BEILSTEIN JOURNAL OF NANOTECHNOLOGY

Advanced atomic force microscopy techniques III

Edited by Thilo Glatzel

Imprint

Beilstein Journal of Nanotechnology
www.bjnano.org
ISSN 2190-4286
Email: journals-support@beilstein-institut.de

The *Beilstein Journal of Nanotechnology* is published by the Beilstein-Institut zur Förderung der Chemischen Wissenschaften.

Beilstein-Institut zur Förderung der
Chemischen Wissenschaften
Trakehner Straße 7–9
60487 Frankfurt am Main
Germany
www.beilstein-institut.de

BEILSTEIN JOURNAL OF NANOTECHNOLOGY

Advanced atomic force microscopy techniques III

Thilo Glatzel[*1] and Thomas Schimmel[2]

Editorial

Address:
[1]Department of Physics, University of Basel, Klingelbergstrasse 82, 4056 Basel, Switzerland and [2]Institute of Nanotechnology (INT), Karlsruhe Institute of Technology (KIT), 76021 Karlsruhe, Germany

Email:
Thilo Glatzel[*] - thilo.glatzel@unibas.ch

* Corresponding author

Keywords:
atomic force microscopy

Beilstein J. Nanotechnol. **2016,** *7,* 1052–1054.
doi:10.3762/bjnano.7.98

Received: 02 June 2016
Accepted: 21 June 2016
Published: 21 July 2016

This article is part of the Thematic Series "Advanced atomic force microscopy techniques III".

Editor-in-Chief: T. Schimmel

Atomic force microscopy (AFM) celebrates its 30th anniversary this year. It was presented by Binnig, Quate and Gerber in 1986 as an extension of the scanning tunneling microscope (STM) with the possibility to measure forces as small as 10^{-18} N [1]. Since then many different variations of the force detection method and various applications have appeared [2,3] and still the scientific community is inventing advanced and improved detection mechanisms and fields of operation. The limits of resolution are not reached yet, however, some research groups start characterizing even ”bond-like” features in high-resolution measurements in between atoms of single molecules or molecular assemblies at positions where chemical bonds are expected [4-6]. However, the origin of this contrast is under intense discussion [7,8]. The extension of the technique towards other physical properties in surface science is pushed continuously. Combined AFM and STM measurements reveal related force and electronic properties [9], energy dissipation in manipulation processes can be examined via the excitation voltage needed to keep a constant amplitude of the probe oscillation [10,11], pulling forces of atomic or molecular wires can be determined and compared with theoretical predictions [12,13], and local charges within single molecules can be measured [14,15], however, the quantification is still under intense discussion. Chemical reactions are triggered and imaged by the AFM tip [16,17] and of course the technique is not limited to ultrahigh-vacuum (UHV) and low-temperature conditions. Therefore, the traditional field in surface science based on diffraction and scattering of charged particles, mostly electrons, which are used as probes in a variety of experimental methods is extended by a powerful local and real space imaging and characterization technique.

This third Thematic Series of „advanced atomic force microscopy techniques“ assembles 22 exciting articles around the improvement and application of this technique which appeared in the *Beilstein Journal of Nanotechnology* within the past 1.5 years. The articles can roughly be grouped in two major categories: local measurements of mechanical properties and high resolution force measurements and spectroscopy.

The characterization of mechanical properties by AFM manifests themselve primarily in the local detection of adhesion, friction and elasticity. Georg Fantner and his co-workers developed an advanced microscope capable of obtaining nanoscale topography as well as mechanical properties by multifrequency AFM at high speed. They combined recent progress in increased imaging speed and photothermal actuation in a unique and versatile AFM head using ultrasmall cantilevers [18]. Single-cell force spectroscopy is used by a biophysics group around Jonne Helenius to quantify the contribution of cell adhesion to specific substrates at both the cell and single molecule level [19]. Furthermore, physico-mechanical properties of intestinal cells were elucidated by force curve measurements by Eva Roblegg and co-workers [20]. The local elastic stiffness and damping of individual phases in a titanium alloys was measured by using atomic force acoustic microscopy (AFAM) and mapping of contact-resonance spectra [21]. Another alloy, namely a Pt containing metallic glass, was characterized by AFM indentation in UHV to quantitatively determine the hardness and deformation mechanisms by Arnaud Caron and Roland Bennewitz [22]. Santiago Solares and Enrique A. López-Guerra presented different approaches to model such viscoelastic properties within AFM simulations [23]. Sliding contact properties like several transitions in the friction coefficient with increasing load have been found on Au(111) in sulfuric acid electrolyte containing Cu ions by Helmut Baltruschat an co-workers [24] and the stiffness of micron-sized sphere-plate contacts was studied by Diethelm Johannsmann et al. by employing high frequency tangential excitation [25].

On the other hand, force spectroscopy and advanced imaging and analysis techniques form a major part of this Thematic Series. For all AFM experiments the tip condition is one of the most critical parameters, Fei Long et al. presented a method for single-molecule probe modification by using a Cu-catalyzed alkyne–azide cycloaddition reaction [26]. To quantify the performed measurements in a reproducible way is still a challenging topic in all AFM measurements. In amplitude modulation AFM higher harmonic signals can be used, Kfir Kuchuk and Uri Sivan presented a mathematical model to derive an accurate and explicit formulae for both conservative and dissipative forces in terms of an arbitrary single harmonic [27], while Luca Costa and Mario S. Rodrigues derived formulas for the tip–sample interactions and investigated the effect of spurious resonances on the measured interaction in liquid media [28]. A software package, dForce, was also presented that allows for a better understanding of amplitude modulation and bimodal AFM experiments in air or liquid [29]. A method for the calibration of the torsional force by using human fibronectin and its monoclonal antibody was presented by Andrzej J. Kulik and co-workers [30]. High-resolution measurements of the adhesion effect of a water film on CaF_2 [31], electric and transport phenomena determined by liquid KPFM in ionically-active and -inactive liquids [32], the spray deposition of single molecules to insulating and ionic surfaces [33], and combined STM and AFM measurements on single-layer graphene on SiC(0001) [34] have been investigated, discussed, and presented. Another combined STM-AFM study determines very accurately the probe-nanocrystal interaction potential [35]. Finally, enhanced information can also be achieved by more accuratly adjust the used parameters and intensivly analyse the results [36-38].

As detailed above this Thematic Series “Advanced atomic force microscopy techniques III” sums up fundamental and applied progresses in surfaces science with a clear focus on advanced atomic force microscopy. It continues the Thematic Series “Advanced atomic force microscopy techniques I and II” [39,40]. The articles demonstrate again, that despite the already 30th anniversary of AFM, current developments in this research field are impressive and by far not finished and we hope to stimulate also further research groups to take part and apply these successful techniques to many other exciting surfaces, systems and materials.

Finally, we want to thank all authors for contributing their excellent work to this series and especially the referees for their continuous support by providing sound and objective reports. Here, we also want to acknowledge the more and more important Open Access policy of the *Beilstein Journal of Nanotechnology* providing the possibility to continue this exciting and stimulating Thematic Series freely accessible worldwide. Moreover, we would like to thank the editing team of the Beilstein-Institut for the excellent and professional framework and support allowing for the collection, review, publishing, and distribution of research results in an easy and excellent way.

Thilo Glatzel and Thomas Schimmel

Basel and Karlsruhe, June 2016

References

1. Binnig, G.; Quate, C. F.; Gerber, C. *Phys. Rev. Lett.* **1986,** *56,* 930. doi:10.1103/PhysRevLett.56.930
2. Morita, S.; Giessibl, F. J.; Meyer, E.; Wiesendanger, R., Eds. *Noncontact Atomic Force Microscopy;* Springer International Publishing, 2015; Vol. 3.
3. Sadewasser, S.; Glatzel, T., Eds. *Kelvin Probe Force Microscopy Measuring and Compensating Electrostatic Forces;* Springer Series in Surface Sciences, Vol. 48; Springer-Verlag: Berlin, Heidelberg, 2011.
4. Kawai, S.; Sadeghi, A.; Xu, F.; Peng, L.; Orita, A.; Otera, J.; Goedecker, S.; Meyer, E. *ACS Nano* **2015,** *9,* 2574–2583. doi:10.1021/nn505876n
5. Zhang, J.; Chen, P.; Yuan, B.; Ji, W.; Cheng, Z.; Qiu, X. *Science* **2013,** *342,* 611–614. doi:10.1126/science.1242603
6. Gross, L.; Mohn, F.; Moll, N.; Schuler, B.; Criado, A.; Guitián, E.; Peña, D.; Gourdon, A.; Meyer, G. *Science* **2012,** *337,* 1326–1329. doi:10.1126/science.1225621
7. Neu, M.; Moll, N.; Gross, L.; Meyer, G.; Giessibl, F. J.; Repp, J. *Phys. Rev. B* **2014,** *89,* 205407. doi:10.1103/PhysRevB.89.205407

8. Hapala, P.; Kichin, G.; Wagner, C.; Tautz, F. S.; Temirov, R.; Jelinek, P. *Phys. Rev. B* **2014,** *90,* 085421. doi:10.1103/PhysRevB.90.085421
9. Pawlak, R.; Ouyang, W.; Filippov, A. E.; Kalikhman-Razvozov, L.; Kawai, S.; Glatzel, T.; Gnecco, E.; Baratoff, A.; Zheng, Q.; Hod, O.; Urbakh, M.; Meyer, E. *ACS Nano* **2016,** *10,* 713–722. doi:10.1021/acsnano.5b05761
10. Hauptmann, N.; Berndt, R. *Phys. Status Solidi B* **2013,** *250,* 2403–2407. doi:10.1002/pssb.201349210
11. Kawai, S.; Glatzel, T.; Such, B.; Koch, S.; Baratoff, A.; Meyer, E. *Phys. Rev. B* **2012,** *86,* 245419. doi:10.1103/PhysRevB.86.245419
12. Kawai, S.; Benassi, A.; Gnecco, E.; Söde, H.; Pawlak, R.; Feng, X.; Müllen, K.; Passerone, D.; Pignedoli, C. A.; Ruffieux, P.; Fasel, R.; Meyer, E. *Science* **2016,** *351,* 957–961. doi:10.1126/science.aad3569
13. Kawai, S.; Koch, M.; Gnecco, E.; Sadeghi, A.; Pawlak, R.; Glatzel, T.; Schwarz, J.; Goedecker, S.; Hecht, S.; Baratoff, A.; Grill, L.; Meyer, E. *Proc. Natl. Acad. Sci. U. S. A.* **2014,** *111,* 3968–3972. doi:10.1073/pnas.1319938111
14. Gross, L.; Mohn, F.; Liljeroth, P.; Repp, J.; Giessibl, F. J.; Meyer, G. *Science* **2009,** *324,* 1428–1431. doi:10.1126/science.1172273
15. Kawai, S.; Sadeghi, A.; Feng, X.; Lifen, P.; Pawlak, R.; Glatzel, T.; Willand, A.; Orita, A.; Otera, J.; Goedecker, S.; Meyer, E. *ACS Nano* **2013,** *7,* 9098–9105. doi:10.1021/nn403672m
16. Riss, A.; Wickenburg, S.; Gorman, P.; Tan, L. Z.; Tsai, H.-Z.; de Oteyza, D. G.; Chen, Y.-C.; Bradley, A. J.; Ugeda, M. M.; Etkin, G.; Louie, S. G.; Fischer, F. R.; Crommie, M. F. *Nano Lett.* **2014,** *14,* 2251–2255. doi:10.1021/nl403791q
17. Albrecht, F.; Pavliček, N.; Herranz-Lancho, C.; Ruben, M.; Repp, J. *J. Am. Chem. Soc.* **2015,** *137,* 7424–7428. doi:10.1021/jacs.5b03114
18. Nievergelt, A. P.; Adams, J. D.; Odermatt, P. D.; Fantner, G. E. *Beilstein J. Nanotechnol.* **2014,** *5,* 2459–2467. doi:10.3762/bjnano.5.255
19. Yu, M.; Strohmeyer, N.; Wang, J.; Müller, D. J.; Helenius, J. *Beilstein J. Nanotechnol.* **2015,** *6,* 157–166. doi:10.3762/bjnano.6.15
20. Schimpel, C.; Werzer, O.; Fröhlich, E.; Leitinger, G.; Absenger-Novak, M.; Teubl, B.; Zimmer, A.; Roblegg, E. *Beilstein J. Nanotechnol.* **2015,** *6,* 1457–1466. doi:10.3762/bjnano.6.151
21. Phani, M. K.; Kumar, A.; Jayakumar, T.; Arnold, W.; Samwer, K. *Beilstein J. Nanotechnol.* **2015,** *6,* 767–776. doi:10.3762/bjnano.6.79
22. Caron, A.; Bennewitz, R. *Beilstein J. Nanotechnol.* **2015,** *6,* 1721–1732. doi:10.3762/bjnano.6.176
23. López-Guerra, E. A.; Solares, S. D. *Beilstein J. Nanotechnol.* **2014,** *5,* 2149–2163. doi:10.3762/bjnano.5.224
24. Podgaynyy, N.; Wezisla, S.; Molls, C.; Iqbal, S.; Baltruschat, H. *Beilstein J. Nanotechnol.* **2015,** *6,* 820–830. doi:10.3762/bjnano.6.85
25. Vlachová, J.; König, R.; Johannsmann, D. *Beilstein J. Nanotechnol.* **2015,** *6,* 845–856. doi:10.3762/bjnano.6.87
26. Long, F.; Cao, B.; Khanal, A.; Fang, S.; Shahbazian-Yassar, R. *Beilstein J. Nanotechnol.* **2014,** *5,* 2122–2128. doi:10.3762/bjnano.5.221
27. Kuchuk, K.; Sivan, U. *Beilstein J. Nanotechnol.* **2015,** *6,* 149–156. doi:10.3762/bjnano.6.14
28. Costa, L.; Rodrigues, M. S. *Beilstein J. Nanotechnol.* **2015,** *6,* 420–427. doi:10.3762/bjnano.6.42
29. Guzman, H. V.; Garcia, P. D.; Garcia, R. *Beilstein J. Nanotechnol.* **2015,** *6,* 369–379. doi:10.3762/bjnano.6.36
30. Kulik, A. J.; Lekka, M.; Lee, K.; Pyka-Fościak, G.; Nowak, W. *Beilstein J. Nanotechnol.* **2015,** *6,* 1164–1175. doi:10.3762/bjnano.6.118
31. Caló, A.; Robles, O. V.; Santos, S.; Verdaguer, A. *Beilstein J. Nanotechnol.* **2015,** *6,* 809–819. doi:10.3762/bjnano.6.84
32. Collins, L.; Jesse, S.; Kilpatrick, J. I.; Tselev, A.; Okatan, M. B.; Kalinin, S. V.; Rodriguez, B. J. *Beilstein J. Nanotechnol.* **2015,** *6,* 201–214. doi:10.3762/bjnano.6.19
33. Hinaut, A.; Pawlak, R.; Meyer, E.; Glatzel, T. *Beilstein J. Nanotechnol.* **2015,** *6,* 1927–1934. doi:10.3762/bjnano.6.195
34. Telychko, M.; Berger, J.; Majzik, Z.; Jelínek, P.; Švec, M. *Beilstein J. Nanotechnol.* **2015,** *6,* 901–906. doi:10.3762/bjnano.6.93
35. Sweetman, A.; Goubet, N.; Lekkas, I.; Pileni, M. P.; Moriarty, P. *Beilstein J. Nanotechnol.* **2015,** *6,* 1229–1236. doi:10.3762/bjnano.6.126
36. Melcher, J.; Stirling, J.; Shaw, G. A. *Beilstein J. Nanotechnol.* **2015,** *6,* 1733–1742. doi:10.3762/bjnano.6.177
37. Wang, Y.; Wang, H.; Bi, S.; Guo, B. *Beilstein J. Nanotechnol.* **2015,** *6,* 952–963. doi:10.3762/bjnano.6.98
38. Damircheli, M.; Payam, A. F.; Garcia, R. *Beilstein J. Nanotechnol.* **2015,** *6,* 1072–1081. doi:10.3762/bjnano.6.108
39. Glatzel, T.; Hölscher, H.; Schimmel, T.; Baykara, M. Z.; Schwarz, U. D.; Garcia, R. *Beilstein J. Nanotechnol.* **2012,** *3,* 893–894. doi:10.3762/bjnano.3.99
40. Glatzel, T.; Garcia, R.; Schimmel, T. *Beilstein J. Nanotechnol.* **2014,** *5,* 2326–2327. doi:10.3762/bjnano.5.241

License and Terms

The definitive version of this article is the electronic one which can be found at:
doi:10.3762/bjnano.7.98

BEILSTEIN JOURNAL OF NANOTECHNOLOGY

Modification of a single-molecule AFM probe with highly defined surface functionality

Fei Long[‡1], Bin Cao[‡2], Ashok Khanal[2], Shiyue Fang[*2] and Reza Shahbazian-Yassar[*1]

Full Research Paper

Open Access

Address:
[1]Department of Mechanical Engineering-Engineering Mechanics, Michigan Technological University, 1400 Townsend Drive, Houghton, Michigan, USA and [2]Department of Chemistry, Michigan Technological University, 1400 Townsend Drive, Houghton, Michigan, USA

Email:
Shiyue Fang[*] - Shifang@mtu.edu; Reza Shahbazian-Yassar[*] - reza@mtu.edu

* Corresponding author ‡ Equal contributors

Keywords:
atomic force microscopy; click reaction; force spectroscopy; single molecule modification

Beilstein J. Nanotechnol. **2014,** *5,* 2122–2128.
doi:10.3762/bjnano.5.221

Received: 16 July 2014
Accepted: 31 October 2014
Published: 14 November 2014

This article is part of the Thematic Series "Advanced atomic force microscopy techniques III".

Guest Editor: T. Glatzel

Abstract

Single-molecule force spectroscopy with an atomic force microscope has been widely used to study inter- and intramolecular interactions. To obtain data consistent with single molecular events, a well-defined method is critical to limit the number of molecules at the apex of an AFM probe to one or to a few. In this paper, we demonstrate an easy method for single-molecule probe modification by using the Cu-catalyzed alkyne–azide cycloaddition reaction. Excess terminal alkynes were covalently attached to the probe, and a bi-functional molecule containing an azide at one end and a carboxylic acid at the other was dissolved in the reaction solution. By simply contacting the probe and the Cu substrate, controlled carboxylation on the probe apex could be achieved, since the 'click' reaction requires the co-exist of alkyne, azide and Cu(I). The finite contact area would result in a highly defined surface functionality of the probe down to single molecule level with high reproducibility.

Introduction

Single-molecule force spectroscopy (SMFS) has become one of the most powerful tools for studying inter- and intramolecular interactions [1]. The information revealed is highly significant for the understanding of the fundamental relationship between molecular structures and their functions [2-5]. Among the SMFS toolbox, atomic force microscopy (AFM) [6] is the most popular one due to high force sensitivity from pico- to nanonewtons, and ease of use under various environment including ambient, aqueous and vacuum [7]. By attaching a single molecule between an AFM probe and a substrate, intramolecular interactions could be studied through stretching the molecule from the entropic form to the extended form. Also, intermolecular interactions could be investigated by attaching one molecule to a probe and the other to a substrate. Examples include the unfolding of proteins [8,9], dissociation of receptors from ligands [10,11], and un-zipping double-stranded RNA and DNA molecules [12]. Despite all the success in these studies, one significant challenge remains in AFM-based SMFS, that is to attach only one or a few molecules to the AFM probes. In previous studies, the most common method depended on non-specific adhesions [13,14], which resulted in uncertainties concerning quantity and location of molecules being studied [1]. To improve the reproducibility of experimental results, covalent attachment methods are preferred. Wong and co-authors attached a single-wall carbon nanotube (SW-CNT) to the tip of an AFM probe [15]. The carboxylic acid group on the open end of the CNT could be further modified with amino and phenyl groups. In this way, the modification of a single-molecule probe with acidic, basic and neutral functionalities could be achieved. Gu and co-authors reported an electrochemical oxidation method for the modification of a single-molecule probe [16]. They applied a bias voltage between an oligo(ethylene glycol) (OEG)-modified AFM probe and an Au film substrate. Carboxylic acid groups were selectively generated at the tip apex through electrochemical oxidation of OEG. The carboxylic acid group was then used to attach the molecules to be studied. All these methods have improved the reproducibility of results from AFM-based single-molecule studies. However, it is not trivial either to attach CNT to an AFM probe, or to adjust bias amplitude/duration in OEG oxidation.

Copper-catalyzed alkyne–azide cycloaddition, which is also called a ‘click’ reaction, has been widely used for surface functionalization and linking of biomolecules [17]. The reaction is compatible with a wide variety of polar functional groups that commonly exist in biomolecules and is highly efficient in various solvents. Chen and co-authors reported the pioneer work of using this ‘click’ reaction to modify AFM probes, taking advantage of the mild reaction condition and simple operation [18]. However, this method is based on a bulk solution and loses the ‘spatial resolution’ in terms of functionality, since the reaction happens anywhere on the probe surface. In this paper, we report a new method for the modification of a single-molecule probe with highly defined surface functionality by using copper-catalyzed alkyne–azide cycloaddition (Figure 1). A probe with a monolayer of terminal alkynes was easily prepared by immersing an amino-functionalized silicon probe in a solution containing 4-pentynoic acid and acetic acid (molar ratio 1:7) through amide bond formation followed by washing and drying (for experimental details see Supporting Information File 1). The probe was then mounted onto an AFM, and brought into contact with a copper-film-coated substrate for 5 to 10 s in a solution containing bi-functional molecules with a carboxylic acid group at one end and an azide group at the other end. Cu(I) was believed to be sparsely scattered over the surface of the copper film. Because the Cu(I)-catalyzed alkyne–azide reaction could only occur at the location where Cu(I), alkyne and azide co-exist, carboxylic acid groups would be attached to the probe during contact. According to DMT model [19], the ~200 pN contact force would result in a contact area within 1 nm in radius. Therefore, the chances for multiple reactions were predicted to be low and single molecular probe modification could be expected. For demonstrating the reproducibility and flexibility, three additional silicon probes and one Au-coated probe were modified under the same conditions.

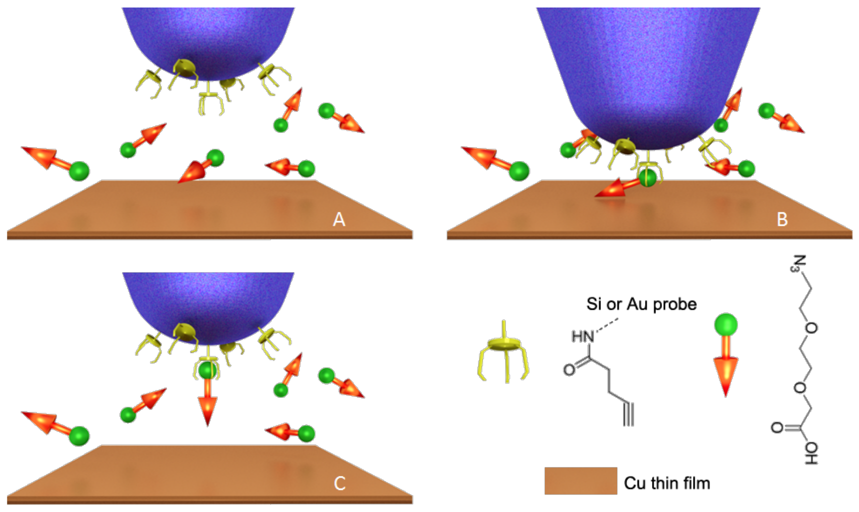

Figure 1: Schematic illustration of the functionalization of a single-molecule probe by using the ‘click’ reaction. (A) An alkyne-modified AFM probe is immersed in a solution of azide/carboxylic acid bi-functional molecules. (B) The probe is brought into contact with a substrate coated with a Cu film for one to two seconds. The Cu(I)-catalyzed alkyne–azide ‘click’ reaction occurs at the contacting area of the probe and substrate. (C) The probe is withdrawn, and single carboxylic acid group is attached to the apex of the probe.

Results and Discussion

To evaluate the results of the modification, a glass slide with a monolayer of amino-terminated poly(ethylene glycol) (PEG) was prepared. PEG was used to reduce the background adhesion force, and as a spacer to better discriminate between specific and non-specific interactions in the force curves [20]. The functionalized probes after ‘click’ modification were ramped over the surface in isopropanol, and more than 1000 force curves were recorded for each of the five probes. Among them, 17–26% showed adhesive interactions appearing at a tip–surface separation greater than zero. Typical force curves obtained were shown in Figure 2A and Figure 2B for the Si probe and the Au-coated probe, respectively. The other force curves showed either no obvious adhesion or only forces at zero separation (due to non-specific interaction). The forces that appear at non-zero tip–surface separations are believed to result from the rupture of a hydrogen bond between the carboxylic acid group on the probe and the amino group on the substrate. Two facts supported this hypothesis. (1) The forces appeared at a tip–surface separation of around 25 nm, which is the contour length of the PEG we used. (2) The force curves fitted well with the worm-like chain (WLC) model [21] with a persistence length of 0.35–0.40 nm, shown as green solid lines in Figure 2. This persistence length agreed well with the extension behavior of PEG molecule [22]. Therefore, it was reasonable to believe that carboxylic groups from the azide molecules had been ‘clicked’ onto the AFM probes through our method.

Three control experiments were carried out to confirm that the ‘click’ reaction indeed occurred at the tip apex of the probes. In these experiments, one of the three components in the ‘click’ reaction (1) the alkyne on the probe, (2) the azide/carboxylic acid bi-functional molecule in the solution, and (3) the Cu film on the substrate, was eliminated. For each control probe, less than 2% of 1000 force curves showed the PEG extension behavior against the amino-terminated PEG monolayer. The significantly lowered probability compared to 17–26% for the probes modified with our method, confirmed that our method can successfully attach carboxylic acid groups to the probe through the ‘click’ reaction.

To further quantify the carboxylic acid groups on a probe, the widely used Poisson statistical method was employed [23,24]. This method assumes the adhesion force is composed of specific interactions, such as hydrogen bonds, and non-specific interactions, such as van der Waals forces,

$$F_{\mathrm{av}} = n_{\mathrm{av}} F_{\mathrm{i}} + F_0 \tag{1}$$

where F_{av} is the total average adhesion force, n_{av} is the average number of specific interactions, which is hydrogen bonding in our case, F_{i} is the magnitude of the specific interaction, and F_0 is non-specific interaction. This method also assumes that the distribution of the average number of interactions at the pull-off point follows a Poisson distribution,

$$P(n) = \frac{(n_{\mathrm{av}})^n}{n!} e^{-n_{\mathrm{av}}} \tag{2}$$

$$\delta_n^2 = n_{\mathrm{av}} \tag{3}$$

where $P(n)$ is the possibility of the specific interaction, and δ_n^2 is the variance of the number of interacting bonds. The expectation of a Poisson-distributed random variable is equal to its variance,

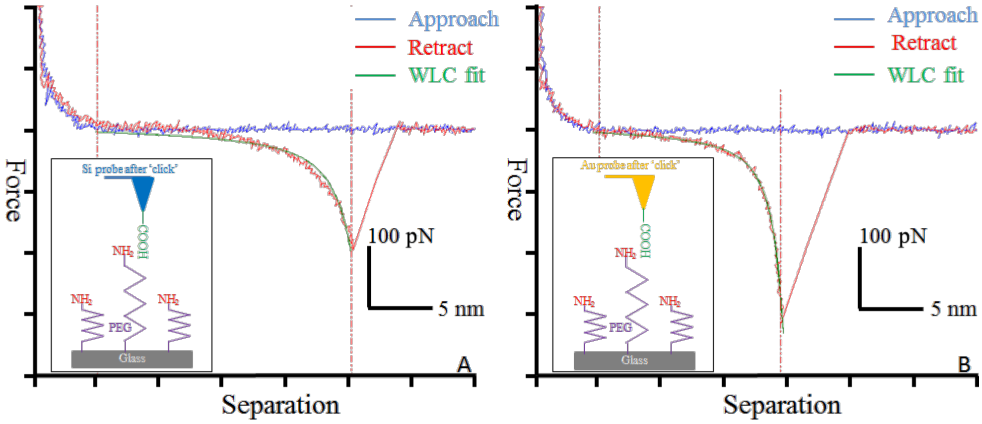

Figure 2: Typical force curves of modified single-molecule (A) Si probes and (B) Au-coated probes interacting with an amino-terminated PEG monolayer on a glass slide. The approach (blue) and retract (red) curves along with worm-like chain model fitting curves (green) are shown, demonstrating the stretching behavior of a single PEG molecule between the probes and the substrate.

$$\delta_F^2 = n_{\mathrm{av}} F_{\mathrm{i}}^2 = F_{\mathrm{av}} F_{\mathrm{i}} - F_{\mathrm{i}} F_0 \qquad (4)$$

Therefore, by plotting δ_F^2 against F_{av}, a linear relationship is expected with the slope F_{i} and intercept $-F_{\mathrm{i}}F_0$.

The linear fitting results are shown in Figure 3 for one silicon probe and one Au-coated probe. The deduced F_{i}, F_0 and n_{av} are 99 ± 57 pN, 84 ± 45 pN and 1.1–1.5, respectively, for the silicon probe, and 95 ± 64 pN, 111 ± 33 pN, and 3.5–4.4, respectively, for the Au-coated probe. Both probes had similar values of F_{i}, showing the same nature of the specific hydrogen bond interaction between the carboxylic acid groups on the probe and amino groups on the substrate. These values agreed with single hydrogen bond rupture forces of 50–250 pN reported in the literature [23,25]. The F_0 value of the Au-coated probe was larger than that of the Si probe. This can be attributed to the larger radius of Au-coated probe due to coating layer of about 35 nm, and the resulting larger contact area between probe and surface during force spectroscopy. The value of n_{av} of the specific interaction was 1.1–1.5 for the Si probe, demonstrating a successful single-molecule modification. Similar values of n_{av} were obtained for the other three Si probes with a maximum value of 2.1. Meanwhile, a larger value of n_{av} = 3.5–4.4 was obtained for the Au-coated probe, which again can be attributed to the larger tip radius resulting in more ‘click’ reactions during modification.

The distribution of the bond-rupture force also supported the above Poisson statistical analysis. A total of 212 measured forces from the Si probes and 145 from the Au-coated probes were plotted in Figure 4. The most probable force for the Si probes was centered at 187 pN, which agreed well with the sum of F_{i} and F_0 in previous Poisson analysis (183 pN for Si

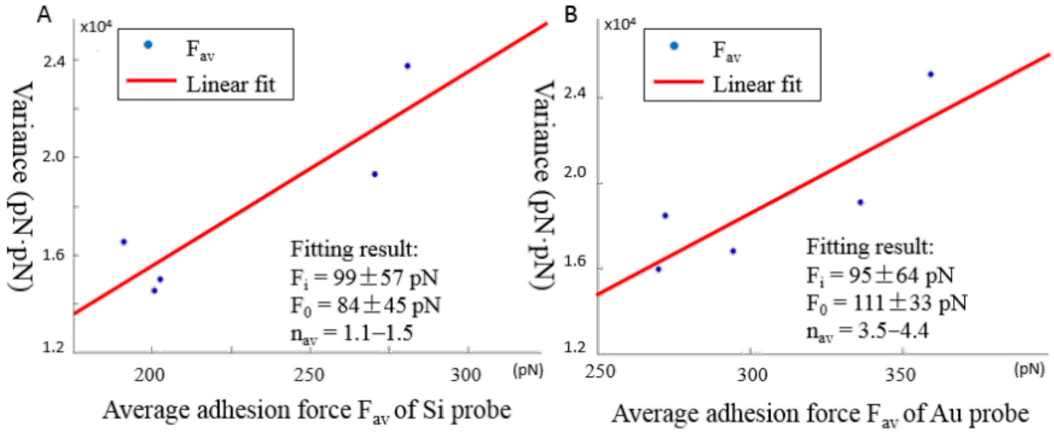

Figure 3: Linear fit of average adhesion force F_{av} against its variance by using the Poisson statistical method for (A) the Si probes and (B) the Au-coated probes, respectively. The fitting result is also shown as inset, in which F_{i} is the specific interaction, F_0 is the non-specific interaction, and n_{av} is the average number of interacting molecules.

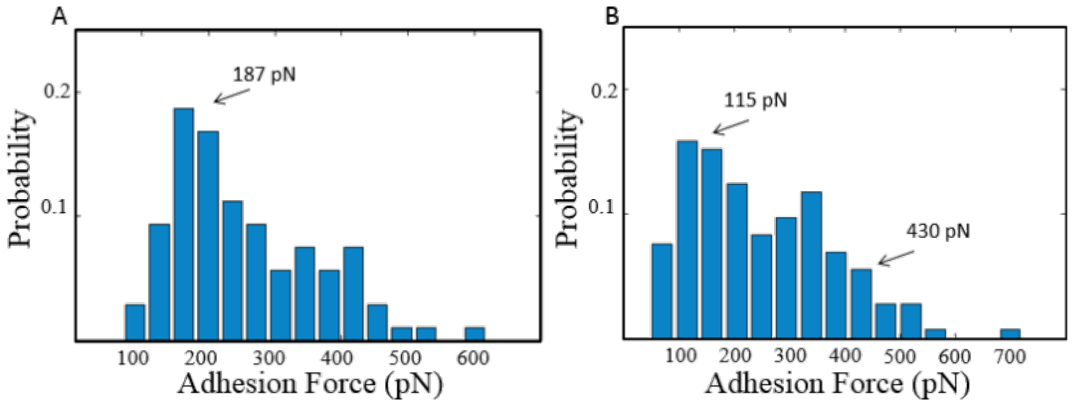

Figure 4: Distribution of bond rupture forces for (A) Si probes (B) Au-coated probes. The most probable force for Si probes was 187 pN, and that for Au-coated probes was 115 pN. In (B), a significant drop of probability was observed for forces larger than 430 pN.

probes). This also indicated that F_i and F_0 had similar probabilities when the probe interacted with the surface. Therefore, it was difficult to distinguish them from the histogram, as shown in Figure 4A. On the other hand, the Au-coated probes showed a much wider distribution with the most probable force centered at 115 pN, as shown in Figure 4B. The value agreed with the F_0 of an Au-coated probe (111 pN). Considering the similar probability of F_i and F_0, the forces obtained from Au-coated probes should be evenly distributed in the range from F_0 to $F_0 + n_{av}F_i$. A significant drop of probability was observed for forces larger than 430 pN. Therefore, it was reasonable to take this threshold value as the upper limit of force range $F_0 + n_{av}F_i$. The resulting value of n_{av} was 3.3, which also agreed well with the theoretical analysis of n_{av} = 3.5–4.4.

The separation between probe and surface when the bond rupture occurred was also summarized and is shown in Figure 5. The PEG molecules on the glass surface had different lateral distances to the tip, and the terminal amino groups had an equal probability to interact with the carboxylic groups on the probe. Therefore, a uniform distribution was expected in the histogram of the probe–sample separation at which specific bond rupture occurred. For both (A) the Si probe and (B) the Au-coated probe, the separation distributions were relatively uniform. The higher probability at 18.0 nm for the Si probe and 9.6 nm for the Au-coated probe were probably due to higher density of carboxylic groups on the surface.

Conclusion

In summary, we have developed a new modification method for single-molecule probes that takes advantage of a highly efficient ‘click’ reaction. As a demonstration, carboxylic acid-terminated azide molecules were successfully ‘clicked’ onto an alkyne-modified probe when the probe was in contact with the Cu substrate, which acts as catalyst. This ‘click’ reaction could only occur within the small contact area, resulting in a highly defined probe functionality. Force spectroscopy analysis along with control experiments proved that a single carboxylic group was successfully modified onto the AFM probe. We believe this method would benefit AFM-based SMFS applications and improve the reproducibility of these studies.

Experimental

Materials

The Fmoc-NH-PEG-NHS (M_p = 3219 Da) was purchased from Rapp Polymere GmbH. The silicon AFM probes (MSNL-C) were purchased from Bruker Nano, Inc. The nominal spring constant is 10 pN/nm and tip curvature is 2 nm. The Au-coated AFM probes (CSG10/Au) were gifts from NT-MDT with 2.5 nm adhesive Ti layer and 35 nm Au layer, the nominal spring constant is 110 pN/nm and tip curvature is 35 nm. The aminopropylsilane-coated glass slides (C18-5131-M20) were purchased from Thermo Scientific. All other chemicals including isopropanol are of reagent grade from Sigma-Aldrich. AFM experiments were carried out on a Bruker Dimension ICON AFM system.

Preparation of AFM probes

Amino-functionalization of Si probes: Si probes were functionalized with amino groups according to a previously reported procedure [26,27]. Briefly, the probes were soaked in chloroform for 10 min, and then, the solvent was removed and the process was repeated. After drying under argon flow, the probes were soaked in a freshly prepared piranha solution (30 vol % H_2O_2/H_2SO_4, 1:3, v/v) for 30 min. After rinsing with water three times, the probes were washed with methanol (two times) and chloroform (two times) and dried in a stream of argon. For amination, the probes were suspended above (3 cm) a solution of 8% (v/v) (3-aminopropyl)triethoxysilane (APTES) in toluene in a desiccator filled with dry nitrogen for 3 h (step a

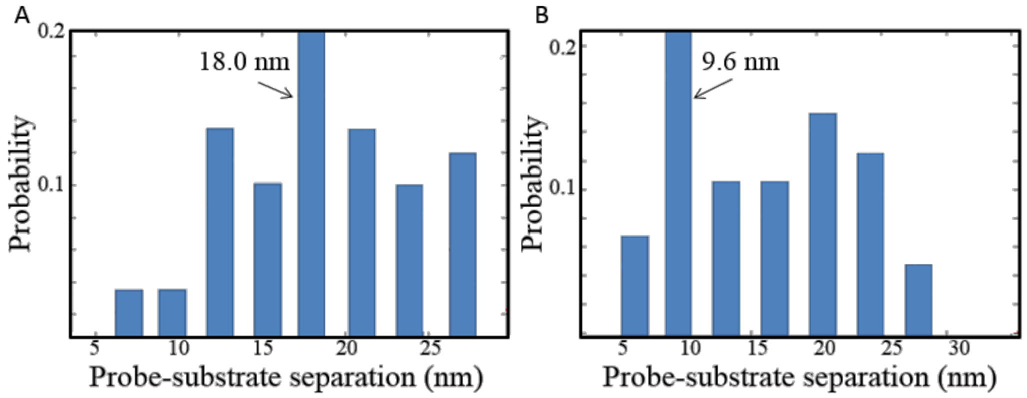

Figure 5: Distribution of probe-substrate separation where maximum adhesion force (bond rupture event) was recorded. (A) The distribution for the Si probe and (B) the distribution for the Au-coated probes.

in Figure S1, Supporting Information File 1). Finally, the probes were treated on a plate at 100 °C in air for 10 min.

Amino-functionalization of Au-coated probes: The amino-functionalized Au-coated probes were prepared by incubating in a 2 mM solution of 2-aminoethanethiol in EtOH overnight (step a in Figure S2, Supporting Information File 1) [28,29]. The probes were washed with water, ethanol and chloroform, and dried in a stream of argon.

Alkynylation of amino-functionalized probes: The amino-functionalized silicon and Au-coated probes were incubated in a solution (4 mL) containing 4-pentynoic acid (1.25 mM), acetic acid (8.75 mM), *O*-benzotriazole-*N*,*N*,*N*’,*N*’-tetramethyluronium hexafluorophosphate (HBTU) (10 mM) and *N*,*N*-diisopropylethylamine (DIPEA) (10mM), in dimethylformamide (DMF) for 3 h (step b in Figure S1 and Figure S2, Supporting Information File 1). The probes were washed with DMF, $CHCl_3$ and CH_3OH, and dried in a stream of argon.

Preparation of amino-PEG-substrates

The aminopropylsilane-coated glass slides were washed with chloroform three times and dried in a stream of argon. They were then incubated in a solution of Fmoc-NH-PEG-NHS (5 mg) and triethylamine (TEA) (5 µL) in $CHCl_3$ (1 mL) at rt under argon overnight (step a in Figure S3, Supporting Information File 1). After washing with chloroform and MeOH, and drying with a stream of argon, the Fmoc protecting groups were removed with 20% piperidine (v/v in DMF) for 30 min (step b in Figure S3, Supporting Information File 1). The slides were washed with DMF, $CHCl_3$, MeOH, and dried in a stream of argon. After each modification process, the probe and substrate surfaces were characterized with FTIR and contact angle measurements. As shown in Figure S4 and Table S1 in Supporting Information File 1.

AFM force spectroscopy experiment

Single-molecule probe modification: The alkyne-modified probe was engaged to the Cu substrate in contact mode with 1 nN force in 0.05 M azide solution. The average surface roughness R_a of the Cu surface was 1.33 ± 0.24 nm determined through AFM topography (shown in Figure S8, Supporting Information File 1). The probe was kept in contact with the substrate for 5 to 10 s giving enough time for the Cu-catalyzed ‘click’ reaction to take place (step c in Figure S1 and Figure S2, Supporting Information File 1). Finally, the probe was retracted and rinsed thoroughly with DI water. The three probes for the control experiments were prepared under the same conditions except that one element, either Cu, alkyne or azide, was lacking. The typical force curves obtained with the control probes are shown in Figure S6 (Supporting Information File 1).

Characterization of single-molecule modified probes: In order to verify the result of the modification, the probe was ramped over a glass slide with a monolayer of amino-terminated poly(ethylene glycol) (PEG) in isopropanol. The amino groups should form hydrogen bonds with the carboxylic acid group on the probe in the contacting period during ramping. When the probe is retracted, the force to break the hydrogen bonds should be detectable. The force spectroscopy experiments were carried out in contact mode at room temperature in isopropanol. The spring constant of the AFM probes were calibrated by using the thermal noise method [30]. The measured values ranged from 15 to 40 pN/nm. Each probe was ramped at five different locations on the substrate, and more than 200 force curves were recorded at each location resulting in more than 1000 force curves per probe. For each ramp, the probes were first brought into contact with the substrate at a contact force of ca. 200 pN for 1 s, and then retracted. The approaching and retracting speed was 300 nm/s. Typical force curves are shown in Figure S7 (Supporting Information File 1). The force curves with either no obvious adhesion events or only non-specific adhesion at zero separation were also shown. Note that sometimes the specific and non-specific interactions co-existed, as in Figure S7D (Supporting Information File 1). The control experiments were carried out under the same conditions.

Supporting Information

Supporting Information File 1

Additional experimental data.
[http://www.beilstein-journals.org/bjnano/content/supplementary/2190-4286-5-221-S1.pdf]

Acknowledgements

The authors gratefully acknowledge the financial support from US NSF (DBI-1225720) and Departments of Chemistry and MEEM, and BRC of MTU; and the NSF equipment grants (CHE-9512445). The authors also thank Dr. J. W. Drelich, Mr. J. L. Lutz and D. W. Seppala for the help on this work.

References

1. Neuman, C. N.; Nagy, A. *Nat. Methods* **2008,** *5,* 491–505. doi:10.1038/nmeth.1218
2. Bustamante, C.; Bryant, Z.; Smith, S. B. *Nature* **2003,** *421,* 423–447. doi:10.1038/nature01405
3. Fazal, F. M.; Block, S. M. *Nat. Photonics* **2011,** *5,* 318–321. doi:10.1038/nphoton.2011.100
4. Hinterdorfer, P.; Dufrêne, Y. F. *Nat. Methods* **2006,** *3,* 347–355. doi:10.1038/nmeth871
5. Evans, E. *Annu. Rev. Biophys. Biomol. Struct.* **2001,** *30,* 105–128. doi:10.1146/annurev.biophys.30.1.105

6. Binnig, G.; Quate, C. F.; Gerber, Ch. *Phys. Rev. Lett.* **1986,** *56,* 930–933. doi:10.1103/PhysRevLett.56.930
7. Müller, D. J.; Dufrêne, Y. F. *Nat. Nanotechnol.* **2008,** *3,* 261–269. doi:10.1038/nnano.2008.100
8. Borgia, A.; Williams, P. M.; Clarke, J. *Annu. Rev. Biochem.* **2008,** *77,* 101–125. doi:10.1146/annurev.biochem.77.060706.093102
9. Puchner, E. M.; Gaub, H. E. *Curr. Opin. Struct. Biol.* **2009,** *19,* 605–614. doi:10.1016/j.sbi.2009.09.005
10. Krasnoslobodtsev, A. V.; Shlyakhtenko, L. S.; Lyubchenko, Y. L. *J. Mol. Biol.* **2007,** *365,* 1407–1416. doi:10.1016/j.jmb.2006.10.041
11. Ashcroft, B. A.; Spadola, Q.; Qamar, S.; Zhang, P.; Kada, G.; Bension, R.; Lindsay, S. *Small* **2008,** *4,* 1468–1475. doi:10.1002/smll.200800233
12. Bustamante, C.; Smith, S. B.; Liphardt, J.; Smith, D. *Curr. Opin. Struct. Biol.* **2000,** *10,* 279–285. doi:10.1016/S0959-440X(00)00085-3
13. Zhang, Q.; Marszalek, P. E. *J. Am. Chem. Soc.* **2006,** *128,* 5596–5597. doi:10.1021/ja058828e
14. Liu, N.; Peng, B.; Lin, Y.; Su, Z.; Niu, Z.; Wang, Q.; Zhang, W.; Li, H.; Shen, J. *J. Am. Chem. Soc.* **2010,** *132,* 11036–11038. doi:10.1021/ja1052544
15. Wong, S. S.; Joselevich, E.; Woolley, A. T.; Cheung, C. L.; Lieber, C. M. *Nature* **1998,** *394,* 52–55. doi:10.1038/27873
16. Gu, J.; Xiao, Z.; Yam, C.-M.; Qin, G.; Deluge, M.; Boutet, S.; Cai, C. *Biophys. J.* **2005,** *89,* L31–L33. doi:10.1529/biophysj.105.069104
17. Binder, W. H.; Sachsenhofer, R. *Macromol. Rapid Commun.* **2007,** *28,* 15–54. doi:10.1002/marc.200600625
18. Chen, G.; Ning, X.; Park, B.; Boons, G.-J.; Xu, B. *Langmuir* **2009,** *25,* 2860–2864. doi:10.1021/la803523b
19. Cappella, B.; Dietler, G. *Surf. Sci. Rep.* **1999,** *34,* 1–104. doi:10.1016/S0167-5729(99)00003-5
20. Hinterdorfer, P.; Baumgartner, W.; Gruber, H. J.; Schilcher, K.; Schindler, H. *Proc. Natl. Acad. Sci. U. S. A.* **1996,** *93,* 3477–3481. doi:10.1073/pnas.93.8.3477
21. Bouchiat, C.; Wang, M. D.; Allemand, J.-F.; Strick, T.; Block, S. M.; Croquette, V. *Biophys. J.* **1999,** *76,* 409–413. doi:10.1016/S0006-3495(99)77207-3
22. Lee, H.; Venable, R. M.; Mackerell, A. D., Jr.; Pastor, R. W. *Biophys. J.* **2008,** *95,* 1590–1599. doi:10.1529/biophysj.108.133025
23. van der Vegte, E. W.; Hadziioannou, G. *Langmuir* **1997,** *13,* 4357–4368. doi:10.1021/la970025k
24. Stevens, F.; Lo, Y.-S.; Harris, J. M.; Beebe, T. P., Jr. *Langmuir* **1999,** *15,* 207–213. doi:10.1021/la980683k
25. Noy, A.; Vezenov, D. V.; Lieber, C. M. *Annu. Rev. Mater. Sci.* **1997,** *27,* 381–421. doi:10.1146/annurev.matsci.27.1.381
26. Razvag, Y.; Gutkin, V.; Reches, M. *Langmuir* **2013,** *29,* 10102–10109. doi:10.1021/la4015866
27. Senapati, S.; Manna, S.; Lindsay, S.; Zhang, P. *Langmuir* **2013,** *29,* 14622–14630. doi:10.1021/la4039667
28. Zeng, X.; Xu, G.; Gao, Y.; An, Y. *J. Phys. Chem. B* **2011,** *115,* 450–454. doi:10.1021/jp109259b
29. Riener, C. K.; Stroh, C. M.; Ebner, A.; Klampfl, C.; Gall, A. A.; Romanin, C.; Lyubchenko, Y. L.; Hinterdorfer, P.; Gruber, H. J. *Anal. Chim. Acta* **2003,** *479,* 59–75. doi:10.1016/S0003-2670(02)01373-9
30. Hutter, J. L.; Bechhoefer, J. *Rev. Sci. Instrum.* **1993,** *64,* 1868–1873. doi:10.1063/1.1143970

License and Terms

The definitive version of this article is the electronic one which can be found at:
doi:10.3762/bjnano.5.221

BEILSTEIN JOURNAL OF NANOTECHNOLOGY

Modeling viscoelasticity through spring–dashpot models in intermittent-contact atomic force microscopy

Enrique A. López-Guerra and Santiago D. Solares*

Full Research Paper

Open Access

Address:
Department of Mechanical Engineering, University of Maryland, College Park, Maryland 20742, United States; Current Address: Department of Mechanical and Aerospace Engineering, George Washington University, Washington, DC 20052, United States

Email:
Santiago D. Solares* - ssolares@gwu.edu

* Corresponding author

Keywords:
atomic force microscopy; creep; dissipated energy; multifrequency; stress relaxation; tapping mode; viscoelasticity

Beilstein J. Nanotechnol. **2014,** *5,* 2149–2163.
doi:10.3762/bjnano.5.224

Received: 16 August 2014
Accepted: 31 October 2014
Published: 18 November 2014

This article is part of the Thematic Series "Advanced atomic force microscopy techniques III".

Guest Editor: T. Glatzel

Abstract

We examine different approaches to model viscoelasticity within atomic force microscopy (AFM) simulation. Our study ranges from very simple linear spring–dashpot models to more sophisticated nonlinear systems that are able to reproduce fundamental properties of viscoelastic surfaces, including creep, stress relaxation and the presence of multiple relaxation times. Some of the models examined have been previously used in AFM simulation, but their applicability to different situations has not yet been examined in detail. The behavior of each model is analyzed here in terms of force–distance curves, dissipated energy and any inherent unphysical artifacts. We focus in this paper on single-eigenmode tip–sample impacts, but the models and results can also be useful in the context of multifrequency AFM, in which the tip trajectories are very complex and there is a wider range of sample deformation frequencies (descriptions of tip–sample model behaviors in the context of multifrequency AFM require detailed studies and are beyond the scope of this work).

Introduction

Atomic force microscopy (AFM) has evolved rapidly since its invention in the mid-1980s [1] and has been used since then for measuring topography and probe–sample forces on micro- and nanoscale surfaces in different environments. Tapping mode AFM (amplitude modulation, AM-AFM) is the most common dynamic method and has been the subject of thorough studies [2-6]. In tapping mode AFM damage or wear of the tip and surface are reduced with respect to contact-mode AFM due to lower friction and lateral forces, which makes it more applicable for imaging soft samples, such as polymers and biological surfaces. Tapping mode AFM has the additional advantage that it records a phase contrast simultaneously with the acquisition of topography, which can be very useful in the study of heterogeneous samples [7-10]. Moreover, the observables in tapping mode AFM (phase and amplitude) can provide quantitative information about the dissipative and conservative tip–sample interactions by converting them to energy-based quantities, namely the dissipated power (P_{ts}) and virial (V_{ts}) [9,11].

Although several authors have achieved quantification of energy dissipation processes [12-15], the further utilization of that information to derive material properties is not trivial in tapping mode AFM. The nature of the technique with its intermittent contact, during which the probe interacts with nonlinear tip–sample forces ranging from attractive to repulsive, hinders the derivation of simple relationships between observables and sample properties. Furthermore, the extraction of sample properties becomes especially challenging when studying viscoelastic materials. Despite the obstacles, analytical and numerical simulations have been performed as an attempt to estimate quantities such the sample loss tangent (a common term used in the characterization of viscoelastic samples) [16] although it has been reported that this approach can be inaccurate for intermittent-contact applications [17]. Notably, one of the key factors preventing the extraction of reliable material information has been the absence of physically accurate models for viscoelastic samples. On the other hand, better quantitative agreement has been accomplished through contact-mode based techniques such as contact resonance AFM (CR-AFM) [17], band excitation AFM (BE-AFM) [18,19] and dual-amplitude resonance tracking AFM (DART-AFM) [20]. These techniques operate in a regime of quasi-linear tip–sample forces by using very small cantilever oscillation amplitudes, but as a result only provide linear viscoelasticity information and characterization can be slow for CR-AFM and BE-AFM due to the pixel-based measurement procedures used.

Significant progress has been recently achieved with regards to fast and simultaneous topographical and spectroscopic characterization of viscoelastic materials through the use of multifrequency AFM [21]. This work represents an important milestone in rapid and quantitative multi-property characterization, although it has so far only been realized in the context of a very simple viscoelastic model that is generally not physically accurate (this model is discussed in detail below). In fact, most of the current models used in AFM simulation do not take into account fundamental viscoelastic behaviors, such as stress relaxation, creep or multiple relaxation times, which are very distinct features in materials that exhibit rate-dependent behaviors, such as polymers [22]. A recent attempt has been made to model viscoelastic samples in AFM by using a standard linear solid (SLS) model (which is also discussed below) in order to include basic rate dependent properties [22-25]. Although this is a reasonable step, further sophistication is still required in order to realistically capture the nonlinear rate-dependent behaviors.

The present paper explores the nature and behavior of spring–dashpot sets as examples of models that can be used for representing viscoelastic surfaces. The first part of the study reviews the simplest models used in the context of linear viscoelasticity within AFM, followed by a discussion of more sophisticated spring–dashpot models. The second part of the study evaluates in detail the force–distance curve and dissipation behavior of these models, focusing on single-eigenmode tip–sample impacts. Throughout the paper, the advantages and disadvantages of the various models are discussed, along with possible enhancements that can lead to more accurate simulation of viscoelastic material characterization with AFM.

Results and Discussion

Model descriptions

Linear Maxwell model

The Linear Maxwell model is one of the simplest spring–dashpot sets. It consists of a spring arranged in series with a dashpot (Figure 1a). This model is known for successfully describing stress relaxation (time-dependent drop in stress under a constant strain) and for failing to describe creep (time-dependent strain relaxation under a constant stress). The latter precludes the existence of a mechanism for surface recovery upon deformation. As a consequence, the sample continuously yields to lower positions when impacted by the AFM tip, such that in subsequent impacts the tip meets the sample at lower and lower heights (see inset of Figure 1c). This also means that a tapping tip would not be able to reach steady state as the surface is continuously yielding (i.e., the probe would reach steady state only when the Linear Maxwell sample has yielded sufficiently to allow the tip to oscillate at its free oscillation amplitude, without any tip–sample interaction). Since we are interested in the response of the Linear Maxwell sample with an intermittent contact probe, we have used a prescribed tip trajectory for the simulations in Figure 1. We have thus prescribed the tip motion as $z(t) = z_c + A \cdot \sin(\omega t)$ while allowing surface relaxation. In this case the tip was forced to travel down to 20 nm below the original surface position for each tap, as shown in the inset of Figure 1c. The inset also shows how the surface yields for each consecutive tap, and it can also be seen that it experiences only a partial recovery without returning to its original position. When the tip goes down, the Linear Maxwell surface partially relaxes through the dashpot, which is the element that causes relaxation of the force stored in the spring. During retraction the sample experiences an elastic recovery that is proportional to the force stored in the spring, which could not fully relax during the approach. However, the sample does not experience viscous recovery because the dashpot does not have a mechanism to travel back up and return to its original position.

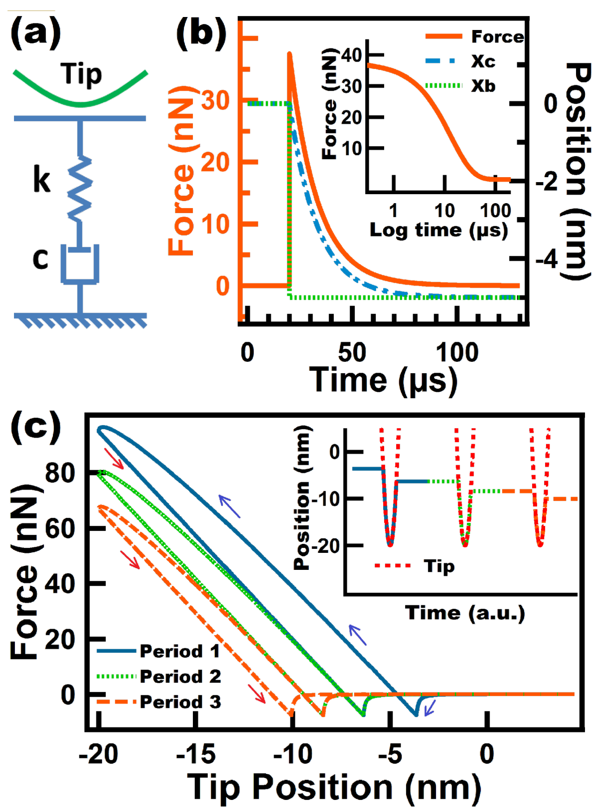

Figure 1: (a) Linear Maxwell model schematic; (b) stress relaxation simulation performed on a Linear Maxwell surface. The surface position (X_b) is depressed to a constant position of 5 nm below its unperturbed state, starting at t = 20 μs. The inset shows the same stress relaxation experiment but starting at t = 0 μs, and the horizontal axis is intentionally plotted by using a logarithmic scale to show the inflection point corresponding to its single relaxation time. (c) Force–distance tip trajectories (the trajectory proceeds in the counterclockwise direction) for a prescribed sinusoidal tip trajectory given by $z(t)$ = 80 nm + (100 nm) sin(ωt), where ω is 2π times 25 kHz. The inset shows three consecutive tip–sample taps, each one separated by a fundamental period equal to 1/25 ms. The Linear Maxwell parameters used were k = 7.5 N/m and $c = 1.0 \times 10^{-4}$ N·s/m. The blue and red arrows in (c) correspond to approach and retraction of the tip, respectively.

Despite the limitations of the Linear Maxwell model, it is able to model dissipation which is evidenced by the presence of a hysteresis loop in the force–distance (FD) curve (see Figure 1c). This dissipation loop arises from the gap between the energy input (energy given by the cantilever to the surface during approach) and the energy output (energy returned by the surface to the cantilever during retract). In spring–dashpot models this gap is caused by the relief of some of the stress accumulated in the springs through the dashpots. Another advantage of the Linear Maxwell model is that it gives a qualitatively accurate description of a FD curve for a viscoelastic sample during a single impact. Figure 1c shows FD curves containing two minima that arise from the fact that the tip encounters and leaves the sample at different heights (the surface remains depressed when the tip leaves the sample). The lack of surface recovery of the Linear Maxwell surface is also evidenced in the force–distance curves of consecutive taps where it can be seen that each loop is shifted to the left where the retract point of a previous tap is the approach point of the subsequent oscillation (see Figure 1c). It is also worth mentioning that all our simulations include long range attractive forces, incorporated through the Hammaker equation (see details in the Methods section) in order to obtain results that are more directly applicable to AFM.

Figure 1b shows a stress relaxation experiment for a Linear Maxwell arm. It can be seen that as time increases the stress over the element drops to zero which is not accurate since it is known that viscoelastic materials (e.g., polymers) retain internal stresses in the chains that are not relaxed over time [26]. The results also indicate the existence of a single relaxation time (c_d/k) which is reflected in the inflection point in Figure 1b. The existence of a single relaxation time is also considered a limitation in depicting true viscoelastic surfaces, which generally have more than one relaxation time [27]. Finally, it is worth mentioning that although a Linear Maxwell arm might appear to be too simplistic, there may be samples whose recovery is so slow that their response could be approximately mimicked by this model [26].

Linear Kelvin–Voigt model

Another simple model comprised by a spring and a dashpot in parallel is known as the Linear Kelvin–Voigt model (Figure 2a). This model is known for successfully describing creep compliance, but failing to describe stress relaxation. The surface lacks a spring that is able to accommodate the immediate force applied to it. Instead, the only spring in the model does not have an immediate response and it only experiences compression until the parallel dashpot starts yielding. As a result, a sudden step appears in the FD curve in Figure 2c upon impact. The magnitude of the step in the force (F) will depend on the instantaneous velocity (v) of the tip when it hits the sample and the viscous coefficient of the damper (c_d), since the force in a linear dashpot is given by $F = c_d \times v$. Since the tip approaches the sample with a velocity governed by the imaging and cantilever parameters, the sample surface experiences an instantaneous velocity *immediately* upon contact, which gives rise to the sudden jump in the FD curve. This is an obvious problem precluding the application of this model to tapping mode AFM. This artifact can also be seen in the inset of Figure 2c which shows the force as a function of time as well as the position of the surface and tip trajectory in time. It can be seen that the discontinuous increment of the force occurs at the moment when the probe encounters the surface.

Figure 2c shows the creep experiment on a Linear Kelvin–Voigt surface. In the inset of the figure, force and surface position are

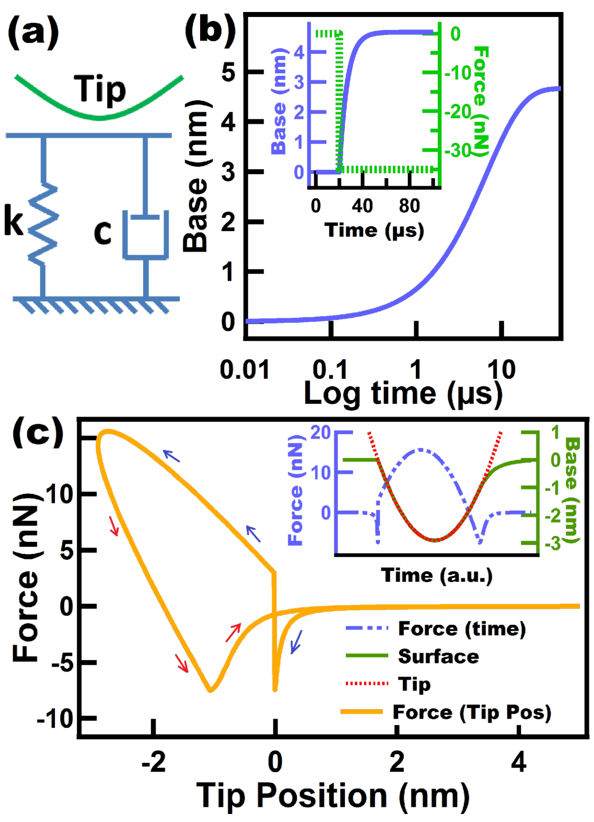

Figure 2: (a) Linear Kelvin–Voigt model scheme; (b) creep simulation performed on a Linear Kelvin–Voigt surface, whereby a force of −35 nN is applied at time zero. The horizontal axis is plotted using a logarithmic scale to show the inflection point corresponding to the single retardation time of the model. The inset shows the same experiment but here the force is applied at time t = 20 µs and the surface creeps. (c) Force–distance tip trajectory corresponding to a tapping tip over a Linear Kelvin–Voigt sample. The inset shows the base (surface) and tip position, and the force along one fundamental oscillation. The tip was oscillated along a numerically simulated trajectory (not prescribed) for tapping mode AFM. The parameters used for (c) are: cantilever position z_c = 80 nm, natural frequency (f_0) = 75 kHz, free amplitude (A_{01}) = 100 nm, cantilever stiffness (k_{m1}) = 4 N/m. The Linear Kelvin–Voigt parameters used for (b) and (c) were k = 7.5 N/m and c = 1.0 × 10^{-6} N·s/m. The blue and red arrows in (c) correspond to approach and retraction of the tip, respectively.

plotted as a function of the time. In this experiment a downward force of 35 nN is applied to the surface, after which the surface immediately starts creeping. When the sample retracts the model behaves as if an upward force is being applied to the surface, which causes the surface to creep back up to its original unperturbed position. This ability of the Linear Kelvin–Voigt model to reproduce creep provides a mechanism for the surface to recover to its original position, which is a feature that is not available in Linear Maxwell surfaces, as previously discussed. It is interesting to see in the inset of Figure 2c that during tip retract the surface does not seem to creep right away but instead it appears that the sample has an initial elastic response and only afterwards exhibits creep behavior, starting when the tip–sample contact is lost. The reason for this is that the surface actually creeps from the beginning but with a higher rate than the tip velocity, so in the simulations a restriction needs to be imposed to keep the surface from overtaking the tip position. As a result, the surface only creeps freely when there is no restriction by the tip, which occurs when the tip leaves the surface. As expected, for higher values of c_d (a less yielding dashpot) the creep phenomenon can be seen from the beginning of the tip retraction because the dashpot creep rate is lower than the tip velocity (Figure S1, Supporting Information File 1). In Figure 2b it can also be seen that the Linear Kelvin–Voigt model only provides one retardation time (the inflection point in the strain–log time curve). The inability of these simple models (Linear Maxwell and Linear Kelvin–Voigt) to capture multiple relaxation and retardation times constitutes a disadvantage when modeling the actual behavior of polymers and in particular when interpreting AFM data, whereby the cantilever and imaging parameters may be such that they favor only a particular relaxation time of the sample or none at all.

Despite the above disadvantages of the Linear Kelvin–Voigt model, it has been previously used in tapping mode AFM, both in experimental and numerical simulation approaches [16,17]. This model is also customarily used in contact-mode methods [28,29], for which there is no transition between contact and noncontact regimes as in tapping mode, so the sudden force artifact discussed above does not occur.

Standard Linear Solid (SLS) model

The SLS model is recognized as being the simplest one that is able to capture both stress relaxation and creep compliance, which are basic time-dependent properties exhibited by viscoelastic surfaces. It is comprised by a Linear Maxwell arm arranged in parallel with a spring (Figure 3a) and has been recently used in the context of multifrequency and spectral inversion AFM simulations [22-24]. Figure 3b illustrates the time-dependent properties of an SLS surface, which captures the advantages of the Linear Maxwell and Linear Kelvin–Voigt models, but exhibiting important differences in the time-dependent experiments. Figure 3b illustrates a relaxation experiment for the SLS model. Here, a restoring force of 75 nN is immediately obtained when the surface is displaced by 5 nm at time 20 µs. Then, the system relaxes through the dashpot located in the Linear Maxwell arm. However in the case of SLS the stress does not relax to zero, but rather, some stress remains stored in the spring parallel to the Linear Maxwell arm (k_{inf}) which in this 1-dimensional case corresponds to a force of 37.5 nN. This behavior is more physically accurate for samples such as polymers, for which it is known that a total relaxation of the stress does not occur [26]. On the other hand, for the creep simulation the SLS shows an immediate response of the surface (attributed to the elastic part) right when the force is applied, before noticeable surface creep occurs (Figure S2, Supporting Information File 1). The above is not observed in the creep simulation of the Linear Kelvin–Voigt surface where creep occurs without showing an immediate elastic response (Figure 2b). In the context of tapping mode AFM the SLS also has advantages when compared to the previous models discussed. First, it provides a mechanism to accommodate the initial force through its springs during tip approach without causing the discontinuous increase in force exhibited by the Linear Kelvin–Voigt model. Second, it provides a mechanism for surface recovery which allows the surface to return to its unperturbed position (this feature is not available in the Linear Maxwell model). Despite the advantages of the SLS model, however, it does not reproduce multiple relaxation times nor nonlinear elastic behavior.

Wiechert model

Modeling of multiple relaxation times has generally been carried out by representing a viscoelastic surface as a series of Linear Maxwell arms in parallel with an equilibrium spring that keeps a residual stress that does not relax in time. This generalized model is known as the Wiechert model. Multiple relaxation times in a real sample are attributed to the presence of molecular segments with different lengths which have different contributions [30]. Figure 3c shows a Wiechert model with two Linear Maxwell arms. We have chosen this particular configuration for simplicity, as the main goal is to illustrate its application in the context of tapping mode AFM. Figure 3d shows a stress relaxation simulation for the Wiechert model chosen, and as expected, the existence of two relaxation times is evidenced by the presence of two inflection points in the inset. Each relaxation time is linked to the relaxation of each of the Linear Maxwell arms. The dashpot constants were intentionally chosen to have significantly different values ($c_1 = 1.0 \times 10^{-5}$ N·s/m and $c_2 = 10.0 \times 10^{-5}$ N·s/m) in order to more clearly show the presence of the multiple relaxation times. In the context of tapping mode AFM this model exhibits a behavior that is qualitatively similar to that of the SLS model. That is, it is able to successfully accommodate the initial force experienced by the surface during the approach of the tip and also provides a mechanism for surface recovery through the stress stored in the equilibrium spring. The FD curve of the Wiechert model (Figure S3, Supporting Information File 1) also looks qualitatively similar to the FD curve of the SLS model. Both are characterized by the presence of two minima and a dissipation loop, and both curves are smooth with no discontinuity artifacts as for the Linear Kelvin–Voigt model.

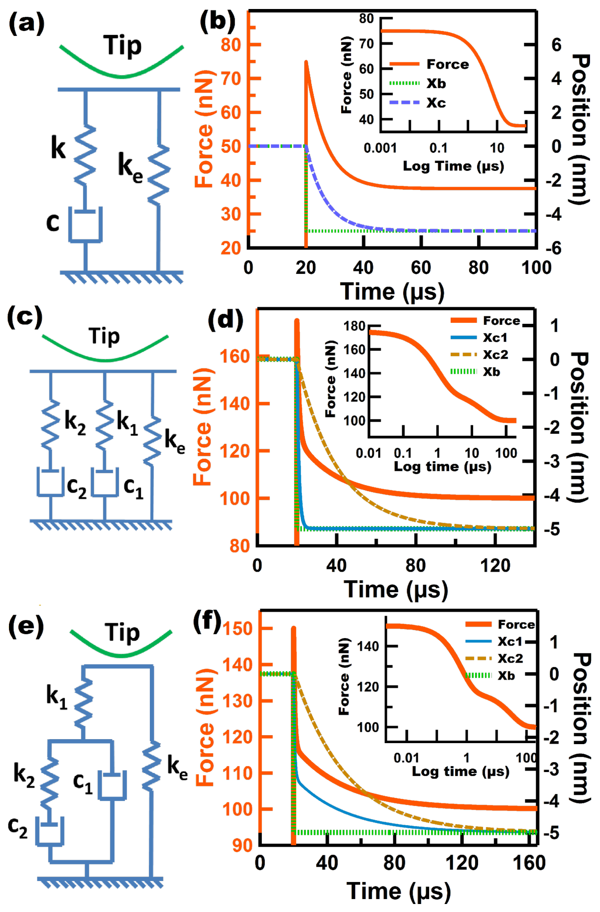

Figure 3: (a), (c), and (e) Standard linear solid (SLS) model, Wiechert model, and Nafion model, respectively; (b), (d), and (f) stress relaxation simulations for SLS, Wiechert, and Nafion models, respectively. The insets show the stress relaxation experiments for which time is plotted in logarithmic scale to show the inflection points corresponding to the relaxation times. The parameters for (b) are: $k_e = k = 7.5$ N/m, $c = 5.0 \times 10^{-5}$ N·s/m. The parameters for (d) and (f) are: $k_e = 20$ N/m, $k_1 = 10$ N/m, $k_2 = 5$ N/m, $c_1 = 1.0 \times 10^{-5}$ N·s/m, $c_2 = 10.0 \times 10^{-5}$ N·s/m.

Nafion® model

The Nafion model was introduced by Boyce and coworkers [31] to mimic the behavior of the Nafion proton exchange polymer in biaxial loading tests. This model, shown in Figure 3e, consists of a standard linear fluid element (a Linear Maxwell arm in parallel with a *dashpot*) in series with a spring and in parallel with an equilibrium spring. The special arrangement in this model attempts to reproduce the molecular and intermolecular rearrangement that Nafion undergoes during the application of stress [31], which motivated us to consider it in the context of AFM. However, it is important to point out that the original model has nonlinear springs and dashpots, whereas the model illustrated here only contains linear elements. This has been done for simplicity, but one must be mindful that nonlinear elements should be present to account for the geometrical aspects of the changing tip–sample contact area during impact. A stress relaxation simulation of the Nafion model is shown in Figure 3f. The inset clearly indicates the presence of two relaxation times in the force–log time curve. Is interesting to see that the rate at which the force drops is proportional to the rate of motion of dashpot c_1. The above is explained by the fact that the drop in the force in spring k_1 is dictated by the motion of dashpot c_1 and, at the same time, the relaxation of the entire model is governed by spring k_1, since the equilibrium spring never relaxes. Is also interesting to mention that the Linear Maxwell arm initially experiences an increase in force, after which the force starts to drop. In this model, as in the two previously described models, the force does not fall to zero but instead reaches a minimum force stored in the equilibrium spring k_e. This model exhibits a very interesting behavior under the influence of a tapping tip, which is discussed in the second part of this study.

Nonlinear models

Typically, viscoelasticity in the context of AFM has been modeled by the addition of a dissipative force term (F_{ts}^{DISS}) to the conservative force term(s) (F_{ts}^{CON}), such that the total tip–sample force can be expressed as $F_{ts} = F_{ts}^{CON} + F_{ts}^{DISS}$. Usually the repulsive conservative portion of the tip–sample interaction force is defined through the Derjaguin–Muller–Toporov (DMT) model or a similar model [6,32] while the conservative attractive force corresponding to van der Waals interactions is modeled through the Hamaker equation [6]. The dissipative portion of the interaction has been typically modeled through a velocity-dependent term. One approach (often used by us) has been to use the model of Gotsmann and coworkers [33], in which the dissipative force, F_{diss}, is proportional to the negative of the tip velocity (that is, acting in opposite direction) through an exponentially decaying coefficient:

$$F_{diss} = -\gamma_0 \exp\left(-\frac{z_{tip}(t)}{z_0}\right)\frac{dz_{tip}(t)}{dt}. \tag{1}$$

Here z_{tip} is the instantaneous cantilever tip position, γ_0 is a dissipation coefficient with units of mass/time and z_0 is a characteristic length over which the dissipation force decays (in this study we will refer to this model as 'DMT-Gotsmann'). Another very widely used approach to incorporate the dissipative portion of the tip–sample forces, is an adapted Voigt model that uses Hertz contact mechanics to incorporate the contact area and sample deformation [7]. The dissipative part of this model, originally introduced by García and coworkers [34] has the following form:

$$F_{diss} = \eta\sqrt{R\delta}\,\frac{d\delta}{dt}, \tag{2}$$

where η is the viscosity, R is the tip radius and δ is the sample deformation (tip–sample indentation). In this model, the linear spring in the Linear Kelvin–Voigt material is also replaced by a nonlinear DMT spring. As a result, this model is able to capture the nonlinear behavior of the tip–sample interactions (this model will be referred to in this study as DMT-García). Typical FD curves of the above two models are shown in Figure 4, in which we show the conservative and dissipative contributions along with the total force. The insets illustrate how the different contributions of the force behave in time. It can be clearly seen that the conservative part is symmetric, the dissipative part is antisymmetric and the total force lacks symmetry. Both approaches (DMT-Gotsmann model and DMT-García) share a similar concept in which the viscous force is proportional to the deformation velocity, and also both include varying contributions due to contact area variations. One important difference is that the DMT-Gotsmann model includes viscoelastic contributions in the conservative *attractive* part of the interaction, which is generally not physically meaningful for viscoelastic surfaces since viscoelastic dissipation only occurs in the contact regime, although there can be other contributions to dissipation in the non-contact regime such as long-range and short-range surface adhesion [7], the discussion of which is beyond the scope of this study. One important disadvantage of the DMT-Gotsmann and DMT-García models is that neither is able to reproduce the fundamental rate-dependent properties of viscoelastic materials, namely stress relaxation and creep. Furthermore, these models do not mimic the behavior of the sample but instead always assume a static unperturbed sample. As a result the FD curves only show one minimum at the fixed point where the tapping probe always finds the sample. On the other hand, one significant advantage of these models over the linear models discussed in previous sections is that they take into account the effect of a varying contact area on the stiffness and dissipative coefficient of the tip–sample interaction.

As an initial attempt to blend the advantages of the linear spring–dashpot models with the advantages of the current nonlinear models used in AFM, we propose here a standard nonlinear solid (SNLS). Figure 5a shows a diagram of the SNLS. The structure resembles the SLS but it incorporates a nonlinear DMT spring as the equilibrium spring. This configuration was chosen because the SLS is the simplest model that is able to describe stress relaxation and creep, and the DMT is a widely used model in contact mechanics that is typically used in the context of AFM. We include both DMT contact forces and long-range van der Waals forces [6,32].

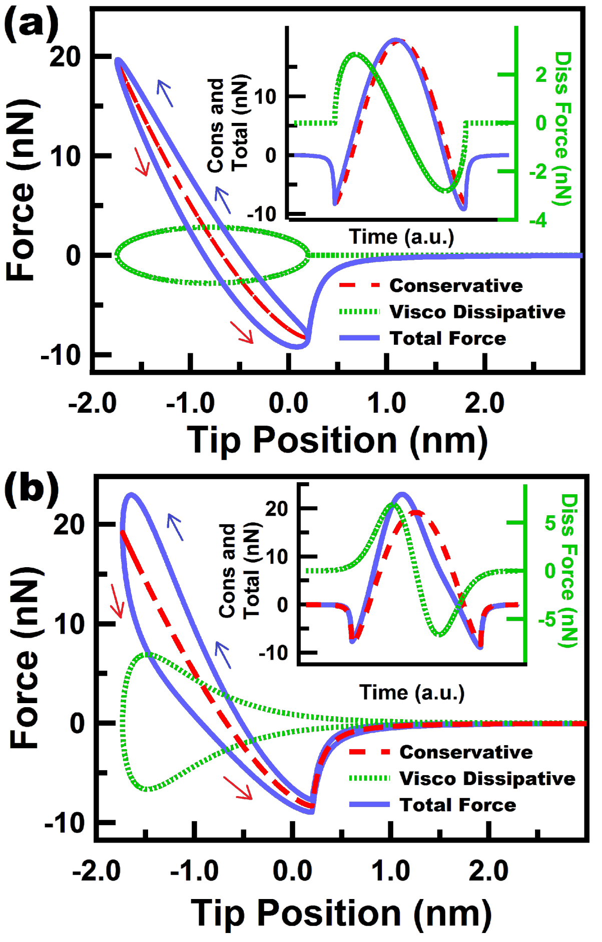

Figure 4: (a) and (b) show force trajectories for a tip under a numerically simulated (not prescribed) single tapping mode trajectory for a DMT-García sample and a DMT-Gotsmann sample, respectively. The figures show the individual contribution of the conservative and dissipative forces, along with the total force. The insets show the behavior of the force contributions over time and reflect the symmetry aspects discussed in the main text. The simulation parameters for the cantilever dynamics in (a) and (b) are: cantilever position z_c = 80 nm, natural frequency (f_0) = 50 kHz, free amplitude (A_{01}) = 50 nm, cantilever stiffness (k_{m1}) = 10 N/m. The model parameters for (b) and (c) associated with the DMT contribution are: elastic sample modulus (E_s) of 3 GPa, elastic tip modulus (E_t) of 150 GPa, Poisson's ratio of tip and sample (υ_t and υ_s, respectively) of 0.3, tip radius of curvature (R) of 10 nm, Hamaker constant of 2×10^{-19} J. For (a) a viscosity (η) value of 400 N·s/m^2 was used. For (b) a dissipation coefficient (γ_0) of 3×10^{-7} kg/s, and a characteristic dissipation length (z_0) of 0.75 nm were used. The blue and red arrows correspond to approach and retraction of the tip, respectively.

$$F_{\text{DMT}} = \frac{-HR}{6z^2} \text{ if } z > a_0 , \tag{3}$$

$$F_{\text{DMT}} = \frac{-HR}{6a_0^2} + \frac{4}{3} E^* \sqrt{R} \left(a_0 - z\right)^{3/2} \text{ if } z \le a_0 , \tag{4}$$

$$\frac{1}{E^*} = \frac{\left(1 - \nu_t\right)}{E_t} + \frac{\left(1 - \nu_s\right)}{E_s} , \tag{5}$$

where H is the Hammaker constant, R is the tip radius, z the tip position with respect to the sample, a_0 the intermolecular distance, E* the effective tip–sample elastic modulus, E_t and E_s the elastic modulus of tip and sample, respectively, and ν_t and ν_s are the Poisson's ratios of the tip and the sample, respectively.

In general, the SNLS works similar to the SLS with the difference that the SNLS includes a DMT element as the equilibrium spring. In Figure 5a we provide a physical representation of the SNLS model in which the DMT spring can be visualized as an infinite collection of springs, for which the number of active elements increases as the tip goes deeper into the sample. The above is mathematically represented with a nonlinear spring whose stiffness depends on the position of the tip and the contact area [32]. A typical FD curve for this model is shown in Figure 5b, in which the nonlinear behavior of the contact region is evident, along with the presence of two force minima, as in the spring–dashpot models.

Dissipation-based analysis

Extracting material properties in a fast and accurate way is one of the ultimate goals in AFM. In order to accomplish this for viscoelastic surfaces, physically accurate models are a requirement. One very distinct feature of viscoelastic materials is that they dissipate energy when they are subjected to dynamic loading. In the particular case of tapping mode AFM, the sample experiences a cyclic, nearly sinusoidal loading. For tapping mode AFM, other authors have derived expressions that link the observables (phase and amplitude) to the energy dissipated [9,35], and these relationships have been widely used [10,11,36,37]. Although the amount of dissipation is an important hint to the nature of the material, it is not possible to derive unambiguous conclusions about the material properties by probing a material with a single condition. With viscoelasticity being a rate-dependent phenomenon, it becomes necessary to characterize the sample at different velocities, which is not trivial in practice for tapping mode AFM. Such characterization would require imaging the sample with cantilevers of different fundamental frequencies or the use of different higher eigenmodes in successive experiments [22]. For this numerical study, we have chosen the first approach and for simplicity we have restricted ourselves to single-eigenmode tapping mode AFM due to the introductory nature of this work and to keep it from becoming excessively lengthy.

Dissipation in AFM has often been studied by using dissipation vs amplitude setpoint (A_1/A_{01}) curves, in which it has been

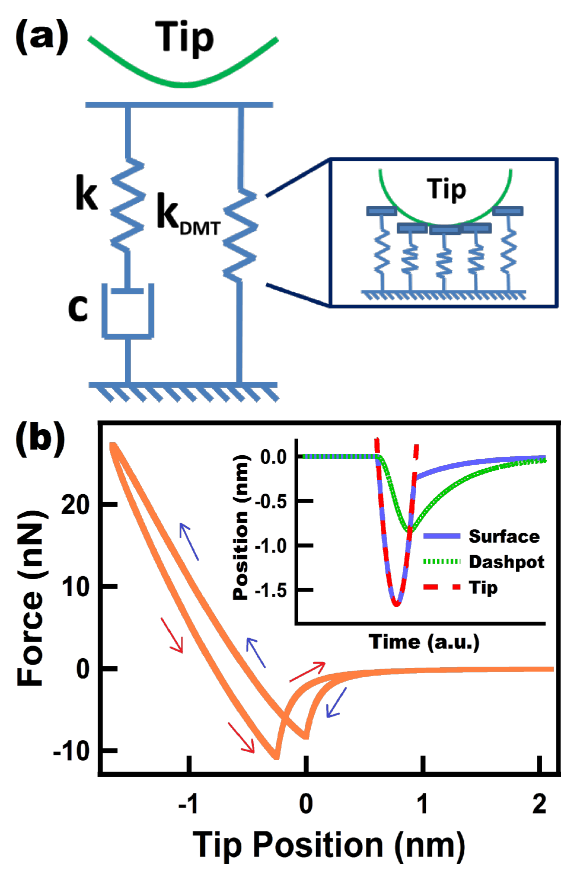

Figure 5: (a) Standard nonlinear solid (SNLS) model. (b) Tip force trajectory for a tip under a numerically simulated (not prescribed) tapping mode trajectory interacting with a SNLS sample. The inset in (b) shows the position of the surface and the dashpot over one fundamental oscillation. The parameters for the cantilever dynamics were the same as in Figure 2b. The parameters for k_{DMT} were the same as in Figure 4. The parameters *k* and *c* were set to 7.5 N/m and 0.5 × 10^{-5} N·s/m, respectively. The blue and red arrows in (b) correspond to approach and retraction of the tip, respectively.

possible to distinguish differences in dissipation arising from viscoelasticity, long- and short-range interactions [34]. We have also followed this approach in the current study. Figure 6 shows the FD behavior of three different models (Linear Kelvin–Voigt, DMT-García and DMT-Gotsmann) for different cantilever frequencies, with the insets showing the corresponding dissipation behavior for different frequencies and different amplitude setpoints (ratio of engaged amplitude to free amplitude A_1/A_{01}). We have analyzed these models together since they share some common features. For the Linear Kelvin–Voigt model (Figure 6a) the dissipation has a direct relation with the velocity, through the linear viscous dashpot in its structure (Figure 2a). For this simple model, which does not include stress relaxation, dissipation arises from the presence of a viscous linear dashpot where the magnitude of the dissipation force is related to the velocity by the simple relation $F_{\text{diss}} = c\dot{z}$. For the other two models in Figure 6, dissipation is incorporated through a nonlinear dashpot, but still the emergence of dissipation is in the form of $F_{\text{diss}} = c(z)\dot{z}$. All the results in Figure 6 show that, regardless of the setpoint, dissipation grows monotonically over the entire range of frequencies studied.

The models in Figure 6 share some common features and the nonlinear models (Figure 6b and Figure 6c) can be considered enhancements of the simple linear Linear Kelvin–Voigt model, which are able to capture the nonlinear interactions of the probe in intermittent contact with the sample. However, we again remind the reader that these models do not exhibit stress relaxation, and in the case of DMT-Gotsmann and DMT-García, they do not exhibit creep either. Nonetheless, the DMT-García model has been able to successfully describe certain viscoelastic materials under specific conditions [21], and even the simple Linear Kelvin–Voigt model has shown applicability in tapping mode AFM for the calculation of loss tangent in simulations [16], although it has shown to be inaccurate in experimental applications, in which real samples are involved [17].

In Figure 7 and Figure 8 we have varied the parameters of the Nafion model in order to tune the importance of the dashpot elements in the viscoelastic model. In this type of model the dissipation per cycle is related to the magnitude of the dashpot constant, where larger dashpot constants lead to lower dissipation (recall that here there are springs that accommodate the immediate response of the cantilever). This does not apply to the case of the Linear Kelvin–Voigt model because there are no springs to accommodate the immediate sample deformation induced by the tip. In the case of the Linear Kelvin–Voigt and other models, in which the dashpot immediately experiences the sample deformation (e.g., in the standard linear fluid element (dashpot in parallel with a Linear Maxwell arm)), the amount of dissipation is proportional to the constant (dissipation coefficient) of the dashpot that immediately experiences strain upon deformation. This discrepancy comes from the fact that the mechanism for the emergence of dissipation for models that accommodate initial response through springs (e.g., standard linear solid and Linear Maxwell) and those that do not (e.g., Linear Kelvin–Voigt and standard linear fluid) is fundamentally different. The latter ones experience immediate viscous dissipation whenever there is a surface displacement while the former experience dissipation through subsequent surface relaxation of stress initially stored in springs.

In the case of the Nafion model we have varied the magnitude of c_1 and c_2 (see Figure 3a) to observe the effect of changing the relative importance of the damping elements. Figure 7 shows the results for the case when both dashpots have the same damping constant. Figure 7a illustrates how dissipation decreases when the frequency increases for the range studied

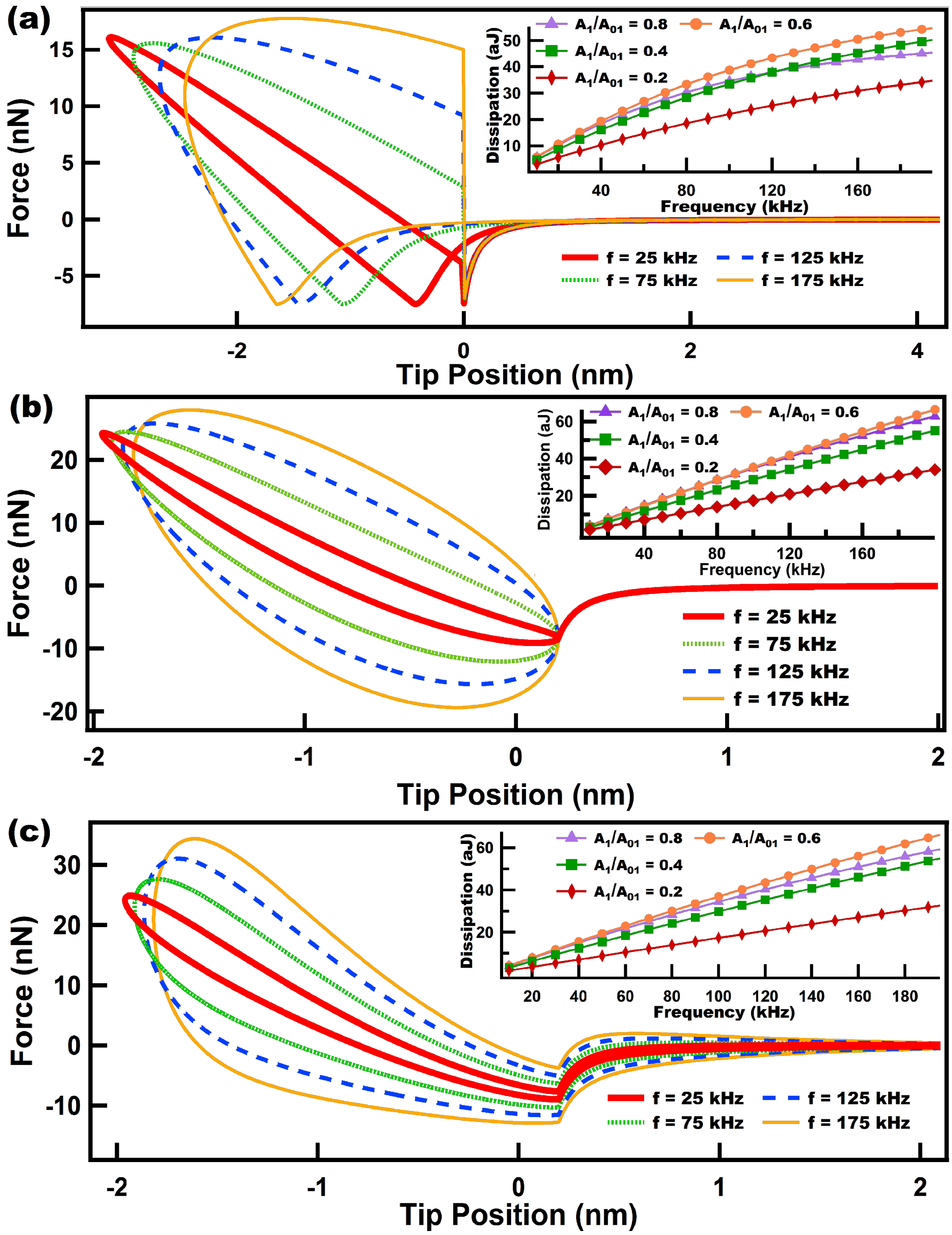

Figure 6: (a), (b) and (c) show force trajectories for a tip following a numerically simulated (not prescribed) single tapping mode trajectory over a Linear Kelvin–Voigt, a DMT-García, and a DMT-Gotsmann sample, respectively. Each of the force trajectories is color-coded according to the cantilever eigenfrequency used in the simulation. The insets in the figures show the behavior of dissipation as the frequency increases, and each color coded line relates to a specific amplitude setpoint (A_1/A_{01}). The simulation parameters for the cantilever dynamics in (a), (b) and (c) are: cantilever position z_c = 80 nm, free amplitude (A_{01}) = 100 nm, cantilever stiffness (k_{m1}) = 4 N/m. The Linear Kelvin–Voigt parameters for (a) were k = 7.5 N/m and $c = 1.0 \times 10^{-6}$ N·s/m. The sample parameters for (b) and (c) are the same as for Figure 4.

here (10–200 kHz). It is interesting to see in Figure 7b that regardless of the amplitude setpoint (A_1/A_{01}) the level of dissipation was higher for lower frequencies along the entire range of parameters studied here. That is, there is no overlap of the dissipation vs amplitude setpoint curves for different frequencies in Figure 7b. The slope of the dissipation vs amplitude setpoint curves is an important parameter in characterizing dissipation [34], which also facilitates the determination of the

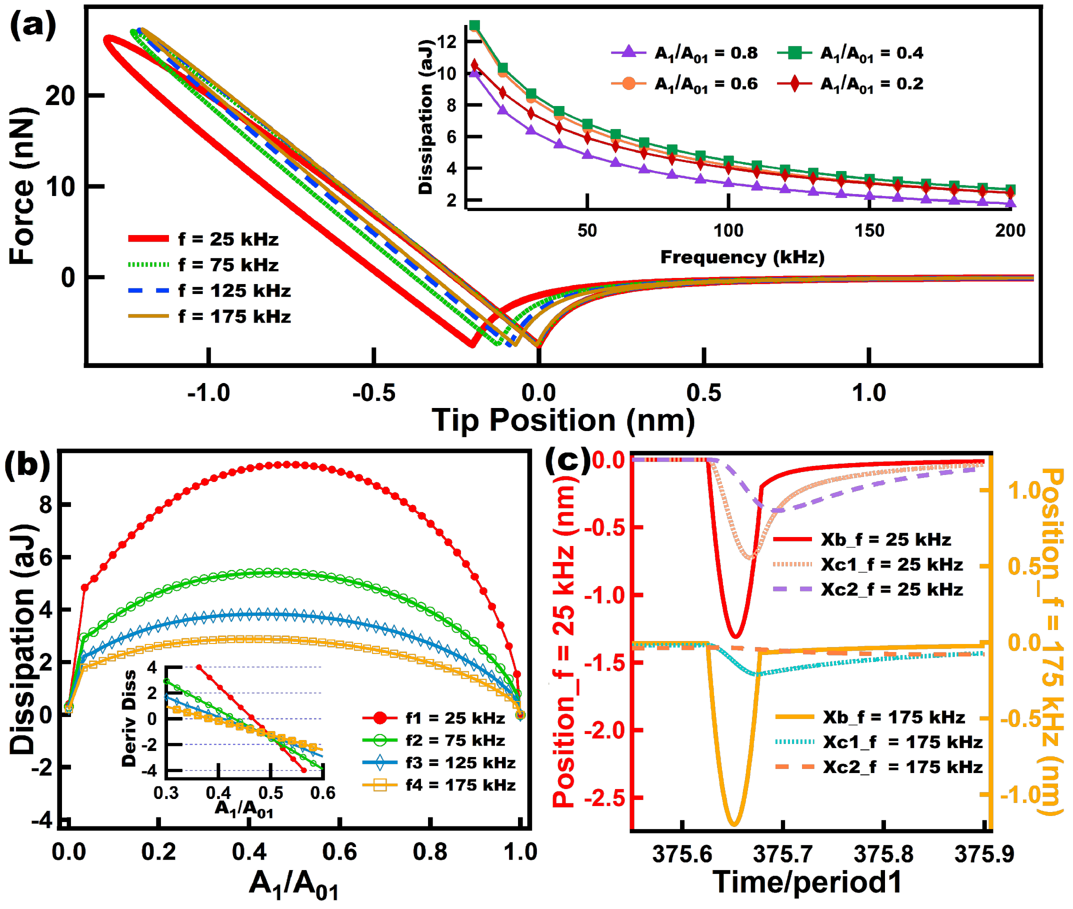

Figure 7: Results of energy dissipation when a numerically simulated tip trajectory in intermittent contact AFM interacts with a Nafion model. (a) shows force–distance curves for tips driven at different eigenfrequencies (color coded). The inset in (a) shows the behavior of the dissipation as the frequency grows, and each color-coded line relates to a specific amplitude setpoint (A_1/A_{01}). (b) shows dissipation vs amplitude setpoint (A_1/A_{01}) curves in which each color-coded line corresponds to a specific eigenfrequency. The inset in (b) shows the slope of the curves in (b) near the range where the slopes cross the *x*-axis in order to easily locate the maxima of the curves in (b). (c) shows the response of the surface and dashpots of the Nafion model for two cases at different cantilever eigenfrequencies. The parameters for the cantilever dynamics are the same as in Figure 6. The sample parameters use were: k_e = 20 N/m, k_1 = 10 N/m, k_2 = 5 N/m, and $c_1 = c_2 = 1.0 \times 10^{-5}$ N·s/m. Time normalization has been carried out in (c) with respect to the fundamental period for ease of comparison.

maximum in these curves. The inset in Figure 7b was plotted for a range in which it is easy to inspect where the derivative crosses the *x*-axis. For this case the maximum of the curves slightly shift to the left as the frequency increases within a range of 0.4 to 0.5 of the ratio A_1/A_{01}.

In contrast, for Figure 8, when the dashpot c_2 is set to a high damping value compared to c_1 (notice that the dashpot c_2 in Figure 3a hardly yields when compared to c_1) the behavior of dissipation changes drastically compared to the results of Figure 7. In the inset of Figure 8a it can be seen that for the range of frequency studied, for every setpoint dissipation increases until it reaches a certain maximum, depending on the setpoint, and then decreases to lower values. In dynamic loading experiments in the polymer literature this maximum is related to a glass transition temperature T_g where the loss modulus (which is proportional to dissipation) peaks within that frequency range [27]. Figure 8b confirms the trend in the inset of Figure 8a. It can be seen that from 25 kHz to 75 kHz dissipation increases almost for all the setpoints (except for high setpoints) and then decreases for higher frequencies (from 75 kHz to 175k Hz) almost for all setpoints (except for low setpoints where A_1/A_{01} is lower than 0.15). The inset in Figure 8b shows that the maximum of the dissipation vs setpoint curve shifts to the left as the frequency increases. The behavior of this model (Figure 8) is more intricate than the one shown in Figure 7 and illustrates the challenges in choosing the ideal parameters when an experimentalist wants to maximize dissipation in tailoring a material that follows this model.

Figure 9 shows dissipation behaviors when performing tapping mode AFM over two different viscoelastic samples:

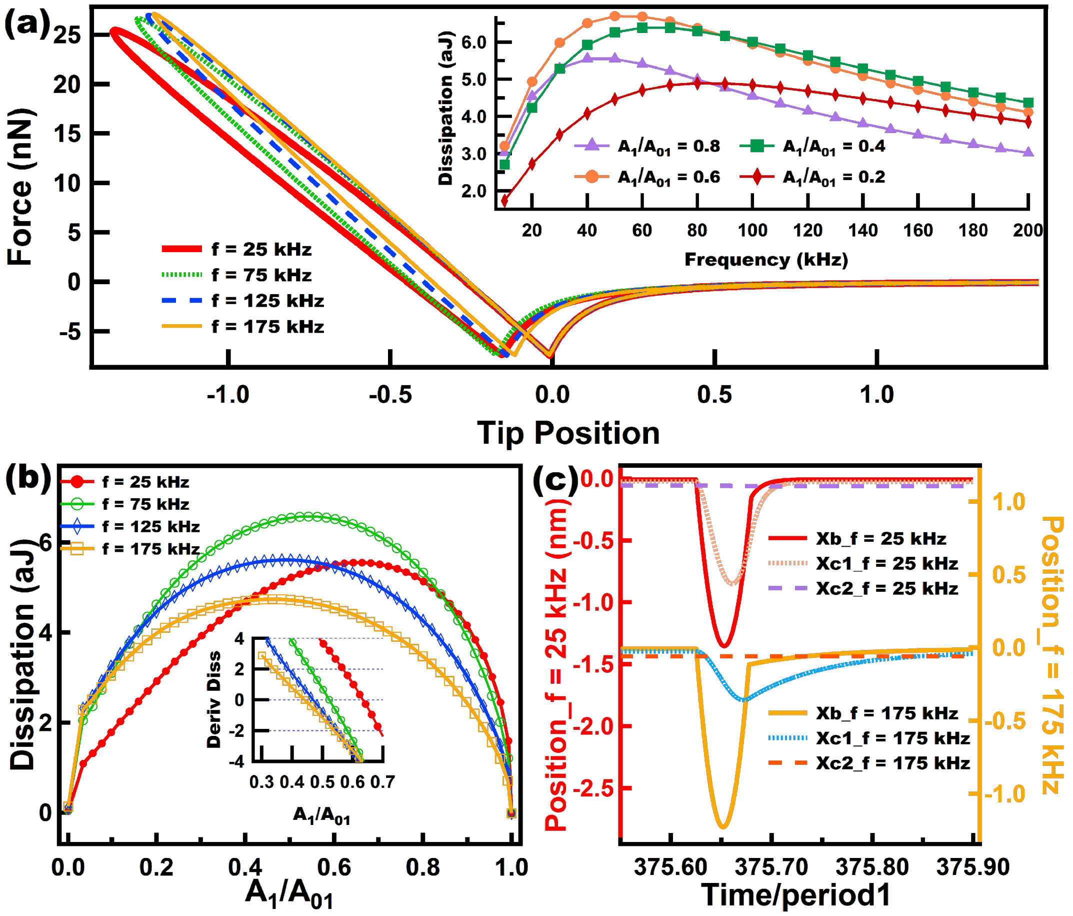

Figure 8: Results of energy dissipation when a tip interacts with a Nafion model under a numerically simulated trajectory. (a) Shows force distance curves for tips driven at different eigenfrequencies (color coded). The inset in (a) shows the behavior of dissipation as the frequency increases, and each color coded line relates to a specific amplitude setpoint (A_1/A_{01}). (b) shows dissipation vs amplitude setpoint (A_1/A_{01}) curves, where each color coded line corresponds to a specific eigenfrequency. The inset in (b) shows the slope of the curves in (b) near the range where the slopes cross the *x*-axis in order to easily locate the maxima of the curves in (b). (c) shows the response of the surface and dashpots of the Nafion model for two cases at different cantilever eigenfrequencies. The parameters for the cantilever dynamics were the same as in Figure 6 and Figure 7. The sample parameters were: k_e = 20 N/m, k_1 = 10 N/m, k_2 = 5 N/m, c_1 = 0.5 × 10^{-5} N·s/m, and c_2 = 100.0 × 10^{-5} N·s/m. Time normalization has been carried out in (c) with respect to the fundamental period for ease of comparison.

Figure 9a and Figure 9b show results for the Wiechert model, and Figure 9c and Figure 9d for the SLS model. For this set of simulations the Wiechert model (see diagram in Figure 3c) had a value of c_2 that was much higher than the value of c_1, with the purpose of making c_2 less relevant in terms of the amount of dissipation observed. Afterwards, an SLS model was simulated with parameters that approximate the response of the more complex Wiechert model (see the caption of Figure 9). The dissipation results show very similar trends for both models and also a close quantitative agreement between both, which is reasonable since the Wiechert model was set in a way that one of the dashpots dominates during the intermittent tip–sample interactions, and as previously stated, the mechanism of dissipation of this spring–dashpot models is surface relaxation which happens when the force, built up in the springs, drops through the yielding of the dashpots. There is still a small difference between the models, which can be observed in Figure 9b and Figure 9d where the values of the dissipation are slightly higher for the Wiechert model. This difference is attributed to the modest contribution of dissipation arising from the stress relaxation that occurs through c_2 in the Wiechert model.

Figure 10 shows dissipation results for the standard nonlinear solid model (SNLS). Figure 10a shows FD curves at different frequencies, from which it is clear that at low frequencies the dissipation loop is larger and also the tip position reaches lower values corresponding to a greater tip–sample indentation. As the tip reaches lower values, the minimum of the FD curve when the tip *leaves* the sample (the left-most minimum in the FD curves, corresponding to the tip retract) is also lower. The above is explained by the fact that lower frequencies allow for a

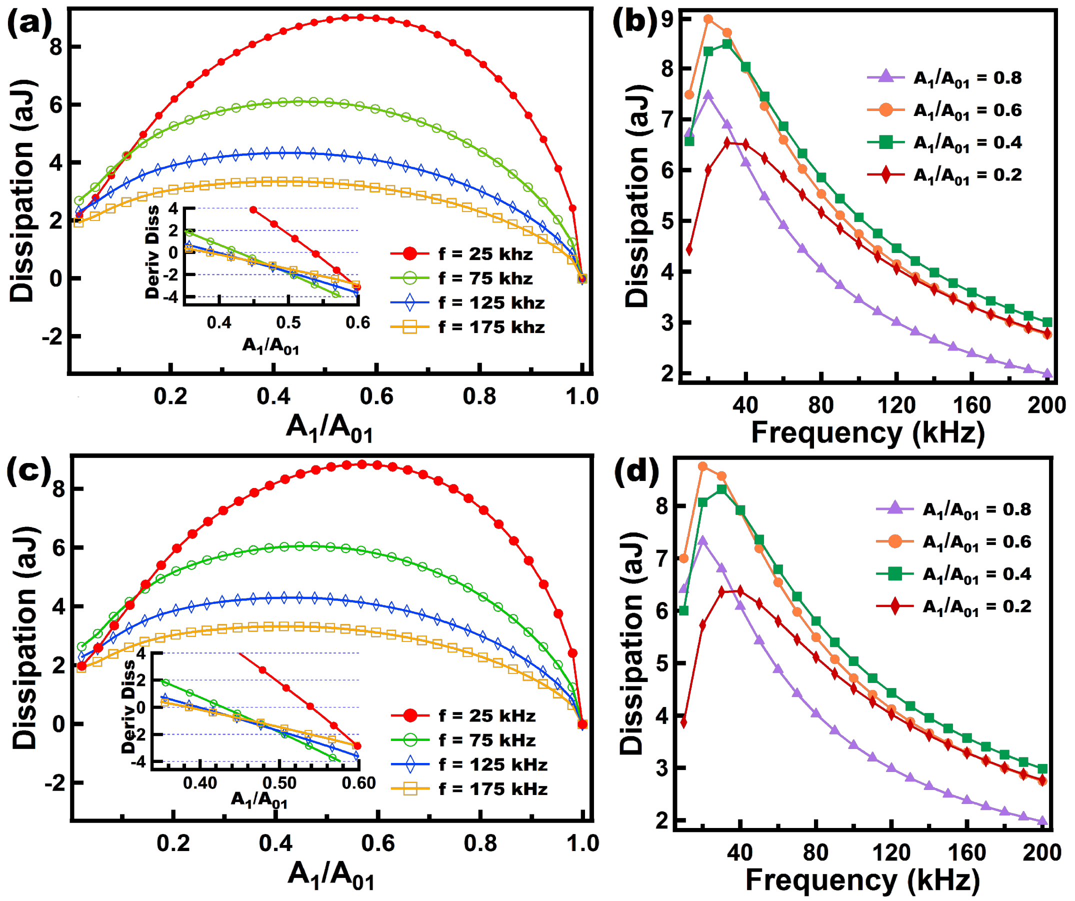

Figure 9: (a) and (c) show dissipation vs amplitude setpoint (A_1/A_{01}) curves where each color coded line corresponds to a specific eigenfrequency, for the Wiechert and the SLS models, respectively. The insets in (a) and (c) show the slope of the curves in (a) and (c) plotted over a range near where the slopes cross the *x*-axis, in order to easily locate the maxima of the curves in (a) and (c). (b) and (d) show the behavior of dissipation as frequency increases, and each color coded line relates to a specific amplitude setpoint (A_1/A_{01}) for the Wiechert and the SLS models, respectively. The parameters for the cantilever dynamics were the same as in Figures 6 to 8. The sample parameters for (a) and (b) were: k_e = 10 N/m, k_1 = 7.5 N/m, k_2 = 7.5 N/m, c_1 = 0.5 × 10^{-5} N·s/m, and c_2 = 100.0 × 10^{-5} N·s/m. The sample parameters for (c) and (d) were: k_e = 17.5 N/m, k = 7.5 N/m, c = 0.5 × 10^{-5} N·s/m.

longer time for relaxation of the dashpots. The inset in Figure 10 shows the behavior of dissipation at different frequencies, exhibiting a similar trend as for the SLS model where the two extremes of frequencies show low dissipation, coinciding with the behavior of amorphous polymers, which in dynamic loading tests are expected to undergo highly elastic behavior in the two extremes of frequencies [27]. Figure 10b also shows similar qualitative behavior to that of the SLS model, with the maxima in the inset shifting to the left for larger frequencies. Finally, Figure 10c shows the response of the surface and the dashpot of the SNLS model to different frequencies. This figure shows clearly than at 25 kHz the dashpot in the model is able to respond significantly while at 175 kHz the dashpot response is much smaller. As a result, the surface is able to experience greater surface relaxation (leading to greater dissipation) at 25 kHz.

Conclusion

Different approaches to model viscoelasticity within intermittent contact AFM have been studied with special emphasis on spring–dashpot models. We summarize the models that have been frequently used in AFM, highlighting their strengths and deficiencies. We also propose different spring–dashpot models that can be used to mimic the response of viscoelastic surfaces, especially polymers, under interactions with the AFM tip. Most of the models included display distinct features observed in polymers, namely stress relaxation and creep, and some of them exhibit multiple relaxation times, as in realistic samples. The level of complexity and physical accuracy is different for each model and good judgment is advised in selecting the proper model for the type of sample or dynamic phenomenon under investigation. Although this paper is not intended to serve as an exhaustive manual for modeling viscoelasticity in AFM, it is

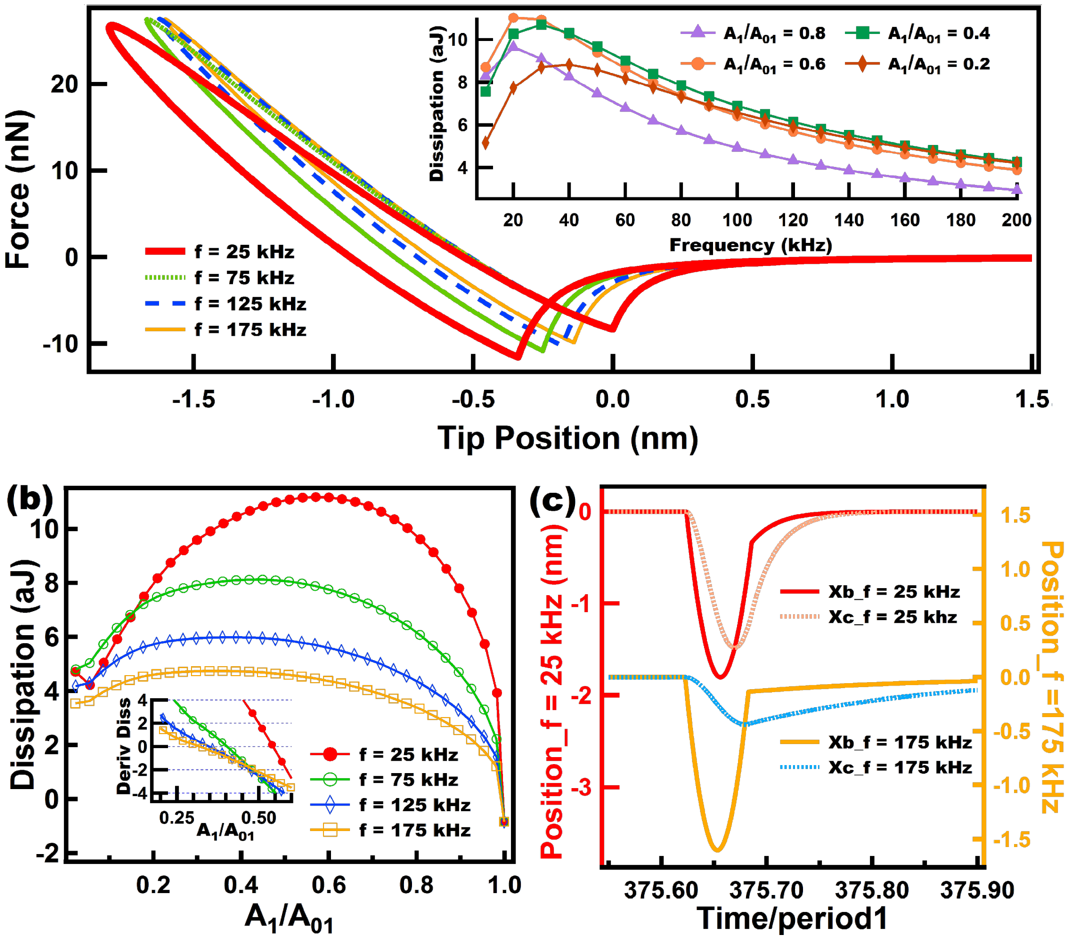

Figure 10: Results of energy dissipation when a realistic tip interacts in intermittent contact AFM with a standard nonlinear solid (SNLS). (a) Shows force–distance curves for tips driven at different eigenfrequencies (color coded). The inset in (a) shows the behavior of dissipation as frequency increases, and each color coded line relates to a specific amplitude setpoint (A_1/A_{01}). (b) Shows dissipation vs amplitude setpoint (A_1/A_{01}) curves where each color coded line corresponds to a specific eigenfrequency. The inset in (b) shows the slope of the curves in (b) plotted in the range where the slopes cross the *x*-axis in order to easily determine the maxima of the curves in (b). (c) Shows the response of the surface and dashpots of the SNLS model for two different cantilever eigenfrequencies. The parameters for the cantilever dynamics were the same as in Figures 6 to 9. The sample parameters were the same as for Figure 5.

our aim that it sparks further theoretical developments, which are much needed especially as new rapid AFM-based spectroscopy techniques are developed [21].

Methods

Numerical simulations of the cantilever dynamics were performed for most of the cases according to single-eigenmode tapping mode AFM, unless otherwise indicated. To model the dynamics of the cantilever we included the contribution of the first three flexural modes of the cantilever (although only the first one was excited). Each mode was described through an individual equation of motion, and the three single equations were coupled through the tip–sample interaction forces as in previous studies [19,22,24,37,38]. The first eigenmode (the only one actively driven) was excited at its natural frequency. The first three quality factors of the cantilever were set to $Q_1 = 220$, $Q_2 = 450$, and $Q_3 = 750$ in all cases, and the rest of the parameters are indicated in the figure captions for each case. The equations of motion were integrated numerically and the amplitude and phase for the first eigenmode were calculated using the in-phase (I_i) and quadrature (K_i) terms:

$$I_i = \int_{N\tau} z_i(t)\cos(\omega t)dt \tag{6}$$

$$K_i = \int_{N\tau} z_i(t)\sin(\omega t)dt \tag{7}$$

where $z_i(t)$ is the i-th eigenmode response in the time domain, N is the number of periods over which the phase and amplitude were averaged, ω is the excitation frequency, and τ is the fundamental period of one oscillation. The amplitude and phase (used in the dissipation analysis) were calculated, respectively, as:

$$A_i = \frac{\omega}{\pi N}\sqrt{I_i^2 + K_i^2} \tag{8}$$

$$\varphi_i = \tan^{-1}\left(K_i / I_i\right) \tag{9}$$

The repulsive tip–sample forces were simulated through the various models discussed throughout the paper, and the parameters for each of the models are provided in the respective figure captions.

Supporting Information

Supporting Information features additional simulation data, namely the surface response of Linear Kelvin–Voigt samples and its dependency on its dissipation coefficient, the creep simulation of a SLS sample, and the comparison between the force–distance curves of the SLS and the Nafion model.

Supporting Information File 1

Additional simulation data.
[http://www.beilstein-journals.org/bjnano/content/supplementary/2190-4286-5-224-S1.pdf]

Acknowledgements

The authors gratefully acknowledge support from the U.S. Department of Energy, Office of Science, Basic Energy Sciences, through award DESC0008115.

References

1. Binnig, G.; Quate, C. F.; Gerber, C. *Phys. Rev. Lett.* **1986,** *56,* 930–933. doi:10.1103/PhysRevLett.56.930
2. García, R.; San Paulo, A. *Phys. Rev. B* **1999,** *60,* 4961–4967. doi:10.1103/PhysRevB.60.4961
3. García, R.; San Paulo, A. *Phys. Rev. B* **2000,** *61,* R13381. doi:10.1103/PhysRevB.61.R13381
4. García, R.; San Paulo, A. *Ultramicroscopy* **2000,** *82,* 79–83. doi:10.1016/S0304-3991(99)00132-1
5. San Paulo, A.; García, R. *Phys. Rev. B* **2002,** *66,* 041406. doi:10.1103/PhysRevB.66.041406
6. García, R.; Pérez, R. *Surf. Sci. Rep.* **2002,** *47,* 197–301. doi:10.1016/S0167-5729(02)00077-8
7. Gómez, C. J.; García, R. *Ultramicroscopy* **2010,** *110,* 626–633. doi:10.1016/j.ultramic.2010.02.023
8. Tamayo, J.; García, R. *Appl. Phys. Lett.* **1997,** 2394–2396. doi:10.1063/1.120039
9. Cleveland, J. P.; Anczykowski, B.; Schmid, A. E.; Elings, V. B. *Appl. Phys. Lett.* **1998,** *72,* 2613–2615. doi:10.1063/1.121434
10. Martínez, N. F.; García, R. *Nanotechnology* **2006,** *17,* S167. doi:10.1088/0957-4484/17/7/S11
11. San Paulo, A.; García, R. *Phys. Rev. B* **2001,** *64,* 193411. doi:10.1103/PhysRevB.64.193411
12. Anczykowski, B.; Gotsmann, B.; Fuchs, H.; Cleveland, J. P.; Elings, V. B. *Appl. Surf. Sci.* **1999,** *140,* 376–382. doi:10.1016/S0169-4332(98)00558-3
13. Sasaki, N.; Tsukada, M. *Jpn. J. Appl. Phys.* **2000,** *39,* L1334–L1337. doi:10.1143/JJAP.39.L1334
14. Kantorovich, L. N.; Trevethan, T. *Phys. Rev. Lett.* **2004,** *93,* 236102. doi:10.1103/PhysRevLett.93.236102
15. Schirmeisen, A.; Hölscher, H. *Phys. Rev. B* **2005,** *72,* 045431. doi:10.1103/PhysRevB.72.045431
16. Proksch, R.; Yablon, D. G. *Appl. Phys. Lett.* **2012,** *100,* 073106. doi:10.1063/1.3675836
17. Yablon, D. G.; Grabowski, J.; Chakraborty, I. *Meas. Sci. Technol.* **2014,** *25,* 055402. doi:10.1088/0957-0233/25/5/055402
18. Jesse, S.; Kalinin, S.; Proksch, R.; Baddorf, A.; Rodriguez, B. *Nanotechnology* **2007,** *18,* 435503. doi:10.1088/0957-4484/18/43/435503
19. Kareem, A. U.; Solares, S. D. *Nanotechnology* **2012,** *23,* 015706. doi:10.1088/0957-4484/23/1/015706
20. Rodriguez, B. J.; Callahan, C.; Kalinin, S. V.; Proksch, R. *Nanotechnology* **2007,** *18,* 475504. doi:10.1088/0957-4484/18/47/475504
21. Herruzo, E. T.; Perrino, A. P.; García, R. *Nat. Commun.* **2014,** *5,* 3126. doi:10.1038/ncomms4126
22. Solares, S. D. *Beilstein J. Nanotechnol.* **2014,** *5,* 1649–1663. doi:10.3762/bjnano.5.176
23. Williams, J. C.; Solares, S. D. *Beilstein J. Nanotechnol.* **2013,** *4,* 87–93. doi:10.3762/bjnano.4.10
24. Ebeling, D.; Eslami, B.; Solares, S. D. *ACS Nano* **2013,** *7,* 10387–10396. doi:10.1021/nn404845q
25. Chyasnavichyus, M.; Young, S. L.; Tsukruk, V. V. *Langmuir* **2014,** *30,* 10566–10582. doi:10.1021/la404925h
26. Wineman, A. S. *Mechanical response of polymers: an introduction;* Cambridge University Press: Cambridge, U.K, 2000.
27. Painter, P. C.; Coleman, M. M. *Essentials of Polymer Science and Engineering;* DSTech Publications Inc.: Lancaster, U.S.A., 2009.
28. Yuya, P. A.; Hurley, D. C.; Turner, J. A. *J. Appl. Phys.* **2008,** *104,* 074916. doi:10.1063/1.2996259
29. Yuya, P. A.; Hurley, D. C.; Turner, J. A. *J. Appl. Phys.* **2011,** *109,* 113528. doi:10.1063/1.3592966
30. Roylance, D. *Engineering Viscoelasticity;* Independent publication: Cambridge, U.S.A., 2001.
31. Silberstein, M. N.; Priam, V. P.; Boyce, M. C. *Polymer* **2011,** *52,* 529–539. doi:10.1016/j.polymer.2010.11.032
32. Derjaguin, B. V.; Muller, V. M.; Toporov, Y. P. *J. Colloid Interface Sci.* **1975,** *53,* 314–326. doi:10.1016/0021-9797(75)90018-1
33. Gotsmann, B.; Seidel, C.; Anczykowski, B.; Fuchs, H. *Phys. Rev. B* **1999,** *60,* 11051–11061. doi:10.1103/PhysRevB.60.11051
34. García, R.; Gómez, C. J.; Martinez, N. F.; Patil, S.; Dietz, C.; Magerle, R. *Phys. Rev. Lett.* **2006,** *97,* 016103. doi:10.1103/PhysRevLett.97.016103
35. Tamayo, J.; García, R. *Appl. Phys. Lett.* **1998,** *73,* 2926–2928. doi:10.1063/1.122632
36. Chawla, G.; Solares, S. D. *Appl. Phys. Lett.* **2011,** *99,* 074103. doi:10.1063/1.3626847
37. Diaz, A. J.; Eslami, B.; López-Guerra, E. A.; Solares, S. D. *J. Appl. Phys.* **2014,** *116,* 104901. doi:10.1063/1.4894837
38. Solares, S. D.; Chawla, G. *Meas. Sci. Technol.* **2010,** *21,* 125502. doi:10.1088/0957-0233/21/12/125502

License and Terms

BEILSTEIN JOURNAL OF NANOTECHNOLOGY

High-frequency multimodal atomic force microscopy

Adrian P. Nievergelt, Jonathan D. Adams, Pascal D. Odermatt and Georg E. Fantner*

Full Research Paper

Open Access

Address:
Laboratory for Bio- and Nano-Instrumentation, École Polytechnique Fédérale de Lausanne, Batiment BM 3109 Station 17, 1015 Lausanne, Switzerland

Email:
Adrian P. Nievergelt - adrian.nievergelt@epfl.ch;
Jonathan D. Adams - jonathan.adams@epfl.ch; Pascal D. Odermatt - pascal.odermatt@epfl.ch; Georg E. Fantner* - georg.fantner@epfl.ch

* Corresponding author

Keywords:
atomic force microscopy; multifrequency imaging; nanomechanical characterization; photothermal excitation; small cantilevers

Beilstein J. Nanotechnol. **2014,** *5,* 2459–2467.
doi:10.3762/bjnano.5.255

Received: 02 September 2014
Accepted: 26 November 2014
Published: 22 December 2014

This article is part of the Thematic Series "Advanced atomic force microscopy techniques III".

Guest Editor: T. Glatzel

Abstract

Multifrequency atomic force microscopy imaging has been recently demonstrated as a powerful technique for quickly obtaining information about the mechanical properties of a sample. Combining this development with recent gains in imaging speed through small cantilevers holds the promise of a convenient, high-speed method for obtaining nanoscale topography as well as mechanical properties. Nevertheless, instrument bandwidth limitations on cantilever excitation and readout have restricted the ability of multifrequency techniques to fully benefit from small cantilevers. We present an approach for cantilever excitation and deflection readout with a bandwidth of 20 MHz, enabling multifrequency techniques extended beyond 2 MHz for obtaining materials contrast in liquid and air, as well as soft imaging of delicate biological samples.

Introduction

The atomic force microscope (AFM) has developed into an extremely useful and versatile tool for nanometre-scale visualization and mechanical characterization. In recent years, several methods have been developed for simultaneous measurement of topographical and mechanical information by using AFM, opening up new possibilities for biology and materials science [1-9]. A key enabling trend in the technological development of AFM has been the drive to minimize the cantilever size and maximize the resonance frequency, while maintaining acceptable spring constants [10-12]. Increasing the cantilever resonance frequency enables faster imaging and force spectroscopy [12-17], and small, high-frequency AFM cantilevers have less viscous drag, lowering force noise [18]. Many of the techniques for extracting mechanical information during imaging utilize higher cantilever resonant modes. Here, the ability to detect cantilever motion at high-frequencies becomes an increasingly critical requirement that is often beyond current instrument capabilities.

In addition to the availability of small, high-frequency cantilever probes and optical beam deflection (OBD) systems with a sufficiently small focus spot to use small cantilevers [12,19], two key practical aspects have limited the widespread use of AFM imaging at frequencies beyond 2 MHz: cantilever drive and deflection readout. In liquids, traditional piezo-based cantilever excitation leads to the generation of numerous system resonances that can mask or fail to drive the desired cantilever resonances and complicate subsequent interpretation and analysis. This problem is accentuated at high frequencies. Alternately, the cantilever can be directly driven by using techniques including magnetic [20], resistive thermal [21], integrated piezotransducer [22] or photothermal [23,24] excitation, eliminating this effect. Of the direct drive techniques, photothermal-based excitation has the benefit that it is compatible with most standard AFM cantilevers and, although long-established, has recently gained renewed interest [25-30]. Although the efficiency of photothermal excitation varies with different coatings, even uncoated cantilevers have been shown to work [31]. Furthermore, photodiode readout electronics in the OBD system typically have been restricted to approx. 2 MHz for standard systems and a maximum of 10 MHz for highly-optimized systems [27]. Even for cantilevers with fundamental resonances of 1–2 MHz, at the second or higher modes this limit is quickly reached. Only a small number of alternative approaches for moving past this limitation have been explored; these include heterodyne optical beam and interferometric detection [32-34] and current-based translinear readout circuitry [35]. Of these approaches, the latter shows excellent potential for low-noise and high-bandwidth direct OBD readout.

Surmounting these technological challenges has thus far remained the domain of a handful of highly-specialized instruments. In this report, we present high-resonance-frequency bimodal AFM imaging by using an AFM readout head designed for high-frequency drive and readout of small cantilevers. Our head is compatible with the Bruker MultiMode AFM, a widely used commercial system. We show that our system has the ability to stably drive small AFM cantilevers in both air and fluid at in bandwidth exceeding 20 MHz, with a detection noise floor comparable to lower bandwidth commercial systems. We demonstrate the application of our instrument towards multifrequency materials contrast imaging of a polymer blend in both air and fluid, and gentle, high-resolution imaging of an F-actin fibre in fluid.

Results and Discussion

Instrument design

The basis for our optical design is a modular AFM readout head design we have reported earlier [36]. The modular nature of this head permits the easy exchange of the optical assembly, allowing for the integration of custom optics elements such as a photothermal drive. Figure 1a illustrates the architecture of our photothermal optical assembly, and Figure 1b shows a picture of the optical and head assembly. The optical design uses a spatial separation approach to separate the incident and reflected light paths, with the additional photothermal drive laser mounted onto the core optics block via an adjustable kinematic mount (see section “Optical beam deflection setup”). Since the drive laser diode has to be modulated at frequencies beyond the capability of most commercial drivers, we used a custom-built wideband constant-current source (Figure 1c). Adjustment of the incidence angle of the collimated drive beam onto the focusing lens translates the focal position. This architecture permits the relative position of the two laser spots to stay fixed when the lasers are aligned to the cantilever. Furthermore, because the optical axis of the assembly is normal to the cantilever top surface, we eliminate the need for refocusing when positioning the foci on the cantilever.

Voltage-based arithmetic, which is used by most quadrant photodiode readouts, uses operational amplifiers to calculate the vertical and horizontal deflections of the laser spot. Our readout in contrast uses translinear loops, allowing us to calculate both deflections in currents as shown by Enning et al. [35]. Figure 1d shows a conceptual schematic of the readout circuit. The photodiode currents are first copied with current mirrors. The currents are then added or subtracted as necessary to generate the sum, vertical and horizontal signals as currents. Finally, transimpedance amplifiers convert the current signals into voltages. The use of current mirror based readout has two major advantages over a conventional, purely operational amplifier based readout. The large increase in speed is achieved by the very low input impedance of current mirrors, thus countering the negative impact of diode parasitics on the total bandwidth. Additionally, the serial nature of the inherently slow voltage-based addition–substraction–division circuits poses a significant bandwidth limitation to voltage-based readouts, which can be circumvented by using current-based arithmetic, which is only limited by an inherently fast transimpedance stage. Besides the increased bandwidth, as operational amplifiers are very complex many-transistor devices, the effective reduction in the total number of transistors used has the potential to allow for a very low electronic noise floor.

Characterization

We characterized the performance of the major optical components in our optical design by using a spectrometer (9405CB, Hamamatsu, Hamamatsu City, Japan). Figure 2a presents the normalised spectra for the two lasers, the bandpass filter and the dichroic mirror. The peak emission wavelengths of the readout and drive lasers were measured at 645 nm and 686 nm, respectively. The readout laser sits well within the pass-band of the bandpass filter, measured at 618 nm to 656 nm at 50% transmission. At the drive laser emission wavelength we measured an extinction higher than OD3 from the bandpass filter, effectively reducing cross-talk from the drive laser to below 0.03% at

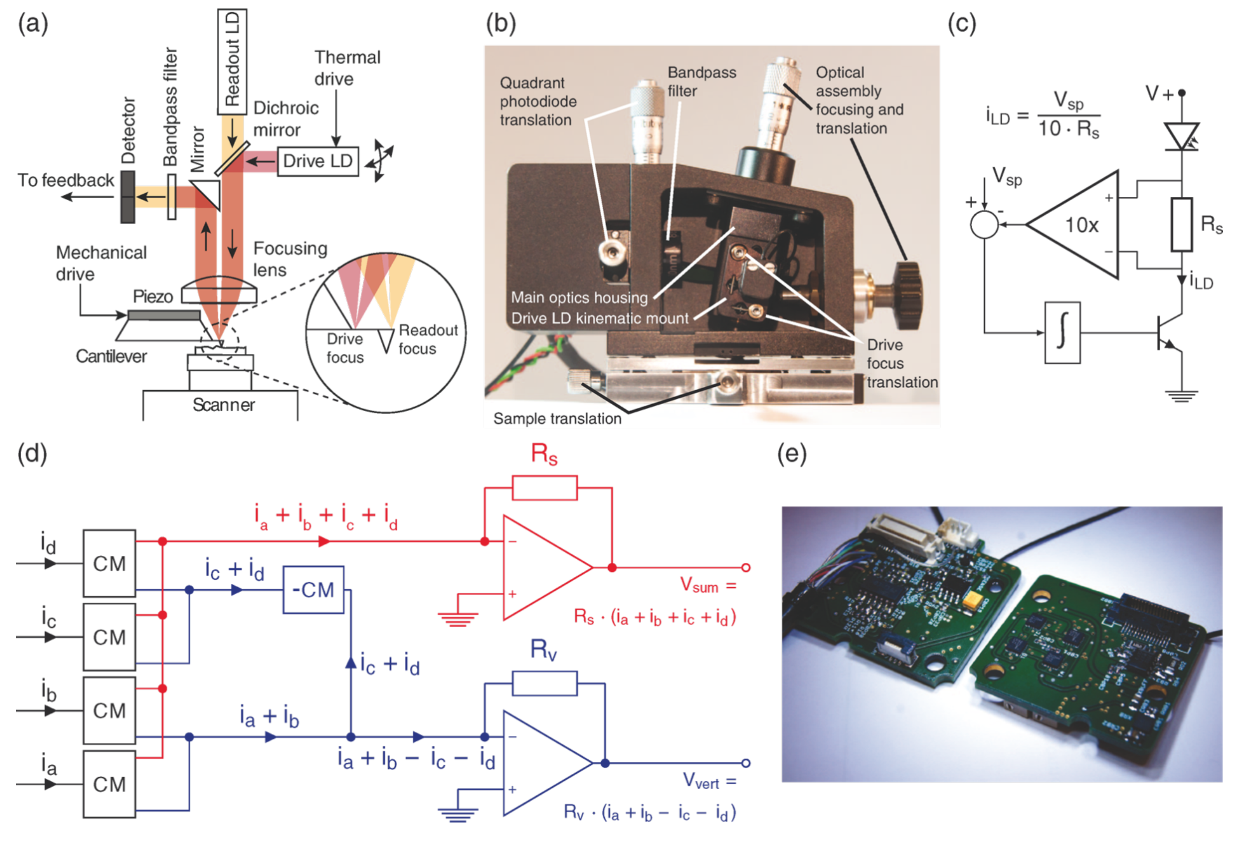

Figure 1: a) Schematic of the optical drive and detection setup. The drive laser focus can be positioned relative to the readout laser focus through an adjustable kinematic mount. b) Photograph of the assembled readout head. The head can be mounted directly onto Bruker MultiMode scanners. c) Schematic of the constant current driver circuit for the photothermal drive laser. d) Simplified functional schematic of the high-bandwidth readout electronics. Transistor-based current arithmetic greatly improves bandwidth and reduces noise. Only the sum and vertical channels are shown for clarity; the horizontal deflection is also calculated. (CM = current mirror, −CM = current subtractor). e) Photograph of the readout electronics circuitry. One circuit board provides power conditioning and the drive laser control, the second board calculates the readout arithmetic.

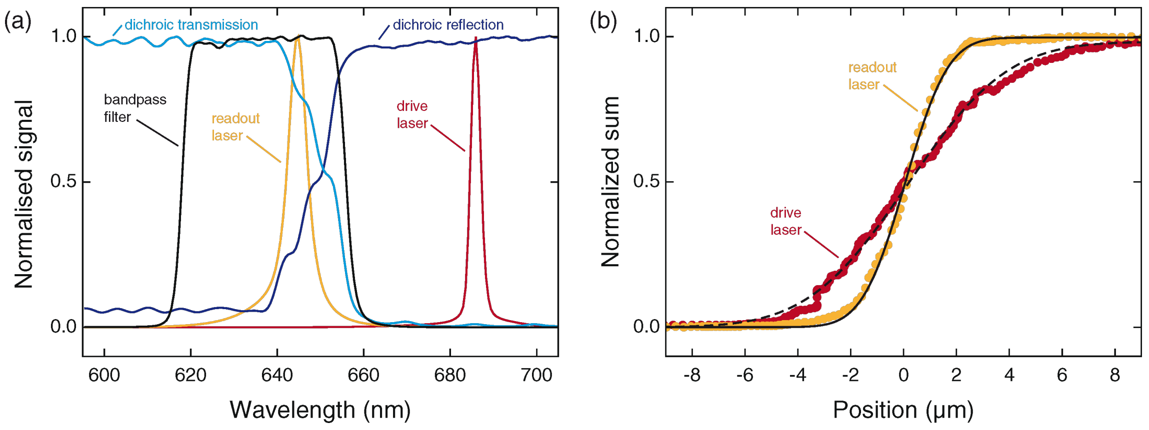

Figure 2: a) Measured spectra of the major optical components in the readout design. b) Measurement of the beam waist of the readout and drive laser. The $1/e^2$ waist of the readout and drive laser are 2.6 µm and 5.9 µm, respectively.

typical optical powers used during imaging (approx. 1 mW for the readout and approx. 0.2 mW for the AC component of the drive). We measured that the dichroic mirror has only 80% transmission at the readout laser wavelength. While the readout laser power can be adjusted to maintain sufficient intensity at the photodiode, this clipping introduces some additional stray light in the system. We chose the dichroic mirror primarily for cost reasons, and expect that a minor performance increase could be obtained by choosing a dichroic mirror with a tailored stop-band transition.

We measured the beam waist of the readout and drive lasers by using a modified knife-edge technique. An interferometer (NA, SIOS Meßtechnik, Ilmenau, Germany) tracked the position of the optics block as it was swept across a cantilever, and the sum signal from the photodiode was recorded. We inferred the spatial position of the focal spot relative to the optics block geometrically. An error function fit to the data yielded a beam waist measurement of 2.6 µm for the readout laser and 5.9 µm for the drive laser (Figure 2b). In contrast to other implementations [27,29,30], our choice of two closely-spaced laser wavelengths simplifies the simultaneous focusing of the two laser spots. For these beam waists, we calculate Rayleigh lengths of 33 µm and 160 µm, well within the estimated 13 µm chromatic focal shift of our optical system obtained by using Zemax 13 (Radiant Zemax LLC, Redmond, WA, USA).

While piezo-driven tapping mode imaging in liquid is used extensively in the literature, the strong dependence of the excitation efficiency on the geometry around the cantilever makes driving high-resonance-frequency cantilevers difficult or impossible. Changes in the surrounding liquid, which conducts acoustic energy from the piezo into the surrounding structures, can drastically alter the cantilever drive efficiency. These effects also make long term imaging difficult and hard to control. Localized excitation techniques such as photothermal excitation cause negligible ambient vibrations, therefore the excitation efficiency does not depend on the total liquid volume surrounding the cantilever and generally yields a much cleaner drive. Figure 3a illustrates this effect. A FastScan C cantilever (Bruker AFM Probes, Camarillo, CA, USA) was placed in a hanging water droplet and alternately driven with photothermal and piezo excitation. The first two resonant modes are clearly visible in the photothermally-driven amplitude signal, whereas they are hidden within the "forest of peaks" [37] in the piezo-driven amplitude signal. As the droplet dried over a period of approx. 100 min, the piezoelectric tune changed significantly, while the photothermal tune shows nearly no variation. In particular, the second resonance excitation (Figure 3a) increases by 50% to 100% under piezo excitation, but by only 3% under photothermal excitation.

We measured the ability of our system to drive and detect multiple cantilever eigenmodes at the corresponding high frequencies by using a FastScan A cantilever (Bruker AFM probes). Figure 3b shows the driven response of the cantilever with clearly detected resonant modes up to 20 MHz (blue curve). The first three flexural modes, the first two torsional modes, and a complex higher mode are visible. The lower part of Figure 3b shows clear phase shifts of 180° through each of the first three flexural resonances and the complex higher mode. Translating the drive laser focus spot can preferentially excite different resonant modes of the cantilever. We enhanced the excitation of the first two torsional modes by approximately one order of magnitude by placing the drive laser spot offset from the middle of the cantilever (red curve in Figure 3b). We

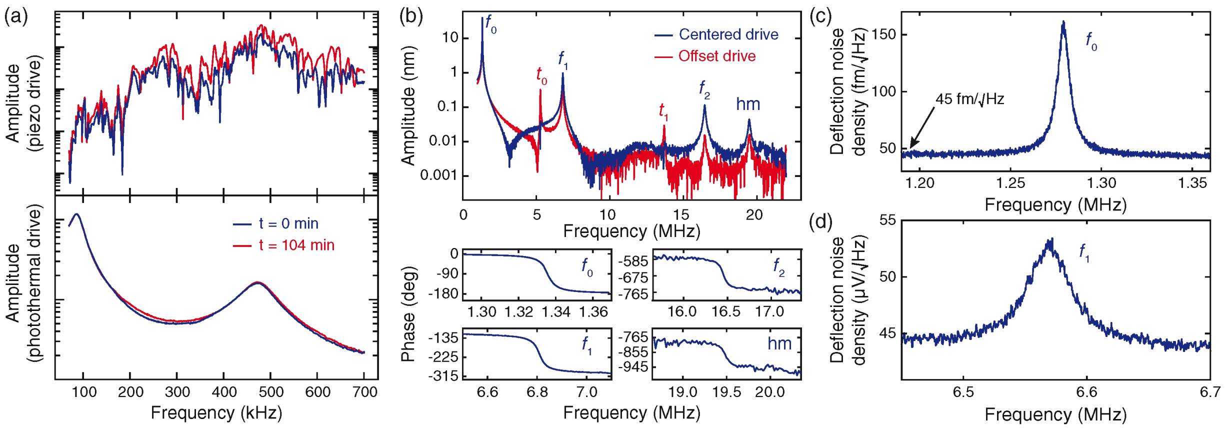

Figure 3: Cantilever drive and deflection readout characterization. a) In contrast to piezo excitation (top curves), photothermal excitation (lower curves) cleanly and consistently drives the first two resonances for more than 100 min. b) The photothermal tunes show resonances up to 19.5 MHz, demonstrating the wide bandwidth with clean phase responses for selected modes. By offsetting the drive laser laterally on a triangular cantilever (Bruker FastScan C), torsional resonances can be excited (red curve). Visible are the first three flexural modes (f_0, f_1 and f_2), the first two torsional modes (t_1 and t_2), and a complex higher resonant mode (hm). c) Thermal noise peak of the first flexural mode of a FastScan A cantilever, with a baseline noise floor of 45 fm/$\sqrt{\text{Hz}}$. d) Thermal noise peak of the second flexural mode of a FastScan A at 6.6 MHz.

confirmed our identification of the resonant modes by using a finite element model of the cantilever (Comsol 4.3b, Comsol, Inc., Burlington, MA, USA).

By using the thermal tune method and a FastScan A cantilever in air, we measured a baseline noise level of 45 $\text{fm}/\sqrt{\text{Hz}}$ for our deflection readout. Figure 3c shows the thermal noise peak of the first flexural mode, while Figure 3d shows the thermal noise peak of the second flexural mode. We expect that further optimization of our system for noise performance will decrease the baseline noise value further [35].

Dissipation imaging

Bimodal imaging

The capability for clean, high-frequency cantilever excitation, and low-noise, high-frequency deflection readout provide a powerful platform for extending multifrequency techniques to higher frequencies. For simultaneous high-frequency imaging and mechanical property mapping, we use a bimodal resonant technique which tracks topography in amplitude modulation on the first eigenmode [5,38]. This mode is one of the possibilities of achieving materials contrast while simultaneously tracking topography. The resonant excitation power needed to keep the second eigenmode at a specific amplitude is mapped, while a phase locked loop (PLL) ensures resonant excitation. Topography feedback deconvolutes material specific effects acting on the second resonance. As the resonant amplification is kept constant with the PLL, the amount of drive signal needed to keep the amplitude constant is proportional to the power dissipated in the tip–sample interaction. The power dissipation (P_{diss}) is calculated from the applied excitation signal ($V_{\text{ex}}\cdot\sin(2\pi f)$) and the intrinsic power dissipation of the cantilever (P_0) as

$$P_{\text{diss}} = P_0\cdot\left(\frac{V_{\text{ex}}}{V_0}-\frac{f}{f_0}\right), \qquad P_0 = \pi f_0\cdot\frac{k\cdot A^2}{Q}, \qquad (1)$$

where V_0 is the excitation voltage, f_0 the excitation frequency, k the spring constant, A the amplitude and Q the quality factor far from the surface [39]. The acquired dissipation is, to a first approximation, only dependent on the materials properties and the additional squeeze-film damping of the cantilever, the latter of which is roughly constant while in feedback.

We used a thin-film blend of polystyrene (PS) and poly(methyl methacrylate) (PMMA) as a sample (PS–PMMA–15M, Bruker AFM probes); its separation into soft and hard domains makes it a widely used standard for materials contrast imaging. For

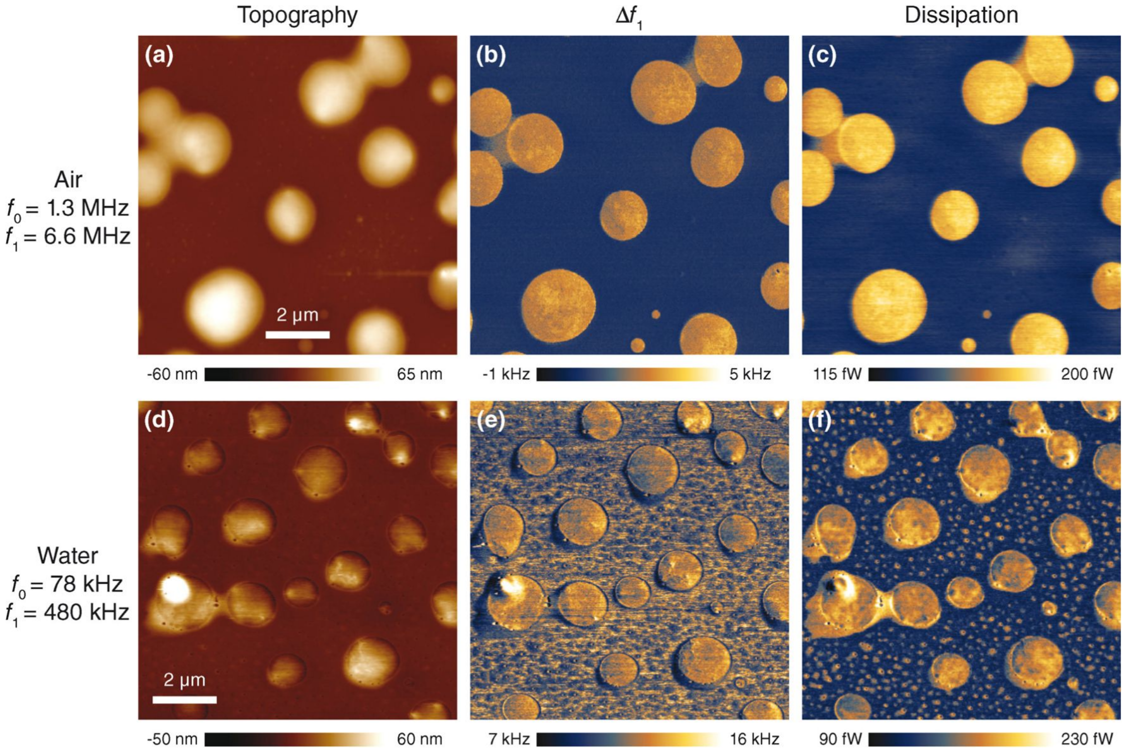

Figure 4: Bimodal AFM imaging of a PS/PMMA polymer blend with small, high-frequency cantilevers in both air (panels a–c) and water (panels d–f). Panels a and c show topography based on amplitude modulation of the fundamental resonance. Panels b and e show the resonance frequency shift of the first higher resonant mode, and panels c and f show the drive amplitude needed to keep the first higher resonant mode at constant amplitude, related to the energy dissipation in the tip–sample interaction.

imaging in air, we used a FastScan A cantilever with the fundamental and first higher flexural resonant modes at 1.3 MHz and 6.6 MHz, respectively. Figure 4a shows the resulting topography image, while Figure 4b and Figure 4c show the frequency shift and dissipation images, respectively. A clear difference in dissipative properties of the two phases can be observed, as is expected. For imaging in water, we used a FastScan C cantilever with drive frequencies at 78 kHz and 480 kHz for the fundamental and first higher resonant modes, respectively. Amplitudes of the first eigenmode were set to 8 nm free amplitude with a setpoint of around 50–60% for both air and water imaging. The second eigenmode was set to 54 pm in air and 86 pm in water. Figure 4d–f present the topography, frequency shift and dissipation images, respectively. The dissipation images show a very clear step contrast for the softer globular areas with no visible effects from the topography feedback. At present, we are uncertain of the source of the apparent contrast inversion at the edges of the globular areas in Figure 4d versus Figure 4a, although it may be due to surface restructuring of the polymer blend in water [40].

One issue of note is that higher eigenmodes have an inherently higher dynamic stiffness that can be up to two orders of magnitude larger than the fundamental mode. This can be problematic for softer samples, as the power dissipated into the sample increases linearly with the spring constant according to Equation 1. The increased optical lever sensitivity (OLS) of the second mode helps in being able to use smaller amplitudes, which reduces the power dissipation and, consequently, the damage to the sample. In order to improve the topography tracking, the bandwidth of the first eigenmode should be increased. Moving to smaller cantilevers allows for higher resonance frequencies which improves the detection bandwidth, while at the same time keeping spring constants low. In the case of imaging in a highly damped environment such as water, the bandwidth of the cantilever will increase due to viscous damping, however the detection bandwidth scales linearly with the dissipated power. The linear scaling is due to the fact that both the dissipated power (see Equation 1) and the cantilever AC-bandwidth, which is proportional to (f_0/Q), scale proportionally with the resonance frequency and inversely with the quality factor. The increased ratio of resonance frequency to spring constant makes it clear that the use of small cantilevers is ideally suited for low-dissipation imaging on multiple dynamic modes.

Drive amplitude modulation imaging

For biophysical imaging with atomic force microscopy, the ability to scan delicate samples in high resolution is required when investigating soft nanostructures. A related technique to the dissipation imaging described above, drive amplitude modulation (DAM) is an imaging mode that allows for the control of the dissipation in the AC-mode tip–sample interaction [41]. Figure 5a provides a schematic of the drive amplitude modulation imaging setup. By using a PLL in combination with an automatic gain controller, the amplitude of the first eigenmode of the cantilever is kept at a constant setpoint while the resonance frequency of the mode is tracked. The scanner feedback loop is then closed by enforcing a higher drive amplitude than the free drive amplitude. As the tip–sample distance decreases, the force interaction becomes stronger and energy is lost from the cantilever oscillation. By using this technique, the non-monotonic tip–surface interaction potential is mapped onto a monotonic function. By controlling for a constant energy loss in this way, soft imaging with very small amplitudes down to 100 pm can be realized; however, an unclean cantilever excitation can negatively impact the imaging. Our photothermal readout head provides the capability for a clean drive and thus enables this technique in water. Figure 5b demonstrates gentle imaging of a sample of F-actin fibres deposited on a (3-aminopropyl)triethoxysilane-coated glass surface in liquid. F-actin is a fibre-forming protein that plays a role in the cytoskeleton.

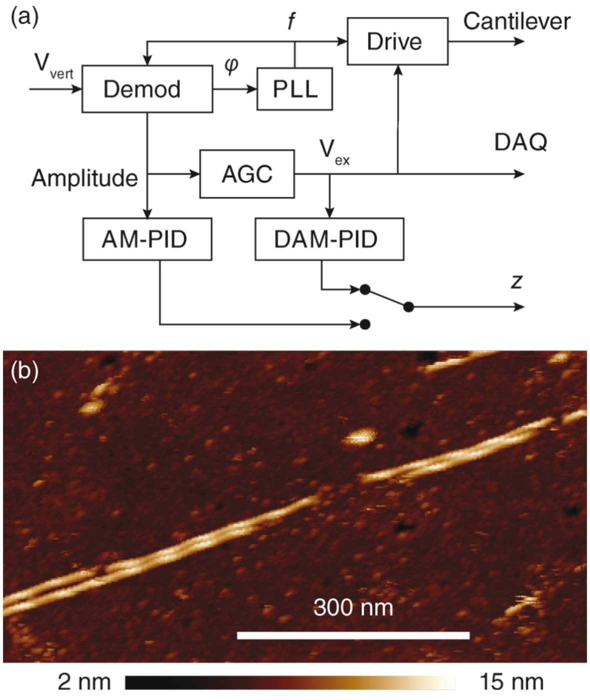

Figure 5: a) Schematic of the drive amplitude modulation feedback compared with standard amplitude modulation imaging. Instead of using the oscillation amplitude as feedback variable like in conventional amplitude modulation mode, the oscillation amplitude is kept constant and the drive amplitude required to keep it constant is used as feedback variable. The drive is then enforced to a setpoint above the free drive, resulting in a stable topography feedback. b) High-resolution DAM imaging in liquid of soft F-actin fibres on (3-aminopropyl)triethoxysilane coated glass. Both the sub- and superstructure of the protein are visible.

F-actin filaments are a notoriously difficult sample for AFM due to their fragility and quick contamination of the cantilever tip. Thus far, successful AFM imaging reports have used either extremely soft cantilevers or hopping-mode imaging methods with very low trigger forces [42-44]. By using our system we were successfully able to take high resolution images of deposited fibres showing the helical structure of the fibre and an underlying substructure related to the individual protein subunits. Even by using a comparatively stiff cantilever for biological imaging (k = 0.8 N·m^{-1}) with a high resonance frequency in fluid, there was little apparent imaging damage to the structure once the feedback gains were adjusted properly.

Conclusion

Imaging gently and quickly is a constant challenge in AFM. Small cantilevers are well suited to low-dissipation imaging, especially in multifrequency imaging modes, since the spring constants of higher eigenmodes can be kept at reasonable values without sacrificing imaging bandwidth. However, their application in multifrequency techniques has been restricted due to instrument capability limitations. By using photothermal actuation of small cantilevers along with a current-based deflection readout, we have shown bimodal imaging of a polymer blend in both air and liquid, with amplitudes of the second mode well below a nanometre at previously inaccessible cantilever resonance frequencies. We furthermore demonstrated gentle, low-dissipation imaging of F-actin in drive amplitude modulation mode with oscillation amplitude below 1 nm. We believe that the combination of small cantilevers, clean photothermal actuation and high-frequency, low-noise deflection readout will be of great benefit for multifrequency AFM imaging faster and with less tip–sample dissipation.

Experimental

Optical beam deflection setup

In our optical beam deflection system, we combine a collimated 5 mW 637 nm readout laser diode (HL6355MG, Conrad, Dietikon, Switzerland) and a 50 mW 685 nm drive laser diode (HL6750MG, Thorlabs, Newton, NJ, USA) by using a 650 nm short-pass dichroic mirror (69-218, Edmund Optics, Barrington, NJ, USA). The laser diodes are each collimated in individual housings by using an aspheric lens (A390-A, Thorlabs). The readout laser diode is driven from an external commercial laser diode driver (LDX3412, ILX Lightwave, Irvine, CA, USA) and modulated with a custom-built push–pull oscillator circuit (EL6204, Intersil, Milpitas, CA). The incident and reflected beam paths are spatially separated such that they use separate parts of the focussing lens (A390-A, Thorlabs). A right angle mirror (48-383, Edmund Optics) redirects the reflected laser beams towards a quadrant photodiode (S4349, Hamamatsu, Hamamatsu City, Japan). A 625 nm centre wavelength 50 nm bandpass filter (86-941, Edmund Optics) blocks the drive laser beam from the quadrant photodiode. 0.20 mm pitch adjustment screws (F2D5ES10, Thorlabs) permit translation of the drive laser focal spot with approximately 0.34 μm and 0.18 μm per degree of screw rotation along the cantilever length and width, respectively.

Actin filament preparation

A 12 mm diameter glass coverslip (Novoglas Labortechnik) was cleaned with piranha solution (1:3 ratio of hydrogen peroxide to sulphuric acid), rinsed with distilled water and dried by a nitrogen stream. The coverslip was then immersed in a solution of (3-aminopropyl)triethoxysilane (0.5% in water) (A3648, Sigma-Aldrich, St. Louis, MO, USA) for 10 min then rinsed. The coverslip was then dried in an oven for approximately one hour at 65 °C in a vertical position and subsequently glued onto a steel disc for imaging. F-actin was prepared according to the protocol of the manufacturer (BK003, Cytoskeleton, Inc., Denver, CO, USA). An amount of 1 μL F-actin was stabilized with 3 μL Alexa Fluor 488 Phalloidin (A12379, Life Technologies, Carlsbad, CA, USA) and diluted to a final volume of 40 μL in buffer (2 mM $MgCl_2$, 1 mM EGTA, 20 mM imidazole·HCl, pH 7.6). Of this, 10 μL was deposited onto the coverslip and incubated for one minute before more buffer was added onto the sample prior to imaging.

Dissipation imaging setup

The imaging modes as described in section “Dissipation imaging” were implemented by using a commercial controller (Nanoscope 5, Bruker) in combination with a digital high-frequency multifunction instrument (UHFLI, Zurich Instruments, Zurich, Switzerland), interfaced via a signal access module (SAM III, Bruker). The scan generation and data acquisition is handled by the AFM controller while feedback and PLL are provided by the multifunction instrument. A custom-built wideband up/down-scaling amplifier provides voltage level compatibility between the two components. The vertical signal from the detector is accessed directly from the detector via a 50 Ω coax cable and wired to the downscaler and the AFM controller. A external high-voltage amplifier, identical to the one in the Nanoscope 5 controller, is driven off the multifunction instrument to displace the piezo tube in the z-direction.

The dissipation images are calibrated by Equation 1. Since the amplitude of the second eigenmode is difficult to calibrate by approach curves due to the motion of the first eigenmode, we estimate the difference in sensitivity from eigenmode calculations using finite element analysis. We find the ratio of the second eigenmode OLS with respect to the first eigenmode OLS to be a factor 5.85 and 6.0 for the FastScan A and FastScan C cantilevers, respectively. The spring constants of the two cantilevers are calibrated by using the thermal noise method. We measure $k_0 = 15.4\ \mathrm{N{\cdot}m^{-1}}$, $k_1 = 470\ \mathrm{N{\cdot}m^{-1}}$ for the first and second eigenmode of the used FastScan A and $k_0 = 0.85\ \mathrm{N{\cdot}m^{-1}}$, $k_1 = 94\ \mathrm{N{\cdot}m^{-1}}$ analogous for the FastScan C cantilever. We calculate $P_0 = 176$ fW for a 54 pm amplitude in air with the FastScan A and $P_0 = 150$ fW for a 86 pm amplitude in water with the FastScan C. Stock coatings were used (approx. 100 nm Al for the FastScan A and approx. 60 nm Ti/Au for the FastScan C).

Acknowledgements

We thank the Atelier de l'institut de production et robotique at EPFL for fabrication of the mechanical components, Aleksandra Radenovic for use of the spectrometer, and SCL-Sensor.tech. for use of the interferometer. This work was funded by the European Union's Seventh Framework Programme FP7/2007-2011 under grant agreement 286146 and the European Union's Seventh Framework Programme FP7/2007-2013/ERC grant agreement 307338, European Community and EUREKA through Eurostars E!8213 TRIPLE-S Microscope, and the Swiss National Science Foundation through grants 205321_134786 and 205320_152675.

References

1. Proksch, R. *Appl. Phys. Lett.* **2006,** *89,* 113121. doi:10.1063/1.2345593
2. García, R.; Magerle, R.; Perez, R. *Nat. Mater.* **2007,** *6,* 405–411. doi:10.1038/nmat1925
3. Pittenger, B.; Erina, N.; Su, C. Quantitative mechanical property mapping at the nanoscale with PeakForce QNM – Application Note Veeco Instruments, Inc. http://www.veeco.com/pdfs/appnotes/Quantitative-Mechanical-Property-Mapping-at-the-Nanoscale-with-PeakForce-QNM-AN128-LoRes.pdf (accessed Sept 1, 2014).
4. Jesse, S.; Kalinin, S. V. *J. Phys. D: Appl. Phys.* **2011,** *44,* 464006. doi:10.1088/0022-3727/44/46/464006
5. Garcia, R.; Herruzo, E. T. *Nat. Nanotechnol.* **2012,** *7,* 217–226. doi:10.1038/nnano.2012.38
6. Dufrêne, Y. F.; Martínez-Martín, D.; Medalsy, I.; Alsteens, D.; Müller, D. J. *Nat. Methods* **2013,** *10,* 847–854. doi:10.1038/nmeth.2602
7. Martinez-Martin, D.; Herruzo, E. T.; Dietz, C.; Gomez-Herrero, J.; Garcia, R. *Phys. Rev. Lett.* **2011,** *106,* 198101. doi:10.1103/PhysRevLett.106.198101
8. Platz, D.; Forchheimer, D.; Tholén, E. A.; Haviland, D. B. *Nat. Commun.* **2013,** *4,* No. 1360. doi:10.1038/ncomms2365
9. Herruzo, E. T.; Perrino, A. P.; Garcia, R. *Nat. Commun.* **2014,** *5,* No. 3126. doi:10.1038/ncomms4126
10. Walters, D. A.; Cleveland, J. P.; Thomson, N. H.; Hansma, P. K.; Wendman, M. A.; Gurley, G.; Elings, V. *Rev. Sci. Instrum.* **1996,** *67,* 3583–3590. doi:10.1063/1.1147177
11. Fantner, G. E.; Schitter, G.; Kindt, J. H.; Ivanov, T.; Ivanova, K.; Patel, R.; Holten-Andersen, N.; Adams, J.; Thurner, P. J.; Rangelow, I. W.; Hansma, P. K. *Ultramicroscopy* **2006,** *106,* 881–887. doi:10.1016/j.ultramic.2006.01.015
12. Ando, T.; Kodera, N.; Takai, E.; Maruyama, D.; Saito, K.; Toda, A. *Proc. Natl. Acad. Sci. U. S. A.* **2001,** *98,* 12468–12472. doi:10.1073/pnas.211400898
13. Ando, T.; Uchihashi, T.; Fukuma, T. *Prog. Surf. Sci.* **2008,** *83,* 337–437. doi:10.1016/j.progsurf.2008.09.001
14. Fantner, G. E.; Barbero, R. J.; Gray, D. S.; Belcher, A. M. *Nat. Nanotechnol.* **2010,** *5,* 280–285. doi:10.1038/nnano.2010.29
15. Kodera, N.; Yamamoto, D.; Ishikawa, R.; Ando, T. *Nature* **2010,** *468,* 72–76. doi:10.1038/nature09450
16. Uchihashi, T.; Iino, R.; Ando, T.; Noji, H. *Science* **2011,** *333,* 755–758. doi:10.1126/science.1205510
17. Braunsmann, C.; Seifert, J.; Rheinlaender, J.; Schäffer, T. E. *Rev. Sci. Instrum.* **2014,** *85,* 073703. doi:10.1063/1.4885464
18. Viani, M. B.; Schäffer, T. E.; Chand, A.; Rief, M.; Gaub, H. E.; Hansma, P. K. *J. Appl. Phys.* **1999,** *86,* 2258–2262. doi:10.1063/1.371039
19. Viani, M. B.; Schäffer, T. E.; Paloczi, G. T.; Pietrasanta, L. I.; Smith, B. L.; Thompson, J. B.; Richter, M.; Rief, M.; Gaub, H. E.; Plaxco, K. W.; Cleland, N.; Hansma, H. G.; Hansma, P. K. *Rev. Sci. Instrum.* **1999,** *70,* 4300. doi:10.1063/1.1150069
20. Han, W.; Lindsay, S. M.; Jing, T. *Appl. Phys. Lett.* **1996,** *69,* 4111. doi:10.1063/1.117835
21. Fantner, G. E.; Burns, D. J.; Belcher, A. M.; Rangelow, I. W.; Youcef-Toumi, K. *J. Dyn. Syst., Meas., Control* **2009,** *131,* 061104. doi:10.1115/1.4000378
22. Sulchek, T.; Hsieh, R.; Adams, J. D.; Yaralioglu, G. G.; Minne, S. C.; Quate, C. F.; Cleveland, J. P.; Atalar, A.; Adderton, D. M. *Appl. Phys. Lett.* **2000,** *76,* 1473. doi:10.1063/1.126071
23. Umeda, N.; Ishizaki, S.; Uwai, H. *J. Vac. Sci. Technol., B* **1991,** *9,* 1318–1322. doi:10.1116/1.585187
24. Ratcliff, G. C.; Erie, D. A.; Superfine, R. *Appl. Phys. Lett.* **1998,** *72,* 1911. doi:10.1063/1.121224
25. Jayanth, G. R.; Jeong, Y.; Menq, C.-H. *Rev. Sci. Instrum.* **2006,** *77,* 053704. doi:10.1063/1.2200874
26. Ramos, D.; Tamayo, J.; Mertens, J.; Calleja, M. *J. Appl. Phys.* **2006,** *99,* 124904. doi:10.1063/1.2205409
27. Fukuma, T. *Rev. Sci. Instrum.* **2009,** *80,* 023707. doi:10.1063/1.3086418
28. Nishida, S.; Kobayashi, D.; Sakurada, T.; Nakazawa, T.; Hoshi, Y.; Kawakatsu, H. *Rev. Sci. Instrum.* **2008,** *79,* 123703. doi:10.1063/1.3040500
29. Labuda, A.; Kobayashi, K.; Miyahara, Y.; Grütter, P. *Rev. Sci. Instrum.* **2012,** *83,* 053703. doi:10.1063/1.4712286
30. Adam, H.; Rode, S.; Schreiber, M.; Kobayashi, K.; Yamada, H.; Kühnle, A. *Rev. Sci. Instrum.* **2014,** *85,* 023703. doi:10.1063/1.4864084
31. Kiracofe, D. R.; Yazdanpanah, M. M.; Raman, A. *Nanotechnology* **2011,** *22,* 295504. doi:10.1088/0957-4484/22/29/295504
32. Dupas, E.; Gremaud, G.; Kulik, A.; Loubet, J.-L. *Rev. Sci. Instrum.* **2001,** *72,* 3891. doi:10.1063/1.1403009
33. Fukuma, T.; Kimura, K.; Kobayashi, K.; Matsushige, K.; Yamada, H. *Appl. Phys. Lett.* **2004,** *85,* 6287. doi:10.1063/1.1842368
34. Kawai, S.; Kawakatsu, H. *Appl. Phys. Lett.* **2006,** *88,* 133103. doi:10.1063/1.2189193
35. Enning, R.; Ziegler, D.; Nievergelt, A.; Friedlos, R.; Venkataramani, K.; Stemmer, A. *Rev. Sci. Instrum.* **2011,** *82,* 043705. doi:10.1063/1.3575322
36. Adams, J. D.; Nievergelt, A.; Erickson, B. W.; Yang, C.; Dukic, M.; Fantner, G. E. *Rev. Sci. Instrum.* **2014,** *85,* 093702. doi:10.1063/1.4895460

37. Schäffer, T. E.; Cleveland, J. P.; Ohnesorge, F.; Walters, D. A.; Hansma, P. K. *J. Appl. Phys.* **1996,** *80,* 3622. doi:10.1063/1.363308
38. Ebeling, D.; Solares, S. D. *Beilstein J. Nanotechnol.* **2013,** *4,* 198–207. doi:10.3762/bjnano.4.20
39. Loppacher, C.; Bennewitz, R.; Pfeiffer, O.; Guggisberg, M.; Bammerlin, M.; Schaer, S.; Barwich, V.; Baratoff, A.; Meyer, E. *Phys. Rev. B* **2000,** *62,* 13674–13679. doi:10.1103/PhysRevB.62.13674
40. Woodcock, S. E.; Chen, C.; Chen, Z. *Langmuir* **2004,** *20,* 1928–1933. doi:10.1021/la035698j
41. Jaafar, M.; Martínez-Martín, D.; Cuenca, M.; Melcher, J.; Raman, A.; Gómez-Herrero, J. *Beilstein J. Nanotechnol.* **2012,** *3,* 336–344. doi:10.3762/bjnano.3.38
42. Lehto, T.; Miaczynska, M.; Zerial, M.; Müller, D. J.; Severin, F. *FEBS Lett.* **2003,** *551,* 25–28. doi:10.1016/S0014-5793(03)00867-6
43. Sharma, S.; Grintsevich, E. E.; Phillips, M. L.; Reisler, E.; Gimzewski, J. K. *Nano Lett.* **2011,** *11,* 825–827. doi:10.1021/nl104159v
44. Schmitz, S.; Schaap, I. A. T.; Kleinjung, J.; Harder, S.; Grainger, M.; Calder, L.; Rosenthal, P. B.; Holder, A. A.; Veigel, C. *J. Biol. Chem.* **2010,** *285,* 36577–36585. doi:10.1074/jbc.M110.142638

License and Terms

The definitive version of this article is the electronic one which can be found at:
doi:10.3762/bjnano.5.255

BEILSTEIN JOURNAL OF NANOTECHNOLOGY

Accurate, explicit formulae for higher harmonic force spectroscopy by frequency modulation-AFM

Kfir Kuchuk and Uri Sivan[*]

Letter

Address:
Department of Physics and The Russell Berrie Nanotechnology Institute, Technion – Israel Institute of Technology, Haifa 32000, Israel

Email:
Uri Sivan[*] - phsivan@tx.technion.ac.il

* Corresponding author

Keywords:
atomic force spectroscopy; higher harmonic FM-AFM

Beilstein J. Nanotechnol. **2015,** *6,* 149–156.
doi:10.3762/bjnano.6.14

Received: 07 August 2014
Accepted: 09 December 2014
Published: 13 January 2015

This article is part of the Thematic Series "Advanced atomic force microscopy techniques III".

Guest Editor: T. Glatzel

Abstract

The nonlinear interaction between an AFM tip and a sample gives rise to oscillations of the cantilever at integral multiples (harmonics) of the fundamental resonance frequency. The higher order harmonics have long been recognized to hold invaluable information on short range interactions but their utilization has thus far been relatively limited due to theoretical and experimental complexities. In particular, existing approximations of the interaction force in terms of higher harmonic amplitudes generally require simultaneous measurements of multiple harmonics to achieve satisfactory accuracy. In the present letter we address the mathematical challenge and derive accurate, explicit formulae for both conservative and dissipative forces in terms of an arbitrary single harmonic. Additionally, we show that in frequency modulation-AFM (FM-AFM) each harmonic carries complete information on the force, obviating the need for multi-harmonic analysis. Finally, we show that higher harmonics may indeed be used to reconstruct short range forces more accurately than the fundamental harmonic when the oscillation amplitude is small compared with the interaction range.

Introduction

AFM measurements are presently utilized to generate atomic resolution [1,2], 3D force maps that carry unprecedented information on the interfacial properties of soft matter [3], water structure [1,2] and ion ordering [4]. The generation of such force maps relies invariably on AC detection methods, most commonly at frequencies in the vicinity of the cantilever's fundamental resonance frequency. In frequency modulation-AFM (FM-AFM), the force is usually reconstructed from the resonance frequency shift, which in the small amplitude regime is proportional to the derivative of the force with respect to tip–surface distance. Similarly, it has been recognized that higher harmonics generated by the nonlinear tip–surface interaction (to be distinguished from higher flexural modes of the cantilever) are related to higher derivatives of the force, and thus carry additional information on the interaction [5-11]. Broad implementation of force spectroscopy by analysing higher harmonics has been nevertheless impeded by the lack of a closed-form expression for the force in terms of measured quantities, namely, the lack of a higher harmonics analogue of the Sader–Jarvis formula for the fundamental harmonic [12,13]. In the present letter we fill this gap by providing such formulae for both conservative and dissipative forces.

In FM-AFM, a cantilever is oscillated at its resonance frequency using an external driving force and a feedback loop. The motion of the cantilever is often modelled as a driven damped harmonic oscillator with an additional force, F_{ts}, stemming from tip–surface interaction

$$\frac{k}{\omega_0^2}\ddot{q}+\gamma\dot{q}+kq=F_0\sin(\omega t)+F_{\text{ts}}(q,\dot{q},t). \qquad (1)$$

Here, k is the effective cantilever spring constant, ω_0 is the fundamental resonance frequency in the absence of tip–surface interaction, $q(t)$ is the tip position, γ is the damping coefficient, and F_0 and ω are the amplitude and frequency of the driving force, respectively. As the cantilever is brought close to a surface, the tip–surface interaction forces shift the resonance frequency. The relation between the frequency shift and F_{ts}, in the case where the force depends only on tip position, was first derived by Giessibl as [14]

$$\frac{\Delta\omega}{\omega_0}=\frac{1}{\pi ak}\int_{-1}^{1}F_{\text{ts}}(z+a(1+u))\frac{u}{\sqrt{1-u^2}}du. \qquad (2)$$

Here, $\Delta\omega$ is the frequency shift, a is the oscillation amplitude and z is the distance of closest approach to the surface in the oscillation cycle. Various techniques have been proposed to invert the convolution in Equation 2 and extract the interaction force from the measured shift in frequency. At first, these were either numerical solutions or analytic approximations of large or small amplitudes [15], but later Sader and Jarvis derived an interpolation formula which is valid for all amplitudes [12,13] (the Sader–Jarvis formula). Its application has also been extended to AM-AFM [16].

Expressions similar to Equation 2, relating the Fourier components of higher harmonics to a convolution over F_{ts}, have been derived [15,17], but existing methods to recover F_{ts} from higher harmonics rely on spectral analysis of the AFM signal [18,19], and require the measurement of a significant number of harmonics to obtain reasonable accuracy [5,17]. Although measurement of all spectral components would theoretically enable fast reconstruction of the force while scanning, the simultaneous acquisition of many harmonics is demanding and requires multiple lock-in amplifiers. For the generation of 3D force maps, the multi-harmonic reconstruction is further complicated since multiple scans must be performed at different heights. Additionally, higher harmonic amplitudes decrease rapidly with harmonic number, limiting the number of measurable harmonics and, hence, the accuracy of force reconstruction. Some methods to amplify the signals of higher harmonics have been exercised [6,20], but these do not completely alleviate the problem. Here, we show that a full force curve can be extracted from the amplitude of any single higher harmonic. We provide simple, explicit expressions for the interaction force in terms of higher harmonic amplitudes, allowing the benefits of high-harmonics force spectroscopy with no need for multiple-harmonics measurements and analysis.

There are several advantages to be gained by expressing the force as a function of higher harmonic amplitudes. First, the existence of these amplitudes depends entirely on the presence of nonlinear interaction forces. Higher harmonic amplitudes may therefore be measured with greater precision compared with fundamental harmonic measurements. While the former are measured with reference to zero, the latter are obtained by offsetting large, inherently noisy signals, such as the driving frequency in FM-AFM or oscillation amplitude in AM-AFM. Second, there is evidence [5-11] that higher harmonics are more sensitive to short-range forces than the fundamental harmonic. This becomes evident when the cantilever oscillation amplitude is small compared with the interaction length. As we show, the frequency shift in this case is related to the first derivative of the force, while higher harmonics are related to higher derivatives. The nth harmonic therefore probes directly the nth derivative of the force, enhancing the sensitivity to short range forces. The main difficulty in measuring higher harmonics is their small magnitude due to the weak response of the cantilever to frequencies far from its resonance. At these frequencies, the noise in well-designed AFMs is dominated by the shot noise of the photodiode in the optical detection system. The SNR of higher harmonic amplitudes is therefore expected to deteriorate with harmonic order, but in many cases a significant number of higher harmonics can still be measured [10,21]. Unlike previous higher harmonic reconstruction methods, the disclosed scheme can be applied also to cases where only a few harmonics are measurable.

Results and Discussion

Consider Equation 1 with the interaction force expressed by its Fourier components:

$$\frac{k}{\omega_0^2}\ddot{q}+\gamma\dot{q}+kq=F_0\sin(\omega\,\mathrm{t}) \\ +\sum_{n=1}^{\infty}a_n\cos(\mathrm{n}\omega t)+\sum_{n=1}^{\infty}b_n\sin(\mathrm{n}\omega t). \qquad (3)$$

The cantilever motion is assumed to be nearly that of a free harmonic oscillator with small harmonic contributions, μ_n and ν_n, generated by the nonlinear tip–surface interaction

$$q(t)=a\cos(\omega t)+\sum_{n=1}^{\infty}\mu_n\cos(\mathrm{n}\omega t)+\sum_{n=1}^{\infty}\nu_n\sin(\mathrm{n}\omega t), \qquad (4)$$

with μ_n/a and $\nu_n/a \ll 1$ for all n.

We begin by analysing the even, conservative part of the force [13], which depends only on tip–sample separation. Substituting Equation 4 into Equation 3 and using orthogonality, one arrives at the relation

$$a_n=k\frac{(\omega_0^2-n^2\omega^2)}{\omega_0^2}\mu_n+n\gamma\omega\nu_n. \qquad (5)$$

Using the definition of a_n and changing variables one finds

$$\Pi_n(z)=\int_{-1}^{1}F_{\text{even}}\left(z+a(1+u)\right)\frac{T_n(u)}{\sqrt{1-u^2}}du, \qquad (6)$$

where

$$\Pi_n(z)\equiv\frac{\pi}{2}\left[\frac{k}{\omega_0^2}\left(\omega_0^2-n^2\omega^2\right)\mu_n+n\gamma\omega\nu_n\right], \qquad (7)$$

and $T_n(u)=\cos(n\cos^{-1}(u))$ is the nth order Chebyshev polynomial of the first kind. As expected, by setting $\gamma=0$ in (7), we recover the result obtained by Dürig [17].

To invert the integral in Equation 6 and express the force in terms of the measured amplitudes μ_n and ν_n, we generalize the derivation of the Sader–Jarvis formula [12] to an arbitrary harmonic, n. First, we express F_{even} in terms of its inverse Laplace transform, $\tilde{F}(\lambda)$:

$$\Pi_n(z)=\int_0^{\infty}\tilde{F}(\lambda)e^{-\lambda z}\int_{-1}^{1}e^{-\lambda a(u+1)}\frac{T_n(u)}{\sqrt{1-u^2}}du\,d\lambda. \qquad (8)$$

Using the integral representation [22] of I_n, the nth order, modified Bessel function of the first kind, along with the Rodrigues' representation [22] of T_n,

$$I_n(x)=\frac{(x/2)^n}{\pi^{1/2}\Gamma(n+1/2)}\int_{-1}^{1}(1-t^2)^{n-1/2}e^{\pm xt} \\ T_n(x)=\frac{(-1)^n\sqrt{\pi}(1-x^2)^{1/2}}{2^n\Gamma(\mathrm{n}+1/2)}\frac{d^n}{dx^n}(1-x^2)^{n-1/2}, \qquad (9)$$

the integral over u can be evaluated

$$\Pi_n(z)=\int_0^{\infty}\pi e^{-\lambda a}(-1)^n I_n(\lambda a)\tilde{F}(\lambda)e^{-\lambda z}d\lambda. \qquad (10)$$

Comparison between Π_n and F_{even} in Laplace space shows that

$$F_{\text{even}}(z)=L\left\{B_n(\lambda a)L^{-1}\left\{\Pi_n(z)\right\}\right\}, \qquad (11)$$

where $B_n(x)=(-1)^n e^x/\pi I_n(x)$. Making use of the asymptotic forms [22] of I_n, an approximation to $B_n(x)$ is constructed

$$B_n^{\text{approx}}(x)=\frac{(-1)^n n!}{\pi}\left(\frac{x}{2}\right)^{-n}\left(1+\sum_{\mathrm{i}}c_{\mathrm{i}}x^{d_{\mathrm{i}}} \right. \\ \left. +\frac{\sqrt{2\pi}}{2^n n!}x^{n+1/2}\right). \qquad (12)$$

For $0<d_{\mathrm{i}}<n+1/2$, Equation 12 has the correct asymptotic behaviour for very small and very large x. An arbitrary number of terms of the form $c_{\mathrm{i}}x^{d_{\mathrm{i}}}$, for some set of coefficients c_{i}, can be fitted to improve the accuracy of Equation 12 as needed. This is in fact what the Sader–Jarvis formula does for the fundamental harmonic – it interpolates between the regimes of large and

small amplitudes, where analytic solutions exist, by fitting terms in the intermediate regime.

Substituting Equation 12 into Equation 11 and using the following results of fractional calculus [12],

$$I_-^{\alpha} g(\lambda) \equiv \frac{1}{\Gamma(\alpha)} \int_{\lambda}^{\infty} \frac{g(\tau)}{(\tau-\lambda)^{1-\alpha}} d\tau$$

$$D_-^{\alpha} g(\lambda) \equiv \frac{(-1)^m}{\Gamma(m-\alpha)} \frac{d^m}{d\lambda^m} \int_{\lambda}^{\infty} \frac{g(\tau)}{(\tau-\lambda)^{\alpha-m+1}} d\tau \qquad (13)$$

$$L\left\{\lambda^{-\alpha} Y(\lambda)\right\} = I_-^{\alpha}\, L\{Y(\lambda)\}$$

$$L\left\{\lambda^{\alpha} Y(\lambda)\right\} = D_-^{\alpha}\, L\{Y(\lambda)\},$$

where $\alpha > 0$ and $m = [\alpha] + 1$, the force is expressed explicitly in terms of the interpolation parameters c_{i}, d_{i}. In particular, if d_{i} are chosen to be integers, the force is given by

$$F_{\mathrm{even}}(z) = \frac{1}{\pi}(-1)^n 2^n n! \left(a^{-n} I_-^{\,n} + \sum_{i=1}^{n-1} c_{\mathrm{i}} a^{-(n-i)} I_-^{\,n-i} + c_n + \frac{a^{1/2}\sqrt{2\pi}}{2^n n!} D_-^{\,1/2} \right) \Pi_n. \qquad (14)$$

The force may thus be derived in terms of any harmonic, provided that the interpolation coefficients c_{i} approximate B_n sufficiently well. Explicit formulae for the force in terms of harmonics 2–6 of the fundamental frequency are given in Table 1, where the interpolation coefficients were calculated such that $\left|B_n - B_n^{\mathrm{approx}}\right| / \left|B_n\right| < 2\%$ for all positive x. The force formulae in terms of other higher harmonics may be derived in a similar way. In the special case $n = 2$ (Equation 15),

$$F_{\mathrm{even}}(z) = \frac{0.8}{\pi}\Pi_2(z) + \frac{1}{\pi}\int_z^{\infty} \left[\left(8.8a^{-1} + 8a^{-2}(\tau - z) \right) \Pi_2(\tau) - \frac{\sqrt{2}a^{1/2}}{(\tau - z)^{1/2}} \frac{d\Pi_2(\tau)}{d\tau} \right] d\tau. \qquad (15)$$

A similar procedure can be applied to recover the odd, dissipative, part of the force from higher harmonics, but a subtlety must first be addressed. The derivation of F_{even} relies on its sole dependence upon tip–sample separation in Equation 6. This is not the case for F_{odd}, which is out of phase with $q(t)$. This issue is resolved by noting that many dissipative forces have the form [13]

$$F_{\mathrm{odd}}(q, \dot{q}, t) = \Gamma(q)\dot{q} \qquad (16)$$

with Γ, the generalised damping coefficient, depending only upon tip–sample separation. It then follows from Equation 3 that

$$\Lambda_n(z) = \frac{a}{n} \int_{-1}^{1} \Gamma(z + a(1+u)) U_{n-1}(u) \sqrt{1-u^2}\, du, \qquad (17)$$

where $U_{n-1}(u) = \sin(n \cos^{-1} u) / \sin(\cos^{-1} u)$ is the nth order Chebyshev polynomial of the second kind and

$$\Lambda_n(z) \equiv -\frac{\pi}{2n\omega}\left[k \frac{\omega_0^2 - n^2\omega^2}{\omega_0^2} \nu_n - n\gamma\omega\mu_n \right]. \qquad (18)$$

Integrating by parts and using the identity $(x^2-1)U'_{n-1} = nT_n(x) - xU_{n-1}(x)$, Equation 17 assumes the form

$$\Lambda_n(z) = \int_{-1}^{1} H(z + a(1+u)) \frac{T_n(u)}{\sqrt{1-u^2}} du, \qquad (19)$$

where $H(x) = -\int_x^{\infty} \Gamma(s) ds$. Comparing Equation 19 with Equation 6, we see that these expressions are identical and therefore have the same solutions. We may then refer to Table 1 for these solutions. For example, using Equation 15, the formula for the generalized damping coefficient for $n = 2$ is readily derived as (Equation 20):

$$\Gamma(z) = \frac{d}{dz}\left\{ \frac{0.8}{\pi}\Lambda_2(z) + \frac{1}{\pi}\int_z^{\infty} \left[\left(8.8a^{-1} + 8a^{-2}(\tau - z) \right) \Lambda_2(\tau) - \frac{\sqrt{2}a^{1/2}}{(\tau - z)^{1/2}} \frac{d\Lambda_2(\tau)}{d\tau} \right] d\tau \right\}. \qquad (20)$$

Table 1: Formulae for the force in terms of harmonics 1–6. The Sader–Jarvis formula for *n* = 1 is given here for completeness. An implementation of these formulae is available in the supplementary Mathematica file.

n	F_{even} in terms of the *n*th harmonic
1	$F_{\text{even}}(z) = 2ka\left(a^{-1}I_-^{1} + \frac{a^{-1/2}}{8}I_-^{1/2} + a^{1/2}\sqrt{\frac{\pi}{2}}D_-^{1/2}\right)\frac{\Delta\omega}{\omega_0}$
2	$F_{\text{even}}(z) = \frac{8}{\pi}\left(a^{-2}I_-^{2} + 1.1a^{-1}I_-^{1} + 0.1 + \frac{a^{1/2}\sqrt{2\pi}}{8}D_-^{1/2}\right)\Pi_2$
3	$F_{\text{even}}(z) = -\frac{48}{\pi}\left(\begin{array}{l} a^{-3}I_-^{3} + 0.89a^{-2}I_-^{2} + 0.58a^{-1}I_-^{1} + 0.024 \\ + \frac{a^{1/2}\sqrt{2\pi}}{48}D_-^{1/2} \end{array}\right)\Pi_3$
4	$F_{\text{even}}(z) = \frac{384}{\pi}\left(\begin{array}{l} a^{-4}I_-^{4} + 1.05a^{-3}I_-^{3} + 0.31a^{-2}I_-^{2} + 0.18a^{-1}I_-^{1} \\ +0.004 + \frac{a^{1/2}\sqrt{2\pi}}{384}D_-^{1/2} \end{array}\right)\Pi_4$
5	$F_{\text{even}}(z) = -\frac{3840}{\pi}\left(\begin{array}{l} a^{-5}I_-^{5} + 0.98a^{-4}I_-^{4} + 0.56a^{-3}I_-^{3} + 0.049a^{-2}I_-^{2} \\ +0.0375a^{-1}I_-^{1} + 0.0005 + \frac{a^{1/2}\sqrt{2\pi}}{3840}D_-^{1/2} \end{array}\right)\Pi_5$
6	$F_{\text{even}}(z) = \frac{46080}{\pi}\left(\begin{array}{l} a^{-6}I_-^{6} + 0.96a^{-5}I_-^{5} + 0.469a^{-4}I_-^{4} + 0.185a^{-3}I_-^{3} \\ +0.0022a^{-2}I_-^{2} + 0.0058a^{-1}I_-^{1} + 0.000045 + \frac{a^{1/2}\sqrt{2\pi}}{46080}D_-^{1/2} \end{array}\right)\Pi_6$

Expressions in terms of higher harmonics may be similarly derived.

We have shown that by measuring any pair of higher harmonic amplitudes, μ_n and ν_n, the full force profile can be recovered. However, the same information can be derived by analysing the first harmonic frequency shift. This begs the question, what new information have we gained in the process? Several experiments [5,7,8] show that for small oscillation amplitudes, higher harmonics enhance the sensitivity to short range interactions compared with first harmonic FM-AFM. This sensitivity has been reasoned by an expression derived by Giessibl [6], which relates the *n*th harmonic to a convolution over the *n*th derivative of the interaction force. In the small oscillation amplitude limit, the two are proportional. Using Equation 14, we reaffirm this relation. For small amplitudes, Equation 14 is dominated by the term proportional to a^{-n}, and the even force term can be approximated by

$$F_{\text{even}}(z) \approx \text{const} \times \int_z^{\infty} \Pi_n(\tau)(\tau - z)^{n-1} d\tau. \tag{21}$$

Integrating Equation 21 by parts and then differentiating *n* times with respect to *z* one finds

$$\frac{d^n F_{\text{even}}}{dz^n} \propto \Pi_n(z), \tag{22}$$

which is similar to the small amplitude approximation derived from Equation 2

$$\frac{dF_{\text{even}}}{dz} \propto \frac{\Delta\omega}{\omega_0}. \tag{23}$$

As expected, higher harmonics are proportional to higher derivatives, while the frequency shift used in first harmonic force spectroscopy is proportional to the first derivative. This suggests that reconstruction of the force using higher harmonics is more sensitive to short range forces compared with reconstruction using the Sader–Jarvis formula, as long as the oscillation amplitude is small compared with the characteristic interaction length.

To test the accuracy of our force inversion formulae, we insert a known conservative force into Equation 6, a generalized damping coefficient into Equation 17, and then recover them with second harmonic analysis, namely with Equation 15 and Equation 20. For the conservative interaction, we employ a Lennard–Jones force law

$$F(z) = F_0\left[\left(\frac{\ell}{z}\right)^{13} - \left(\frac{\ell}{z}\right)^{7}\right], \qquad (24)$$

Where F_0 is constant and ℓ is the interaction length scale. For the dissipative interaction, we use a viscoelastic type of force [23], characterized by the generalized damping coefficient

$$\Gamma(z) = \begin{cases} 0 & z \geq 0 \\ \eta\sqrt{R|z|} & z < 0\,, \end{cases} \qquad (25)$$

where η is the viscosity, R is the tip radius, and the sample surface is assumed to be at $z = 0$. The results displayed in Figure 1 and Figure 2 demonstrate the accuracy of our formulae. Figure 1a,b confirms, in the small amplitude regime, the increased sensitivity to short range interaction of force reconstruction using higher harmonics compared with the Sader–Jarvis formula. As the oscillation amplitude grows smaller compared with the range of the Lennard–Jones potential, the Sader–Jarvis formula grows inaccurate, while reconstruction using the second harmonic maintains its accuracy. When the amplitude is increased (Figure 1c), the accuracy of the Sader–Jarvis formula improves and for large amplitudes (Figure 1d) both methods yield satisfactory results. Figure 2 depicts the reconstruction of the generalized damping coefficients. Both the Sader–Jarvis formula for dissipative forces and the second harmonic reconstruction lose accuracy as the indentation into the simulated surface increases to the order of the oscillation amplitude, but second harmonic reconstruction remains the more accurate of the two.

Conclusion

We have derived a general procedure yielding both conservative and dissipative forces in terms of cantilever oscillations at an arbitrary harmonic, and provided explicit formulae for harmonics 2–6. This procedure reconstructs the full interaction

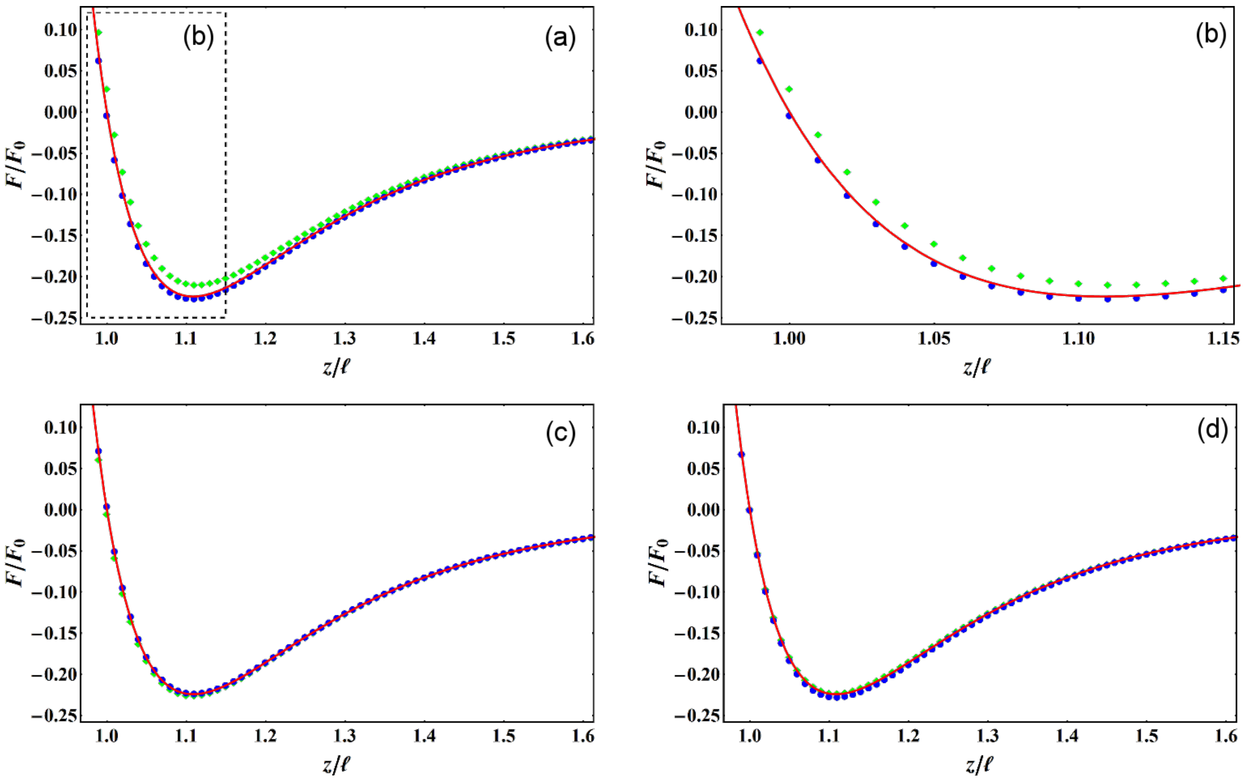

Figure 1: Lennard–Jones interaction (solid red line) and reconstructed forces. Blue circles depict reconstruction using the second harmonic. Green diamonds depict reconstruction using the Sader–Jarvis formula for the fundamental harmonic. Amplitudes of oscillation used are $a/\ell = 0.1$ (a), $a/\ell = 1$ (c), $a/\ell = 10$ (d). (b) depicts magnification of the dashed frame marked in (a).

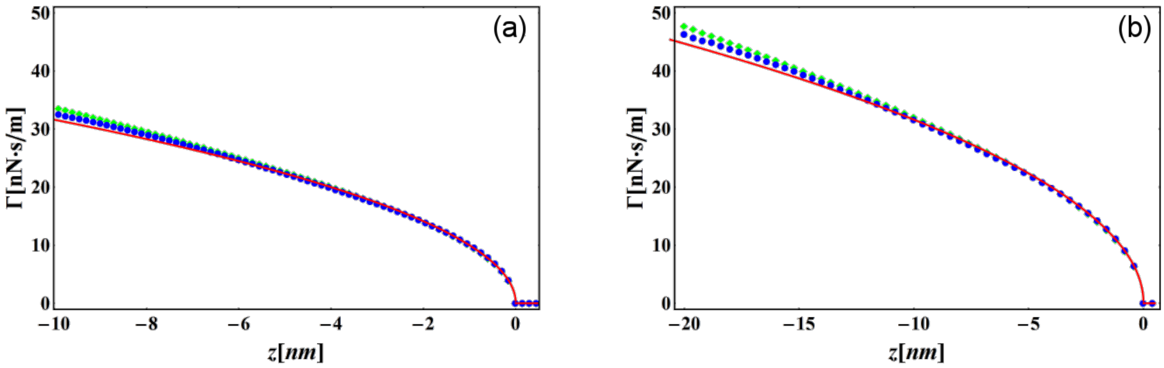

Figure 2: Generalized damping coefficient of a viscous interaction (solid red line) and its reconstructions. Blue circles depict reconstruction using the second harmonic. Green diamonds depict reconstruction using the Sader–Jarvis formula for the fundamental harmonic. The tip radius and viscosity are R = 10 nm and η = √10 Pa·s. The amplitudes of oscillation are a = 10 nm (a) and a = 20 nm (b).

force curve from any single harmonic, obviating existing reconstruction methods based on simultaneous measurement of multiple higher harmonics. In addition, it was shown that in the small amplitude regime, short range forces are reconstructed more accurately by higher harmonic analysis compared with the fundamental harmonic one.

Supporting Information

A supplementary Mathematica notebook file containing an implementation of the formulae of Table 1 for reconstruction of simulated conservative forces can be found in the ZIP file of the Supporting Information.

Supporting Information File 1

Force reconstruction.
[http://www.beilstein-journals.org/bjnano/content/supplementary/2190-4286-6-14-S1.zip]

Acknowledgements

This work was supported by the Israeli Science Foundation under grants 1403/12 and I-Core 1902/12.

References

1. Fukuma, T.; Ueda, Y.; Yoshioka, S.; Asakawa, H. *Phys. Rev. Lett.* **2010,** *104,* 016101. doi:10.1103/PhysRevLett.104.016101
2. Herruzo, E. T.; Asakawa, H.; Fukuma, T.; Garcia, R. *Nanoscale* **2013,** *5,* 2678–2685. doi:10.1039/c2nr33051b
3. Higgins, M. J.; Polcik, M.; Fukuma, T.; Sader, J. E.; Nakayama, Y.; Jarvis, S. P. *Biophys. J.* **2006,** *91,* 2532–2542. doi:10.1529/biophysj.106.085688
4. Loh, S.-H.; Jarvis, S. P. *Langmuir* **2010,** *26,* 9176–9178. doi:10.1021/la1011378
5. Garcia, R.; Herruzo, E. T. *Nat. Nanotechnol.* **2012,** *7,* 217–226. doi:10.1038/nnano.2012.38
6. Giessibl, F. J. *Surf. Interface Anal.* **2006,** *38,* 1696–1701. doi:10.1002/sia.2392
7. Hembacher, S.; Giessibl, F. J.; Mannhart, J. *Science* **2004,** *305,* 380–383. doi:10.1126/science.1099730
8. Wright, C. A.; Solares, S. D. *Nano Lett.* **2011,** *11,* 5026–5033. doi:10.1021/nl2030773
9. Santos, S.; Barcons, V.; Font, J.; Verdaguer, A. *Beilstein J. Nanotechnol.* **2014,** *5,* 268–277. doi:10.3762/bjnano.5.29
10. Preiner, J.; Tang, J.; Pastushenko, V.; Hinterdorfer, P. *Phys. Rev. Lett.* **2007,** *99,* 046102. doi:10.1103/PhysRevLett.99.046102
11. Stark, R. W.; Heckl, W. M. *Rev. Sci. Instrum.* **2003,** *74,* 5111. doi:10.1063/1.1626008
12. Sader, J. E.; Jarvis, S. P. *Appl. Phys. Lett.* **2004,** *84,* 1801. doi:10.1063/1.1667267
13. Sader, J. E.; Uchihashi, T.; Higgins, M. J.; Farrell, A.; Nakayama, Y.; Jarvis, S. P. *Nanotechnology* **2005,** *16,* 94–101. doi:10.1088/0957-4484/16/3/018
14. Giessibl, F. J. *Phys. Rev. B* **1997,** *56,* 16010. doi:10.1103/PhysRevB.56.16010
15. Dürig, U. *Appl. Phys. Lett.* **1999,** *75,* 433. doi:10.1063/1.124399
16. Katan, A. J.; van Es, M. H.; Oosterkamp, T. H. *Nanotechnology* **2009,** *20,* 165703. doi:10.1088/0957-4484/20/16/165703
17. Dürig, U. *New J. Phys.* **2000,** *2,* 5. doi:10.1088/1367-2630/2/1/005
18. Stark, M.; Stark, R. W.; Heckl, W. M.; Guckenberger, R. *Proc. Natl. Acad. Sci. U. S. A.* **2002,** *99,* 8473–8478. doi:10.1073/pnas.122040599
19. Legleiter, J.; Park, M.; Cusick, B.; Kowalewski, T. *Proc. Natl. Acad. Sci. U. S. A.* **2006,** *103,* 4813–4818. doi:10.1073/pnas.0505628103
20. Sahin, O.; Quate, C.; Solgaard, O.; Atalar, A. *Phys. Rev. B* **2004,** *69,* 165416. doi:10.1103/PhysRevB.69.165416
21. Sahin, O.; Magonov, S.; Su, C.; Quate, C. F.; Solgaard, O. *Nat. Nanotechnol.* **2007,** *2,* 507–514. doi:10.1038/nnano.2007.226
22. Milne-Thomson, L. M.; Abramowitz, M.; Stegun, I. A. *Handbook of Mathematical Functions;* Dover: New York, 1972; pp 375–377.
23. Garcia, R.; Gómez, C. J.; Martinez, N. F.; Patil, S.; Dietz, C.; Magerle, R. *Phys. Rev. Lett.* **2006,** *97,* 016103. doi:10.1103/PhysRevLett.97.016103

License and Terms

The definitive version of this article is the electronic one which can be found at:
doi:10.3762/bjnano.6.14

BEILSTEIN JOURNAL OF NANOTECHNOLOGY

Increasing throughput of AFM-based single cell adhesion measurements through multisubstrate surfaces

Miao Yu[1,2,§], Nico Strohmeyer[1,§], Jinghe Wang[2], Daniel J. Müller[1] and Jonne Helenius[*1]

Full Research Paper

Open Access

Address:
[1]Department of Biosystems Science and Engineering, ETH Zurich, Mattenstrasse 26, 4058 Basel, Switzerland and [2]Center for Precision Engineering, Harbin Institute of Technology, Harbin 150001, China

Email:
Jonne Helenius* - jonne.helenius@bsse.ethz.ch

* Corresponding author
§ Equal contributers

Keywords:
atomic force microscopy; cell adhesion; collagen I; fibroblasts; fibronectin; HeLa; laminin; MDCK; PC3; single cell assay; single cell force spectroscopy

Beilstein J. Nanotechnol. **2015,** *6,* 157–166.
doi:10.3762/bjnano.6.15

Received: 22 August 2014
Accepted: 10 December 2014
Published: 14 January 2015

This article is part of the Thematic Series "Advanced atomic force microscopy techniques III".

Guest Editor: T. Glatzel

Abstract

Mammalian cells regulate adhesion by expressing and regulating a diverse array of cell adhesion molecules on their cell surfaces. Since different cell types express distinct sets of cell adhesion molecules, substrate-specific adhesion is cell type- and condition-dependent. Single-cell force spectroscopy is used to quantify the contribution of cell adhesion molecules to adhesion of cells to specific substrates at both the cell and single molecule level. However, the low throughput of single-cell adhesion experiments greatly limits the number of substrates that can be examined. In order to overcome this limitation, segmented polydimethylsiloxane (PDMS) masks were developed, allowing the measurement of cell adhesion to multiple substrates. To verify the utility of the masks, the adhesion of four different cell lines, HeLa (Kyoto), prostate cancer (PC), mouse kidney fibroblast and MDCK, to three extracellular matrix proteins, fibronectin, collagen I and laminin 332, was examined. The adhesion of each cell line to different matrix proteins was found to be distinct; no two cell lines adhered equally to each of the proteins. The PDMS masks improved the throughput limitation of single-cell force spectroscopy and allowed for experiments that previously were not feasible. Since the masks are economical and versatile, they can aid in the improvement of various assays.

Introduction

The regulated adhesion of mammalian cells with the extracellular matrix (ECM) and surrounding cells is crucial in biological processes such as cell migration, differentiation, proliferation, and apoptosis. Since impaired cell adhesion causes a wide range of diseases, the study of cell adhesion is an important field of research [1-5]. Cell adhesion is predominantly mediated by cell adhesion molecules (CAMs), which comprise different protein families, including integrins and cadherins [6].

Cells express and regulate CAMs in order to control whether they adhere to surfaces they encounter, and if so, how strong and for how long [7-10]. Extracellular cues and intracellular signaling tightly regulate cell adhesion. Furthermore, the outside-in signaling of CAMs regulate cellular processes including the adhesive properties of the cell [11]. Among CAMs, integrins dominantly facilitate adhesion of cells to ECM proteins. Integrins are heterodimers composed of non-covalently linked α- and β-subunits, both of which consist of a large extracellular domain, a short transmembrane domain, and a cytoplasmic domain of variable length. In mammalian cells, the 18 α-subunits and 8 β-subunits are known to form 24 different integrins, which have specific, but overlapping, adhesion functions and often bind to more than one ECM protein [12]. To adapt their adhesion to the ECM, cells regulate the surface expression of integrins [13]. Importantly, cells differ in their adherence to various ECM proteins, necessitating the investigation of the adhesive properties of the cells.

Atomic force microscopy (AFM)-based single-cell force spectroscopy (SCFS) provides a versatile tool to quantify the adhesion of single cells in near-physiological conditions [14-16]. In AFM-based SCFS, a single cell is attached to a cantilever (Figure 1A,B), commonly facilitated by an adhesive coating (e.g., concanavalin A, poly-L-lysine or CellTak) [17-22]. The attached cell is lowered (approach) onto a substrate (Figure 1A(i)), which is a protein-coated surface, another cell or a biomaterial [23], until a set force is reached and the cell is kept stationary for a set time to allow the formation of adhesive interactions (Figure 1A(ii)). During the subsequent raising (retraction) of the cantilever (Figure 1A(iii)), the force acting on the cell and the distance between cell and substrate is recorded in a force–distance curve (Figure 1C). The force range that can be detected with AFM-based SCFS is from ≈10 pN up to ≈100 nN [14], thereby, SCFS allows both the overall cell adhesion and the contribution of single adhesion receptors to be quantified. During initial cantilever retraction the upward acting

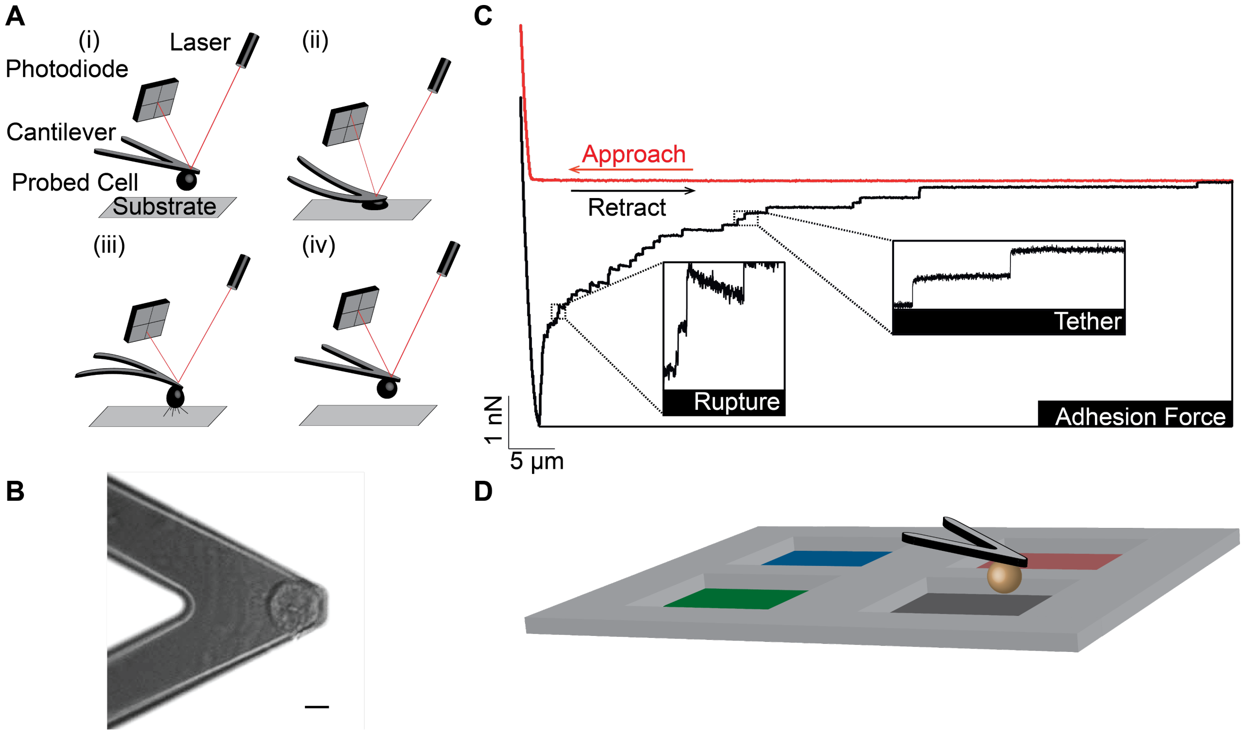

Figure 1: Depiction of AFM-based SCFS. (A,B) A single cell is bound to a tip-less AFM cantilever via a receptor specific or unspecific substrate (scale bar, 10 µm). (A) (i and ii) The cantilever-bound cell is brought into contact with the substrate until a preset force is recorded. After a specified contact time, (iii) the cantilever is retracted until the cell is fully detached from the substrate. During the experimental cycle, the deflection (force) of the cantilever and the distance between cell and surface is recorded in a force–distance curve (red). (C) The force–distance curve shows distinct features: In the approach segment of the force–distance curve, the deflection of the cantilever is recorded while the cell is lowered onto the substrate; the retraction segment of the force–distance curve (black) records the adhesion force of the cell, which is the maximum force acting on the cantilever and, thus, the force needed to initiate the detachment of the cell from its substrate. Subsequently, single receptor unbinding events are observed. Rupture events are recorded when the CAM–ligand bond of a cytoskeleton-linked CAM fails. Tether events are recorded when a membrane tether is extruded from the cell membrane with the CAM at its tip (tethers). In the latter case, attachment of the CAM to the cytoskeleton is either too weak to resist the mechanical stress applied or non-existent. (D) To improve the throughput of SCFS experiments, a four-segmented coating mask is used, allowing adhesion force measurements of one cell to different adhesives substrates.

force on the cell increases until the force needed to initiate cell de-adhesion is reached, thereafter, unbinding events occur (Figure 1C). The maximum force is called the adhesion force and is a measure of how strong the cell adhered to the substrate. Unbinding events correlate with the unbinding of either single or clustered CAMs and can be characterized as either rupture or tether events [15,17,20]. The analysis of these unbinding events may be used to characterize the strength of single bonds and cell membrane properties [17,24,25]. Examples of the utility of SCFS include studies of the adhesion of two *Dictyostelium discoideum* cells via glycoproteins [26], dendritic cells via activated leukocyte cell adhesion molecules [17], Chinese hamster ovary cells to collagen I via $\alpha_2\beta_1$-integrins [22], pre-osteoblasts to denatured collagen I via $\alpha_5\beta_1$-integrins and integrins containing α_v-subunits [27], Jurkat T cells to the vascular cell adhesion molecule VCAM-1 via $\alpha_4\beta_1$-integrins [28], and the contribution of galectins to the overall cell adhesion of MDCK cells to collagens [29]. In addition to studying the adhesion of cells to a substrate, the regulation of one CAM by another CAM has been studied by SCFS. It was shown by SCFS that collagen I binding integrins down-regulate the avidity of fibronectin binding integrins by an increased endocytosis in HeLa cells [30].

The classical SCFS setup, where the adhesion of a cantilever-bound cell to a substrate is probed, has a limited throughput because only one substrate is examined per cantilever. Therefore, an alternative method has been used to quantify the adhesive properties of several cells using one cantilever. Thereto, in an inverted assay, a ligand-functionalized (e.g., ECM protein) cantilever or a cantilever with a functionalized bead is lowered on round or spread cells that are seeded on a Petri dish [31,32]. After the designated contact time has been reached, the cantilever is retracted from the cell and the adhesion of the cell to the cantilever or bead is measured. Thereafter, the cantilever can be moved above another cell and the adhesion experiment cycle repeated. With this inverted approach, several cells can be examined using one cantilever. However, a surface that has been in contact with a cell may be contaminated with debris from the cell or restructured by the cell, especially after longer contact times [16,33]. Due to the limited surface areas at the ends of the cantilevers and beads, the coating is compromised after a few measurements and the cantilever must be replaced to ensure consistent assay conditions.

An alternative method to increase the throughput of adhesion measurements in the classical setup is to microstructure the surface such that it presents areas having different properties. Examples used for SCFS include: microstructured surfaces with two different polymers [34], different nanoscale groves [35] and the use of two different ECM proteins [36]. However, the equipment needed for these approaches are uncommon in biological laboratories.

In order to increase the throughput, we chose to modify Petri dishes using polydimethylsiloxane (PDMS) masks with four distinct areas (Figure 1D). The four segments separate the Petri dish surface into four independent 4 × 4 mm^2 wells, which allow one dish to be coated with different substrates and, thus, characterization of the adhesion of the same cell to four substrates. The masks are thin enough to remain on the Petri dish while performing adhesion measurements. These multi-segmented substrates not only increase the rate at which SCFS measurements can be made but also improve their reliability and comparability, because the adhesion of cells of the same type can vary considerably [37]. Therefore, the number of cells probed can be reduced. In addition, the masks decrease the coating area, reduce experimental material and improve experimental efficiency. We implemented the masks to characterize the adhesion of different cell lines to collagen I, fibronectin and laminin 332 and found that the cell lines had unique adhesion profiles, which likely reflect differences in the CAMs they expressed.

Results

PDMS masks for single-cell force spectroscopy

To increase throughput of AFM-based SCFS, we developed segmented PDMS masks (Figure 1D and Figure 2B) that allow the adhesion of one cell to different substrates to be characterized. Using this mask, four wells having an area of 16 mm^2 and a depth of 150 µm (Figure 2B) can be coated in one Petri dish and SCFS adhesion measurements can be performed with the same cell in each segment without removing the mask. Since the non-specific adhesion of different cell lines to either glass or PDMS varies, we developed two types of PDMS masks with a protein coating on either a glass or PDMS surface. The mask type can be chosen to minimize the background adhesion of the cell line. The production process as well as the handling of the PDMS mask is described in the next sections. In addition, the characterization of surface topography, protein coating and microscopy utility of both types of PDMS masks is presented.

Characterization of the protein coating on PDMS masks

To characterize the surface roughness and the protein coating, glass and PDMS surfaces were imaged using AFM. Several protein-coated surfaces of both PDMS and glass were imaged. Surfaces of protein-coated glass were smooth with height variations of ≈4 nm (Figure 3A). In contrast, the protein-coated PDMS surfaces were rougher, with height differences of >40 nm (Figure 3B).

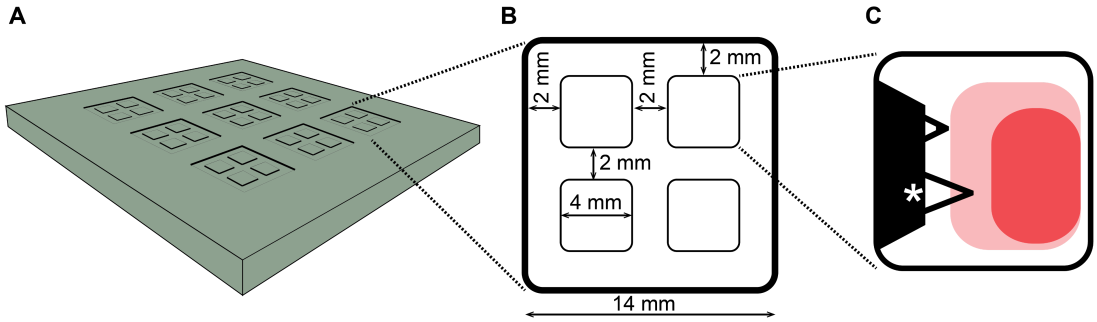

Figure 2: Technical details of the PDMS coating mask. (A) For the production of the PDMS masks, an aluminum mold is produced with nine casting molds for the PDMS masks. Dimensions of the masks are shown in (B). The height of the wells is 150 µm. (C) AFM cantilever (starred, NP-O, Bruker) accessible area usually used for SCFS adhesion experiments. Dark red indicates the area where the PDMS masks do not interfere with measurements, where the pale red area indicates regions where small interference occurs, and white areas are where measurements are not possible.

To verify that the surfaces were coated with proteins, we tried to physically remove the protein coating over a 10 × 10 μm^2 area of the sample by applying a high contact force (≈95 nN) during contact-mode AFM imaging, that is, by scratching the coating with the AFM cantilever. An area was scratched several times before the scanning angle was rotated 90° and the same area was scratched several more times. After scratching, a 20 × 20 μm^2 area surrounding the scratched area was imaged. On the glass surface, the protein was removed from the scratched area (Figure 3A’’). The protein-coating depth was 3.2 ± 0.5 nm (n = 5) for BSA and 4.5 ± 0.4 nm (n = 5) for collagen I (Figure 3C). The AFM images of the PDMS coatings (Figure 3B,D) revealed an uneven surface with features exceeding 40 nm in height. These are replications of imperfections in the aluminum mold. Although the sensitivity of AFM imaging is high enough to detect protein coatings, the overall roughness of the surface conceals the thin protein layers, and, thus, detection of the presence of a scratched protein patch was not possible.

Since we were unable to confirm a protein coating on PDMS by the AFM scratching experiments, we coated the glass and PDMS surfaces with fluorescent-conjugated proteins used in the later adhesion study: fluorescein isothiocyanate (FITC) conjugated BSA, rhodamine-conjugated laminin, FITC-conjugated collagen I and HiLyte488-conjugated fibronectin. For each protein, confocal images show nearly homogeneous surface signals when absorbed on both PDMS (Figure 3E’–H’) and glass (Figure 3E–H). In a smaller area the fluorescence was bleached using an excitation wavelength of either 488 nm or 555 nm. On both surfaces the fluorescence signal was quenched, demonstrating that the ECM proteins did in fact coat the surfaces. Negative controls (uncoated glass or PDMS) showed background fluorescence that did not decrease with bleaching (data not shown). These experiments confirm homogeneous protein coatings on glass surfaces and indicate that the PDMS surfaces were similarly coated.

Accessibility of the coated area with cantilever-bound cells

The accessible area at the bottom of a SCFS well is limited by the geometry of the mask and the AFM cantilever. If these come into contact with each other, the recorded force–distance curves will be corrupted or, worse, the AFM cantilever may be displaced and the cantilever can be damaged. Both the height of the coating mask and the 10° angle of the cantilever determine the accessible area. Unfortunately, PDMS masks thinner than 150 µm are fragile and difficult to handle, making the production of masked-dishes cumbersome. The area suitable for adhesion measurements is depicted in Figure 2C. Since the AFM chip must clear the chip-side of the mask, an approximately 4 mm^2 area at the chip-side cannot be used for adhesion measurements (see Figure 2C, white area). How close the cantilever can be moved towards the side borders of the well is determined by the position of the cantilever on the chip and how the chip is mounted. The tip-side area is accessible until the cantilever makes contact with the mask. When the cantilever was too close to the chip boarder, both approach- and retraction-force–distance curves showed a distinct bending in the baseline force. When the cantilever was too close to a side border, no obvious features were found in force–distance curves. The sensitivity of the cantilever was determined by pressing it onto a surface either outside the mask or close to the tip-side border of a well.

Evaluation of the PDMS masks for light microscopy

Light microscopy is essential for many SCFS experiments. Therefore, we tested the optical behavior of the masks with PDMS surfaces. UV–vis spectra of 1 mm thick PDMS slices

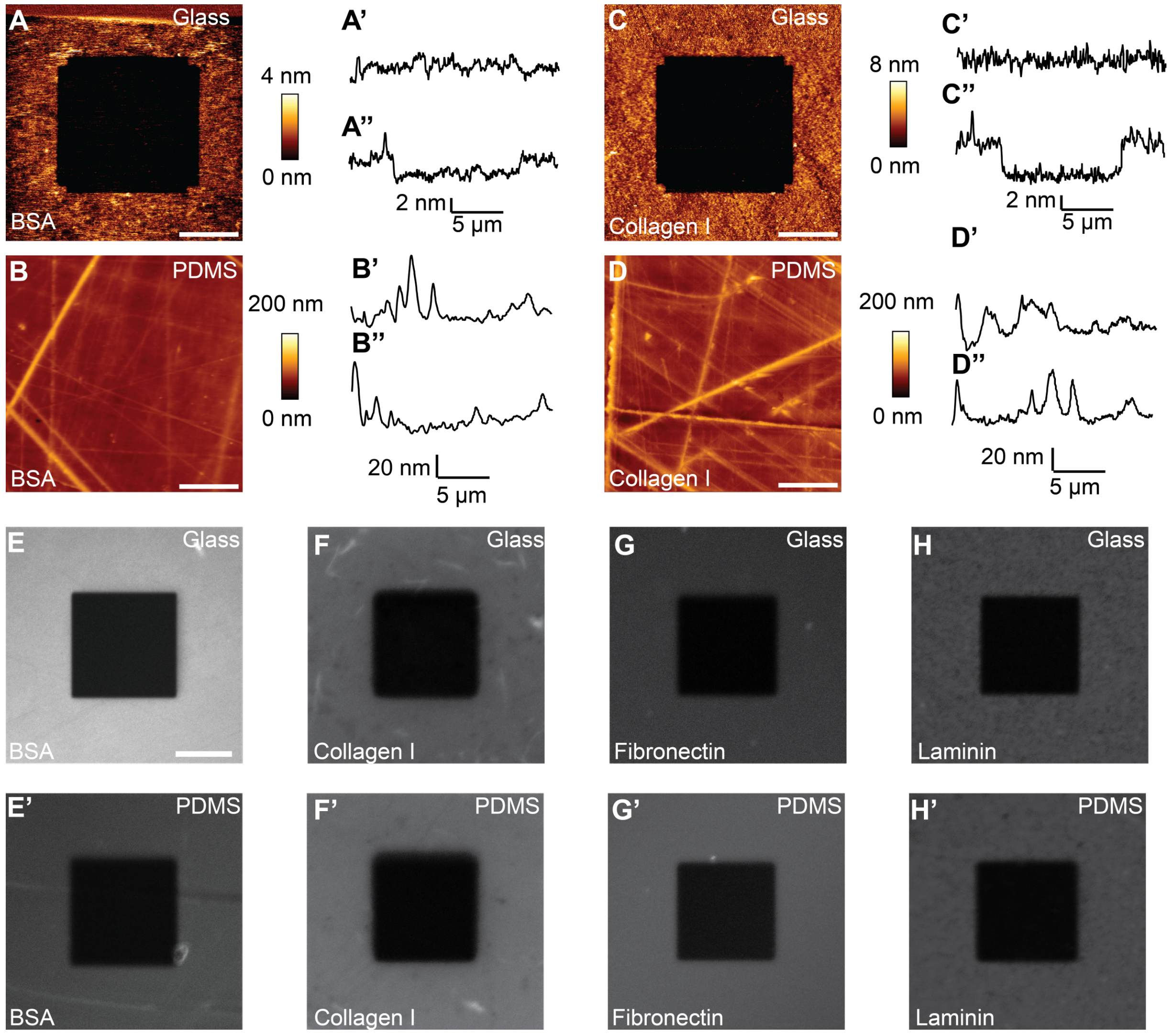

Figure 3: Surface characterization. Representative topographies of BSA-coated (A) and collagen I-coated (C) glass surfaces, and BSA-coated (B) and collagen I-coated (D) PDMS surfaces. A 20 × 20 µm^2 area of the coated surface was imaged with AFM after a 10 x 10 µm^2 area was repeatedly scratched by contact-mode AFM imaging using a high contact force. Images show a cavity in the scratched area for BSA- (A) and collagen I-coated (C) glass surfaces. The thicknesses of the coatings were similar, ≈3.5 nm for BSA (A”) and ≈4.5 nm for collagen I (C”). The PDMS surface showed a rough surface with height differences of >40 nm (B and D). On PDMS, the displacement of proteins by AFM scratching was not evident (B, B” and D, D”). Scale bars, 5 µm. Since a protein coating was not demonstrated, we coated PDMS wells with fluorescently labeled BSA (FITC), collagen I (FITC), fibronectin (rhodamine) and laminin (HiLyte488) and imaged the glass (E–H, respectively) and PDMS (E’–F’) surfaces. Using confocal microscopy, a 20 × 20 µm^2 area was bleached with maximum laser power before the 50 × 50 µm^2 area was imaged (E–H and E’–H’). Scale bar, 10 µm.

showed that cured PDMS did not absorb light at wavelengths important for light microscopy (230–840 nm, data not shown). PDMS masks did not appear to reduce the quality of wide field and fluorescence images. However, the *z*-resolution and calibration will be suboptimal since the refractive index of PDMS (1.415, as measured) does not match that of water. Furthermore, the working distance of the microscope objective must exceed the thickness of the PDMS layer, thus, these masks are not suitable for short distance, high numerical aperture objectives. Although the masks with PDMS surfaces show technical limitations in optical microscopy, they are usable for standard microscopy mostly used in combination with SCFS. If the PDMS masks interfere with optical microscopy, the masks with glass surfaces are recommended.

Comparison of the non-specific adhesion force on glass and PDMS surfaces

In our experience, non-specific cell adhesion to clean glass is higher than the adhesion of cells to ConA-coated cantilevers. In order to attach cells to ConA-coated cantilevers, it was necessary to passivate glass surfaces onto which cells were pipetted. We found that both HeLa and PC3 cells also strongly adhere to PDMS (Figure 4). Therefore, it was necessary to passivate the PDMS surfaces. BSA is commonly used to block non-specific adhesion of cells to different surfaces [38]. To address non-specific cell adhesion, we coated glass and PDMS wells with BSA. To our surprise, the adhesion of PC3 cells was higher for BSA when BSA was adsorbed onto glass than when absorbed onto PDMS (Figure 4). Thus, we decided to use PDMS masks in subsequent experiments. Furthermore, the cells were collected with the cantilever from BSA-coated wells because their adhesion to BSA is lower than to the ConA-coated cantilevers.

Cell line-dependent adhesion to extracellular matrix proteins

To demonstrate that PDMS masks are a useful tool to increase throughput and comparability of results on different ECM proteins in SCFS, we conducted a small adhesion-force screening with four cell lines and three different ECM proteins. Thereto, we coated the wells in the PDMS-coated masks with collagen I, fibronectin, and laminin 332. We evaluated cell adhesion of PC3, HeLa, mouse kidney fibroblast and MDCK cells to different extracellular matrix proteins. The fourth well of the PDMS mask was coated with BSA from which cells were picked up. We measured the adhesion force to all three ECM proteins for at least 11 cells of each cell line (Figure 5). As expected, the cell lines differed in their adhesion to the ECM proteins. For example, PC3 cells showed similar adhesion to collagen I and fibronectin and a higher adhesion to laminin 332, while mouse kidney fibroblast showed very low adhesion to collagen I and laminin 332, but high adhesion to fibronectin. This indicates that cell lines express different patterns of CAMs. Besides the cell line-dependent adhesion forces, contact time-dependent strengthening also differed between cell lines, indicating difference in the dynamic regulation of adhesion. These results show that the PDMS masks can be used to evaluate the adhesive properties that distinguish different cell lines from each other and perhaps reflect unique cell line-specific adhesion signatures.

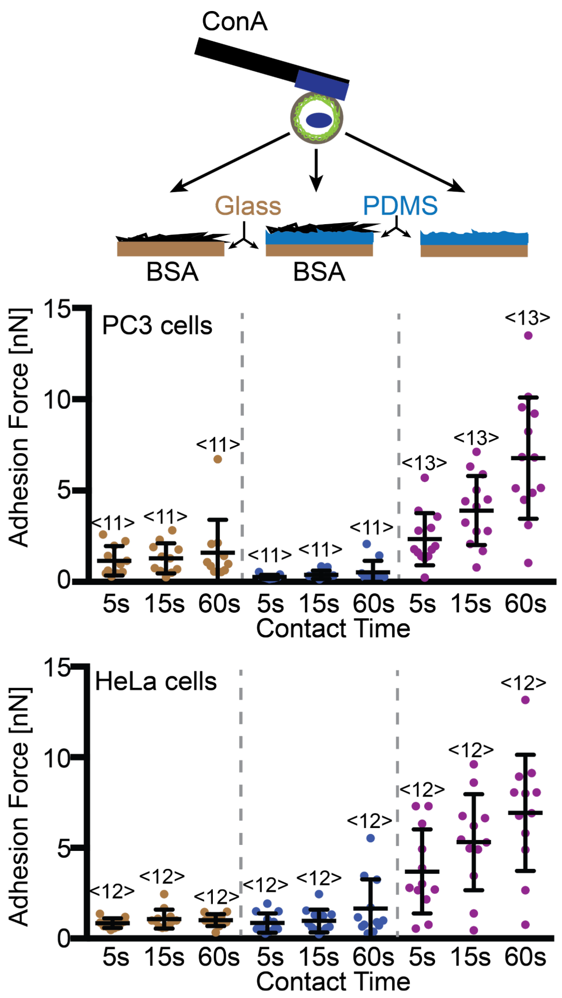

Figure 4: Comparisons of glass-surface and PDMS-surface masks**.** Top, depiction of the SCFS assay used to quantify the adhesion of PC3 and HeLa cells. Single cells were bound to ConA-coated cantilevers and approached BSA-coated glass or PDMS and a clean PDMS surface until a force of 2 nN was recorded. After the denoted contact time, the cantilever was retracted to detach the cantilever-bound cell and substrate. During retraction, the adhesion force of cell and substrate was measured. Bottom: adhesion forces recorded for PC3 and HeLa cells during their detachment from substrates. Each dot represents the measurement of one cell with the number of cells assayed for each condition given by <*n*> The *x*-axis indicates the duration (5, 15 and 60 s) that the cell was in contact with the substrate before being detached. The error bars indicate mean force and standard deviation.

Discussion

Adhesion is a fundamental aspect of both healthy and diseased cells. In the last decade, single cell adhesion studies have contributed to the understanding of adhesion proteins and their regulation. AFM-based SCFS has been used to quantify adhesion of numerous cell types to a diverse set of substrates, include ECM proteins, biomaterial and cell–cell adhesion proteins [14,15,26]. However, since only one cell can be examined at a time, the number of conditions that can be studied efficiently by SCFS is limited. To help alleviate this problem, we designed two kinds of PDMS masks that allow adhesion of one cell to multiple adhesive substrates to be measured. The masks were cast in aluminum molds, which can be made in most mechanical workshops.

We characterized the masks with regard to surface topography, protein coating ability and applicability for light microscopy. While the PDMS surface was very rough compared to the glass surface, both could be well-coated with proteins. The height

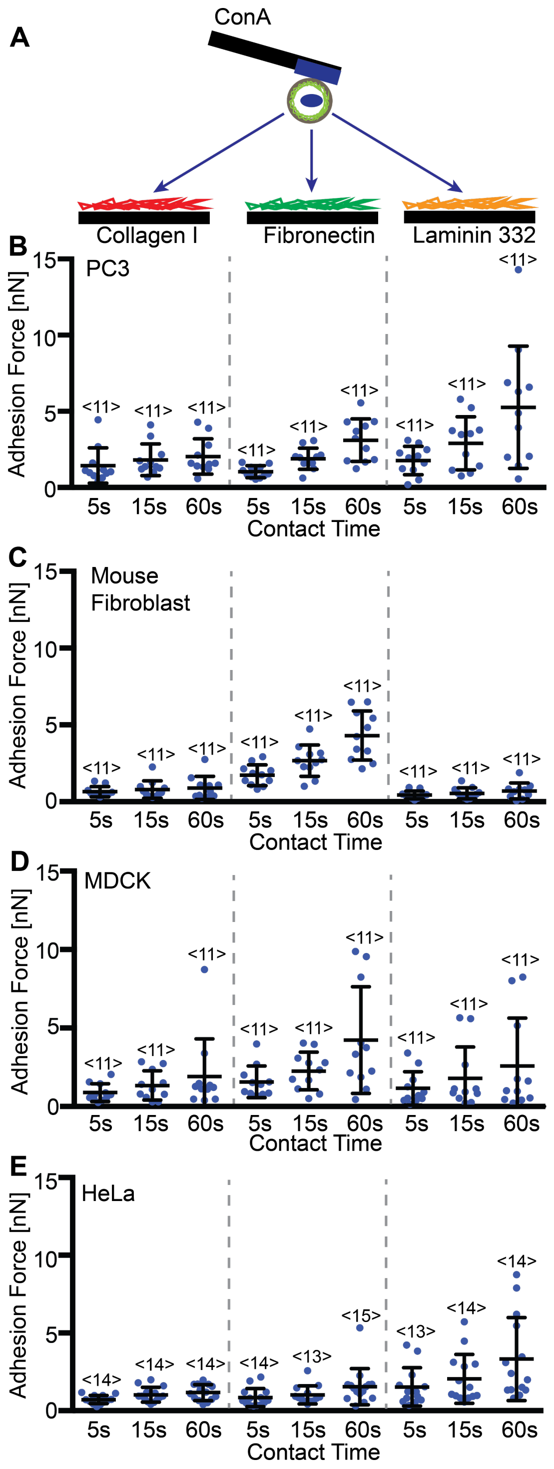

Figure 5: Cell line-dependent adhesion of ECM proteins. (A) Depiction of the SCFS experimental setup, where the adhesion of a ConA bound cell is measured to different protein-coated surfaces. Graphs of the adhesion forces measured for PC3 (B), mouse fibroblasts (C), MDCK (D) or HeLa (E) cells to collagen I, fibronectin and laminin 332 coated PDMS surfaces after contact times of 5, 15 and 60 s. Each dot represents the measurement of one cell. The number of cells assayed for each condition is given by <*n*>. Error bars indicate mean force and standard deviation.

variation of the PDMS surface (>40 nm), although small compared the size of cells examined (diameter, 15 µm), may be the cause of the differences in HeLa cell adhesion to BSA-coated substrates observed in Figure 4. Other differences between the glass and PDMS surfaces, such as hydrophobicity or the specifics of protein absorption, may also account for this difference. However, since the difference in adhesion to BSA only occurred for PC3 cells (Figure 4) and was minor compared to specific adhesion, we conclude that both glass and PDMS surfaces can be coated and used for cell adhesion measurements. Fluorescently labeled proteins adsorbed on glass and PDMS showed homogenous protein coatings on both surfaces (Figure 3), and confirmed this conclusion. Further experiments showed that like glass-bottomed wells, PDMS-bottomed wells are suitable for light microscopy. Thus, neither mask lowered the quality of possible SCFS experiments, even in combination with light microscopy. If SCFS is combined with advanced light microscopy and objectives with short working distances and high numerical apertures are used, the glass surface masks are preferable.

Finally, we used the PDMS masks to characterize and compare the adhesion of four cell lines to collagen I, fibronectin and laminin 332. HeLa (Kyoto), PC3, mouse kidney fibroblast and MDCK cells where chosen based on their widespread use. The masks allowed us to profile the adhesion properties of the cells quickly and efficiently, requiring ≈2 days for each cell line. By measuring the adhesion of a single cell to different matrix proteins, a smaller number of cells need to be assayed. These measurements show that cell lines have specific ECM protein adhesion profiles. This is likely due to difference in their expression of integrins. To profile cell adhesion of different cell lines, the used substrates could be readily extended to more ECM proteins and cell–cell adhesion proteins, such as E-cadherin. Further, contact times could be increased to address long-term CAM regulation, which would increase the accuracy of the profiles. With the help of the PDMS-coated masks, a semi-automated adhesion measurement setup is feasible.

Our masks compare favorably to commercially available silicone masks, such as those offered by Ibidi. The production of the mask is easy and commercially available equivalents are commonly expensive. The masks described herein require a mold, which can be easily produced in workshop, and the PDMS components. The usage of the mask is not limited to AFM-based SCFS, as the four-well mask is only one of many possible dimensions and forms. For example, migration or spreading experiments on different proteins could be conducted using PDMS masks. Further examples where masks could be used include wound-healing assays and experiments that require more complex surfaces.

Experimental

Production of PDMS masks

To produce the PDMS masks, a casting mold with cavities for nine masks was used (Figure 2A). For the mold, 150 µm-deep cavities were machined in an 8 mm-thick aluminum plate (Figure 2B), which was then anodized to harden its surface. To reduce adhesion of PDMS to the mold, the mold was silanized overnight with 200 µL of perfluorooctyltrichlorosilane in a vacuum chamber at room temperature. After silanization, the mold was washed extensively with water and ethanol. It was important that the cavities were free of any residues before casting. The PDMS elastomer (Sylgard 184, Dow Corning) was mixed in a 10:1 oil to base ratio. The mixture was placed in a vacuum chamber for 20 min to remove dissolved gases. Approximately 2 mL of the uncured PDMS mixture was poured on the top of the aluminum mold and spread uniformly over the mold using a straightedge. For glass surface masks, only the cavities of the mold were filled and, importantly, the inner squares (future wells of the mask) were wiped free of PDMS. In contrast, to produce masks with PDMS surface wells, the entire top of aluminum mold was left covered with a thin PDMS layer. The mold was place in an oven at 80 °C for at least 2 h to fully cure the PDMS. After cooling, the glass-bottom masks were carefully lifted out of the cavities and excess PDMS removed from the edges of the wells. In contrast, PDMS-surface masks where cut out of the continuous PDMS layer before they were lifted from the mold. Subsequently, both types of masks were placed topside down in the middle of a glass bottom Petri dish (WPI) and any air bubbles were removed by gently pushing them out with tweezers before the dishes were heated at 80 °C for 20 min. To enhance the binding of the PDMS mask to the glass, both surfaces can be plasma cleaned in air for one minute before they are joined. However, PDMS surfaces become hydrophilic during plasma treatment, and thus, liquid coating drops spread over the masks. Storing the PDMS in air will restore the hydrophobicity of the surface.

Cell culture

PC3 cells were maintained in RPMI-1640-supplemented (Gibco-Life technologies) 1 mM sodium pyruvate; HeLa cells (Kyoto) and mouse kidney fibroblasts were maintained in DMEM GlutaMAX supplemented with 10% (v/v) FCS; MDCK cells were maintained in MEM supplemented with 5% FCS. All media also contained 100 units/mL penicillin and 100 µg/mL streptomycin (Gibco-Life technologies).

Protein functionalization of PDMS masks and the AFM cantilever

Before the PDMS or glass surface was coated with proteins, the Petri dish containing the PDMS masks was washed with ethanol and ultrapure water to remove any residue. After drying the Petri dishes, 16 µL solutions of 160 µg/mL collagen I (Inamed Biomaterials), 50 µg/mL fibronectin (Merck), 50 µg/mL laminin 332 (Abcam) or 2% (w/v) BSA (Sigma) in PBS were added to the separate wells and left to adsorb overnight at 4 °C. In order to minimize uncoated glass areas, all wells were incubated with 2% BSA in PBS for 30 min at room temperature. The glass and PDMS were coated with fluorescently labeled proteins as described for non-labeled proteins. The cantilever coating was performed as previously described [30]. In short, the cantilevers were plasma-cleaned and incubated overnight in 2 mg/mL ConA (Sigma) containing PBS at 4 °C.

Characterization of protein coatings

To characterize surface roughness and protein coatings of PDMS and glass-surfaced wells, a NanoWizzard II AFM (JPK Instruments) mounted on an inverted microscope (Axio Observer.Zi, Zeiss) was used. AFM imaging was performed in intermittent contact mode with a v-shaped cantilever (SNL, Brucker) having a nominal spring constant of 0.58 N/m. First, an area of 20 × 20 µm^2 was imaged at a line rate of 0.7 Hz and with a resolution of 512 × 512 pixels. During the scan, the force acting on the surface was kept low by manually adjusting the drive voltage between 0.5 and 1 V, which compensated for the thermal drifts. AFM scratching was done in contact mode on an area of 10 × 10 µm^2 with a cantilever deflection of 8 V (≈95 nN), a line rate of 10 Hz and an image size of 128 × 128 pixels. After performing 10 scratches, the scan direction was rotated 90° and another 10 scratches were performed. Thereafter, the original 20 × 20 µm^2 surface area was reimaged using the original AFM settings.

Single-cell force spectroscopy

For SCFS, a CellHesion200 (JPK Instruments) device mounted on an inverted optical microscope (Axio Observer.Z1, Zeiss) in a temperature-controlled, noise cancellation box was used. The temperature was set to 37 °C throughout the experiments. 200 µm-long, tip-less, v-shaped, silicon nitride cantilevers having nominal spring constants of 0.06 N/m (NP-O, Bruker) were used for adhesion measurements. The spring constant of every cantilever was determined prior to the experiment using the thermal noise method.

Prior to experiments, cells grown to ≈80% confluency were detached from culture flasks by trypsin/EDTA and washed off with measurement media (cell line-specific media supplemented with 20 mM HEPES) containing 10% FCS. Cells were pelleted (420 g for 90 s) and resuspended in measurement media. Petri dishes with PDMS masks were washed with measurement media to exchange coating buffers and remove loosely bound protein from the surface. Throughout the experiments, the PDMS mask remained on Petri Dish. After a recovery time of at least 45 min in the measurement media [20], cell suspensions were pipetted onto the BSA well and cells were allowed to settle. To attach a cell, the calibrated and functionalized cantilever was lowered onto a cell at a velocity of 10 µm/s until an upward force of 5 nN was recorded and was then raised after remaining for 5 s at a constant height. The presence of a cell at the apex of the cantilever was visually confirmed. Cantilever-bound cells were incubated for 10 min to ensure firm binding on the cantilever. For adhesion measurements, single cantilever-bound cells were moved over the protein-coated wells and lowered onto the protein-coated surface with a velocity of 5 µm/s until a contact force of 2 nN was reached. The cantilever was maintained at a constant height for 5, 15 or 60 s (contact time) and subsequently retracted a distance of >90 µm at a speed of 5 µm/s until the cell was fully detached from the substrate. After each adhesion cycle, the cell was allowed to recover for a time at least equal to the contact time before a new adhesion cycle was performed. The spot at which each cell adhesion was quantified was changed with each adhesion cycle. After quantifying the cell adhesion with the three contact times, the cell was moved to another protein-coated well and adhesion measurements were repeated. To avoid possible systematic errors caused by substrate-specific cell activation or deactivation, we varied the order in which cell adhesion to the substrates was measured. After adhesion measurements were performed for all protein coatings, the cell was exchanged. The Petri dish was replaced after characterizing 4 cells on each coating. If a cell showed morphological changes during the experiments, it was discarded. Adhesion forces were extracted from force–distance curves using JPK data processing software.

Fluorescence microscopy and UV–vis spectroscopy

Fluorescence microscopy was performed with an inverted scanning confocal microscope (Axio Observer.Z1, LSM 700, Zeiss) equipped with a plan, apochromat, 25×, 0.8 numerical aperture, water-immersion objective lens (Zeiss). FITC–albumin (Sigma), fibronectin–HiLyte488 (LuBioScience), laminin–rhodamine (LuBioScience) and FITC-collagen I (Sigma) were dissolved at a concentration of 20 µg/mL in PBS and absorbed as described above. For fluorophore bleaching, the laser power of the 488 or 555 nm laser was set to the maximum intensity. A limited area ($20 \times 20\ \mu m^2$) was bleached using a single 156 × 156 pixel scan, before a $50 \times 50\ \mu m^2$ image (448 × 448 pixels) was recorded at 4% laser intensity. UV–vis spectra were acquired using a NanoDrop 2000c (Thermo Scientific) for 1 mm-thick PDMS slices.

Acknowledgements

We thank Mitasha Bharadwaj and Joost te Riet for their help developing and evaluating the masks and Paul Argast for developing the aluminum molds. We thank Hongxiang Wang for supervising the Ph.D. research of Miao Yu at the Harbin Institute of Technology. The mouse kidney fiboblasts, MDCK and PC3 cell lines were kindly provided by Reinhard Fässler, Aki Manninen and the Oncology Group of the Institute for Surgical Research and Hospital Management at University Hospital Basel, respectively. The Swiss National Science Foundation (Grant 31003A_138063) and the NCCR Molecular Systems Engineering supported this work. Miao Yu was supported by the National Natural Science Foundation of China (51175124).

References

1. Winograd-Katz, S. E.; Fässler, R.; Geiger, B.; Legate, K. R. *Nat. Rev. Mol. Cell Biol.* **2014,** *15,* 273–288. doi:10.1038/nrm3769
2. Hegde, S.; Raghavan, S. *Cell Adhes. Commun.* **2013,** *20,* 155–169. doi:10.3109/15419061.2013.854334
3. Barone, V.; Heisenberg, C.-P. *Curr. Opin. Cell Biol.* **2012,** *24,* 148–153. doi:10.1016/j.ceb.2011.11.006
4. El-Amraoui, A.; Petit, C. Cadherin Defects in Inherited Human Diseases. In *Progress in Molecular Biology and Translational Science;* van Roy, F., Ed.; Elsevier: Burlington, 2013; Vol. 116, pp 361–384.
5. Gumbiner, B. M. *Cell* **1996,** *84,* 345–357. doi:10.1016/S0092-8674(00)81279-9
6. Juliano, R. L. *Annu. Rev. Pharmacol. Toxicol.* **2002,** *42,* 283–323. doi:10.1146/annurev.pharmtox.42.090401.151133
7. Crossin, K. L.; Prieto, A. L.; Hoffman, S.; Jones, F. S.; Friedlander, D. R. *Exp. Neurol.* **1990,** *109,* 6–18. doi:10.1016/S0014-4886(05)80004-4
8. Meager, A. *Cytokine Growth Factor Rev.* **1999,** *10,* 27–39. doi:10.1016/S1359-6101(98)00024-0
9. Hynes, R. O. *Cell* **1992,** *69,* 11–25. doi:10.1016/0092-8674(92)90115-S
10. Sutherland, A. E.; Calarco, P. G.; Damsky, C. H. *Development* **1993,** *119,* 1175–1186.
11. Shen, B.; Delaney, M. K.; Du, X. *Curr. Opin. Cell Biol.* **2012,** *24,* 600–606. doi:10.1016/j.ceb.2012.08.011
12. Hynes, R. O. *Cell* **2002,** *110,* 673–687. doi:10.1016/S0092-8674(02)00971-6
13. Kim, L. T.; Yamada, K. M. *Exp. Biol. Med.* **1997,** *214,* 123–131. doi:10.3181/00379727-214-44078
14. Helenius, J.; Heisenberg, C.-P.; Gaub, H. E.; Muller, D. J. *J. Cell Sci.* **2008,** *121,* 1785–1791. doi:10.1242/jcs.030999
15. Müller, D. J.; Helenius, J.; Alsteens, D.; Dufrêne, Y. F. *Nat. Chem. Biol.* **2009,** *5,* 383–390. doi:10.1038/nchembio.181
16. Friedrichs, J.; Legate, K. R.; Schubert, R.; Bharadwaj, M.; Werner, C.; Müller, D. J.; Benoit, M. *Methods* **2013,** *60,* 169–178. doi:10.1016/j.ymeth.2013.01.006
17. te Riet, J.; Helenius, J.; Strohmeyer, N.; Cambi, A.; Figdor, C. G.; Müller, D. J. *J. Cell Sci.* **2014,** *127,* 1595–1606. doi:10.1242/jcs.141077
18. Wojcikiewicz, E. P.; Zhang, X.; Moy, V. T. *Biol. Proced. Online* **2004,** *6,* 1–9. doi:10.1251/bpo67
19. Fichtner, D.; Lorenz, B.; Engin, S.; Deichmann, C.; Oelkers, M.; Janshoff, A.; Menke, A.; Wedlich, D.; Franz, C. M. *PLoS One* **2014,** *9,* e93123. doi:10.1371/journal.pone.0093123
20. Schubert, R.; Strohmeyer, N.; Bharadwaj, M.; Ramanathan, S. P.; Krieg, M.; Friedrichs, J.; Franz, C. M.; Muller, D. J. *FEBS Lett.* **2014,** *588,* 3639–3648. doi:10.1016/j.febslet.2014.06.012

21. Friedrichs, J.; Helenius, J.; Muller, D. J. *Nat. Protoc.* **2010,** *5,* 1353–1361. doi:10.1038/nprot.2010.89
22. Taubenberger, A.; Cisneros, D. A.; Friedrichs, J.; Puech, P.-H.; Muller, D. J.; Franz, C. M. *Mol. Biol. Cell* **2007,** *18,* 1634–1644. doi:10.1091/mbc.E06-09-0777
23. Taubenberger, A. V.; Hutmacher, D. W.; Muller, D. J. *Tissue Eng., Part B* **2014,** *20,* 40–55. doi:10.1089/ten.teb.2013.0125
24. Krieg, M.; Helenius, J.; Heisenberg, C.-P.; Muller, D. J. *Angew. Chem., Int. Ed.* **2008,** *47,* 9775–9777. doi:10.1002/anie.200803552
25. Benoit, M.; Gaub, H. E. *Cells Tissues Organs* **2002,** *172,* 174–189. doi:10.1159/000066964
26. Benoit, M.; Gabriel, D.; Gerisch, G.; Gaub, H. E. *Nat. Cell Biol.* **2000,** *2,* 313–317. doi:10.1038/35014000
27. Taubenberger, A. V.; Woodruff, M. A.; Bai, H.; Muller, D. J.; Hutmacher, D. W. *Biomaterials* **2010,** *31,* 2827–2835. doi:10.1016/j.biomaterials.2009.12.051
28. Alon, R.; Feigelson, S. W.; Manevich, E.; Rose, D. M.; Schmitz, J.; Overby, D. R.; Winter, E.; Grabovsky, V.; Shinder, V.; Matthews, B. D.; Sokolovsky-Eisenberg, M.; Ingber, D. E.; Benoit, M.; Ginsberg, M. H. *J. Cell Biol.* **2005,** *171,* 1073–1084. doi:10.1083/jcb.200503155
29. Friedrichs, J.; Torkko, J. M.; Helenius, J.; Teräväinen, T. P.; Füllekrug, J.; Muller, D. J.; Simons, K.; Manninen, A. *J. Biol. Chem.* **2007,** *282,* 29375–29383. doi:10.1074/jbc.M701867200
30. Friedrichs, J.; Helenius, J.; Müller, D. J. *Proteomics* **2010,** *10,* 1455–1462. doi:10.1002/pmic.200900724
31. Kim, H.; Arakawa, H.; Osada, T.; Ikai, A. *Ultramicroscopy* **2003,** *97,* 359–363. doi:10.1016/S0304-3991(03)00061-5
32. Hyonchol, K.; Arakawa, H.; Osada, T.; Ikai, A. *Colloids Surf., B* **2002,** *25,* 33–43. doi:10.1016/S0927-7765(01)00299-5
33. Friedrichs, J.; Taubenberger, A.; Franz, C. M.; Muller, D. J. *J. Mol. Biol.* **2007,** *372,* 594–607. doi:10.1016/j.jmb.2007.06.078
34. Canale, C.; Petrelli, A.; Salerno, M.; Diaspro, A.; Dante, S. *Biosens. Bioelectron.* **2013,** *48,* 172–179. doi:10.1016/j.bios.2013.04.015
35. Lamers, E.; te Riet, J.; Domanski, M.; Luttge, R.; Figdor, C. G.; Gardeniers, J. G. E.; Walboomers, X. F.; Jansen, J. A. *Eur. Cells Mater.* **2012,** *23,* 182–194.
36. Dao, L.; Weiland, U.; Hauser, M.; Nazarenko, I.; Kalt, H.; Bastmeyer, M.; Franz, C. M. *Exp. Cell Res.* **2012,** *318,* 2155–2167. doi:10.1016/j.yexcr.2012.06.017
37. Dao, L.; Gonnerman, C.; Franz, C. M. *J. Mol. Recognit.* **2013,** *26,* 578–589. doi:10.1002/jmr.2303
38. Lee, M. H.; Brass, D. A.; Morris, R.; Composto, R. J.; Ducheyne, P. *Biomaterials* **2005,** *26,* 1721–1730. doi:10.1016/j.biomaterials.2004.05.026

License and Terms

The definitive version of this article is the electronic one which can be found at:
doi:10.3762/bjnano.6.15

BEILSTEIN JOURNAL OF NANOTECHNOLOGY

Kelvin probe force microscopy in liquid using electrochemical force microscopy

Liam Collins[1,2], Stephen Jesse[3], Jason I. Kilpatrick[2], Alexander Tselev[3],
M. Baris Okatan[3], Sergei V. Kalinin[3,4] and Brian J. Rodriguez[*1,2]

Full Research Paper

Open Access

Address:
[1]School of Physics, University College Dublin, Belfield, Dublin 4, Ireland, [2]Conway Institute of Biomolecular and Biomedical Research, University College Dublin, Belfield, Dublin 4, Ireland, [3]Center for Nanophase Materials Sciences, Oak Ridge National Laboratory, Oak Ridge, Tennessee 37831, USA and [4]Institute for Functional Imaging of Materials, Oak Ridge National Laboratory, Oak Ridge, Tennessee 37831, USA

Email:
Brian J. Rodriguez[*] - Brian.Rodriguez@ucd.ie

* Corresponding author

Keywords:
diffuse charge dynamics; double layer charging; electrochemical force microscopy; electrochemistry; Kelvin probe force microscopy

Beilstein J. Nanotechnol. **2015,** *6,* 201–214.
doi:10.3762/bjnano.6.19

Received: 14 August 2014
Accepted: 10 December 2014
Published: 19 January 2015

This article is part of the Thematic Series "Advanced atomic force microscopy techniques III".

Guest Editor: T. Glatzel

Abstract

Conventional closed loop-Kelvin probe force microscopy (KPFM) has emerged as a powerful technique for probing electric and transport phenomena at the solid–gas interface. The extension of KPFM capabilities to probe electrostatic and electrochemical phenomena at the solid–liquid interface is of interest for a broad range of applications from energy storage to biological systems. However, the operation of KPFM implicitly relies on the presence of a linear lossless dielectric in the probe–sample gap, a condition which is violated for ionically-active liquids (e.g., when diffuse charge dynamics are present). Here, electrostatic and electrochemical measurements are demonstrated in ionically-active (polar isopropanol, milli-Q water and aqueous NaCl) and ionically-inactive (non-polar decane) liquids by electrochemical force microscopy (EcFM), a multidimensional (i.e., bias- and time-resolved) spectroscopy method. In the absence of mobile charges (ambient and non-polar liquids), KPFM and EcFM are both feasible, yielding comparable contact potential difference (CPD) values. In ionically-active liquids, KPFM is not possible and EcFM can be used to measure the dynamic CPD and a rich spectrum of information pertaining to charge screening, ion diffusion, and electrochemical processes (e.g., Faradaic reactions). EcFM measurements conducted in isopropanol and milli-Q water over Au and highly ordered pyrolytic graphite electrodes demonstrate both sample- and solvent-dependent features. Finally, the feasibility of using EcFM as a local force-based mapping technique of material-dependent electrostatic and electrochemical response is investigated. The resultant high dimensional dataset is visualized using a purely statistical approach that does not require a priori physical models, allowing for qualitative mapping of electrostatic and electrochemical material properties at the solid–liquid interface.

Introduction

Many important physical, chemical and biological processes including wetting, adsorption, electronic transfer and catalysis take place at the solid–liquid interface [1,2]. Very often these processes involve charge storage through the formation of electric double layers adjacent to an electrode surface (i.e., capacitive storage) and/or transfer of electrons across an electrode–electrolyte interface (i.e., pseudocapacitive storage). Consequently, understanding the local electrostatic, electrochemical and double layer ion dynamics at the solid–liquid interface is crucial to the study of corrosion, sensing, energy storage and bioelectric interfaces [3]. These processes are dynamic in nature, involving changes of the local concentration of ions through migration (field-driven ion transport) and diffusion (concentration-gradient-driven transport) both to and from the solid–liquid interface as well as electron transfer reactions across the interface, resulting in a broad spectrum of charge relaxation timescales (ns–s) [4-10].

In electrochemical systems, the local reactivities and overpotentials of nucleation centers across micro- to nanometer length scales ultimately govern the electrochemical functionality, lifetime and failure mechanisms of materials and devices. Understanding such systems necessitates the development of characterization techniques capable of operating in ionically-active liquids across multiple length scales from a single step edge or point defect up to the device level. While macroscopic electrochemical measurements are capable of probing material properties on the device level, few techniques are capable of operating below the micron length scale [11]. Scanning probe microscopy (SPM) techniques are uniquely positioned to probe structure on nano- to micrometer length scales and can do so under vacuum, ambient or liquid environments. Thus, the development of SPM techniques that are capable of obtaining both structural information and information on local electrochemical functionality is a natural combination of capability and necessity [12-15].

In the past few decades, a plethora of SPM techniques capable of probing electrostatic, [16,17] electromechanical [18], electrochemical [19] and ionic [15] functionality on the nanoscale have been developed. A paradigmatic example of such development is closed loop-Kelvin probe force microscopy (KPFM) [20], which has become a widely used voltage-modulated SPM technique for the measurement of surface potential distribution, and has proven to be an important technique for studying electronic functionality at the solid–gas interface. KPFM measurements have previously been utilized to investigate surface photo-voltage in photovoltaics [21-23] and charging dynamics in ferroelectric [24-26], dielectric [27] and ionic materials [14,28,29]. When operated in ultra-high vacuum, KPFM has been demonstrated to provide absolute surface potential measurements, with molecular and atomic scale resolution previously reported [30-32]. Interpretation of surface potential values from this technique can, however, become complicated by feedback artefacts and stray capacitance even in vacuum [33-35]. In ambient environments, the interpretation of surface potential values increases in complexity due to the possible shielding of the surface by mobile adsorbates and the presence of a thin water layer, resulting in an unknown background potential [36].

The study of, e.g., biological systems and battery materials necessitates the application of KPFM-like techniques in ionically-active liquids whilst presenting an opportunity to overcome the difficulties present under ambient conditions. Despite the urgent need for KPFM-like measurements in ionically-active liquids, suitable techniques have yet to be established due to complications arising from the broad spectrum of relaxation timescales associated with diffuse charge dynamics [37,38].

Previous attempts to implement KPFM in liquid aimed to avoid ion dynamics and electrochemical processes [39-43]. One approach to avoid diffuse charge dynamics has been to implement KPFM in non-polar solutions [39]. Open loop-KPFM approaches, offering a promising approach for measuring electrostatic properties in ionically-active liquids, have also been previously reported [40-43]. In general, open loop-KPFM does not require the application of a DC bias via a feedback loop and can be performed by utilizing either (i) both AC voltage and DC bias (referred to here as open loop bias spectroscopy, OLBS) [44], or (ii) AC voltage alone (referred to here as dual harmonic KPFM, DH-KPFM) [34,45]. Kobayashi et al. [40-42] have previously demonstrated the application of DH-KPFM for surface potential mapping in low molarity solutions (<10 mM). However, for energy or biological applications, where solution concentrations are often >>10 mM, ion dynamics occur at timescales <<100 ns [43]. The broad distribution of timescales associated with electrochemical processes necessitates the development of techniques capable of probing ion dynamics and electrochemical processes taking place between the probe and sample as a function of time.

Here, OLBS measurements in air and milli-Q water are compared to illustrate the infeasibility of implementing KPFM in ionically-active liquids. A multidimensional (i.e., bias- and time-resolved) spectroscopy method, referred to as electrochemical force microscopy (EcFM) [38], is subsequently investigated for performing electrostatic measurements in both ionically-active and -inactive liquids. EcFM is employed to detect the bias- and time-dependent electrostatic and electrochemical forces between probe and sample under ambient, non-polar (ionically-inactive decane) and polar (ionically-active isopropanol, milli-Q water and aqueous NaCl) environments. The measurement of bias- and time-dependent ion dynamics allows different electrokinetic phenomena to be separated and a set of environmental and measurement timescale requirements for determining CPD under conditions comparable with KPFM to be delineated. Finally, the applicability of EcFM to resolve local electrostatic and electrochemical properties at the solid–liquid interface in the presence of diffuse ion dynamics is demonstrated. The increase in both size and complexity of the resulting data necessitates simple analysis methods capable of dealing with high dimensional information without relying on a priori physical models. Multivariate statistical approaches are implemented in order to map the local electrochemical behavior across a metal-insulator junction.

Results and Discussion

OLBS in air and milli-Q water

Assuming a lossless dielectric between probe and sample, the static and dynamic components of the electrostatic force resulting when a DC bias, V_{dc}, and AC voltage, V_{ac}, at a frequency, ω, is applied between a conducting probe and a sample ($V_{probe} = V_{dc} + V_{ac}\cos(\omega t)$) are given by:

$$F_{dc} = -\frac{1}{2}C_z'\left[\left(V_{dc} - V_{cpd}\right)^2 + \frac{1}{2}V_{ac}^{\ 2}\right] \qquad (1)$$

$$F_{\omega} = -C_z'\left(V_{dc} - V_{cpd}\right)V_{ac}\sin(\omega t) \qquad (2)$$

$$F_{2\omega} = C_z'\frac{1}{4}V_{ac}^{\ 2}\cos(2\omega t) \qquad (3)$$

where C_z' is the capacitance gradient, governed by the geometry and permittivity of the probe–sample capacitor system and V_{cpd} is the CPD or electrochemical potential between the probe and sample. Equation 2 and Equation 3 describe the bias-dependent first harmonic force, F_{ω}, and the bias-independent second harmonic force, $F_{2\omega}$, acting on the probe, which are detected as the first and second harmonic cantilever amplitude (A_{ω} and $A_{2\omega}$) and phase (θ_{ω} and $\theta_{2\omega}$) using lock-in techniques. Equation 2 predicts a linear dependence of F_{ω} with respect to the probe–sample DC bias, which is minimized when $V_{dc} = V_{cpd}$. KPFM employs this principle via a feedback loop to minimize A_{ω}. Depending on the material under investigation and the environment in which the measurement is performed, the CPD can then be related to various electrostatic and electrochemical properties. For example, in the case of a metal probe with known work function in vacuum, the CPD provides a measurement of the work function of the sample. For non-conducting materials, such as semiconductors, dielectrics and ferroelectrics, additional Columbic terms arising from static charges and polarizability may also contribute to the detected force [46]. $F_{2\omega}$ can be used to study local dielectric properties [47,48], and has recently been used to quantify dielectric constants in low molarity (<10 mM) solutions at high frequency (>MHz) [49,50].

In deriving Equation 2, an implicit assumption of a linear lossless dielectric between probe and sample is made. This has two major implications, which underpin the operation of KPFM. First, the electrostatic force must be measured under equilibrium conditions and secondly, F_{ω} must have a linear V_{dc} dependence. In ionically-active liquids, however, where a lossy polarizable dielectric is present between probe and sample, Equation 2 is insufficient to accurately describe the system. In particular, if the measurement timescale >> relaxation time of the system, the system will be in equilibrium with the double layer fully formed, whereas for a measurement timescale << the relaxation time of the system, the system will behave similar to a linear dielectric. Finally, intermediate relaxation times can give rise to complex dynamic responses. Hence, bias-induced charge dynamics (e.g., electromigration and ion diffusion) as well as steric effects [6-9] and electrochemical processes at larger biases, need to be detected and separated experimentally in order to fully characterize the system, which is beyond the capabilities of KPFM.

The bias dependence of A_{ω} and $A_{2\omega}$ recorded during OLBS is shown in Figure 1. Here, V_{ac} was applied to the probe at a fixed distance (200 nm) above the surface as V_{dc} was ramped linearly to a set potential, at which point the V_{dc} ramp was inverted. Measurements were performed in air and milli-Q water with the same Pt/Ir coated probe. Figure 1a,b shows the bias dependence of A_{ω} for highly ordered pyrolytic graphite (HOPG) and Au surfaces, respectively. For both HOPG and Au, a linear dependence of A_{ω} to the applied V_{dc} was observed in air, and the minimum of A_{ω} corresponds to the measured CPD of the probe–sample system, as described by Equation 2. Thus, the CPD was estimated to be ≈420 mV for HOPG and ≈−60 mV for Au.

To investigate the operation of KPFM in liquid, the measurements were repeated in milli-Q water, which has a minimum ion concentration of $\approx 4 \times 10^{-7}$ M [51]. In a first set of experiments, small bias sweeps (±300 mV) were performed to reduce the likelihood of inducing irreversible electrochemical processes. For HOPG, a minimum was observed at ≈370 mV, close to the measured CPD in air, but no minimum was observed for Au. The observed A_{ω} for Au is weakly dependent

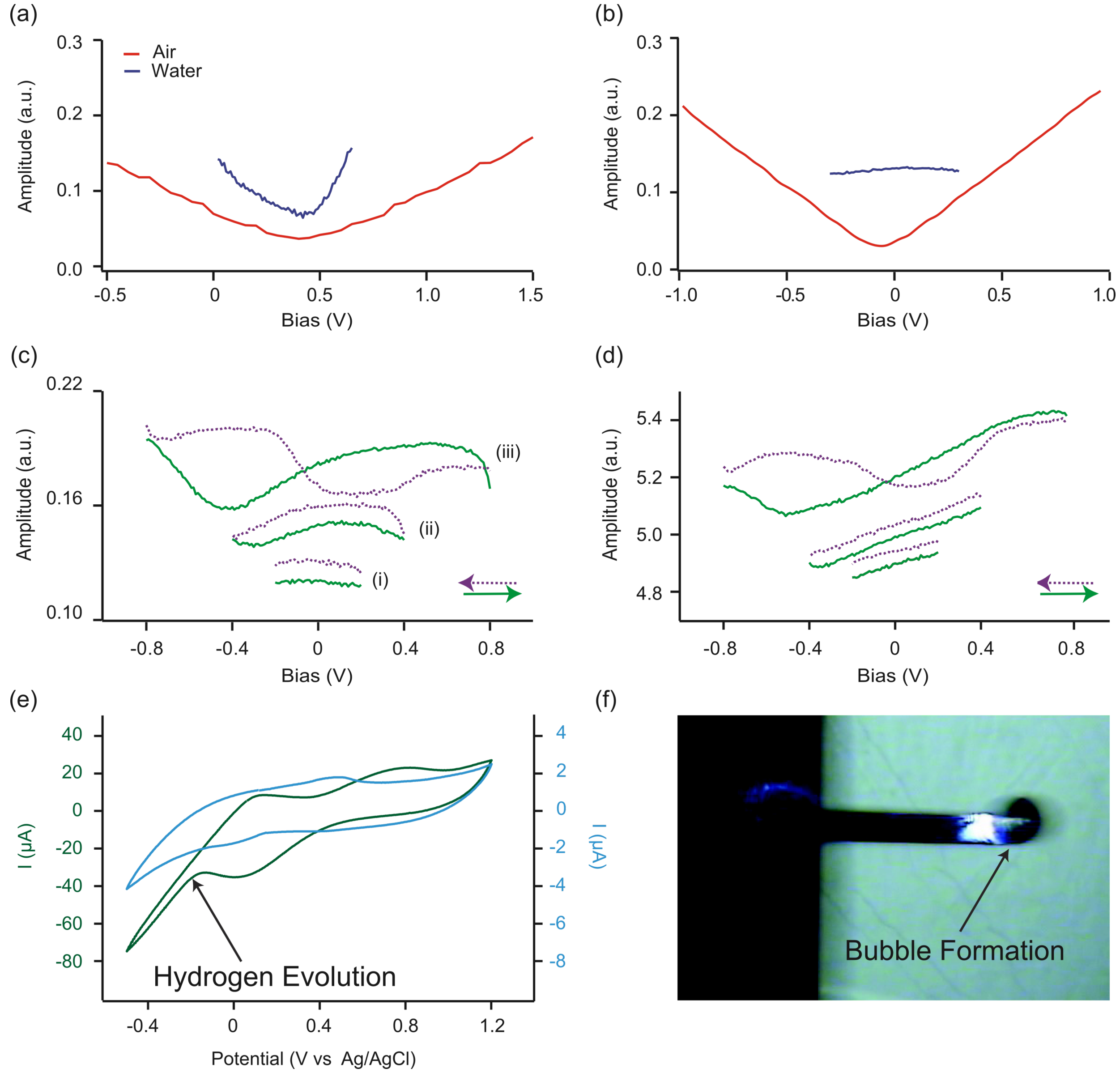

Figure 1: A_ω recorded in air (red) and milli-Q water (blue) 50 nm above (a) HOPG and (b) Au surfaces as a function of the DC bias applied to the probe. (c) A_ω and (d) $A_{2\omega}$ recorded 50 nm above an Au surface in the order of (i) small (±200 mV), (ii) medium (±400 mV) and (iii) large (±800 mV) bias ranges. Measurements were performed using a sweep rate of 500 $\mathrm{mVs^{-1}}$ for HOPG and 100 $\mathrm{mVs^{-1}}$ for Au in air and 100 $\mathrm{mVs^{-1}}$ for both surfaces in milli-Q water, with V_{ac} = 0.5 V [5 kHz] applied to the probe. (e) Cyclic voltammetry measurements in milli-Q water of HOPG (blue) and Au (green) electrodes were performed using a sweep rate of 50 $\mathrm{mVs^{-1}}$. (f) Optical image of bubble formation between the probe and HOPG surface in response to the application of a 2 V DC bias (nominal cantilever length is 225 μm).

on bias in this range, suggesting the mechanisms at play are significantly different from those described by Equation 2. In aqueous solutions, charge screening from ions, adsorption of water molecules and surface dipoles at the probe and/or sample surface could also play a role in shifting the measured CPD of the Au surface outside of the bias range studied.

In order to investigate the possibility that the CPD of Au was shifted in liquid, and to further investigate the dependence of electrostatic forces at larger biases, A_ω and $A_{2\omega}$ were probed under increasing bias ranges, i.e., adopting a first order reversal curve approach. Previously, this approach was demonstrated to be highly effective in exploring local bias-induced phenomena that are reversible for small biases and irreversible at high biases [14,52,53].

Typical results for A_ω and $A_{2\omega}$ above an Au surface for three bias ranges are shown in Figure 1c,d. Data sweeps were collected for a small (±200 mV), medium (±400 mV) and large (±800 mV) bias range, consecutively. For small bias sweeps

(±200 mV), finite shifts in the magnitude of A_ω between negative and positive (green) and between positive and negative (purple) bias sweeps were observed, likely resulting from a redistribution of ions. For medium bias sweeps (±400 mV), hysteretic behavior was observed between sweeps. Large bias sweeps (±800 mV) resulted in complex responses including hysteretic behavior and the presence of maxima and minima. Raiteri et al. reported similar hysteretic behavior in the static electrochemical stress experienced for biased Au electrodes in a variety of electrolytes [54]. Umeda et al. also observed similar hysteresis in this bias range for a cantilever above a platinum surface in water [55]. For all bias sweeps shown here, the general shapes of the OLBS curves were reproducible when using the same sweep rate; however, the shape and magnitude of the response was found to depend heavily on sweep rate (not shown), suggesting an underlying temporal dependence of the response.

The differences in the bias-dependent A_ω response in milli-Q water and air for HOPG and Au are attributed to the differences in electronic and electrochemical properties of the materials. This was confirmed macroscopically using cyclic voltammetry (CV) measurements [56]. Typical CV traces for both HOPG and Au electrodes in milli-Q water are shown in Figure 1e. In some respects, OLBS (Figure 1a–d) is a force-based analogue of the macroscopic current-based CV measurement.

Hydrogen evolution can be observed for Au at potentials of <−200 mV (Figure 1e), but not for HOPG, showing that HOPG is more electrocatalytically inert than the Au electrode. In OLBS measurements, when using bias sweeps larger than 2 V, large changes in the AFM cantilever deflection signal occurred (not shown), often followed by visible bubble nucleation in the probe–sample gap (e.g., Figure 1f). Attempts at implementing KPFM in ionically-active liquids will often result in similar, if not more catastrophic, bubble formation by virtue of the absence of a defined minimum, which may result in the application of large DC biases by the feedback loop.

Figure 1 demonstrates that the universal application of KPFM across all materials, all bias ranges and all solutions is not viable. In particular, the absence of a unique minimum in A_ω and the presence of hysteresis and irreversible reactions at larger biases observed for Au (Figure 1c,d) are fundamental barriers to the proper application of KPFM in milli-Q water and other ionically-active liquids.

Bias- and time-resolved EcFM

The hysteresis observed in Figure 1 illustrates that the response in milli-Q water is more complex than expected from the electrostatic force interactions described by Equations 1–3. This is not surprising as the underlying assumption of a lossless dielectric is no longer valid in the presence of diffuse ion dynamics, precluding the use of KPFM. The observed hysteretic response can be explained as a combination of tip–sample interactions caused by field-driven migration and concentration-gradient-driven diffusion of ions in the bulk electrolyte, as well as possible steric effects, double layer charging and electrochemical processes at larger biases. This necessitates making simultaneous measurements as a function of both bias and time. As a relevant parallel, macroscopic analysis of diffuse charge dynamics or electrochemical processes also requires separation of the electrokinetic effects, which cannot be obtained using linear bias sweeps (e.g., CV measurements), ultimately requiring either pulsed electrochemical or impedance measurements [57].

To achieve this goal, a multidimensional spectroscopic strategy was implemented, which is capable of probing both the bias- and time-dependent dynamic probe-sample interaction, referred to as EcFM [38]. In EcFM the probe is electrically modulated with a high frequency AC voltage used to detect the dynamic cantilever response using lock-in amplifiers while the system is perturbed by DC bias waveforms applied, in the present study, to the probe. Ideally, the AC voltage excitation should be at sufficiently high frequency such that AC voltage-induced electrochemical processes do not dominate the response mechanism and thus the system is probed under quasistatic conditions. In EcFM, the data is collected both during the bias application (bias-on state) and following the bias application (bias-off state), as the magnitude of the bias pulses is increased linearly with time. Figure 2a shows a section of the DC bias waveform applied to the probe with the corresponding response recorded in air. Here, data is presented as the mixed response ($A_\omega^{\text{mixed}} = A_\omega \cos(\theta_\omega)$) which contains information on the polarity and magnitude of the signal. Little to no relaxation of the electrostatic force is observed, with A_ω^{mixed} following the applied bias, and therefore satisfying the second principle of KPFM, a time-invariant electrostatic response. This is expected for a purely electrostatic response, or more generally when the force experienced by the system is governed purely by the time-independent Maxwell stress tensor directly related to the charge density between probe and sample [58].

The data can be presented as an EcFM spectra representing the bias- and time-dependent A_ω^{mixed} for a single location, e.g., Figure 2b. In ionically-inactive non-polar liquids, such as decane, Figure 2d,e,f, a similar response is observed to that observed in air, where again the electrostatic force follows the applied DC bias and is time-invariant. In ionically-active polar liquids, such as isopropanol (Figure 2g,h,i) or milli-Q water (Figure 2j,k,l), a very different response mechanism is observed. For these systems, a large increase in $A_{\omega}^{\text{mixed}}$ is observed at the instant the bias pulse is applied, which relaxes within ≈10 ms to below ≈30% of the peak value. In isopropanol, a smooth transient decay of the response is observed for all biases measured. The relaxation could be well-described by a double exponent decay having a fast relaxation time (τ_1) of 1.2 ms to 6.3 ms and a slower relaxation time (τ_2) between 11 ms and 47 ms (see Supporting Information File 1, Figure S1 for full fitting results). For milli-Q water, regions of varying transient response could be identified. For bias values between −1.5 V and 0.6 V a smooth transient decay having a τ_1 of 4.4 ms and a slower relaxation τ_2 between 12 ms and 50 ms were determined (see Supporting Information File 1, Figure S2 for full fitting results). In milli-Q water for larger positive biases (>600 mV), a more complex response with local minima were observed (>3 ms), as seen in Figure 2j, which could not be described by exponential fitting alone and are likely indicative of the initiation of Faradaic processes between tip and sample.

Similar information can be obtained from the bias-off state. For both air and decane the bias-off state was time-invariant for the entire bias range, Figure 2c,f. For isopropanol (Figure 2i) and milli-Q water (Figure 2l), transient responses were detected for the bias-off state and the magnitude of the response was bias-

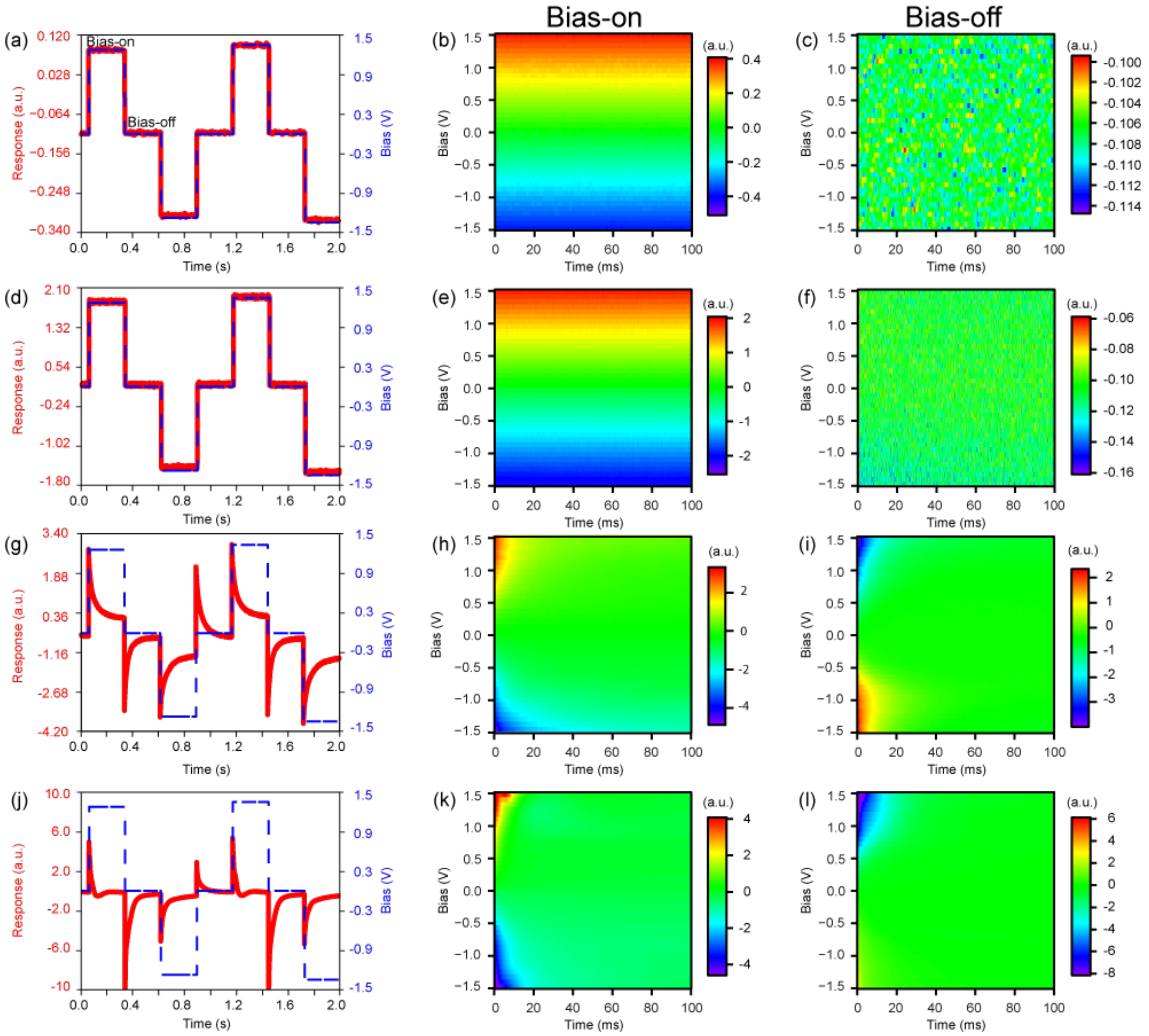

Figure 2: EcFM $A_{\omega}^{\text{mixed}}$ response collected 200 nm above a grounded Au electrode in (a, b, c) air, (d, e, f) decane and (g, h, i) isopropanol and (j, k, l) milli-Q water. (a, d, g, j) Temporal response (solid red line) of $A_{\omega}^{\text{mixed}}$ in response to the applied DC bias waveform (dashed blue line). Single-point EcFM $A_{\omega}^{\text{mixed}}$ spectra showing bias-on (b, e, h, k) and bias-off (c, f, i, l) states. Measurements were performed with V_{ac} = 0.5 V [25 kHz] applied to the probe.

dependent. This response is attributed to the redistribution of ions in the double layer that occurs when the bias is switched off. For milli-Q water (Figure 2l), the largest response (including for bias-on states) was seen after the application of positive bias pulses greater than +600 mV. Interestingly, this is also the region where deviations from an exponential decay in the bias-on state are detected, which may be indicative of, e.g., steric effects or Faradaic reactions being induced at large positive biases. EcFM measurements in a three electrode configuration with a reference and counter electrode would be beneficial for elucidating the precise bias at which electron transfer reactions are initiated. This is the subject of ongoing investigation.

The time-independent response for decane suggests that KPFM in liquid is possible in ionically-inactive liquids, as was previously reported [39]. In ionically-active liquids, however, the large peak and subsequent exponential relaxation of the cantilever response observed is likely associated with diffuse ion dynamics. To account for these effects, an equivalent circuit approach is adopted, in which the double layer charging is modelled as an idealized capacitor [6] and the ion dynamics can be described in terms of equivalent circuits, where the double layer remains in quasi-equilibrium with the neutral bulk electrolyte. The charging is governed by the transport of ions into the double layer. During the double layer charging, the bulk electrolyte concentration remains nearly uniform, and thus, the bulk electrolyte acts as a resistor in series with the double layer capacitors at each interface. Equivalent circuit models are commonly used in electrochemical measurements, and reportedly describe the electrostatic actuation of microelectromechanical systems [59] and electrostatic force microscopy (EFM) [50] in liquid, analysis of which was performed analytically and verified experimentally to establish the critical actuation frequency such that the timescale is shorter than required for double layer screening.

The associated *RC* timescale can be expressed as

$$\tau_{RC} = RC = \frac{\lambda L/2}{D} \qquad (4)$$

where D is the diffusivity of the ions in solution, L is the separation of the electrodes and λ is the Debye screening length, given by

$$\lambda = \sqrt{\frac{\varepsilon kT}{2z^2e^2C_\mathrm{b}}} \qquad (5)$$

where k is Boltzmann's constant, C_b is the molar concentration, ε is the dielectric permittivity of the solvent, T is the temperature, e is the electronic charge and z is the ion valence. At low biases ($V_\mathrm{dc} < kT/e \approx 25$ mV) and in the absence of Faradaic reactions, this *RC* time is the relevant timescale of the transient response, e.g., in high-frequency impedance spectroscopy experiments or induced charge electrokinetics, where high-frequency alternating currents are applied [5]. Thus, it would be expected that the *RC* time is the relevant timescale of the transient response in isopropanol or milli-Q water (Figure 2g,j), suggesting a similarity between τ_1 and τ_{RC}, as previously reported [38].

Despite the broad applicability of equivalent circuit models in electrochemistry, and the success shown in describing imaging mechanisms in low molarities (≈10 mM) using high frequency (>>MHz) EFM [50], their suitability across all biases (particularly large biases where $V_\mathrm{dc} >> 25$ mV) and timescales as well as at higher ion concentration is unclear, particularly as the non-uniform evolution of ion concentration (e.g., ion depletion in the neutral bulk electrolyte) cannot be adequately modelled by homogenous circuit elements [37]. Furthermore, the *RC* time is not the only relevant timescale for equilibration of an electrochemical cell, as illustrated by the apparent double exponential decay of A_ω^mixed in ionically-active liquids (see Supporting Information File 1, Figure S1 and Figure S2). As previously described [38], the bulk electrolyte diffusion timescale (τ_L) (i.e., the time it takes an ion to diffuse from the bulk electrolyte into the diffuse charge layer), ($\tau_L = (L/2)^2/D$), which is much larger than the *RC* time for thin double layers ($L >> 2\lambda$) becomes increasingly important in the presence of Faradaic reactions or at large applied biases ($V_\mathrm{dc} >> 25$ mV) for blocking electrodes where the electric double layer adsorbs neutral salt such that the bulk electrolyte becomes depleted [5]. It is likely that τ_2 is related to ion depletion and subsequent ion diffusion from the bulk electrolyte, suggesting a similarity to τ_L as previously reported [38]. As seen in Figure 2j, more sophisticated descriptions of the electrostatic force than those described in Equations 1–3 are required to account for non-linear effects (e.g., ion crowding and Faradaic reactions) across all bias ranges. Towards a complete understanding of these phenomena, it is expected that the full time-dependent ion transport dynamics, recently developed for ideally polarizable electrodes, will need to be solved numerically for the complex probe–sample geometry [4]. In the presence of Faradaic reactions, this approach must be extended to include the Frumkin correction and other non-linear modifications of the reaction rate associated with diffuse charge [5].

The presence of a non-linear bias dependence (Figure 1) and time-dependent response (Figure 2) currently precludes the application of KPFM in ionically-active liquids. Figure 3a,b,c show A_ω^{mixed} collected in decane, isopropanol and milli-Q water, respectively. Here, A_ω^{mixed} is plotted as a function of V_{dc}, while the color scale represents the timescale. In decane, A_ω^{mixed} follows a linear bias dependence and no deviation from linearity was observed for all times probed. Under these conditions, EcFM "converges" to KPFM in the sense that EcFM can be used to determine the CPD by linear fitting as is done in OLBS (see Supporting Information File 1, Figure S3) to find the bias at which A_ω^{mixed} is minimized. The CPD was determined for each time slice as $A_\omega^{\text{mixed}} = 0$ and the slope of a linear fit was used to measure C_z' [44]. For decane (Figure 3a,d), both the CPD (85 ± 2 mV) and C_z' were constant within experimental error with any variations likely to be a result of small changes in probe–sample geometry due to drift in the probe–sample separation during the measurement. These results validate the implementation of KPFM in decane [39]. Since the decane acts like a near-perfect lossless dielectric between probe and sample, the dynamic response is purely capacitive and can be effectively described by Equation 2. The extension of KPFM to operation in ionically-active liquids provides an opportunity to study, e.g., multi-layered charge structures in non-polar electrified interfaces and electrochemical potentials of thin layers and surfactants.

In isopropanol or milli-Q water, when the measurement timescale $<<\tau_{RC}$, i.e., faster than the time it takes ions in solution to fully screen the charged surface from the probe, a measured value for the CPD can be obtained in a manner similar to that used for decane. In the case of milli-Q water, the bias dependence was fit in a smaller bias window (−500 to +500 mV) to avoid including the observed non-linear behavior at higher biases (see Supporting Information File 1, Figure S2). From the first 2 ms of data the CPD of the Au electrode was found to be 158 ± 8 mV in isopropanol and 112 ± 14 mV in milli-Q water, close to that observed in decane (85 ± 2 mV). The discrepancies between the measured CPD values likely result from physisorption of molecules at the solid–liquid interface [39]. The error is greater for the measured CPD recorded in ionically-active polar solvents than in decane due to gradual changes of the measured CPD in milli-Q water and isopropanol (Figure 3e,f), which varies by >650 mV in both ionically-active polar liquids within the 100 ms measurement as a result of screening by the double layers between probe and sample. This is also reflected in the transient behavior in the capacitance gradient, shown in Figure 3e,f. Again, this transient response was well-described by a double exponent fit (blue line) having relaxation times of $\tau_1 = 5.4$ ms and $\tau_2 = 23.7$ ms in isopropanol and $\tau_1 = 4.2$ ms and $\tau_2 = 31.7$ ms in milli-Q water. This time dependence in polar liquids, which is absent in decane, prohibits the implementation of KPFM in ionically-active liquids and necessitates the adoption of multidimensional bias- and time-resolved techniques, as demonstrated here.

Most electrochemical systems of interest (i.e., energy or biological systems), however, require characterization at high ion

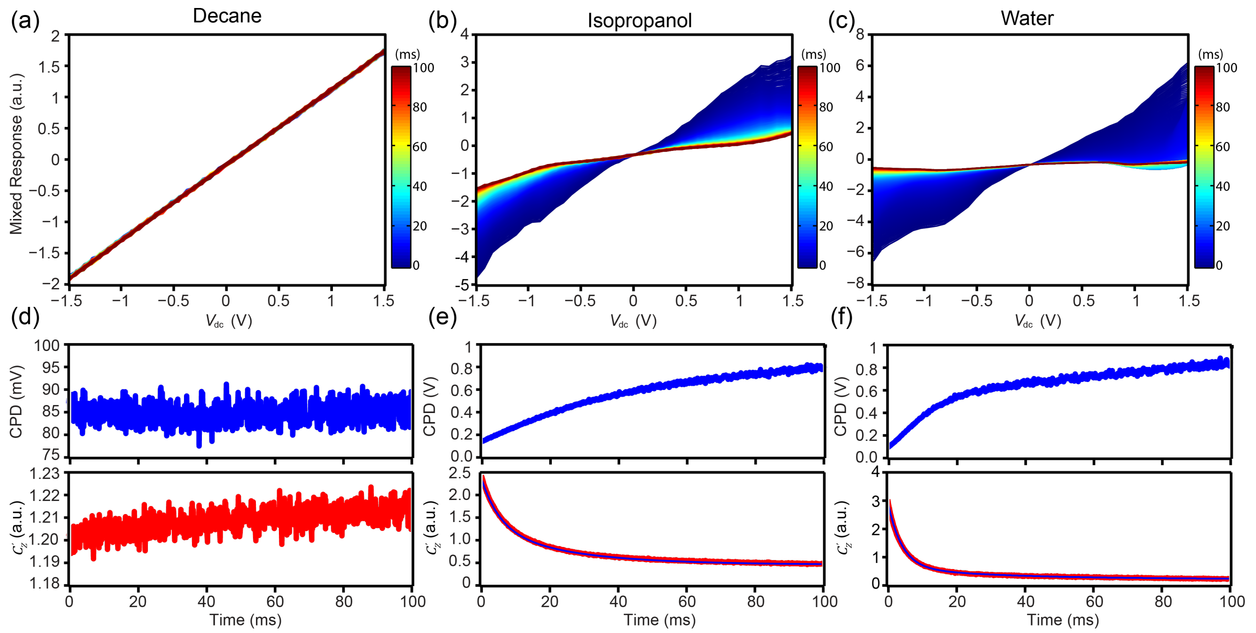

Figure 3: EcFM measurements [bias-on] in (a, d) decane (b, e) isopropanol and (c, f) milli-Q water recorded 200 nm above a grounded Au electrode. (a, b, c) EcFM bias-resolved A_ω^{mixed} with time represented on the color scale. (d, e, f) The measured CPD and C_z' determined from linear fitting of A_ω^{mixed} (Supporting Information File 1, Figure S3). Measurements were performed with $V_{\text{ac}} = 0.5$ V [25 kHz] applied to the probe.

concentration >100 mM. Thus, to explore the dependence of the ion concentration on the EcFM response, single-point EcFM measurements were performed as a function of NaCl concentration (Figure 4). For measurements performed in the presence of NaCl, the data shows a non-linear bias dependence of A_ω^{mixed}. In addition, bubble formation was observed within the applied bias range ≥10 mM, with the threshold for bubble formation being lower for larger salt concentrations. When bubbles became visible, data collection was stopped.

For concentrations ≥10 mM, A_ω^{mixed} did not fully relax within the measurement time following the application of negative bias. The calculated double layer charging times for Figure 4b, τ_{RC} = 0.8 µs between tip and sample and τ_{RC} = 22.8 µs between cantilever and sample (λ = 3.04 nm, L_{tip} = 500 nm, $D = 1 \times 10^{-9}$ m^{2}s^{-1} and $L_{\text{cantilever}}$ = 15 µm), are both well outside the current temporal resolution, which is currently determined by the low pass filter of the lock-in amplifier (100 µs). The slower processes (>>10 ms) are likely a result of irreversible Faradaic reactions.

In Figure 1, HOPG and Au demonstrated different electrochemical response for both OLBS and CV measurements. The differences in electrochemical properties are also visible in single-point EcFM spectra recorded above both surfaces. A_ω^{mixed} was observed to be non-linear across the full bias range for both Au and HOPG in milli-Q water (Figure 5). The response of A_ω^{mixed} to negative V_{dc} for both surfaces were similar in magnitude, however, the response to positive V_{dc} was significantly larger for Au than for HOPG. In addition, the signal was less likely to relax within the measurement time for Au than for HOPG. The lower response to positive V_{dc} for HOPG as compared to Au can be explained by the inert electrochemical nature of the basal plane of HOPG and the low electrocatalytic activity of HOPG for many redox reactions in comparison to Au, as was previously demonstrated in Figure 1e.

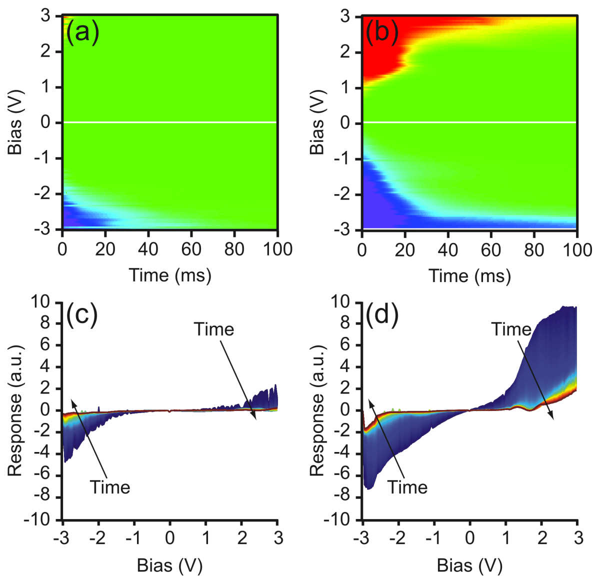

Figure 5: EcFM A_ω^{mixed} spectra [bias-on] collected 500 nm above (a) HOPG and (b) Au in milli-Q water (vertical color scale ±3 a.u. and 0–4 a.u., respectively). Evolution of A_ω^{mixed} response as a function of time for (c) HOPG and (d) Au surfaces (vertical color scale 100 ms). Measurements were performed with V_{ac} = 1 V [15 kHz] applied to the probe.

Mapping local electrochemical reactivity using EcFM

Finally, the different electrochemical properties of HOPG and Au are leveraged to assess the spatial variability in the EcFM response for both materials, and thus, the utility of EcFM for spatially-resolved imaging. To show the localization of the EcFM response, a model sample comprising an electrode of Au deposited on a HOPG surface is used. Shown in Figure 6 is an example of EcFM point spectroscopy across a HOPG/Au boundary in milli-Q water. The variability of the spectral data can be seen across the sample surface and a transition close to the boundary of the materials is observed. This variability

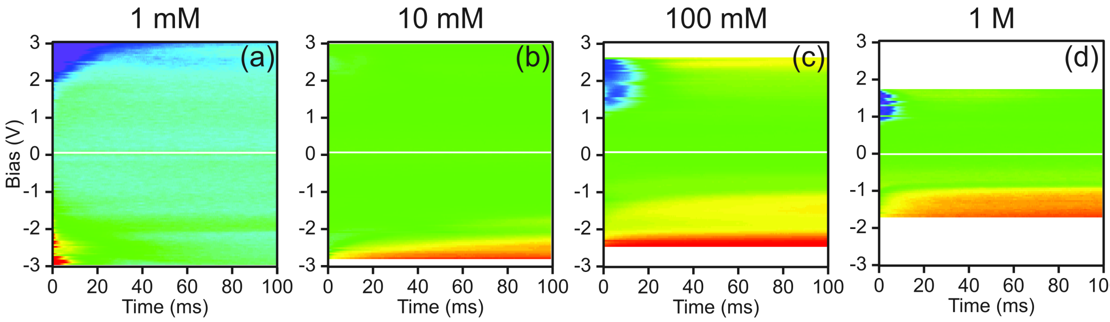

Figure 4: EcFM A_ω^{mixed} spectra [bias-on] collected 500 nm above HOPG in aqueous solutions of increasing salt concentration (1 mM–1 M NaCl). Measurements were recorded from low to high concentrations using the same probe. Vertical scale ±5 a.u. (data normalized by the mean value at the smallest positive V_{dc}). Measurements were performed with V_{ac} = 1 V [15 kHz] applied to the probe.

supports the previously reported conclusion that the data is localized and dependent on the material below the probe, which allows spatially-resolved mapping of electrochemical reactivity using force-based detection [38].

Statistical analysis of EcFM

The complexity of the electrochemical processes taking place between tip and sample requires the adoption of a multidimensional approach to capture the bias (V) and time (t) dependence of the response at each spatial (x,y) location on the sample. The corresponding multidimensional data (x,y,V,t) can become difficult to analyze, particularly if it cannot be reduced by using phenomenological fitting procedures with parameters having a known physical relationship. Indeed, the development of fitting procedures, based on analytical models, is a key requirement for the broad applicability of EcFM across all areas of electrochemistry. However, in the short term, the significant increase in both size and complexity of the data necessitates simple analysis methods capable of dealing with high dimensional information and without relying on a priori physical models. One possible solution to overcome the difficulty in dealing with such high dimensional data sets is by using multivariate statistical approaches. Here, principal component analysis (PCA) [60] is applied to visualize spatial variability within the EcFM data. PCA selects and ranks relevant response components based on variance within the data purely on statistical methods, without employing assumptions regarding underlying physical behavior. In this way, the first eigenvector contains the most statistically relevant information (defined as variance) within the dataset, while the second contains the most statistically rele-

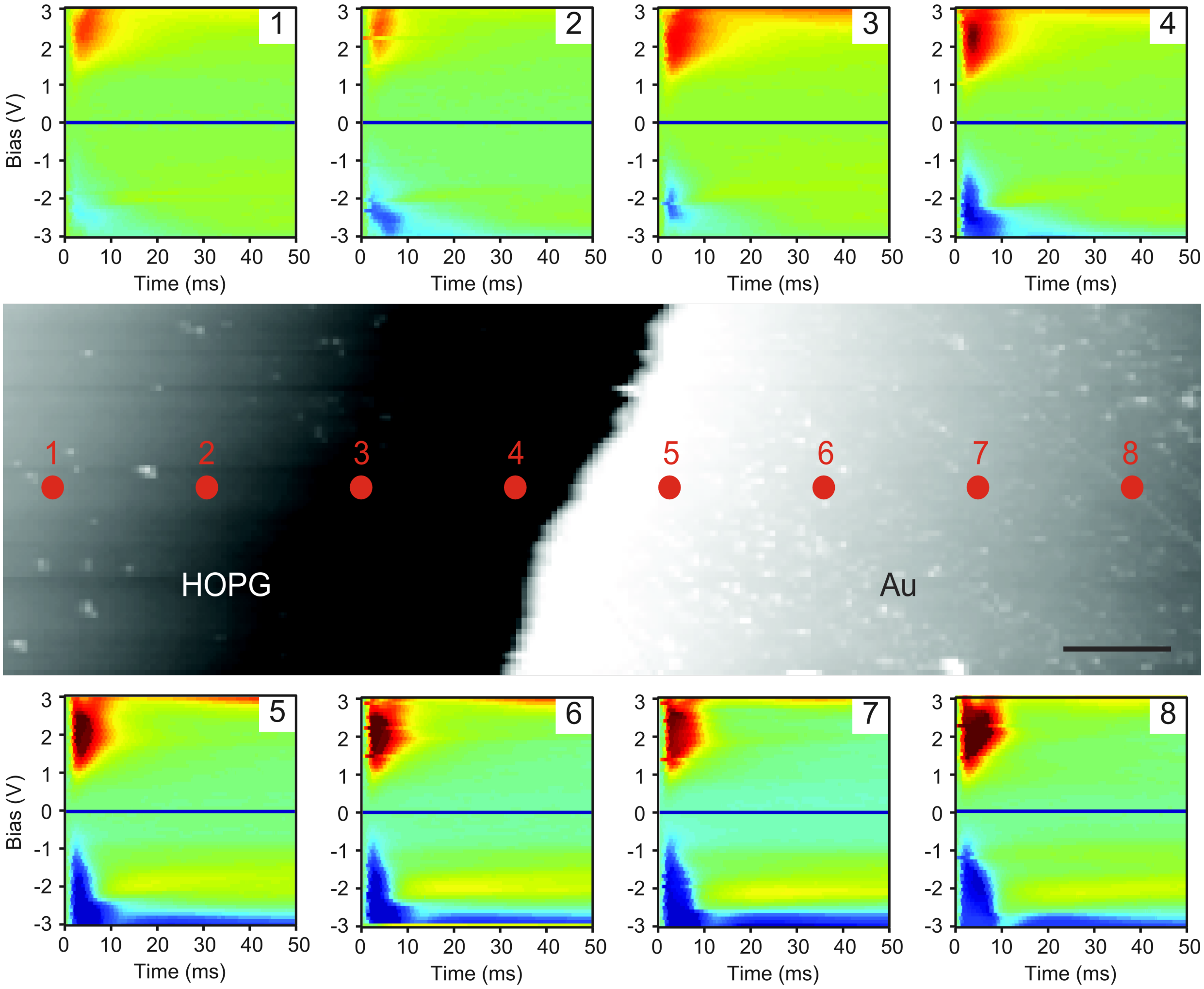

Figure 6: Variability of EcFM $A_{\omega}^{\text{mixed}}$ spectra [bias-on] recorded 500 nm above a HOPG/Au boundary in milli-Q water. Topography and markers indicate positions at which the single-point data was collected (scale bar = 5 μm). Vertical color scale ±10 a.u. for inserts 1–8. Measurements were performed with V_{ac} = 0.5 V [17.5 kHz] applied to the probe.

vant information after subtraction of the first, and so on. PCA is used to transform a number of correlated variables into a smaller number of uncorrelated variables called principal components (PCs), where each PC can be represented as an eigenvector and corresponding loading (eigenvalue) map.

Figure 7 demonstrates the usefulness of the application of PCA to EcFM data. The EcFM data analyzed was of the first harmonic (bias on) mixed response recorded on a 50 × 15 grid across a metal/insulator boundary. The spatial distribution of the first component demonstrates that PCA separates the overall behavior into metal and insulator regions. The first two PCs contain >97% of the statistically relevant information as shown from the dominance plot in Figure 7a. Loading maps beyond 2nd PC are dominated by noise. Note that within the first two PCs, isolated regions or hot spots demonstrate a different elec-

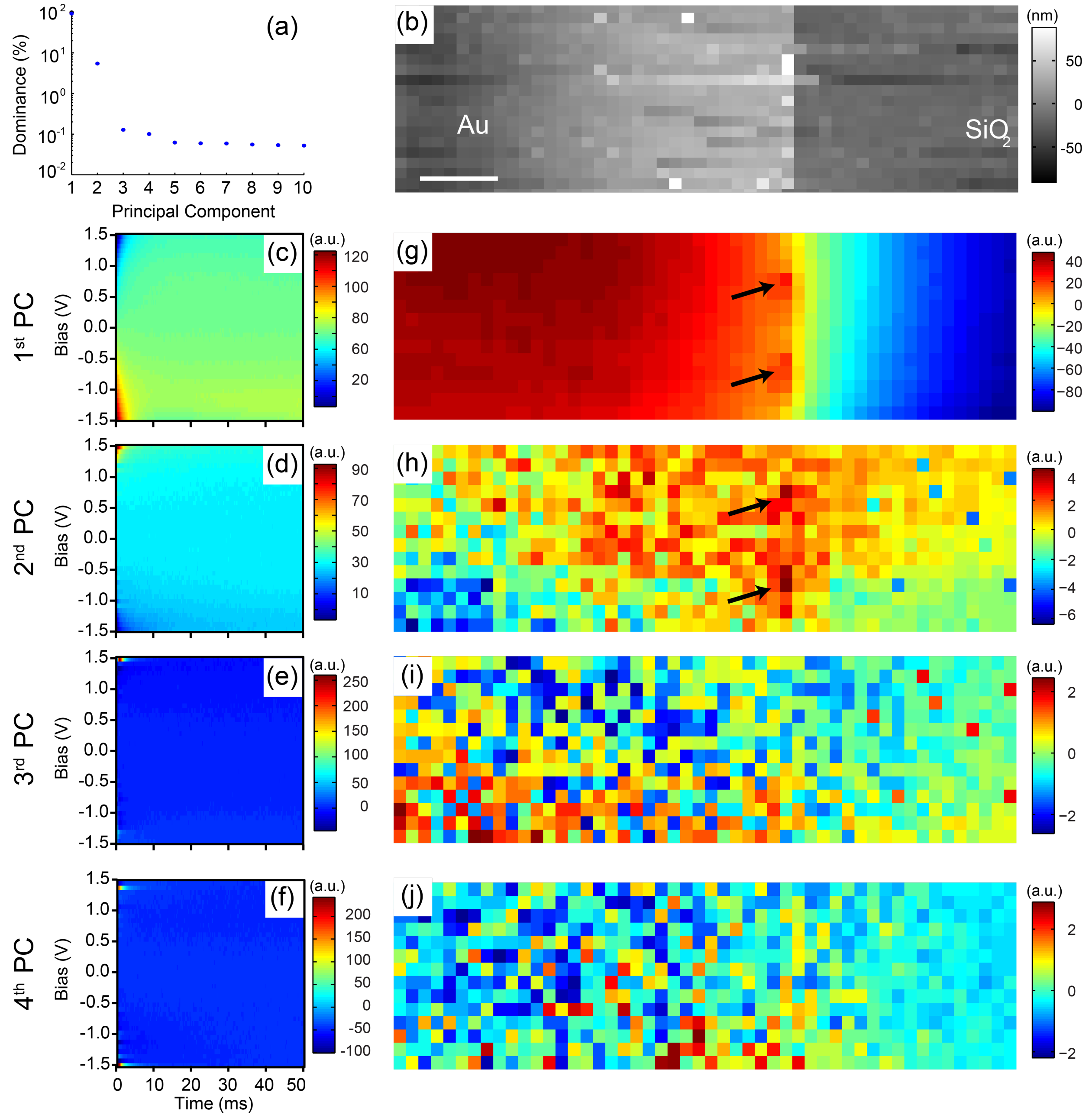

Figure 7: PCA results of a first harmonic EcFM data set on a 50 × 15 grid recorded at a distance of 200 nm above an Au/SiO$_2$ boundary (scale bar = 5 µm). (a) Plot of the dominance of the response versus principal component (PC). (b) Reconstructed topography from force measurements during EcFM data acquisition. (c–f) show the first 4 PC eigenvectors respectively and (g–j) showing their corresponding PC spatial maps. Black arrows in the (g) first and (h) second PC spatial maps highlight electrochemical hotspots recognized using PCA.

trochemical behavior from their immediate surroundings. This highlights the usefulness of PCA for dimensionality reduction and qualitative visualization of spatial variations in the EcFM measurements. The corresponding eigenvectors have complicated behavior and do not allow for direct physical interpretation, however, PCA may act as a precursor for more suitable multivariate statistical approaches which do allow physical interpretation (e.g., Bayesian demixing analysis) of the response when combined with analytical modelling [61].

Conclusion

The feasibility of force-based electrostatic and electrochemical measurements was investigated in liquid by probing the bias- and time-dependent response to a biased probe. The implementation of conventional closed loop-KPFM has been determined to be possible only when the first harmonic response is linear with applied bias and the measurement is performed under equilibrium conditions (i.e., time-invariant response). The operation of KPFM in non-polar liquids was justified by demonstrating a linear bias dependence and a time-invariant relaxation of the first harmonic cantilever response. In the presence of diffuse charge dynamics, however, the linear bias dependence detected at timescales $<<\tau_{RC}$ was found to quickly relax as a result of ion dynamics, precluding the use of KPFM in ionically-active liquids. To overcome this and to further probe bias- and time-dependent ion dynamics and material-dependent electrochemical processes at the probe-sample junction, EcFM was implemented.

Unlike KPFM, EcFM provides a framework to separate different electrochemical processes at the solid–liquid interface based on their bias- and time-dependent response, and thus, has the potential to provide fundamental insights into diffuse charge dynamics. In this work, EcFM has been implemented in ionically-active and -inactive liquids and the usefulness of principal component analysis, which does not require assumptions on physical tip–sample interactions, to map electrochemical behavior across a metal–insulator junction has been demonstrated. It is anticipated that EcFM measurements will be useful in the study of local electro-osmotic flow in microelectrode devices, ion intercalation in capacitor materials, changes in reaction kinetics due to ion adsorption/desorption at the solid–liquid interface and other phenomena central to biological and energy research.

Experimental

HOPG (Agar Scientific) was cleaved immediately prior to use. Au-coated borosilicate glass substrates (Arrandee) were cleaned in isopropanol and ethanol and rinsed in milli-Q water prior to use. For the Au/HOPG sample, ≈45 nm of Au was deposited on ≈5 nm of Ti by evaporation on top of a freshly cleaved HOPG surface. For the Au/SiO_2 sample, ≈50 nm of Au was deposited by evaporation on the SiO_2 surface. During measurements all samples were mounted on a conductive surface using silver paint which was at ground potential with respect to the tip.

All OLBS and EcFM measurements were performed using a commercial AFM system (Asylum Research, MFP-3D) and as-received Pt/Ir-coated (Nanosensors, PPP-EFM) cantilevers with a nominal mechanical resonant frequency and spring constant of 75 kHz and 2.8 N/m, respectively. Linear bias sweeps were performed using a procedure implemented using Igor Pro (Wavemetrics) and the AFM controller, which was used to control the DC bias added to the AC voltage from the lock-in amplifier. For EcFM measurements the tip position was controlled by a custom program written in Igor Pro (Wavemetrics). After positioning the tip in the correct location, the tip was then retracted a predefined distance from the surface and a trigger was used to initiate the electrochemical measurement. In all measurements shown the tip–sample distance was chosen to ensure the interaction was purely long range and that any changes in separation due to drift were small compared to the tip–sample distance. Measurements in Figures 1–3 were performed using a multifrequency lock in amplifier (Zurich Instruments, HF2LI) having a built in electronic adder and Figures 4–7 were performed using two lock-in amplifiers (Stanford research, SR830 and Signal Recovery, 7280) and an external electronic adder (Nanonis, SA4). EcFM measurements were performed with a LabView/MatLab controller implemented on National Instruments PXIe-6124 (Figures 1–3) or 5122/5412 (Figures 4–7) fast AWG and DAQ cards.

Isopropyl alcohol (isopropanol) (≥99.7%, Sigma-Aldrich) and deionized water (milli-Q, Gradient A10, resistance of 18.2 MΩ·cm) was used for measurements reported in polar solvents. CV traces were collected using a potentiostat (Biologic, SP300) and an Ag/AgCl reference electrode.

Supporting Information

Double exponent fitting of the transient EcFM mixed response in isopropanol (Figure S1), double exponent fitting of the transient EcFM mixed response in milli-Q water (Figure S2) and linear fitting of the EcFM mixed response for determination of CPD (Figure S3).

Supporting Information File 1

Additional figures.
[http://www.beilstein-journals.org/bjnano/content/supplementary/2190-4286-6-19-S1.pdf]

Acknowledgements

This publication has emanated from research conducted with the financial support of UCD Research (R11335 and SF938) and NANOREMEDIES, which is funded under the Programme for Research in Third Level Institutions Cycle 5 and co-funded by the European Regional Development Fund. This research was conducted at the Center for Nanophase Materials Sciences, which is sponsored at Oak Ridge National Laboratory by the Scientific User Facilities Division, Office of Basic Energy Sciences, U.S. Department of Energy (CNMS2012-036 and CNMS2013-339).

References

1. Somorjai, G. A.; Li, Y. *Introduction to Surface Chemistry and Catalysis;* John Wiley & Sons, 2010.
2. Adamson, A. W.; Gast, A. P. *Physical Chemistry of Surfaces,* 6th ed.; Wiley & Sons: New York, 1967.
3. Zaera, F. *Chem. Rev.* **2012,** *112,* 2920–2986. doi:10.1021/cr2002068
4. Bazant, M. Z.; Kilic, M. S.; Storey, B. D.; Ajdari, A. *Adv. Colloid Interface Sci.* **2009,** *152,* 48–88. doi:10.1016/j.cis.2009.10.001
5. van Soestbergen, M.; Biesheuvel, P. M.; Bazant, M. Z. *Phys. Rev. E* **2010,** *81,* 021503. doi:10.1103/PhysRevE.81.021503
6. Kilic, M. S.; Bazant, M. Z.; Ajdari, A. *Phys. Rev. E* **2007,** *75,* 021502. doi:10.1103/PhysRevE.75.021502
7. Kilic, M. S.; Bazant, M. Z.; Ajdari, A. *Phys. Rev. E* **2007,** *75,* 021503. doi:10.1103/PhysRevE.75.021503
8. Storey, B. D.; Edwards, L. R.; Kilic, M. S.; Bazant, M. Z. *Phys. Rev. E* **2008,** *77,* 036317. doi:10.1103/PhysRevE.77.036317
9. Bazant, M. Z.; Kilic, M. S.; Storey, B. D.; Ajdari, A. *New J. Phys.* **2009,** *11,* 075016. doi:10.1088/1367-2630/11/7/075016
10. Biesheuvel, P. M.; Fu, Y.; Bazant, M. Z. *Phys. Rev. E* **2011,** *83,* 061507. doi:10.1103/PhysRevE.83.061507
11. Bard, A. J.; Mirkin, M. V. *Scanning Electrochemical Microscopy,* 2nd ed.; CRC Press: Florida, 2012. doi:10.1201/b11850
12. Balke, N.; Bonnell, D.; Ginger, D. S.; Kemerink, M. *MRS Bull.* **2012,** *37,* 633–637. doi:10.1557/mrs.2012.141
13. Black, J.; Strelcov, E.; Balke, N.; Kalinin, S. V. *Electrochem. Soc. Interface* **2014,** *23,* 53–59.
14. Strelcov, E.; Kim, Y.; Jesse, S.; Cao, Y.; Ivanov, I. N.; Kravchenko, I. I.; Wang, C.-H.; Teng, Y.-C.; Chen, L.-Q.; Chu, Y. H.; Kalinin, S. V. *Nano Lett.* **2013,** *13,* 3455–3462. doi:10.1021/nl400780d
15. Balke, N.; Jesse, S.; Morozovska, A.; Eliseev, E.; Chung, D. W.; Kim, Y.; Adamczyk, L.; Garcia, R. E.; Dudney, N.; Kalinin, S. V. *Nat. Nanotechnol.* **2010,** *5,* 749–754. doi:10.1038/nnano.2010.174
16. Martin, Y.; Abraham, D. W.; Wickramasinghe, H. K. *Appl. Phys. Lett.* **1988,** *52,* 1103–1105. doi:10.1063/1.99224
17. Terris, B. D.; Stern, J. E.; Rugar, D.; Mamin, H. J. *Phys. Rev. Lett.* **1989,** *63,* 2669. doi:10.1103/PhysRevLett.63.2669
18. Kalinin, S. V.; Bonnell, D. A. *Phys. Rev. B* **2002,** *65,* 125408. doi:10.1103/PhysRevB.65.125408
19. Kumar, A.; Ciucci, F.; Morozovska, A. N.; Kalinin, S. V.; Jesse, S. *Nat. Chem.* **2011,** *3,* 707–713. doi:10.1038/nchem.1112
20. Nonnenmacher, M.; O'Boyle, M. P.; Wickramasinghe, H. K. *Appl. Phys. Lett.* **1991,** *58,* 2921–2923. doi:10.1063/1.105227
21. Weber, S. A. L.; Butt, H. J.; Berger, R. Electrical Characterization of Solar Cell Materials Using Scanning Probe Microscopy. *Scanning Probe Microscopy in Nanoscience and Nanotechnology 3;* Springer: Berlin, 2013; pp 551–573.
22. Liscio, A.; De Luca, G.; Nolde, F.; Palermo, V.; Müllen, K.; Samorì, P. *J. Am. Chem. Soc.* **2008,** *130,* 780–781. doi:10.1021/ja075291r
23. Loppacher, C.; Zerweck, U.; Teich, S.; Beyreuther, E.; Otto, T.; Grafström, S.; Eng, L. M. *Nanotechnology* **2005,** *16,* S1–S6. doi:10.1088/0957-4484/16/3/001
24. Collins, L.; Kilpatrick, J. I.; Bhaskaran, M.; Sriram, S.; Weber, S.; Jarvis, S.; Rodriguez, B. Dual Harmonic Kelvin Probe Force Microscopy for Surface Potential Measurements of Ferroelectrics. In *Applications of Ferroelectrics held jointly with 2012 European Conference on the Applications of Polar Dielectrics and 2012 International Symp Piezoresponse Force Microscopy and Nanoscale Phenomena in Polar Materials (ISAF/ECAPD/PFM),* 2012 Intl Symp; IEEE, 2012; pp 1–4.
25. Kalinin, S. V.; Bonnell, D. A. *Phys. Rev. B* **2001,** *63,* 125411. doi:10.1103/PhysRevB.63.125411
26. Kalinin, S. V.; Bonnell, D. A. *J. Appl. Phys.* **2000,** *87,* 3950. doi:10.1063/1.372440
27. Lubarsky, G.; Shikler, R.; Ashkenasy, N.; Rosenwaks, Y. *J. Vac. Sci. Technol., B* **2002,** *20,* 1914–1917. doi:10.1116/1.1502701
28. Bocquet, F.; Nony, L.; Loppacher, C.; Glatzel, T. *Phys. Rev. B* **2008,** *78,* 035410. doi:10.1103/PhysRevB.78.035410
29. Egberts, P.; Filleter, T.; Bennewitz, R. *Nanotechnology* **2009,** *20,* 264005. doi:10.1088/0957-4484/20/26/264005
30. Enevoldsen, G. H.; Glatzel, T.; Christensen, M. C.; Lauritsen, J. V.; Besenbacher, F. *Phys. Rev. Lett.* **2008,** *100,* 236104. doi:10.1103/PhysRevLett.100.236104
31. Okamoto, K.; Yoshimoto, K.; Sugawara, Y.; Morita, S. *Appl. Surf. Sci.* **2003,** *210,* 128–133. doi:10.1016/S0169-4332(02)01492-7
32. Mohn, F.; Gross, L.; Moll, N.; Meyer, G. *Nat. Nanotechnol.* **2012,** *7,* 227–231. doi:10.1038/nnano.2012.20
33. Polak, L.; de Man, S.; Wijngaarden, R. J. *Rev. Sci. Instrum.* **2014,** *85,* 046111. doi:10.1063/1.4873331
34. Collins, L.; Kilpatrick, J. I.; Weber, S. A.; Tselev, A.; Vlassiouk, I.; Ivanov, I.; Jesse, S.; Kalinin, S.; Rodriguez, B. *Nanotechnology* **2013,** *24,* 475702. doi:10.1088/0957-4484/24/47/475702
35. Barbet, S.; Popoff, M.; Diesinger, H.; Deresmes, D.; Théron, D.; Mélin, T. *J. Appl. Phys.* **2014,** *115,* 144313. doi:10.1063/1.4870710
36. Sugimura, H.; Ishida, Y.; Hayashi, K.; Takai, O.; Nakagiri, N. *Appl. Phys. Lett.* **2002,** *80,* 1459–1462. doi:10.1063/1.1455145
37. Bazant, M. Z.; Thornton, K.; Ajdari, A. *Phys. Rev. E* **2004,** *70,* 021506. doi:10.1103/PhysRevE.70.021506
38. Collins, L.; Jesse, S.; Kilpatrick, J. I.; Tselev, A.; Varenyk, O.; Okatan, M. B.; Weber, S. A. L.; Kumar, A.; Balke, N.; Kalinin, S. V. *Nat. Commun.* **2014,** *5,* 3871. doi:10.1038/ncomms4871
39. Domanski, A. L.; Sengupta, E.; Bley, K.; Untch, M. B.; Weber, S. A. L.; Landfester, K.; Weiss, C. K.; Butt, H.-J.; Berger, R. *Langmuir* **2012,** *28,* 13892. doi:10.1021/la302451h
40. Kobayashi, N.; Asakawa, H.; Fukuma, T. *J. Appl. Phys.* **2011,** *110,* 044315. doi:10.1063/1.3625230
41. Kobayashi, N.; Asakawa, H.; Fukuma, T. *Rev. Sci. Instrum.* **2012,** *83,* 033709. doi:10.1063/1.3698207
42. Kobayashi, N.; Asakawa, H.; Fukuma, T. *Rev. Sci. Instrum.* **2010,** *81,* 123705. doi:10.1063/1.3514148
43. Collins, L.; Kilpatrick, J. I.; Vlassiouk, I. V.; Tselev, A.; Weber, S. A.; Jesse, S.; Kalinin, S. V.; Rodriguez, B. J. *Appl. Phys. Lett.* **2014,** *104,* 133103. doi:10.1063/1.4870074

44. Guo, S.; Kalinin, S. V.; Jesse, S. *Nanotechnology* **2012,** *23,* 125704. doi:10.1088/0957-4484/23/12/125704
45. Takeuchi, O.; Ohrai, Y.; Yoshida, S.; Shigekawa, H. *Jpn. J. Appl. Phys., Part 1* **2007,** *46,* 5626. doi:10.1143/JJAP.46.5626
46. Cherniavskaya, O.; Chen, L.; Weng, V.; Yuditsky, L.; Brus, L. E. *J. Phys. Chem. B* **2003,** *107,* 1525–1531. doi:10.1021/jp0265438
47. Fumagalli, L.; Esteban-Ferrer, D.; Cuervo, A.; Carrascosa, J. L.; Gomila, G. *Nat. Mater.* **2012,** *11,* 808–816. doi:10.1038/nmat3369
48. Fumagalli, L.; Gramse, G.; Esteban-Ferrer, D.; Edwards, M.; Gomila, G. *Appl. Phys. Lett.* **2010,** *96,* 183107. doi:10.1063/1.3427362
49. Gramse, G.; Edwards, M. A.; Fumagalli, L.; Gomila, G. *Appl. Phys. Lett.* **2012,** *101,* 213108. doi:10.1063/1.4768164
50. Gramse, G.; Edwards, M.; Fumagalli, L.; Gomila, G. *Nanotechnology* **2013,** *24,* 415709. doi:10.1088/0957-4484/24/41/415709
51. Pashley, R. M.; Rzechowicz, M.; Pashley, L. R.; Francis, M. J. *J. Phys. Chem. B* **2005,** *109,* 1231–1238. doi:10.1021/jp045975a
52. Kim, Y.; Kumar, A.; Ovchinnikov, O.; Jesse, S.; Han, H.; Pantel, D.; Vrejoiu, I.; Lee, W.; Hesse, D.; Alexe, M.; Kalinin, S. V. *ACS Nano* **2011,** *6,* 491–500. doi:10.1021/nn203831h
53. Arruda, T. M.; Kumar, A.; Kalinin, S. V.; Jesse, S. *Nano Lett.* **2011,** *11,* 4161–4167. doi:10.1021/nl202039v
54. Raiteri, R.; Butt, H.-J. *J. Phys. Chem.* **1995,** *99,* 15728–15732. doi:10.1021/j100043a008
55. Umeda, K.; Kobayashi, K.; Oyabu, N.; Hirata, Y.; Matsushige, K.; Yamada, H. *J. Appl. Phys.* **2014,** *116,* 134307. doi:10.1063/1.4896881
56. Nicholson, R. S. *Anal. Chem.* **1965,** *37,* 1351–1355. doi:10.1021/ac60230a016
57. Bard, A. J.; Faulkner, L. R. *Electrochemical Methods: Fundamentals and Applications;* Wiley: New York, 1980; Vol. 2.
58. Butt, H.-J. *Biophys. J.* **1991,** *60,* 777–785. doi:10.1016/S0006-3495(91)82112-9
59. Sounart, T. L.; Michalske, T. A.; Zavadil, K. R. *J. Micromech. Microeng.* **2005,** *14,* 125–133. doi:10.1109/JMEMS.2004.839006
60. Jolliffe, I. *Principal component analysis;* John Wiley & Sons, Ltd, 2005.
61. Strelcov, E.; Belianinov, A.; Hsieh, Y.-H.; Jesse, S.; Baddorf, A. P.; Chu, Y.-H.; Kalinin, S. V. *ACS Nano* **2014,** *8,* 6449–6457. doi:10.1021/nn502029b

License and Terms

The definitive version of this article is the electronic one which can be found at:
doi:10.3762/bjnano.6.19

BEILSTEIN JOURNAL OF NANOTECHNOLOGY

Dynamic force microscopy simulator (dForce): A tool for planning and understanding tapping and bimodal AFM experiments

Horacio V. Guzman, Pablo D. Garcia and Ricardo Garcia*

Full Research Paper

Open Access

Address:
Instituto de Ciencia de Materiales de Madrid, CSIC, Sor Juan Inés de la Cruz 3, 28049 Madrid, Spain

Email:
Ricardo Garcia* - r.garcia@csic.es

* Corresponding author

Keywords:
bimodal AFM; dynamic AFM; nanomechanics; numerical simulations; tapping mode AFM

Beilstein J. Nanotechnol. **2015,** *6,* 369–379.
doi:10.3762/bjnano.6.36

Received: 23 September 2014
Accepted: 08 January 2015
Published: 04 February 2015

This article is part of the Thematic Series "Advanced atomic force microscopy techniques III".

Guest Editor: T. Glatzel

Abstract

We present a simulation environment, dForce, which can be used for a better understanding of dynamic force microscopy experiments. The simulator presents the cantilever–tip dynamics for two dynamic AFM methods, tapping mode AFM and bimodal AFM. It can be applied for a wide variety of experimental situations in air or liquid. The code provides all the variables and parameters relevant in those modes, for example, the instantaneous deflection and tip–surface force, velocity, virial, dissipated energy, sample deformation and peak force as a function of time or distance. The simulator includes a variety of interactions and contact mechanics models to describe AFM experiments including: van der Waals, Hertz, DMT, JKR, bottom effect cone correction, linear viscoelastic forces or the standard linear solid viscoelastic model. We have compared two numerical integration methods to select the one that offers optimal accuracy and speed. The graphical user interface has been designed to facilitate the navigation of non-experts in simulations. Finally, the accuracy of dForce has been tested against numerical simulations performed during the last 18 years.

Introduction

Numerical simulations have played a pivotal role to advance the understanding and, in the process, to improve the performance of amplitude modulation atomic force microscopy (AM-AFM), usually known as tapping mode AFM. The following discussion provides some examples. Simulations provided the first estimation of the forces and deformations involved in tapping mode AFM [1,2]. They explained the origin of the phase contrast observed on heterogeneous samples by tapping mode AFM in air [3] and liquid [4,5]. In the process, simulations validated the theory of AFM phase imaging in air [6,7], its use to identify energy dissipation processes [7] or to measure the energy dissipated in the sample [8-10]. Numerical simulations have provided critical insight to understand the subtle nonlinear dynamics aspects present in AM-AFM, such as the existence of multiple interaction regimes [11-13] or the presence of chaotic tip motion [14]. Similarly, simulations have linked the presence of higher harmonic components in the tip motion with the presence of nonlinear interactions [15]. In the process, the cross talk between modes and harmonics has been clarified [16-20]. The complicated cantilever motion in liquid and the differences observed between the excitation methods have been analyzed by simulations [21-23].

The tip–surface force controls the cantilever motion, however, the force itself is not an observable. Numerical simulations have been used to derive parametric approximations [24], scaling laws [25] and insights about the role of different material properties [25-27] in obtaining the maximum force. Simulations can generate maps that provide the estimation of the peak forces for a large variety of conditions [27,28]. The range of applicability of the force reconstruction methods has also been verified by numerical simulations [29]. The spatial resolution and contrast of different dynamic AFM methods has also been studied by simulations [28,30,31]. Finally, the emergence of multifrequency AFM [32] in particular bimodal [33,34], trimodal [35], intermodulation [36] or torsional harmonics [37] has been supported by simulations [38]. In the case of bimodal AFM, numerical simulations [39] preceded and paved the way to its experimental development [33,40].

The complexity of amplitude modulation AFM makes it difficult to develop reliable code accessible for both the large community of tapping mode AFM users and the emerging community of multifrequency AFM. The future applications and understanding of dynamic AFM operation will be enhanced if accurate simulators are easily accessible to the experimentalist. These factors promote the development of AFM simulation platforms such as VEDA [41,42].

Here we present a dynamic AFM simulator (dForce), which is based on the experience and knowledge accumulated from nearly 20 years of simulations. The interactive simulator has a modular structure that allows AFM users from the unexperienced to the most advanced to simulate a wide variety of experimental conditions and/or operational modes. The code is valid for air or liquid environments, soft or hard materials, small or large amplitudes, conservative and non-conservative forces and single or bimodal excitation modes. Its accuracy has been tested against previous numerical simulations. The dForce simulator will be useful to either devise the optimal experimental conditions in terms of amplitudes, peak forces, material property sensitivity and spatial resolution, or to explain the experimental data in standard and non-standard dynamic AFM configurations.

The code is written in Python/SciPy, which is embedded with open source features. It can be run on Windows, Mac and Linux operating systems. It can be freely downloaded from our website [43]. The user interface has been designed to mimick some of the main steps of an amplitude modulation AFM experiment (Figure 1).

The dForce user must be aware that the accuracy of the simulations to describe an experiment cannot be better than the accuracy of the model used to describe it. In addition, the use of dForce should be accompanied by an understanding of the physics of dynamic AFM methods. There are many instances where a poor selection of the different parameters in the code could generate incorrect results without producing errors in either the model or the code.

Results and Discussion

Cantilever–tip dynamics

In amplitude modulation AFM the equation of motion for the microcantilever–tip system is approximated by using the point-mass model [11],

$$\ddot{z}(t) = -\omega_0^2 z(t) - \frac{\omega_0}{Q}\dot{z}(t) + \frac{F_{\mathrm{ts}}(d)}{m} + \frac{F_0 \cos\omega t}{m}, \qquad (1)$$

where m is the effective mass of the cantilever tip, ω_0 is the angular resonant frequency, Q the quality factor, k the spring constant of the fundamental resonance (first flexural mode) and F_{ts} is the tip–sample interaction force. The above equation is applicable when the contributions from higher modes to the cantilever motion are negligible [15].

The presence of higher flexural modes in the the cantilever–tip motion can be described by using a continuos beam theory [15,16]. The extended Euler–Bernoulli equation considers the cantilever as a continuous and uniform rectangular beam under the action of external forces,

$$\begin{aligned} EI\frac{\partial}{\partial x^4}\left[w(x,t) + \alpha_1 \frac{\partial w(x,t)}{\partial t}\right] + \rho bh \frac{\partial^2 w(x,t)}{\partial t^2} = \\ -\alpha_0 \frac{\partial w(x,t)}{\partial t} + \delta(x-L)\left[F_0 \cos\omega t + F_{\mathrm{ts}}(d)\right], \end{aligned} \qquad (2)$$

where E is the Young modulus of the cantilever, I the area moment of inertia, α_1 the internal damping coefficient of the

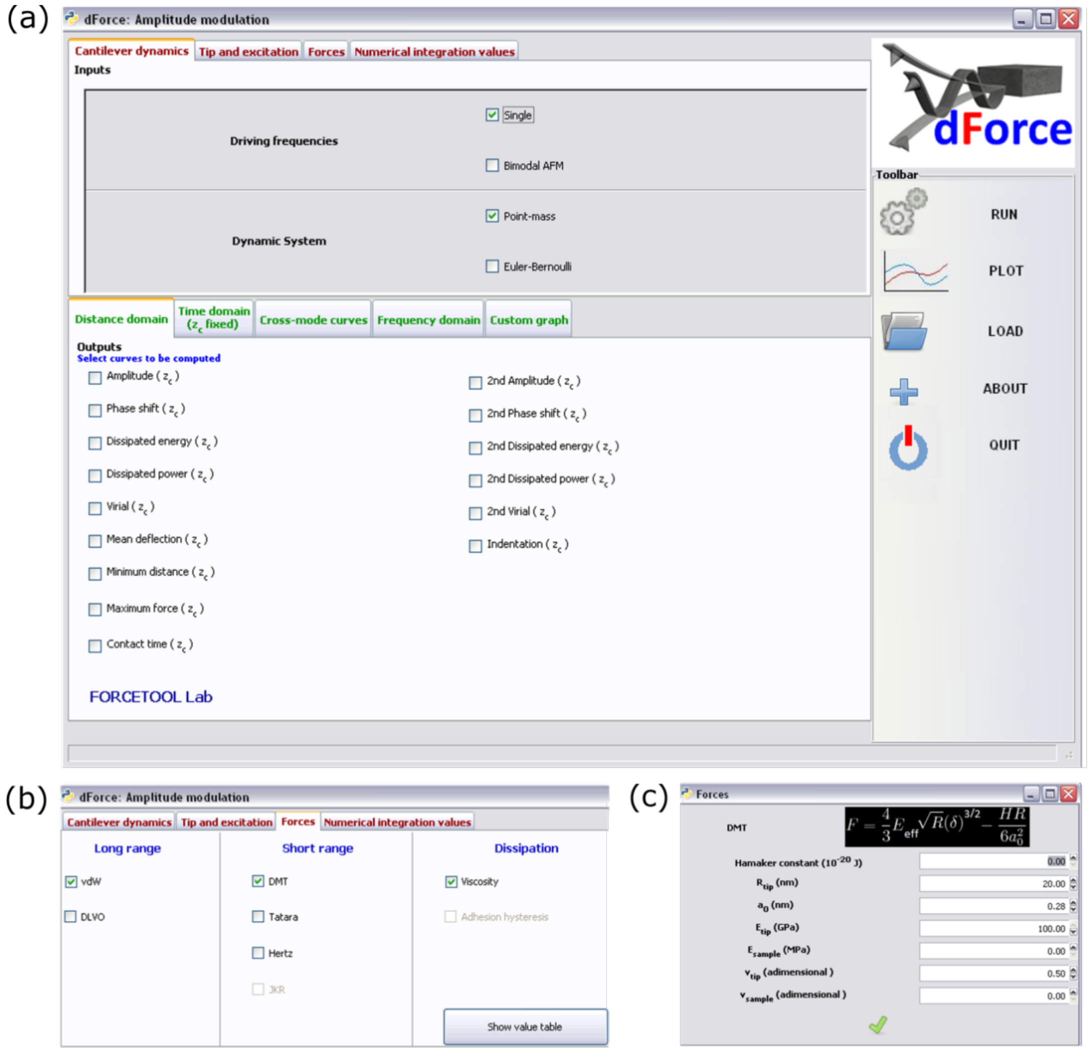

Driving frequencies: ☑ Single ☐ Bimodal AFM

Dynamic System: ☑ Point-mass ☐ Euler-Bernoulli

☐ Amplitude (z_c)
☐ Phase shift (z_c)
☐ Dissipated energy (z_c)
☐ Dissipated power (z_c)
☐ Virial (z_c)
☐ Mean deflection (z_c)
☐ Minimum distance (z_c)
☐ Maximum force (z_c)
☐ Contact time (z_c)
☐ 2nd Amplitude (z_c)
☐ 2nd Phase shift (z_c)
☐ 2nd Dissipated energy (z_c)
☐ 2nd Dissipated power (z_c)
☐ 2nd Virial (z_c)
☐ Indentation (z_c)

Long range: ☑ vdW ☐ DLVO

Short range: ☑ DMT ☐ Tatara ☐ Hertz ☐ JKR

Dissipation: ☑ Viscosity ☐ Adhesion hysteresis

DMT $F = \frac{4}{3}E_{\text{eff}}\sqrt{R}(\delta)^{3/2} - \frac{HR}{6a_0^2}$

Hamaker constant (10^{-20} J): 0.00
R_{tip} (nm): 20.00
a_0 (nm): 0.28
E_{tip} (GPa): 100.00
E_{sample} (MPa): 0.00
ν_{tip} (adimensional): 0.50
ν_{sample} (adimensional): 0.00

Figure 1: Graphical user interface of dForce. (a) Main menu. It is divided in three sections, two horizontal and one vertical. The top tabs contain all panels relevant for AFM simulations. The bottom panel enables selection of the output plots. The vertical panel contains the tabs for running the program and managing the output. (b) Force panel that shows the different tip–surface force models implemented in dForce. (c) Example of the input panel for the DMT model.

cantilever, ρ the cantilever mass density, b, h and L are the width, thickness and length of the cantilever, respectively, α_0 is the hydrodynamic damping of the medium, and $w(x,t)$ is the time-dependent, vertical displacement of the differential beam's element placed at the x position. To numerically solve the above equation, we replace it by a system of point-mass equations, one for each relevant mode, n = 1, 2, etc. as described by [16,44,45]

$$\ddot{z}_n(t) + \frac{\omega_n}{Q_n}\dot{z}_n(t) + \omega_n^2 z_n(t) = \frac{F_0\cos\omega t + F_{\text{ts}}(d)}{m} \qquad (3)$$

with $m = 0.25 \cdot m_c$ and $1 + \cos(\kappa_n)\cosh(\kappa_n) = 0$, where κ_n is the nth positive real root of the above equation and m_c is the real mass of the cantilever. Additionally, the quality factor is defined as

$$Q_n = \frac{\omega_n}{\frac{\alpha_1}{\rho b h} + \alpha_0\omega_n^2}, \qquad (4)$$

where

$$\omega_n = \left(\frac{\kappa_n}{L}\right)^4 \frac{EI}{\rho b h}. \qquad (5)$$

Tip–sample interaction forces

The simulator includes a variety of models and tip–surface force interactions. The interactions are separated in long range and short range. The user has the option of combining a long range with a short range interaction to produce the full tip–surface force. It is also possible to add one or several non-conservative interactions such as adhesion hysteresis and/or viscoelasticity. We briefly describe the resulting expressions.

van der Waals

The van der Waals interaction between a sphere and a half-space is calculated by [46]

$$F_{\mathrm{vdW}} = -\frac{HR_{\mathrm{t}}}{6d^2} \text{ if } a_0 - d < 0, \tag{6}$$

where R_{t} is the tip radius, H is the Hamaker constant, d is the distance between the tip's apex the sample surface and a_0 is the intermolecular distance (0.165 nm).

Derjaguin–Landau–Verbey–Overbeek (DLVO)

The DLVO force [46] describes interactions in liquid by including the contributions from the electrical double layer and the van der Waals interactions. The DLVO force is given by

$$F_{\mathrm{DLVO}} = \frac{4\pi R_{\mathrm{t}}}{\varepsilon\varepsilon_0}\sigma_{\mathrm{t}}\sigma_{\mathrm{s}}\lambda_{\mathrm{D}}\mathrm{e}^{-d/\lambda_{\mathrm{D}}} - \frac{HR_{\mathrm{t}}}{6d^2} \text{ if } a_0 - d < 0, \tag{7}$$

where λ_{D} is the Debye length, ε is the relative permeability, ε_0 is the vacuum permeability, σ_{t} is the tip–surface charge density and σ_{s} is the sample surface charge density.

Hertz contact mechanics

The elastic contact between the tip and sample is usually modelled with the Hertz model [46] whereby for a spherical tip and a half-space sample the force is given by

$$F_{\mathrm{Hertz}} = \frac{4}{3}E_{\mathrm{eff}}\sqrt{R}\delta^{3/2}, \tag{8}$$

where δ is the indentation and E_{eff} is the effective Young modulus of the interface defined by

$$\frac{1}{E_{\mathrm{eff}}} = \frac{1-\upsilon_{\mathrm{t}}^2}{E_{\mathrm{t}}} + \frac{1-\upsilon_{\mathrm{s}}^2}{E_{\mathrm{s}}}, \tag{9}$$

where E_{t} and E_{s} are the Young's modulus of the tip and sample, respectively, and υ_{t} and υ_{s} are the Poisson coefficients of the tip and sample, respectively.

Derjaguin–Mueller–Toporov contact mechanics (DMT)

The DMT model is valid for describing stiff and small contacts with low adhesion forces. The DMT model [47] considers an elastic term given by Hertz contact mechanics as

$$F_{\mathrm{DMT}} = \frac{4}{3}E_{\mathrm{eff}}\sqrt{R}\delta^{3/2} - 4\pi R\gamma \tag{10}$$

and an adhesion force that acts outside the contact area given by

$$F_{\mathrm{adh}} = 4\pi R\gamma = \frac{HR}{6a_0^2}, \tag{11}$$

where γ is the sample surface energy.

Johnson–Kendall–Roberts contact mechanics (JKR)

The JKR model is applied to describe contacts characterized by a relatively small Young modulus, and large adhesion and contact area [48]. In this model the force is calculated as an implicit equation of the indentation

$$\begin{aligned}\bar{\delta} &= 3\left(\overline{F_{\mathrm{JKR}}} + 2 + 2\sqrt{1+\overline{F_{\mathrm{JKR}}}}\right)^{2/3} \\ &\quad -4\left(\overline{F_{\mathrm{JKR}}} + 2 + 2\sqrt{1+\overline{F_{\mathrm{JKR}}}}\right)^{1/6},\end{aligned} \tag{12}$$

where

$$\bar{\delta} = \delta\left(\frac{\gamma^2 R\pi^2}{3E_{\mathrm{eff}}^2}\right)^{-1/3} \tag{13}$$

and

$$\overline{F_{\mathrm{JKR}}} = \frac{F_{\mathrm{JKR}}}{R\gamma\pi}. \tag{14}$$

Tatara contact mechanics

The Tatara contact mechanics are applied to describe a sample with a finite size with respect to the tip. It releases the vertical load into both vertical and lateral deformations [49]. The deformation is symmetrically generated on both sides of the sample, one that is in contact with the tip and the one in contact with the substrate. The force is calculated by

$$F_{\mathrm{Tatara}} = \frac{n}{2^{2/3}}\delta^{3/2} + \frac{3n^2}{8n_{\mathrm{c}}^2}\delta^2 + \frac{15n^3}{2^{11/2}n_{\mathrm{c}}^2}\delta^{5/2}, \tag{15}$$

with

$$n = \frac{4}{3}E_{\mathrm{eff}}\sqrt{R_{\mathrm{eff}}} \tag{16}$$

$$n_c = \frac{4\pi E_t R_t E_s R_s}{6 + \upsilon_t - 2\upsilon_t^2 + \upsilon_s - 2\upsilon_s^2} \tag{17}$$

$$\frac{1}{R_{\text{eff}}} = \frac{1}{R_t} + \frac{1}{R_s}, \tag{18}$$

where R_t and R_s are the tip and the sample radius, respectively.

Bottom effect cone correction (BECC)

This model was recently introduced by Gavara and Chadwick to suppress the influence of the stiffness of the substrate on the stiffness measured by AFM on very soft and thin materials deposited on them [50]. The expression is valid when the Young modulus of the substrate is several orders of magnitude higher than that of the sample. The force is calculated by

$$F_{\text{BECC}} = \frac{8E_{\text{eff}}\tan\theta}{3\pi}\delta^2 \left\{1 + 1.7795\frac{2\tan\theta}{\pi^2}\frac{\delta}{h_s} + 50.67\tan^2\theta\frac{\delta^2}{h_s^2}\right\} \tag{19}$$

where θ is the half-cone angle and h_s is the thickness of the sample.

Linear viscosity force

The linear viscosity force deduced by Garcia and San Paulo [51] combines the relationship between the stress and strain given by the Kelvin–Voigt model and the sample deformation given by Hertz contact mechanics as

$$F_{\text{vis}} = -\eta\sqrt{R_t\delta}\frac{d\delta}{dt} \tag{20}$$

where η is the viscosity coefficient.

Standard linear solid viscoelastic model (SLS)

The SLS model is considered to represent the time-dependent behavior of a viscoelastic material without residual strains [52]. The model characterizes a viscoelastic material as an elastic element, which is coupled in series with a system that includes another elastic element and a viscous response. The equivalent mechanical system is a spring in series with a spring and a dashpot. By assuming a contact mechanism as described by Hertz contact mechanics, we deduce the force as

$$F_{\text{SLS}} = -\frac{E_0\eta}{E_0 + E_\infty}\left(\sqrt{R\delta}\frac{d\delta}{dt} - \frac{dF_{\text{SLS}}/dt}{E_0}\right) \tag{21}$$

where E_0 and E_∞ represent the Young's modulus of the material at fast and slow loading rates, respectively.

Customized force

The code also enables the definition of other types of forces. For that purpose, the advanced user could use any of the variables and/or parameters defined in the above force models, or could use any or several of the four undefined parameters $P1$, $P2$, $P3$ and $P4$ allowed by the code. In this manner, the code has the capability to simulate the dynamics of the microscope under a force that includes any of the variables of the above models and up to four new parameters generally defined as

$$F_{\text{custom}} = F_{\text{custom}}(z, \dot{z}, t, R, H, k, \ldots P1, P2, P3, P4). \tag{22}$$

Numerical integration methods

To obtain the cantilever–tip motion in AM-AFM we have considered a point-mass model with the parameters of the first flexural model of the cantilever. For bimodal AM we have considered a system of equations involving the first three flexural modes [39,45]. Each mode was described by a point-mass model. In this system the modes are coupled by the tip–sample interaction force. The equations of motion were integrated numerically using the Livermore solver for ordinary differential equations (LSODA) of the scipy library (scipy.ode) [53-55]. LSODA uses an algorithm to adapt the integration step for a given numerical tolerance of the numerical integration [51]. We have chosen this numerical method because it offers faster integration times as compared to the commonly used fourth-order Runge–Kutta algorith (RK-4) [56]. We have compared the numerical integration for AM-AFM and bimodal AM microscopy examples (see Table 1). The results presented in

Table 1: Parameters used to compare the performance of the numerical integration algorithms LSODA and Runge–Kutta 4 (RK-4) for z_c = 4 nm.

AFM configuration	R (nm)	f_1 (kHz)	k_1 (N/m)	Q_1	A_{01} (nm)	f_2 (kHz)	k_2 (N/m)	Q_2	A_{02} (nm)	E_s (Pa)	H (J)
AM-AFM	2	48.9	0.9	100	5	–	–	–	–	1 G	0
Bimodal AM	20	48.9	0.9	100	5	282	28	200	1	1 G	0

Table 2 show the performace of LSODA with respect to RK-4. In all the cases, LSODA performs the simulations significantly faster than RK-4. In fact, when higher accuracy is demanded (higher *m* values), LSODA also performs better. We note that the comparison applies only to the part of the code that involves the integration methods and not to the code as a whole, which involves other operations such as data storing and visualization.

Table 2: Comparison between two different numerical integration algorithms, LSODA and RK-4. The numbers indicate the factor by which LSODA is faster than RK-4 for two dynamic AFM configurations (see Table 1); *m* is the number of points per period to represent the oscillation.

	$m = 128$	$m = 256$	$m = 512$
AM-AFM	2.8	4.3	6.5
Bimodal AM	4.5	7.3	11.1

For the simulations, it is important to choose appropriate values for the numerical integrator, in particular the number of periods, interval of periods (to calculate the steady state), and the average tip–surface distance step to guarantee that the simulations reflect the proper oscillation conditions. In general, the main interest is in the steady state solutions, that is, when the transient term has practically vanished [46]. For a driven and damped harmonic oscillator, the transient terms are reduced by a factor of 1/e after a time $t = QT/\pi$ where T is the natural period of the oscillation. Consequently, the number of periods should be at least 2–5 times larger than Q/π for quality factors above 30. For a smaller Q values, it should involve about 30 periods. The interval of periods to calculate the steady state solution refers to the number periods in the oscillation that will be used in the calculations. These are the last periods of the total number of periods and typically 8 periods are sufficient. The last key parameter is the tip step. This refers to the amplitude of the motion of the tip (phase shift) versus distance curves. Smaller steps will give better results but they imply larger computation times. A 1 nm z_c step is a good starting value, however, smaller values could be necessary depending, for example, on the coexistence of attractive and repulsive interaction regimes.

Graphical user interface

The graphical user interface is divided into three main sections: microscope input data, the output section and the toolbar for running the program and handling files. Figure 1a shows a screenshot of the interface. In the AFM data panel some tabs facilitate the introduction of the relevant information for the simulation such as the type of AFM configuration (AM-AFM versus bimodal AFM) or the model to describe the tip–surface forces. By activating any of the tabs a new panel will show the available options. Figure 1b shows the options available to model the tip–surface interactions. An example of force data panel is shown in Figure 1c.

Amplitude modulation AFM simulations

The results presented in this section describe steady-state conditions. Consequently, the numerical integration values have been adjusted to integrate the tip's deflection once the transient component has faded away [57]. The parameters characterizing the AFM operation used in the Figures of this section are summarized in Table 3.

Figure 2 shows the tip motion under the influence of a force that includes van der Waals and Hertz contact mechanics (see Table 3 for the parameters). The instantaneous tip deflection, velocity and force are shown. The tip oscillates between ±0.47 nm while the velocity changes between zero and 141 μm/s. The instantaneous force shows the presence of a non-interacting region for distances larger than the set point amplitude, the region of the attractive force and the region of repulsive forces. In this case, attractive and repulsive peak forces are about −92 and 112 pN, respectively. One useful feature provided by dForce is the capability to combine different data in a single plot. Figure 2d shows the cantilever deflection, the velocity and the force.

Coexistence of interaction regimes

The existence of different interaction regimes in AM-AFM is a direct consequence of the nonlinear character of the tip–surface force [11,46]. The amplitude versus the average tip–surface distance z_c curve shows a sudden increase at $z_c = 9.3$ nm

Table 3: Summary of the parameters used in the numerical simulations described in Figures 2–5.

Figure	R (nm)	f_1 (kHz)	k_1 (N/m)	Q_1	A_0 (nm)	E_s (Pa)	H (J)	η (Pa·s)
2	2	49.9	0.9	100	1	1 G	0.8×10^{-20}	0
3 (air) (water)	2	48.9	0.9	255 2	10	1 G	2×10^{-20} 0	0 0
4	2	48.9	10	100	10	50 G (hard) 50 M (soft)	0	0
5	2	49	0.9	50	10	50 M	0	100

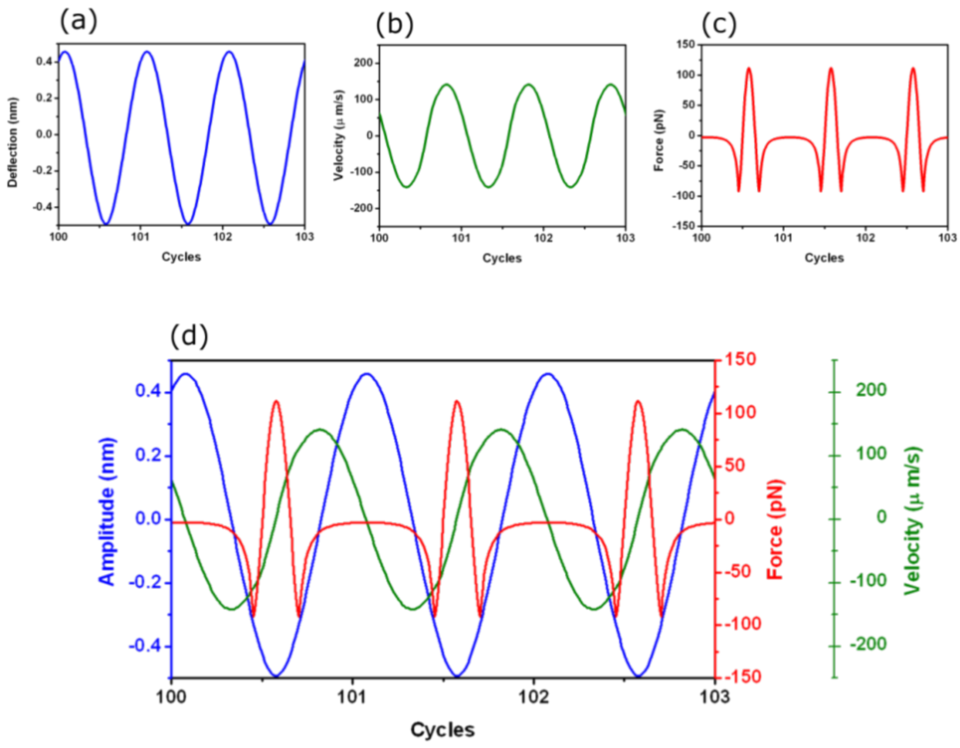

Figure 2: dForce simulation of AM-AFM for a tip–surface force that includes van der Waals and DMT. (a) Instantaneous tip deflection. (b) Instantaneous velocity. (c) Instantaneous force. (d) Combining different plots in a single figure. Deflection (blue), velocity (green) and force (red). The simulations were performed for z_c = 0.5 nm.

(Figure 3a).This increase marks the transition between a tip oscillation dominated by attractive forces to a tip oscillation dominated by repulsive forces. The increase in the amplitude curve is also reflected in the phase shift curve (Figure 3b) where the phase shift changes from about 110° to 65°. The initial values of the deflection, position and velocity determine the z_c value where the jump occurs. The inset (Figure 3a) shows the coexistence of two amplitude values for the same z_c. This coexistence generates a hysteresis loop [11]. We note that in the attractive regime, the phase shift increases from the non-interacting value (90°) with decreasing z_c. However, in the repulsive regime, ϕ decreases with decreasing z_c.

Low versus high Q values

The above considerations apply for environments with relatively high Q values (10–500), which experimentally usually implies air environments. For simulations performed in liquid, $Q \approx 1$–5, and the tip motion is markedly different [20,22-24,58]. First, the AFM operation is controlled by repulsive forces because the attractive forces are highly screened in liquid. The absence of an attractive regime in liquid implies that the phase shift decreases by decreasing z_c. Second, for the same instrument, the noise in the amplitude is higher in liquid. This happens because the noise is proportional to $1/(dA/dz_c)$ [47]. The slope of the amplitude curve in liquid is 0.7 while in air for the same system it is 1 (Figure 3a). Third, in liquid the observed cantilever motion depends on the microcantilever excitation method [22,58]. The code is written to simulate the dynamics of directly excited microcantilevers (photo-thermal or magnetic excitation).

The amplitude spectrum also depends on the medium (z_c = 5 nm). The anharmonicity of the motion is higher in liquid [20,59]. For all the frequencies except the fundamental, the amplitude of the harmonics is higher in water (Figure 3c).

Imaging soft and hard materials

The cantilever dynamics in AM-AFM shows some subtle differences depending on the effective Young's modulus of the interaction. Figure 4 shows the amplitude, phase shift and harmonic components for two materials characterized by an E_s of 50 MPa and 50 GPa. The amplitude curve shows a significant difference in the slope. In the stiffer material the slope is nearly 1 while for the softer material the slope is about 0.7. Because the noise in the amplitude depends on the slope as 1/slope, the smaller value of the slope implies that in softer materials it is more difficult to achieve high resolution. The phase shift (Figure 4b) decreases more rapidly with the average distance in

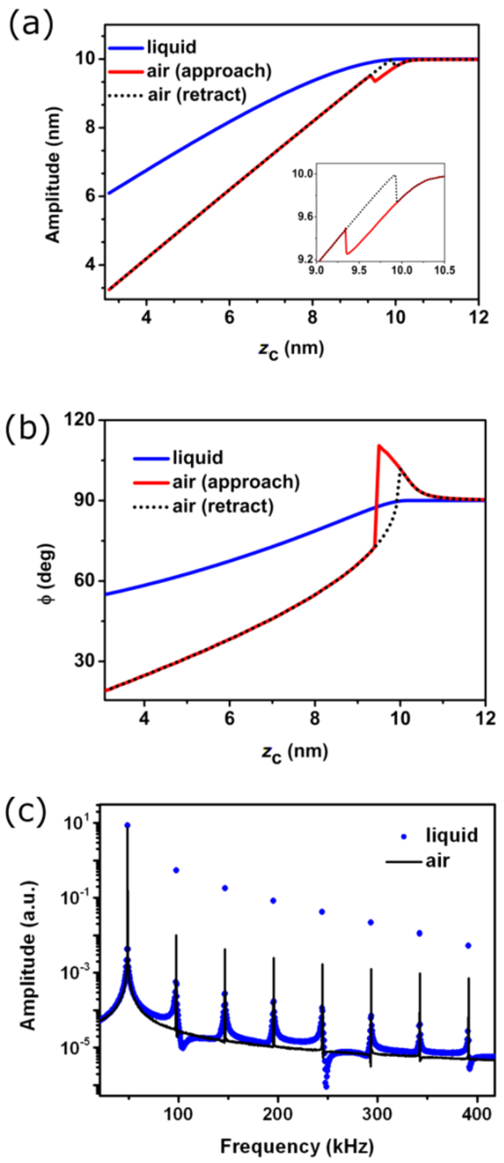

Figure 3: AM-AFM comparison of cantilever dynamics, air versus liquid. (a) Amplitude versus average tip–surface distance curves for low and high Q values. The inset shows the details of the hysteresis in the amplitude (approaching and retraction cycles). (b) Corresponding phase shift curves. (c) Spectra of the amplitude components taken at z_c = 7 nm. The approaching (continuous line) and retraction curves (dots) are also shown in (a) and (b) for Q = 255.

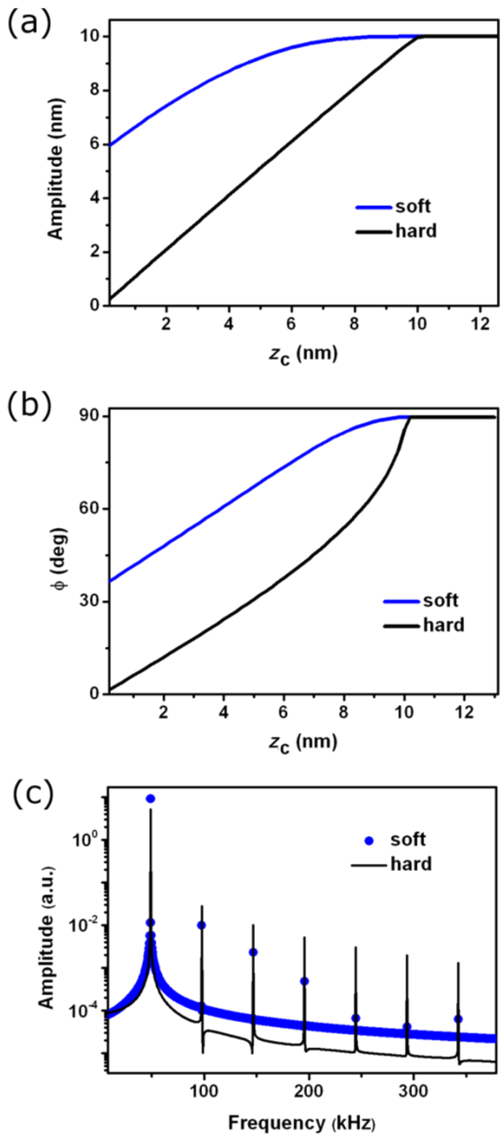

Figure 4: AM-AFM comparison of cantilever dynamics, hard versus soft materials. (a) Amplitude versus average tip–surface distance curves for hard and soft surfaces. (b) Corresponding phase shift curves. (c) Spectra of the amplitude components taken at z_c = 5 nm.

the stiffer material. The amplitude spectrum shows that strength of the higher harmonics also depends on the material. Higher components are observed in the stiffer material (Figure 4c).

Viscoelastic materials

Experiments involving soft matter usually imply the existence of a viscoelastic response. Figure 5a shows the viscoelastic force calculated with the Garcia–San Paulo expression (Equation 20). Far from the sample surface, the force is zero (not including long-range forces) and upon contact, the repulsive force increases until a maximum is reached. During retraction, an attractive force appears due to the viscoelastic response of the material. Then the force depends on the direction the tip motion. The thick blue line shows the elastic component of the force.

The tip deflection is shown in Figure 5b. The amplitude is slightly smaller in presence of viscous material and the oscillation is phase shifted with respect to the absence of a viscoelastic response. The instantaneous force shows a region of attractive force when the tip withdraws from the sample surface (Figure 5c). This effective attractive force originates from the viscoelastic interactions.

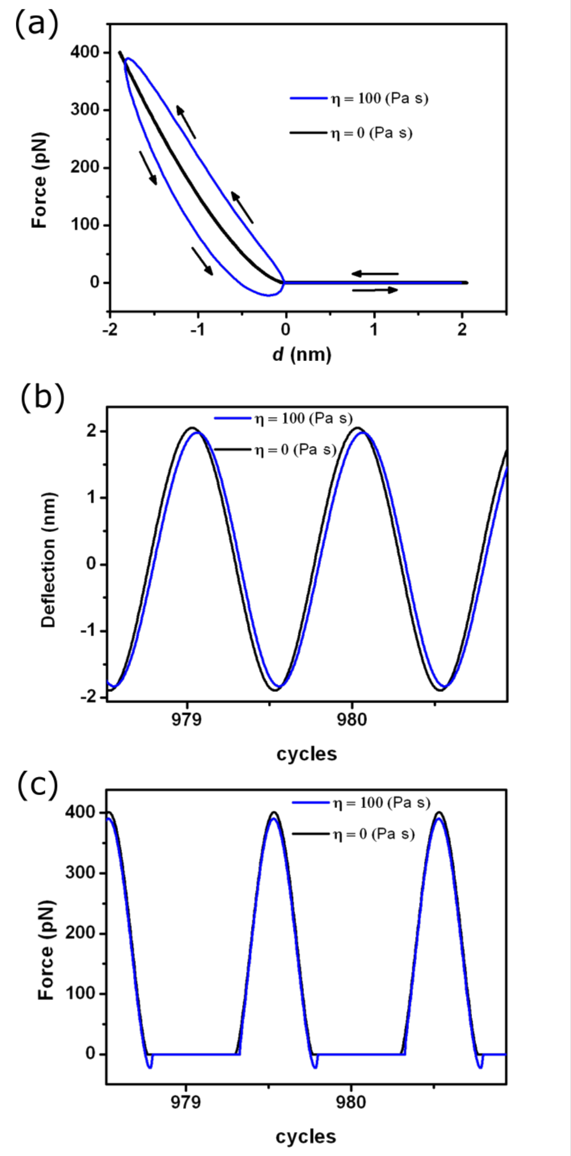

Figure 5: AM-AFM simulations for a viscoelastic material. (a) Force–distance curve for the linear viscous model. The blue curve represents the conservative force given by the Hertz model. (b) Tip deflection as a function of time for an elastic and a viscoelastic material. (c) Instantaneous force at z_c = 0.2 nm.

We have also compared dForce and VEDA simulations [41,42] for several AM-AFM cases. Both simulators give similar results with some minor numerical differences. The compatibility of dForce with different operating systems (Windows, Mac and Linux), the autonomy of running dForce without internet access, and the flexibility by offering customizable plots and interactions forces, highlight several advantages dForce offers.

Bimodal AM

The simulations were performed for the bimodal AM configuration where the first two flexural modes are excited and an amplitude modulation feedback controls the amplitude of the first mode [33]. The parameters used in the bimodal AM simulations are presented in Table 4.

Figure 6 shows the tip response under the influence of excitation and the tip–surface interactions. The periodicity of the signal occurs at a frequency that is a multiple of both the first and the second modes. The instantaneous force shows the region of attractive and repulsive forces and the variation of the peak forces over different periods of the first mode.

In bimodal AM, the phase shift of the second mode is the observable used in heterogeneous samples to separate regions of different material properties. Figure 7 shows the dependence of the phase shift as a function of the set-point amplitude and the material properties (changes in the Hamaker constant). The phase shift ϕ_2 (attractive regime) has a sudden increase that it is followed by a region where the ϕ_2 seems to saturate but then suddenly increases for small z_c values. The shape of the curve is reproduced for other materials (H values).

To illustrate the differences with the AM-AFM operation we also plot the phase shift for the same values of H (in this case ϕ_1). The phase shift in AM-AFM is not sensitive to changes in the conservative terms of the interaction. We remark that the above result holds for a system without dissipative elements [5].

Conclusion

We have developed an interactive simulation environment, based on open source code, to simulate the full cantilever dynamics in both amplitude modulation and bimodal AM force microscopies. The code is both robust and numerically accurate. It incorporates the most relevant interaction force models that apply for dynamic AFM experiments in air and liquid. The simulator has been tested over the years on a wide variety of different AFM conditions.

Table 4: Summary of the parameters used in the numerical simulations of bimodal AFM described in Figure 6 and Figure 7.

Figure	R (nm)	f_1 (kHz)	k_1 (Nm)	Q_1	A_{01} (nm)	f_2 (kHz)	k_2 (Nm)	Q_2	A_{02} (nm)	E_s (Pa)	H (J)
6	1	50	0.9	10	10	310	35.2	62.7	1	1 G	4×10^{-20}
7	20	48.9	0.9	255	17	306.6	35.2	1000	1	1 G	4×10^{-20} 9×10^{-20}

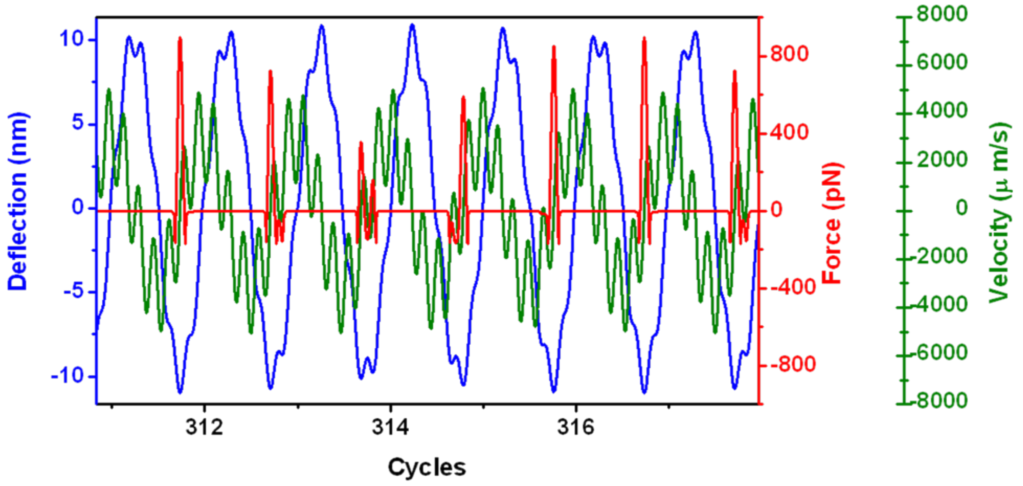

Figure 6: Bimodal AFM tip motion. The tip oscillation (blue), instantaneous force (red) and velocity (green) are shown. Notice that in this particular case the period of the oscillation is 6 times the period of the first mode. Data obtained at z_c = 9 nm.

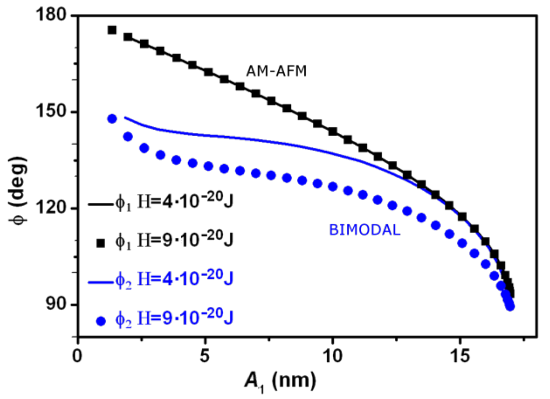

Figure 7: Material contrast in bimodal AFM. Phase shift as a function of the set-point amplitude in bimodal AFM (ϕ_2 versus A_1). To illustrate the bimodal effect, we show the simulations for regular AM-AFM (ϕ_1 versus A_1).

The simulator will help to clarify and understand any arising complexity in the tip motion found in both amplitude modulation and bimodal AFM and, in the process, to establish the relationship between material properties, forces and observables for a given experiment. Because this is open source software, the advanced user could incorporate additional libraries as desired. Finally, the use of dForce must be accompanied by an understanding of the physics behind the simulations in order to select appropriate input parameters that will generate meaningful and correct results.

Acknowledgements

This work was funded by the European Research Council ERC-AdG-340177 (3DNanoMech) and the Spanish Ministry of Economy (MINECO) through grant CSD2010-00024.

References

1. Anczykowski, B.; Krüger, D.; Fuchs, H. *Phys. Rev. B* **1996,** *53,* 15485. doi:10.1103/PhysRevB.53.15485
2. Tamayo, J.; García, R. *Langmuir* **1996,** *12,* 4430–4435. doi:10.1021/la960189l
3. Tamayo, J.; García, R. *Appl. Phys. Lett.* **1997,** *71,* 2394. doi:10.1063/1.120039
4. Melcher, J.; Carrasco, C.; Xu, X.; Carrascosa, J. L.; Gómez-Herrero, J.; de Pablo, P. J.; Raman, A. *Proc. Natl. Acad. Sci. U. S. A.* **2009,** *106,* 13655–13660. doi:10.1073/pnas.0902240106
5. Payam, A. F.; Ramos, J. R.; Garcia, R. *ACS Nano* **2012,** *6,* 4663–4670. doi:10.1021/nn2048558
6. Tamayo, J.; García, R. *Appl. Phys. Lett.* **1998,** *73,* 2926. doi:10.1063/1.122632
7. Garcia, R.; Gómez, C. J.; Martinez, N. F.; Patil, S.; Dietz, C.; Magerle, R. *Phys. Rev. Lett.* **2006,** *97,* 016103. doi:10.1103/PhysRevLett.97.016103
8. Garcia, R.; Magerle, R.; Perez, R. *Nat. Mater.* **2007,** *6,* 405–411. doi:10.1038/nmat1925
9. Anczykowski, B.; Gotsman, B.; Fuchs, H.; Cleveland, J. P.; Elings, V. B. *Appl. Surf. Sci.* **1999,** *140,* 376–382. doi:10.1016/S0169-4332(98)00558-3
10. Santos, S.; Gadelrab, K. R.; Souier, T.; Stefancich, M.; Chiesa, M. *Nanoscale* **2012,** *4,* 792–800. doi:10.1039/c1nr10954e
11. García, R.; San Paulo, A. *Phys. Rev. B* **1999,** *60,* 4961. doi:10.1103/PhysRevB.60.4961
12. García, R.; San Paulo, A. *Phys. Rev. B* **2000,** *61,* R13381. doi:10.1103/PhysRevB.61.R13381
13. Hölscher, H.; Schwarz, U. D. *Int. J. Nonlinear Mech.* **2007,** *42,* 608–625. doi:10.1016/j.ijnonlinmec.2007.01.018
14. Stark, R. W. *Mater. Today* **2010,** *13,* 24–32. doi:10.1016/S1369-7021(10)70162-0
15. Rodríguez, T. R.; García, R. *Appl. Phys. Lett.* **2002,** *80,* 1646. doi:10.1063/1.1456543
16. Stark, R. W.; Heckl, W. M. *Surf. Sci.* **2000,** *457,* 219–228. doi:10.1016/S0039-6028(00)00378-2

17. Stark, R. W. *Nanotechnology* **2004,** *15,* 347–351. doi:10.1088/0957-4484/15/3/020
18. Sahin, O.; Quate, C. F.; Solgaard, O.; Atalar, A. *Phys. Rev. B* **2004,** *69,* 165416. doi:10.1103/PhysRevB.69.165416
19. Balantekin, M.; Atalar, A. *Phys. Rev. B* **2005,** *71,* 125416. doi:10.1103/PhysRevB.71.125416
20. Xu, X.; Melcher, J.; Basak, S.; Reifenberger, R.; Raman, A. *Phys. Rev. Lett.* **2009,** *102,* 060801. doi:10.1103/PhysRevLett.102.060801
21. Lantz, M.; Liu, Y. Z.; Cui, X. D.; Tokumoto, H.; Lindsay, S. M. *Surf. Interface Anal.* **1999,** *27,* 354–360. doi:10.1002/(SICI)1096-9918(199905/06)27:5/6<354::AID-SIA541>3.0.CO;2-4
22. Herruzo, E. T.; Garcia, R. *Appl. Phys. Lett.* **2007,** *91,* 143113. doi:10.1063/1.2794426
23. Basak, S.; Raman, A. *Appl. Phys. Lett.* **2007,** *91,* 064107. doi:10.1063/1.2760175
24. Hu, S.; Raman, A. *Appl. Phys. Lett.* **2007,** *91,* 123106. doi:10.1063/1.2783226
25. Solares, S. D.; Chang, J.; Seog, J.; Kareem, A. U. *J. Appl. Phys.* **2011,** *110,* 094904. doi:10.1063/1.3657940
26. Kumar, B.; Pifer, P. M.; Giovengo, A.; Legleiter, J. *J. Appl. Phys.* **2010,** *107,* 044508. doi:10.1063/1.3309330
27. Guzman, H. V.; Perrino, A. P.; Garcia, R. *ACS Nano* **2013,** *7,* 3198–3204. doi:10.1021/nn4012835
28. Guzman, H. V.; Garcia, R. *Beilstein J. Nanotechnol.* **2013,** *4,* 852–859. doi:10.3762/bjnano.4.96
29. Holscher, H. *Appl. Phys. Lett.* **2006,** *89,* 123109. doi:10.1063/1.2355437
30. Font, J.; Santos, S.; Barcons, V.; Thomson, H. N.; Verdaguer, A.; Chiesa, M. *Nanoscale* **2012,** *4,* 2463–2469. doi:10.1039/c2nr12012g
31. Melcher, J.; Martínez-Martín, D.; Jaafar, M.; Gómez-Herrero, J.; Raman, A. *Beilstein J. Nanotechnol.* **2013,** *4,* 153–163. doi:10.3762/bjnano.4.15
32. Garcia, R.; Herruzo, E. T. *Nat. Nanotechnol.* **2012,** *7,* 217–226. doi:10.1038/nnano.2012.38
33. Martinez, N. F.; Patil, S.; Lozano, J. R.; Garcia, R. *Appl. Phys. Lett.* **2006,** *89,* 153115. doi:10.1063/1.2360894
34. Garcia, R.; Proksch, R. *Eur. Polym. J.* **2013,** *49,* 1897–1906. doi:10.1016/j.eurpolymj.2013.03.037
35. Solares, S. D.; Chawla, G. *J. Appl. Phys.* **2010,** *108,* 054901. doi:10.1063/1.3475644
36. Hutter, C.; Platz, D.; Tholén, E. A.; Hansson, T. H.; Haviland, D. B. *Phys. Rev. Lett.* **2010,** *104,* 05801. doi:10.1103/PhysRevLett.104.050801
37. Sahin, O.; Magonov, S.; Su, C.; Quate, C. F.; Solgaard, O. *Nat. Nanotechnol.* **2007,** *2,* 507–514. doi:10.1038/nnano.2007.226
38. Solares, S. D.; Hoelscher, H. *Nanotechnology* **2010,** *21,* 075702. doi:10.1088/0957-4484/21/7/075702
39. Rodríguez, T. R.; García, R. *Appl. Phys. Lett.* **2004,** *84,* 449–451. doi:10.1063/1.1642273
40. Proksch, R. *Appl. Phys. Lett.* **2006,** *89,* 113121. doi:10.1063/1.2345593
41. Melcher, J.; Hu, S.; Raman, A. *Rev. Sci. Instrum.* **2008,** *79,* 061301. doi:10.1063/1.2938864
42. Kiracofe, D.; Melcher, J.; Raman, A. *Rev. Sci. Instrum.* **2012,** *83,* 013702. doi:10.1063/1.3669638
43. dForce. http://www.icmm.csic.es/forcetool/images/DFORCE/dForce%20simulator.zip (accessed Jan 4, 2015).
44. Melcher, J.; Hu, S.; Raman, A. *Appl. Phys. Lett.* **2007,** *91,* 053101. doi:10.1063/1.2767173
45. Lozano, J. R.; Garcia, R. *Phys. Rev. B* **2009,** *79,* 014110. doi:10.1103/PhysRevB.79.014110
46. García, R. *Amplitude Modulation Atomic Force Microscopy;* Wiley-VCH: Weinheim, Germany, 2010. doi:10.1002/9783527632183
47. Derjaguin, B. V.; Muller, V. M.; Toporov, Yu. P. *J. Colloid Interface Sci.* **1975,** *53,* 314–326. doi:10.1016/0021-9797(75)90018-1
48. Johnson, K. L.; Kendall, K.; Roberts, A. D. *Proc. R. Soc. London, Ser. A* **1971,** *324,* 301. doi:10.1098/rspa.1971.0141
49. Tatara, Y. *JSME Int. J., Ser. A* **1993,** *36,* 190–196.
50. Gavara, N.; Chadwick, R. S. *Nat. Nanotechnol.* **2012,** *7,* 733–736. doi:10.1038/nnano.2012.163
51. San Paulo, A.; García, R. *Surf. Sci.* **2001,** *471,* 71–79. doi:10.1016/S0039-6028(00)00883-9
52. Chyasnavichyus, M.; Young, S. L.; Tsukruk, V. V. *Langmuir* **2014,** *30,* 10566–10582. doi:10.1021/la404925h
53. Blanco-Silva, F. J. *Learning SciPy for Numerical and Scientific Computing;* Packt Publishing: Birmingham, U. K., 2013.
54. Ivan, I. *NumPy,* 2nd ed.; Packt Publishing: Birmingham, U. K., 2013.
55. Scipy.org. http://www.scipy.org (accessed Jan 4, 2015).
56. Hairer, E.; Nørsett, S. P.; Wanner, G. *Solving Ordinary Differential Equations I: Nonstiff Problems,* 2nd ed.; Springer Series in Computational Mathematics, Vol. 8; Springer-Verlag, 1993.
57. García, R.; Pérez, R. *Surf. Sci. Rep.* **2002,** *47,* 197–301. doi:10.1016/S0167-5729(02)00077-8
58. Xu, X.; Raman, A. *J. Appl. Phys.* **2007,** *102,* 034303. doi:10.1063/1.2767202
59. Voïtchovsky, K. *Phys. Rev. E* **2013,** *88,* 22407. doi:10.1103/PhysRevE.88.022407

License and Terms

The definitive version of this article is the electronic one which can be found at:
doi:10.3762/bjnano.6.36

BEILSTEIN JOURNAL OF NANOTECHNOLOGY

Influence of spurious resonances on the interaction force in dynamic AFM

Luca Costa[1] and Mario S. Rodrigues*[2]

Full Research Paper

Open Access

Address:
[1]ESRF, The European Synchrotron, 71 Rue des Martyrs, 38000 Grenoble, France and [2]CFMC/Dep. de Física, Universidade de Lisboa, Campo Grande 1749-016 Lisboa, Portugal

Email:
Mario S. Rodrigues* - mmrodrigues@fc.ul.pt

* Corresponding author

Keywords:
acoustic excitation; amplitude modulation; atomic force microscopy; fluid borne excitation; interferometric detection; laser-beam detection; spurious resonances

Beilstein J. Nanotechnol. **2015,** *6,* 420–427.
doi:10.3762/bjnano.6.42

Received: 26 August 2014
Accepted: 09 January 2015
Published: 10 February 2015

This article is part of the Thematic Series "Advanced atomic force microscopy techniques III".

Guest Editor: T. Glatzel

Abstract

The quantification of the tip–sample interaction in amplitude modulation atomic force microscopy is challenging, especially when measuring in liquid media. Here, we derive formulas for the tip–sample interactions and investigate the effect of spurious resonances on the measured interaction. Highlighting the differences between measuring directly the tip position or the cantilever deflection, and considering both direct and acoustic excitation, we show that the cantilever behavior is insensitive to spurious resonances as long as the measured signal corresponds to the tip position, or if the excitation force is correctly considered. Since the effective excitation force may depend on the presence of such spurious resonances, only the case in which the frequency is kept constant during the measurement is considered. Finally, we show the advantages that result from the use of a calibration method based on the acquisition of approach–retract curves.

Introduction

Dynamic atomic force microscopy (AFM) was introduced in the late 1980s [1] as the natural evolution of the first atomic force microscopes [2]. Thanks to its flexibility, amplitude modulation AFM (AM-AFM) [3] has become successful and widely employed to characterize surfaces at the nanoscale. It has continuously evolved in terms of achievable lateral resolution and scan speed, producing impressive results both at solid/gas interfaces under ambient conditions [4] and at solid/liquid interfaces [5]. A complete overview is given in [3] and [6]. In AM-AFM, micro-sized cantilevers are conventionally excited at a frequency close to their first eigenmode. The oscillation amplitude of the tip is the feedback signal that is kept constant to obtain the sample morphology during the scan. Obviously, the cantilever excitation plays a central role in AM-AFM. Conventionally, mechanical vibration of the cantilever holder is provided through the excitation of a small piezoelectric element (dither). The setup is widely employed in many commercial and custom-made AFMs and permits measurements both in air and in liquids. Despite the success of this method, the cantilever transfer function presents a forest of spurious peaks particularly when measuring in liquid media. As a consequence, a quantitative estimation of the interaction between the probe and the sample is complicated. Moreover, it has already been observed that the motion of the cantilever base due to the acoustic excitation is not negligible in situations in which the Q factor is low – a typical situation when measuring in liquids. The same holds if the cantilever is not excited close to its resonance frequency. Several solutions have been proposed to overcome the presence of spurious peaks in the cantilever transfer function. One possibility is the development of custom-made liquid cells which limit these excitations [7]. Another possibility is the direct excitation of the tip bypassing the conventional piezoelectric excitation. In particular, in the last decade magnetic [8,9], capacitive [10] and photothermal [11,12] actuation schemes have been introduced. The differences between the direct excitation of the tip and the conventional dither excitation have already been studied and reported [13,14]. Consistent efforts have been made to properly quantify the conservative and dissipative interactions when using acoustically excited cantilevers in liquids [15,16]. Here we show that direct excitation is not needed if the position of the cantilever is detected instead of the cantilever bending angle. We report a general study of the dynamics of excited cantilevers and lay-down formulas for deriving the conservative and dissipative interactions considering different types of detection methods. Additionally, this work addresses the consistent advantages that result from the use of approach–retract curves as calibration method [17-19] compared to the standard characterization of the cantilever transfer function.

Results and Discussion

Interaction stiffness and damping

In this section we review two general formulas for the interaction stiffness k_i and damping γ_i without using the assumption that the whole system has a specific transfer function, and assuming only that all the forces involved are additive. However, one should note that if we talk of the interaction stiffness, k_i, this contains the implicit assumption that the interaction force, F_i, in the vicinity of the tip oscillation can be expressed approximately as $F_\text{i} = F_0 - k_\text{i}x$, with F_0 being a constant and x being the tip position.

Consider a point mass which is being acted by two forces. One unknown force given by $F_y(t)$ and another known force $F_x(t) = A_x \cos(\omega t)$. The two forces add together to give a resultant force $F_\text{r}(t) = A_\text{r}\cos(\omega t + \phi)$, which determines the motion of the mass: $x(t) = A\cos(\omega t + \phi)$, which from Newton's second law implies $A_\text{r} = -mA\omega^2$. Hence, from basic trigonometric relationships:

$$\begin{aligned} F_y(t) = &\left[-mA\omega^2 - A_x\cos(\phi)\right]\cos(\omega t+\phi) \\ &-A_x\sin(\phi)\sin(\omega t+\phi). \end{aligned} \tag{1}$$

Consider that the force $F_y(t)$ has two contributions, a restoring force F_rest and a damping force F_damp, so that $F_y(t) = F_\text{rest}(t) + F_\text{damp}(t)$. The restoring force is directly proportional to the position of the moving mass, whereas the damping is directly proportional to its velocity. Let us define k as being the proportionality constant between the force and the position and γ the proportionality constant between the damping force and the speed of the mass. Hence,

$$F_y(t) = -kA\cos(\omega t+\phi) + \gamma\omega A\sin(\omega t+\phi). \tag{2}$$

Comparing Equation 2 with Equation 1 gives

$$\begin{aligned} k &= m\omega^2 + \frac{A_x}{A}\cos(\phi) \\ \gamma &= -\frac{A_x}{\omega A}\sin(\phi). \end{aligned} \tag{3}$$

Suppose that the proportionality constant k depends on an external parameter z so that it can be set $k = k_0 + k_\text{i}(z)$, and in the same way $\gamma = \gamma_0 + \gamma_\text{i}(z)$. In this case

$$\begin{aligned} k_\text{i}(z) &= -k_0 + m\omega^2 + \frac{A_x}{A}\cos(\phi) \\ \gamma_\text{i}(z) &= -\gamma_0 - \frac{A_x}{\omega A}\sin(\phi). \end{aligned} \tag{4}$$

Setting $k_\text{i}(\infty) = 0$ and $\gamma_\text{i}(\infty) = 0$ yields

$$\begin{aligned} a \equiv \frac{A_x^\infty}{A^\infty} &= \sqrt{(k_0 - m\omega^2)^2 + \gamma_0^2\omega^2} \\ \phi^\infty &= \arctan\left(\frac{\gamma_0\omega}{k_0 - m\omega^2}\right). \end{aligned} \tag{5}$$

The superscript "infinity" above means that those constants are evaluated far from the surface. In practice, due to the squeeze film effect, they have to be evaluated just before the short range forces occur. We can then write a final relationship:

$$\begin{aligned} k_\text{i}(z) &= a\left[n\cos(\phi) - \cos(\phi^\infty)\right] \\ \gamma_\text{i}(z) &= \frac{a}{\omega}\left[\sin(\phi^\infty) - n\sin(\phi)\right], \end{aligned} \tag{6}$$

where

$$n \equiv \frac{A_x A^\infty}{A A_x^\infty} . \tag{7}$$

The amplitudes of excitation and tip motion have been normalized to n which is $n = 1$ far from the surface. As long as the excitation force remains directly proportional to the excitation signal, it is not necessary to know its actual value, nor how is the cantilever excited. Thus, as far as the quantifying forces is concerned, squeeze film effects or spurious peaks will not affect the quantification of forces. We will come back to this later when considering specifically spurious forces.

If the cantilever spectrum shows a well defined transfer function, then it is straightforward to obtain a and ϕ^∞ needed to quantify the interaction forces. If the spectrum however is deformed by spurious resonances, then the constants a and ϕ^∞ cannot be evaluated from a simple analysis of the spectrum. This does not mean, however, that Equation 6 is incorrect. An important note is that even if the resonance curve is calibrated close to the sample, we assume that k is the spring constant of the cantilever, so that a resonance frequency different from the natural frequency is accounted for only through a rescaling of the effective mass and quality factor. Whereas, if a and ϕ^∞ are calibrated, the cantilever spring constant is not fixed to any value.

The reasoning above assumes that the measurement corresponds to the position of the particle to which the forces are applied. Most of the AFMs employ however optical beam deflection schemes [20], providing the measurement of the tip bending angle instead of the tip position. If the cantilever is directly excited so that the base of the cantilever is not displaced [8-12], then Equation 6 is still valid, because in that case the deflection is indeed proportional to the position. If the tip position is not measured and the cantilever is not directly excited, then Equation 6 does not hold, particularly away from the resonance frequency or when the Q factor is small.

Coupling with additional resonances

Consider now that the cantilever is coupled to another oscillator giving rise to one extra peak in the spectrum. The cantilever may be coupled in different ways. Let us consider firstly the case where the coupling is described by

$$\begin{aligned} m_\mathrm{l}\ddot{x}_\mathrm{l} + k_\mathrm{l}\left(x_\mathrm{l} - x_\mathrm{s}\right) + \gamma_\mathrm{l}\dot{x}_\mathrm{l} &= 0 \\ m_\mathrm{s}\ddot{x}_\mathrm{s} + k_\mathrm{l}\left(x_\mathrm{s} - x_\mathrm{l}\right) + k_\mathrm{s}\left(x_s - x_0\right) + \gamma_\mathrm{s}\dot{x}_\mathrm{s} &= 0 . \end{aligned} \tag{8}$$

This case corresponds to situations in which additional resonances in the cantilever transfer function are due to the piezoelectric dither in the cantilever holder or due to the cantilever holder itself. The subscript “l” stands for lever and “s” for spurious. Equation 8 is straightforward to solve considering spurious peaks at frequencies close to the cantilever frequency and assuming that nothing else in the system is as soft as the cantilever. If the frequency is comparable to the cantilever resonance frequency, then the ratio $k_\mathrm{s}/m_\mathrm{s}$ is also comparable. If the spurious motion is comparable to the cantilever motion, then the situation is such that the term $k_\mathrm{l}(x_\mathrm{s}-x_\mathrm{l})$ is negligible when compared to the other terms. This implies that the spurious motion is insensitive to motions of the cantilever, i.e., the spurious motion is the same regardless of the cantilever vibrations. Thus, this motion depends only on the excitation signal. As a matter of fact, if the set-up cannot fulfill this requirement, then the cantilever spring constant can not be used for any quantitative evaluation of the interaction, because in this case the cantilever deflection is not directly proportional to the inverse of its spring constant. Therefore the above condition/simplification must, and it does, correspond to the real situation. The above implies Equation 8 can be rewritten as:

$$\begin{aligned} m_\mathrm{l}\ddot{x}_\mathrm{l} + k_\mathrm{l}\left(x_\mathrm{l} - x_\mathrm{s}\right) + \gamma_\mathrm{l}\dot{x}_\mathrm{l} &= 0 \\ m_\mathrm{s}\ddot{x}_\mathrm{s} + k_\mathrm{s}\left(x_\mathrm{s} - x_0\right) + \gamma_\mathrm{s}\dot{x}_\mathrm{s} &= 0 . \end{aligned} \tag{9}$$

The second equation has a very well-known steady-state solution. Given the amplitude $A_\mathrm{s} = x_0 \big/ \sqrt{(k_\mathrm{s} - m_\mathrm{s}\omega^2)^2 + \gamma_\mathrm{s}^2\omega^2}$ and phase $\phi_\mathrm{s} = \arctan[\gamma_\mathrm{s}\omega \big/ (k_\mathrm{s} - m_\mathrm{s}\omega^2)]$, a spurious oscillation will occur. The problem then simplifies and can be summarized in the solution of

$$m_\mathrm{l}\ddot{x}_\mathrm{l} + k_\mathrm{l}\left[x_\mathrm{l} - A_\mathrm{s}\cos\left(\omega t + \phi_\mathrm{s}\right)\right] + \gamma_\mathrm{l}\dot{x}_\mathrm{l} = 0 , \tag{10}$$

which has the following steady state amplitude and phase:

$$\begin{aligned} A_\mathrm{l} &= \frac{k_\mathrm{l} A_\mathrm{s}}{\sqrt{(k_\mathrm{l} - m\omega^2)^2 + \gamma_\mathrm{l}^2\omega^2}} \\ \phi_\mathrm{l} &= -\arctan\left(\frac{\gamma_\mathrm{l}\omega}{k_\mathrm{l} - m_\mathrm{l}\omega^2}\right) + \phi_\mathrm{s} . \end{aligned} \tag{11}$$

Clearly, at a given frequency, the effect of this spurious resonance is that the excitation signal is amplified (A_s) and a phase lag is introduced. However, if the frequency is kept constant, this amplification factor and phase lag remain constant, hence the quantification of the interaction forces is not affected.

Let us consider now that the liquid motion results in an additional force on the cantilever that does not depend on the cantilever bending, i.e., the fluid is moving at the excitation frequency but it does so, independently of the tip oscillation, as in

$$m_1\ddot{x}_1+k_1x_1+\gamma_1\dot{x}_1=kx_\text{b}\cos(\omega t)+F_\text{liquid}\cos(\omega t-\phi_\text{liquid}). \quad (12)$$

Note that the amplitude of F_liquid may be a function of the excitation frequency and in particular present resonances, but because we fixed the excitation frequency, this does not matter. If c_1 and c_2 are the proportionality constants between the excitation signal and kx_b and F_liquid, respectively, then the amplitude and phase of the force acting on the tip are given by:

$$\begin{aligned} A_x &= v_x\sqrt{\left[c_1+c_2\cos\left(\phi_\text{liquid}\right)\right]^2+c_2^2\sin^2\left(\phi_\text{liquid}\right)} \\ \phi_x &= \arctan\frac{c_2\sin\left(\phi_\text{liquid}\right)}{c_1+c_2\cos\left(\phi_\text{liquid}\right)}, \end{aligned} \quad (13)$$

where v_x is the output voltage used to excite the cantilever. If the value inside the square root remains constant then it cancels out when the amplitude is normalized. It is obvious then that such a force will not have any effect in the quantification of the forces if Equation 6 is used. The value of F_liquid and, hence, of c_2 may however change locally depending on the tip being far away from the sample or at its vicinity or even depending on the sample itself. Such changes will cause variations in both the measured amplitude and phase according to the equations above, hence, explaining changes in amplitude and in phase observed for example in [21]. Therefore, a, and ϕ^∞ must be evaluated close to the sample surface and assume they remain approximately constant at very short tip–sample distances where the actual interaction takes place.

To experimentally demonstrate the assumptions above we coated an optical fiber with 30 nm of gold at its ends and 300 nm of gold at its edges as illustrated in Figure 1.

We applied a harmonic oscillating signal $V(\omega)$ around a given ΔV_0 which results in a direct electrostatic actuation of the tip. Figure 2a shows the resonance of the excited cantilever in air (black) and in deionized water (blue). The cantilevers have a nominal spring constant of 0.8 N/m. Figure 2b shows the resonance of the cantilever in liquid with direct excitation (blue) and with a conventional piezoelectric excitation (red), showing the presence of spurious resonances.

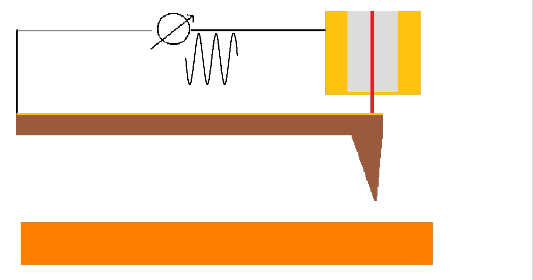

Figure 1: Setup employed for the direct excitation of the tip. A gold coated optical fiber is used to measure the tip position and to apply an electrostatic excitation to the conductive cantilever at a frequency close to resonance.

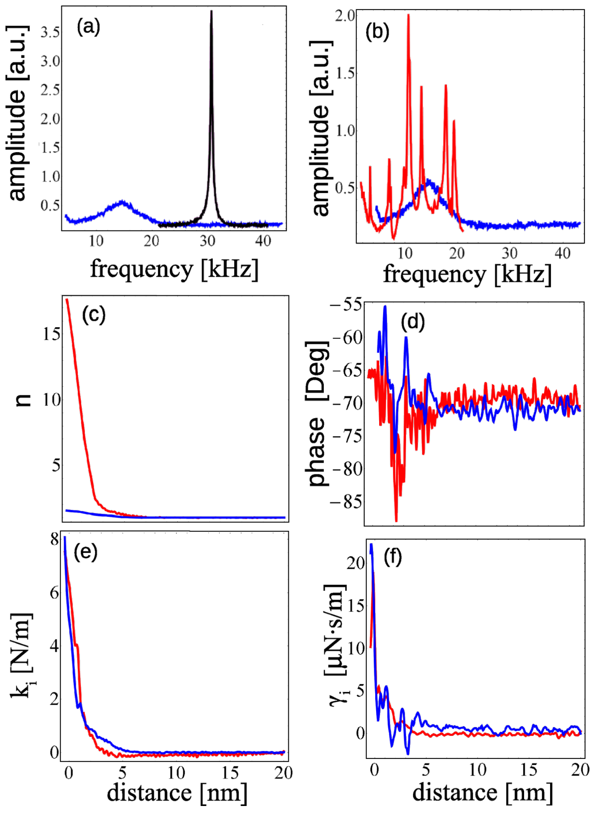

Figure 2: Excitation of the tip in air and in liquid with different actuation methods: a) electrostatic excitation of the cantilever in air (black) and in liquid (blue); b) Amplitude of the tip directly excited (blue) and mechanically excited (red) in liquid; (c and d) normalized excitation and phase, respectively; e) force gradient and f) dissipation measured at the mica/deionized water interface with electrostatic excitation of the tip (blue) and conventional piezoelectric excitation (red).

Approach force curves were acquired in force feedback mode [17,18] at the mica/deionized water interface. The oscillation amplitude of the tip was 0.3 nm. Amplitude and phase were recorded and converted into conservative and dissipative interactions by using Equation 6 and the equality $F = -\int k_\text{i}\text{d}z$. The same measurement was repeated while using conventional piezoelectric excitation instead. Even in the presence of spurious peaks, we converted the amplitude and phase into conservative and dissipative interactions. The force gradient and the dissipation are shown in Figure 2e and Figure 2f. In both cases it is possible to observe the same results in terms of force gradient and dissipation, the main difference between the two excitation methods being only the calibration parameters a and ϕ^{∞}, which were in the case of electrostatic excitation $\phi^{\infty} = -0.6$ rad and $a = 2$ N/m, and for the conventional acoustic excitation $\phi^{\infty} = -0.3$ rad and $a = 0.2$ N/m.

Measurement based on the deflection angle

If the measurement is not directly proportional to the position of the tip but to the cantilever deflection, then the displacement of the base has to be added to the measured signal. Considering Equation 4 and recomputing both $\cos(\phi)/A$ and $\sin(\phi)/A$, the position of the moving mass, given by its deflection plus the motion of the base, is $A\cos(\omega t + \phi) = A_{\mathrm{m}}\cos(\omega t + \phi_{\mathrm{m}}) + A_{\mathrm{b}}\cos(\omega t)$, where A_{m} is the amplitude of the measured signal and A_{b} the oscillation amplitude of the cantilever anchoring point. To simplify, as both A_{b} and A_x are proportional to the excitation signal, we can put $A_x\alpha = kA_{\mathrm{b}}$ where α is zero in case of direct excitation. We can also define a proportionality constant between the measured amplitude and the excitation $nrkA_{\mathrm{m}} = A_x$ where n is again the normalized amplitude and r is a constant such that $n = 1$ in the absence of interactions. Equation 4 becomes

$$
\begin{aligned}
k_{\mathrm{i}} &= -k + m\omega^2 + \frac{knr\left[\alpha nr + \cos\left(\phi_{\mathrm{m}}\right)\right]}{1 + \alpha^2 n^2 r^2 + 2\alpha nr\cos\left(\phi_{\mathrm{m}}\right)} \\
\gamma_{\mathrm{i}} &= -\gamma_0 - \frac{1}{\omega}\frac{knr\sin\left(\phi_{\mathrm{m}}\right)}{1 + \alpha^2 n^2 r^2 + 2\alpha nr\cos\left(\phi_m\right)}.
\end{aligned}
\qquad (14)
$$

Note that Equation 14 is the same as Equation 4 if one of the following is true:

1. The measured signal corresponds to the position of the moving tip, in which case the terms with α do not appear in the equation.
2. The base of the cantilever does not move (direct excitation), in which case α = 0.
3. It is possible to state that $A_{\mathrm{m}} >> A_{\mathrm{b}}$, which implies $\alpha \approx 0$.
4. If there is a liquid cell resonance such that $F_{\mathrm{liquid}} >> kA_{\mathrm{b}}$, in which case the cantilever behaves as being directly excited.

If none of the above is true, then there is one particular noteworthy case that corresponds to an excitation force solely due to the cantilever base displacement. Note that this implies the absence of spurious forces. In that case α = 1 and Equation 14 simplifies to

$$
\begin{aligned}
k_{\mathrm{i}} &= m\omega^2 - \frac{k\left[1 + nr\cos\left(\phi_{\mathrm{m}}\right)\right]}{1 + n^2 r^2 + 2nr\cos\left(\phi_{\mathrm{m}}\right)} \\
\gamma_{\mathrm{i}} &= \gamma_0 - \frac{k}{\omega}\frac{nr\sin\left(\phi_{\mathrm{m}}\right)}{1 + n^2 r^2 + 2nr\cos\left(\phi_{\mathrm{m}}\right)}.
\end{aligned}
\qquad (15)
$$

Far from the sample surface, Equation 15 must equal zero. We can solve Equation 15 to find the constants ϕ_m^{∞} and r:

$$
\begin{aligned}
r &\equiv \frac{A_x^{\infty}}{kA_m^{\infty}} = \sqrt{\frac{\gamma^2\omega^2 + \left(k - m\omega^2\right)^2}{\gamma^2\omega^2 + m^2\omega^4}} \\
\phi_m^{\infty} &= \arccos\left[\frac{\omega\left[\gamma^2 + m\left(m\omega^2 - k\right)\right]}{\sqrt{\left(\gamma^2 + m^2\omega^2\right)\left[\gamma^2\omega^2 + \left(k - m\omega^2\right)^2\right]}}\right].
\end{aligned}
\qquad (16)
$$

The first terms in Equation 15 can be computed from the information far from the sample:

$$
\begin{aligned}
m\omega^2 &= \frac{k\left[1 + r\cos\left(\phi_{\mathrm{m}}^{\infty}\right)\right]}{1 + r^2 + 2r\cos\left(\phi_{\mathrm{m}}^{\infty}\right)} \\
\gamma_0 &= \frac{k}{\omega}\frac{r\sin\left(\phi_{\mathrm{m}}^{\infty}\right)}{1 + r^2 + 2r\cos\left(\phi_{\mathrm{m}}^{\infty}\right)}.
\end{aligned}
\qquad (17)
$$

This highlights the fact that if the cantilever spring constant k is known, then the evaluation of either γ and m, or r and ϕ^{∞} is needed to quantify the interaction. The first couple of constants can be found from a resonance curve if it is well-defined in the spectrum. The second couple can be found from a calibration curve obtained from a known force or by using for example an approach curve and the fit of $F = -\int k_{\mathrm{i}}\mathrm{d}z$ as in [17,18]. In air it is straightforward to calibrate these constants by using for instance an electrostatic force.

Finally, some considerations regarding the case in which $\alpha \neq 1$. This case depicts piezoelectric actuation resulting in a non-negligible liquid-borne excitation. First note that this situation poses no difficulty in the case in which the tip position is measured. It is more complicated in the case of beam deflection because Equation 14 is more difficult to analyze. The values of A_x and A_{b}, or their ratios, are not acquired from a conventional analysis of the transfer function nor from fitting the Brownian motion of the cantilever. One could perhaps use the equality

$F = \int \nabla F \mathrm{d}z$ to calibrate Equation 14. However, it turns out that for $0 < \alpha < 1$ the solution lies somewhere between those given by Equation 6 and Equation 17 (see Figure 3). As such, either Equation 6 or Equation 17 can be used to effectively calibrate the required constants. When $\alpha >> 1$, the situation is more complicated. Fortunately, this will happen only in very particular cases. Going back to Equation 13 one concludes

$$\alpha = c_1 \Big/ \sqrt{\left[c_1 + c_2 \cos\left(\phi_{\text{liquid}}\right)\right]^2 + c_2^2 \sin^2\left(\phi_{\text{liquid}}\right)}, \quad (18)$$

which means $\alpha >>1$ only when $c_1 \approx c_2$ and $\phi_{\text{liquid}} \approx -\pi$.

To further prove the statements in the last paragraph, and because one usually does not measure α, we have considered a force gradient going from $-k/3$ up to $k/3$ for different α by using Equation 14, Equation 6 ($\alpha = 0$) and Equation 17 ($\alpha = 1$). The latter was done considering three cantilevers all with the same resonance frequency but with rather different Q factors from high to low. In Figure 3 we show what would be the amplitude and phase measured for five different values of α (represented with different colors) and for three different Q factors. For high Q factors and small interactions all expressions lead to about the same values (Figure 3), meaning that in such cases it is not necessary to worry about the constant α. However, for lower values of Q the solutions give quite different results. Figure 3 illustrates the rather large errors that can be made if the excitation force is not well taken into account showing the advantages of measuring position rather than deflection.

To experimentally illustrate the situation described above, we have prepared a cantilever holder that excites the cantilever by a combination of rotation and translation [22]. In this case $A_x \neq kA_b$. Furthermore, this particular holder shows many spurious resonances. We applied an electrical potential difference between a conductive cantilever and a conductive sample which results in an electrostatic interaction. Three approach curves were taken at selected arbitrary frequencies (Figure 4b) and Equation 17 was used to account for the interaction. All the measurements provide the same force gradient (Figure 4e) regardless of the presence of spurious resonances (Figure 4a), whereas the dissipation remains constant and approximately equal to zero. The force was used to obtain all unknown constants.

Interestingly, the values of r and ϕ^∞ that result from the calibration are those that would be expected if the spurious peaks were not present. Notice in Figure 4d that the phase is close to 0, −90 and −180°, when the cantilever is, respectively, excited below, close to, and above the resonance frequency. To ease the task of

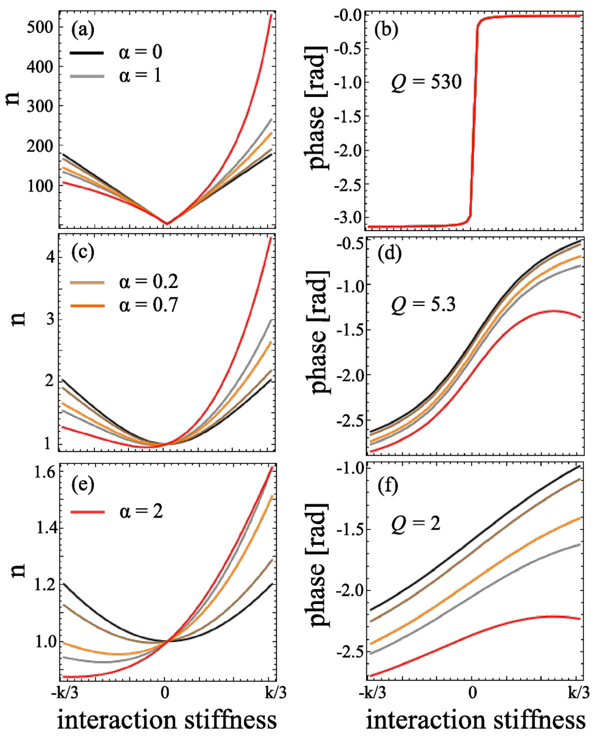

Figure 3: Equation 14 simulating amplitude (left) and phase (right) for three different quality factors from high (top) to low (bottom). Each plot contains five curves, each corresponding to a different α. If α = 0 (black) then the solution is equal to that given by Equation 6, for α = 1 (gray) the solution is equal to that given by Equation 15. For 0 < α < 1, the solution lies somewhere between that given by Equation 6 and Equation 15. The red curve shows the solution for α = 2.

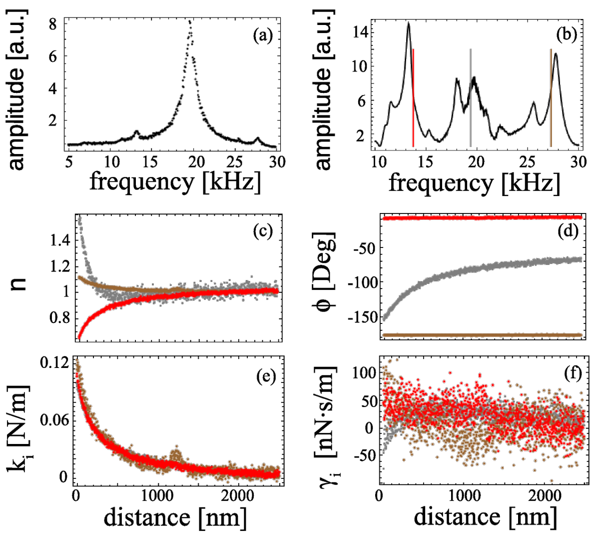

Figure 4: Characterization of a tip–sample electrostatic interaction at resonance (gray) and off resonance (red and brown). a) Cantilever Brownian motion; b) spectrum of the excited cantilever; c) normalized amplitude at three selected frequencies indicated in the spectrum; d) measured phase (offset so that at infinity it gives ϕ_m^∞); e) and f) force gradient and dissipation measured at the three selected frequencies.

calibrating the cantilever, r and ϕ^{∞} were initially guessed from Equation 16, for which the constants were obtained from the analysis of the tip Brownian motion shown in Figure 4a. The resulting r^{*} and $\phi^{\infty*}$ are listed in Table 1 together with r and ϕ^{∞} values obtained from the analysis of the Brownian motion. This result shows that the change in amplitude and phase due to the interaction force were about the same, regardless of the presence of spurious peaks.

Table 1: Calibration based on matching the integral of the force gradient to the force (r^{*}, $\phi^{\infty*}$), and using directly the constants determined from fitting the Brownian motion of the tip (r, ϕ^{∞}).

f_x	13734 Hz	19393 Hz	27315 Hz
r	1.05 N/m	0.059 N/m	0.48
r^{*}	1.05	0.056	0.4
ϕ^{∞}	−8°	−66°	−178°
$\phi^{\infty*}$	−8°	−66°	−177°

Conclusion

We have introduced a methodology to directly derive the conservative and dissipative interactions between the AFM probe and the sample in dynamic AFM experiments when small oscillation amplitudes of the tip are used, and for different tip excitation and detection schemes. We considered both direct detection of the tip position, for example with Fabry–Perot interferometers, and classic optical beam deflection scheme, showing that the first method allows a much easier calculation of the interactions. We have proposed a calibration method of the cantilever response that is not based on the measurement of its transfer function, but it is based on the acquisition of the tip position/deflection, amplitude and phase during approach curves and consequently the assumption of the equality $F = -\int k_i \mathrm{d}z$. The method has been employed to compare the interaction force at the mica/deionized water interface measured with a conventional piezoelectric dither excitation and direct electrostatic excitation. The different setups provide the same evaluation of the force gradient although the calibration parameters are different. Finally, we have highlighted the changes that have to be introduced into the formulas for optical beam deflection based AFMs. With the described procedure, it is possible to ignore the effects of spurious resonances even when using optical beam deflection-based AFMs.

Acknowledgements

Luca Costa acknowledges COST Action TD 1002. Mario S. Rodrigues acknowledges financial support from Fundação para a Ciência e Tecnologia SFRH/BPD/69201/2010. The authors thank Fabio Comin and Joel Chevrier for discussions and Irina Snigireva for the preparation of the gold coated optical fibers.

References

1. Martin, Y.; Williams, C. C.; Wickramasinghe, H. K. *J. Appl. Phys.* **1987,** *61,* 4723–4729. doi:10.1063/1.338807
2. Binnig, G.; Quate, C. F.; Gerber, C. *Phys. Rev. Lett.* **1986,** *56,* 930–933. doi:10.1103/PhysRevLett.56.930
3. García, R. *Amplitude modulation atomic force microscopy;* Wiley-VCH, 2010.
4. Santos, S.; Barcons, V.; Christenson, H. K.; Billingsley, D. J.; Bonass, W. A.; Font, J.; Thomson, N. H. *Appl. Phys. Lett.* **2013,** *103,* 063702. doi:10.1063/1.4817906
5. Ando, T. *Nanotechnology* **2012,** *23,* 062001. doi:10.1088/0957-4484/23/6/062001
6. Baro, A. M.; Reifenberger, R. G., Eds. *Atomic Force Microscopy in Liquid: Biological Applications;* Wiley, 2012.
7. Maali, A.; Cohen-Bouhacina, T.; Couturier, G.; Aimé, J.-P. *Phys. Rev. Lett.* **2006,** *96,* 086105. doi:10.1103/PhysRevLett.96.086105
8. Han, W.; Lindsay, S. M.; Jing, T. *Appl. Phys. Lett.* **1996,** *69,* 4111–4113. doi:10.1063/1.117835
9. Revenko, I.; Proksch, R. *J. Appl. Phys.* **2000,** *87,* 526–533. doi:10.1063/1.371894
10. Umeda, K.-i.; Oyabu, N.; Kobayashi, K.; Hirata, Y.; Matsushige, K.; Yamada, H. *Appl. Phys. Express* **2010,** *3,* 065205. doi:10.1143/APEX.3.065205
11. Ratcliff, G. C.; Erie, D. A.; Superfine, R. *Appl. Phys. Lett.* **1998,** *72,* 1911–1913. doi:10.1063/1.121224
12. Ramos, D.; Tamayo, J.; Mertens, J.; Calleja, M. *J. Appl. Phys.* **2006,** *99,* 124904. doi:10.1063/1.2205409
13. Herruzo, E. T.; Garcia, R. *Appl. Phys. Lett.* **2007,** *91,* 143113. doi:10.1063/1.2794426
14. Xu, X.; Raman, A. *J. Appl. Phys.* **2007,** *102,* 034303. doi:10.1063/1.2767202
15. Kiracofe, D.; Raman, A. *Nanotechnology* **2011,** *22,* 485502. doi:10.1088/0957-4484/22/48/485502
16. de Beer, S.; van den Ende, D.; Mugele, F. *Nanotechnology* **2010,** *21,* 325703. doi:10.1088/0957-4484/21/32/325703
17. Rodrigues, M. S.; Costa, L.; Chevrier, J.; Comin, F. *Appl. Phys. Lett.* **2012,** *101,* 203105. doi:10.1063/1.4766172
18. Costa, L.; Rodrigues, M. S.; Newman, E.; Zubieta, C.; Chevrier, J.; Comin, F. *J. Mol. Recognit.* **2013,** *26,* 689–693. doi:10.1002/jmr.2328
19. Rodrigues, M. S.; Costa, L.; Chevrier, J.; Comin, F. *J. Appl. Phys.* **2014,** *115,* 054309. doi:10.1063/1.4864127
20. Meyer, G.; Amer, N. M. *Appl. Phys. Lett.* **1988,** *53,* 1045–1047. doi:10.1063/1.100061
21. Cartagena, A.; Raman, A. *Biophys. J.* **2014,** *106,* 1033–1043. doi:10.1016/j.bpj.2013.12.037
22. Vitorino, M. V.; Carpentier, S.; Costa, L.; Rodrigues, M. S. *Appl. Phys. Lett.* **2014,** *105,* 013106. doi:10.1063/1.4887484

License and Terms

BEILSTEIN JOURNAL OF NANOTECHNOLOGY

Mapping of elasticity and damping in an α + β titanium alloy through atomic force acoustic microscopy

M. Kalyan Phani[1], Anish Kumar[1], T. Jayakumar[1], Walter Arnold*[2,3] and Konrad Samwer[3]

Full Research Paper

Open Access

Address:
[1]Metallurgy and Materials Group, Indira Gandhi Centre for Atomic Research, Kalpakkam-603102, Tamil Nadu, India, [2]Department of Materials and Materials Technology, Saarland University, Campus D 2.2, D-66123 Saarbrücken, Germany and [3]1. Physikalisches Institut, Georg-August-Universität, Friedrich Hund Platz 1, D-37077 Göttingen, Germany

Email:
Walter Arnold* - w.arnold@mx.uni-saarland.de

* Corresponding author

Keywords:
atomic force acoustic microscopy; contact resonances; damping; indentation modulus; Ti-6Al-4V

Beilstein J. Nanotechnol. **2015,** *6,* 767–776.
doi:10.3762/bjnano.6.79

Received: 08 October 2014
Accepted: 15 February 2015
Published: 18 March 2015

This article is part of the Thematic Series "Advanced atomic force microscopy techniques III".

Guest Editor: T. Glatzel

Abstract

The distribution of elastic stiffness and damping of individual phases in an α + β titanium alloy (Ti-6Al-4V) measured by using atomic force acoustic microscopy (AFAM) is reported in the present study. The real and imaginary parts of the contact stiffness k^* are obtained from the contact-resonance spectra and by using these two quantities, the maps of local elastic stiffness and the damping factor are derived. The evaluation of the data is based on the mass distribution of the cantilever with damped flexural modes. The cantilever dynamics model considering damping, which was proposed recently, has been used for mapping of indentation modulus and damping of different phases in a metallic structural material. The study indicated that in a Ti-6Al-4V alloy the metastable β phase has the minimum modulus and the maximum damping followed by α′- and α-phases. Volume fractions of the individual phases were determined by using a commercial material property evaluation software and were validated by using X-ray diffraction (XRD) and electron back-scatter diffraction (EBSD) studies on one of the heat-treated samples. The volume fractions of the phases and the modulus measured through AFAM are used to derive average modulus of the bulk sample which is correlated with the bulk elastic properties obtained by ultrasonic velocity measurements. The average modulus of the specimens estimated by AFAM technique is found to be within 5% of that obtained by ultrasonic velocity measurements. The effect of heat treatments on the ultrasonic attenuation in the bulk sample could also be understood based on the damping measurements on individual phases using AFAM.

Introduction

The physical and mechanical properties of the individual phases govern the respective properties of the multiphase structural materials. The knowledge of elastic properties of the individual phases is important for studying their deformation behavior, crack nucleation and propagation, dislocation activity and interaction with grain boundaries and also even helps in understanding the bulk elastic properties of multiphase materials [1,2]. Over the last two decades many contact-resonance-based atomic force microscopy (AFM) techniques, such as ultrasonic atomic force microscopy (UAFM) [3], and atomic force acoustic microscopy [4] have emerged for the characterization of elastic properties of materials with nanometer resolution. UAFM and AFAM work with a similar principle and only vary in the excitation of the cantilever. In UAFM the cantilever is excited by attaching a transducer to the cantilever base. In AFAM, the transducer is placed under the sample and periodic displacements of the sample are sensed by the cantilever when in contact. Rabe et al. [4], Hurley et al. [5] have discussed in detail the development of contact-resonance force microscopy techniques for quantitative measurements of nanomechanical properties. Ogi et al. [6] have studied elastic and damping properties in a dual-phase steel by using resonance ultrasound microscopy (RUM), which is a contact-resonance based technique but limited to micrometer resolution. An improved UAFM technique was used for mapping the resonance frequency and the quality factor, Q, in carbon reinforced plastics composites [7]. In recent years, AFAM has been extensively used to determine elastic stiffness or damping properties in nano-crystalline nickel [2], PMMA films [8], NiMnGa films [9], Arabidopsis plant [10], polystyrene–propylene blends [11], nickel base alloys [12,13], ferritic steels [13], and metallic glasses [14]. Besides contact-resonance based methods, multifrequency AFM techniques have also been used for measurement of elastic and damping properties in living cells [15], proteins [16] and polymers [17,18]. They have been found to be useful in probing material properties with enhanced sensitivity, less surface damage and also at larger distances [18,19]. However, these techniques were developed for soft materials with moduli smaller than 10 GPa.

The type and amount of various phases formed during thermal/thermo-mechanical treatments influence both the mechanical as well as the elastic properties of α + β titanium alloys [1]. By varying the volume fractions of the two phases present in the alloy, various combinations of strength and toughness can be achieved. Ti-6Al-4V combines the benefits of high strength, light weight, formability and corrosion resistance and finds applications in aircraft structural components, aerospace fasteners, high-performance automotive parts, marine applications, medical devices, and sports equipment. Owing to the good corrosion resistance and biocompatibility, Ti-6Al-4V is also widely used in making load-bearing metal implants [20]. Different studies have been reported on phase transformations [21] and mechanical property variations with various phases [22] in Ti-6Al-4V. Kumar et al. [1] have successfully mapped the indentation modulus of α- and β-phases in a Ti-6Al-4V alloy by using AFAM while using a cantilever dynamic model in which damping, however, was neglected. In this paper, we report mapping of elastic modulus and damping using a modified cantilever dynamic model in various phases, such as α, β and α′ in Ti-6Al-4V alloy heat-treated at different temperatures. The modulus of individual phases measured by AFAM has been used to calculate the average modulus of the alloy in different heat treatment conditions, which is correlated with the modulus obtained by the bulk ultrasonic velocity measurements.

Measurement of elastic stiffness and damping through AFAM

In AFAM, longitudinal waves are injected into the specimen from its bottom by using a transducer, which leads to periodic displacements of the specimen surface. These vibrations are sensed by a probe (cantilever + tip) during contact. The amplitude of the vibrations of the probe after excitation at various frequencies is detected through the AFM photodiode signal by the use of a lock-in-amplifier [14]. The response of the probe as a function of the frequency can be acquired by sweeping a wide range of frequencies. The obtained contact-resonance spectra are used to calculate the contact stiffness k^* and the local contact damping E''/E' by employing suitable models for the tip–specimen contact, and in turn enabling one to image and to measure the local elasticity or the storage modulus E' and the damping or loss modulus E'' of the specimen surfaces with a spatial resolution of a few tens of nanometers. A schematic representation of set-up of AFAM is shown in Figure 1.

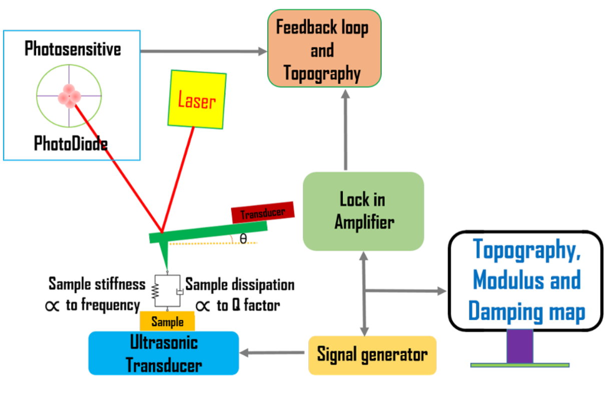

Figure 1: Schematic setup of atomic force acoustic microscopy.

Detailed descriptions of the theory and calculations of the indentation modulus and damping are given elsewhere [4,23,24]. In particular for measuring contact damping, the cantilever model must be taken into account [8], and this has been applied recently to metallic glasses by Wagner et al. [24]. They have successfully demonstrated a quantitative approach to determine the local internal friction or loss at a nanometer scale, using the evaluation procedure of the cantilevers distributed mass model with damped flexural modes on amorphous PdCuSi metallic glass.

The solution of the characteristic dispersion equation of the 'cantilever dynamics' model was presented in many publications, also in [24]:

$$\begin{aligned}
&\frac{2}{3}\frac{k_c}{k^*}\left(k_nL_1\right)^4 A+\left(k_nL_1\right)^3\frac{h^2}{L_1^2}\left[\sin^2\theta+c_P\cos^2\theta\right]\\
&\times\left[D_1\times A_2-D_2\times C_1\right]+2\left(k_nL_1\right)^2\frac{h}{L_1}\sin\theta\cos\theta\left(c_p-1\right)\\
&\times\left[\sin\left(k_nL_1\right)\sinh\left(k_nL_1\right)\times A_2+\sin\left(k_nL_2\right)\sinh\left(k_nL_2\right)\times C_1\right] \quad (1)\\
&+\left(k_nL_1\right)\left[\cos^2\theta+c_p\sin^2\theta\right]\times\left[B_1\times A_2-B_2\times C_1\right]\\
&+c_p\left(3\frac{k^*h^2}{k_cL_1^2}C_1\times A_2\right)=0\,,
\end{aligned}$$

where

$$\begin{aligned}
A&=1+\cos\left(k_nL\right)\cosh\left(k_nL\right),\\
B&=\sin\left(k_nL\right)\cosh\left(k_nL\right)-\sinh\left(k_nL\right)\cos\left(k_nL\right),\\
C&=1-\cos\left(k_nL\right)\cosh\left(k_nL\right),\\
D&=\sin\left(k_nL\right)\cosh\left(k_nL\right)+\sinh\left(k_nL\right)\cos\left(k_nL\right).
\end{aligned}$$

The subscripts 1, 2 used here are for L_1 and L_2 and hold for all *A, B, C and D* for example:

$$\begin{aligned}
D_1&=\sin\left(k_nL_1\right)\cosh\left(k_nL_1\right)+\sinh\left(k_nL_1\right)\cos\left(k_nL_1\right),\\
D_2&=\sin\left(k_nL_2\right)\cosh\left(k_nL_2\right)+\sinh\left(k_nL_2\right)\cos\left(k_nL_2\right).
\end{aligned}$$

L is the total cantilever length and L_1 is the distance between the tip position and the free end of the cantilever, and $L_2 = L - L_1$. The values used for the calculations in the present study are $L_1/L = 0.94$, the angle of inclination of the cantilever $\theta = 12°$ and the ratio of the lateral to the vertical contact stiffnesses $c_p = 0.85$ given by the Poisson's ratio of the materials examined [4,23].

When damping is taken into account, the wave-vector k_n describing the motion of the cantilever becomes complex with a_n being its real part and b_n being its imaginary part. The imaginary part is caused by the damping of the tip–specimen configuration, i.e., the damping in the contact zone, and the damping of the cantilever motion in air. The cantilever resonance frequencies determine the real part a_n, and the imaginary part b_n is determined by the width of the contact resonance curves [8,11]:

$$\begin{aligned}
k_n&=\left(a_n+ib_n\right)/L\text{ , where}\\
a_n&=C_n\sqrt{\frac{f_{\text{cont}}}{f_{\text{free}}}},\\
b_n&=\frac{2\pi f_{\text{cont}}-\dfrac{2\pi f_{\text{free}}}{Q_{\text{free}}}Q_{\text{cont}}}{8\pi f_{\text{cont}}Q_{\text{cont}}}\,.
\end{aligned}\qquad(2)$$

Here, $n = 1, 2,\ldots\infty$ are the mode numbers, e.g., $C_1 = 1.875$ for the first free resonance. In Equation 2 it is neglected that the damping of the cantilever during its motion in air is not the same for the free cantilever and the cantilever in contact [24]. However, due to the relative high contact damping E''/E', which we observe in our experiments, we neglect this effect.

The values for a_n and b_n are obtained by fitting Lorentzians to the experimentally obtained resonances curves of the free and contact resonances. Due to the local damping in the contact zone the contact stiffness becomes a complex quantity, i.e., $k^* = k_r + ik_i$, where k_r is the real part of the contact stiffness and k_i is the imaginary part of the contact stiffness. In case there is viscous damping in the contact zone, $k_i = \omega\gamma$, where ω is the angular frequency. Neither k_r nor k_i can be measured directly. The local damping Q_{loc}^{-1} is given by the ratio of the imaginary part of the contact stiffness to the real part. The above set of equations was solved by using the LabVIEW® program, in order to obtain the real and imaginary parts of the wave vectors and the contact stiffness using the procedures employed by Yuya et al. [8,25] and Killgore et al. [11]. Here, it is convenient to introduce:

$$\lambda_n=\frac{k_r}{k_c}\text{ and }\eta_n=\gamma\sqrt{\frac{L_1^2}{9EI\rho A}}\,,\qquad(3)$$

where λ_n is the normalized contact stiffness and η_n is the normalized damping constant. The parameter γ stands for the interaction damping in the contact zone, generally represented by a dashpot parallel to a spring. I is the area moment of inertia.

By using an appropriate contact mechanics model, one can convert the obtained stiffness values to the reduced elastic modulus E^* and then to the indentation modulus M. The contact mechanics for AFM tips is very difficult to model as the exact shape of the tip in contact with the sample is usually unknown. The Hertz model is a simplified and the most widely used contact mechanics model for AFM contacts. It assumes each contact to be an elastic half space with relatively small strains at the frictionless contact with elliptical shape [26]. The tip radius and the applied load are considered to be constant during a scan. Hence, the modulus of one phase could be considered as reference for obtaining the modulus of the other phases. If we assume the tip to be spherical, the real part of the contact stiffness, k_r, is related to E^* through the following equation [1,8,12,13]:

$$k_r = \sqrt[3]{6RPE^{*2}} \,. \tag{4}$$

Here, E^* is the reduced elastic modulus, R is the radius of curvature of the cantilever tip and P is the load applied on the specimen through the cantilever. There is one unknown, R, which can be eliminated by using a reference method. Reference material can either be a single crystal with known orientations or an amorphous material. Recently, Phani et al. [12] have demonstrated an approach that circumvents the problem of the change in the tip condition by simultaneous acquisition of two contact-resonance frequencies and by selecting a few points in the matrix in each scan line as a reference. This methodology eliminates repeated switching between an unknown specimen and a reference specimen for quantitative measurement of the indentation modulus. The calibration procedure is based on the equation:

$$\frac{E_s^*}{E_{\text{ref}}^*} = \left(\frac{k_s^*}{k_{\text{ref}}^*}\right)^{3/2} . \tag{5}$$

E_s^* is governed by the elastic properties of the specimen and the tip. The relation between the indentation moduli M_{tip} and M_{sample} and E_s^* is given by:

$$\frac{1}{E_s^*} = \frac{1}{M_{\text{tip}}} + \frac{1}{M_{\text{sample}}} , \tag{6}$$

with

$$M = E \big/ \left(1 - \nu^2\right) , \tag{7}$$

where ν is the Poisson’s ratio. By using the values obtained for k_r and k_i and, hence, λ_n and η_n from the dispersion equation, one can get the local damping $Q_{\text{loc}}{}^{-1} = E''/E'$ values of the specimen at the nanometer scale. The damping for the first mode can be derived from the equation:

$$\begin{aligned} Q_{n,\text{loc}}^{-1} &= \frac{\omega\gamma}{k_r} \\ &= \frac{\eta_n}{\lambda_n} \frac{L}{L_1} \frac{\omega_{c,n} \times \left(k_n L\right)^2}{\omega_{\text{free},n}} \\ &\approx 3.516 \frac{n_1}{\lambda_1} \frac{L}{L_1} \frac{\omega_{c,1}}{\omega_{\text{free},1}} . \end{aligned} \tag{8}$$

Here, ω and ω_{free} are the contact and the free angular resonance frequencies, respectively. The lower approximation of Equation 8 holds for the first cantilever mode.

Experimental

Three specimens of Ti-6Al-4V of dimensions of about 25 × 25 × 4 mm^3 were solution-annealed at 1323 K (above the β-transus temperature) for one hour, followed by water quenching. The solution-annealed specimens were then heat-treated at 923, 1123 and 1223 K, respectively, for one hour, followed by water quenching. The specimens were prepared by using an automatic polishing machine down to 0.25 µm diamond solution. Further, the specimens were polished by using a 50 nm colloidal silica suspension at a very low load to obtain the strain-free specimen surfaces. Plane parallelism of the specimens was maintained throughout the polishing.

An NTEGRA AFAM system supplied by M/s. NT-MDT Co., Zelenograd, Russia was used in the study. A stiff cantilever with a spring constant, k_c, of about 30 N/m and the first free resonance frequency f_0 of about 171 kHz was used in the study. The surface topography of the specimens was obtained in tapping mode to select an area with sufficient flatness for acquiring the contact-resonance spectra. A topographical variation is always observed for different phases upon mechanical/chemical-mechanical polishing of a sample due to difference in their mechanical/chemical properties. Even differences in the crystallographic orientation of the phase exhibit different topography upon polishing. In order to avoid excessive damage to the cantilever tip during contact scanning, an area with sufficient flatness was selected, where the maximum height variation for different phases was found to be less than 10 nm. An area of about 5 × 5 μm^2 was selected for the AFAM measurements. The AFAM data was acquired by using cantilevers with similar dimensions and stiffness values. A step of 50 nm was chosen and the contact resonance spectrum of the first flexural mode was acquired with a resolution of about 0.1 Hz in the range of 650–850 kHz for all the specimens heat-treated at different temperatures. In order to effectively obtain the contribution of local internal friction Q_{loc}^{-1} from the sample, the load of the cantilever onto the sample was chosen to be about 1200 nN for all the measurements. Caron et al. [2] have observed that a background damping in the material related to the global ultrasonic absorption is obtained at higher loads only. Hence, a slightly higher value of load was selected at which no noticeable wear of the tip and no slipping in the tip–sample contact were observed and, hence, uniform measurements throughout the scan were assured. The contact-resonance spectra were analyzed using software specifically developed in LabVIEW to obtain the maps of the indentation modulus and damping (i.e., local internal friction). The indentation modulus of the individual phases obtained by AFAM measurements was used to estimate the average modulus of the specimens, using the volume fractions of the phases present in the specimens. The volume fractions of the phases were estimated using JMatPro® [27,28] simulation software. The volume fractions obtained by JMatPro® were validated on one of the samples experimentally by X-ray diffraction (XRD) measurements, using an INEL make XRG3000 diffractometer operated at 40 kV and 30 mA with monochromatic Cu Kα_1 radiation. The XRD spectrum was recorded in the 2θ range of 10 to 100° using a curved position-sensitive (CPS) detector with a step size of 0.011°.

In order to identify various phases present in the specimen microstructure, an electron back-scatter diffraction (EBSD) study was performed using a Zeiss SUPRA 55 Gemini field emission gun (FEG) scanning electron microscope (SEM) at an accelerating voltage of 20 kV, an aperture of 120 µm, a working distance of 16 mm, a tilt angle of 70° and a specimen–detector distance of 178 mm. An indexing algorithm based on eight detected bands was utilized.

Results and Discussion

The amount of the α- and β-phases present at different heat-treatment temperatures for Ti-6Al-4V alloy, as obtained by the JMatPro® simulation, is shown in Figure 2. The volume fraction of the β-phase is very low (ca. 6.57%) at 923 K and it increases to 26% and 70.9% at 1123 K and 1223 K, respectively. The JMatPro® simulation indicates a β-transus temperature of 1275 K, above which only the β-phase is observed. This is in good agreement with the earlier reported experimental value of the β-transus temperature of 1268 K for the alloy [29].

Figure 3 shows the XRD spectrum for the specimen heat-treated at 923 K. The volume fraction of the β-phase obtained by using XRD is 6.61%, which is in excellent agreement with that obtained using JMatPro®.

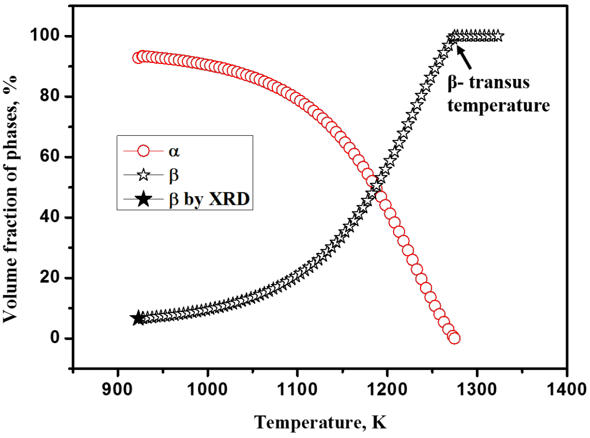

Figure 2: Variations in the volume fraction of α- and β-phases with the heat treatment temperature as obtained by the JMatPro® simulation software and XRD measurement.

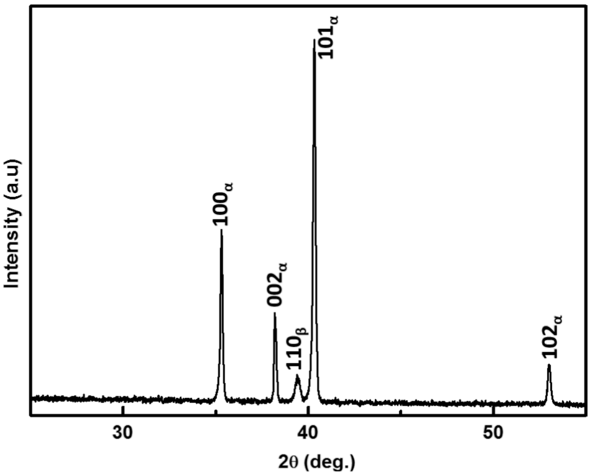

Figure 3: XRD spectrum obtained using the profile fitting method for Ti-6Al-4V sample heat-treated at 923 K for one hour, followed by water quenching.

Typical AFM topography images for the specimens heat-treated at 923, 1123 and 1223 K are shown in Figure 4a–c, respectively. The topography indicates the presence of two different phases in the specimens heat-treated at 923 and 1123 K. The increase in the size and volume fraction of the bright phase (with higher topography) can be clearly seen in the topography image of the specimen heat-treated (SHT) at 1123 K (Figure 4b), as compared to that for the SHT at 923 K (Figure 4a). Based on the volume fraction of phases, the brighter phase is identified as the β-phase. Based on the topography, three different phases can be observed in the SHT at 1223 K (Figure 4c). The topography line profile corresponding to the dotted line (in blue) shown in Figure 4c is given in Figure 4d. A maximum of 10 nm height variation is observed in

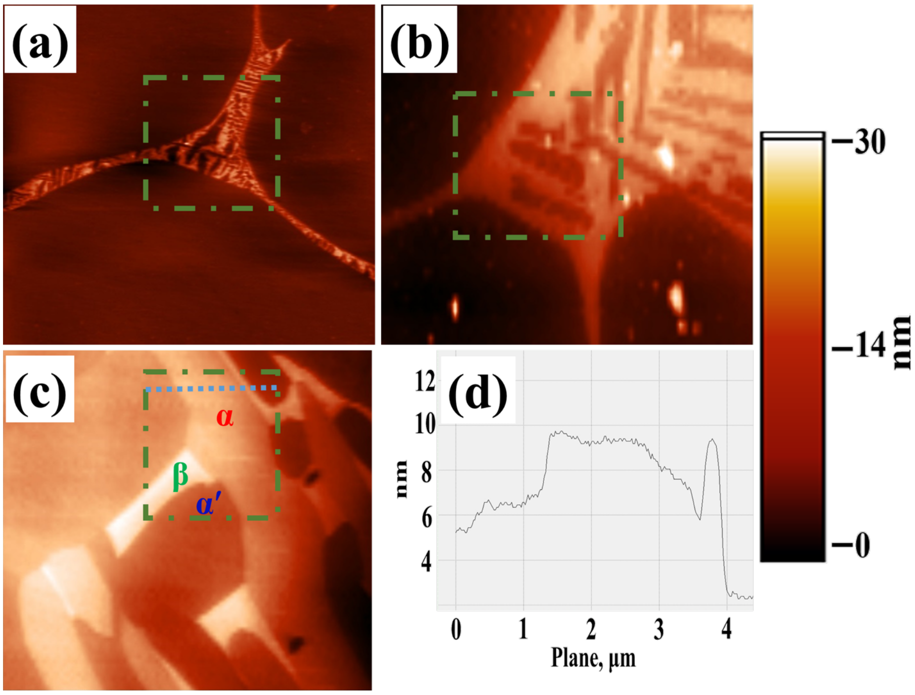

Figure 4: Topography of Ti-6Al-4V specimens heat-treated at (a) 923 K; (b) 1123 K; (c) 1223 K for one hour followed by water quenching and (d) topography line-profile corresponding to the dotted line marked in (c).

Figure 4d for the different phases. The surface roughness (S_{RMS}) is found to be less than 0.33 nm for the individual phases.

In order to unambiguously identify these phases, SEM and EBSD studies were carried out on this specimen. Figure 5a shows the topography image obtained by using a forward scattering detector (FSD) in the FEG-SEM. The topography image indicates the presence of three different phases viz., the matrix with the low topography, a lath-like phase with intermediate height and a bright phase at the boundary. The EBSD analysis indicates that both the matrix and the lath-like phase with intermediate height are of hexagonally closed package (HCP) structure, whereas, the phase at the boundary is of body-centered cubic (BCC) structure. This can clearly be seen in the composite image shown in Figure 5b, which consists of an inverse-pole-figure map along with the band contrast for the HCP phases and the BCC phase is shown in red. The matrix is identified as α′ martensite with HCP structure, which the high temperature β-phase in an α + β titanium alloy transforms to,

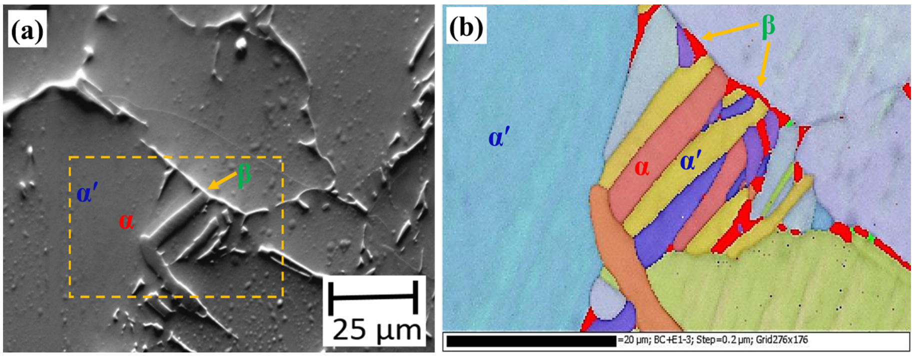

Figure 5: (a) Topography image and (b) a composite image showing typical microstructure in a Ti-6Al-4V specimen heat-treated at 1223 K for one hour followed by water quenching. The topography image is obtained by a forward scattering detector in a FEG-SEM. The composite image consists of an inverse-pole-figure map along with band contrast for the HCP (α and α′) phases and the BCC (β) phase is shown in red.

upon quenching from temperature above about 1123 K [29]. The presence of untransformed β-phase along with α′ matrix and α lath has also been reported by Pederson [30] in Ti-6Al-4V alloy heat-treated at 1223 K and followed by water quenching. With the help of the EBSD analysis, it becomes clear that the matrix in Figure 4c is α′ martensite and the two phases with intermediate and high topography are the α- and β-phases, respectively.

A map of the peak frequency in the contact-resonance spectra for the SHT at 1223 K is shown in Figure 6a. The presence of three phases with different contact-resonance frequencies can be clearly seen in Figure 6a. Figure 6b shows the typical contact-resonance spectra for the three phases. The α′-matrix phase exhibited an intermediate value of the contact-resonance frequency, whereas, the α lath and the retained β exhibit the highest and the lowest contact-resonance frequencies, respectively. This indicates that the α-phase has the highest modulus followed by the α′- and β-phases, respectively.

This is in agreement with the values reported on the basis of ultrasonic velocity measurements on bulk samples heat-treated at different temperatures in the range of 923 to 1323 K [31]. Table 1 and Table 2 summarize the elastic properties and ultrasonic attenuation values obtained in the bulk specimens heat-treated at 923, 1123, 1223 and 1323 K. The modulus was found to be the highest in the sample heat-treated at 923 K that has the maximum volume fraction of the α-phase. The attenuation was found to be highest in the sample heat-treated at 1223 K that has the maximum amount of β-phase. The SHT at 1323 K is comprised of a single-phase α′ microstructure. Hence, the isotropic indentation modulus of the α′-phase can be obtained by using the bulk E and ν values of the SHT at 1323 K. Kumar et al. [13] reported that the isotropic indentation modulus obtained with the bulk measurements does not vary much with the anisotropic modulus measured on different crystallographic planes. By using a similar approach, the isotropic indentation modulus of the α′-phase is used as a reference for obtaining the indentation modulus of the other phases in the present study. The M value for the α′-phase as determined by the ultrasonic velocity measurements is 127.8 GPa [31].

By using the software developed in LabVIEW® incorporating the cantilever dynamics model (Equations 1–3), the contact-stiffness map is obtained based on the contact-resonance frequencies shown in Figure 6a. After obtaining the k_r map, a small area in the *α′* region was selected as a reference to obtain the indentation modulus map of the SHT at 1223 K, as shown in

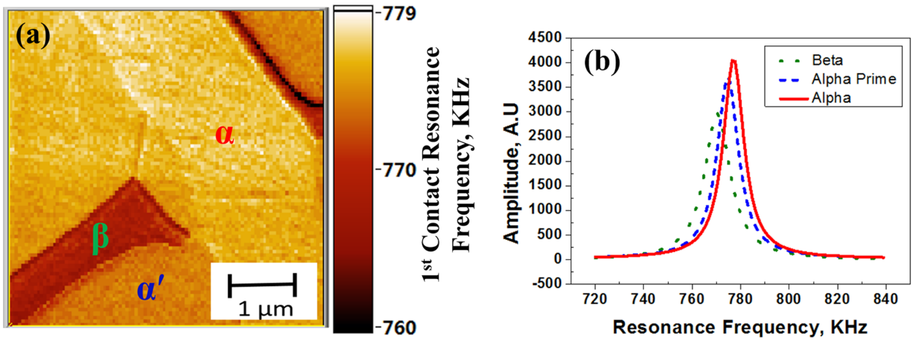

Figure 6: (a) First contact resonance frequency map for a Ti-6Al-4V specimen heat-treated at 1223 K for one hour, followed by water quenching and (b) the typical resonance spectra for the three different phases identified as α, β, and α′.

Table 1: Ultrasonic velocity measurements obtained from literature for Ti-6Al-4V bulk samples heat-treated at different temperatures.

temperature [K]	volume fraction (%) by JMatPro® simulation			ultrasonic data on bulk sample [23]			
	α	β	α′	E [GPa]	attenuation [dB/mm]	Poisson’s ratio ν	M_{BS} [GPa]
923	93.3	6.6	0	115.7	0.36	0.321	132.7
1123	74	26	0	111.5	0.42	0.326	130
1223	29	5[a]	66[a]	114	0.36	0.323	128.8
1323	0	0	100	114.5	0.38	0.323	127.8 (ref)

[a] The volume fraction of the retained β-phase given is approximate, based on the AFM and SEM microstructure. The volume fraction of the α′-phase is calculated based on the difference in the volume fraction of the β-phase estimated by the JMatPro® and the volume fraction of the retained β-phase. The values of the Poisson’s ratio are $\nu_\alpha = 0.32$ and $\nu_\beta = 0.33$.

Table 2: AFAM measurements obtained for the individual phases present in Ti-6Al-4V samples heat-treated at different temperatures.

temperature [K]	AFAM measurements						
	M_α [GPa]	M_β [GPa]	E_α [GPa]	E_β [GPa]	E_{BS} [GPa]	$(E''/E')_\alpha$	$(E''/E')_\beta$
923	133.5	120	119.7	106.9	119.1	0.013	0.028
1123	133.5	118.7	119.7	105.7	116.2	0.044	0.056
1223	133.5	117	119.7	104.2	115.4	0.019	0.028

Figure 7a. Statistical analysis was carried out on the data of Figure 7a to obtain the average (mode) values of M for α- (M_α) and β- (M_β) phases in the SHT at 1223 K, which are found to be 133.5 GPa and 117 GPa, respectively. The three phases are labeled in the figure for better understanding. The modulus of the α-phase is reported to be less influenced by the composi-

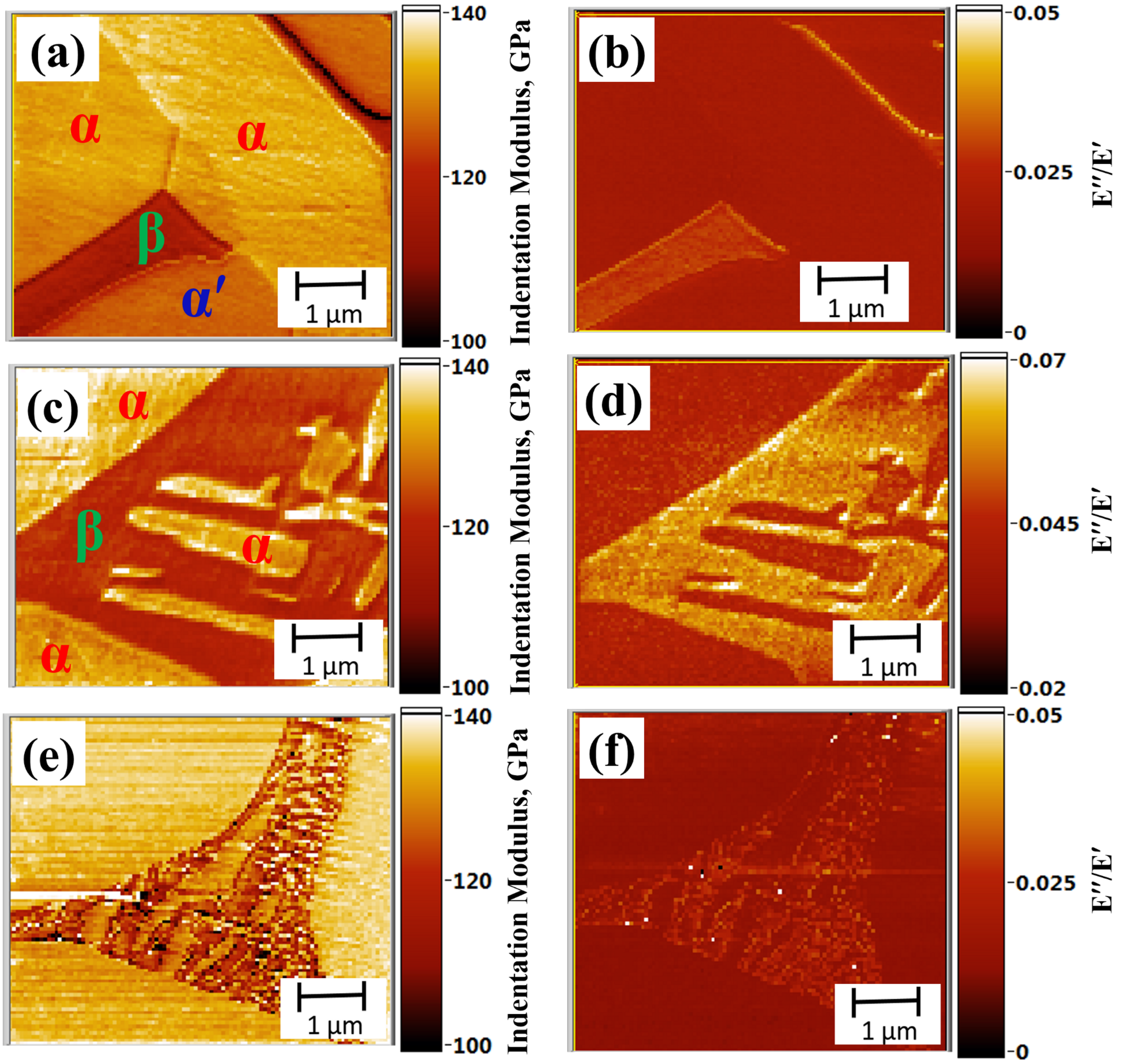

Figure 7: Modulus and damping maps of the Ti-6Al-4V specimen's heat-treated at (a and b) 1223 K, (c and d) 1123 K, and (e and f) 923 K for 1 h, followed by water quenching, respectively.

tional variations [31], hence the M_α obtained for the 1223 K sample is used as a reference to get the average M_β in the other two SHT at 1123 K and 923 K.

Figure 7c shows the modulus map for the SHT at 1123 K. Using the M_α obtained for the SHT at 1223 K as a reference, the average value for M_β was obtained as 118.7 GPa. Figure 7e shows the modulus map for the SHT at 923 K. The average value for M_β is obtained as 120 GPa. The relative modulus values measured using AFAM is found to be similar for α- and β-phases in the specimens heat-treated at different temperatures. The Young's modulus of the individual phases can be approximated by using M values for the respective phases and Equation 6. Poisson's ratio values as a function of heat-treatment temperature for Ti-6Al-4V samples are discussed in detail elsewhere [31]. The Poisson's ratios used for the calculations for the α and β phases are $\nu_\alpha = 0.32$ and $\nu_\beta = 0.33$, respectively. By knowing the E and volume fraction of each phase, the average E of the bulk sample can be calculated using the rule of mixture as given below [32]:

$$E_{\mathrm{BS}} = E_\alpha V_\alpha + E_\beta V_\beta + E_{\alpha'} V_{\alpha'} \qquad (9)$$

where V_α, V_β and $V_{\alpha'}$ are the volume fractions of α, β and α′ phases in the sample and E_{BS} is the average Young's modulus of the bulk sample.

Substituting the values for E_α and E_β, obtained by AFAM and V_α and V_β obtained by JMatPro® simulation for specimens heat-treated at 923, 1123 and 1223 K in Equation 9, the E_{BS} values are obtained as 119.1, 116.2 and 115.4 GPa, respectively. These values are compared with those obtained with the bulk ultrasonic velocity measurements averaging over the whole sample, in Table 1. The maximum deviation in the E_{BS} values calculated using the AFAM is 5% compared to those calculated by using ultrasonic velocity measurements. This variation is essentially attributed to the effect of crystallographic orientation on the modulus, which is not considered in the present study.

In Figure 6b, the width of the contact-resonance spectrum is larger by about 30% for the β-phase than for the α′- and α-phases, indicating a higher damping in the β-phase for the sample heat-treated at 1223 K. Therefore, along with the modulus, damping was also mapped simultaneously for all three heat-treated specimens. Equations 1–3 and Equation 8 have been used for calculation of the damping in different samples.

Figure 7 (panels b, d and f) shows the damping maps for specimens heat-treated at 923, 1123 and 1223 K. For all the three heat-treated samples, the β-phase exhibits the highest damping followed by α′ and α. The obtained results for damping are in line with the ultrasonic attenuation measurements carried out on bulk Ti-6Al-4V samples heat-treated at 923, 1123 and 1223 K, as shown in Table 1 [31]. The SHT at 1123 K having the highest amount of β-phase exhibited the maximum attenuation. Even though the absolute values of the damping are not the same for the phases in the three specimens, the relative damping values for of the α- and the β-phase are similar in all three samples. The higher absolute value of damping in the SHT at 1123 K is attributed to the larger tip radius, as is evident from the contact-resonance frequency values. The first contact-resonance frequency values for the SHT at 1123 K was found to be in the range of 821–837 kHz, as compared to 710–750 kHz for the SHT at 923 K and 760–780 kHz for the SHT at 1223 K. The contact-radius values calculated by using Equation 4 for the measurements made on the SHT at 923, 1123 and 1223 K are found to be 27.4, 28.1 and 63.8 nm, respectively. The study demonstrates the uniqueness of AFAM for modulus and damping mapping in multiphase structural alloys with a lateral spatial resolution of better than 50 nm.

Conclusion

Simultaneous mapping of elastic and damping properties in a multiphase structural alloy by using an AFM technique is reported for the first time in the present study, in which a cantilever dynamics model is used that also considers damping. The β-phase exhibited minimum modulus and maximum damping followed by α′- and α-phases in all three heat-treated Ti-6Al-4V alloy samples. The relative modulus values measured by using AFAM are found to be similar for α- and β-phases in the specimens heat-treated at different temperatures. The study also demonstrates that the micro-scale elastic properties measured by using AFAM can also be used for obtaining the average elastic properties of the bulk samples.

Acknowledgements

The authors are grateful for the support of the German Science Foundation within the "Sonderforschungsbereich SFB 1073" and a grant (DLR 01DQ12033) within the framework of Indo-German collaboration supported by the Federal Ministry of Education and Research (BMBF) via the International Office of the DLR, Cologne. A.K. thanks the Board of Research in Nuclear Sciences (BRNS) for financial support in the form of a DAE-SRC Outstanding Researcher Award and M.K.P. thanks IGCAR for providing fellowship to carry out this research work. Authors are thankful to Dr. (Mrs.) Vani Shankar for her help in the EBSD study.

References

1. Kumar, A.; Rabe, U.; Arnold, W. *Jpn. J. Appl. Phys.* **2008,** *47,* 6077–6080. doi:10.1143/JJAP.47.6077

2. Caron, A.; Arnold, W. *Acta Mater.* **2009,** *57,* 4353–4363. doi:10.1016/j.actamat.2009.05.030
3. Yamanaka, K.; Nakano, S. *Jpn. J. Appl. Phys.* **1996,** *35,* 3787–3792. doi:10.1143/JJAP.35.3787
4. Rabe, U. Atomic Force Acoustic Microscopy. In *Applied Scanning Probe Methods II;* Bhushan, B.; Fuchs, H., Eds.; Springer: Heidelberg, Germany, 2006; p 37.
And references contained therein.
5. Hurley, D. Contact Resonance Force Microscopy Techniques for Nanomechanical Measurements. In *Applied Scanning Probe Methods XI;* Bhushan, B.; Fuchs, H., Eds.; Springer: Berlin, Heidelberg, Germany, 2009; pp 97–138.
6. Ogi, H.; Niho, H.; Hirao, M. *Appl. Phys. Lett.* **2006,** *88,* 141110. doi:10.1063/1.2194479
7. Yamanaka, K.; Maruyama, Y.; Tsuji, T.; Nakamoto, K. *Appl. Phys. Lett.* **2001,** *78,* 1939–1942. doi:10.1063/1.1357540
8. Yuya, P. A.; Hurley, D. C.; Turner, J. A. *J. Appl. Phys.* **2008,** *104,* 074916. doi:10.1063/1.2996259
9. Luo, Y.; Büchsenschütz-Göbeler, M.; Arnold, W.; Samwer, K. *New J. Phys.* **2014,** *16,* 013034. doi:10.1088/1367-2630/16/1/013034
10. Kos, A. B.; Killgore, J. P.; Hurley, D. C. *Meas. Sci. Technol.* **2014,** *25,* 025405. doi:10.1088/0957-0233/25/2/025405
11. Killgore, J. P.; Yablon, D. G.; Tsou, A. H.; Gannepalli, A.; Yuya, P. A.; Turner, J. A.; Proksch, R.; Hurley, D. C. *Langmuir* **2011,** *27,* 13983–13987. doi:10.1021/la203434w
12. Phani, M. K.; Kumar, A.; Jayakumar, T. *Philos. Mag. Lett.* **2014,** *94,* 395–403. doi:10.1080/09500839.2014.920538
13. Kumar, A.; Rabe, U.; Hirsekorn, S.; Arnold, W. *Appl. Phys. Lett.* **2008,** *92,* 183106. doi:10.1063/1.2919730
14. Wagner, H.; Bedorf, D.; Küchemann, S.; Schwabe, M.; Zhang, B.; Arnold, W.; Samwer, K. *Nat. Mater.* **2011,** *10,* 439–442. doi:10.1038/nmat3024
15. Dulebo, A.; Preiner, J.; Kienberger, F.; Kada, G.; Rankl, C.; Chtcheglova, L.; Lamprecht, C.; Kaftan, D.; Hinterdorfer, P. *Ultramicroscopy* **2009,** *109,* 1056–1060. doi:10.1016/j.ultramic.2009.03.020
16. Dong, M.; Husale, S.; Sahin, O. *Nat. Nanotechnol.* **2009,** *4,* 514–517. doi:10.1038/nnano.2009.156
17. Garcia, R.; Proksch, R. *Eur. Polym. J.* **2013,** *49,* 1897–1906. doi:10.1016/j.eurpolymj.2013.03.037
18. Lozano, J. R.; Garcia, R. *Phys. Rev. Lett.* **2008,** *100,* 076102. doi:10.1103/PhysRevLett.100.076102
19. Wadu-Mesthrige, K.; Amro, N. A.; Garno, J. C.; Cruchon-Dupeyrat, S.; Liu, G.-Y. *Appl. Surf. Sci.* **2001,** *175–176,* 391–398. doi:10.1016/S0169-4332(01)00131-3
20. Bandyopadhyay, A.; Espana, F.; Balla, V. K.; Bose, S.; Ohgami, Y.; Davies, N. M. *Acta Biomater.* **2010,** *6,* 1640–1648. doi:10.1016/j.actbio.2009.11.011
21. Elmer, J. W.; Palmer, T. A.; Babu, S. S.; Zhang, W.; DebRoy, T. *J. Appl. Phys.* **2004,** *95,* 8327–8339. doi:10.1063/1.1737476
22. Homporova, P.; Poletti, C.; Stockinger, M.; Warchomicka, F. Dynamic phase evolution in titanium alloy Ti-6Al-4V. In *Proc. 12th World Conference on Titanium,* Beijing, China; Zhou, L., Ed.; 2011; pp 19–42.
23. Rabe, U.; Kopycinska-Müller, M.; Hirsekorn, S. Atomic Force Acoustic Microscopy. In *Acoustic Scanning Probe Microscopy;* Marinello, F.; Passeri, D.; Savio, E., Eds.; Springer: Berlin, Heidelberg, Germany, 2013; pp 123–153. doi:10.1007/978-3-642-27494-7_5
24. Wagner, H.; Büchsenschütz-Göbeler, M.; Luo, Y.; Kumar, A.; Arnold, W.; Samwer, K. *J. Appl. Phys.* **2014,** *115,* 134307. doi:10.1063/1.4874264
25. Yuya, P. A.; Hurley, D. C.; Turner, J. A. *J. Appl. Phys.* **2011,** *109,* 113528. doi:10.1063/1.3592966
26. Johnson, K. L. *Contact Mechanics;* Cambridge University Press: Cambridge, UK, 1985. doi:10.1017/CBO9781139171731
27. Guo, Z.; Saunders, N.; Schillé, J. P.; Miodownik, A. P. *Mater. Sci. Eng., A* **2009,** *499,* 7–13. doi:10.1016/j.msea.2007.09.097
28. Saunders, N.; Guo, U. K. Z.; Li, X.; Miodownik, A. P.; Schillé, J.-P. *JOM* **2003,** *55,* 60–65. doi:10.1007/s11837-003-0013-2
29. Kumar, A.; Jayakumar, T.; Raj, B.; Banerjee, D. *Philos. Mag.* **2008,** *88,* 327–338. doi:10.1080/14786430701837015
30. Pederson, R. Microstructure and Phase transformation of Ti-6Al-4V. Licentiate Thesis, Lulea University of Technology, Sweden, 2002.
31. Kumar, A. Correlation of Microstructure and Mechanical Properties with Ultrasonic Parameters in metallic materials. Ph.D. Thesis, Indian Institute of Technology, Kharagpur, India, 2005.
32. Tilley, R. J. D. *Understanding Solids: The Science of Materials,* 2nd ed.; Wiley: Hoboken, NJ, USA, 2013; p 319.

License and Terms

The definitive version of this article is the electronic one which can be found at:
doi:10.3762/bjnano.6.79

BEILSTEIN JOURNAL OF NANOTECHNOLOGY

Capillary and van der Waals interactions on CaF_2 crystals from amplitude modulation AFM force reconstruction profiles under ambient conditions

Annalisa Calò[1], Oriol Vidal Robles[1], Sergio Santos[2] and Albert Verdaguer*[1,3]

Full Research Paper

Open Access

Address:
[1]Institut Català de Nanociència i Nanotecnologia (ICN2), Campus UAB, Bellaterra, Barcelona, 08193, Spain, [2]Departament de Disseny i Programació de Sistemes Electrònics, Universitat Politècnica de Catalunya (UPC), Av. Bases 61, Manresa, Barcelona, 08242, Spain and [3]Consejo Superior de Investigaciones Científicas (CSIC), ICN2 Building, Bellaterra, Barcelona, 08193, Spain

Email:
Albert Verdaguer* - averdaguer@cin2.es

* Corresponding author

Keywords:
amplitude modulation (AM) AFM; dynamic capillary interactions; dissipative nanoscale interactions; CaF_2 wetting; force reconstruction

Beilstein J. Nanotechnol. **2015,** *6,* 809–819.
doi:10.3762/bjnano.6.84

Received: 29 September 2014
Accepted: 26 February 2015
Published: 25 March 2015

This article is part of the Thematic Series "Advanced atomic force microscopy techniques III".

Guest Editor: T. Glatzel

Abstract

There has been much interest in the past two decades to produce experimental force profiles characteristic of the interaction between nanoscale objects or a nanoscale object and a plane. Arguably, the advent of the atomic force microscope AFM was instrumental in driving such efforts because, in principle, force profiles could be recovered directly. Nevertheless, it has taken years before techniques have developed enough as to recover the attractive part of the force with relatively low noise and without missing information on critical ranges, particularly under ambient conditions where capillary interactions are believed to dominate. Thus a systematic study of the different profiles that may arise in such situations is still lacking. Here we employ the surfaces of CaF_2, on which nanoscale water films form, to report on the range and force profiles that might originate by dynamic capillary interactions occurring between an AFM tip and nanoscale water patches. Three types of force profiles were observed under ambient conditions. One in which the force decay resembles the well-known inverse-square law typical of van der Waals interactions during the first 0.5–1 nm of decay, a second one in which the force decays almost linearly, in relatively good agreement with capillary force predicted by the constant chemical potential approximation, and a third one in which the attractive force is almost constant, i.e., forms a plateau, up to 3–4 nm above the surface when the formation of a capillary neck dominates the tip–sample interaction.

Introduction

The study of the forces and energies released when a nanometric tip and a surface are progressively brought into contact has driven much of the recent investigation in atomic force microscopy (AFM) and has allowed for the mapping of materials properties while scanning [1-3] besides finding optimal imaging conditions [4,5]. Furthermore, understanding and distinguishing among relevant interactions in a broad range of materials at the nanoscale and in different environmental conditions is important from the fundamental point of view [6,7]. This is particularly true when working in air under ambient conditions, where the presence of thin layers of water is ubiquitous even on highly hydrophobic surfaces [8-10] and specific interactions (hydration, capillary forces) [11] need to be accounted for, which can be effective at relatively large tip–sample distances [12,13] and can exhibit unexpected distance dependencies [14].

Contact AFM measurements, in which the force is determined from the static deflection of the cantilever during approach [15], can readily record the tip–sample interaction force and have been used extensively to characterize a variety of nanoscale materials, from soft biomaterials (vesicles, viruses) [16,17], to organic thin films [18-21] and self-assembled monolayers [22] in liquid and in air, especially at those short separations where breakthrough events and sample mechanical deformations occur. However, in such experiments, the jump-to-contact instability [6,7] screens even strong (van der Waals, capillary) [13,23] interactions and actually prevented the experimental access to that region in force curves where attractive forces dominate. This instability has been especially observed when working in air and when soft cantilevers were employed to increase the sensitivity [6,7,15,24].

Dynamic modes proved to overcome the limitations of contact measurements in detecting attractive forces [11,25-27]. In these modes the cantilever is mechanically driven at a fixed oscillation frequency and interaction forces can be determined through analytical descriptions [28] or numerical methods [29] from minute changes in the amplitude [30] or in the frequency [6,7] of the oscillation when the tip–sample separation distance is changed. Furthermore, the advantage of performing dynamic AFM measurements, as for example amplitude modulation AM-AFM measurements, is that experimental observables, i.e., the phase lag of the cantilever relative to the driving force, can be directly related to the energy dissipated in the tip–sample interaction [31-33]. Identifying and separating individual contributions to the net energy dissipation by their physical origin and/or distance-dependence [34] has been the object of recent efforts in the direction of performing quantitative measurements with the AFM [35,36]. For example, Gadelrab and coauthors showed that the difference in the phase signal compared to a purely conservative attractive interaction ($\Delta\Phi$) can be used to distinguish between dissipative processes (hysteresis, viscosity) occurring in non-contact [37].

In this work, we used the Sader–Jarvis–Katan method [38,39] to reconstruct force vs minimum distance of approach (F_{ts} vs d_{min}) curves [24] from amplitude and phase distance (APD) curves collected on CaF_2 crystals containing water patches on their surface. We then compared the obtained profiles with those observed under low humidity conditions, i.e., when water is not present on the crystals. The Sader–Jarvis–Katan method has been recently applied to reconstruct the force on mica and graphite samples and changes in the shape of the resulting profiles were studied under different environmental conditions. An evolution in the force curves was observed keeping these surfaces at high humidity levels for long times [9,10]. At high humidity and long times of exposure plateau-like features where force was approximately constant for 1–2 nm before contact were observed. This kind of force profile, approximating a square well [14], has been already proposed to explain, from the phenomenological point of view, typical APD curves observed in dynamic AFM and interpreted as the result of dynamic capillary interactions. In the experiments reported on graphite additional spectroscopic IR measurements were performed [9,10] to exclude that the observed change in force profiles could depend on chemical contamination or aging of the sample. For example, carbonates could be present on the surface due to the exposure to a set of environmental conditions for prolonged times. Although IR measurements seemed to prove an increase in the intensity of the peaks related to water with time, in the AM-AFM experiments water was not visualized on the surface, making it impossible to distinguish between dry, wet or contaminated regions of the sample or to have an estimation of the thickness of the water layer adsorbed on the surface.

In the case of CaF_2, well-defined water patches on the crystals surface can be induced by controlling the environmental humidity [40], which are recognizable through AM-AFM images [41,42]. Thus, direct correlations between the reconstructed force profiles and topographical data are possible in situ and the evolution of force curves during the patch formation can be followed in short time experiments, thus limiting sample contamination. In these crystals we unambiguously identified fingerprints of capillary interactions, i.e., their onset and distance dependencies, from force curves on top of the water patches and from the simultaneous observation of both the corresponding dissipated energy, calculated according to the Cleveland equation [31], and the $\Delta\Phi$ vs distance evolution [27]. Our results indicate that standard expressions for capillary forces based on a constant chemical potential can also be a valuable tool to predict the experimental phenomena observed in dynamic AFM [14].

Results

Figure 1a and Figure 1b show AFM images of the surface of a CaF_2 crystal before (a) and after (b) the formation of water patches has been induced (see Experimental section). In the

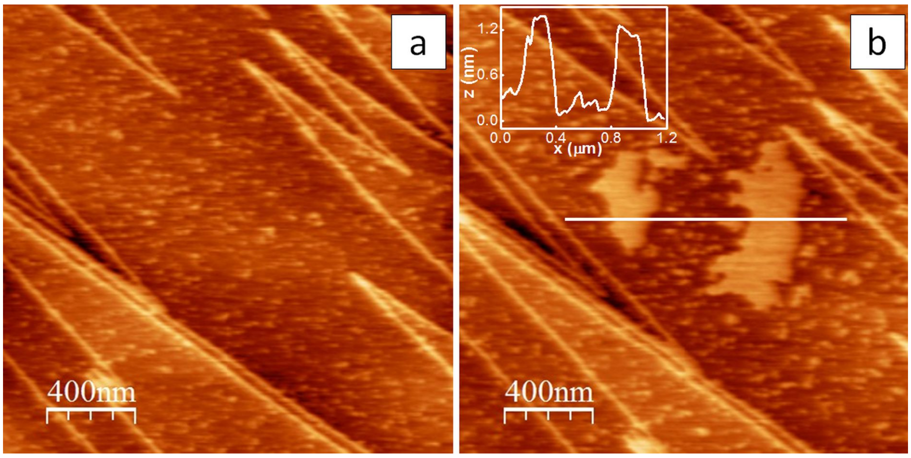

Figure 1: (a, b) AM-AFM images of a CaF_2 crystal taken immediately after cleavage (a) and after a water patch is formed on the crystal surface (b). Z_{scale} is 3 nm for both images. (b, Inset). Topographic profile corresponding to the white line in the image in (b).

image in Figure 1a a micrometer-sized terrace is visible, which is delimited by triangular (V-shaped) steps. These features are characteristic of freshly cleaved CaF_2 (111) surfaces, for which the shape of the steps (triangular or long parallel) depends on the cleavage direction [40]. Water is already present on top of the crystal surface after cleavage and accumulates in small drops about 1 nm thick, as inferred from the topographic profile of the AFM image in Figure 1a. At ambient temperature and RH (RH ca. 40%) water accumulates at the flat terraces on the crystal surface forming rounded islands [40] (see Figure 1b and Experimental section) over a time scale of few minutes. Under our experimental conditions, the islands exhibited a typical thickness of 1–1.5 nm (see the inset of Figure 1b) that did not change during experiments, i.e., by repeatedly scanning or collecting APD curves on the same area [41].

In Figure 2a and Figure 2b typical F_{ts} vs d_{min} curves are reported, which have been reconstructed according to Equation 2 (see Experimental section) from APD curves collected respectively in the middle of the terrace in Figure 1a and on top of the bigger water patch in Figure 1b. Raw and smooth data are respectively indicated as solid circles in grey and as continuous lines in blue. Curves such as the one shown in Figure 2a exhibit an approximately linear decay in the force, starting at relatively large tip–sample distances ≥2 nm and terminating at the contact with the hard CaF_2 surface. Curves such as the one shown in Figure 2b exhibit an abrupt jump in the long range, followed by an almost constant plateau, which spans nearly 4 nm of vertical distance. Then F_{ts} increases very rapidly with d_{min} and the force profile is similar to that observed at distances past the minima in force in Figure 2a. Here mechanical contact occurs and repulsive forces dominate the tip–sample interaction [27]. We set d_{min} = 0 by eye at the point where F_{ts} changes its slope and starts to increase rapidly, corresponding to the beginning of the mechanical contact between the tip and the surface.

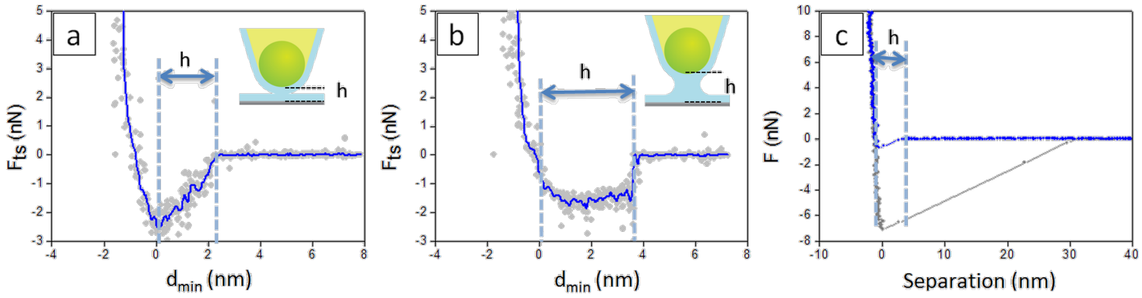

Figure 2: (a,b) Reconstructed force curves on top of the terrace in Figure 1a (a) and on top of the bigger water patch in Figure 1b (b); free amplitude of tip oscillation: A_0 = 23 nm. Raw and smooth data are, respectively, indicated as solid circles in grey and as continuous lines in blue. (c) *F* vs separation curves acquired in contact mode on a wet CaF_2 crystal. The extension and retraction paths are indicated, respectively, in blue and in grey only in (c).

We found that the distance from the decay of F_{ts} in the long range to $d_{min} = 0$ is 2.33 ± 0.17 nm for curves like the one shown in Figure 2a and 3.66 ± 0.20 nm for curves like the one shown in Figure 2b. A similar distance of 3.93 ± 0.40 nm from the jump-to-contact to the point of zero separation is found in the approach path of force curves collected in contact mode on CaF_2 crystals with adsorbed water layers on top of the surface (see Figure 2c) at ca. 40% RH.

Force profiles such as the ones in Figure 2a and Figure 2b indicate that capillary interactions, i.e., intermolecular attractive forces acting between water layers present on the surface of the tip and of the crystal, take place, which involve the formation and the rupture of a capillary bridge [3,14].

A linear decay of the force vs tip–sample distance such as that shown in Figure 2a is predicted in the limit of constant chemical potential or constant vapor pressure, according to which, when the tip approaches the sample, water condensation can induce the formation of a nanometer-size water bridge [43-45]. Expressions for the capillary force (F_{CAP}) based on these assumptions (see Equation 10 in the Experimental section) have been employed in dynamic AFM, together with more complex derivations based on the limit of a constant meniscus volume [3,14]. The approximation that assumes a constant volume of the meniscus considers that water in the capillary bridge essentially derives from water layers already present at the surface of the tip and the sample, rather than from the condensation of ambient vapor due to tip proximity. The choice of the more realistic model in specific contexts should take into account the timescale of water condensation and the tapping frequency [43,44].

The force profile shown in Figure 2b resembles force evolutions employed in the context of dynamic AFM, in which the predominantly attractive component of the net force is relatively independent on the distance and covers a range of some nanometers above the surface [14]. In Equation 11 it has been assumed that when the capillary forms the force is constant and equal to the adhesion force (F_{AD}) (see Experimental section).

In this work, Equation 10 and 11 have been employed to reconstruct force curves according to the Sader–Jarvis–Katan formalism in numerical simulations (see Experimental section).

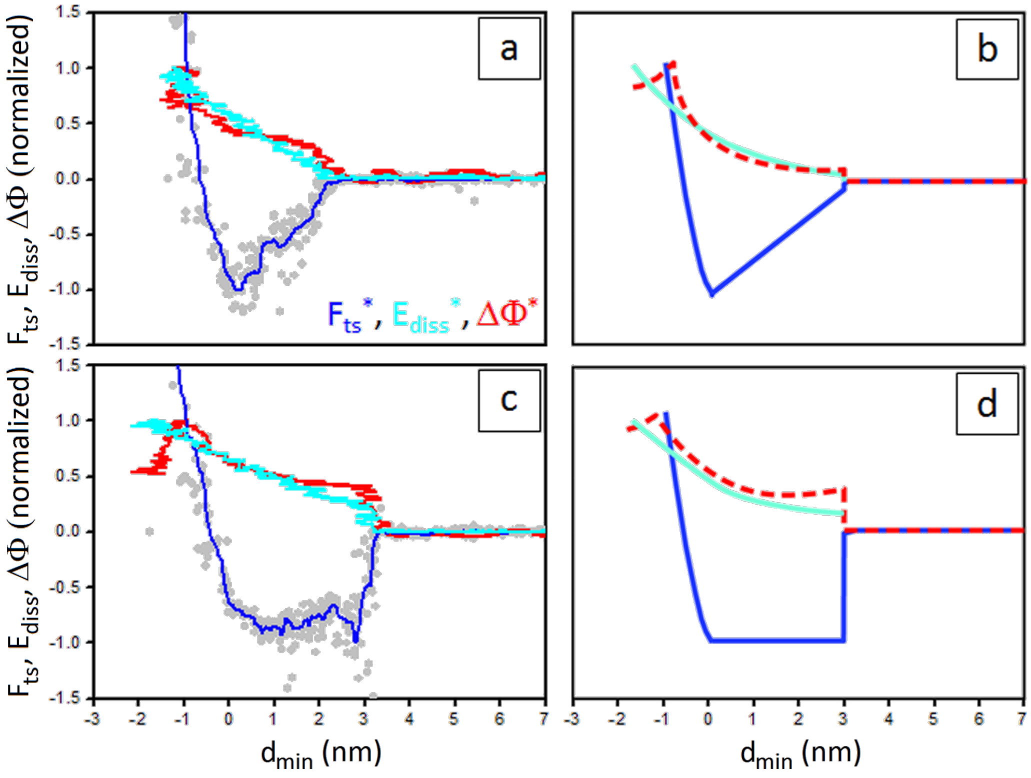

Figure 3: (a,c) Experimental normalized F_{ts}, E_{diss} and ΔΦ curves vs d_{min} collected on a CaF_2 sample containing water droplets (a) and on a water patch on top of the CaF_2 crystal (c). F_{AD} = 2.8 nN, E_{max} = 82 eV, $\Delta\Phi_{max}$ = 11.0° in (a) and F_{AD} = 2.0 nN, E_{max} = 114 eV, $\Delta\Phi_{max}$ = 13.9° in (c) (see main text). A_0 in (a) and (c) is 23 nm. (b,d) Simulated normalized F_{ts}, E_{diss} and ΔΦ curves in which the capillary force is expressed by Equation 10 (b) and Equation 11 (d). The forces and parameters employed in the simulation are described in the Experimental section. F_{ts}^*, E_{diss}^* and $\Delta\Phi^*$ are respectively indicated in blue, cyan and red.

The results of the simulations are shown in Figure 3, in which simulated F_{ts} curves (Figure 3b and Figure 3d) are compared with the experimental curves (Figure 3a and Figure 3c).

Forces such as those in Equation 10 and Equation 11 suppose a d_{on}/d_{off} mechanism. They act at a distance $d < d_{on}$ on tip approach and at $d < d_{off}$ on tip retraction, with $d_{off} \geq d_{on}$ [14]. The difference between these two distances leads to hysteresis in the long range. That is, as the tip approaches the sample a capillary bridge forms at $d = d_{on}$, which ruptures on tip retraction at $d = d_{off}$. If the distances of formation and rupture of the capillary bridge do not coincide, i.e., if $d_{off} > d_{on}$, hysteresis occurs and energy is dissipated in the interaction. If $d_{off} = d_{on}$ there is no hysteresis and the interaction is conservative [14].

In the reconstructed force curve of Figure 2a a step-like discontinuity that could be associated with the formation of a capillary bridge is not distinguishable. Instead, a slow decay is observed in the force at a distance, 2.33 nm, that approximately matches the sum of the height of the absorbed water droplets on top of hydrated CaF_2 and the expected thickness of the water layer on top of the tip (1 nm at room temperature, RH ca. 40% and in the absence of contamination) [46]. This distance indicates that water meniscus forms upon geometrical contact of the absorbed water layers on top of the tip and the crystal (see the sketch in Figure 2a) or that capillary condensation due to tip–sample proximity or other instabilities (for example, van der Waals interactions) can be considered negligible in this case [45]. Alternatively, the measured distance could point out that water layers on the tip and the sample simply overlap on approach, i.e., a capillary neck does not form at all in this case, and the decaying region in the force marks the tip penetration into confined water, a scenario that seems also plausible in dynamic AFM [14].

When a continuous water patch is present on top of the CaF_2 crystal, a linear increase in the attractive force was still observed for some reconstructed force curves but a different feature appeared regularly. In most of the force curves an abrupt drop followed by a constant force plateau was observed (Figure 2b), similarly to what reported for graphite exposed to high humidity for long times [9]. The abrupt drop occurs at a distance of 3.66 nm that approximately corresponds to three times the thickness of the water islands as measured by AFM topography. This number is in impressive agreement with $d_{on} = 3h$, with h being the height of adsorbed water layers on the hydrated surfaces of the tip and the sample (here $h_{tip} \approx h_{sample}$) and it is expected when instabilities due to van der Waals attraction and/or capillary condensation take place under approach [14,44]. Interestingly, we found $d_{on} = 3h$ only when stable water patches were present on the surface, a condition that is obtained experimentally by leaving the ambient humidity spontaneously increase from 10% to the ambient value of 40% after sample preparation (see Experimental section). This increase of RH should reduce the free energy barrier for water nucleation, thus increasing the water condensation rate [3]. It is worth to point out that force vs distance evolutions changing from almost linear decays to abrupt jumps followed by a constant plateau have been shown in function of the increasing relative vapor pressure in Monte Carlo simulations of the interaction forces between nanoparticles [13] and between a rigid nanoparticle and a flat plate [47].

Finally notice that, due to the imaging conditions (see Experimental section), the apparent height of the water droplets/layers measured by AFM topography (Figure 1a and Figure 1b) should be equal or close to the true value as water perturbation due to mechanical contact is avoided [41,42].

Discussion

The different dynamic interactions in the two situations depicted in Figure 2a and Figure 2b is corroborated by the analysis of the normalized dissipated energy and phase difference evolutions vs d_{min} in the long range (see also Equation 4 and Equation 5 of the Experimental section). Here, the asterisk indicates normalization, $E_{diss}^* = E_{diss}/E_{max}$ and $\Delta\Phi^* = \Delta\Phi/\Delta\Phi_{max}$, with E_{max} and $\Delta\Phi_{max}$ corresponding to the maxima in the approach curve [27]. This is shown in Figure 3, in which the reported force curves are also normalized, i.e., F_{ts} is divided by the minimum force F_{AD}.

The simulated curves in Figure 3b and Figure 3d reproduce very well the experimental observations Figure 3a and Figure 3c. When a long range hysteretic force with a d_{on}/d_{off} mechanism such as the one described in Equation 10 is activated in the simulation (here $d_{on} = 3$ nm and $d_{off} = 3.3$ nm), a small step-like discontinuity is observed at $d = d_{on}$ in the F_{ts}^*, E_{diss}^* and $\Delta\Phi^*$ signals (see respectively the blue, the cyan and the dashed red lines in Figure 3b). This effect becomes more pronounced when a capillary force such as the one described in Equation 11 is employed (see the blue, cyan and dashed red lines in Figure 3d, here being $d_{on} = 3$ nm and $d_{off} = 5$ nm) [14]. The jump in E_{diss} should correspond to the difference between the area of the approach and retraction force curves used in the simulation [27].

Notice that the force reconstruction process according to the Sader–Jarvis–Katan formalism recovers the conservative tip–sample force and fails to record events that occur at distances larger than d_{on} [27]. Thus, the footprints of a d_{on}/d_{off} dissipative mechanism result in the observed steps in the E_{diss}^* and $\Delta\Phi^*$ signals [27,37].

In experimental E_{diss} and $\Delta\Phi$ vs d_{min} curves collected on water patches on CaF_2 we measured, respectively, a step of (25.17 ± 4.82) eV and of (5.52 ± 0.70)° in correspondence of the abrupt drop in force (see Figure 3c). The value obtained for E_{diss} is in the expected range (20–50 eV) for the formation and the rupture of a capillary neck by means of tips with a radius of about 20 nm [3,45]. For curves collected under low humidity conditions (see Figure 3a) E_{diss} did not show any step-like discontinuity, while $\Delta\Phi$ exhibited a smaller step (3.78 ± 0.75)°. Both signals indicate that a lower amount of energy is dissipated in the process of forming and breaking the capillary bridge in this case or, equivalently, that the distances of formation and rupture of the capillary bridge are similar.

In Figure 4 normalized force curves reconstructed on CaF_2 crystals in dry conditions (Figure 4a), are compared with the results of numerical simulations (Figure 4b). Both panels include $E_{diss}{}^*$ and $\Delta\Phi^*$ signals. Force curves reconstructed from experiments in dry conditions, i.e. after incubating CaF_2 crystals for 30 minutes at 120 °C under N_2 flow before measurements, usually show a well-defined curvature around $d_{min} \sim 1$ nm from contact, resembling an inverse-square law decay (see the blue line in Figure 4a). At this distance, $E_{diss}{}^*$ and $\Delta\Phi^*$ start to increase continuously with diminishing d_{min} (see the lines in cyan and in red in Figure 4a). The simulated curves show a similar behavior (Figure 4b).

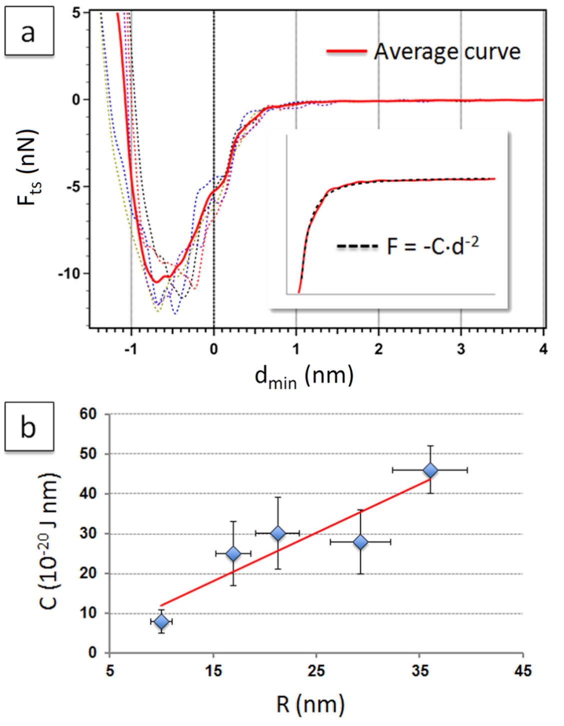

Figure 5: (a) Experimental (dotted lines) and average (red line) F_{ts} vs d_{min} curves collected on a CaF_2 crystal in the absence of water droplets and/or patches (A_0 = 80 nm). (a, Inset) Detail of the average curve in the region 0.2 nm < d_{min} < 1.8 nm and corresponding fit according to Equation 1. (b) Dependence of the fitting parameter C on the tip radius. A linear fit of the data is indicated in red.

In Figure 5a five different reconstructed F_{ts} vs d_{min} curves, represented as dotted lines, are shown which are taken in the same region of a dry CaF_2 crystal. The strong adhesion force ($F_{AD} \approx 10$ nN) depends on tip radius ($R \approx 40$ nm in this case, see Supporting Information File 1, Figure S2). Curves were aligned and averaged before fitting in order to minimize noise in the region of interest. Alignment of individual curves at $d_{min} = 0$ in the graph was established according to the distance at which discontinuities, in the form of changes of slope, were observed in the $E_{diss}{}^*$ and $\Delta\Phi^*$ signals vs d_{min}

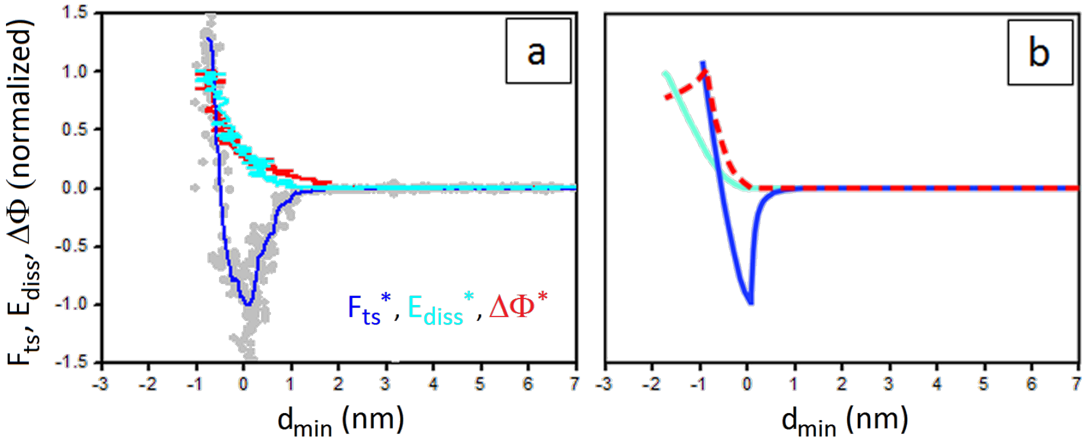

Figure 4: (a) Experimental $F_{ts}{}^*$, $E_{diss}{}^*$ and $\Delta\Phi^*$ curves vs d_{min} collected on a dry CaF_2 sample. F_{AD} = 11.4 nN, E_{max} = 418 eV, $\Delta\Phi_{max}$ = 12.3°; A_0 = 80 nm. (b) Simulated $F_{ts}{}^*$, $E_{diss}{}^*$ and $\Delta\Phi^*$ curves. For the forces and parameters employed in this case in the simulation see Experimental section. $F_{ts}{}^*$, $E_{diss}{}^*$ and $\Delta\Phi^*$ are indicated as blue, cyan and red lines, respectively.

(data not shown). As it can be observed in Figure 5a, the force around $d_{\mathrm{min}} = 0$ contains an inflection point, or a shoulder. For some curves this point was very clear, while for other curves we found its position quite arbitrary to determine in a range of ± 0.4 nm (see also Supporting Information File 1, Figure S2).

The average force curve, shown as a continuous line in red in Figure 5a, was fitted with a power law decay [48]:

$$F_{\mathrm{ts}} = C \cdot d_{\mathrm{min}}{}^{-n}, \text{ with } d_{\mathrm{min}} \geq 0\,, \tag{1}$$

leaving C and n as free parameters. In general, good fittings were obtained with $n = 2$, according to the χ^2 values (see the inset of Figure 5a). In Supporting Information File 1, Figure S3, the effect of a slight modification of the point at zero distance in the average curve on the fitting results is reported.

Obtained values for C from the fitting were stable in the same experiment and in different experiments with tips of similar radius. The fitting parameter C showed a strong dependency on the tip radius. In Figure 5b its average value is reported as a function of the tip radius R, determined from the onset of the smooth transition between the attractive and the repulsive regime (see Experimental section). By using this method, we estimated an error of ca. 20% for the tip radius [49]. The experimental C vs tip radius values adapt to a linear tendency with a coefficient of determination of $R^2 = 0.84$.

Based on these results, the observed force could be explained as a pure van der Waals attractive force operating between the tip and the CaF_2 crystal according to Equation 7 [27,50]. From the fitting of the linear tendency, and according to the simplified model of van der Waals interactions used in Equation 7, we estimated a value for the Hamaker constant of $(7.3 \pm 0.4) \cdot 10^{-20}$ J. Although this value has not to be taken as an accurate measurement of the Hamaker constant, it is in the range of the experimental and theoretical values reported in the literature for the CaF_2/SiO_2 pair [50].

Conclusion

Force vs distance curves were collected in both contact mode AFM and reconstructed from dynamic AM-AFM experiments on CaF_2 crystals exhibiting water patches on the surface. Results indicate that dissipative processes occur that involve the formation and the rupture of a capillary bridge. This can be inferred from the high hysteresis in the retracting portion of the static force curves, which spans an average distance of about 30 nm and exhibits an adhesion force of almost 6 nN compared to the approach path. But it is only from dynamic AFM experiments that interactions in the long (attractive) range can be truly probed and their effect on the energy stored by the cantilever during interaction with the sample accurately measured. In this work, two different interaction regimes have been identified in the force vs minimum tip–sample separation distance in the attractive range, in which (a) the force decreases almost linearly with separation or (b) exhibits an abrupt drop followed by a constant plateau. These regimes, which are indistinguishable in contact mode experiments, have been here related to the occurrence of dynamic capillary interactions during tip approach when relative humidity is allowed to spontaneously reach the ambient value of about 40% and homogeneous micrometer-sized water patches stabilize on top of the crystals surface. The dissipation induced by the capillary bridge formation is unambiguously identified in experimental E_{diss} and $\Delta\Phi$ curves and force profiles are compared with simulations in the long range, where the contact between water layers on top of the tip and the surface occurs. CaF_2 is demonstrated to be an ideal surface to probe the presence of these interactions, as it allows correlating directly force profiles and topographical data from AFM images and distinguishing force profiles in wet and in dry samples. Under dry conditions, van der Waals interactions seem to be the main contribution to the net tip–sample attractive force.

Experimental

Materials and Methods

All the experiments were performed using an Asylum Research AFM MFP-3D microscope equipped with a cooler/heater sample stage and operating in AM mode. APD curves (rate: 1.5 Hz) were collected on top of CaF_2 crystals at free amplitudes above the critical region of bi-stability [51,52], in order to achieve a smooth transition from the attractive to the repulsive regime as the amplitude is reduced to approximately 10% of its free value in a distance range of 15 nm. In this way, force profiles can be reconstructed in the whole range of distances, from long range interactions to tip–sample mechanical contact, without discontinuities [9,27]. Cantilevers with resonance frequency $f_0 \approx 300$ kHz, spring constant $k \approx 45$ N/m and nominal tip radius $R_0 \approx 10$ nm were employed (Nanosensors PPP-NCHR), for which avoiding discontinuity requires a free amplitude $A_0 \approx 23$ nm. The conversion of the amplitude in volts to amplitude in nm was determined by adjusting the tilt of d_{min} vs z_c curves in the repulsive region till a flat plateau was obtained [34]. The resonance frequency, spring constant and quality factor ($Q \approx 400$) of the cantilever were calibrated in situ at a distance smaller than 200 nm from the surface. The resonance frequency was found to decrease approximately 30 Hz with respect to the calibrated value at a few micrometers above the surface. The tip radius R was constantly monitored in situ as well, by checking that the onset of the smooth transition remained constant during experiments [49]. When free amplitudes $A_0(R)$ higher than 23 nm were employed, the tip radius was estimated to be $R = R_0 \cdot (A_0(R)/A_0)^{1.1}$, according to the experimental observations reported for the case of the critical amplitude A_c [49].

When force curves were collected in contact mode, cantilevers with resonance frequencies $f_0 \approx 15$ kHz, spring constant $k \approx 0.2$ N/m and $R \approx 10$ nm were used (Nanosensors PPP-CONTR). The cantilever spring constant was calibrated in situ using the thermal noise method implemented in the MFP-3D microscope and the deflection in volts converted to deflection in nanometers by means of sensitivity calculations on dry CaF_2 crystals.

Thin slices of CaF_2 single crystals a few millimeters thick (Crystal GmbH, Berlin, Germany) were cleaved parallel to the (111) plane [40] in ambient conditions and kept under low humidity conditions before experiments. A low humidity level (RH < 10%) was achieved by mounting the samples on a cooler/heater holder for environmental control in the MFP-3D microscope and circulating dry nitrogen for 30 min after positioning the AFM head on top of the sample. Then the nitrogen flow was suspended and the cantilevers k, f_0 and Q calibrated. AFM images of 2×2 µm^2 were recorded before collecting APD curves in order to verify that no extended water patches were present on the surface.

When dry samples were needed, the crystals were kept at 120 °C for 30 min under nitrogen flow before calibrating the cantilevers.

In general, repeatedly scanning and/or collecting curves at ambient relative humidity RH ≈ 40% results in the formation of mesoscopic water patches on the surface of the crystals. Once the patches containing region was imaged (2×2 µm^2) APD curves were collected on top of the patches. Images were collected at the lowest free amplitude ($A_0 = 9$ nm) and with the highest amplitude set-point, in order to minimize sample deformation while scanning [41,42].

APD curves were converted into force curves by numerically integrating the Sader–Jarvis–Katan equation [38,39] in Matlab [53]. In this formalism, the conservative force F_{ts} vs d_{min} is recovered from variations in the oscillation amplitude (A) and in the frequency shift (Ω) that occur by decreasing the cantilever-surface separation (z). This is shown in Equation 2 where d_{min} is related to z and to A as: $d_{min} \approx z - A$.

$$F_{ts}\left(d_{min}\right) = 2k \int_{u=d_{min}}^{u=\infty} \left[\left(1 + \frac{A^{1/2}}{8\sqrt{\pi\left(u - d_{min}\right)}}\right)\Omega(u) - \frac{A^{3/2}}{\sqrt{2\left(u - d_{min}\right)}} \frac{d\Omega(u)}{du}\right] du\,, \qquad (2)$$

The normalized frequency shift Ω is derived from observables in AM-AFM. When $f = f_0$, Equation 3 is obtained [38].

$$\Omega\left(d_{min}\right) = \left[1 + \frac{A_0}{QA}\cos\left(\Phi\left(d_{min}\right)\right)\right]^{1/2} - 1\,, \qquad (3)$$

where Φ is the phase lag relative to the drive force, and Q is the quality factor due to dissipation with the medium.

The experimental APD curves cover the approach and the retract part during one cycle, with a drift smaller than 0.5 nm (see Supporting Information File 1, Figure S1). Only approach curves for which the cantilever–sample separation is decreased were employed to reconstruct the tip–sample force [27]. In this work raw (solid circles in grey) and smooth (continuous line in blue) data are reported for the reconstructed force curves [53].

The dissipated energy (E_{diss}) and $\Delta\Phi$ were also calculated for each APD curve vs d_{min}. The energy dissipated per cycle was determined with the use of the expression derived by Cleveland et al. [31,32]:

$$E_{diss} = \frac{\pi k A_0 A}{Q}\left[\sin(\Phi) - \frac{A}{A_0}\right]. \qquad (4)$$

$\Delta\Phi$ was calculated by subtracting the phase lag relative to the drive force, i.e., the experimental observable Φ, from the conservative angle Φ_{cons} defined as:

$$\Phi_{cons} = \sin^{-1}\left(\frac{A}{A_0}\right). \qquad (5)$$

From Equation 5 it follows that if there is no energy dissipation, $\Delta\Phi = 0$.

Numerical integration method

The standard (single mode) equation of motion [27,51] of the cantilever has been implemented in the programming language C and solved with the use of a standard Euler algorithm,

$$m\frac{d^2z}{dt^2}+\frac{m\omega}{Q}\frac{dz}{dt}+kz=F_{\text{ts}}+F_{\text{D}}\ , \qquad (6)$$

where ω is the angular drive frequency, the effective mass is $m = k/\omega^2$, F_D is the driving force and F_{ts} is the net tip–sample force. Typically, the drive frequency is set equal to the natural frequency ω_0 since this leads to convenient simplifications. Furthermore, z is the position of the tip relative to its unperturbed equilibrium position.

The reconstruction of the conservative force and the determination of the energy dissipation have been carried out by implementing the expressions in Equation 2 and Equation 4 in Matlab [53]. The raw amplitude and phase data have been processed both when dealing with the experimental data and when dealing with the data from the numerical integration of the equation of motion with the same code implemented in Matlab. The expression in Equation 2 has been turned into a finite sum and numerically integrated in Matlab in both cases.

In the simulations three force profiles have been accounted for:

1) One where van der Waals (vdW) forces are present in the long range and repulsive forces are present in the short range. Long-range conservative vdW forces have been modeled, as it is customary in dynamic AFM theory [14,27,30,51], as:

$$F_{\text{vdW}}=-\frac{HR}{6d^2}\ , \qquad (7)$$

where H is the Hamaker constant.

Viscosity in the short range has been modeled with the Kelvin–Voigt model as [27,34,35]:

$$F_{\eta}=-\eta\left(R\delta\right)^{1/2}\dot{\delta}\ ;\text{with } d\le a_0\ , \qquad (8)$$

where η is the viscosity in Pascal·second, a_0 is an intermolecular distance [14,27] and δ is the tip–sample deformation, i.e., $\delta = a_0 - d$. In this work η = 50 Pa·s throughout. In the short range the standard Derjaguin–Muller–Toporov (DMT) model of contact mechanics [54] has been employed to account for short range repulsion:

$$F_{\text{DMT}}=-\frac{HR}{6a_0^2}+\frac{4}{3}E^*\sqrt{R\delta}^{\,3/2}\ ;\text{with } d\le a_0\ , \qquad (9)$$

where E^* is the effective Young's modulus that includes the elastic modulus of the tip and of the sample [14]. This profile is shown in Figure 4b.

2) The second profile corresponds to a linear decay in the long range force corresponding to the capillary interaction F_{CAP}. F_{CAP} is written as:

$$F_{\text{CAP}}=-2\pi\gamma RX\left(1-\frac{d}{d_{\text{off}}}\right);\text{with } d>a_0\ , \qquad (10)$$

where γ is the surface energy and X is the average contact coefficient [3,14]. Equations 7, 8 and 9 have also been included. The resulting force profile is shown in Figure 3b.

For distances $d < d_{\text{on}}$ hysteresis has been considered also and modeled simply as a difference in the Hamaker constant H during tip retraction relative to tip approach. In particular, $H_{\text{retraction}} = 1.5\cdot H_{\text{approach}}$. This term accounts for long-range dissipation in Figure 3b and could be identified with dissipation due to contact between the tip and the surface water layers. The relationship between γ and H is $H = 24\pi\gamma(a_0)^2$. For this profile d_{on} = 3 nm and d_{off} = 3.3 nm.

3) The third profile corresponds to a force curve displaying a plateau, such as the one shown in Figure 3c. In this case the van der Waals force in Equation 7 has been ignored, because it plays a minimal role as deduced by inspecting the experimental curves. Furthermore Equation 10 has been replaced by:

$$F_{CAP}=-4\pi\gamma R\ ;\text{with } a_0<d<d_{\text{on}}\ . \qquad (11)$$

This profile is shown in Figure 3d. In the simulations d_{on} = 3 nm and d_{off} = 5 nm. The force has been assumed to remain constant and equal to that in Equation 11 in the $d_{\text{on}}/d_{\text{off}}$ region.

The common parameters in the simulations throughout this work are: k = 40 N/m, f_0 = 300 kHz, Q = 450, A_0 = 25 nm, E_{tip} = 120 GPa, E_{sample} = 1 GPa, $H = 2.5 \times 10^{-20}$ J, R = 8 nm.

Supporting Information

Supporting Information File 1

APD curves, reconstructed force curves vs tip radius, effect of the choice of the "0" distance on the fitting parameters according to Equation 1.
[http://www.beilstein-journals.org/bjnano/content/supplementary/2190-4286-6-84-S1.pdf]

Acknowledgements

This work was supported by the Ministerio de Economía y Competitividad (MINECO), Spain, through project MAT2012-38319-C02-01. ICN2 acknowledges support from the Severo Ochoa Program (MINECO, Grant SEV-2013-0295).

References

1. García, R.; Magerle, R.; Perez, R. *Nat. Mater.* **2007,** *6,* 405–411. doi:10.1038/nmat1925
2. Herruzo, E. T.; Perrino, A. P.; Garcia, R. *Nat. Commun.* **2014,** *5,* No. 3126. doi:10.1038/ncomms4126
3. Sahagún, E.; García-Mochales, P.; Sacha, G. M.; Sáenz, J. J. *Phys. Rev. Lett.* **2007,** *98,* 176106. doi:10.1103/PhysRevLett.98.176106
4. Santos, S.; Barcons, V.; Font, J.; Thomson, N. H. *Nanotechnology* **2010,** *21,* 225710. doi:10.1088/0957-4484/21/22/225710
5. Santos, S.; Barcons, V.; Font, J.; Thomson, N. H. *J. Phys. D: Appl. Phys.* **2010,** *43,* 275401. doi:10.1088/0022-3727/43/27/275401
6. Gotsmann, B.; Seidel, C.; Anczykowski, B.; Fuchs, H. *Phys. Rev. B* **1999,** *60,* 11051–11061. doi:10.1103/PhysRevB.60.11051
7. Sader, J. E.; Jarvis, S. P. *Appl. Phys. Lett.* **2004,** *84,* 1801–1803. doi:10.1063/1.1667267
8. Verdaguer, A.; Sacha, G. M.; Bluhm, H.; Salmeron, M. *Chem. Rev.* **2006,** *106,* 1478–1510. doi:10.1021/cr040376l
9. Amadei, C. A.; Santos, S.; Pehkonen, S. O.; Verdaguer, A.; Chiesa, M. *J. Phys. Chem. C* **2013,** *117,* 20819–20825. doi:10.1021/jp408984h
10. Amadei, C. A.; Tang, T. C.; Chiesa, M.; Santos, S. *J. Chem. Phys.* **2013,** *139,* 084708. doi:10.1063/1.4819267
11. Katan, A. J.; Oosterkamp, T. H. *J. Phys. Chem. C* **2008,** *112,* 9769–9776. doi:10.1021/jp711017n
12. Wastl, D. S.; Weymouth, A. J.; Giessibl, F. J. *ACS Nano* **2014,** *8,* 5233–5239. doi:10.1021/nn501696q
13. Leroch, S.; Wendland, M. *Langmuir* **2013,** *29,* 12410–12420. doi:10.1021/la402002f
14. Barcons, V.; Verdaguer, A.; Font, J.; Chiesa, M.; Santos, S. *J. Phys. Chem. C* **2012,** *116,* 7757–7766. doi:10.1021/jp2107395
15. Heinz, W. F.; Hoh, J. H. *Trends Biotechnol.* **1999,** *17,* 143–150. doi:10.1016/S0167-7799(99)01304-9
16. Hernando-Pérez, M.; Miranda, R.; Aznar, M.; Carrascosa, J. L.; Schaap, I. A. T.; Reguera, D.; de Pablo, P. J. *Small* **2012,** *8,* 2366–2370. doi:10.1002/smll.201200664
17. Calò, A.; Reguera, D.; Oncins, G.; Persuy, M.-A.; Sanz, G.; Lobasso, S.; Corcelli, A.; Payot-Augy, E.; Gomila, G. *Nanoscale* **2014,** *6,* 2275–2285. doi:10.1039/c3nr05107b
18. Garcia-Manyes, S.; Redondo-Morata, L.; Oncins, G.; Sanz, F. *J. Am. Chem. Soc.* **2010,** *132,* 12874–12886. doi:10.1021/ja1002185
19. Oncins, G.; Picas, L.; Hernández-Borrell, J.; Garcia-Manyes, S.; Sanz, F. *Biophys. J.* **2007,** *93,* 2713–2725. doi:10.1529/biophysj.107.110916
20. Dols-Pérez, A.; Fumagalli, L.; Cohen-Simonsen, A.; Gomila, G. *Langmuir* **2011,** *27,* 13165–13172. doi:10.1021/la202942j
21. Dols-Pérez, A.; Fumagalli, L.; Gomila, G. *Colloids Surf., B* **2014,** *116,* 295–302. doi:10.1016/j.colsurfb.2013.12.049
22. Oncins, G.; Vericat, C.; Sanz, F. *J. Chem. Phys.* **2008,** *128,* 044701. doi:10.1063/1.2813434
23. Stifter, T.; Marti, O.; Bhushan, B. *Phys. Rev. B* **2000,** *62,* 13667–13673. doi:10.1103/PhysRevB.62.13667
24. Santos, S.; Gadelrab, K.; Font, J.; Chiesa, M. *New J. Phys.* **2013,** *15,* 083034. doi:10.1088/1367-2630/15/8/083034
25. Rodrigues, M. S.; Costa, L.; Chevrier, J.; Comin, F. *J. Appl. Phys.* **2014,** *115,* 054309. doi:10.1063/1.4864127
26. Costa, L.; Rodrigues, M. S.; Newman, E.; Zubieta, C.; Chevrier, J.; Comin, F. *J. Mol. Recognit.* **2013,** *26,* 689–693. doi:10.1002/jmr.2328
27. Santos, S.; Amadei, C. A.; Verdaguer, A.; Chiesa, M. *J. Phys. Chem. C* **2013,** *117,* 10615–10622. doi:10.1021/jp4039732
28. Giessibl, F. J. *Phys. Rev. B* **1997,** *56,* 16010–16015. doi:10.1103/PhysRevB.56.16010
29. Krüger, D.; Anczykowski, B.; Fuchs, H. *Ann. Phys.* **1997,** *509,* 341–363. doi:10.1002/andp.19975090502
30. García, R.; Pérez, R. *Surf. Sci. Rep.* **2002,** *47,* 197–301. doi:10.1016/S0167-5729(02)00077-8
31. Cleveland, J. P.; Anczykowsky, B.; Schmid, A. E.; Elings, V. B. *Appl. Phys. Lett.* **1998,** *72,* 2613–2615. doi:10.1063/1.121434
32. Tamayo, J.; García, R. *Appl. Phys. Lett.* **1998,** *73,* 2926–2928. doi:10.1063/1.122632
33. Santos, S.; Gadelrab, K. R.; Barcons, V.; Stefancich, M.; Chiesa, M. *New J. Phys.* **2012,** *14,* 073044. doi:10.1088/1367-2630/14/7/073044
34. Gadelrab, K. R.; Santos, S.; Chiesa, M. *Langmuir* **2013,** *29,* 2200–2206. doi:10.1021/la3044413
35. Garcia, R.; Gómez, C. J.; Martinez, N. F.; Patil, S.; Dietz, C.; Magerle, R. *Phys. Rev. Lett.* **2006,** *97,* 016103. doi:10.1103/PhysRevLett.97.016103
36. Santos, S.; Gadelrab, K. R.; Souier, T.; Stefancich, M.; Chiesa, M. *Nanoscale* **2012,** *4,* 792–800. doi:10.1039/c1nr10954e
37. Gadelrab, K. R.; Santos, S.; Souier, T.; Chiesa, M. *J. Phys. D: Appl. Phys.* **2012,** *45,* 012002. doi:10.1088/0022-3727/45/1/012002
38. Katan, A. J.; van Es, M. H.; Oosterkamp, T. H. *Nanotechnology* **2009,** *20,* 165703–165711. doi:10.1088/0957-4484/20/16/165703
39. Sader, J. E.; Uchihashi, T.; Higgins, M. J.; Farrel, A.; Nikayama, Y.; Jarvis, S. P. *Nanotechnology* **2005,** *16,* S94–S101. doi:10.1088/0957-4484/16/3/018
40. Cardellach, M.; Verdaguer, A.; Fraxedas, J. *Surf. Sci.* **2011,** *605,* 1929–1933. doi:10.1016/j.susc.2011.07.003
41. Santos, S.; Verdaguer, A.; Souier, T.; Thomson, N. H.; Chiesa, M. *Nanotechnology* **2011,** *22,* 465705. doi:10.1088/0957-4484/22/46/465705
42. Verdaguer, A.; Santos, S.; Sauthier, G.; Segura, J. J.; Chiesa, M.; Fraxedas, J. *Phys. Chem. Chem. Phys.* **2012,** *14,* 16080–16087. doi:10.1039/c2cp43031b
43. Butt, H.-J.; Kappl, M. *Adv. Colloid Interface Sci.* **2009,** *146,* 48–60. doi:10.1016/j.cis.2008.10.002
44. Yaminsky, V. V. *Colloids Surf., A* **1999,** *159,* 181–195. doi:10.1016/S0927-7757(99)00173-9
45. Zitzler, L.; Herminghaus, S.; Mugele, F. *Phys. Rev. B* **2002,** *66,* 155436. doi:10.1103/PhysRevB.66.155436
46. Verdaguer, A.; Weis, C.; Oncins, G.; Ketteler, G.; Bluhm, H.; Salmeron, M. *Langmuir* **2007,** *23,* 9699–9703. doi:10.1021/la700893w
47. Shinto, H.; Uranishi, K.; Miyahara, M.; Higashitani, K. *J. Chem. Phys.* **2002,** *116,* 9500–9509. doi:10.1063/1.1473817
48. *Igor Pro 6;* WaveMetrics Inc.: Lake Oswego, Oregon, USA.
49. Santos, S.; Guang, L.; Souier, T.; Gadelrab, K.; Chiesa, M.; Thomson, N. H. *Rev. Sci. Instrum.* **2012,** *83,* 043707. doi:10.1063/1.4704376
50. Israelachvili, J. *Intermolecular and Surface Forces,* 2nd ed.; Academic Press: New York, NY, USA, 1991.

51. García, R.; San Paulo, A. *Phys. Rev. B* **1999,** *60,* 4961–4967. doi:10.1103/PhysRevB.60.4961
52. García, R.; San Paulo, A. *Ultramicroscopy* **2000,** *82,* 79–83. doi:10.1016/S0304-3991(99)00132-1
53. *MATLAB R2010b;* The MathWorks Inc.: Natick, Massachusetts, USA.
54. Derjaguin, B. V.; Muller, V. M.; Toporov, Yu. P. *J. Colloid Interface Sci.* **1975,** *53,* 314–326. doi:10.1016/0021-9797(75)90018-1

License and Terms

The definitive version of this article is the electronic one which can be found at:
doi:10.3762/bjnano.6.84

BEILSTEIN JOURNAL OF NANOTECHNOLOGY

Stick–slip behaviour on Au(111) with adsorption of copper and sulfate

Nikolay Podgaynyy, Sabine Wezisla, Christoph Molls, Shahid Iqbal
and Helmut Baltruschat*

Full Research Paper

Open Access

Address:
Institute of Physical and Theoretical Chemistry, University of Bonn,
Roemerstrasse 164, D-53117 Bonn, Germany

Email:
Helmut Baltruschat* - baltruschat@uni-bonn.de

* Corresponding author

Keywords:
AFM; friction; friction force microscopy; nanotribology; underpotential deposition

Beilstein J. Nanotechnol. **2015,** *6,* 820–830.
doi:10.3762/bjnano.6.85

Received: 21 July 2014
Accepted: 04 March 2015
Published: 26 March 2015

This article is part of the Thematic Series "Advanced atomic force microscopy techniques III".

Guest Editor: T. Glatzel

Abstract

Several transitions in the friction coefficient with increasing load are found on Au(111) in sulfuric acid electrolyte containing Cu ions when a monolayer (or submonolayer) of Cu is adsorbed. At the corresponding normal loads, a transition to double or multiple slips in stick–slip friction is observed. The stick length in this case corresponds to multiples of the lattice distance of the adsorbed sulfate, which is adsorbed in a $\sqrt{3} \times \sqrt{7}$ superstructure on the copper monolayer. Stick–slip behaviour for the copper monolayer as well as for 2/3 coverage can be observed at $F_N \geq 15$ nN. At this normal load, a change from a small to a large friction coefficient occurs. This leads to the interpretation that the tip penetrates the electrochemical double layer at this point. At the potential (or point) of zero charge (pzc), stick–slip resolution persists at all normal forces investigated.

Introduction

Atomic-scale friction processes constitute a fascinating field of research which has been opened by the invention of the atomic force microscope (AFM) [1]. The AFM allows us to determine the force necessary to move a cantilever tip laterally across the surface with atomic resolution. A theoretical model describing this so-called stick–slip motion was provided by Tomlinson [2]. Tip atoms in contact with the surface remain at a certain surface position with a minimum of potential energy until the increasing lateral force initiates a slip toward the next potential minimum. Many interesting aspects on the origin of friction and the underlying dissipative processes have been elucidated so far, but an overall understanding is still far from being complete [3-6].

Investigations at surfaces performed under electrochemical conditions offer some advantages compared to those performed in air or under ultra high vacuum (UHV) conditions: simply by varying the potential of the working electrode, the electrode surface can quickly and reversibly be modified by adsorption of a foreign metal or other substances, while the degree of unwanted contamination can be kept as low as under UHV conditions.

There are only a few older publications reporting on AFM friction studies on HOPG (highly oriented pyrolytic graphite) and polycristalline Ag under electrochemical conditions, examining the dependence of friction on potential and the adsorption of anions [7-9]. Our group recently started to study friction forces on single crystal electrodes under electrochemical conditions. In [10,11] we investigated the effect of copper under potential deposition (UPD) on Au(111) and Pt(111) on friction and found an increase in friction force after adsorption of a sub- or monolayer of copper. A particularly high friction was observed at the potential where the 2/3 Cu adlayer was formed. This was later corroborated by Bennewitz and coworkers [12]. A transition in friction coefficient was found at a certain normal load on a copper monolayer which was ascribed to a normal load dependent penetration of the double layer or even displacements of adsorbates [10,13]. We showed that the pressure necessary for the displacement of adsorbates such as a UPD metal calculated from a typical pressure dependence of the adsorption free enthalpy (as given by the adsorption volume, cf. [14,15]) does correspond to the pressure exerted by the tip. The friction force on UPD copper in presence of chloride is much smaller than in sulfuric acid solution. Upon the adsorption of sulfate ions on Au(111), we observed a considerable increase in friction force [10,13].

Bennewitz, Hausen and Gosvami showed that stick–slip resolution can be obtained for this adlayer [12] Labuda et al. [16] found that atomic resolution on gold is most easily achieved at the potential of zero charge (pzc). They observed "blurred" resolution at higher potential where oxygen starts being adsorbed. Hausen et al. observed a stick–slip periodicity equal to the lattice distance of sulfate anions, which is adsorbed in a $\sqrt{3} \times \sqrt{7}$ superstructure [17]. They found an increase in friction force upon the adsorption of anions only at normal loads above a certain threshold. As an explanation, the authors consider the squeezing out of water layer when the normal force exceeds a certain threshold [18]. The behaviour of water on crystalline surfaces was described as a viscous structure, which can resist to the tip pressure up to 4 water layers [19]. On the other hand, the properties of viscous water on a gold surface are dependent on the surface potential. For Au(111) in 0.05 M sulfuric acid solution + 1 mM $CuSO_4$ the pzc is 0.22 V vs Cu/Cu^{2+} [20]. Labuda et al. [21] obtained atomic resolution of a copper submonolayer on gold(111) in perchloric acid solution. They found an increase in friction force after metal adsorption as compared to a clean gold surface.

When the tip is scanning across a monatomic step, friction is largely increased due to the Schwoebel barrier, as has been shown for the NaCl(001)/gas interfaces [22]. We observed the same effect at the Au(111)/electrolyte interfaces [10,13]. Correspondingly, we have shown that friction is higher when the tip is scanning perpendicular to the steps of a stepped Au(665) electrode surface than when scanning parallel; only in the latter case, the effects of Cu UPD on the stepped Au(665) on friction is similar to that on the Au(111) electrode surface [23].

The objective of the present work is a detailed study of the nature of atomic-scale friction with respect to the Au(111) surface, covered with different adsorbates. We would like to find out what factors influence friction and to learn more about the role of the double layer thereupon. It is also our ongoing interest to elucidate whether findings obtained at the solid/gas interface are also valid at the solid electrolyte interface.

In this paper we present the results of investigations of friction forces during UPD and dissolution of Cu/Au(111) and also during sulfate adsorption in sulfuric acid solution. We extend previous measurements to lower loads and also elucidate the conditions for atomic stick–slip. This system has been well studied in a large number of publications and therefore is a model system for fundamental studies. Many different methods have been used including STM [24,25], and also ex situ experiments such as LEED, AES and RHEED [26]. The given results reveal the coverage and the structure of adsorbed copper and sulfate anions on Au(111) and the potential regions at which the different structures can be observed. Gordon et al. [27] found a $\sqrt{3} \times \sqrt{3}$ copper structure in the 2/3 coverage region using X-ray and QCM methods. Lipkowski et al. [28] used standard electrochemical instrumentation in order to determine the Gibbs excess of copper coadsorbed with SO_4^{2-} anions.

Experimental

AFM measurements were performed with a Nanoscope III E controller (Digital Instruments, Santa Barbara, CA) and a commercially available AFM scanner (Molecular Imaging) fitted with an electrochemical cell. The nominal spring constants of the commercial Si cantilevers used (Veeco MPP-31100) were 0.65 N/m. The torsional force constant was determined via Sader's method [29] to be 190 N/m. This method is based on the measurement of the resonant frequency and quality factor of the cantilever. All AFM measurements were performed at room temperature.

Friction force maps shown here are the difference images between both scan directions. Due to the relatively high load used in our experiments, the tip radius quickly approached a value of around 100 nm, but then stayed constant as revealed by SEM images obtained after different usage times. Using the formulae given in [4], the real contact area at a normal load of 15 nN was estimated to around 30 nm^2 and at 60 nN around 70 nm^2 [30].

Cyclic voltammograms were recorded with standard electrochemical equipment. The solutions were made of ultrapure H_2SO_4 (Merck, suprapure), $CuSO_4$ (Merck, >99%, p.a.) and high purity water (millipore, toc < 3 ppb, 18.2 MΩ·cm). The Au(111) single crystal (obtained from Metal Crystals & Oxides) was oriented with an accuracy of 0.5°. The preparation of the single crystal was performed by flame annealing to red heat for two minutes. The crystal was cooled in argon atmosphere and brought into contact with the deaerated solution at room temperature. All potentials were measured and are quoted with respect to a Cu/Cu^{2+} reference electrode. Cleanliness was controlled by cyclic voltammetry in sulfuric acid.

Results and Discussion

Figure 1 shows a cyclic voltammogram of Au(111) in 0.05 M $H_2SO_4 + 4 \times 10^{-4}$ M $CuSO_4$ in the AFM cell. The voltammogram can be split into three potential regions (see Figure 1). At potentials $E \geq 250$ mV only sulfate is adsorbed to the Au(111) surface. The sulfate coverage increases with potential. Between peak A1 and B1, the copper coverage is $\Theta_{Cu} = 2/3$ of a monolayer; copper has a $\sqrt{3} \times \sqrt{3}$ honeycomb structure. Negative of peaks B and positive of peak C, the latter corresponding to copper bulk deposition, a full monolayer of copper is present. Both the monolayer of copper and the copper 2/3 layer are covered by sulfate anions, adsorbed from solution at potentials $E \leq 0.2$ V vs Cu/Cu^{2+}. On the copper 2/3 layer, sulfate anions occupy the holes in the honeycomb structure, therefore forming a $\sqrt{3} \times \sqrt{3}$ structure as well. On the copper monolayer, sulfate is adsorbed in a $\sqrt{7} \times \sqrt{3}$ structure. At the potential of zero charge (pzc) at $E = 0.22$ V, just positive of peak A2 or A1, only a small amount of adsorbate covers the gold surface, according to [28] $\Theta_{Cu} = 9\%$; $\Theta_{sulfate} = 5\%$.

In Figure 2 the friction image (difference image of trace and retrace signals) of the Au(111) surface at the pzc is presented. The figure also illustrates how the friction force was determined as a function of normal load.

The results of these investigations for different potentials are given in Figure 3a,b. Figure 3a shows the dependency of friction force versus normal load for a set of four selected potentials corresponding to different adsorbate structures. As already reported before [11], a transition in the coefficient of friction is observed for a copper monolayer at $F_N = 70$ nN. Here, we extended the study to lower normal loads and observed another transition in the friction coefficient at a normal load of $F_N \approx 15$ nN.

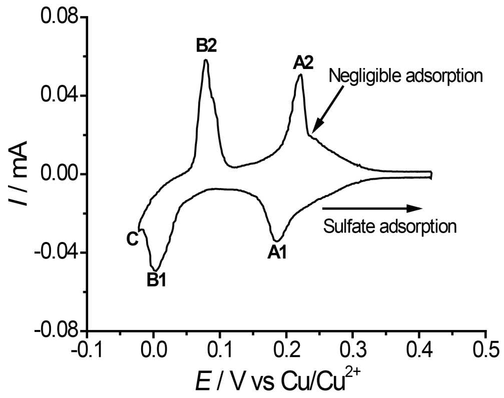

Figure 1: Cyclic voltammogram in 0.05 M $H_2SO_4 + 4 \times 10^{-4}$ M $CuSO_4$. v = 50 mV/s.

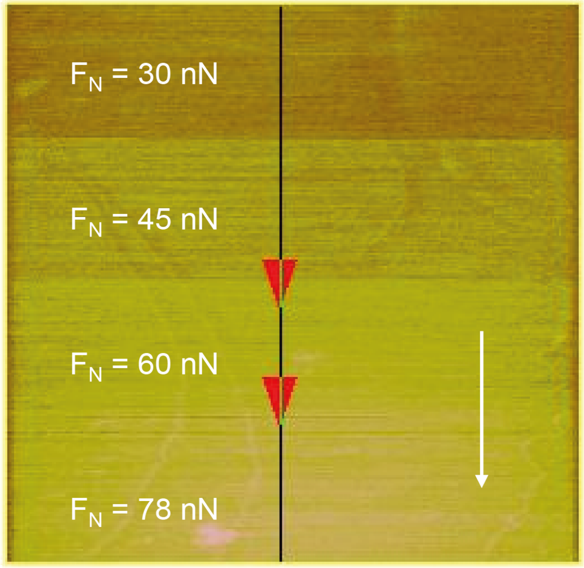

Figure 2: Friction image of Au(111) (in 0.05 M $H_2SO_4 + 4 \times 10^{-4}$ M $CuSO_4$) with a variation of normal load; E = 0.22 V (pzc); image size 600 nm × 600 nm.

The dependency of friction force on potential is shown in Figure 3b. The friction force is independent of potential as long as the adsorbate structure is preserved but changes when the adsorbate structure is changed; it is minimal at the pzc (E = 0.22 V). Due to adsorption of sulfate, positive of the pzc, friction force increases with increasing potential, as already shown before for Au(111) in H_2SO_4 [13]. The high friction value at $E \approx 0.2$ V, which exceeds the friction value in the copper 2/3 adlayer region, is constant with time and is found at all normal loads investigated. This potential corresponds to the

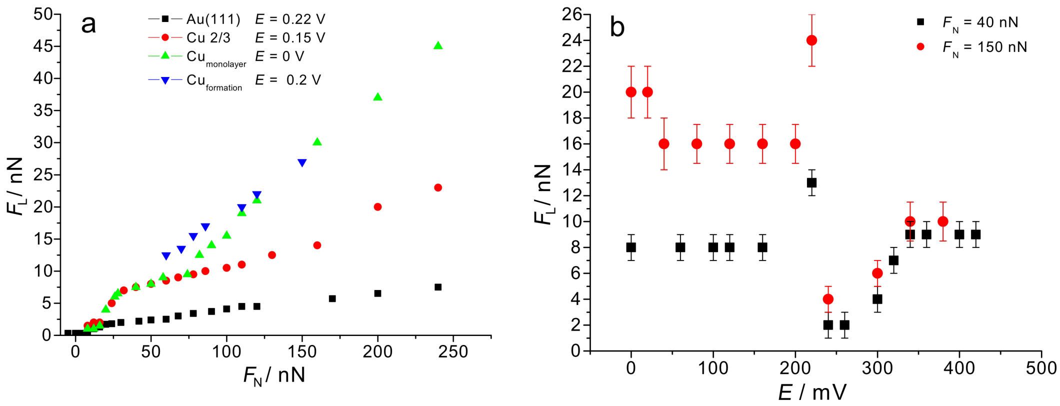

Figure 3: a) Friction force as a function of normal load. Green triangles: *E* = 0 V (Cu monolayer); red circles: *E* = 0.15 V (2/3 Cu coverage); black squares: *E* = 0.22 V (Au pzc). b) Friction force as a function of potential. Black: F_N = 40 nN; red: F_N = 150 nN.

peak in the cyclic voltammogram which is due to formation of the copper 2/3 layer. At this peak potential, copper makes up about 30% surface coverage. In our previous experiments, such a large friction value was observed when stepping the potential from a potential of zero Cu coverage into the copper 2/3 adlayer region [10]. A similar effect was observed previously on Pt(111) during the formation of a copper monolayer [11]. Bennewitz et al. observed such an increase on Au(111) upon Cu adsorption during potential cycling [12]. Obviously, this increase in friction is not a transient behaviour as we assumed from the above mentioned previous results involving cyclic voltammetry and potential steps across the peaks. In this context it is noteworthy that Hölzle and Kolb observed a nucleation and growth mechanism for peaks A2, B1 and B2, but not for A1 [31]. It is therefore not clear whether at the peak potential of A1/A2 the surface is covered by many small 2D nuclei or a high density of (freely diffusing) Cu adatoms; whereas the explanation of the increased friction due to many 2D islands involving many steps leading to an increased friction due to the Schwoebel barrier is straightforward, the explanation of the friction increase by adatoms would involve a more sophisticated model.

Figure 4 shows atomically resolved images with high resolution of atoms for Au(111) (Figure 4a) and for Cu 2/3 (Figure 4b). The stick–slip periodicity on Au(111) (here at an angle of 30° to the lattice vector) equals 2.4 Å (error estimated from many images ±0.3 Å), which corresponds to $\sqrt{3}/2$ of the lattice vector. From that, the lattice vector is calculated to 2.71 Å. For the 2/3 copper layer the distance between two neighbouring potential minima from the stick–slip signal (now in the direction of the substrate lattice vector) equals 4.4 Å, which corresponds to 1.5 of the Au(111) periodicity, from which a lattice vector of 2.9 Å is calculated. Both values agree fairly well with the lattice vector of Au of 2.77 Å.

The slope of the sawtooth stick–slip curve (section analysis below the figure) characterizes the effective lateral stiffness of the surface–tip contact. In our case it is 10 N/m and therefore much smaller than the lateral stiffness of the cantilever (190 N/m). The somewhat rounded shape might be due to a not completely commensurable tip–substrate contact [32]. Figure 5 shows the change of the structure during a potential step from the sulfate covered Au(111) surface to the Cu 2/3 adlayer. The increase in friction at the transition (cf. Figure 3b) is clearly seen.

Figure 6 shows the friction force map during a change from the Cu monolayer to the 2/3 Cu layer. The slope of the stick curve is 12 N/m. In all cases it is between 10 and 12 N/m and independent of potential. It is important to mention that at all potentials the surface is very resistant to wear; even at high normal loads of about 250 nN, atomic resolution is always visible. At the pzc the quality of stick–slip resolution on gold is much better than at potentials of high sulfate coverage, in accordance with the results in [16].

On the copper monolayer, stick–slip behaviour can be observed while atomic resolution (in y-direction) is completely absent in all applicable regimes of normal load. Figure 7 shows four friction force maps for eight normal loads at constant potential (E = 0 mV). At first sight the images appear irregular but the particular analysis of stick–slip behaviour shows astonishing results: With an increase of normal load the stick–slip periodicity increases.

Figure 8a presents three typical cross sections from Figure 7. Typical slip distances are 4.6 Å or less for $F_N \approx 15$ nN, 9.5–11 Å for $27 < F_N < 55$ nN and 16.5 Å or more for $70 < F_N < 100$ nN. This leads to the conclusion that at high normal loads, slips across multiple potential minima are

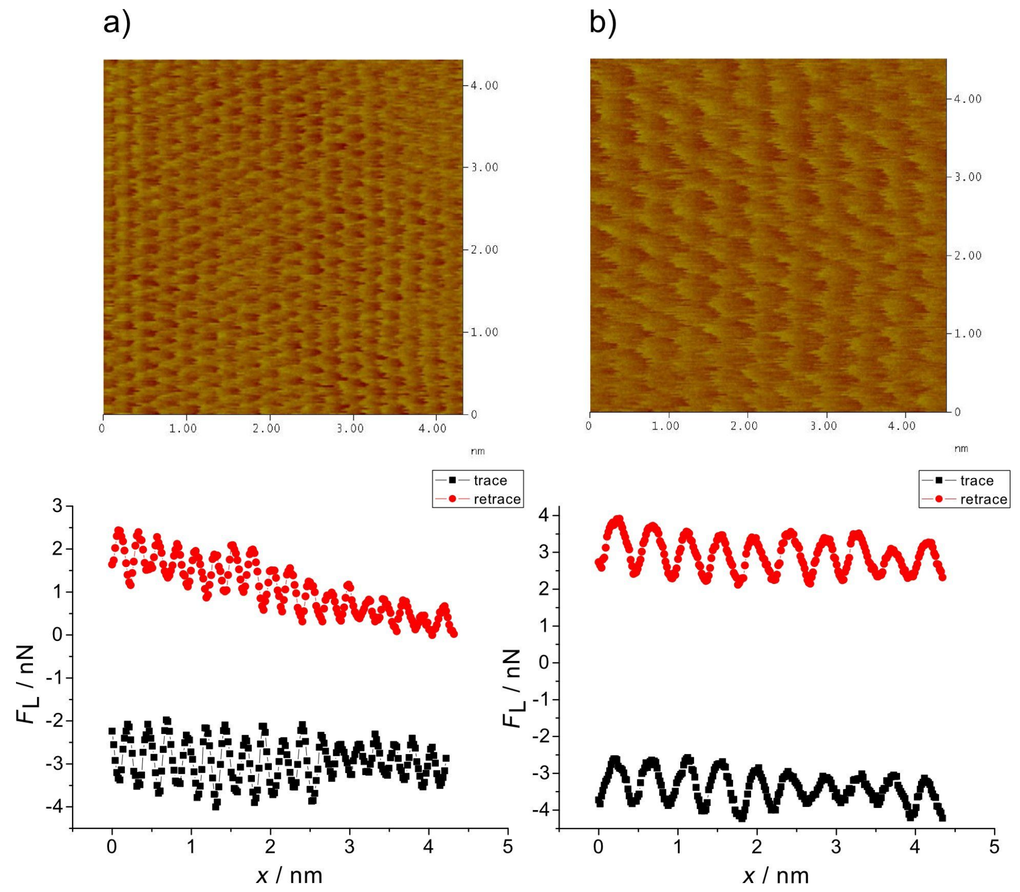

Figure 4: Stick–slip atomic resolution and cross section analysis for a) Au(111) at E = 270 mV; F_N = 80 nN; scan rate 106 nm/s; b) Cu 2/3, E = 100 mV; F_N = 45 nN; scan rate 92 nm/s.

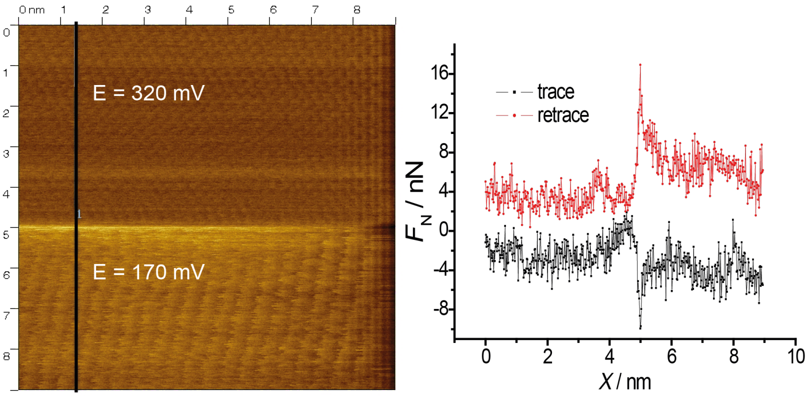

Figure 5: Stick–slip atomic resolution and cross section analysis for **a** potential jump from 320 mV (Au(111)/sulfate) to 170 mV (2/3 Cu adlayer), cross section along the vertical line as indicated; F_N = 45 nN; scan rate 275 nm/s.

observed. A similar effect was observed by Meyer and coworkers [33]: Upon an increase in normal load on a NaCl(001) surface a transition to multiple slip was found. According to [34], who predicted such transitions from theory for low damping conditions and also observed it on HOPG, this process is based on energy minimisation and caused by the increase in normal load.

A schematic model of the √7 × √3 sulfate structure on the Cu monolayer is presented in Figure 8b. Arrows represent a

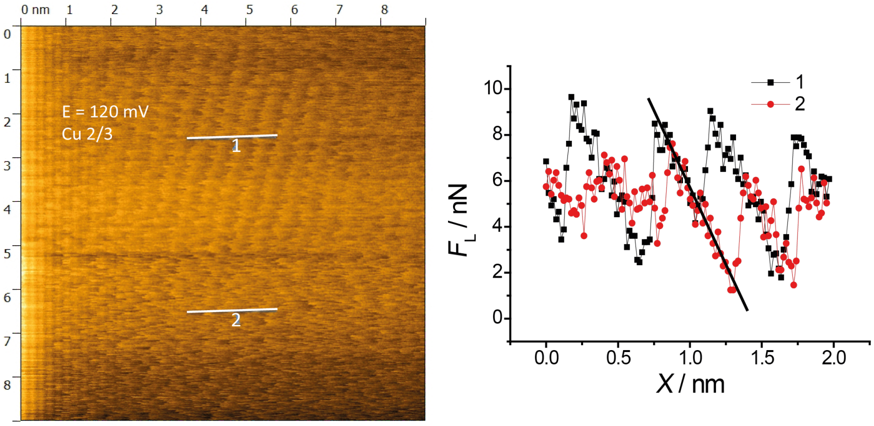

Figure 6: Stick–slip atomic resolution and cross section analysis for a potential jump from 0 mV (full Cu adlayer) to 120 mV (2/3 Cu adlayer), cross section along the two short horizontal lines F_N = 45 nN; scan rate 275 nm/s.

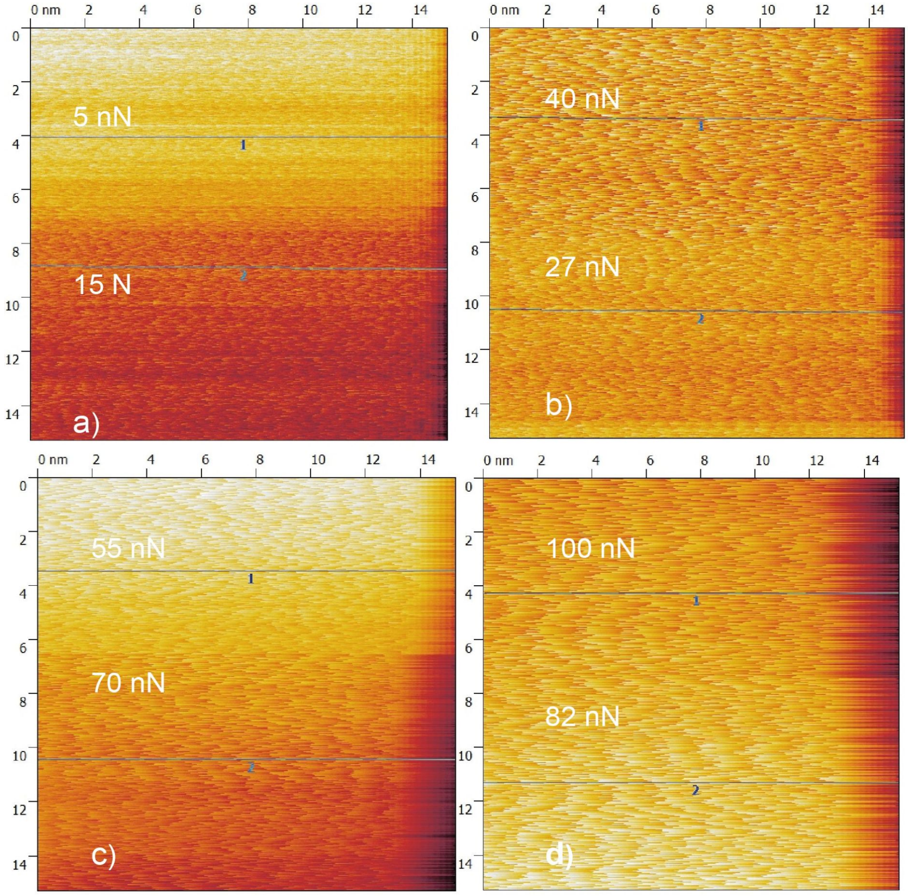

Figure 7: Copper monolayer friction images at F_N = a) 5, 15 nN; b) 27, 40 nN; c) 55, 70 nN and d) 82, 100 nN.

possible slip pathway for the different slip lengths. It is based on the crystal orientation as obtained from the Au(111) and Cu 2/3 structures. We assume that the tip apex is mobile enough in order to have a small variation in direction perpendicular to the tip motion. Black dotted lines on the Figure 8b show the path of tip apex while the red arrows represent the cantilever motion in scan direction. For a single jump, an average value of 0.46 nm (3 jumps within a distance of 5 lattice constants) is obtained, for

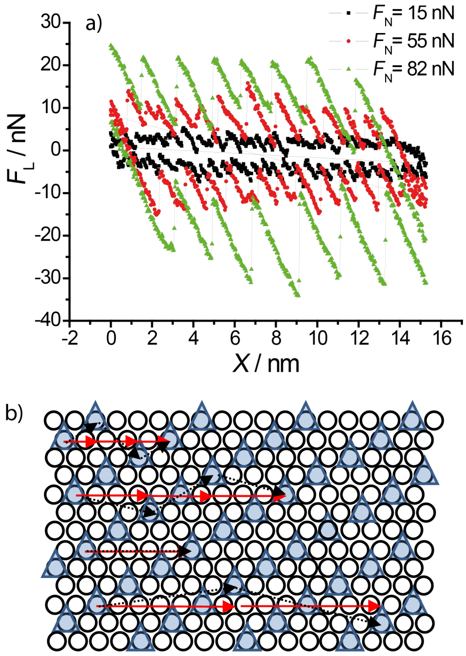

Figure 8: a) Typical cross sections from Figure 7 at F_N = 15, 55 and 82 nN. b) Schematic illustration of the √7 × √3 structure of sulfate anions (triangles) on a copper monolayer (circles): arrows (black, dotted) denote a possible jumping pathway for the AFM tip in a single, double, triple and quadruple slip. (Of course, triangles may as well reflect minimal energy positions between the sulfate ions.)

a double jump 0.92 nm, for a triple jump 1.39 nm and for a quadruple jump 1.8 nm. These values agree fairly well with the experimental data.

A plot of the nano-scale friction force as a function of normal load on a copper monolayer is given in Figure 9. The friction coefficient changes from 0.12 to 0.5 at a normal load of approximately 70 nN. This change corresponds to change in friction coefficient presented on Figure 3a. This transition in friction coefficient goes along with a change in slip length, as indicated by the bars at the bottom. These friction data obtained from high resolution images agree well with those obtained from large scale images (cf. Figure 3a), although the transition at 15 nN is less visible than in Figure 3a because of the much lower density of data points.

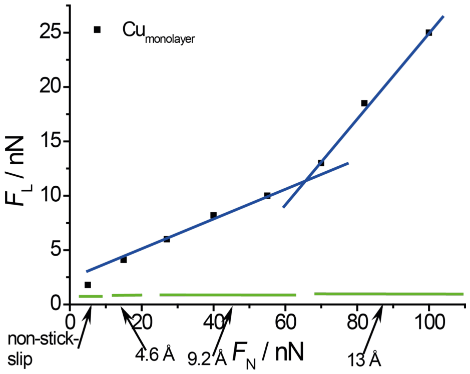

Figure 9: Friction force as a function of normal load (data, e.g., from Figure 8a).

An important point is the vanishing of stick–slip behaviour at normal loads of less than 15 nN. In spite of non-stick–slip resolution the contact between tip and surface is preserved and energy dissipation is still observed. A transition to superlubricity would involve disappearing friction [35,36]. Since this is not the case here one might speculate about different contributions to friction, only one of which is disappearing with decreasing load. Figure 10 demonstrates the transition from non- to regular stick–slip on a Cu monolayer on Au(111). A similar effect is also observed at a 2/3 Cu monolayer and at the sulfate covered gold surface.

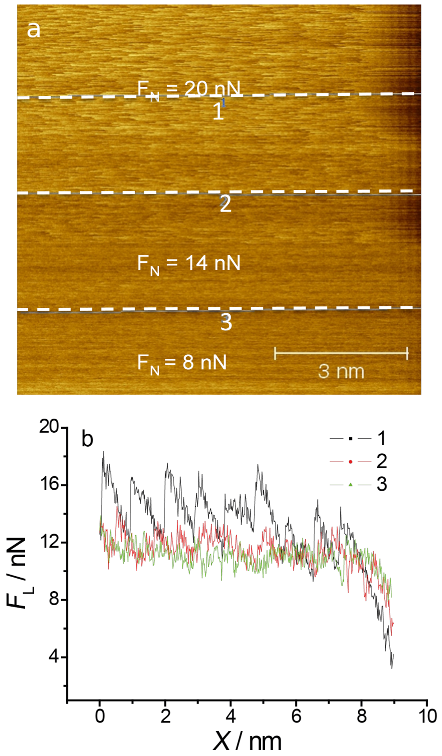

Figure 10: Transition from irregular to regular stick–slip on a copper monolayer a) AFM image at three different normal loads; b) cross sections along the lines from image a). *E* = 10 mV; scan rate 213 nm/s.

The transition between non-stick–slip and stick–slip on the copper sub-monolayer is shown in Figure 11. At normal loads above 10 nN regular atomic stick–slip without resolution in the slow scan direction is observed. Comparison of Figure 11a and b shows that the transition is reversible with regard to whether

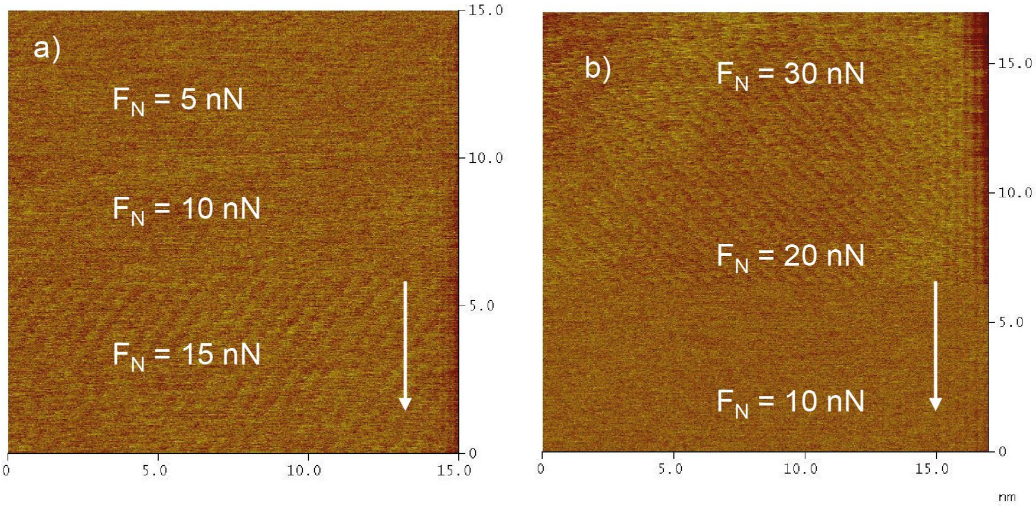

Figure 11: Transition between regular and irregular stick–slip on copper 2/3 during an increase (a) and a decrease (b) of normal load. E = 100 mV; scan rate 180 nm/s.

the normal load is increased or decreased. Good atomic resolution was only observed at higher normal loads (cf. Figure 4–6). Since stick slip disappears rather abruptly and reproducibly upon decreasing the normal load, we believe that this is a true physical effect and that stick slip does not just become indistinguishable from noise at lower normal loads.

Figure 12 shows friction force maps for two different potentials. At the pzc on clean gold (Figure 12a), stick–slip behaviour is present even at very small normal loads of nominally $F_N = -5$ nN. (The negative normal load is possible here because of adhesion, see below.) At normal loads below this value the contact between tip and surface is broken. On sulfate-covered gold at E = 420 mV (Figure 12b), a transition from non- to regular stick–slip behaviour is found for positive F_N.

For Figure 13, all experimentally observed transition forces were collected and correlated to the applied potential. Orange

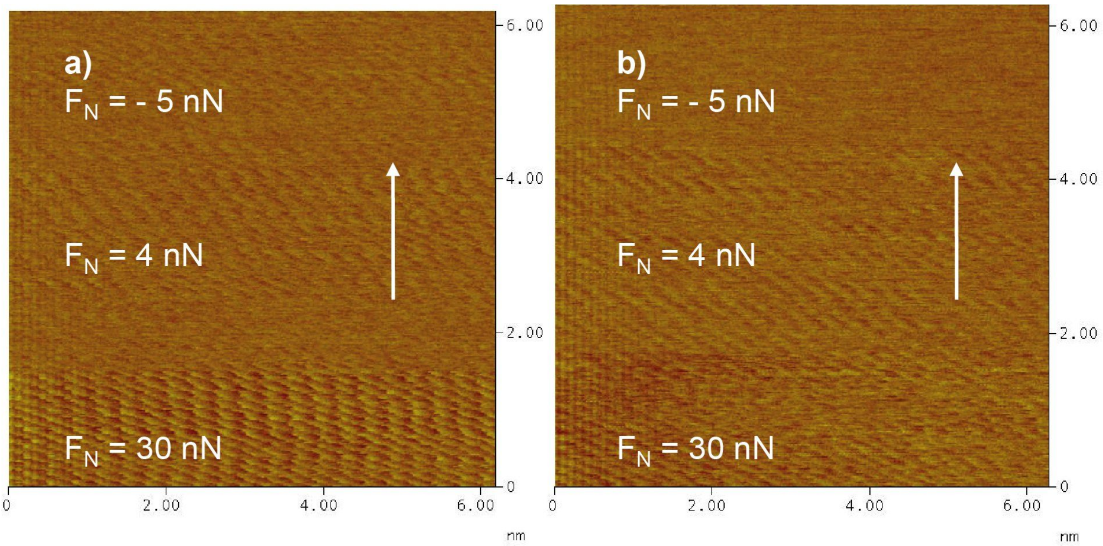

Figure 12: Friction images on Au(111). a) atomic resolution on Au(111) (no transition to non-stick–slip at this potential); $F_N = -5, 4, 30$ nN; E = 250 mV; scan rate 154 nm/s. (In this image, the apparent gradual change of the lattice direction at the beginning of the upward scan – lower part of the image – is an artefact probably due to the hysteresis of the scanner piezo.) b) Transition from non- to regular stick–slip behaviour at F_N = 4 nN; E = 420 mV; scan rate 154 nm/s.

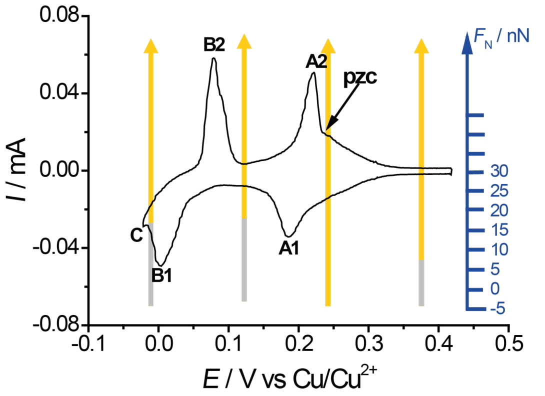

Figure 13: Cyclic voltammogram of Au(111) in 0.05 M H_2SO_4 + 4×10^{-4} M $CuSO_4$ as shown in Figure 1. Normal force regions of different behaviours are inset as arrows. Orange: atomic-resolution stick–slip; grey: non-stick–slip behaviour.

arrows mark the force region where stick–slip is observed. The grey parts of the arrows correspond to regions of non-stick–slip. Figure 13 shows that for both the sub- and monolayer of copper the transition to regular stick–slip starts at the same normal load of about 15 nN. At this same normal load we observed a transition in friction coefficient on the microscale for Cu covered gold (Figure 3). As mentioned before, sulfate is adsorbed to the copper layer for both the 2/3- and the monolayer. Also positive of the pzc, where only sulfate is adsorbed, such a transisiton is observed, but not at the pzc, where atomic stick–slip is observed even at low normal loads. These effects lead to the conclusion that the transition is strongly dependent on adsorption. The onset of stick–slip may be caused by a tip penetration through the electrochemical double layer, which effectively is not existent at the pzc. Possibly at potentials other than the pzc, the tip is scanning above or in a viscous layer of water above the double layer at low loads.

Figure 14 shows force–distance curves at different potentials. A curve showing strong adhesion (Figure 14a) is observed in the potential region positive of and at the pzc where the gold surface is free of adsorbates or covered with a sulfate layer; the value of the adhesion is independent of the potential. For all potentials negative of the pzc including the copper monolayer the adhesion disappears (Figure 14b). This could be related to a different orientation of water molecules in the double layer and a possible formation of hydrogen bonds to the OH groups of the surface oxide of the Si tip. (In principle, these tip approach curves should also reveal the above mentioned penetration of the tip into the double layer. Unfortunately, at present the resolution is not sufficient to reveal the corresponding small vertical tip displacement of about 0.2 nm corresponding to the atomic diameter of, e.g., a Cu atom. Corresponding work is in progress.)

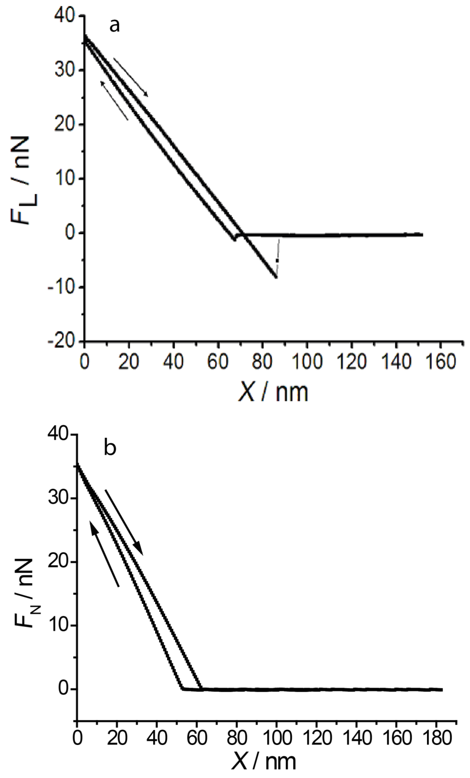

Figure 14: Force–distance curves at potentials of a) 220 mV, b) 150 mV. A large snap-off force due to adhesion is only found for potentials positive of the pzc.

An origin of the attractive interaction positive of the pzc is also the electrostatic interaction between the positively (protonated) charged tip and the negatively charged surface (caused by the specific adsorption of sulfate). The irreversibility may also be caused by a mutual penetration of the two double layers (that of the surface and that of the tip) into each other and an irreversibility of the building up of the original double layer upon withdrawal of the tip. At low potentials, due to the Cu adlayer, the double layer of the substrate could be much more rigid. This could also explain the non-stick–slip behaviour at Cu-covered surfaces: at low normal loads, tip and surface are separated by their own double layers and atomic resolution is not obtained.

Conclusion

Friction forces on Au(111) covered by a copper monolayer in sulfuric acid solution show several transitions in friction coefficient which are also related to a transition to multiple-slip. The stick length corresponds to multiples of the distance of adsorbed sulfate. Stick–slip behaviour for both the copper monolayer and 2/3 Cu coverage can be observed at normal loads above F_N = 15 nN. (This value is certainly dependent on the tip radius, which, as mentioned above, is around 100 nm.) At the same normal load a change in friction coefficient on the microscale can be found. This may suggest that at this normal load, the tip penetrates an outer water layer of the electrical double layer. Stick–slip resolution at potentials close to the pzc can be observed at all normal forces investigated.

Friction is minimal at the potential of zero charge, suggesting again the role of adsorbates for frictional energy dissipation. On the other hand, friction is particularly large when the adlayer is disordered at the potential of a phase transition, as shown here for the formation of the $\sqrt{3} \times \sqrt{3}$ adlayer. Whether these phenomena can be generalized has to be elucidated in further studies.

Acknowledgements

Thanks are due to the Deutsche Forschungsgemeinschaft for financial support (Ba 1008/16-1).

References

1. Binnig, G.; Quate, C. F.; Gerber, C. *Phys. Rev. Lett.* **1986,** *56,* 930–933. doi:10.1103/PhysRevLett.56.930
2. Tomlinson, G. A. *Philos. Mag.* **1929,** *7,* 905. doi:10.1080/14786440608564819
3. Ruan, J.-A.; Bhushan, B. *J. Tribol.* **1994,** *116,* 378–388. doi:10.1115/1.2927240
4. Gnecco, E.; Bennewitz, R.; Gyalog, T.; Meyer, E. *J. Phys.: Condens. Matter* **2001,** *13,* R619–R642. doi:10.1088/0953-8984/13/31/202
5. Persson, B. N. J. *Sliding Friction: Physical Principles and Applications;* Springer: Berlin, Heidelberg, 2000. doi:10.1007/978-3-662-04283-0
6. Gnecco, E.; Meyer, E. *Fundamentals of Friction and Wear on the Nanoscale;* Springer: Berlin, Heidelberg, 2007. doi:10.1007/978-3-540-36807-6
7. Binggeli, M.; Christoph, R.; Hintermann, H.-E.; Colchero, J.; Marti, O. *Nanotechnology* **1993,** *4,* 59–63. doi:10.1088/0957-4484/4/2/001
8. Weilandt, E.; Menck, A.; Marti, O. *Surf. Interface Anal.* **1995,** *23,* 428–430. doi:10.1002/sia.740230616
9. Kautek, W.; Dieluweit, S.; Sahre, M. *J. Phys. Chem. B* **1997,** *101,* 2709–2715. doi:10.1021/jp962724w
10. Nielinger, M.; Baltruschat, H. *Phys. Chem. Chem. Phys.* **2007,** *9,* 3965–3969. doi:10.1039/b706804b
11. Nielinger, M.; Hausen, F.; Podghainiy, N.; Baltruschat, H. Nanotribology at Electrodes: Influence of Adsorbates and Potential on Friction Forces Studied with Atomic Force Microscopy. In *Friction, Wear and Wear Protection,* 1st ed.; Fischer, A.; Bobzin, K., Eds.; Wiley-VCH: Weinheim, Germany, 2009; pp 178–184.
12. Bennewitz, R.; Hausen, F.; Gosvami, N. N. *J. Mater. Res.* **2013,** *28,* 1279–1288. doi:10.1557/jmr.2013.103
13. Hausen, F.; Nielinger, M.; Ernst, S.; Baltruschat, H. *Electrochim. Acta* **2008,** *53,* 6058–6063. doi:10.1016/j.electacta.2008.03.053
14. Wang, H.-C.; Baltruschat, H. *ChemPhysChem* **2010,** *11,* 2798–2801. doi:10.1002/cphc.201000253
15. Loewe, T.; Baltruschat, H. *Phys. Chem. Chem. Phys.* **2005,** *7,* 379–384. doi:10.1039/B412505N
16. Labuda, A.; Hausen, F.; Gosvami, N. N.; Grütter, P. H.; Lennox, R. B.; Bennewitz, R. *Langmuir* **2011,** *27,* 2561–2566. doi:10.1021/la104497t
17. Hausen, F.; Gosvami, N. N.; Bennewitz, R. *Electrochim. Acta* **2011,** *56,* 10694–10700. doi:10.1016/j.electacta.2011.03.013
18. Briscoe, W. H.; Titmuss, S.; Tiberg, F.; Thomas, R. K.; McGillivray, D. J.; Klein, J. *Nature* **2006,** *444,* 191–194. doi:10.1038/nature05196
19. Li, T.-D.; Gao, J.; Szoszkiewicz, R.; Landman, U.; Riedo, E. *Phys. Rev. B* **2007,** *75,* 115415. doi:10.1103/PhysRevB.75.115415
20. Dietterle, M.; Will, T.; Kolb, D. M. *Surf. Sci.* **1995,** *342,* 29–37. doi:10.1016/0039-6028(95)00756-3
21. Labuda, A.; Paul, W.; Pietrobon, B.; Lennox, R. B.; Grütter, P. H.; Bennewitz, R. *Rev. Sci. Instrum.* **2010,** *81,* 083701. doi:10.1063/1.3470107
22. Meyer, E.; Lüthi, R.; Howald, L.; Bammerlin, M.; Guggisberg, M.; Güntherodt, H.-J. *J. Vac. Sci. Technol., B* **1996,** *14,* 1285–1288. doi:10.1116/1.589082
23. Podgaynyy, N.; Iqbal, S.; Baltruschat, H. *Surf. Sci.* **2015,** *631,* 67–72. doi:10.1016/j.susc.2014.07.026
24. Magnussen, O. M.; Hotlos, J.; Nichols, R. J.; Kolb, D. M.; Behm, R. J. *Phys. Rev. Lett.* **1990,** *64,* 2929. doi:10.1103/PhysRevLett.64.2929
25. Kolb, D. M. *Ber. Bunsen-Ges. Phys. Chem.* **1994,** *98,* 1421–1432. doi:10.1002/bbpc.19940981110
26. Zei, M. S.; Qiao, G.; Lehmpfuhl, G.; Kolb, D. M. *Ber. Bunsen-Ges. Phys. Chem.* **1987,** *91,* 349–353. doi:10.1002/bbpc.19870910423
27. Gordon, J. G.; Melroy, O. R.; Toney, M. F. *Electrochim. Acta* **1995,** *40,* 3–8. doi:10.1016/0013-4686(94)00238-V
28. Shi, Z.; Lipkowski, J. *J. Electroanal. Chem.* **1994,** *365,* 303–309. doi:10.1016/0022-0728(93)03207-6
29. Sader, J. E.; Chon, J. W. M.; Mulvaney, P. *Rev. Sci. Instrum.* **1999,** *70,* 3967–3969. doi:10.1063/1.1150021
30. Podgaynyy, N. AFM-Untersuchungen auf Elektrodenoberflächen. Ph.D. Thesis, University of Bonn, Bonn, Germany, May 2013.
31. Hölzle, M. H.; Retter, U.; Kolb, D. M. *J. Electroanal. Chem.* **1994,** *371,* 101–109. doi:10.1016/0022-0728(93)03235-H
32. Dong, Y.; Perez, D.; Voter, A. F.; Martini, A. *Tribol. Lett.* **2011,** *42,* 99–107. doi:10.1007/s11249-011-9750-5
33. Roth, R.; Glatzel, T.; Steiner, P.; Gnecco, E.; Baratoff, A.; Meyer, E. *Tribol. Lett.* **2010,** *39,* 63–69. doi:10.1007/s11249-009-9567-7
34. Medyanik, S. N.; Liu, W. K.; Sung, I.-H.; Carpick, R. W. *Phys. Rev. Lett.* **2006,** *97,* 136106. doi:10.1103/PhysRevLett.97.136106
35. Dienwiebel, M.; Verhoeven, G. S.; Pradeep, N.; Frenken, J. W. M.; Heimberg, J. A.; Zandbergen, H. W. *Phys. Rev. Lett.* **2004,** *92,* 126101. doi:10.1103/PhysRevLett.92.126101
36. Li, H.; Wood, R. J.; Rutland, M. W.; Atkin, R. *Chem. Commun.* **2014,** *50,* 4368–4370. doi:10.1039/c4cc00979g

License and Terms

BEILSTEIN JOURNAL OF NANOTECHNOLOGY

Stiffness of sphere–plate contacts at MHz frequencies: dependence on normal load, oscillation amplitude, and ambient medium

Jana Vlachová, Rebekka König and Diethelm Johannsmann*

Full Research Paper

Address:
Clausthal University of Technology, Institute of Physical Chemistry,
Arnold-Sommerfeld-Straße 4, 38678 Clausthal-Zellerfeld, Germany

Email:
Diethelm Johannsmann* - johannsmann@pc.tu-clausthal.de

* Corresponding author

Keywords:
contact mechanics; contact splitting; contact stiffness; partial slip;
quartz crystal microbalance

Beilstein J. Nanotechnol. **2015,** *6,* 845–856.
doi:10.3762/bjnano.6.87

Received: 16 October 2014
Accepted: 09 March 2015
Published: 30 March 2015

This article is part of the Thematic Series "Advanced atomic force microscopy techniques III".

Guest Editor: T. Glatzel

Abstract

The stiffness of micron-sized sphere–plate contacts was studied by employing high frequency, tangential excitation of variable amplitude (0–20 nm). The contacts were established between glass spheres and the surface of a quartz crystal microbalance (QCM), where the resonator surface had been coated with either sputtered SiO_2 or a spin-cast layer of poly(methyl methacrylate) (PMMA). The results from experiments undertaken in the dry state and in water are compared. Building on the shifts in the resonance frequency and resonance bandwidth, the instrument determines the real and the imaginary part of the contact stiffness, where the imaginary part quantifies dissipative processes. The method is closely analogous to related procedures in AFM-based metrology. The real part of the contact stiffness as a function of normal load can be fitted with the Johnson–Kendall–Roberts (JKR) model. The contact stiffness was found to increase in the presence of liquid water. This finding is tentatively explained by the rocking motion of the spheres, which couples to a squeeze flow of the water close to the contact. The loss tangent of the contact stiffness is on the order of 0.1, where the energy losses are associated with interfacial processes. At high amplitudes partial slip was found to occur. The apparent contact stiffness at large amplitude depends linearly on the amplitude, as predicted by the Cattaneo–Mindlin model. This finding is remarkable insofar, as the Cattaneo–Mindlin model assumes Coulomb friction inside the sliding region. Coulomb friction is typically viewed as a macroscopic concept, related to surface roughness. An alternative model (formulated by Savkoor), which assumes a constant frictional stress in the sliding zone independent of the normal pressure, is inconsistent with the experimental data. The apparent friction coefficients slightly increase with normal force, which can be explained by nanoroughness. In other words, contact splitting (i.e., a transport of shear stress across many small contacts, rather than a few large ones) can be exploited to reduce partial slip.

Introduction

Partial slip is a widespread and multifacetted phenomenon. When a contact experiences partial slip, parts of a contact stick to each other under a tangential stress, while others slide. Partial slip is found in many tribological situations of practical relevance. This includes fretting wear [1,2] granular media [3], earthquakes [4], and the collision between particles [5]. Early models of partial slip were formulated independently by Cattaneo [6] and Mindlin [7], who were concerned with a Hertzian contact. If the entire contact area sticks, a continuum treatment predicts a stress singularity at the rim of the contact (Figure 1A). However, infinite stress is unrealistic, and among the mechanisms removing the singularity is partial slip. Partial slip implies that those areas, where the tangential stress exceeds a certain critical value, slide and thereby lower the local stress. Cattaneo and Mindlin assumed that the frictional stress in the sliding zone, σ, is proportional to the normal pressure, p, as in Coulomb friction (Figure 1C). The ratio of σ and p is the friction coefficient, μ. From the Cattaneo–Mindlin (CM) model, one can derive predictions for the width of the sliding region (which is of annular shape) and for the force–displacement relation (Figure 2D below) [8,9].

Partial slip as such is an accepted and frequently observed phenomenon. The details of the CM model, however, are being debated for a variety of reasons. Etsion [11] gives a detailed account. The first category of problems originates from the numerous assumptions in the formulation of the model. For example, the normal pressure is assumed to stay constant during tangential loading. A second set of limitations is related to the idealized conditions. The CM model ignores roughness, capillary forces, plastic deformation, and the effects of contamination. In particular, plastic deformation can lead to junction growth, which stiffens the contact rather than weakening it [12,13].

There is a particular shortcoming that is on the one hand widely observed, but also easily fixed on a heuristic level on the other. The CM model ignores viscous dissipation. In consequence, the energy dissipated in reciprocating sliding scales as the cube of the oscillation amplitude in the low-amplitude limit. Following from this scaling law, the damping of a resonator, which experiences particle slip in one way or another, should go to zero at small amplitudes. An explanation of the contact resonance method, which probes these relations, is given below. Deviating from this scaling prediction, the contacts usually do damp a resonance even at the smallest accessible amplitudes. This type of damping must be related to linear viscoelasticity, meaning that the corresponding stresses are proportional to displacement (Figure 2C). While such viscous processes are not contained in

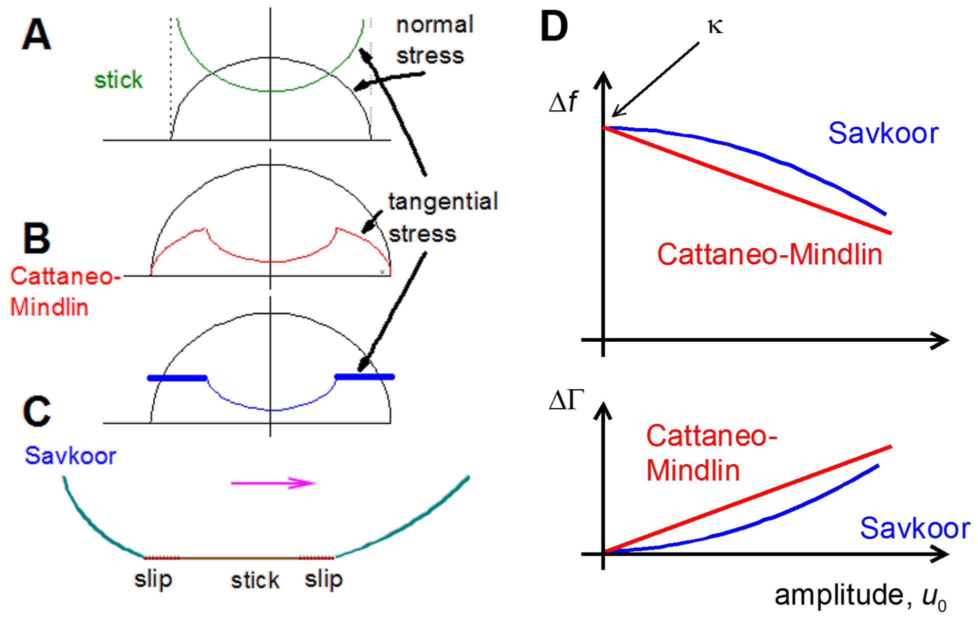

Figure 1: Sketch of the mechanisms underlying partial slip. A Hertzian contact under a tangential load has infinite tangential stress at the edge of the contact (A). This singularity is removed by allowing for slip in a circular region close to the edge. In CM theory, the tangential stress in the sliding region is proportional to the normal stress, where the latter follows the Hertz model (B). In an alternative model formulated by Savkoor, the tangential stress in the sliding region is constant (C). When probing such contacts with the contact resonance method, the two models lead to different dependences of the shifts in frequency, Δf, and shifts in bandwidth, $\Delta\Gamma$, on the amplitude, u_0. Δf and $\Delta\Gamma$ depend linearly and quadratically on amplitude for the CM model and the Savkoor model, respectively (D).

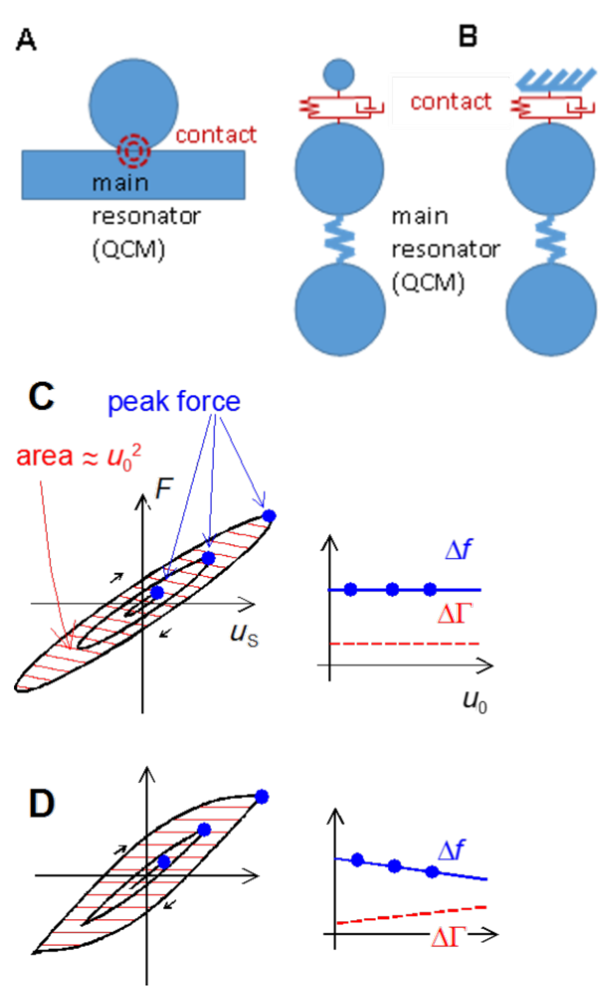

Figure 2: (A) For a narrow contact between a sphere and a plate, deformation occurs close to the contact, only. The contact may be depicted as a spring, or more generally, as a Voigt element, where the latter also accounts for viscous dissipation (B). In the case, where the sphere is heavy enough to be clamped in space by inertia, it can be depicted as a wall (right-hand side in B). (C,D): Illustration of how Δf and $\Delta\Gamma$ depend on the shape of the force–displacement loop. (C): viscoelastic contact and (D): partial slip according to Cattaneo and Mindlin. The frequency shift is roughly proportional to the ratio of force and displacement at the turning point (full dots). $\Delta\Gamma$ is proportional to the area inside the loop divided by u_0^2 (hatched). (C) and (D) adapted with permission from [10], copyright 2013 the American Physical Society.

the CM model, they can be added into it in an ad hoc manner (see Equation 12).

In the Results and Discussion section, we address a further rather fundamental criticism of the CM model, which starts out from the extent to which a macroscopic view of friction guides its formulation. Macroscopic concepts enter the CM model at two separate instances. Firstly, a sliding stress proportional to the normal pressure is commonly associated with Coulomb friction. In Coulomb friction, the tangential force is related to the actual area of contact, to be distinguished from the nominal area of contact due to surface roughness. These arguments should not apply on the nanoscale. Savkoor has responded to this criticism with a modified model of partial slip, which assumes the tangential stress in the sliding zone to be constant, independent of normal pressure [14,15]. The value of the constant stress, τ_0, is the free parameter of the model. Savkoor solved the equations of continuum elasticity and derived the force–displacement relations. These relations differ from the CM model in the details, but deciding between the two models based on the shape of the force–displacement loop is somewhat of a challenge. Interestingly, it is rather easy to distinguish between the Savkoor model and the Cattaneo–Mindlin model with the contact resonance method because the Cattaneo–Mindlin model predicts a linear dependence of frequency and bandwidth on amplitude, while the same relations are parabolic if derived from the Savkoor model. This difference is easily observed in experiment [16].

A second element of the CM model of genuinely macroscopic nature is the notion of a stress singularity at the edge of the contact. It is essential that this peak in stress at the edge is indeed strong enough to locally initiate sliding. Gao and Yao have mathematically analyzed a related problem, namely the detachment of a fiber end from a flat surface under tensile load [17]. Such a contact displays a peak in tensile stress at the edge, which governs the pull-off force if the contact diameter is larger than about 100 nm. Pull-off then results in crack propagation. Partial slip in the Cattaneo–Mindlin sense also results in crack propagation, where the modes of crack opening are II and III, as opposed to mode I, which operates during pull-off [18]. Gao and Yao find that the crack propagation mechanism becomes inefficient once the contact diameter falls to below 100 nm. For small contacts, the stress concentration at the edge becomes less and less significant. Translated to the tangential load problem, the analysis by Gao and Yao shows that the transition from stick to slip may occur by crack propagation (that is, by partial slip in the Cattaneo–Mindlin sense), but that small contacts may also start to slide as a whole. Even if partial slip at individual contacts is found, it is expected to be more prominent for larger contacts because the maximum level of stress depends on the ratio of the contact diameter to the radius of the crack tip.

From an engineering perspective, partial slip (also called microslip) has a slightly different meaning. It mostly denotes a small tangential displacement at contacts between rough surfaces. These small displacements per se have little influence on the strength of the contact. They are still of immense practical relevance because they cause fretting wear [19-21], which is a special type of corrosion. Microslip at multicontact interfaces is different from partial slip in the Cattaneo–Mindlin sense because it involves a debonding of the weakly coupled load–bearing asperities and, also, because new contacts can form at large relative displacements [22]. Depending on the distance between the individual load–bearing asperities, these are elastically coupled to each other [23]. If the contacts are tightly coupled, there is crack propagation with a peak in stress at the crack tip. Otherwise, the analysis should be based on an ensemble of contacts with a distribution in contact stiffness and contact stress. Bureau et al. have provided such a model [24], making extensive use of the Greenwood–Williamson formalism [25].

The experiments below rely on the contact resonance method. The contact resonance method is also applied on the macroscopic scale [26] and in AFM-based metrology [27]. In particular, the mathematics is closely related to what was reported in [28] and [29]. Differing from many experiments performed with AFM [30,31], the contacts here have a substructure and it is this substructure, which gives rise to the phenomena under discussion. Also, hysteresis is more important in QCM experiments than in AFM experiments. A contact is established between a resonator (which is a quartz crystal microbalance here and is the cantilever in AFM experiments) and an external object. The geometry is configured such that the contact does not overdamp the resonance, but rather shifts the resonance frequency and the resonance bandwidth by small amounts (termed Δf and $\Delta\Gamma$ below). The contact resonance method is well suited to detect nonlinear force–displacement relations because nonlinear behavior leads to a dependence of Δf and $\Delta\Gamma$ on amplitude, u_0, while such a dependence is absent when the system obeys a linear response. Partial slip results in a nonlinearity and whether or not a contact undergoes partial slip can therefore be inferred from the dependence of Δf and $\Delta\Gamma$ on the amplitude. More quantitatively, the Cattaneo–Mindlin model predicts Δf and $\Delta\Gamma$ to scale linearly with u_0 in the low-amplitude limit and this prediction can be tested easily.

The experiments were undertaken with a quartz crystal microbalance (QCM). The QCM is mostly known as a device for thickness determination, but it can equally well be employed to measure contact stiffness. In this regard, it is helpful to view the QCM as a shear wave reflectometer. The amplitude and the phase of the wave reflected at an interface is related to the stiffness of this interface. Acoustic reflectometry was used to measure contact stiffness as early as 1971 [32]. The work reported below is concerned with discrete contacts (as opposed to a multicontact interface), but the physical picture is closely analogous to what is developed in [32]. The presence of contacts at a resonator surface changes the reflectivity of the resonator surface and thereby changes the resonator's frequency and its bandwidth [26].

There is a different (but equivalent) way of explaining the measurement principle. The resonator can be represented by a lumped element circuit [33], as shown in Figure 2B. The main resonator is at the bottom. Its resonance frequency is given as $2\pi(\kappa_R/M_R)^{1/2}$ where κ_R is the effective stiffness and M_R is the effective mass. The sample is the small sphere at the top. Because the contact zone is small (Figure 2A), it can be represented by a spring and a dashpot arranged in parallel (a Voigt element). If the resonator is coated with a rigid thin film (or with nanoparticles rigidly attached to the surface), this load increases the resonator's effective mass, thereby lowering the resonance frequency. In the lumped element representation, this amounts to the sphere at the top in Figure 2B being small and the spring being stiff. Applied in this mode, the QCM determines the value of the effective mass, hence the name "microbalance". However, millimeter-sized spheres such as the ones studied here are not samples of this kind. They are so heavy that they do not follow the resonator's MHz motion, but rather are clamped in space by inertia [34]. In the lumped element representation, they are depicted as a wall, attached to the surface across a spring and a dashpot (a Voigt element). It is essential that the contact diameter is much smaller than both the sphere diameter and the wavelength of sound. The deformation is then localized; the bulk of the sphere remains undeformed. The force follows from integration of the stress distribution over the contact area; the displacement is evaluated in the undeformed regions far outside the contact zone. The ratio of force and displacement is the contact stiffness. As we show in the modeling section, the spring constant and the dashpot's drag coefficient can be easily determined from the shifts of frequency and bandwidth. The ratio of the two represents the loss tangent.

The representation of the contact as a Voigt element only holds as long as the contact behaves linearly. Partial slip, however, results in a nonlinear behavior. Even in the precense of partial slip, one can use the lumped element representation for the sake of an intuitive understanding. Roughly speaking, the apparent contact stiffness decreases at elevated amplitudes because the sticking portion of the contact decreases. The "apparent contact stiffness" here is the stiffness as derived from the frequency shift (Equation 2 below). This intuitive picture can be backed up with a rigorous mathematical model. We briefly recapitulate the mathematics in the modeling section.

In previous work [10], we have reported details of the experimental setup and elaborated on the mathematical details of what the Cattaneo–Mindlin model and the Savkoor model predict for the functions $\Delta f(u_0)$ and $\Delta\Gamma(u_0)$. The authors in [10] focused on how the amount of partial slip depends on contact size. For the current work, the sphere size was chosen large enough to always guarantee partial slip. An improved experimental setup allowed for a detailed quantitative analysis in both the linear and the nonlinear regime. All experiments were repeated 9 times, which allows for a robust analysis of statistical errors. Finally, we compare experiments undertaken in air to experiments using the same sample, but immersed in water.

Experimental

Modeling

A QCM loaded with discreate contacts: linear and nonlinear regime

We first consider the viscoelastic contact. According to the small-load approximation, the complex frequency shift at small amplitude is given as [35,36]

$$\Delta f + \mathrm{i}\Delta\Gamma = \frac{\mathrm{i}f_{\mathrm{F}}}{\pi Z_{\mathrm{q}}}\frac{\langle\sigma_0\rangle}{\mathrm{i}\omega u_0} = \frac{n_{\mathrm{P}}}{2n\pi^2 A_{\mathrm{eff}} Z_{\mathrm{q}}}\left(\kappa + \mathrm{i}\omega\xi\right). \qquad (1)$$

Δf and $\Delta\Gamma$ are the shifts of the frequency and the half-bandwidth at half-height, respectively. The parameter Γ is related to the dissipation factor, D, by $D = \Gamma/(2f)$. f_{F} is the fundamental frequency, which is often 5 MHz. $Z_{\mathrm{q}} = 8.8 \times 10^6$ kg·m^{-2}s^{-1} is the shear wave impedance of AT-cut quartz. $\langle\sigma_0\rangle$ is the area-averaged complex amplitude of the tangential stress at the resonator surface, and u_0 is the amplitude of oscillation. The ratio of stress and velocity (where the latter is equal to $\mathrm{i}\omega u_0$) is the complex load impedance, Z_{L}. In the second step in Equation 1, the stress was converted to force by area. The force, in turn, was expressed as tangential stiffness times amplitude (that is, as κu_0). n is the overtone order, n_{P} is the number of spheres, and A_{eff} is the acoustically effective area (similar to the electrode area, A_{eff} can be derived from the experimental data [10]). κ is the tangential stiffness of an individual contact (to be distunguished from the stiffness of a multi-contact interface [22]). The term $\mathrm{i}\omega\xi$ acounts for viscous dissipation, where ξ is the drag coefficient. ξ quantifies linear processes in the sense that the stress is proportional to the rate of displacement. No statement is made on the mechanism(s) leading to dissipation. The drag coefficient may be linked to the viscoelastic nature of the materials involved, but also to interfacial processes (as long as these obey linear mechanics). Equation 1 can be inverted as

$$\kappa + \mathrm{i}\omega\xi = \frac{2n\pi^2 A_{\mathrm{eff}} Z_{\mathrm{q}}}{n_{\mathrm{p}}}\left(\Delta f + \mathrm{i}\Delta\Gamma\right). \qquad (2)$$

As shown in Equation 2, the complex frequency shift is easily converted to a complex contact stiffness.

Up to now, linear force–displacement relations were assumed. If linearity does not hold, the stress, $\sigma(t)$, is no longer time harmonic. In consequence, there is no complex amplitude, σ_0, which could be inserted into Equation 1. Importantly, a non-trivial time dependence can be accounted for in an expanded model. As long as stress is periodic with the frequency of the resonator (but of any other shape otherwise), the QCM measures the first Fourier component of $\sigma(t)$. It then follows that [36,37]

$$\begin{aligned}\Delta f(u_0) + \mathrm{i}\Delta\Gamma(u_0) &= \frac{1}{2n\pi^2 Z_{\mathrm{q}}}\frac{2}{u_0}\left\langle\sigma(t)\exp(\mathrm{i}\omega t)\right\rangle_{\mathrm{area,time}} \\ &= \frac{n_{\mathrm{P}}}{2n\pi^2 A_{\mathrm{eff}} Z_{\mathrm{q}}}\frac{2}{u_0}\left\langle F(t)\exp(\mathrm{i}\omega t)\right\rangle_{\mathrm{time}}\end{aligned} \qquad (3)$$

In the 2nd line of Equation 3, stress was replaced by the force at the contacts, $F(t)$, multiplied by the number density of the contacts, $n_{\mathrm{P}}/A_{\mathrm{eff}}$. There is a close analogy between Equation 3 and the principle of operation of lock-in amplifiers. Δf and $\Delta\Gamma$ are proportional to the in-phase and the out-of-phase components of the force.

Underlying both Equation 1 and Equation 3 is the small load approximation, which states that the load impedance (often called Z_{L}, the ratio of σ_0 and $\mathrm{i}\omega u_0$) is much smaller than the acoustic shear wave impedance of the crystal, Z_{q}. The small load approximation holds as long as $\Delta f/f_{\mathrm{F}} << 1$, which is almost always true. If the load is small in this sense, the magnitude of the force is so small that the motion of the resonator surface remains approximately sinusoidal. Put differently, the QCM surface is under displacement control. For that reason, the time average in Equation 3 can be converted to an average over displacement, u. Note: In general, the force, F, will not only depend on displacement, u, but also on the maximum displacement, u_0, and on the frequency, ω. Because the trajectories differ between the two directions of motion, averaging must occur separately for the two directions. The two forces are called $F_{-}(u,u_0,\omega)$ and $F_{+}(u,u_0,\omega)$, in the following, where the indices “−” and “+” denote movement toward negative and positive u. The chain of algebraic conversions must be $F_{\pm}(u,u_0,\omega) \rightarrow F(t) \rightarrow \{\Delta f(u_0), \Delta\Gamma(u_0)\}$. The first entry must be $F_{\pm}(u,u_0,\omega)$, not $F(u)$. By letting the forces depend on u, u_0, and ω, we do not mean to exclude a dependence on velocity. Such a dependence on velocity would implicitly enter $F_{+}(u,u_0,\omega)$ and $F_{-}(u,u_0,\omega)$ since the velocity itself is a function of u and ω, given as $\mathrm{i}\omega u$.

The transformation from $F_{\pm}(u,u_0,\omega)$ to $\Delta f(u_0)$ and $\Delta\Gamma(u_0)$ take the form [10] of Equation 4 and Equation 5. The frequency

$$\begin{aligned}\Delta f\left(u_0\right) &= \frac{n_\mathrm{P}}{n\pi^2 A_\mathrm{eff} Z_\mathrm{q}} \frac{1}{u_0^2} \frac{1}{2\pi} \int_{-u_0}^{u_0} \left(F_-\left(u,u_0,\omega\right)+F_+\left(u,u_0,\omega\right)\right) \frac{u/u_0}{\sqrt{1-\left(u/u_0\right)^2}} \mathrm{d}u \\ &= \frac{n_\mathrm{P}}{n\pi^2 A_\mathrm{eff} Z_\mathrm{q}} \frac{1}{u_0} \frac{1}{2\pi} \int_{-1}^{1} \left(F_-\left(u,u_0,\omega\right)+F_+\left(u,u_0,\omega\right)\right) \frac{u/u_0}{\sqrt{1-\left(u/u_0\right)^2}} \mathrm{d}\left(\frac{u}{u_0}\right)\end{aligned} \tag{4}$$

$$\Delta\Gamma\left(u_0\right) = \frac{n_P}{n\pi^2 A_{eff} Z_q} \frac{1}{u_0^2} \frac{1}{2\pi} \int_{-u_0}^{u_0} \left(F_+\left(u,u_0,\omega\right)-F_-\left(u,u_0,\omega\right)\right)\mathrm{d}u \tag{5}$$

shift, Δf, is proportional to a weighted sum of F_+ and F_-. The integrand in Equation 4 is symmetric in u/u_0. The integral may therefore be evaluated at positive values of u/u_0, only. The term $u/u_0(1-(u/u_0)^2)^{-1/2}$ then is positive and takes the role of a statistical weight. Δf is proportional to a weighted average of $|F_- + F_+|$, where the weight function has a sharp peak at $u \approx u_0$. As the relation in the second line of Equation 4 shows, Δf roughly scales as the force at the turning point divided by u_0. The shift in bandwidth is proportional to the difference of F_+ and F_- (Equation 5). In essence, it is the area under the force–displacement loop and thereforce scales as u_0^2. The bandwidth is proportional to this area divided by u_0^2.

Figure 2C, D illustrates the content of Equation 4 and Equation 5 in graphical form. For viscoelastic contacts, the force–displacement loop is an ellipse. The ratio of force and displacement at the peak (full dots) is independent of amplitude, u_0, and Δf therefore also is independent of u_0. The area inside the friction loop scales as u_0^2, and $\Delta\Gamma$ therefore also is independent of u_0. This may change, if the force–displacement loop takes some other shape. Figure 2D shows the force–displacement loop according to Cattaneo and Mindlin. For contacts following the CM model, Δf and $\Delta\Gamma$ decrease and increase with amplitude, respectively.

Partial slip and its consequences for a QCM experiment: predictions derived from the Cattaneo–Mindlin model and the Savkoor model

In Cattaneo–Mindlin theory, the tangential force, F_x, and the tangential displacement, u, are related as [8]

$$\frac{F_x}{\mu F_\mathrm{N}} = 1-\left(1-\frac{2}{3}\frac{\kappa u}{\mu F_\mathrm{N}}\right)^{3/2} \tag{6}$$

F_N is the normal force and μ is the friction coefficient in the Coulomb sense. No distinction is made between the static and the dynamic friction coefficient. $\kappa = 2G^*a$ is the contact stiffness in the low-amplitude limit. a is the contact radius and G^* is an effective modulus. The frequency shift, Δf, is related to the contact stiffness, κ, by Equation 2. G^* is the effective modulus, given as

$$G^* = \left(\frac{2-\nu_1}{4G_1}+\frac{2-\nu_2}{4G_2}\right)^{-1} \tag{7}$$

G and v are the shear modulus and the Poisson ratio, respectively. The indices 1 and 2 label the contacting media. Given that the contact diameter can be estimated to be larger than 1 µm, we ignore the thin films present (SiO_2, PMMA, gold) and use the same values on both sides.

For the sake of quantitative modeling (see Figure 5 below) we keep the Poisson number fixed at $v_1 = v_2 = 0.17$ and express the shear modulus as

$$G = \frac{E}{2\left(1+v\right)} \tag{8}$$

where E is the Young's modulus and E is a fit parameter. The contact radius, a, is assumed to obey the JKR equation, which is

$$a^3 = \frac{3R}{4E^*}\left(F_\mathrm{N}+6\pi\gamma R+\left(12\pi\gamma R F_\mathrm{N}+\left(6\pi\gamma R\right)^2\right)^{1/2}\right) \tag{9}$$

where R is the (known) sphere radius, γ is the energy of adhesion and E^* is another effective modulus, given as

$$\frac{1}{E^*} = \frac{1-v_1^2}{E_1}+\frac{1-v_2^2}{E_2}. \tag{10}$$

As before, $v_1 \approx v_2 \approx 0.17$ is assumed. Also, E_1 was assumed to be the same as E_2 ($E_1 \approx E_2 = E$) with E a fit parameter. The energy of adhesion, γ, was also a fit parameter. All other parameters were fixed.

Inserting the force–displacement relation from Equation 6 into Equation 4 and Equation 5 and, further, expanding the result to first order in u_0, one finds [10]

$$\begin{aligned}\Delta f\left(u_0\right) &\approx \frac{n_\mathrm{P}}{2n\pi^2 A_\mathrm{eff} Z_\mathrm{q}}\kappa\left(1-\frac{\kappa}{3\mu F_\mathrm{N}}u_0\right)\\ \Delta\Gamma\left(u_0\right) &\approx \frac{n_\mathrm{P}}{2n\pi^2 A_\mathrm{eff} Z_\mathrm{q}}\frac{4}{9\pi}\frac{\kappa^2}{\mu F_\mathrm{N}}u_0\end{aligned} \tag{11}$$

At this point, we slightly extend the CM model by including viscous dissipation. On a heuristic basis, we add a viscous term into ΔΓ which accounts for dissipative processes with a linear dependence on stress:

$$\begin{aligned}\Delta f\left(u_0\right) &\approx \frac{n_\mathrm{P}}{2n\pi^2 A_\mathrm{eff} Z_\mathrm{q}}\kappa\left(1-\frac{\kappa}{3\mu F_\mathrm{N}}u_0\right)\\ \Delta\Gamma\left(u_0\right) &\approx \frac{n_\mathrm{P}}{2n\pi^2 A_\mathrm{eff} Z_\mathrm{q}}\omega\xi\left(1+\frac{4}{9\pi}\frac{\kappa}{\omega\xi}\frac{\kappa}{\mu F_\mathrm{N}}u_0\right)\end{aligned} \tag{12}$$

As Equation 12 shows, the Cattaneo–Mindlin theory predicts Δf and $\Delta\Gamma$ to depend linearly on u_0.

Savkoor [14,38] has formulated a modified model of partial slip, which assumes the traction in the sliding zone to be constant with a value of τ_0, rather than being proportional to the normal stress as in CM theory. The force–displacement relation resulting from the Savkoor model is

$$F_x = 2\tau_0 a^2\left(\arccos\left(\frac{c}{a}\right)+\frac{c}{a}\sqrt{1-\frac{c^2}{a^2}}\right) \tag{13}$$

where a is the radius of contact and c is the radius of the sticking area, given as

$$c = a\sqrt{1-\frac{G^{*2}}{\left(2\tau_0 a\right)^2}u^2} \tag{14}$$

Inserting Equation 13 into Equation 4 and Equation 5 and, further, expanding the result to second order in u_0, one finds [10]:

$$\begin{aligned}\Delta f\left(u_0\right) &\approx \frac{n_\mathrm{P}}{2n\pi^2 A_\mathrm{eff} Z_\mathrm{q}}\kappa\left(1-\frac{5}{8}\left(\frac{\kappa u_0}{4\tau_0 a^2}\right)^2\right)\\ \Delta\Gamma\left(u_0\right) &\approx \frac{n_\mathrm{P}}{2n\pi^2 A_\mathrm{eff} Z_\mathrm{q}}\omega\xi\left(1+\frac{8}{6\pi}\left(\frac{\kappa}{\omega\xi}\frac{\kappa u_0}{2\tau_0 a^2}\right)^2\right)\end{aligned} \tag{15}$$

The dependence of Δf and $\Delta\Gamma$ on amplitude is now parabolic, whereas it is linear in the CM model.

Experimental details

The geometry of the experiment was based on a tripod configuration as shown in Figure 3. Three glass spheres with a diameter of either 2.2 mm or 1.2 mm were glued to a backing plate in the form of an equilateral triangle. The tripod was placed onto the center of the plate, where the distance of the individual contacts to the center was less than 3 mm. The three points of contact experience the same normal force and the same amplitude of motion. The weight of the tripod alone was 0.5 g. Additional weights between 0.5 and 2.5 g were added onto the backing plate, thereby increasing the normal force. There was a frame with a cylindrical hole around the backing plate, which prevented its lateral movement. With this frame in place, the sample did not shift laterally when the weight was added. The frame was essential for obtaining reproducible results.

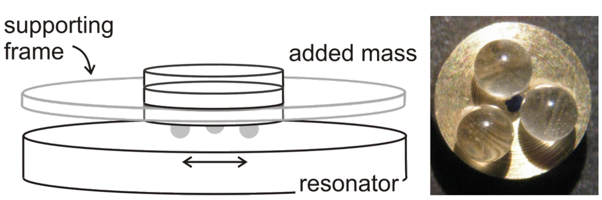

Figure 3: Left: Sketch of the experimental geometry. The contacts are formed between a tripod (center top) and the resonator plate. The three spheres (in grey) carry an equal normal load and experience equal amplitudes of oscillation. The normal force is changed by adding weight on the top. A fixed frame around the tripod ensures that the tripod does not shift when weight is added or removed at the top. Right: Image of a Tripod.

Shifts of frequency and bandwidth were acquired with impedance analysis. One frequency sweep took about 1 s. Each amplitude ramp consisted of 10–15 steps. All ramps were repeated four times (two increasing and two decreasing ramps). The first ramp often gave results different from the following three ramps. This type of running-in behavior was not further investigated. Most of the time, the data from ramps 2– 4 agreed with each other within the experimental error. In particular, there were no systematic differences between increasing and decreasing ramps. Occasionally, a slow drift was superimposed onto the ramps. Quartz resonators respond to changes in temperature and static stress with slow drifts. Drifts can be reduced by mounting the crystals in the holder one day before the experiment and by controlling temperature, but they cannot be avoided altogether. Experiments were undertaken in ambient air with no additional control of temperature or humidity. For further details on the experiment (on the processing of raw data and on the calculation of the amplitudes, in particular) see [10]. Experiments were carried out with either SiO_2-coated resonators (purchased from Inficon) or PMMA-coated resonators. The thickness of the spin-cast PMMA layer was 250 nm. Previous experiments did not find evidence of an influence of the thickness of a glassy polymer on the contact stiffness.

All experiments were carried out in both air and water. Deionized water was used throughout, but the water was not degassed. A sample, which had been previously studied in air, was flooded with water. The water level was about 3 mm; however, the exact height was not an important parameter because the QCM only senses the conditions inside the first micron of a liquid sample.

Results and Discussion

Figure 4 shows a number of amplitude sweeps. The four graphs at the top and the four graphs at the bottom display data acquired in air and in water, respectively. Because water damps the crystal's resonance, the maximum amplitude achieved was 6 nm (compared to an amplitude of ≈20 nm in air). $\Delta f\,(u_0)$ is always a decreasing function of amplitude, u_0 (panels on the left-hand side), while $\Delta\Gamma$ increases with u_0 (on the right). Figure 4A,B,E,F displays what was observed most of the time (in >80% of the experiments): Most of the time, Δf and $\Delta\Gamma$ were linear functions of u_0. Occasionally, the data show a plateau at small amplitudes. These plateaus have been discussed in detail in [39]. They can be associated with a critical minimum amplitude for partial slip. A plateau occurred often for the small spheres (diameters <500 µm) examined in [10]. Further discussion is outside the scope of this work. Large spheres were chosen here in order to achieve a linear dependence of Δf and $\Delta\Gamma$ on u_0. If linear behavior is observed, the complex spring constant in the low-amplitude limit is readily extracted from the data by extrapolation (see Figure 5 and Figure 7 below). Likewise, the friction coefficient as derived from the slopes of $\Delta f(u_0)$ and $\Delta\Gamma(u_0)$ is a robust parameter (see Figure 8 below).

Very rarely, we see an increase of Δf with amplitude (data not shown). This behavior might tentatively be associated with junction growth [12]. Most of the time Δf and $\Delta\Gamma$ decrease and increase with amplitude, characteristic for partial slip.

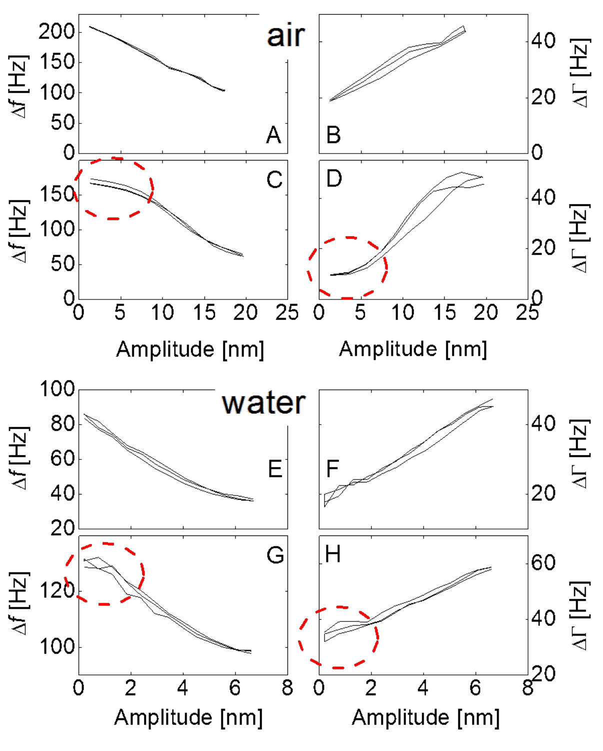

Figure 4: Data traces of frequency shift, Δ*f*, and bandwidth shift, ΔΓ, versus amplitude of oscillation. All data sets contain four amplitude sweeps. Data shown in the four panels at the top and the four panels at the bottom were acquired in air and in water, respectively. In liquids, the maximum achievable amplitude is lower than in air because of damping. Δ*f* and ΔΓ decrease and increase with amplitude, respectively, as is characteristic for partial slip. Panels A, B, E, and F show typical data traces. In these cases, the amplitude dependence is linear. Occasionally, one also finds plateaus at small amplitudes (dashed ellipses in panels C, D, G, and H). In these cases, the edge of the contact sticks at small amplitudes, where the exact conditions, under which such a stick occurs, are unclear. Even in these cases, the frequency–amplitude traces are clearly not parabolic (which should result if the Savkoor model was applicable).

Figure 5 shows the low-amplitude limits of Δf for the three different configurations studied. Full and open symbols correspond to data taken in air and in water, respectively. The fact that Δf_0 increases with normal load is easy to understand. With increasing load, the contact radius increases and the contact stiffness increases correspondingly. The dotted lines show an attempt to bring this understanding in line with the known models of contact mechanics. We fitted the data with the JKR model. (The Tabor parameter of the geometry under study is 10, which says that the JKR model should be applied, rather than the DMT model.)

Table 1 shows the derived values of the interfacial energy, γ, and the effective Young's modulus, *E*. While the values are reasonable, they scatter quite significantly between the different experiments and the different configurations. As far as the interfacial energy, γ, is concerned, part of the problem is that the

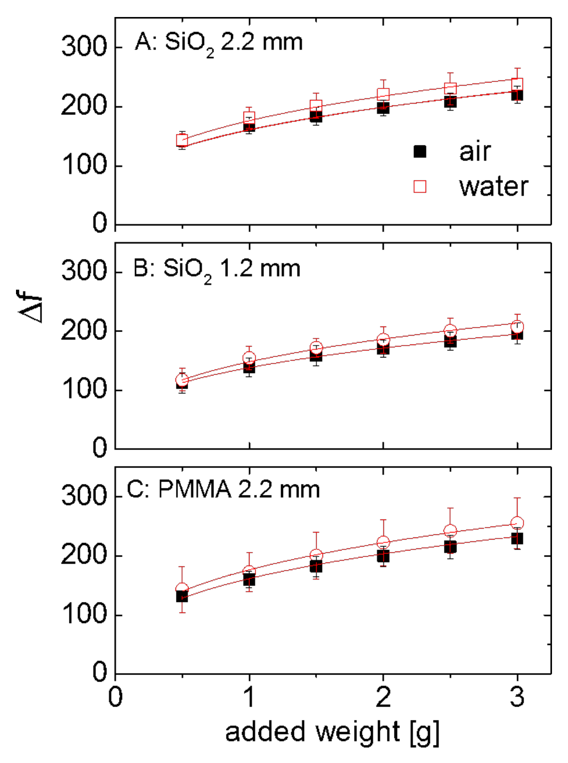

Figure 5: Frequency shifts in the low-amplitude limit obtained on silica surfaces (A and B) and on a PMMA surface (C). All data shown are averages from 9 experiments. Error bars are standard deviations. Dotted lines show JKR fits with parameters as given in Table 1.

loads are rather high. A more reliable determination of γ would require more data points close to the point of zero added weight. Clearly, the numbers must be interpreted with some caution. Possible sources of artifacts are roughness, contamination, and of course the idealized assumptions of the model. The high excitation frequency may also play a role. A systematic comparison with the tangential contact stiffness determined at low frequencies would certainly be worthwhile. Unfortunately, such experiments are difficult.

The contact stiffness increased when the sample was immersed in water. Note: The contacts were not broken between the two experiments. Water was admitted to the sample compartment without removing the spheres from the resonator. An increased stiffness in water contradicts intuition insofar, as one would expect the liquid to lower the effective van der Waals attraction. With lowered adhesive forces, the contact area should decrease and the contact stiffness should decrease, in consequence. However, this was not observed. The contact stiffness increased by about 10% in all cases.

At this point, the high frequency of the measurement presumably comes into play in the sense that the small compressibility of the liquid contributes to the contact stiffness. Figure 6 provides a sketch. When the resonator surface oscillates tangentially, the material close to the contact responds with a tangential movement, mostly, but one can also expect a small amount of rotation. The rotational component changes the width of the liquid wedge close to the contact, thereby inducing a squeeze flow of liquid. However, the mass involved in this movement is so large that inertia strongly resists the flow. (The sphere itself is clamped in space for the same reason). Because of inertial clamping, the sphere's rocking motion compresses the liquid and the liquid responds elastically to compression. The liquid's high bulk modulus in this way stiffens the contact. Again, this effect is genuinely linked to the experiment occurring at MHz frequency. It will be important when applying this methodology to biomaterials (which are usually studied in the liquid phase). The above interpretation clearly is tentative. Roughness may also play role. When water fills the micro-voids between the two surfaces, this may also increase the elastic stiffness of the contact.

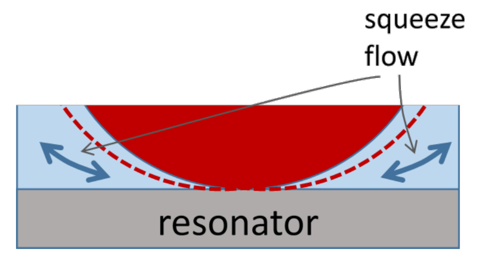

Figure 6: A sketch of an explanation for the increase in MHz contact stiffness when an experiment is undertaken in liquid rather than in air. A rocking motion of the sphere couples to a squeeze flow of liquid in the wedge next to the edge of the contact. Since inertia immobilizes the liquid, there is a significant amount of volume compression. The liquid responds elastically to compression.

Figure 7 addresses the linear components of the dissipative processes, quantified by the low-amplitude limit of ΔΓ, termed

Table 1: Fit Parameters for the data in Figure 5.

	air, γ [mN/m]	air, *E* [GPa]	water, γ [mN/m]	water, *E* [GPa]
SiO_2, 2.2 mm	190 ± 20	100 ± 3	50 ± 40	63 ± 6
SiO_2, 1.2 mm	30 ± 10	61 ± 2	20 ± 30	47 ± 5
PMMA, 2.2 mm	10 ± 10	70 ± 2	0	45 ± 3

$\Delta\Gamma_0$. In Figure 7B, Γ_0 was converted to a loss tangent by taking the ratio of $\Delta\Gamma_0$ and Δf_0. Interestingly, $\Delta\Gamma$ does not increase with normal load in the same way as Δf. It stays approximately constant. For that reason the loss tangent is a decreasing function of normal load. This result implies that the finite values of $\Delta\Gamma_0$ should not be viewed as a consequence of viscous dissipation inside the materials involved. If $\Delta\Gamma/\Delta f$ were a materials parameter, it should not depend on the normal load. Also, a loss tangent of 0.1 would be unreasonably high for fused silica. Rather, these dissipative processes should be attributed to the interface. Linear contributions to the dissipation in contact resonance experiments are well known [8,40]. While the exact nature of these processes would be interesting, the present experiments do not allow for a statement other than that they must be connected to interfacial friction in one way or another.

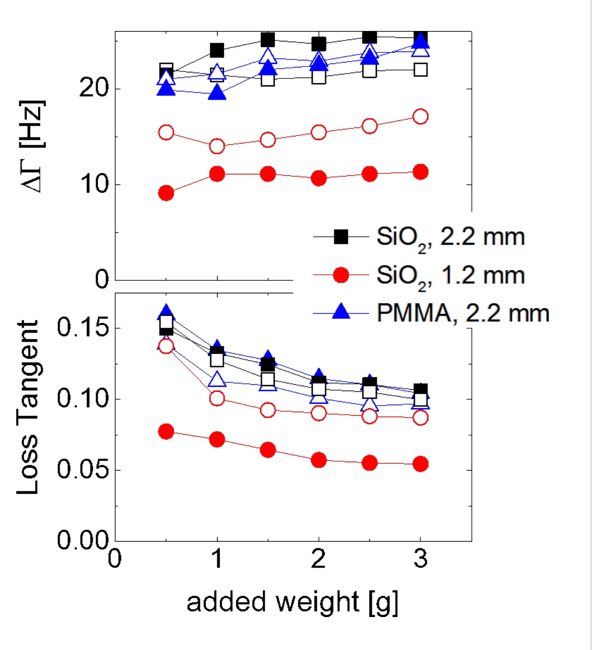

Figure 7: Shift in bandwidth, $\Delta\Gamma$ (top) and loss tangent, $\Delta\Gamma/\Delta f$, (bottom) in the low-amplitude limit. Full and open symbols denote measurements in air and water, respectively. The fact that $\Delta\Gamma$ is a constant independent of the normal load, suggests interfacial processes as the source of dissipation. If the dissipation were to occur in the material, one would expect the loss tangent to be constant, rather than $\Delta\Gamma$ itself, because a materials parameter should not depend on the normal load.

So far, the discussion has been concerned with linear contact mechanics. The experiment is easy and there are few other techniques that give access to the same data (mostly the AFM and ultrasonic reflectometry). Importantly, the QCM also accesses the (weakly) nonlinear regime and it does so rather easily, as well. As shown in Figure 4, most data sets show a linear dependence of Δf and $\Delta\Gamma$ on u_0. In the following, we use these data to derive the apparent friction coefficient from the slopes, following Equation 12.

Figure 8 displays these apparent friction coefficients. Firstly, the two ways to derive the friction coefficient (from $\Delta f(u_0)$ and $\Delta\Gamma(u_0)$) give reasonable agreement with each other. Secondly, the friction coefficients that result are in the range known from macroscopic mechanics (that is, on the order of unity). Thirdly, and importantly, the friction coefficients all decrease with normal load. The larger the contact area, the more pronounced is the partial slip. This finding is in line with the treatment of the pulling problem by Gao and Yao referred to in the Introduction. Partial slip occurs if the stress singularity at the edge is strong. The peak stress depends on the ratio of the contact radius to the radius of the crack tip and therefore increases as the normal force becomes larger. A different (but related) explanation builds on nanoscale roughness. Nanoroughness rounds off the stress profile at the edge, which avoids the stress singularity similarly to a finite radius of a crack tip. The load dependence of μ points to yet another benefit of “contact splitting” [40,41]. A large number of small contacts will experience less partial slip (less fretting wear) than a small number of correspondingly larger contacts.

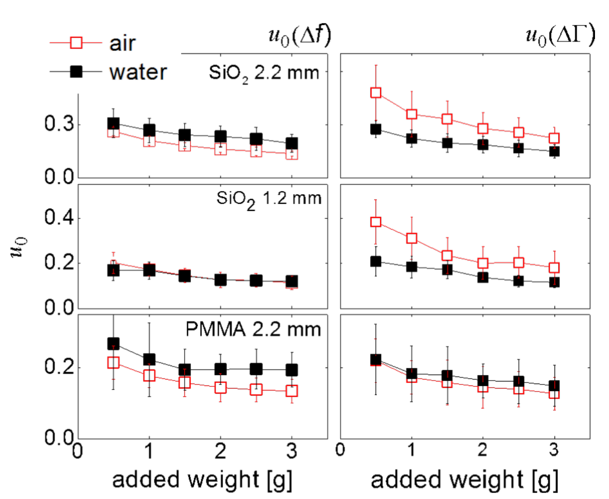

Figure 8: Friction coefficients, μ, obtained by analyzing the slopes in plots of Δf versus u_0 (left) and $\Delta\Gamma$ versus u_0 (right), following Equation 12. The two ways to derive μ should lead to the same values, ideally. Further, μ should be of the order of unity. The decrease of μ with increasing normal force can be explained with an increased contact area and a concomitant increase in the stress concentration at the edge of the contact.

A side remark: The agreement between the two friction coefficients (determined from $\Delta f(u_0)$ and $\Delta\Gamma(u_0)$) is better in water than in air. We suspect that capillary forces affect $\Delta\Gamma(u_0)$ stronger than $\Delta f(u_0)$. A more detailed discussion of the matter would require an extension of the Cattaneo–Mindlin model by specific contributions from different forces. Such an extension is outside the scope of this work, but it is possible. It is even worthwhile, if the role contact mechanics in acoustic sensing shall be expanded.

Conclusion

Using a QCM-based contact resonance method, the stiffness of sphere–plate contacts was studied at MHz frequencies. The linearcontact stiffness increases with normal load. A fit using JKR theory is possible. The fit parameters are in the expected range, but there is a significant amount of scatter between experiments. A quantitative interpretation must be undertaken with some care. The contact stiffness increases in the presence of a liquid. Possibly, this increase is rooted in a squeeze flow close to the edge of the contact. The loss tangent is of the order of 0.1 and decreases with normal force, F_N. The F_N-dependence suggests that the dissipation is connected to interfacial processes. At elevated amplitudes, it was also observed that there is partial slip. The amplitude dependence of frequency and bandwidth can be fitted with the Cattaneo–Mindlin model, which suggests that the frictional forces are proportional to the normal pressure as in macroscopic friction. The friction coefficients were found to be on the order of unity. The friction coefficients as derived from $\Delta f(u_0)$ and $\Delta\Gamma(u_0)$ agree with each other reasonably well. The agreement is better in water than in air. Finally, the friction coefficients were found to decrease slightly with increasing normal force (that is, with increasing contact area). This can explained by the finite radius of the crack tip at the edge of the contact or by nanoscale roughness. These effects are most pronounced for the smallest contacts. Contact splitting can lower the amount of partial slip and fretting wear.

Acknowledgements

This work strongly builds on instrumental developments by Andreas Böttcher and Sylvia Kerl (née Hanke). J. V. acknowledges a stipend by the Ministry of Education, Youth and Sports of the Czech Republic.

References

1. Hurricks, P. L. *Wear* **1970,** *15,* 389. doi:10.1016/0043-1648(70)90235-8
2. Varenberg, M.; Etsion, I.; Halperin, G. *Tribol. Lett.* **2005,** *18,* 493–498. doi:10.1007/s11249-005-3609-6
3. Gardiner, B. S.; Tordesillas, A. *Int. J. Solids Struct.* **2004,** *41,* 5885–5901. doi:10.1016/j.ijsolstr.2004.05.051
4. Ciamarra, M. P.; Lippiello, E.; Godano, C.; de Arcangelis, L. *Phys. Rev. Lett.* **2010,** *104,* 238001. doi:10.1103/PhysRevLett.104.238001
5. Di Renzo, A.; Di Maio, F. P. *Chem. Eng. Sci.* **2004,** *59,* 525–541. doi:10.1016/j.ces.2003.09.037
6. Cattaneo, C. *Atti Accad. Naz. Lincei, Cl. Sci. Fis., Mat. Nat., Rend.* **1938,** *27,* 342–348.
7. Mindlin, R. D.; Deresiewicz, H. *Trans. ASME* **1953,** *20,* 327–344.
8. Johnson, K. L. *Contact Mechanics;* Cambridge University Press: Cambridge, United Kingdom, 1985. doi:10.1017/CBO9781139171731
9. Popov, V. L. *Contact Mechanics and Friction: Physical Principles and Applications,* 1st ed.; Springer: Berlin, Germany, 2010. doi:10.1007/978-3-642-10803-7
10. Hanke, S.; Petri, J.; Johannsmann, D. *Phys. Rev. E* **2013,** *88,* 032408. doi:10.1103/PhysRevE.88.032408
11. Etsion, I. *J. Tribol.* **2010,** *132,* 020801. doi:10.1115/1.4001238
12. Tabor, D. *Proc. R. Soc. London, Ser. A* **1959,** *251,* 378–393. doi:10.1098/rspa.1959.0114
13. Brizmer, V.; Kligerman, Y.; Etsion, I. *J. Tribol.* **2007,** *129,* 783. doi:10.1115/1.2772322
14. Savkoor, A. R. Dry adhesive contact of elastomers. M. S. Thesis, Technical University Delft, Netherlands, 1987.
15. Johnson, K. L. *Proc. R. Soc. London, Ser. A* **1997,** *453,* 163–179. doi:10.1098/rspa.1997.0010
16. Mazeran, P.-E.; Beyaoui, M. *Tribol. Lett.* **2008,** *30,* 1–11. doi:10.1007/s11249-008-9304-7
17. Gao, H. J.; Yao, H. M. *Proc. Natl. Acad. Sci. U. S. A.* **2004,** *101,* 7851–7856. doi:10.1073/pnas.0400757101
18. Lawn, B. *Fracture in brittle solids;* Cambridge University Press: Cambridge, United Kingdom, 1993. doi:10.1017/CBO9780511623127
19. Berthier, Y.; Vincent, L.; Godet, M. *Tribol. Int.* **1989,** *22,* 235–242. doi:10.1016/0301-679X(89)90081-9
20. Szolwinski, M. P.; Farris, T. N. *Wear* **1996,** *198,* 93–107. doi:10.1016/0043-1648(96)06937-2
21. Leidich, E.; Maiwald, A.; Vidner, J. *Wear* **2013,** *297,* 903–910. doi:10.1016/j.wear.2012.11.006
22. Baumberger, T.; Caroli, C. *Adv. Phys.* **2006,** *55,* 279–348. doi:10.1080/00018730600732186
23. Persson, B. N. J. *Surf. Sci. Rep.* **2006,** *61,* 201–227. doi:10.1016/j.surfrep.2006.04.001
24. Bureau, L.; Caroli, C.; Baumberger, T. *Proc. R. Soc. London, Ser. A* **2003,** *459,* 2787–2805. doi:10.1098/rspa.2003.1146
25. Greenwood, J. A.; Williamson, J. B. P. *Proc. R. Soc. London, Ser. A* **1966,** *295,* 300. doi:10.1098/rspa.1966.0242
26. Fuadi, Z.; Takagi, T.; Miki, H.; Adachi, K. *Proc. Inst. Mech. Eng., Part J* **2013,** *227,* 1117–1128. doi:10.1177/1350650113481293
27. Rabe, U.; Amelio, S.; Kester, E.; Scherer, V.; Hirsekorn, S.; Arnold, W. *Ultrasonics* **2000,** *38,* 430–437. doi:10.1016/S0041-624X(99)00207-3
28. Giessibl, F. J. *Appl. Phys. Lett.* **2001,** *78,* 123–125. doi:10.1063/1.1335546
29. Hölscher, H.; Schwarz, U. D.; Wiesendanger, R. *Appl. Surf. Sci.* **1999,** *140,* 344–351. doi:10.1016/S0169-4332(98)00552-2
30. Pfeiffer, O.; Bennewitz, R.; Baratoff, A.; Meyer, E.; Grütter, P. *Phys. Rev. B* **2002,** *65,* 161403. doi:10.1103/PhysRevB.65.161403
31. Giessibl, F. J.; Herz, M.; Mannhart, J. *Proc. Natl. Acad. Sci. U. S. A.* **2002,** *99,* 12006–12010. doi:10.1073/pnas.182160599
32. Kendall, K.; Tabor, D. *Proc. R. Soc. London, Ser. A* **1971,** *323,* 321. doi:10.1098/rspa.1971.0108
33. Martin, S. J.; Bandey, H. L.; Cernosek, R. W.; Hillman, A. R.; Brown, M. J. *Anal. Chem.* **2000,** *72,* 141–149. doi:10.1021/ac9908290
34. Dybwad, G. L. *J. Appl. Phys.* **1985,** *58,* 2789–2790. doi:10.1063/1.335874
35. Laschitsch, A.; Johannsmann, D. *J. Appl. Phys.* **1999,** *85,* 3759–3765. doi:10.1063/1.369745
36. Johannsmann, D. *Phys. Chem. Chem. Phys.* **2008,** *10,* 4516–4534. doi:10.1039/b803960g
37. Berg, S.; Prellberg, T.; Johannsmann, D. *Rev. Sci. Instrum.* **2003,** *74,* 118–126. doi:10.1063/1.1523647
38. Johnson, K. L. *Proc. Inst. Mech. Eng., Part C* **1961,** *3,* 362.

39. Léopoldès, J.; Jia, X. *Phys. Rev. Lett.* **2010,** *105,* 266101. doi:10.1103/PhysRevLett.105.266101
40. Kamperman, M.; Kroner, E.; del Campo, A.; McMeeking, R. M.; Arzt, E. *Adv. Eng. Mater.* **2010,** *12,* 335–348. doi:10.1002/adem.201000104
41. Majumder, A.; Sharma, A.; Ghatak, A. Bio-Inspired Adhesion and Adhesives: Controlling by Micro-nano Structuring of Soft Surfaces. In *Microfluidics and Microfabrication;* Chakraborty, S., Ed.; Springer: Berlin, Germany, 2010; pp 283–307. doi:10.1007/978-1-4419-1543-6_7

License and Terms

The definitive version of this article is the electronic one which can be found at:
doi:10.3762/bjnano.6.87

BEILSTEIN JOURNAL OF NANOTECHNOLOGY

Graphene on SiC(0001) inspected by dynamic atomic force microscopy at room temperature

Mykola Telychko[1,2], Jan Berger[1,3], Zsolt Majzik[1], Pavel Jelínek[1] and Martin Švec*[1]

Full Research Paper

Open Access

Address:
[1]Institute of Physics, Academy of Sciences of the Czech Republic, Cukrovarnická 10, CZ-16200 Prague, Czech Republic, [2]Charles University, Faculty of Mathematics and Physics, V Holešovičkách 2, Praha 8, Czech Republic and [3]Department of Physical Electronics, Faculty of Nuclear Sciences and Physical Engineering, Czech Technical University in Prague, Břehová 7, CZ-11519 Prague, Czech Republic

Email:
Martin Švec* - svec@fzu.cz

* Corresponding author

Keywords:
AFM; electron scattering; graphene; SiC; STM

Beilstein J. Nanotechnol. **2015,** *6,* 901–906.
doi:10.3762/bjnano.6.93

Received: 24 September 2014
Accepted: 02 March 2015
Published: 07 April 2015

This article is part of the Thematic Series "Advanced atomic force microscopy techniques III".

Guest Editor: T. Glatzel

Abstract

We investigated single-layer graphene on SiC(0001) by atomic force and tunneling current microscopy, to separate the topographic and electronic contributions from the overall landscape. The analysis revealed that the roughness evaluated from the atomic force maps is very low, in accord with theoretical simulations. We also observed that characteristic electron scattering effects on graphene edges and defects are not accompanied by any out-of-plane relaxations of carbon atoms.

Introduction

Graphene epitaxially grown on a substrate differs in many aspects from free-standing graphene or graphene exfoliated onto insulating surfaces. The influence of the substrate hinders applications of epitaxial graphene in the nanoelectronics [1]. The two main methods of epitaxial graphene growth are chemical vapor deposition (CVD) on metal surfaces [2] and annealing of silicon carbide (SiC) [3]. The large conductivity of metal substrates leaves graphene on metals as model-only systems. Alternatively, graphene on SiC(0001) is a more promising candidate for applications [4,5]. But its electronic behaviour is still strongly affected by intrinsic properties of the substrate and the morphology of the interface [6].

Understanding the interplay between atomic and electronic structure of graphene grown on SiC substrate is a crucial factor for device construction. In this respect structural properties of graphene were extensively studied by atomic force microscopy (AFM) [7-9] and scanning tunneling microscopy (STM) [10-12]. STM measurements of single-layer (SLG) as well as bi-layer graphene (BLG) grown epitaxially on 6H- or 4H-SiC(0001) show a characteristic $6\sqrt{3} \times 6\sqrt{3}$ quasi-periodic corrugation (q-$6\sqrt{3}$ hereafter) [3,13-15]. It has not been clarified yet whether STM contrast on this surface has electronic or topographic origin. There is a lack of knowledge about the real physical corrugation of SLG and its contribution to the observed STM contrast, as it has already been successfully studied on graphene/Ir(111) [16-18]. However, it is well-known that the morphological modulations of the SLG arise from the interaction with the so-called buffer layer – a C-rich phase, which separates graphene from the SiC substrate [19-21].

Until now, the morphology of SLG on SiC(0001) has been studied by STM and AFM separately. Therefore, an investigation using the combined STM–AFM technique, that has simultaneous access to the electronic and topographic channels, is needed.

For the first time we bring experimental data, that can distinguish the topographic landscape from the local electronic structure of SLG on a 6H-SiC(0001) substrate. At room temperature we employed a combined STM and dynamic atomic force microscopy (dAFM) based on the Q-plus sensor working under UHV conditions. We observe the $\sqrt{3}\times\sqrt{3}\mathrm{R}30°$ ($\sqrt{3}$) modulations, characteristic for the areas of graphene edges and point defects. Our results complement the previous findings about the origin of scattering at the defects and also serve for a comparison with properties of different kinds of epitaxial graphene.

Experimental

The experiments were performed in an ultra-high vacuum (UHV) environment with a base pressure not exceeding 1×10^{-10} mbar. N-doped Si-face 6H-SiC(0001) wafers purchased from CREE Inc., were cut into 3 mm × 10 mm stripes and mounted onto sample holders constructed for a direct-current sample heating. After inserting into the UHV, the samples were degassed at 600 °C and annealed to 800–850 °C under a Si flux for 30 min, which resulted in a perfect Si type 3 × 3 reconstruction and typical terrace widths above 50 nm. As the source of the Si flux we used a Si wafer, which was annealed up to 1200 °C by passing the direct current. The deposition rate was 1 mL per 5 min. The temperature of the sample was measured using an optical pyrometer with spectral emissivity set to 0.6, operating at 1.6 µm wavelength, focused onto a spot on the sample with a diameter <2 mm. Buffer layer and graphene growth were achieved by further annealing of the sample up to 1150 °C, repeated in 10 min increments, until the desired coverage of graphene was achieved (about 2/3 of the surface) [13,14] and terrace widths reached 100 nm. All intermediate steps were monitored both by the low energy electron diffraction and STM. A custom-built quartz-tuning fork sensor was used for the measurements. It had a main resonance frequency of 51294 Hz, a quality factor above 1000 and an estimated stiffness of ≈3800 $\mathrm{N{\cdot}m^{-1}}$ [22]. The contact to the tungsten tip was made of a thin golden wire in order to avoid crosstalk with the deflection signal from the tuning fork piezo [22,23]. The tip has been treated by annealing to 1200 °C in contact with a hot tungsten filament. The simultaneous current and frequency shift measurements were done in constant height mode. A very slow tunneling current feedback was applied for compensation of the sample tilt. The reason to use current as a feedback, as opposed to using the frequency shift (Δf), is the possibility of doing measurements in the region of a negative frequency shift gradient (repulsive regime), even at room temperature, without enhanced risk of losing the tip apex. This approach is specifically chosen for the conditions when the graphene contrast provided by the Δf is not giving atomic resolution in the attractive regime. Kelvin probe force measurements (KPFM) were also done in the constant-height mode, with a slow feedback between the measurement points, to compensate the tilt of the sample. KPFM parabola was measured by sweeping the bias voltage and measuring the Δf value [24].

In order to estimate the SLG corrugation we carried out large scale total energy density functional theory (DFT) calculations. We used local-orbital FIREBALL code [25,26]. FIREBALL uses an optimized [27] spatially-confined pseudo-atomic numerical orbital basis set. In our case, an *ss** basis set was used for the H atoms, a *sp* basis set for the Si and C atoms. The cutoff radii of the pseudo-atomic basis functions were as follows: $R(\mathrm{H},s)$ = 4.5 a.u., $R(\mathrm{H},s^*)$ = 4.5 a.u., $R(\mathrm{C},s)$ = 4.5 a.u, $R(\mathrm{C},s)$ = 4.5 a.u., $R(\mathrm{Si},s)$ = 6.0 a.u., $R(\mathrm{Si},p)$ = 6.00 a.u. Local density approximation is used for the exchange correlation functional. Our atomic models of the SLG-SiC(0001) surface consisted of a slab of 1648 atoms, 10 atomic layers thick (including the buffer and SLG layer) with an additional passivating hydrogen layer on the underside. The lateral size of the supercell was $6\sqrt{3}\times 6\sqrt{3}$. The calculations were restricted to the Γ point of the first surface Brillouin zone. The bottom Si atomic layer as well as the hydrogen layer were kept fixed during the geometry optimization while all other atoms were allowed to relax freely into their equilibrium positions. The criterion for terminating the relaxation was that maximal forces on free atoms had to be below 0.05 eV/Å and the change of total energy between subsequent iterations had to be smaller than 10^{-4} eV per unit cell.

Results

Figure 1 shows a compilation of STM images taken over an incomplete layer of graphene grown on 6H-SiC(0001). Figure 1a shows the main features of the surface morphology, terraces divided by steps of various heights, areas covered with SLG and BLG and areas of buffer layer. All of them have a common pattern – the quasiperiodic (q-$6\sqrt{3}$) modulation corresponding to the $6\sqrt{3}\times 6\sqrt{3}\mathrm{R}30°$ quasiperiodic structure detected by low-energy electron diffraction [3,14]. Figure 1b shows a detail of the SLG, measured at a bias voltage 0.5 V,

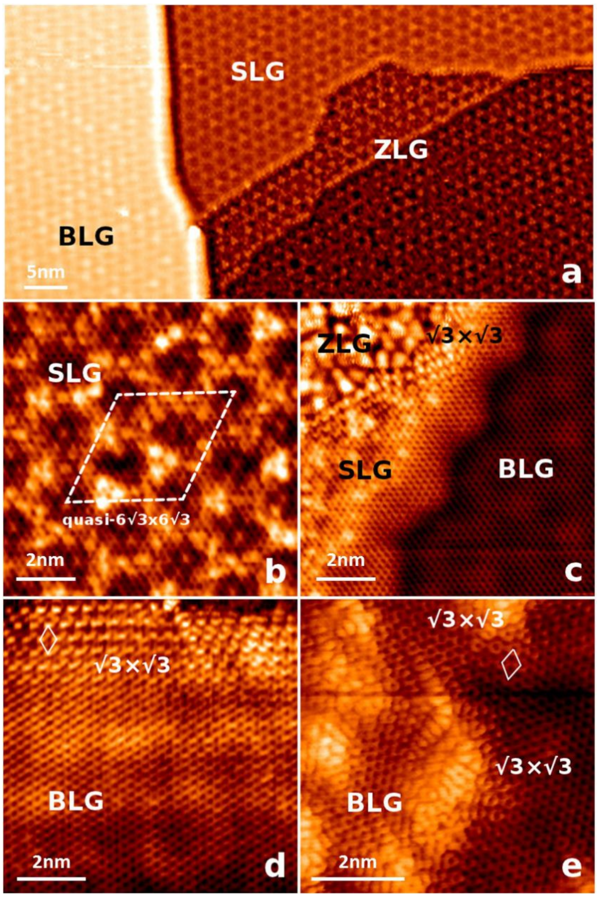

Figure 1: Constant-current STM images taken over an incomplete graphene layer grown on the 6H-SiC(0001) (color online). (a) 67 × 33 nm^2, V_bias = −1.5 V, I = 0.15 nA; overview of an area containing the buffer layer (ZLG) and single- and bi-layer graphene (SLG and BLG). (b) 10 × 10 nm^2, V_bias = 0.5 V, I = 0.18 nA; subsurface features bonds of the buffer layer visible through a sheet of graphene, the characteristic $6\sqrt{3}$ quasiperiodicity is indicated. (c) 10 × 10 nm^2, V_{bias} = 0.5 V, I = 0.18 nA; example of a characteristic $\sqrt{3}\times\sqrt{3}$ rippling of SLG near to an armchair edge, step overgrown by graphene without any extra rippling, (d) 8.5 × 8.5 nm^2, V_bias = 0.2 V, I = 0.16 nA; rippling at a boundary between SLG and BLG graphene, (e) 6.4 × 6.4 nm^2, V_bias = −0.2 V, I = 0.16 nA; $\sqrt{3}\times\sqrt{3}$ near to vacancies created by ion etching.

with a stable tip that provides a good resolution, allowing the detection of buffer layer features. These are responsible for the characteristic modulation of SLG. The roughness measured by the STM at voltages below 0.5 V has a typical value of 21 pm RMS and peak-to-peak value of 60 pm. Figures Figure 1c,d show rippled boundaries of graphene. The edges are rippled, regardless whether it is a BLG or SLG boundary, zigzag or armchair termination of the graphene domain. In a closer inspection of the armchair-type termination (FigureFigure 1d), it can be identified locally as a $\sqrt{3}$ periodicity. This characteristic feature has been observed before, not only near to the graphene boundaries, but also around single-point defects in graphene and graphite [3,13,28,29] and adsorbates [30-32]. We also recorded a prominent example of this effect at ion-etched graphene – see Figure 1e. This effect is generally explained by intervalley scattering of electrons in graphene [33]. In contrast, in a special case where the graphene overgrows a step (see Figure 1c), there is no visible rippling.

The set of curves in Figure 2a shows local spectroscopy taken just before the imaging above the single-layer graphene with the tuning-fork-based dAFM sensor, oscillating at amplitudes of 150 pm. The Δf, time-averaged current ($<I_t>$) are measured vs the tip–sample relative distance (Z) during an approach and retraction of the tip. Voltage is kept at 100 mV. The $<I_t>$ grows exponentially with Z and the Δf has a minimum near to −80 Hz. The value of $Z = 0$ corresponds to the tip–sample separation at $<I_t>$ setpoint of 0.46 nA. In the region of the set point, the Δf is rising at a rate of (0.98 ± 0.04) Hz/pm, as determined by the least-square fitting. Force (F) is calculated from the Δf signal, using the approach proposed by Sader et al. [34]. Maximum attractive force amounts roughly to −0.3 nN.

To identify any charge transfer effects within the q-$6\sqrt{3}$ structure of graphene a Kelvin-probe measurement [24] has been performed on the bright and dark areas (highs and lows of the q-$6\sqrt{3}$ modulation) in the Δf image, at 0.5 nm from the setpoint, further from the sample. In Figure 2b, the two corresponding parabolas show no difference neither in the shape nor in their maxima. The contact potential between the tip and the sample corresponds to maxima in the parabolas and is located at −0.32 eV.

In Figure 3, the Δf and $<I_t>$ maps are presented for the same area of the sample, taken in a constant height regime with a slow feedback setpoint at 0.46 nA, producing a tip–sample separation close to the $Z = 0$ in Figure 2a. The $<I_t>$ map shows an image resembling the STM topography in Figure 1b, however with a slightly sharper contrast, which is a common aspect of current images taken in the constant-height regime [35]. It shows the characteristic graphene honeycomb structure modulated by the q-$6\sqrt{3}$ periodicity. The Δf signal shows the honeycomb structure and the q-$6\sqrt{3}$ modulation as well. In this case, the slow feedback control of the tip–sample distance allows us to stay in the repulsive regime, achieving atomic resolution. This would be otherwise possible only at very stable conditions, e.g., at low temperatures. The lower part of the $<I_t>$ image in Figure 3 (also zoomed in the inset) possesses features arising from armchair graphene boundaries. The boundaries residing in the left and right lower corners, produce characteristic $\sqrt{3}$ ripples on graphene visible in the $<I_t>$ channel. In contrast, the Δf image shows only a flat honeycomb structure of graphene.

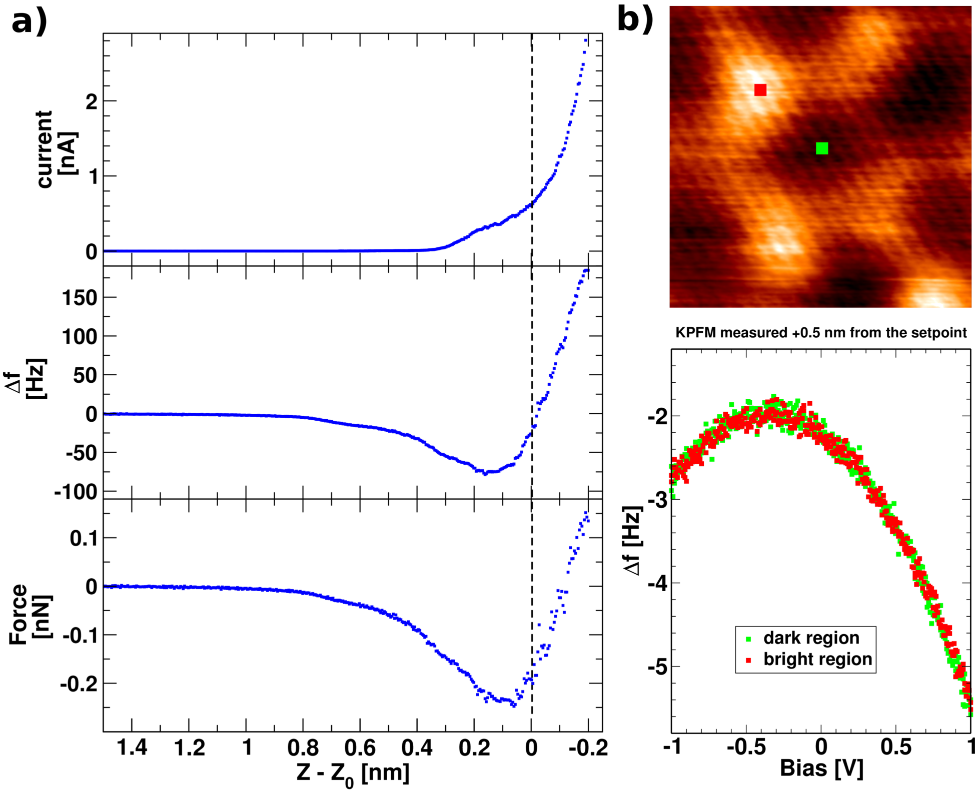

Figure 2: (Color online) (a) Spectroscopy curves of average tunneling current <I_t>, Δf and force F vs the tip–sample distance on graphene/SiC(0001), taken with a bias voltage of 100 mV, just before imaging. The value of Z = 0 corresponds to the tip–sample separation at <I_t> setpoint of 0.46 nA. (b) Example measurements of the local potential at bright and dark regions of the q-(6$\sqrt{3}$) modulation visible in the Δf map, indicating undetectable charge transfer.

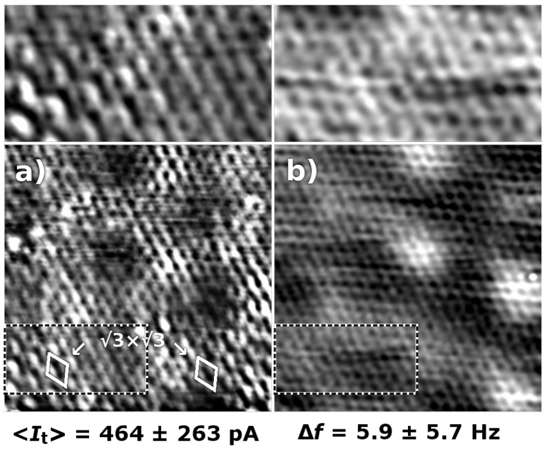

Figure 3: (a) The average tunneling current <I_t> maps (V_{bias} = 100 mV, I = 0.46 nA, 5.5 nm × 7.1 nm and (b) frequency shift Δf acquired on the same area of graphene/SiC(0001). The q-6$\sqrt{3}$ modulation is apparent in both channels, whereas the $\sqrt{3}\times\sqrt{3}$ modulation due to scattering on armchair boundary is detected only in the <I_t> map. The insets on the top show zoomed images of a region that has a $\sqrt{3}\times\sqrt{3}$ modulation in the <I_t> map. The mean value and a standard deviation (RMS) are given for each measured quantity beneath each of the images.

Discussion

The experimental results reveal that the q-6$\sqrt{3}$ modulation of graphene in STM has, apart from a significant electronic contribution, a topographic component. It is a question how strong is the topographic effect and whether it can be evaluated from the semi-constant height data. Neglecting the effect of the slow feedback and by using the Δf(Z) curve from Figure 2a, we estimated the Z height modulation of graphene from the Δf images in Figure 3. Considering that the image is taken in the negative Δf region, which has a of 1.0 Hz/pm, we use the Δf roughness corresponding to the q-6$\sqrt{3}$ modulation (5.7 Hz RMS), to obtain an average value of about 6 pm RMS, corresponding to 16 pm corrugation (peak-to-peak). This is significantly lower than the roughness obtained by standard topographic mode of STM, pointing out the dominant electronic contribution of the buffer layer to the STM topography of SLG. In our fully relaxed theoretical model of SLG on the buffer layer (Figure 4), which is using the 6$\sqrt{3}\times$ 6$\sqrt{3}$ unit cell, the standard deviation of the C atom z-positions in the SLG layer is 4.4 pm (12.4 pm peak-to-peak), which corresponds well to the experimental estimation and is comparable to a similar calculation in [36]. The value is much smaller than the corrugation obtained for graphene/

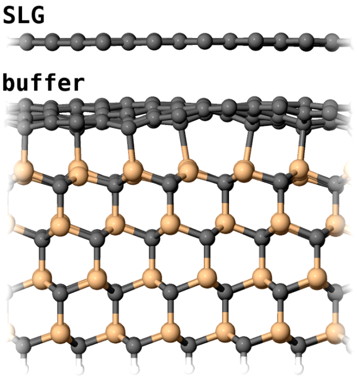

$\bar{z}$(pm)	/	σz(pm)	
652	/	4.4	C
300	/	35.5	C
24	/	9.7	Si
-36	/	7.1	C
-232	/	5.7	Si
-300	/	5.0	C
-495	/	4.4	Si
-564	/	4.0	C
-757	/	3.9	Si
-820	/	3.5	C

Figure 4: The fully relaxed theoretical model of SLG on the buffer layer, that is using the $6\sqrt{3} \times 6\sqrt{3}$ unit cell. The z values in the table correspond to z-positions of C and Si atomic layers in the model, σz is a standard deviation of atom positions. The standard deviation of the C atom z-positions in the SLG layer is 4.4 pm.

Ru(0001) and graphene/Ir(111) that are both claimed to be in the range of 100 pm (corresponding to 35 pm RMS) [37-39].

Most remarkable is the $\sqrt{3}$ pattern (shown in the inset of Figure 3a) emerging due to the scattering at the armchair graphene boundaries. We do not observe any out-of-plane relaxation of the carbon atoms in the honeycomb structure resolved by dAFM (in the inset of Figure 3b). This is a direct evidence that the $\sqrt{3}$ has a purely electronic origin. That is an expected behaviour since the effect has been attributed to scattering of Dirac electrons on graphene sublattices [31]. It also demonstrates that the graphene layer in SLG is weakly bound to the buffer layer through van der Waals interactions. This finding of no atomic relaxations can be extrapolated for the single-point defects and other graphene disruptions for graphene on SiC(0001), since they produce the same type of scattering and do not interact strongly with the substrate. In this entire observation, we can exclude any influence of the so-called phantom force [40], as the Δf signal has no hints of the $\sqrt{3}$.

Considering that the electronic contribution is the major factor that affects the $\langle I_t \rangle$ maps, we can also deduce that these maps taken at low bias reflect a variation of local conductivity. Moreover, the Kelvin parabola measurements do not detect any significant contact potential difference between the dark and bright protrusions of the q-$6\sqrt{3}$ modulation. It can be understood as a negligible workfunction difference between these investigated areas.

Conclusion

In summary, we successfully probed the epitaxial graphene on SiC(0001) by a combined STM and dAFM technique, gathering extended information on its atomic structure near defects. By atomic force microscopy, we detected a topographical corrugation of the q-$6\sqrt{3}$ with an average value of 6 pm RMS (16 pm peak-to-peak). We can conclude that variation at this scale detected by previous STM measurements is caused mainly by electronic contributions arising from the buffer layer. In the case of the characteristic $\sqrt{3}$ rippling of graphene, which occurs due to presence of defects or boundaries, any relaxations of carbon atoms perpendicular to the surface can be excluded. These results are consistent with recent findings and show the single-layer graphene on SiC(0001) as a morphologically very flat substrate.

Acknowledgements

The research was funded by GACR grant no.14-02079S, GACR grant no. EXCELENCE 14-374527G.

References

1. Soukiassian, P. G.; Enriquez, H. B. *J. Phys.: Condens. Matter* **2004,** *16,* S1611–S1658. doi:10.1088/0953-8984/16/17/011
2. Zhang, Y.; Zhang, L.; Zhou, C. *Acc. Chem. Res.* **2013,** *46,* 2329–2339. doi:10.1021/ar300203n
3. Hass, J.; de Heer, W. A.; Conrad, E. H. *J. Phys.: Condens. Matter* **2008,** *20,* 323202–323227. doi:10.1088/0953-8984/20/32/323202
4. Berger, C.; Song, Z.; Li, X.; Wu, X.; Brown, N.; Naud, C.; Mayou, D.; Li, T.; Hass, J.; Marchenkov, A. N.; Conrad, E. H.; First, P. N.; de Heer, W. A. *Science* **2006,** *312,* 1191–1196. doi:10.1126/science.1125925
5. Lin, Y.-M.; Valdes-Garcia, A.; Han, S.-J.; Farmer, D. B.; Meric, I.; Sun, Y.; Wu, Y.; Dimitrakopoulos, C.; Grill, A.; Avouris, P.; Jenkins, K. A. *Science* **2011,** *332,* 1294–1297. doi:10.1126/science.1204428
6. Ristein, J.; Mammadov, S.; Seyller, T. *Phys. Rev. Lett.* **2012,** *108,* 246104. doi:10.1103/PhysRevLett.108.246104
7. Held, C.; Seyller, T.; Bennewitz, R. *Beilstein J. Nanotechnol.* **2012,** *3,* 179–185. doi:10.3762/bjnano.3.19
8. Filleter, T.; Bennewitz, R. *Phys. Rev. B* **2010,** *81,* 155412. doi:10.1103/PhysRevB.81.155412
9. Wastl, D. S.; Weymouth, A. J.; Giessibl, F. J. *ACS Nano* **2014,** *8,* 5233–5239. doi:10.1021/nn501696q
10. Rutter, G. M.; Guisinger, N. P.; Crain, J. N.; Jarvis, E. A. A.; Stiles, M. D.; Li, T.; First, P. N.; Stroscio, J. A. *Phys. Rev. B* **2007,** *76,* 235416. doi:10.1103/PhysRevB.76.235416
11. Biedermann, L. B.; Bolen, M. L.; Capano, M. A.; Zemlyanov, D.; Reifenberger, R. G. *Phys. Rev. B* **2009,** *79,* 125411. doi:10.1103/PhysRevB.79.125411
12. Mallet, P.; Varchon, F.; Naud, C.; Magaud, L.; Berger, C.; Veuillen, J.-Y. *Phys. Rev. B* **2007,** *76,* 041403. doi:10.1103/PhysRevB.76.041403
13. Huang, H.; Chei, W.; Chen, S.; Wee, A. T. S. *ACS Nano* **2008,** *2,* 2513–2518. doi:10.1021/nn800711v
14. Mårtensson, P.; Owman, F.; Johansson, L. I. *Phys. Status Solidi B* **1997,** *202,* 501–528. doi:10.1002/1521-3951(199707)202:1<501::AID-PSSB501>3.0.CO;2-H

15. Riedl, C.; Coletti, C.; Iwasaki, T.; Zakharov, A. A.; Starke, U. *Phys. Rev. Lett.* **2009,** *103,* 246804. doi:10.1103/PhysRevLett.103.246804
16. Boneschanscher, M. P.; Hämäläinen, S. K.; Liljeroth, P.; Swart, I. *ACS Nano* **2014,** *8,* 3006–3014. doi:10.1021/nn500317r
17. Boneschanscher, M. P.; van der Lit, J.; Sun, Z.; Swart, I.; Liljeroth, P.; Vanmaekelbergh, D. *ACS Nano* **2012,** *6,* 10216–10221. doi:10.1021/nn3040155
18. Hämäläinen, S. K.; Boneschanscher, M. P.; Jacobse, P. H.; Swart, I.; Pussi, K.; Moritz, W.; Lahtinen, J.; Liljeroth, P.; Sainio, J. *Phys. Rev. B* **2013,** *88,* 201406. doi:10.1103/PhysRevB.88.201406
19. Varchon, F.; Feng, R.; Hass, J.; Li, X.; Nguyen, B. N.; Naud, C.; Mallet, P.; Veuillen, J.-Y.; Berger, C.; Conrad, E. H.; Magaud, L. *Phys. Rev. Lett.* **2007,** *99,* 126805. doi:10.1103/PhysRevLett.99.126805
20. Kim, S.; Ihm, J.; Choi, H. J.; Son, Y.-W. *Phys. Rev. Lett.* **2008,** *100,* 176802. doi:10.1103/PhysRevLett.100.176802
21. Nemec, L.; Blum, V.; Rinke, P.; Scheffler, M. *Phys. Rev. Lett.* **2013,** *111,* 065502. doi:10.1103/PhysRevLett.111.065502
22. Berger, J.; Švec, M.; Müller, M.; Ledinský, M.; Fejfar, A.; Jelínek, P.; Majzik, Z. *Beilstein J. Nanotechnol.* **2013,** *4,* 1–9. doi:10.3762/bjnano.4.1
23. Majzik, Z.; Setvín, M.; Bettac, A.; Feltz, A.; Cháb, V.; Jelínek, P. *Beilstein J. Nanotechnol.* **2012,** *3,* 249–259. doi:10.3762/bjnano.3.28
24. Nonnenmacher, M.; O'Boyle, M. P.; Wickramasinghe, H. K. *Appl. Phys. Lett.* **1991,** *58,* 2921–2923. doi:10.1063/1.105227
25. Lewis, J. P.; Jelínek, P.; Ortega, J.; Demkov, A. A.; Trabada, D. G.; Haycock, B.; Wang, H.; Adams, G.; Tomfohr, J. K.; Abad, E.; Wang, H.; Drabold, D. A. *Phys. Status Solidi B* **2011,** *248,* 1989–2007. doi:10.1002/pssb.201147259
26. Jelínek, P.; Wang, H.; Lewis, J. P.; Sankey, O. F.; Ortega, J. *Phys. Rev. B* **2005,** *71,* 235101. doi:10.1103/PhysRevB.71.235101
27. Basanta, M. A.; Dappe, Y. J.; Jelínek, P.; Ortega, J. *Comput. Mater. Sci.* **2007,** *39,* 759. doi:10.1016/j.commatsci.2006.09.003
28. Ugeda, M. M.; Brihuega, I.; Guinea, F.; Gómez-Rodríguez, J. M. *Phys. Rev. Lett.* **2010,** *104,* 096804. doi:10.1103/PhysRevLett.104.096804
29. Cockayne, E.; Rutter, G. M.; Guisinger, N. P.; Crain, J. N.; First, P. N.; Stroscio, J. A. *Phys. Rev. B* **2011,** *83,* 195425. doi:10.1103/PhysRevB.83.195425
30. Hornekær, L.; Šljivančanin, Ž.; Xu, W.; Otero, R.; Rauls, E.; Stensgaard, I.; Lægsgaard, E.; Hammer, B.; Besenbacher, F. *Phys. Rev. Lett.* **2006,** *96,* 156104. doi:10.1103/PhysRevLett.96.156104
31. Rutter, G. M.; Crain, J. N.; Guisinger, N. P.; Li, T.; First, P. N.; Stroscio, J. A. *Science* **2007,** *317,* 219–222. doi:10.1126/science.1142882
32. Joucken, F.; Tison, Y.; Lagoute, J.; Dumont, J.; Cabosart, D.; Zheng, B.; Repain, V.; Chacon, C.; Girard, Y.; Botello-Méndez, A. R.; Rousset, S.; Sporken, R.; Charlier, J.-C.; Henrard, L. *Phys. Rev. B* **2012,** *85,* 161408. doi:10.1103/PhysRevB.85.161408
33. Mallet, P.; Brihuega, I.; Bose, S.; Ugeda, M. M.; Gómez-Rodríguez, J. M.; Kern, K.; Veuillen, J. Y. *Phys. Rev. B* **2012,** *86,* 045444. doi:10.1103/PhysRevB.86.045444
34. Sader, J. E.; Jarvis, S. P. *Appl. Phys. Lett.* **2004,** *84,* 1801–1803. doi:10.1063/1.1667267
35. Švec, M.; Jelínek, P.; Shukrynau, P.; González, C.; Cháb, V.; Drchal, V. *Phys. Rev. B* **2008,** *77,* 125104. doi:10.1103/PhysRevB.77.125104
36. Sforzini, J.; Nemec, L.; Denig, T.; Stadtmüller, B.; Lee, T. L.; Kumpf, C.; Soubatch, S.; Starke, U.; Rinke, P.; Blum, V.; Bocquet, F. C.; Tautz, F. S. *arXiv [cond-mat.mtrl-sci]* **2014,** No. 1411.4753.
37. Stradi, D.; Barja, S.; Díaz, C.; Garnica, M.; Borca, B.; Hinarejos, J. J.; Sánchez-Portal, D.; Alcamí, M.; Arnau, A.; Vázques de Parga, A. L.; Miranda, R.; Martín, F. *Phys. Rev. Lett.* **2011,** *106,* 186102. doi:10.1103/PhysRevLett.106.186102
38. Moritz, W.; Wang, B.; Bocquet, M.-L.; Brugger, T.; Greber, T.; Wintterlin, J.; Günther, S. *Phys. Rev. Lett.* **2010,** *104,* 136102. doi:10.1103/PhysRevLett.104.136102
39. Voloshina, E. N.; Fertitta, E.; Garhofer, A.; Mittendorfer, F.; Fonin, M.; Thissen, A.; Dedkov, Yu. S. *Sci. Rep.* **2013,** *3,* No. 1072. doi:10.1038/srep01072
40. Weymouth, A. J.; Wutscher, T.; Welker, J.; Hofmann, T.; Giessibl, F. J. *Phys. Rev. Lett.* **2012,** *106,* 226801. doi:10.1103/PhysRevLett.106.226801

License and Terms

BEILSTEIN JOURNAL OF NANOTECHNOLOGY

Automatic morphological characterization of nanobubbles with a novel image segmentation method and its application in the study of nanobubble coalescence

Yuliang Wang*[1], Huimin Wang[2], Shusheng Bi[1] and Bin Guo[3]

Full Research Paper

Open Access

Address:
[1]School of Mechanical Engineering and Automation, Beihang University, Beijing 100191, P.R. China, [2]Department of Materials Science and Engineering, The Ohio State University, 2041 College Rd., Columbus, OH 43210, USA and [3]School of Material Science and Engineering, Harbin Institute of Technology, Harbin, 150001, P.R. China

Email:
Yuliang Wang* - wangyuliang@buaa.edu.cn; Huimin Wang - wang.1333@osu.edu

* Corresponding author

Keywords:
atomic force microscopy; characterization; coalescence; nanobubbles; segmentation

Beilstein J. Nanotechnol. **2015,** *6,* 952–963.
doi:10.3762/bjnano.6.98

Received: 22 August 2014
Accepted: 26 February 2015
Published: 14 April 2015

This article is part of the Thematic Series "Advanced atomic force microscopy techniques III".

Guest Editor: T. Glatzel

Abstract

Nanobubbles (NBs) on hydrophobic surfaces in aqueous solvents have shown great potential in numerous applications. In this study, the morphological characterization of NBs in AFM images was carried out with the assistance of a novel image segmentation method. The method combines the classical threshold method and a modified, active contour method to achieve optimized image segmentation. The image segmentation results obtained with the classical threshold method and the proposed, modified method were compared. With the modified method, the diameter, contact angle, and radius of curvature were automatically measured for all NBs in AFM images. The influence of the selection of the threshold value on the segmentation result was discussed. Moreover, the morphological change in the NBs was studied in terms of density, covered area, and volume occurring during coalescence under external disturbance.

Introduction

Over the last ten years, spherical-capped bubbles on various hydrophobic surfaces in aqueous solvents have gained increasing attention [1-5].These gas bubbles with dimensions of 5–100 nm in height and 100–800 nm in diameter are often referred to as nanobubbles (NBs). The existence of NBs has been verified through various techniques, including atomic force microscopy (AFM) [1,5-9], rapid cryofixation/freeze fracturing [10], neutron reflectometry [11], X-ray reflectivity measurements [12], spectroscopic methods [13], total internal reflection fluorescence excitation [14], and even using an optical visualization approach with a limited resolution [14,15].

NBs have shown their potential in numerous applications. They can be used as vehicles for drug delivery and agents to enhance ultrasound contrast for tumor imaging [16,17]. Studies show that NBs can promote physiological activity of living organisms and increase cell productivity [18]. They are responsible for long-range attractive hydrophobic forces [19,20]. The coalescence of NBs on hydrophobic surfaces is believed to form a gas bridge and leads to long-range attractive forces [19,21]. They are also believed to be the reason for the breakdown of the no-slip boundary condition at the solid–liquid interface on hydrophobic/superhydrophobic surfaces [22-27].

The interaction between NBs and sample surfaces supporting them was also recently investigated. A phenomenon of NB-induced nanoindentions was reported by Wang et al. on an ultrathin polystyrene (PS) film in water [8], and was further confirmed by Janda et al. [28] and Alsawafta et al. [29] on highly ordered, pyrolytic graphite surfaces and gold–gelatin bionanocomposite films, respectively. This raises the possibility that NBs may be used to fabricate nanopatterned surfaces. By investigating the impact of micro/nanostructures on NBs, Wang et al. found that both nanoindentations on a continuously coated PS film and hydrophobic island structures on partially coated PS films can effectively increase their resistance to external disturbancees, which defines NB immobility [9].

The NB properties, and their response to changing experimental parameters, are widely studied. Several studies have shown that increased solution temperature, under ambient conditions are favorable conditions for the generation of NBs [2,30-32]. An increase of the solution temperature results in an increased NB density when the liquid temperature is lower than about 40 °C with an optimal liquid temperature of ≈35–40 °C [2,30,31]. However, when the temperature is higher than 40 °C, the total volume decreases with temperature [32]. Bhushan et al. studied the impact of an electric field applied to the sample substrates of NBs. They found that the NB density and size increased without obvious change to the area covered by the NBs when the substrate bias was increased from 0 to 100 V [33]. NB nucleation is also a function of gas type [34,35]. Among seven different gas types, H_2, He, CH_4, N_2, O_2, Ar and CO_2, O_2-based NBs had the largest diameter and Ar NBs had the largest volume at 25 °C [35]. They also found that the contact angle of the NB was a function of its radius of curvature.

The NB properties, including diameter, height, contact angle, radius of curvature, density and covered area, are normally studied through morphological characterization from AFM images. The first step in NB characterization is image segmentation – a process of identifying the specific areas covered by NBs. With the segmented images, NB-covered area, density, as well as volume can be obtained. Moreover, the cross sections of the NBs can be extracted after image segmentation. With the selected cross sections, the NB diameter and height can be directly measured. By fitting the cross sections as arcs, the NB contact angle and radius of curvature can be obtained [36-39].

The morphological characterization of NBs suffers from several difficulties. First, NB image segmentation is mainly implemented through the threshold method [31,40]. The areas with height larger than the selected threshold value are considered to be NBs. The threshold-based image segmentation method can process hundreds of NBs in one AFM images. However, this method underestimates the NB height, diameter and covered areas. Moreover, the cross sections extracted through the segmentation method represent only a portion of the actual NB cross sections, which lead to the inaccurate estimation of height and diameter. In some studies, the cross sections were manually selected [6,13]. Although the manual selection of cross sections can guarantee accurate NB characterization, only a limited number of NBs can be processed. When hundreds of NBs are involved, an automatic image segmentation method must be employed [2,32,33,35].

In this study, we provide a systematic approach for NB morphological characterization. Here, a novel method was developed to implement automatic image segmentation, which combines the regular threshold method and the active contour method [41] to achieve optimized image segmentation. With this method, the morphological characterization of hundreds of NBs from AFM images was carried out. Moreover, the method was applied to evaluate the morphological changes occurring during coalescence.

Experimental

NB imaging

A sample was prepared by spin coating a thin film of PS on a silicon (100) substrate at a speed of 500 rpm. The substrate was cleaned in a sonic bath of acetone and then water. PS particles (molecular weight 350,000, Sigma-Aldrich) were dissolved in toluene (Mallinckrodt Chemical) to a concentration of 0.2 wt % to obtain the solution for spin coating. The contact angle of the PS surface with water was measured to be 95 ± 3° using a sessile drop method.

A commercial AFM (MultiMode III, Digital Instruments) operating in tapping mode was used for imaging the sample. A silicon rotated force-modulated etched silicon probe (RFESP, Bruker Corporation) cantilever with a tip radius of 8 nm and a stiffness of 3 N/m was used. A modified tip holder was used for tapping mode atomic force microscopy (TMAFM) scanning, as was used in our previous studies [6,8,9]. In the general tapping mode operation, the whole liquid cell is excited by a piezoelectric element, which results in a multitude of spurious peaks related to the fluid cell eigenfrequencies. It is difficult to accurately determine the resonance frequency of a cantilever. In this study, a tapping mode tip holder for non-fluid use in air was modified, as shown in Figure 1. A horizontal slot was carved out above the piezo element in the opening of the tip holder to insert a glass slide. When the liquid is added between the glass slide and the substrate, a liquid meniscus is formed between the glass and sample surface for fluid imaging.

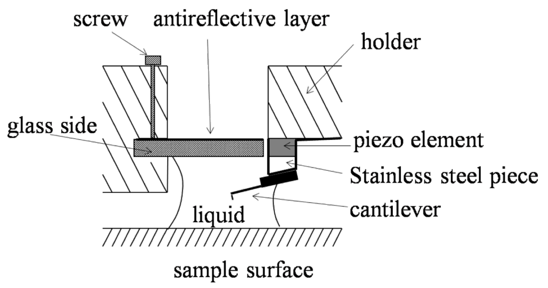

Figure 1: Schematic diagram of the modified tip holder [6].

The sample was first imaged in air, followed by immersion into deionized (DI) water for imaging by TMAFM. While imaging in water, the drive frequency was chosen to be the resonance frequency. The measured resonance frequency in water was about 25 Hz. The free oscillation amplitude of the cantilever at the working frequency was 7.3 nm. To minimize the force applied to the samples, the setpoint was set at 95% of the free amplitude, which was 6.9 nm. The sample surface was scanned at a rate of 2 Hz and the scan angle was 90°. To study the morphological changes occurring during NB coalescence, higher scanning loads with setpoints of 85% (6.2 nm), 79% (5.7 nm), and 66% (4.8 nm) were applied for a given 2 × 2 µm scanning area. After each high-load scan, the 95% setpoint was selected to check the corresponding changes after coalescence.

Parameters for NB characterization

In this section, the parameters involved in the morphological characterization of NBs will be individually introduced. For a given AFM image, the total number of NBs can be directly obtained after image segmentation. The NB density is defined as the number of NBs in a unit area. The covered area is the area of the substrate surface covered by NBs. Once the boundaries of the NBs are determined, the area enclosed by the detected NB boundary can be taken as the covered area.

Other parameters in NB morphology characterization, such as NB diameter, height, contact angle and radius of curvature, are normally obtained from the cross sections of NBs. A schematic of a cross section of a NB on a PS surface is shown in Figure 2.

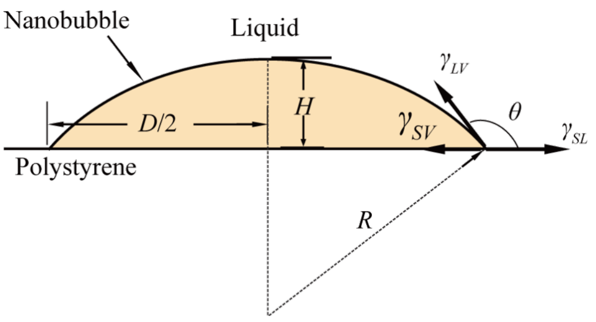

Figure 2: Schematic of a cross section of a NB on a solid PS surface.

In the figure, γ_{SL} (72 mN/m for water), γ_{SV}, and γ_{LV} are the surface tensions at the solid–liquid, solid–vapor, and liquid–vapor interfaces, respectively. *H*, *D*, *R*, and θ are the NB height, diameter, radius of curvature, and contact angle, respectively. *H* and *D* can be directly obtained from the selected cross section. By assuming the cross section is an elliptical arc, *R* and θ are given as:

$$R = \frac{(D/2)^2 + H^2}{2H}, \tag{1}$$

$$\theta = \pi - 2\tan^{-1}\frac{2H}{D}. \tag{2}$$

Algorithms for NB image segmentation

In this section, the principles and algorithms for NB image segmentation will be presented step-by-step. The PS surface was first scanned by TMAFM in air and this image is shown in Figure 3a. The root mean square (rms) roughness R_{rms} of the

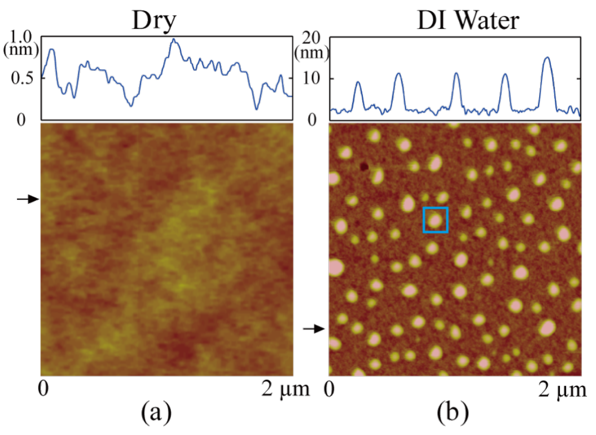

Figure 3: Comparison of AFM images of a PS surface in air (a) and in DI water (b).

image is 0.18 nm. Figure 3b shows the image of the PS surface immersed in DI water. The entire surface is covered with spherical cap-like domains, which are identified as NBs [6]. The R_{rms} is 2.8 nm, which is a value much larger than that obtained in air. Due to the mechanical instrumentation drift [42] that occurs during imaging, the obtained AFM images usually need to be flattened. In the regular flattening method, the average height of each scanned line is set to the height of the whole image. As a result, the scan lines containing less NBs have higher height values and appear brighter in AFM images, which results in artifacts in the post-processed images. In this study, the obtained AFM images were flattened by excluding the small areas containing NBs. This operation is a standard function in the AFM operation software and reduces the above mentioned artifacts. This method is referred to as the excluded area flattening method in this study. Figure 3b is a NB image obtained with the excluded flattening method. Figure S1 in Supporting Information File 1 shows the comparison of the AFM image obtained with the linear flattening method and the excluded flattening method.

Segmentation with the threshold method

The image segmentation was first implemented using the threshold method for the image shown in Figure 3b. Figure 4a–c shows the image segmentation results when the threshold values of 7.0 nm, 7.5 nm and 9.0 nm, respectively, were applied. One can see that when the threshold value is set to 7.0 nm, some of the sample substrate was falsely recognized as NBs, as indicated by the red arrow in Figure 4a. This overestimation is called oversegmentation. Therefore, it is clear that the threshold value should be higher than 7.0 nm to avoid oversegmentation. When the threshold value was increased to 7.5 nm, all NBs in the image could be detected, as shown in Figure 4b.

To test the influence of the threshold value on the segmentation result, a higher threshold value of 9 nm was applied, as shown in Figure 4c. A mesh plot of a NB at the location indicated by the yellow arrows in Figure 4a–c is shown in Figure 4d. The detected boundaries with the three different threshold values are also plotted in the mesh plot. As expected, the lowest threshold value (7.0 nm) gives the largest contour and better boundary detection than the higher ones (7.5 and 9.0 nm). This indicates that the threshold method is sensitive to the selection of the threshold value. Moreover, one can see that the method could not achieve optimized boundary detection results even with the lower threshold value: only part of the NB area is enclosed by the detected boundary.

Optimized NB boundary detection

To obtain an optimized boundary detection, a new approach was proposed in this study. The method utilizes the height distribution information in the AFM images. Figure 5a shows the 3D image of the NB indicated by the yellow arrow in Figure 4a. The apex of NB identifies the NB center, which gradually decreases towards their boundaries, as illustrated in Figure 5b. One can obtain the gradient field of the height by taking the differentiation of the image along both x and y directions, as shown in Figure 5c. This can be used to define the outline of NB boundaries.

Here, the traditional, active contour method is modified to detect NB boundaries. In the traditional, active contour model, a contour in an image is defined as a parametric contour $\nu(s) = (x(s),y(s))$ and has an energy function given as [41]:

$$E = \int_0^1 \left(\frac{1}{2}\alpha \nu_s^2 + \frac{1}{2}\beta \nu_{ss}^2 + E_{\text{ext}} \right) ds, \qquad (3)$$

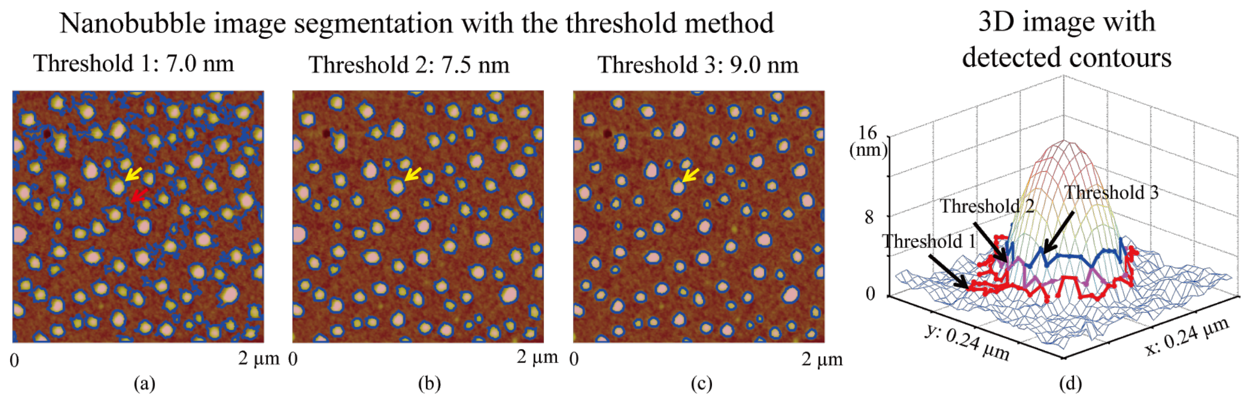

Figure 4: Nanobubble image segmentation using the threshold method with the threshold values of 7.0 nm (a), 7.5 nm (b), and 9.0 nm (c). (d) Mesh plot of a selected NB and the detected contours with the different threshold values. The detected boundaries are strongly related to the selected threshold values.

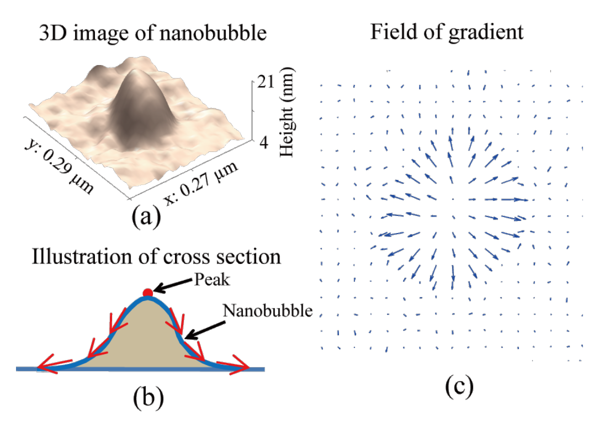

Figure 5: (a) 3D image of a selected NB. (b) Illustration of the NB cross section. (c) Field of gradient of the AFM image.

where ν_s and ν_{ss} are the first and second order partial derivatives, and α and β are scalar coefficients. The first two terms in Equation 3 are related to the internal energy of the contour, while the E_{ext} represents the external energy of the contour. Here, the height of the NBs along the contour is taken as the external energy. The internal energy depends only on the curve geometry and enforces the continuity and smoothness of the curve. The minimization of the total energy E satisfies the associated Euler–Lagrange function given as [41]:

$$\alpha\nu_{ss}(s,t)-\beta\nu_{ssss}(s,t)-\nabla E_{\text{ext}}=0, \tag{4}$$

where ν_{ssss} is the fourth order partial derivative of ν(s).

Equation 4 can be numerically solved, as presented by Kass et al. [41] and here we briefly introduce the process. The discrete form of the contour ν(s) can be expressed as a series of points along the contour, given as $\nu_i = (x_i,y_i) = (x(ih), y(ih))$, where h is the finite step size along the contour. By approximating the derivatives with finite differences, the terms ν_{ss} and ν_{ssss} at point i in Equation 4 can then be given as:

$$\nu_{ss}(i)=(\nu_{i+1}-2\nu_i+\nu_{i-1})/h \tag{5}$$

$$\nu_{ssss}(i)=(\nu_{i+2}-4\nu_{i+1}+6\nu_i-4\nu_{i-1}+\nu_{i-2})/h^4. \tag{6}$$

Given $f_x(i) = \partial E_{\text{ext}} / \partial x_i$ and $f_y(i) = \partial E_{\text{ext}} / \partial y_i$, we have $\nabla E_{\text{ext}} = f_{x,y}(i) = \left(f_x(i), f_y(i)\right)$.

By combining Equation 4, Equation 5 and Equation 6 and substituting $\nabla E_{\text{ext}} = \left(f_x(i), f_y(i)\right)$ into Equation 4, the finite difference form of Equation 4 can be given as:

$$\begin{aligned}&\beta\nu_{i+2}-(\alpha+4\beta)\nu_{i+1}+(2\alpha+6\beta)\nu_i-(\alpha+4\beta)\nu_{i-1}\\&+\beta\nu_{i-2}+\left(f_x(i),f_y(i)\right)=0\end{aligned} \tag{7}$$

The above finite difference form of the Euler–Lagrange function can be written in matrix notation as

$$\mathbf{A}\nu_s+\mathbf{f}_{x,y}=0, \tag{8}$$

where **A** is a pentadiagonal banded matrix. Equation 8 can be solved through an explicit Euler method between two successive instantaneous time points t and t−1, given as:

$$\mathbf{A}\nu_s(t)+\mathbf{f}_{x,y}(t-1)=-\gamma\left(\mathbf{v}_s(t)-\mathbf{v}_s(t-1)\right), \tag{9}$$

where γ is the step size. Equation 9 can be solved as:

$$\mathbf{v_s}(t)=(\mathbf{A}+\gamma\mathrm{I})\left(\gamma\mathbf{v_s}(t-1)-\mathbf{f}_{x,y}(t-1)\right). \tag{10}$$

By iteratively solving the Equation 10, the contour will be deformed and converged towards the NB boundary, where the total energy of the contour is minimized. In this study, all calculations were performed with commercial software (MATLAB, USA).

In practice, the original active contour method requires contour initialization, which gives an initial guess of the actual boundary for calculations. In this study, the threshold method and active contour method were combined to carry out automated image segmentation for all NBs in AFM images. Instead of manually drawing the initial contours for individual NBs, we take the contours detected by the threshold method as the initial guess used further in the implementation of the active contour method. The initial contours are mostly located within the actual boundaries and expand outwards.

Figure 6a demonstrates the boundary detection for a selected NB using the proposed method. The first image is a raw AFM image of a selected NB. A mask was obtained after applying the threshold method (threshold = 10 nm), as shown in the second image. The boundary of the mask is extracted to serve as the initial contour, as shown in the third image. The area enclosed by the initial contour for this image is 9333 nm^2. Driven by the field of gradient, the initial contour expands outwards as indicated by the green contours shown in the fourth image. The contour stops at the NB boundary where it achieves the minimum energy, as shown in the fifth image. The area enclosed by the contour is 16714 nm^2, which is much larger than that obtained with the threshold method. Figure 6b shows a

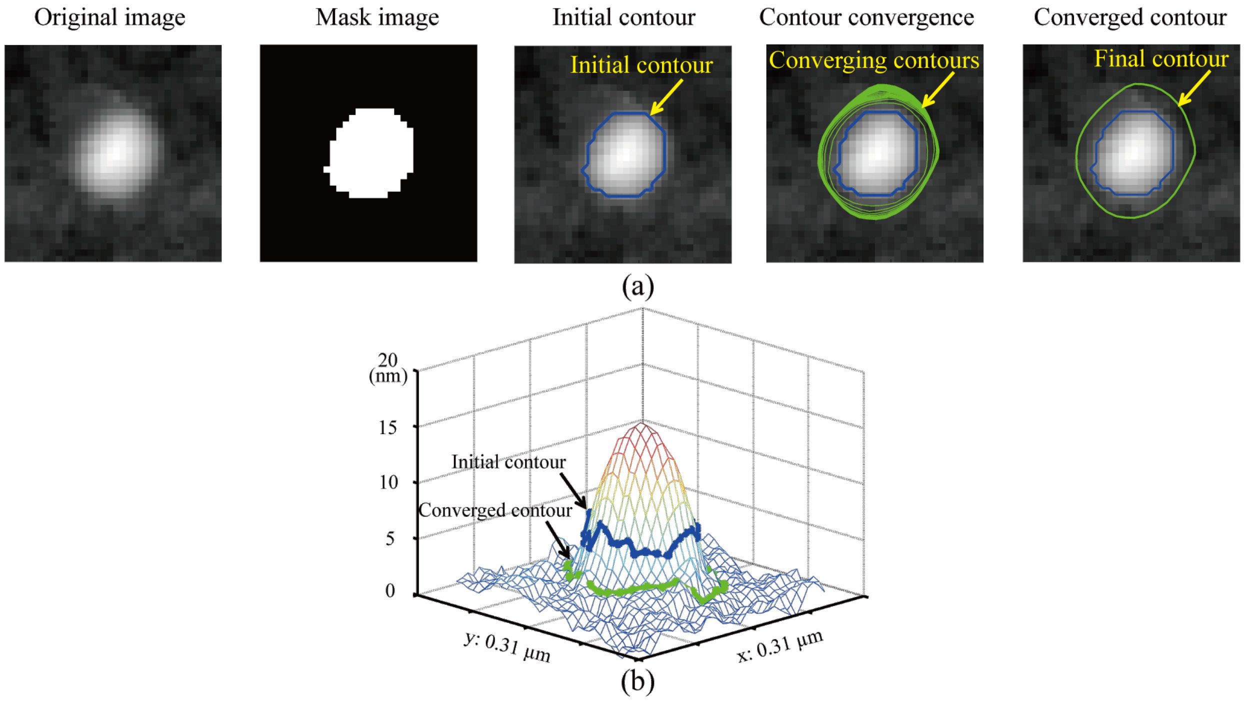

Figure 6: Demonstration of NB image segmentation with the proposed method. (a) The procedure of the NB boundary detection. The first figure shows the raw AFM image. The threshold method is used to select a preliminary mask for the selected NB, as shown in the second figure. The boundary of the mask obtained in the threshold method is extracted and taken as the initial contour (third figure). Driven by the field of gradient of height, the initial contours gradually converge to the boundary, as indicated by the green contours in the fourth figure. The contour is finally converged at the boundary, where the contour achieves the minimum energy (fifth figure). (b) Mesh plot of the NB with the detected boundaries obtained by the threshold method and the proposed method. It is clear that the proposed method provides an optimized boundary detection with a correct detected area as compared with that obtained with the threshold method.

comparison of the contours obtained by the threshold method and the proposed method as a mesh plot of the selected NB. One can see that the contour obtained with the proposed method (green contour) converges to the actual boundary of the NB and provides a much better estimation of the boundary than that obtained with the threshold method (blue contour).

The proposed method can also be used to detect the NB volume. In this study, the average height along detected boundaries is defined as the bottom of NB. The volume enclosed by the NB surface and the horizontal plane determined by the detected bottom is taken as NB volume. The detected volumes for the example given are 3.6×10^4 nm^3 and 6.3×10^4 nm^3 from the threshold method and the proposed method, respectively. One can see that the proposed method has a much better estimation of volume than the threshold method.

Figure 7 shows the comparison of the contour expansion results with different threshold values during contour initialization. The blue contours in Figure 7a,b are initialized contours with threshold values of 10 nm and 18 nm, respectively. The green contour in Figure 7a and the purple contour in Figure 7b are converged contours using the proposed method with corresponding initial contours. Although the initialized contours are quite different, the converged contours are superimposed on one other, as shown in Figure 7c.

Results and Discussion

In this section, NB characterization was implemented using the proposed image segmentation method. Additionally, the change in morphology of the NBs during coalescence was studied.

Image segmentation with the proposed method

The AFM image shown in Figure 3b was segmented with the proposed method. First, the threshold method (threshold = 7.5 nm) was applied to the image. A mask image was obtained, as shown in Figure 8a. The boundaries of the masks were extracted and taken as the initial contours for each NB. In Figure 8b, the blue contours are the initialized contours extracted from Figure 8a. With the proposed method, the initial contours converge towards the actual NB boundaries. The green contours in Figure 8b are the converged contours. They clearly enclose larger areas and thus provide a better estimation of the boundaries. Figure 8c shows the comparison of the covered areas enclosed by the contours detected with the threshold

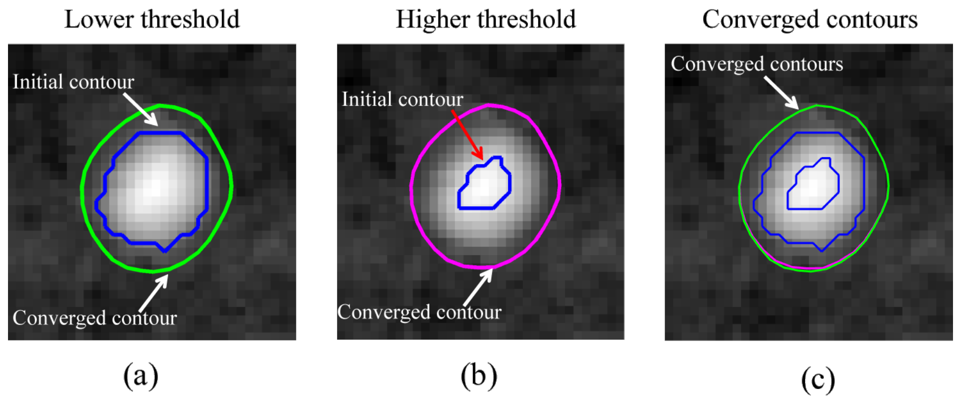

Figure 7: The proposed method is robust to the selection of the threshold value during contour initialization. (a) Initialized contour obtained with a lower threshold value (10 nm) and corresponding converged contour obtained using the proposed method. (b) Initialized contour obtained with a higher threshold value (18 nm) and corresponding converged contour. (c) Comparison of the initialized contours and the converged contours obtained with the different threshold values. The coverged contours are superimposed on each other, which indicates that the proposed method is robust to the selection of the threhold value.

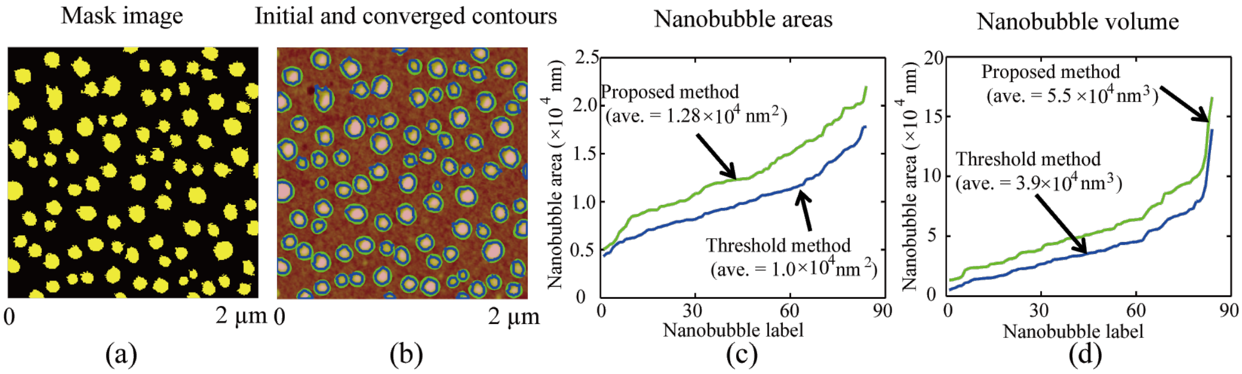

Figure 8: Implementation of image segmentation for all NBs in an AFM image. (a) Mask image obtained using the threshold method. The boundaries of the mask areas were taken as the initial guesses for boundary detection. (b) Initial contours (blue) and converged contours (green) for individual NBs. (c,d) Comparison of covered areas and volumes detected with the threshold method and the proposed method. One can see that both the covered areas and volumes detected with the threshold method are underestimated compared with that obtained by the proposed method.

method and the proposed method. The NBs were numerically labeled by increasing areas detected by the threshold method. The average value of the covered area detected by the proposed method is 1.28 × 10^4 nm^2, which is much larger than that of 1.0 × 10^4 nm^2 detected by the threshold method. Figure 8d compares the detected NB volumes for the two different methods. Similarly, the average volume detected by the proposed method is 5.5 × 10^4 nm^3, which is much larger than that detected by the threshold method (3.9 × 10^4 nm^3).

Morphological characterization of NBs

The morphological characterization for the NBs found in the AFM image was automatically implemented and the NB boundaries were detected. To obtain the height information, the contact angle and radius of curvature, as well as the cross sections for individual NBs were first extracted, whereby the NB centroids must first be determined. In this study, the centroid (x_c, y_c) of a NB was calculated within the detected boundary with the following equation:

$$(x_c, y_c) = \left(\frac{\sum H_i x_i}{\sum H_i}, \frac{\sum H_i y_i}{\sum H_i} \right), \qquad (11)$$

where H_i is the height of the ith point within the detected NB boundary and (x_i, y_i) is the coordinate of the point in the image. To obtain the cross section, a line is automatically drawn along the fast scan direction in the NB image across the detected centroid. The two intersection points of the line with the detected boundary result. The portion of the profile between the two interaction points is selected as the cross section of the NB.

With the detected cross sections, the NB height, width, contact angle and radius of curvature can be obtained.

Figure 9a shows the detected boundaries along with the automatically selected cross sections for all NBs in the AFM image. The blue curve in Figure 9b shows the section profile across a NB, indicated by the blue arrow in Figure 9a. The cross section was automatically selected as previously described. Through the cross section, the NB width D can be directly obtained. The selected cross section was then fitted as an elliptical arc using the least squares fitting method, as shown by the red curve.

Figure 9c–e shows the height, contact angle, and radius of curvature as a function of width, respectively, for all NBs in Figure 9a. One can see that the NB height increases with increasing width. The NB contact angle varies in between 150° and 170° and slightly decreases with increasing width. The measured contact angle and the correlation between contact angle and NB size is consistent with that reported elsewhere [35,43,44]. In their study, they claimed that the contact angle is a function of radius of curvature. This is mainly due to the existence of line tension along the three phase contact line. Here one should note that the tip radius, contact angle, as well as width shown in Figure 9 are the statistical values directly obtained from AFM images. It is known that the AFM images are a combination of sample topography and the shape of the cantilever tip [45,46]. Here we take the radius of curvature as an example. For the tip used in this study, the half cone angle, α_{tip}, is less than 20°. Since contact angle θ for NB imaging is much larger than $(90° + \alpha_{\text{tip}})$, one can assume the NBs are probed only at the spherical tip apex and the side wall of the tip does not touch the NBs. The measured radius of curvature, R', is given as $R' = R + R_{\text{tip}}$, where R_{tip} (8 nm in this case) is the radius of curvature of the AFM tip [46]. One can see that tip convolution leads to an overestimation of the radius of curvature. Assuming the NB heights are not influenced by the tip shape, the NB width and contact angle can then be obtained.

The proposed method was used to study morphological changes in NBs in terms of number, covered area, and volume during coalescence. In this study, a same sample area was imaged with different setpoints and all of the obtained images were postprocessed with the flattening method. For the area, a high setpoint (95%) was first applied to obtain the initial image, as

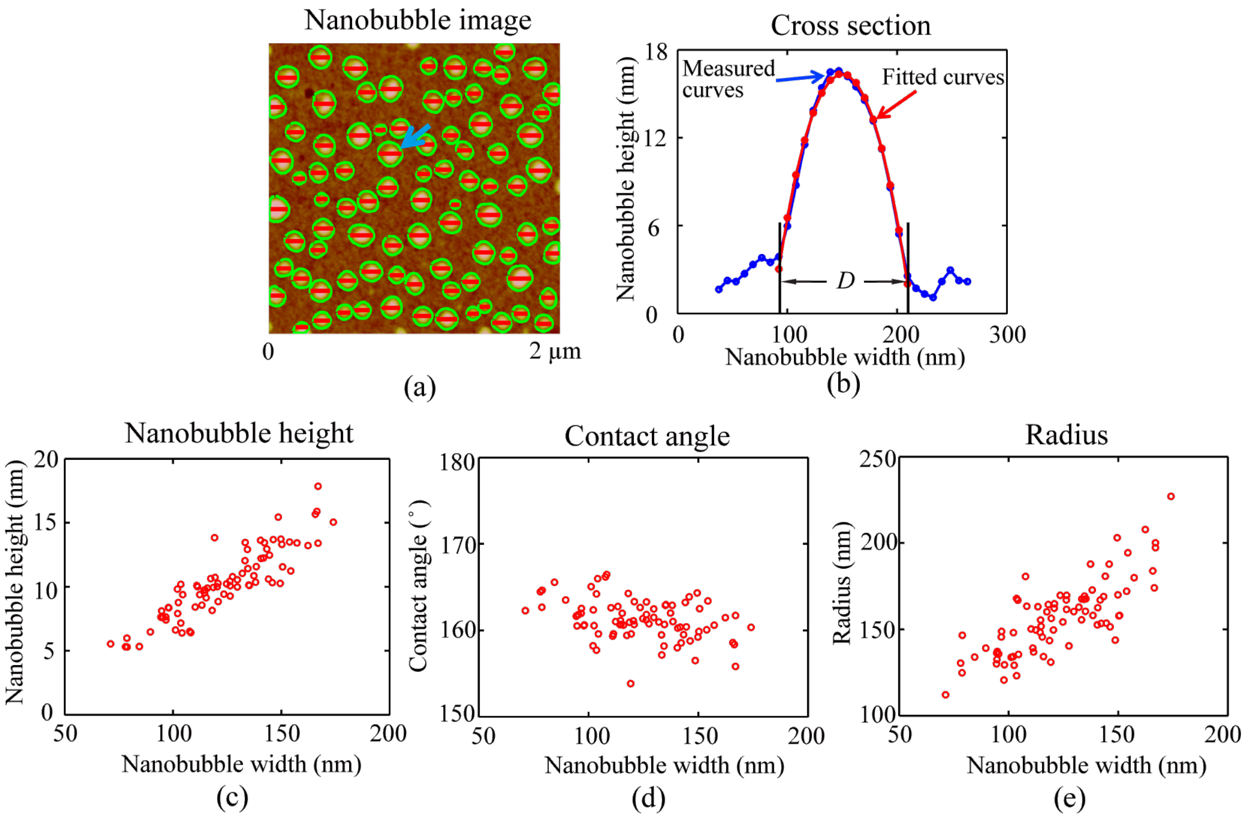

Figure 9: Morphological characterization of NBs detected with the proposed method. (a) Automated extraction of the NB cross sections after image segmentation. (b) Cross section of the NB indicated by the blue arrow in (a) and a corresponding least squares fit curve by fitting the profile as a circular arc. (c–e) The height, contact angle, and radius of curvature as a function of width for all detected NBs in the AFM image, respectively. The NB height and radius of curvature increase with width, while the contact angle decreases with width.

shown in the first image of Figure 10a. After that, a lower setpoint of 85% was applied and NB coalescence occurred [6]. This was confirmed with another high setpoint (95%), as shown in the second figure of Figure 10a. Similarly, setpoints of 79% and 66% were applied to scan the area. After each high-load (lower setpoint) scan, the 95% setpoint scanning was selected to check the corresponding changes after coalescence. The third and fourth images in Figure 10a show images after further NB coalescence. Apparently, the density of NBs decreases with increased scan load.

The AFM images shown in Figure 10a were processed with the proposed image segmentation method. The blue contours in the figures are initial contours extracted using the threshold method and the green contours are detected boundaries with the proposed method. For each image, the threshold value was carefully selected. First, the threshold value should be low enough to cover as large of an area as possible. Second, the selected threshold value should not cause oversegmentation. For the four images shown in Figure 10a, the threshold values of 8.0 nm, 7.5 nm, 7.5 nm, and 7.6 nm were selected. In the images, the blue contours are the initial contours obtained with the threshold method, while the green contours are the detected boundaries with the proposed method. Figure 10b shows the number of NBs as a function of applied setpoint. One can see that the number of NBs first slightly decreased with increased scan load when the setpoint decreased from 95% to 79%. Then, it rapidly decreased when the setpoint decreased from 79% to 66%.

Figure 10c shows the covered area and coverage rate as a function of applied setpoint. Compared with the proposed method, the threshold method underestimated the covered area by about 14%. More importantly, we found the covered area did not monotonically change with decreased setpoint value. The covered area first increases with increased setpoint value when

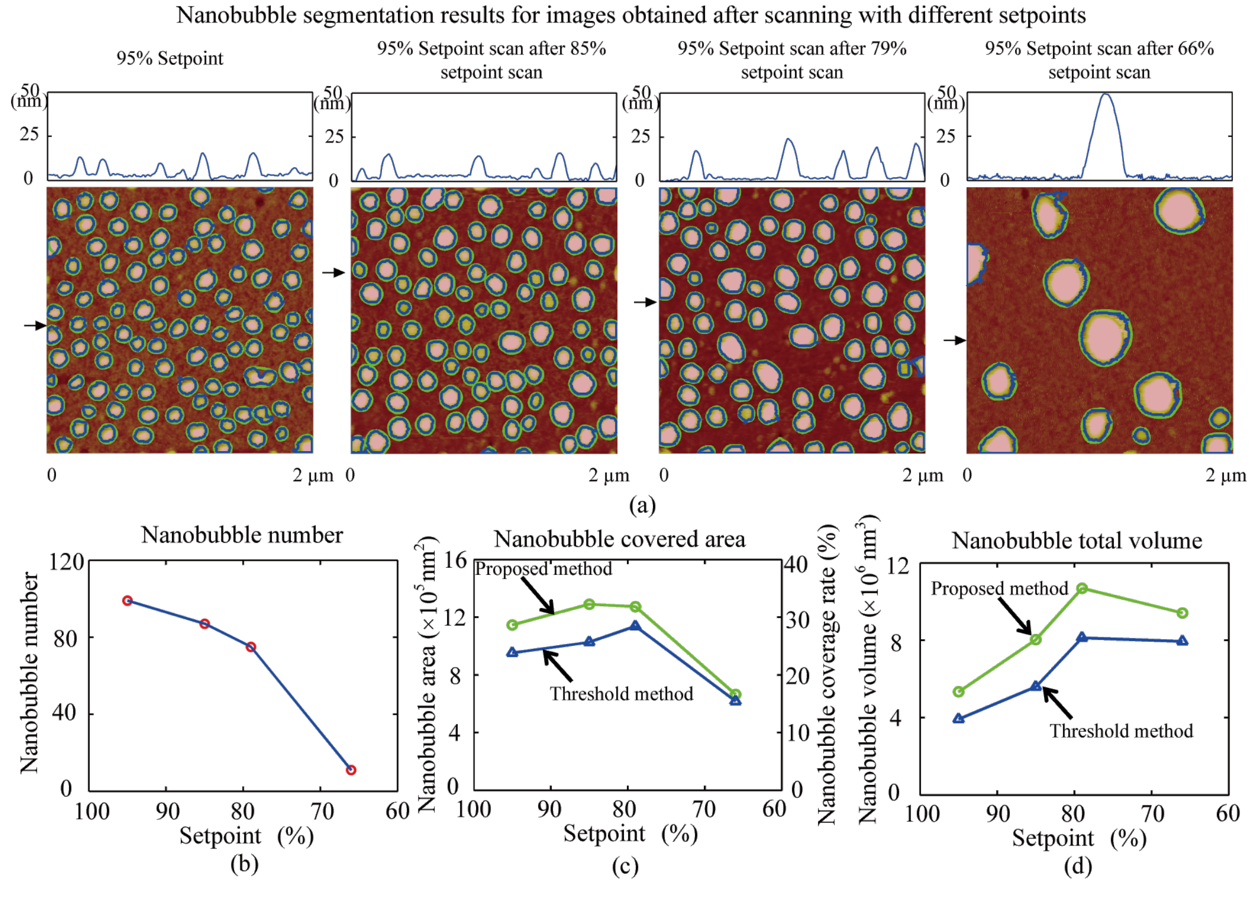

Figure 10: Change in the number of NBs, covered area, and total volume in the same scanning area as a function of decreased setpoint (increased scan load). (a) AFM image and corresponding segmentation results for a series of AFM images scanned with different setpoints. The first figure is the image scanned with a 95% setpoint. The second, third, and fourth images are the obtained with a 95% setpoint preceded by scanning with 85%, 79%, and 66% setpoints, respectively. With decreasing a setpoint, NB coalescence occurred, resulting in a decreased number of NBs and increased NB size. (b–d) number of NBs, covered area, and total volume in the same scan area as a function of applied setpoint. The number of NBs decreases with decreasing setpoint. The total covered area and total volume first increased and then decreased with the setpoint value.

the setpoint is decreased from 95% to 85%. The maximum coverage rate is 32.2%, which was achieved after the 58% setpoint was achieved. Then, the coverage rate decreases from 31.8% to 16.6% when the setpoint is further decreased from 79% to 66%.

In addition to the covered area, the change of the total NB volume in the scan area was studied. The total volume as a function of applied setpoint obtained with the threshold method and the proposed method is shown in Figure 10d. Compared with the proposed method, the threshold method underestimated the volume detection by about 24%. One can see that the total volume first increases when the setpoint is decreased from 95% to 79% and then remains at about 1.0×10^7 nm^3 for setpoint values between 79% and 66%.

One explanation for the increased total volume could be the deceased inner pressure with increasing size. According to the Laplace–Young equation, the pressure difference Δp across a NB can be given as [47]:

$$\Delta p = 2\gamma_{\mathrm{LV}} / R. \quad (12)$$

The inner pressure p can be given as:

$$p = p_0 + \Delta p, \quad (13)$$

where p_0 is the ambient pressure. With a decreasing setpoint, NB coalescence occurred and the NB size (R) increases, which leads to decreased inner pressure, assuming the ambient pressure p_0 is constant during the experiment. The increased NB size will lead to decreased inner pressure. The quantity of gas molecules can be evaluated with $p{\cdot}V$, where V is the NB volume. The decreased pressure will lead to an increased NB volume. In this study, the inner pressure can be obtained by the radius of curvature for each NB using Equation 13. The volume can be directly measured with the detected boundaries. The sum of $p_i{\cdot}V_i$ can then be obtained for NBs in each image shown in Figure 10a**.** The result is shown in Figure 11. From this result, one can see that the $p{\cdot}V$ increases with a decreasing setpoint when the setpoint is decreased from 95% to 79%. After that, $p{\cdot}V$ rapidly decreases with decreasing setpoint when the setpoint is decreased from 79% to 66%.

The measured results indicate that the total number of gas molecules trapped in the NBs may not be constant during coalescence. The observation is consistent with that recently reported by Li et al. [48] In their study, they found that the total number of gas molecules in a newly formed NB after coalescence was 112.5% higher than that in the corresponding NBs before coalescence. They stated that the increased number of gas molecules after coalescence chould be due to the existence of an interfacial gas enrichment layer [11,49] and the dynamic equilibrium mechanism between the influx and the outflux around the three phase contact line of the NBs [50]. The inner pressure decreases with increasing NB size, which increases the gas influx into the newly formed NBs. This results in an increased number of gas molecules. However, the reason for the decreased number of gas molecules when the setpoint is decreased from 79% to 66% is still unknown. For the above analysis, the NBs are assumed to be moved and merged into other NBs during coalescence. However, it is still not clear if some NBs were broken during this process, especially when higher loads were applied. One explanation for the decreased $p{\cdot}V$ when the setpoint was decreased from 79% to 66% could be the dissolution of some NBs during coalescence.

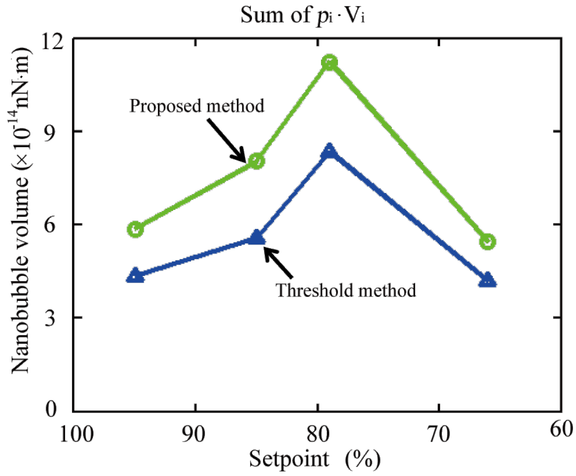

Figure 11: Sum of $p_i{\cdot}V_i$ obtained with the threshold method and the proposed method for images shown in Figure 10a.

Conclusion

In this study, the morphological characterization of NBs was implemented. Here, a new method was developed for image segmentation through the combination of the threshold method and the active contour method. The threshold method was used to locate the NBs and to obtain their preliminary boundaries. In the active contour method, driven by the gradient of the height, the preliminarily obtained boundaries converge towards actual boundaries and achieve the optimized boundary detection. With the proposed image segmentation method, the diameter, contact angle and radius of curvature for all NBs in AFM images were automatically measured. The results showed that the NB height and radius of curvature increase with its width, while contact angle decreases with increasing width.

The morphological changes in the NBs occurring during coalescence were quantitatively characterized for the first time with the proposed method. A series of scans with setpoints of 95%, 85%, 79%, and 66% were applied to a same scan area. The changes in the NB density, covered area, and volume were quantitatively studied. The results showed that the NB density first gradually decreases when the setpoint was decreased from 95% to 79% and then rapidly decreased when the setpoint was decreased from 79% to 66%. The covered area first increased when the setpoint decreased from 95% to 85%. The maximum coverage rate of 32.2% was achieved at an 85% setpoint value. Then, the coverage rate decreased from 31.8% to 16.6% when the setpoint was decreased from 79% to 66%. The total volume first increased when the setpoint was decreased from 95% to 79% and then stayed at about 1.0×10^7 nm^3 between the 79% and 66% setpoint values.

Supporting Information

Supporting Information File 1

Additional experimental information.
[http://www.beilstein-journals.org/bjnano/content/supplementary/2190-4286-6-98-S1.pdf]

Acknowledgements

This work is supported by the National Natural Science Foundation of China (Grant No. 51305019), Beijing Natural Science Foundation (Grant No. 3144030), the Specialized Research Fund for the Doctoral Program of Higher Education (Grant No. 20131102120021) and the China Postdoctoral Science Foundation funded projects (Grant No. 201104421 and 20100471031).

References

1. Lou, S.-T.; Ouyang, Z.-Q.; Zhang, Y.; Li, X.-J.; Hu, J.; Li, M.-Q.; Yang, F.-J. *J. Vac. Sci. Technol., B* **2000,** *18,* 2573. doi:10.1116/1.1289925
2. Yang, S.; Dammer, S. M.; Bremond, N.; Zandvliet, H. J. W.; Kooij, E. S.; Lohse, D. *Langmuir* **2007,** *23,* 7072–7077. doi:10.1021/la070004i
3. Tyrrell, J. W. G.; Attard, P. *Phys. Rev. Lett.* **2001,** *87,* 176104. doi:10.1103/PhysRevLett.87.176104
4. Agrawal, A.; Park, J.; Ryu, D. Y.; Hammond, P. T.; Russell, T. P.; McKinley, G. H. *Nano Lett.* **2005,** *5,* 1751–1756. doi:10.1021/nl051103o
5. Holmberg, M.; Kühle, A.; Garnæs, J.; Mørch, K. A.; Boisen, A. *Langmuir* **2003,** *19,* 10510. doi:10.1021/la0352669
6. Bhushan, B.; Wang, Y.; Maali, A. *J. Phys.: Condens. Matter* **2008,** *20,* 485004. doi:10.1088/0953-8984/20/48/485004
7. Tyrrell, J. W. G.; Attard, P. *Langmuir* **2002,** *18,* 160–167. doi:10.1021/la0111957
8. Wang, Y.; Bhushan, B.; Zhao, X. *Nanotechnology* **2009,** *20,* 045301. doi:10.1088/0957-4484/20/4/045301
9. Wang, Y.; Bhushan, B.; Zhao, X. *Langmuir* **2009,** *25,* 9328–9336. doi:10.1021/la901186a
10. Switkes, M.; Ruberti, J. W. *Appl. Phys. Lett.* **2004,** *84,* 4759–4761. doi:10.1063/1.1755837
11. Steitz, R.; Gutberlet, T.; Hauss, T.; Klösgen, B.; Krastev, R.; Schemmel, S.; Simonsen, A. C.; Findenegg, G. H. *Langmuir* **2003,** *19,* 2409–2418. doi:10.1021/la026731p
12. Poynor, A.; Hong, L.; Robinson, I. K.; Granick, S.; Zhang, Z.; Fenter, P. A. *Phys. Rev. Lett.* **2006,** *97,* 266101. doi:10.1103/PhysRevLett.97.266101
13. Zhang, X. H.; Quinn, A.; Ducker, W. A. *Langmuir* **2008,** *24,* 4756–4764. doi:10.1021/la703475q
14. Chan, C. U.; Ohl, C.-D. *Phys. Rev. Lett.* **2012,** *109,* 174501. doi:10.1103/PhysRevLett.109.174501
15. Karpitschka, S.; Dietrich, E.; Seddon, J. R. T.; Zandvliet, H. J. W.; Lohse, D.; Riegler, H. *Phys. Rev. Lett.* **2012,** *109,* 066102. doi:10.1103/PhysRevLett.109.066102
16. Xing, Z.; Wang, J.; Ke, H.; Zhao, B.; Yue, X.; Dai, Z.; Liu, J. *Nanotechnology* **2010,** *21,* 145607. doi:10.1088/0957-4484/21/14/145607
17. Yin, T.; Wang, P.; Zheng, R.; Zheng, B.; Cheng, D.; Zhang, X.; Shuai, X. *Int. J. Nanomed.* **2012,** *7,* 895–904. doi:10.2147/IJN.S28830
18. Weber, J.; Agblevor, F. A. *Process Biochem.* **2005,** *40,* 669–676. doi:10.1016/j.procbio.2004.01.047
19. Ishida, N.; Sakamoto, M.; Miyahara, M.; Higashitani, K. *J. Colloid Interface Sci.* **2002,** *253,* 112–116. doi:10.1006/jcis.2002.8444
20. Palmer, L. A.; Cookson, D.; Lamb, R. N. *Langmuir* **2011,** *27,* 144–147. doi:10.1021/la1029678
21. Hampton, M. A.; Nguyen, A. V. *Adv. Colloid Interface Sci.* **2010,** *154,* 30–55. doi:10.1016/j.cis.2010.01.006
22. Joseph, P.; Cottin-Bizonne, C.; Benoît, J. M.; Ybert, C.; Journet, C.; Tabeling, P.; Bocquet, L. *Phys. Rev. Lett.* **2006,** *97,* 156104. doi:10.1103/PhysRevLett.97.156104
23. Lauga, E.; Stone, H. A. *J. Fluid Mech.* **2003,** *489,* 55–77. doi:10.1017/S0022112003004695
24. Ou, J.; Perot, B.; Rothstein, J. P. *Phys. Fluids* **2004,** *16,* 4635–4643. doi:10.1063/1.1812011
25. Sbragaglia, M.; Prosperetti, A. *J. Fluid Mech.* **2007,** *578,* 435–451. doi:10.1017/S0022112007005149
26. Wang, Y.; Bhushan, B.; Maali, A. *J. Vac. Sci. Technol., A* **2009,** *27,* 754–760. doi:10.1116/1.3086637
27. Bhushan, B.; Wang, Y.; Maali, A. *Langmuir* **2009,** *25,* 8117–8121. doi:10.1021/la900612s
28. Janda, P.; Frank, O.; Bastl, Z.; Klementová, M.; Tarábkova, H.; Kavan, L. *Nanotechnology* **2010,** *21,* 095707. doi:10.1088/0957-4484/21/9/095707
29. Alsawafta, M.; Badilescu, S.; Truong, V.-V.; Packirisamy, M. *Nanotechnology* **2012,** *23,* 065305. doi:10.1088/0957-4484/23/6/065305
30. Zhang, X. H.; Zhang, X. D.; Lou, S. T.; Zhang, Z. X.; Sun, J. L.; Hu, J. *Langmuir* **2004,** *20,* 3813. doi:10.1021/la0364542
31. Guan, M.; Guo, W.; Gao, L.; Tang, Y.; Hu, J.; Dong, Y. *ChemPhysChem* **2012,** *13,* 2115–2118. doi:10.1002/cphc.201100912
32. Berkelaar, R. P.; Seddon, J. R. T.; Zandvliet, H. J. W.; Lohse, D. *ChemPhysChem* **2012,** *13,* 2213–2217. doi:10.1002/cphc.201100808
33. Bhushan, B.; Pan, Y.; Daniels, S. *J. Colloid Interface Sci.* **2013,** *392,* 105–116. doi:10.1016/j.jcis.2012.09.077
34. Belova, V.; Krasowska, M.; Wang, D.; Ralston, J.; Shchukin, D. G.; Möhwald, H. *Chem. Sci.* **2013,** *4,* 248–256. doi:10.1039/c2sc21321d
35. van Limbeek, M. A. J.; Seddon, J. R. T. *Langmuir* **2011,** *27,* 8694–8699. doi:10.1021/la2005387

36. Zhang, X.; Uddin, M. H.; Yang, H.; Toikka, G.; Ducker, W.; Maeda, N. *Langmuir* **2012,** *28,* 10471–10477. doi:10.1021/la301851g
37. Lüderitz, L. A. C.; von Klitzing, R. *Langmuir* **2012,** *28,* 3360–3368. doi:10.1021/la202635a
38. Zhang, X.; Chan, D. Y. C.; Wang, D.; Maeda, N. *Langmuir* **2013,** *29,* 1017–1023. doi:10.1021/la303837c
39. Walczyk, W.; Schön, P. M.; Schönherr, H. *J. Phys.: Condens. Matter* **2013,** *25,* 184005. doi:10.1088/0953-8984/25/18/184005
40. Guo, W.; Shan, H.; Guan, M.; Gao, L.; Liu, M.; Dong, Y. *Surf. Sci.* **2012,** *606,* 1462–1466. doi:10.1016/j.susc.2012.05.018
41. Kass, M.; Witkin, A.; Terzopoulos, D. *Int. J. Comput. Vision* **1988,** *1,* 321–331. doi:10.1007/BF00133570
42. Wang, Y.; Wang, H.; Bi, S. *AIP Adv.* **2014,** *4,* 057130. doi:10.1063/1.4880242
43. Song, B.; Walczyk, W.; Schönherr, H. *Langmuir* **2011,** *27,* 8223–8232. doi:10.1021/la2014896
44. Yang, J.; Duan, J.; Fornasiero, D.; Ralston, J. *J. Phys. Chem. B* **2003,** *107,* 6139–6147. doi:10.1021/jp0224113
45. Kameda, N.; Sogoshi, N.; Nakabayashi, S. *Surf. Sci.* **2008,** *602,* 1579–1584. doi:10.1016/j.susc.2008.02.023
46. Borkent, B. M.; de Beer, S.; Mugele, F.; Lohse, D. *Langmuir* **2010,** *26,* 260–268. doi:10.1021/la902121x
47. Israelachvili, J. *Intermolecular & Surface Forces;* Academic Press: London, United Kingdom, 1992.
48. Li, D.; Jing, D.; Pan, Y.; Wang, W.; Zhao, X. *Langmuir* **2014,** *30,* 6079–6088. doi:10.1021/la501262a
49. Lu, Y.-H.; Yang, C.-W.; Hwang, I.-S. *Langmuir* **2012,** *28,* 12691–12695. doi:10.1021/la301671a
50. Brenner, M. P.; Lohse, D. *Phys. Rev. Lett.* **2008,** *101,* 214505. doi:10.1103/PhysRevLett.101.214505

License and Terms

The definitive version of this article is the electronic one which can be found at:
doi:10.3762/bjnano.6.98

BEILSTEIN JOURNAL OF NANOTECHNOLOGY

Optimization of phase contrast in bimodal amplitude modulation AFM

Mehrnoosh Damircheli[1,2], Amir F. Payam[1] and Ricardo Garcia*[1]

Full Research Paper

Open Access

Address:
[1]Instituto de Ciencia de Materiales de Madrid, CSIC, Sor Juana Inés de la Cruz 3, 28049 Madrid, Spain and [2]Permanent address: Department of Mechanical Engineering, Shahr-e-Qods Branch, Islamic Azad University, Tehran, Iran

Email:
Ricardo Garcia* - r.garcia@csic.es

* Corresponding author

Keywords:
bimodal AFM; dynamic AFM; tapping mode

Beilstein J. Nanotechnol. **2015,** *6,* 1072–1081.
doi:10.3762/bjnano.6.108

Received: 17 October 2014
Accepted: 30 March 2015
Published: 28 April 2015

This article is part of the Thematic Series "Advanced atomic force microscopy techniques III".

Guest Editor: T. Glatzel

Abstract

Bimodal force microscopy has expanded the capabilities of atomic force microscopy (AFM) by providing high spatial resolution images, compositional contrast and quantitative mapping of material properties without compromising the data acquisition speed. In the first bimodal AFM configuration, an amplitude feedback loop keeps constant the amplitude of the first mode while the observables of the second mode have not feedback restrictions (bimodal AM). Here we study the conditions to enhance the compositional contrast in bimodal AM while imaging heterogeneous materials. The contrast has a maximum by decreasing the amplitude of the second mode. We demonstrate that the roles of the excited modes are asymmetric. The operational range of bimodal AM is maximized when the second mode is free to follow changes in the force. We also study the contrast in trimodal AFM by analyzing the kinetic energy ratios. The phase contrast improves by decreasing the energy of second mode relative to those of the first and third modes.

Introduction

The atomic force microscope is a versatile and powerful tool for imaging, compositional mapping and modification of surfaces with atomic and nanoscale spatial resolutions [1-8]. The evolution of AFM is being shaped by the need to provide images of heterogeneous surfaces with high spatial resolution combined with compositional contrast and/or material properties mapping [7,9]. Amplitude modulation force microscopy (AM-AFM) was designed to excite the cantilever near or at its fundamental free resonant frequency [2]. However, the need to improve and/or provide quantitative compositional contrast without compromising the data acquisition speed has led to the development of several AFM modes, specifically multifrequency force microscopy methods [9-32].

Bimodal force microscopy is a multifrequency AFM method that uses two eigenmode frequencies for excitation and detection (Figure 1) [9]. It has several configurations depending on the feedback schemes [16-24]. In the first bimodal AFM configuration (bimodal AM) [15,16], the feedback acts on the amplitude of the first mode by keeping it at a fixed value during imaging while the second mode operates in an open loop. The ability of bimodal AM to map compositional variations under the influence of conservative forces is a main advantage with respect to AFM phase imaging (tapping mode AFM), where the phase contrast is related to variations in energy dissipation [33].

In AM-AFM there are two interacting regimes, attractive and repulsive [2]. The regimes are defined by the average value of the force [34]. A transition between the regimes is usually accompanied by a sudden change of the observables (amplitude and phase shift). In bimodal AFM some additional contrast regimes has been identified [35-37] where sudden changes of the phase contrast are not associated with changes in the sign of the average value of the force. The origin of those regimes are discussed in terms of the different energies of the system, kinetic energy of the exited modes [35-38], the input energy [36] or the energy transfer between the modes [37]. In general those regimes appear when the modes are highly coupled. This happens when the energy of the first and second mode are comparable [35].

This context has also stimulated other multifrequency AFM variations such as trimodal AFM [39-41]. In trimodal AFM the first three flexural modes are excited and detected. The feedback operates on the amplitude of the first mode while both second and third modes are in open loops. It has been shown the usefulness of the third mode to modulate the indentation [23]. A comparison of the trade-offs in sensitivity and sample depth have been performed with bimodal and trimodal AFM in the repulsive regime [41]. However, a similar comparison has not been reported for the attractive interaction regime.

In bimodal AFM (Figure 1), the advances in instrumentation are ahead of its theoretical understanding. To bridge the gap between experiments and theory we study the conditions to optimize the compositional contrast and material properties sensitivity in bimodal AM. The compositional contrast is usually defined as the phase shift difference of the second mode between two regions of the surface of a heterogeneous material. We study the phase contrast as a function of the amplitude ratio, the amplitude values of the second mode and the kinetic energy ratios of the excited modes. We also study the phase contrast between different materials by including energy dissipation in the tip–sample interaction, by inverting the roles of the excited modes (indirect bimodal AM) as well as in trimodal AFM. In the latter, the phase contrast is maximized when the energy of the second mode is much smaller than the other excited modes.

Results and Discussion

Equation of motion and tip–surface forces

To analyze the dependence of the phase contrast on the values of the different parameters we have used numerical simulations. For this we consider that bimodal AFM is characterized by the simultaneous excitation of two cantilever resonant frequencies,

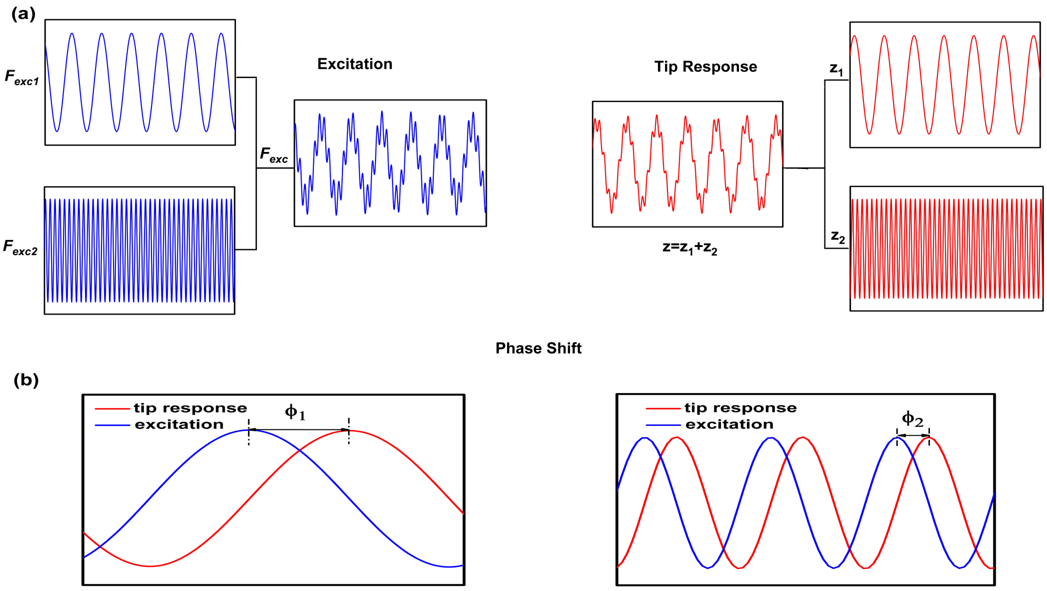

Figure 1: (a) Scheme of the excitation and detection signals in bimodal AM configuration. (b) Definition of phase shifts in bimodal AM for the first and the second modes.

usually the lowest flexural eigenmodes [42]. The total driving force is expressed as

$$F_{\text{exc}} = F_{01}\cos\omega_1 t + F_{02}\cos\omega_2 t \qquad (1)$$

Then, the cantilever–tip ensemble will be described by the system of two differential modal equations,

$$\ddot{z}_i(t) + \frac{\omega_i}{Q_i}\dot{z}_i(t) + \omega_i^2 z_i(t) = \frac{F_{01}\cos\omega_1 t + F_{02}\cos\omega_2 t + F_{\text{ts}}(d)}{m} \qquad (2)$$

$$F_{0i} = \frac{k_i}{Q_i}A_{0i} \qquad (3)$$

$$z_i = A_i\cos(\omega_i t - \phi_i) \qquad (4)$$

with i = 1,2; ω_i, k_i, Q_i, ϕ_i, A_i and A_{0i} are, respectively, the angular frequency, the force constant, quality factor, phase shift, amplitude and free amplitude of mode i; $m = 0.25m_\text{c}$ is an effective mass while m_c is the real cantilever–tip mass. The solution of the above equation has two components z_1 and z_2 that vibrate, respectively, with the eigenmode frequencies ω_1 and ω_2. The instantaneous tip–surface distance d is defined by

$$d = z_0 + z_\text{c} + z_1 + z_2 \qquad (5)$$

where z_0 and z_c are respectively, the average tip deflection and the average tip–surface separation. The tip–surface force is modelled by Equation 6 where a_0 is a molecular distance (0.165 nm).

Material and cantilever–tip parameters

To study the phase contrast we have simulated the bimodal AM operation for two materials gold (Au) and polystyrene (PS). The values of the material properties needed to describe the tip–surface force (Hamaker constant and Young modulus) and the operational values of the microscope are summarized in Table 1 and Table 2.

Table 1: Hamaker and Young modulus values.

H (tip-gold)	*E* (Au)	*H* (tip-PS)	*E* (PS)
12 × 10^{-20} J	75 GPa	7 × 10^{-20} J	3 GPa

Table 2: Cantilever-tip parameters.

R (nm)	k_1 (N/m)	f_1 (kHz)	Q_1	k_2 (N/m)	f_2 (kHz)	Q_2
20	0.896	49.16	254	35.24	308.26	995

For trimodal AFM simulations we have used the parameters shown in Table 3. To minimize some complex non-linear dynamic effects we restrict our study to situations that involve the attractive regime. The attractive forces have been modeled by van der Waals interactions with the Hamaker values given in Table 1.

Phase contrast in the attractive regime (conservative force): $A_{01} > A_{02}$

In bimodal AM the feedback loop operates on A_1, consequently the amplitude of the first mode or its ratio is the relevant parameter to be used as the independent variable. In some cases, the representation with respect to the average tip–surface distance could also provide useful information.

The dependence of ϕ_2 with A_1/A_{01} has been described previously [15,16]. In the attractive regime, it shows an increase with A_1/A_{01} decreasing (A_{01} = 10 nm). The fastest changes happen at the edges of the x-axis (small and large amplitude ratios). This behavior is reproduced for gold (Figure 2a) and PS (Figure 2b) for different values of A_{02}. Interestingly, for the same z_c the phase shift is larger for the material with the smaller Hamaker value. This is at odds what happens in amplitude modulation AFM, where the phase shifts increases with the value of H.

$$F_{\text{ts}}(d) = \begin{cases} F_{\text{vdW}}(d) = -\dfrac{HR}{6d^2} & d \ge a_0 \\[2ex] F_{\text{DMT}}(d) = \dfrac{4E_{\text{eff}}\sqrt{R}}{3}(a_0 - d)^{3/2} - \dfrac{HR}{6a_0^2} & d < a_0 \end{cases} \qquad (6)$$

Table 3: Cantilever–tip parameters in trimodal AFM.

R (nm)	k_1 (N/m)	f_1 (kHz)	Q_1	k_2 (N/m)	f_2 (kHz)	Q_2	k_3 (N/m)	f_3 (kHz)	Q_3
20	0.896	49.16	254	35.24	308.26	995	276.18	862.86	766

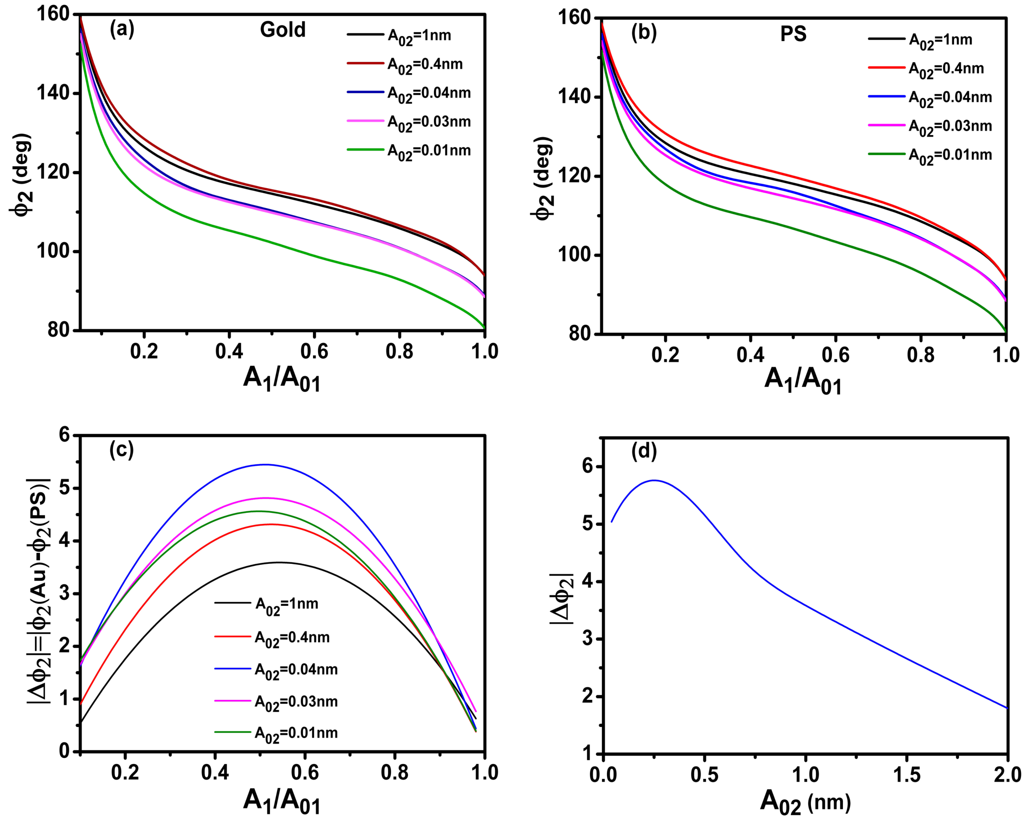

Figure 2: Bimodal AM in the attractive regime. (a) Phase shift dependence on the amplitude ratio of the first mode for different values of A_{02}. The value of the Hamaker constant is set for the Au–air–Si interface. (b) Phase shift dependence on the amplitude ratio of the first mode for different values of A_{02}. The value of the Hamaker constant is set for the PS–air–Si interface. (c) Phase contrast between Au and PS as a function of the amplitude ratio. (d) Phase contrast as a function of A_{02}. A_{01} = 10 nm; see Table 1 and Table 2 for more details.

The phase contrast $|\Delta\phi_2| = |\phi_2\,(\text{gold}) - \phi_2\,(\text{PS})|$ depends on both the A_1/A_{01}-ratio and the value of A_{02}. Two maxima are observed, one with respect to A_1/A_{01} and the other with respect to A_{02}. The first maximum happens near an A_1/A_{01}-ratio of about 0.5. It seems similar to the behavior observed in AM-AFM for the dependence of the minimum distance with A_1/A_{01} [43]. In terms of optimizing the material contrast it is more relevant to pay attention to the behavior with respect to A_{02} (Figure 2d). It shows the phase contrast for A_{01}/A_{02} ratios between 5 and 2000. Small values of A_{02} are needed to enhance the material contrast, however, for very small A_{02} the bimodal enhancement of contrast will disappear as the system becomes monomodal, i.e., tapping mode AFM. For this simulation the best contrast is yielded for an amplitude ratio of 250. This value is significantly larger than the values previously recommended (10–50) which were based on experiments [43-45].

Phase contrast in the attractive regime (dissipation): $A_{01} > A_{02}$

To study the effect of energy dissipation in the bimodal phase contrast, in addition the above conservative force, we introduce the following non-conservative interaction [47]:

$$F_{ts} = -\frac{0.43HR}{6d^2}\frac{\dot{z}}{|\dot{z}|} \qquad d \geq a_0 \tag{7}$$

The power dissipated in the sample for each mode is calculated by [47]

$$P_{\text{ts}}(i) = \frac{\omega_i k_i A_i}{2Q_i}\left(A_{0i}\sin\phi_i - A_i\right) \tag{8}$$

Figure 3a,b show the dependence of ϕ_2 versus A_1/A_{01} when the tip–sample interaction includes non-conservative interactions. The phase shift increases by reducing the A_1/A_{01}-ratio until a maximum is reached for ratios below 0.2. This behavior is reproduced for both gold and PS and for different A_{02} values. The increase of the phase shift by increasing the value of A_{02} is in agreement with experimental observations [36]. The presence of dissipation reduces the phase shift for the same A_1/A_{01}-ratio (see Figure 2). Energy dissipation in the sample softens the resonance curves which in turns reduces the phase shift. This is a common feature of resonators that is not affected by bimodal excitation. The phase contrast

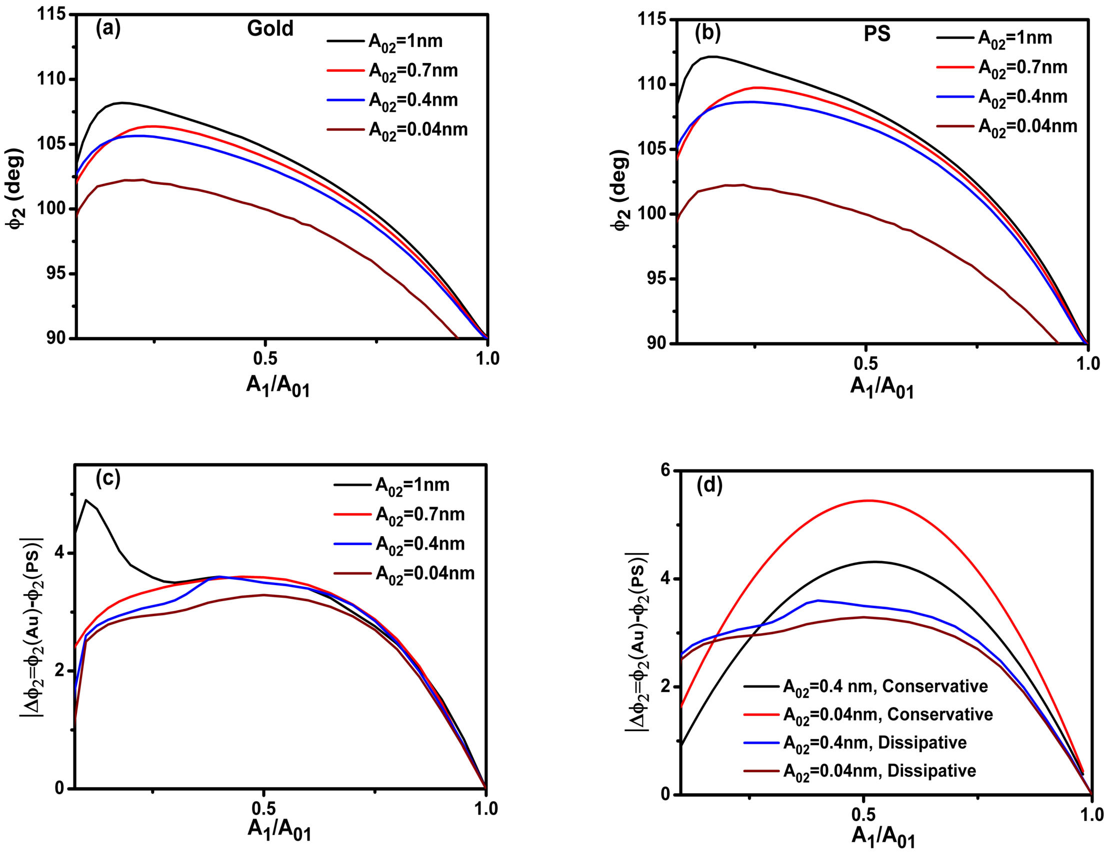

Figure 3: Phase contrast in bimodal AM in the presence of dissipation (attractive regime). (a) Phase shift dependence on the amplitude ratio of the first mode for different values of A_{02}. The value of the Hamaker constant is set for the Au–air–Si interface. (b) Phase shift dependence on the amplitude ratio of the first mode for different values of A_{02}. The value of the Hamaker constant is set for the PS–air–Si interface. (c) Phase contrast between Au and PS as a function of the amplitude ratio. (d) Comparison of the phase contrast between Au and PS with and without dissipation. A_{01} = 10 nm.

$|\Delta\phi_2| = |\phi_2\text{ (gold)} - \phi_2\text{ (PS)}|$ also shows a maximum with respect to A_1/A_{01}. The behavior is very similar to the one observed for conservative interactions (Figure 2c) except for $A_{02} \geq 1$ nm where the maximum is displaced to very small amplitude ratios. This is due to the cross-over in the amount of power dissipated between Au and PS for those amplitude ratios (see below). In general, the introduction of dissipation processes in the tip–sample interaction reduces the material contrast observed in the phase shift of the 2nd mode (Figure 3d). This is in contrast with phase imaging in amplitude modulation AFM, where the contrast is related to energy dissipation processes. It shows that the phase contrast in bimodal AM is dominated by conservative forces [42,47]. The presence of dissipation also modifies the conditions to maximize the phase contrast to smaller A_{01}/A_{02} values (20 versus 250 (no dissipation)).

To clarify the dependence of the phase contrast with the power dissipated by the tip–sample interaction we plot the dissipated power as a function of A_1/A_{01} for different materials. Figure 4a and 4b show, respectively, the total dissipated power for Au and PS. The dissipated power increases with the free amplitude of the 2nd mode and it has a maximum with respect to A_1/A_{01}. This maximum is related to the existence of a minimum in the closest tip–surface separation as a function of A_1/A_{01}. More dissipation is obtained for gold than PS because the Au–air–Si interface has a higher Hamaker constant. The power dissipated by the 2nd mode also shows a maximum with A_1/A_{01} near 0.2 (Figure 4c). A discussion about the energy transfer among different modes is presented by Solares and co-workers [48]. The data plotted in Figure 3 and Figure 4 has been obtained by using the dForce simulator [49].

Phase contrast in the attractive regime (no dissipation): A_{02} > A_{01} (inverted bimodal excitation)

In the first bimodal AM experiments the first mode carried the feedback controls while the second has an open loop (no feedback). This configuration introduced a significant asymmetry between the roles of the excited modes. This raises the question about the equivalence of the excited modes 1 and 2 for bimodal

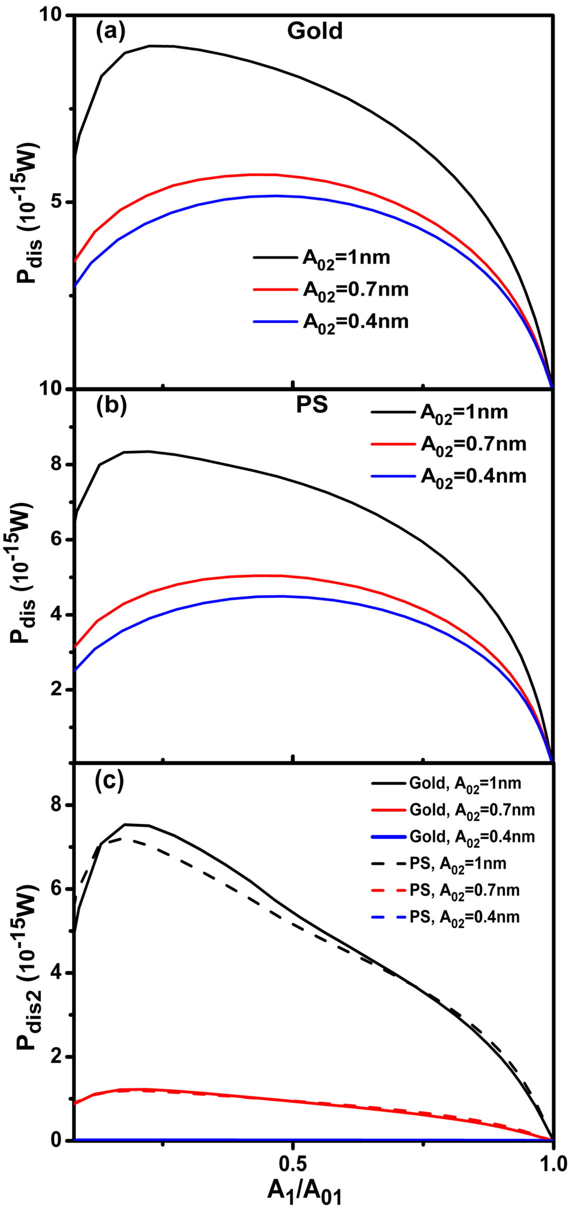

Figure 4: (a) Total dissipated power as a function of A_1/A_{01} (gold). (b) Total dissipated power as a function of A_1/A_{01} (PS). (c) Power dissipated by the second mode for different values of A_{02}. A_{01}= 10 nm. See Table 1 and Table 2 for more details.

AM operation. To answer this question we have simulated a situation where the feedback operates in the second mode while the first mode has an open loop (inverted bimodal excitation). In the simulations, the free amplitude of the second mode is 10 nm while the one of the first ranges between 0.7 and 2 nm. Other relevant parameters are described in Tables 1, 2 and 3. The cross-mode representation has ϕ_1 or $\Delta\phi_1$ as dependent variables with respect to A_2 or its ratio.

The phase shift ϕ_1 versus A_2/A_{02} shows a quick increase from 90° to close to 180° for a rather small reduction of the amplitude ratio (Figure 5a,b). In the inverted bimodal AM there is the phase contrast between Au and PS. In fact the contrast in terms of degrees is comparable to the one observed in bimodal AM, however, it happens for an extremely small range of set-point amplitudes ratios (0.99 and 0.999). This makes it impractical from the experimental point of view. In the direct bimodal AM the phase contrast is observed in almost all the amplitude ratio range from 0.1 to 0.99.

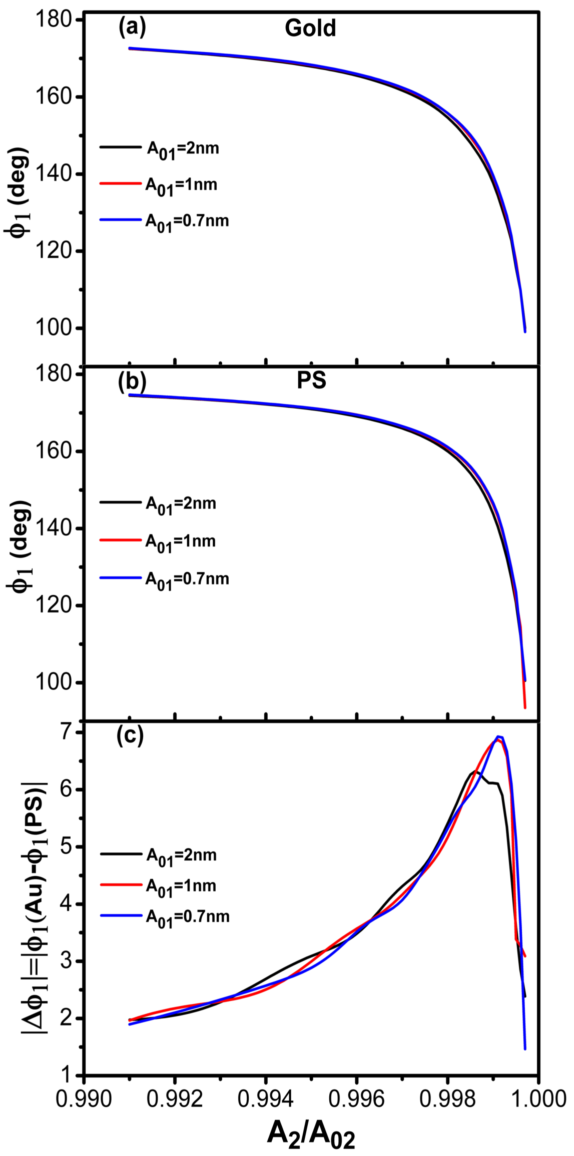

Figure 5: Inverted bimodal AM. (a) Phase shift dependence on the amplitude ratio (A_2/A_{02}). The value of the Hamaker constant is set for the Au–air–Si interface. (b) Phase shift dependence on the amplitude ratio (A_2/A_{02}). The value of the Hamaker constant is set for the PS–air–Si interface. (c) Phase contrast as a function of A_2/A_{02}. A_{02} = 10 nm; see Table 1 and Table 2 for more details.

Consequently, the roles of modes 1 and 2 in bimodal AM are not equivalent. The asymmetry is more clearly seen by plotting the dependences of A_1/A_{01} and A_2/A_{02} with respect to z_c for both the direct and the inverse bimodal AFM configurations (Figure 6). In the direct bimodal AM both A_1 and A_2 decrease with respect z_c over similar range (Figure 6a). However, in inverted bimodal AM, A_1 has almost vanished while A_2 is still starting to notice the presence of the tip–surface force (Figure 6b). The origin of this asymmetry can be traced back to the sensitivity of an oscillating system with respect to Q_i and k_i. It has been shown that the phase shift sensitivity is proportional to the Q_i/k_i ratio [43]. This ratio decreases with increasing the eigenmode index [9].

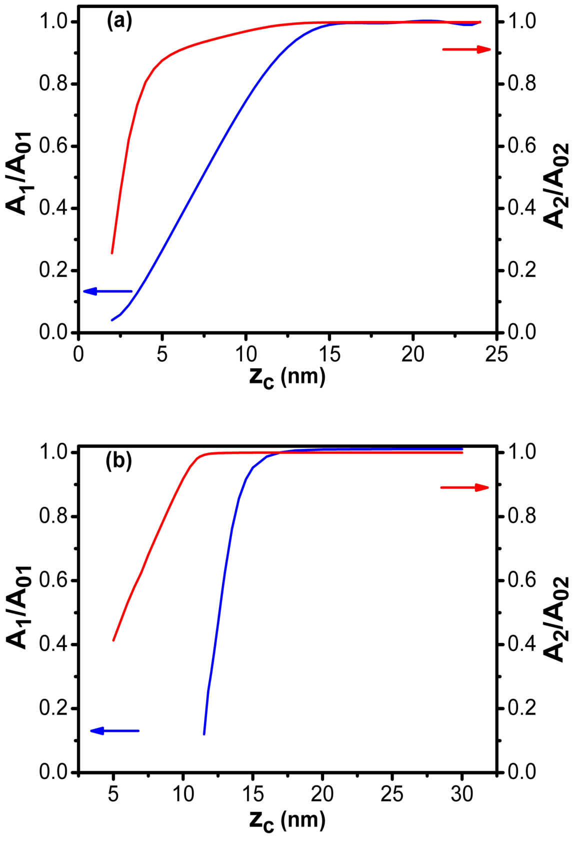

Figure 6: Comparison between direct and inverted bimodal AM. (a) Amplitude ratio dependence on the average tip–surface separation for bimodal AM (feedback on A_1). (b) Amplitude ratio dependence on the average tip–surface separation for the inverted bimodal AM (feedback on A_2).

Phase contrast in the repulsive regime (no dissipation): $A_{01} > A_{02}$

In the repulsive regime, the phase shift decreases from the non-interacting phase shift (90°) with A_1/A_{01} decreasing (Figure 7a and 7b). The decrease depends on the Young modulus and on the value of A_{02}. For the same A_1/A_{01}-ratio lower phase shift values are observed on the stiffer material. The dependence on A_{02} follows the trend observed in the attractive regime. For the same A_1/A_{01}-ratio by reducing the value from 2 to 0.4 nm the phase shift variation (from the non-interacting value, 90°) is increased. More significantly, the phase contrast measured between Au and PS is also enhanced by reducing A_{02}. A maximum is observed in the phase contrast dependence on the A_1/A_{01}-ratio (Figure 7c). The position of the maximum depends on A_{02}. The lower the value of A_{02}, the higher the A_1/A_{01}-ratio where the maximum is observed.

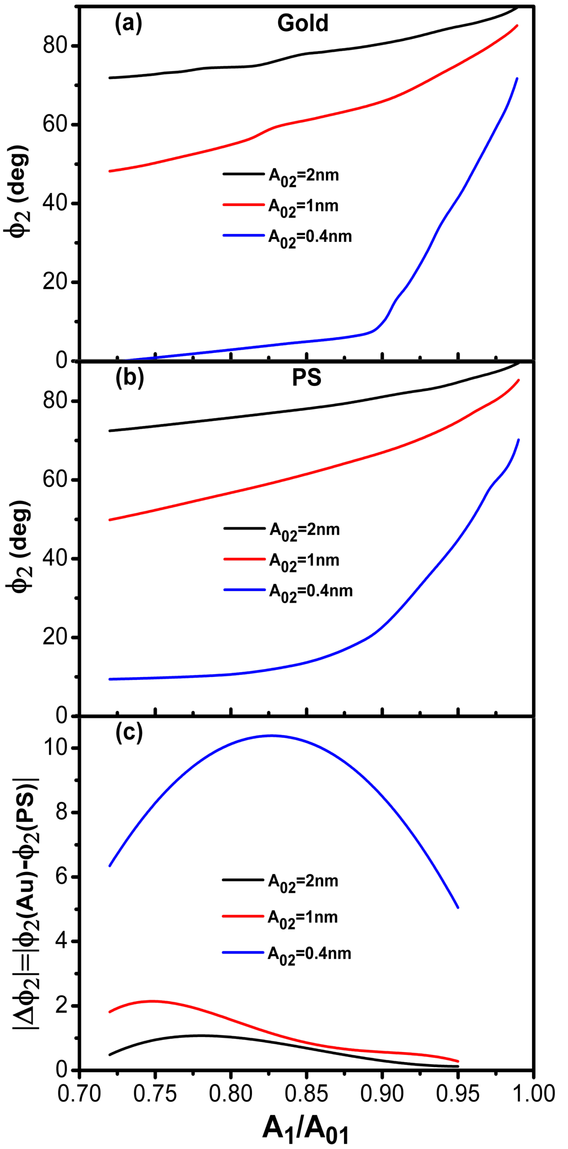

Figure 7: Bimodal AM in the repulsive regime. (a) Phase shift dependence on the amplitude ratio of the first mode for different values of A_{02}. The value of the Young modulus corresponds to Au. (b) Phase shift dependence on the amplitude ratio of the first mode for different values of A_{02}. The value of the Young modulus corresponds to PS. (c) Phase contrast between Au and PS as a function of the amplitude ratio for different A_{02}. A_{01} = 10 nm, see Table 1 and Table 2 for other parameters.

Trimodal AFM in the attractive regime

Solares and co-workers have extended the bimodal scheme by introducing an additional excitation in the third mode [39-41,46]. The third excitation in trimodal AFM offers two additional channels for compositional contrast. The value of A_{03} has been used modulate the indentation while imaging embedded nanoparticles in a soft polymer [23]. To understand some of the fundamental aspects of trimodal AFM and the differences with respect to bimodal AM we study the phase contrast in trimodal AFM in the attractive regime.

We have performed simulations by using an excitation force with contributions to the first three eigenmodes

$$F_{\text{exc}} = F_1 \cos \omega_1 t + F_2 \cos \omega_2 t + F_3 \cos \omega_3 t \qquad (9)$$

The phase contrast is studied in terms of the kinetic energy (KE) of the excited modes [38]. It has been shown that the contrast reversal observed in bimodal AM depends on the relative kinetic energy maxima of the excited modes [35,36].

$$KE_i = \frac{1}{2} k_i A_i^2 \qquad (10)$$

The kinetic energy analysis is applied to establish the optimum conditions for phase contrast in trimodal AFM. Table 4 shows the different amplitudes values used in the simulations and the corresponding kinetic energy relationships.

Table 4: Kinetic energy maxima and free amplitudes in trimodal AFM.

kinetic energy relationship	A_{01} (nm)	A_{02} (nm)	A_{03} (nm)
$KE_1 = KE_2 = KE_3$	10	1.6	0.57
$KE_1 > KE_2$; $KE_2 < KE_3$	10	0.4	0.4
$KE_1 > KE_2 > KE_3$	10	1.2	0.3

Figure 8a,b show the phase shift as function of the set-point amplitude for different energy ratios among modes. Each single curve reproduces the bimodal AM shape described before (Figure 2). Phase contrast between AU and PS is observed in all the cases irrespective of the kinetic energy distribution among the excited modes. However, the maximum contrast is obtained for a situation that minimizes the kinetic energy of the second mode with respect to the other two (Figure 8c). We also observe that the maximum contrast happens for an amplitude ratio about 0.5. This is far from the edge regions where the phase shift changes more rapidly.

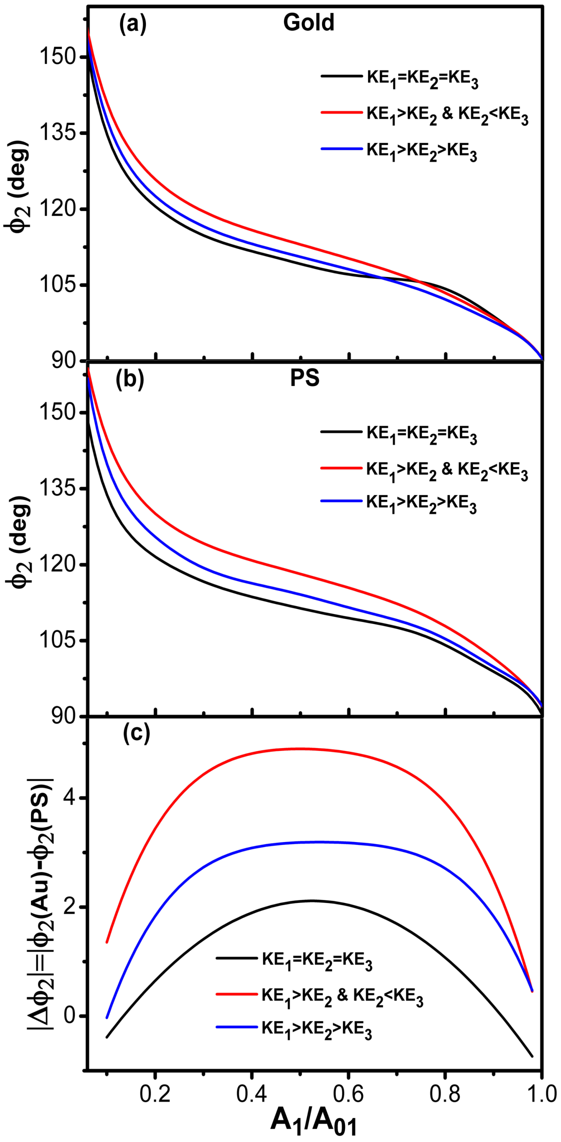

Figure 8: Trimodal AFM in the attractive regime. (a) Phase shift of the second mode dependence on A_1/A_{01} for different kinetic energy ratios. The value of the Hamaker constant corresponds to Au–air–Si interface. (b) Phase shift of the second mode dependence on A_1/A_{01} for different kinetic energy ratios. The value of the Hamaker constant is for the PS–air–Si interface. (c) Phase contrast between Au and PS as a function of the amplitude ratio for different kinetic energy ratios. See Table 3 for parameter values.

We have also compared the phase contrast between bimodal and trimodal AFM (attractive regime). The shape of the phase shift curves are almost identical in bimodal and trimodal AM (Figure 9a,b). However, the introduction of third excitation improves the phase contrast (Figure 9c). This seems an advantage of trimodal with respect to bimodal AM, however, this happens at the expense of introducing additional electronic hardware and increasing the peak force. A more detailed study is needed to stablish the advantages/disadvantages of these multifrequency AFM configurations.

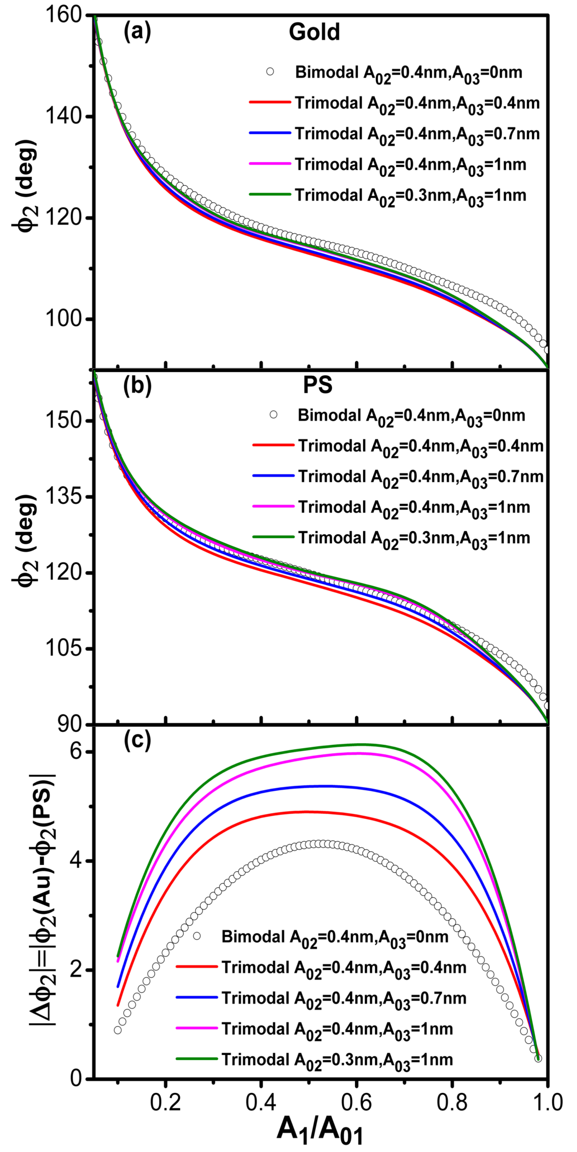

Figure 9: Bimodal versus trimodal AM (attractive regime). (a) Phase shift of the second mode dependence on A_1/A_{01} for different A_{03} values. The value of the Hamaker constant is for the Au–air–Si interface. (b) Phase shift of the second mode dependence on A_1/A_{01} for different A_{03} values. The value of the Hamaker constant is for the PS–air–Si interface. (c) Phase contrast between Au and PS as a function of the amplitude ratio for different kinetic energy ratios. A_{01} = 10 nm in all cases.

Conclusion

We have studied the phase contrast in bimodal amplitude modulation AFM for the attractive and the repulsive interaction regimes as a function of the amplitude and amplitude ratio of the excited modes. We have found that the contrast increases by minimizing the amplitude of the second mode. We have also compared the phase contrast for direct (conventional) and indirect bimodal AM configurations. We have found that bimodal AM favors the use of feedback controls on the amplitude of the lowest excited mode. This excitation/detection scheme maximizes the operational range. In the inverted bimodal AM configuration, the amplitude of the lowest excited mode disappears so quickly that only a very small range of amplitude ratios is left to perform bimodal AM. The origin of this asymmetry lies in the fact that the cantilever sensitivity to forces decreases with the mode number. The presence of tip–sample energy dissipation processes reduces the phase contrast observed between different materials in bimodal AM with respect to have exclusively non-conservative interactions.

The simulations show that in the attractive regime, the introduction of a small excitation in the third flexural mode improves the phase contrast with respect to bimodal AFM. This result is related to the distribution of the kinetic energies among the modes. In terms of compositional contrast it is favored the configuration that minimizes the kinetic energy of the imaging mode (second) with respect to any of the kinetic energies of the other modes. However, the increase in compositional sensitivity happens at the expense of increasing the peak forces.

Acknowledgements

This work was funded by the Spanish Ministry of Economy (MINECO) through grant CSD2010-00024.

References

1. Binnig, G.; Quate, C. F.; Gerber, C. *Phys. Rev. Lett.* **1986,** *56,* 930. doi:10.1103/PhysRevLett.56.930
2. García, R.; Pérez, R. *Surf. Sci. Rep.* **2002,** *47,* 197. doi:10.1016/S0167-5729(02)00077-8
3. Ando, T.; Uchihashi, T.; Fukuma, T. *Prog. Surf. Sci.* **2008,** *83,* 337. doi:10.1016/j.progsurf.2008.09.001
4. Gan, Y. *Surf. Sci. Rep.* **2009,** *64,* 99–121. doi:10.1016/j.surfrep.2008.12.001
5. Barth, C.; Foster, A. S.; Henry, C. R.; Shluger, A. L. *Adv. Mater.* **2011,** *23,* 477–501. doi:10.1002/adma.201002270
6. Payam, A. F.; Ramos, J. R.; Garcia, R. *ACS Nano* **2012,** *6,* 4663–4670. doi:10.1021/nn2048558
7. Dufrêne, Y. F.; Martínez-Martín, D.; Medalsy, I.; Alsteens, D.; Müller, D. J. *Nat. Methods* **2013,** *10,* 847–854. doi:10.1038/nmeth.2602
8. Garcia, R.; Knoll, A. W.; Riedo, E. *Nat. Nanotechnol.* **2014,** *9,* 577–587. doi:10.1038/nnano.2014.157
9. Garcia, R.; Herruzo, E. T. *Nat. Nanotechnol.* **2012,** *7,* 217–226. doi:10.1038/nnano.2012.38
10. Sahin, O.; Magonov, S.; Su, C.; Quate, C. F.; Solgaard, O. *Nat. Nanotechnol.* **2007,** *2,* 507. doi:10.1038/nnano.2007.226
11. Dong, M.; Sahin, O. *Nat. Commun.* **2011,** *2,* No. 247. doi:10.1038/ncomms1246
12. Spitzner, E.-C.; Riesch, C.; Magerle, R. *ACS Nano* **2011,** *5,* 315–320. doi:10.1021/nn1027278
13. Rico, F.; Su, C.; Scheuring, S. *Nano Lett.* **2011,** *11,* 3983–3986. doi:10.1021/nl202351t
14. Raman, A.; Trigueros, S.; Cartagena, A.; Stevenson, A. P. Z.; Susilo, M.; Nauman, E.; Contera, S. A. *Nat. Nanotechnol.* **2011,** *6,* 809–814. doi:10.1038/nnano.2011.186

15. Rodríguez, T. R.; García, R. *Appl. Phys. Lett.* **2004,** *84,* 449. doi:10.1063/1.1642273
16. Martinez, N. F.; Patil, S.; Lozano, J. R.; Garcia, R. *Appl. Phys. Lett.* **2006,** *89,* 153115. doi:10.1063/1.2360894
17. Stark, R. W.; Naujokes, N.; Stemmer, A. *Nanotechnology* **2007,** *18,* 065502. doi:10.1088/0957-4484/18/6/065502
18. Li, Y. J.; Kobayashi, N.; Naitoh, Y.; Kageshima, M.; Sugawara, Y. *Appl. Phys. Lett.* **2008,** *92,* 121903. doi:10.1063/1.2901151
19. Li, J. W.; Cleveland, J. P.; Proksch, R. *Appl. Phys. Lett.* **2009,** *94,* 163118. doi:10.1063/1.3126521
20. Kawai, S.; Glatzel, T.; Koch, S.; Such, B.; Baratoff, A.; Meyer, E. *Phys. Rev. Lett.* **2009,** *103,* 220801. doi:10.1103/PhysRevLett.103.220801
21. Kawai, S.; Canova, F. F.; Glatzel, T.; Hynninen, T.; Meyer, E.; Foster, A. S. *Phys. Rev. Lett.* **2012,** *109,* 146101. doi:10.1103/PhysRevLett.109.146101
22. Garcia, R.; Proksch, R. *Eur. Polym. J.* **2013,** *49,* 1897–1906. doi:10.1016/j.eurpolymj.2013.03.037
23. Ebeling, D.; Eslami, B.; Solares, S. D. J. *ACS Nano* **2013,** *7,* 10387–10396. doi:10.1021/nn404845q
24. Santos, S. *Appl. Phys. Lett.* **2013,** *103,* 231603. doi:10.1063/1.4840075
25. Herruzo, E. T.; Perrino, A. P.; Garcia, R. *Nat. Commun.* **2014,** *5,* No. 3126. doi:10.1038/ncomms4126
26. Sahin, O.; Yaralioglu, G.; Grow, R.; Zappe, S. F.; Atalar, A.; Quate, C.; Solgaard, O. *Sens. Actuators, A* **2004,** *114,* 183–190. doi:10.1016/j.sna.2003.11.031
27. Platz, D.; Tholén, E. A.; Haviland, D. B. *Appl. Phys. Lett.* **2008,** *92,* 153106. doi:10.1063/1.2909569
28. Forchheimer, D.; Platz, D.; Tholén, E. A.; Haviland, D. *Phys. Rev. B* **2012,** *85,* 195449. doi:10.1103/PhysRevB.85.195449
29. Stan, G.; Solares, S. D.; Pittenger, B.; Erina, N.; Su, C. M. *Nanoscale* **2014,** *6,* 962–969. doi:10.1039/C3NR04981G
30. Killgore, J. P.; Kelly, J. Y.; Stafford, C.; Fasolka, M.; Hurely, D. C.; Fasolka, M. J. *Nanotechnology* **2011,** *22,* 175706. doi:10.1088/0957-4484/22/17/175706
31. Jesse, S.; Kalinin, S. V.; Proksch, R.; Baddrof, A. P.; Rodriguez, B. J. *Nanotechnology* **2007,** *18,* 435503. doi:10.1088/0957-4484/18/43/435503
32. Jesse, S.; Vasudevan, R. K.; Collins, L.; Strelcov, E.; Okatan, M. B.; Belianinov, A.; Baddorf, A. P.; Proksch, R.; Kalinin, S. V. *Annu. Rev. Phys. Chem.* **2014,** *65,* 519–536. doi:10.1146/annurev-physchem-040513-103609
33. Garcia, R.; Gómez, C. J.; Martinez, N. F.; Patil, S.; Dietz, C.; Magerle, R. *Phys. Rev. Lett.* **2006,** *97,* 016103. doi:10.1103/PhysRevLett.97.016103
34. García, R.; San Paulo, A. *Phys. Rev. B* **1999,** *60,* 4961. doi:10.1103/PhysRevB.60.4961
35. Kiracofe, D.; Raman, A.; Yablon, D. *Beilstein J. Nanotechnol.* **2013,** *4,* 385–393. doi:10.3762/bjnano.4.45
36. Chakraborty, I.; Yablon, D. G. *Nanotechnology* **2013,** *24,* 475706. doi:10.1088/0957-4484/24/47/475706
37. Santos, S. *Appl. Phys. Lett.* **2014,** *104,* 143109. doi:10.1063/1.4870998
38. Stark, R. W. *Appl. Phys. Lett.* **2009,** *94,* 063109. doi:10.1063/1.3080209
39. Solares, S. D.; Chawla, G. *J. Appl. Phys.* **2010,** *108,* 054901. doi:10.1063/1.3475644
40. Solares, S. D.; Chawla, G. *Meas. Sci. Technol.* **2010,** *21,* 125502. doi:10.1088/0957-0233/21/12/125502
41. Eslami, B.; Ebeling, D.; Solares, S. D. *Beilstein J. Nanotechnol.* **2014,** *5,* 1144–1151. doi:10.3762/bjnano.5.125
42. Lozano, J. R.; Garcia, R. *Phys. Rev. Lett.* **2008,** *100,* 076102. doi:10.1103/PhysRevLett.100.076102
43. Dietz, C.; Herruzo, E. T.; Lozano, J. R.; Garcia, R. *Nanotechnology* **2011,** *22,* 125708. doi:10.1088/0957-4484/22/12/125708
44. Martinez, N. F.; Lozano, J. R.; Herruzo, E. T.; García, F.; Richter, C.; Sulzbach, T.; García, R. *Nanotechnology* **2008,** *19,* 384011. doi:10.1088/0957-4484/19/38/384011
45. Gigler, A. M.; Dietz, C.; Baumann, M.; Martinez, N. F.; Garcia, R.; Stark, R. W. *Beilstein J. Nanotechnol.* **2012,** *3,* 456–463. doi:10.3762/bjnano.3.52
46. Solares, S. D.; An, S.; Long, C. J. *Beilstein J. Nanotechnol.* **2014,** *5,* 1637–1648. doi:10.3762/bjnano.5.175
47. Lozano, J. R.; Garcia, R. *Phys. Rev. B* **2009,** *79,* 014110. doi:10.1103/PhysRevB.79.014110
48. An, S.; Solares, S. D.; Santos, S.; Ebeling, D. *Nanotechnology* **2014,** *25,* 475701. doi:10.1088/0957-4484/25/47/475701
49. Guzman, H. V.; Garcia, P. D.; Garcia, R. *Beilstein J. Nanotechnol.* **2015,** *6,* 369–379. doi:10.3762/bjnano.6.36

License and Terms

The definitive version of this article is the electronic one which can be found at:
doi:10.3762/bjnano.6.108

BEILSTEIN JOURNAL OF NANOTECHNOLOGY

Probing fibronectin–antibody interactions using AFM force spectroscopy and lateral force microscopy

Andrzej J. Kulik[1], Małgorzata Lekka[*2], Kyumin Lee[1], Grazyna Pyka-Fościak[3] and Wieslaw Nowak[4]

Full Research Paper

Address:
[1]Laboratoire de la Physique de la Matière Vivante, Ecole Polytechnique Fédérale de Lausanne (EPFL), CH-1015 Lausanne, Switzerland, [2]Institute of Nuclear Physics, Polish Academy of Sciences, Radzikowskiego 152, 31-342 Kraków, Poland, [3]Department of Histology, Jagiellonian University Medical College, Kopernika 7, 31-034 Kraków, Poland, and [4]Institute of Physics, Faculty of Physics, Astronomy and Informatics, Nicolaus Copernicus University, Grudziądzka 5/7, 87-100 Toruń, Poland

Email:
Małgorzata Lekka* - Malgorzata.Lekka@ifj.edu.pl

* Corresponding author

Keywords:
fibronectin; lateral force microscopy; molecular recognition; torsional forces calibration

Beilstein J. Nanotechnol. **2015,** *6,* 1164–1175.
doi:10.3762/bjnano.6.118

Received: 18 February 2015
Accepted: 22 April 2015
Published: 15 May 2015

This article is part of the Thematic Series "Advanced atomic force microscopy techniques III".

Guest Editor: T. Glatzel

Abstract

The first experiment showing the effects of specific interaction forces using lateral force microscopy (LFM) was demonstrated for lectin–carbohydrate interactions some years ago. Such measurements are possible under the assumption that specific forces strongly dominate over the non-specific ones. However, obtaining quantitative results requires the complex and tedious calibration of a torsional force. Here, a new and relatively simple method for the calibration of the torsional force is presented. The proposed calibration method is validated through the measurement of the interaction forces between human fibronectin and its monoclonal antibody. The results obtained using LFM and AFM-based classical force spectroscopies showed similar unbinding forces recorded at similar loading rates. Our studies verify that the proposed lateral force calibration method can be applied to study single molecule interactions.

Introduction

The invention of atomic force microscopy (AFM) opened up new areas of research as it can probe various biological structures with nanometer resolution, including images of DNA [1], proteins [2], and cellular surfaces [3,4]. Apart from the imaging aspect, AFM can also be applied to probe molecular interactions with a force resolution of tenths of pN. This method enables the measurement of the strength of the interaction forces between a single pair of molecules [5-7] such as biotin–avidin, biotin–streptavidin [8], or lectin–carbohydrate [9]. Direct measurements of intermolecular forces for complementary DNA strands have been carried out as well [10].

Protein–antibody interactions are of particular interest in immunochemical-based diagnosis [11]. Therefore, studies of the interaction forces provide valuable insight into the mechanisms behind biological interactions. AFM allows for a unique opportunity to probe the properties of individual ligand–receptor complexes and provides details on the structure and behavior of single molecules in conditions close to natural ones [6-9]. This technique provides several advantages over traditional methods including, for example, characterization of states that are undetectable in ensemble approaches where the average value of a property is monitored. Thus, any improvements in the cantilevers or measurement methodologies leading to an increase in speed, resolution, and/or force sensitivity are essential in nanotechnology development.

In the majority of AFMs, the cantilever deflection is recorded by an optical detection system composed of a laser and a position-sensitive photodiode having an active area divided into four quadrants. The deflection (referred to here as the normal deflection) and torsion (referred to here as the lateral deflection) signals are determined as follows: the signal difference between the two upper and lower quadrants is a measure of the normal deflection, while torsion of the cantilever is represented as the signal difference between the two left and two right quadrants.

For an AFM working in force spectroscopy mode (referred to here as AFM-FS), the interactions forces are determined from the analysis of force curves. A force curve represents the dependence between the deflection of the AFM cantilever in the direction perpendicular (normal) to the surface and a relative position on a sample. In the AFM-FS measurement, force curves are recorded point-by-point, requiring a precise but tedious and very time consuming procedure.

Lateral force microscopy (LFM), also called friction force microscopy (FFM) is another operational mode in a standard AFM instrument working in contact mode [12]. In LFM, the cantilever is moved laterally over the investigated surface. In this case, the interaction forces cause cantilever torsion and thus, instead of a perpendicular deflection, the torsion is recorded as a function of the relative position on the sample. To determine the magnitude of the interaction forces, the force curves obtained for torsion can be processed in the same way as force curves obtained in AFM-FS. The two main advantages of the LFM mode are: a much higher unbinding speed applied to bonds and faster measurements. The higher velocity that is used during the LFM experiments to break the bonds enables deeper parts of the energy landscape of the studied molecular complex to be probed. The use of LFM working in the "continuous" line scan mode might help to more quickly probe molecular interactions and should give quantitative estimates of interaction forces.

Wider applications of the fast LFM method are hampered by impediments in the quantitative determination of the force value. In contrast to AFM-FS, this requires a reliable and repetitive calibration procedure. Irrespective of the applied experimental methodology (AFM-FS or LFM), the calibration proceeds through similar steps: (1) determination of the photodiode sensitivity converting the measured signal (in V) into a displacement of the cantilever (in nm) and (2) estimation of the cantilever spring constant used to deliver force (in nN). The calibration of normal deflection, typical for AFM-FS, poses no problem and is based on a well-known procedure utilizing thermal excitations of the cantilever. To date, there are only a few methods that can be used for the lateral force calibration [13,14], but unfortunately, none are fully reliable. For example, recently, Dendzik et al. proposed that the stretching of a reference single molecule (e.g., dextran) could be used to determine the normal and lateral AFM cantilever calibration [15]. Although this new method presents a clear improvement over previous attempts to obtain a reliable calibration for lateral measurements, it requires special hardware. Similarly, the method proposed very recently by Wang and Gee requires an additional calibration tool [16], which may be troublesome as well.

In the presented work, we propose an alternative method for torsion force calibration. It is based on the cantilever deflection measurements carried out during the lateral scanning over a rectangular, reference cantilever with a known normal spring constant. Our method is relatively simple to use, fast, and it does not require any special equipment. In order to verify the extent to which the LFM is suitable for probing molecular interactions, we have measured interaction forces between protein fibronectin (FN) and monoclonal antibody against FN (FN-Mab) using both AFM-FS and LFM techniques. The relation between the unbinding force and the loading rate obtained by AFM-FS was compared with the corresponding relation gathered using LFM. Our results show that the new calibration method has potential for applications in LFM quantitative investigations of intermolecular interactions.

Results

Converting torsion into force units

The calibration of the force that acts perpendicular to the investigated surface requires the knowledge of the normal cantilever spring constant and normal photodetector sensitivity.

The nominal, normal spring constant was controlled by monitoring the resonant frequency of a thermally excited cantilever [17], carried out before functionalization with an antibody. Since the resonance frequency of the cantilever was almost constant (8.73 ± 0.07 kHz), the nominal value of the spring constant was used to measure the force value. The photodetector sensitivity (referred to here as normal PSD sensitivity) was determined from the slope of the force curve in the region of tip contact with the reference glass surface (for type C cantilevers, the normal PSD sensitivity was 22.1 ± 3.5 nm/V).

Analogous to the normal force measurement, the lateral force (inferred from the torsion of the cantilever) was determined by multiplying the recorded signal (measured in V) by the torsional spring constant and lateral photodetector sensitivity. Both parameters are difficult to estimate using known methods [14,18], so here we propose a simple, alternative method that allows the measured signal (in V) to be directly converted into force units. The conversion factor is referred to here as the lateral PSD sensitivity.

The calibration concept is presented in Figure 1. Two cantilevers were used: a reference and a probe. The uncharacterized probe cantilever scans over the rectangular reference cantilever of known normal spring constant. The choice of the rectangular shape of the reference cantilever was motivated by the fact that it is easy to bend such a cantilever (one can easily access the end of a cantilever mounted perpendicularly). In our experiments, rectangular cantilevers (micro lever for contact and tapping mode (MLCT), type B) with a nominal spring constant of 0.02 N/m were used.

The lateral signal was recorded while scanning in both directions, as presented schematically in Figure 1A. The optical images of the calibration steps are shown in Figure 1B,C. They were recorded while scanning the reference cantilever with a

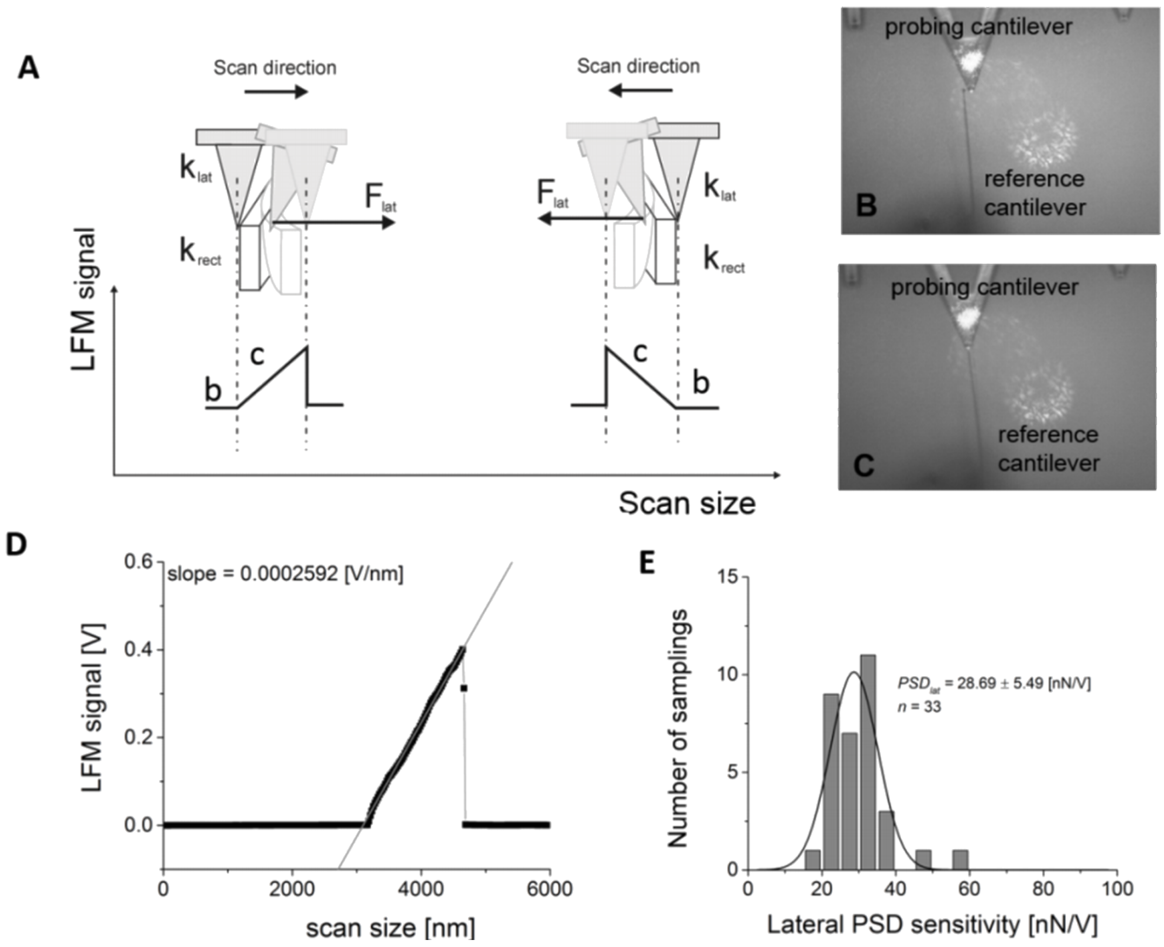

Figure 1: The lateral force calibration concept. (A) An illustration of the calibration approach. (B,C) Images recorded during the scanning of a reference cantilever with a probe MLCT type C cantilever. (D) A calibration curve recorded using the proposed calibration approach. (E) The distribution of the calibration factors (lateral PSD sensitivity) expressed in nN/V.

triangular probe cantilever (MLCT type C, 0.01 N/m). The contour of the LFM signal has a characteristic pyramidal shape that reflects the signal recorded during bending of the reference cantilever (Figure 1D). Each scan consists of 2048 points, recorded over a distance of 6000 nm. From the slope, a lateral calibration factor can be determined by fitting a straight line. A linear regression gives a goodness of fit in the range of 0.992–0.998. The calculated slope was then converted into nN/V by inverting it and multiplying by the known cantilever spring constant of the reference cantilever. From the distribution of the calibration factors (Figure 1E), a mean value of 28.7 ± 5.5 nN/V was calculated, giving a ≈19% accuracy. This is also a measure of the reproducibility (33 cantilevers were calibrated in this manner).

Surface topography

To verify whether the functionalization of a mica surface gave an expected layer of fibronectin molecules, the surface topography was recorded using a bare (non-functionalized) cantilever. As shown in Figure 2, the fibronectin molecules had a regular globular shape and were uniformly distributed over the entire scanned area. The FN height ranged from 0.5 to 3.5 nm with a mean value of 2.4 ± 0.9 nm.

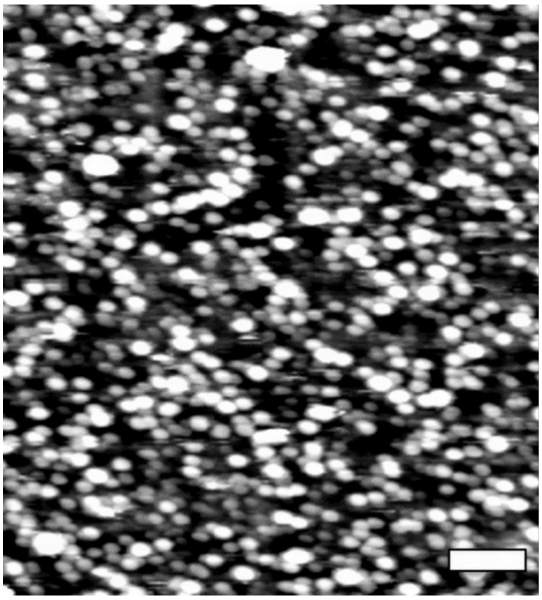

Figure 2: Topography image of FN deposited on a mica surface recorded while scanning in contact mode AFM with a bare AFM tip. Scale bar: 1 µm.

Dependence of friction force on normal load

The frictional interaction between surfaces observed on the macroscale is typically modelled using Amonton’s law, where a frictional force is linearly dependent on a load force. The proportionality factor is the constant friction coefficient. To verify whether any friction force is observed between the FN-coated surface and the FN-Mab-functionalized AFM probe, the LFM images were recorded as a function of the load force from 0.1 to 4 nN.

The friction force value was determined by subtracting the mean values calculated separately for scans running in two opposite directions (i.e., trace and retrace) along the same path (see Figure 3A). Thus, the mean value of the friction force was calculated from the distribution of the friction force recorded

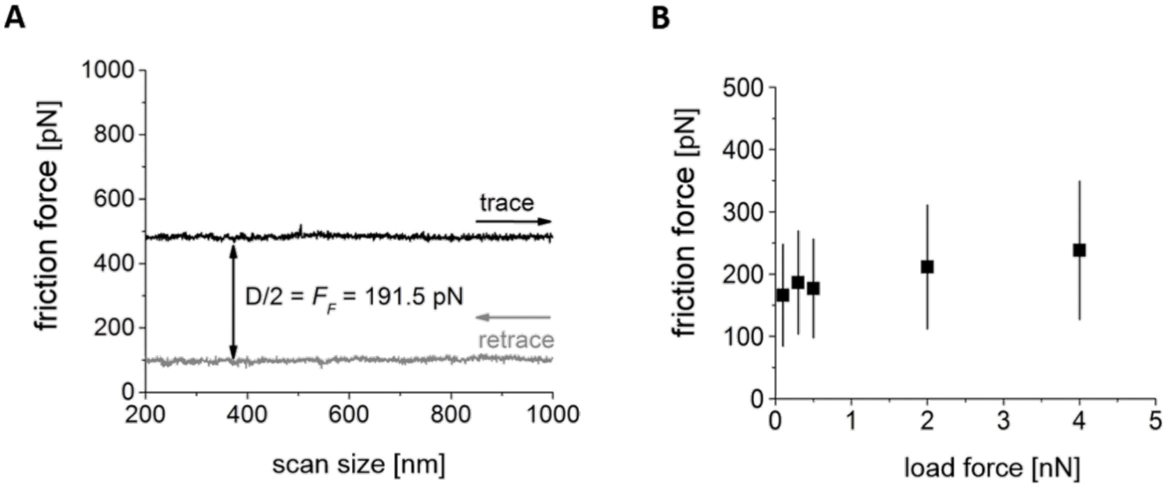

Figure 3: (A) Friction loop determined for a load of 2 nN. The difference, D, between the lateral signal recorded for the trace and retrace modes divided by 2 determines the friction force. (B) The dependence of the friction force on normal load (friction force given as the mean ± standard deviation).

during such a scan in both directions. The width of the distribution represents the measurement error. In the presented measurements, only a weak dependence of the friction force on the normal load was observed (Figure 3B), therefore, all further measurements of the FN-Mab interaction forces were carried out at the set point of 0.1 nN.

Unbinding force determination

To study the unbinding process using both LFM and the AFM-based classical force spectroscopies, the measurements of the unbinding force between fibronectin and monoclonal antibody were carried out. We assume that independent of the applied unbinding direction (i.e., normal or lateral), both methods (AFM-FS and LFM) provide similar values of the interaction force at similar loading rates.

In the AFM-FS method, force curves (i.e., the dependence of the cantilever normal deflection converted into force and displacement in the perpendicular direction) were recorded (Figure 4).

For each curve, an unbinding force, *F*, and the length, *L*, were determined (Figure 4A). These two values were used to calculate the effective spring constant, which was used to calculate the loading rate for a given retraction speed. The effective spring constant varied from 0.0030 N/m to 0.0124 N/m for 0.1 μm/s and 10 μm/s, respectively (MLCT type C and MLCT type D cantilevers were used). Then, for each value of the loading rate, a histogram was formed. Exemplary histograms for loading rates of 360 pN/s and 6740 pN/s are presented in Figure 4B,C together with the corresponding Gaussian fit. The fit was used for the determination of the most probable force leading to unbinding of the fibronectin–antibody complex. For all loading rate values, the most probable rupture lengths varied from 10 to 25 nm. The unbinding probability (defined as the ratio between the number of force curves showing the unbinding events and the total number of measured curves) was 20%. After blocking FN by adding free antibody molecules to the solution, followed by 30 min of incubation, the unbinding probability dropped to 5%.

A similar approach was applied within the LFM in order to measure the unbinding forces. Each signal from the torsional cantilever deflection (representing a trace or a retrace) was analyzed in search for sharp peaks. Sharp peaks correspond to unbinding events (ruptures) during a lateral movement of the

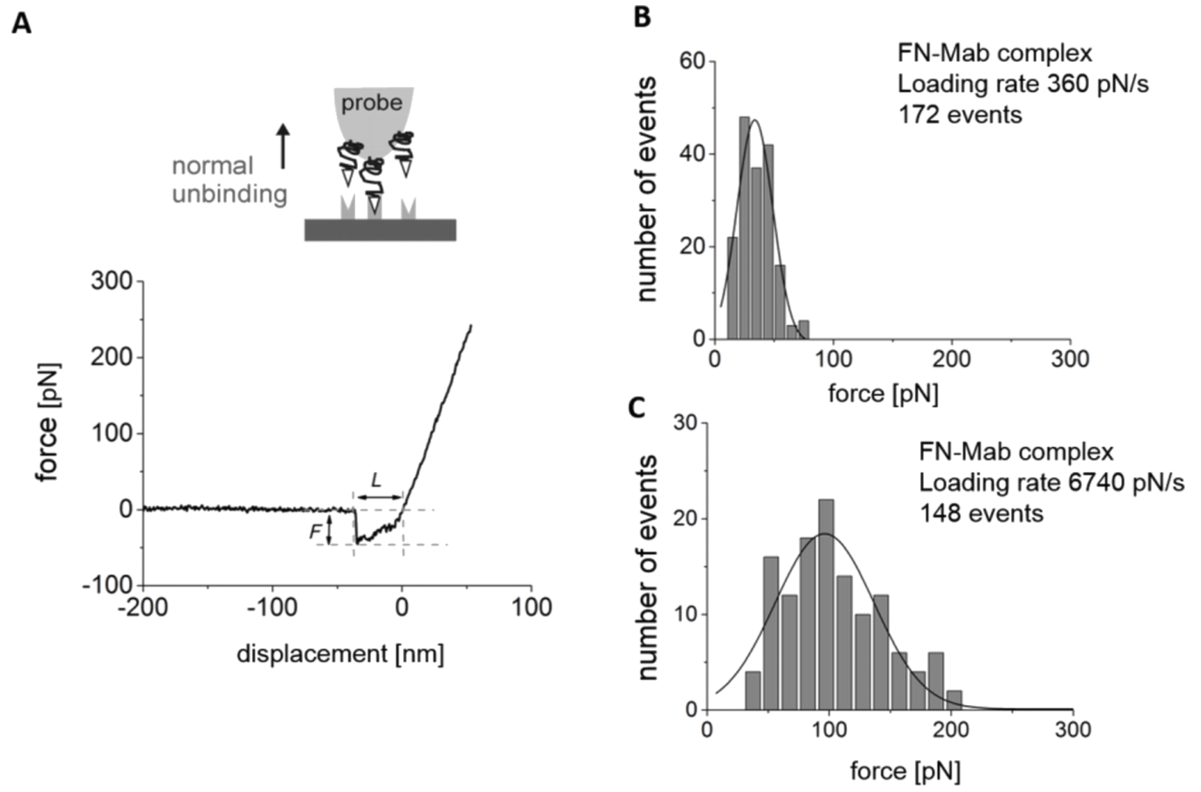

Figure 4: Unbinding of a FN-Mab complex studied using AFM-FS. (A) For each force curve recorded at a given loading rate, the unbinding force, *F*, and unbinding length, *L*, were determined. (B,C) Histograms of unbinding events obtained for two loading rates of 360 pN/s and 6737 pN/s.

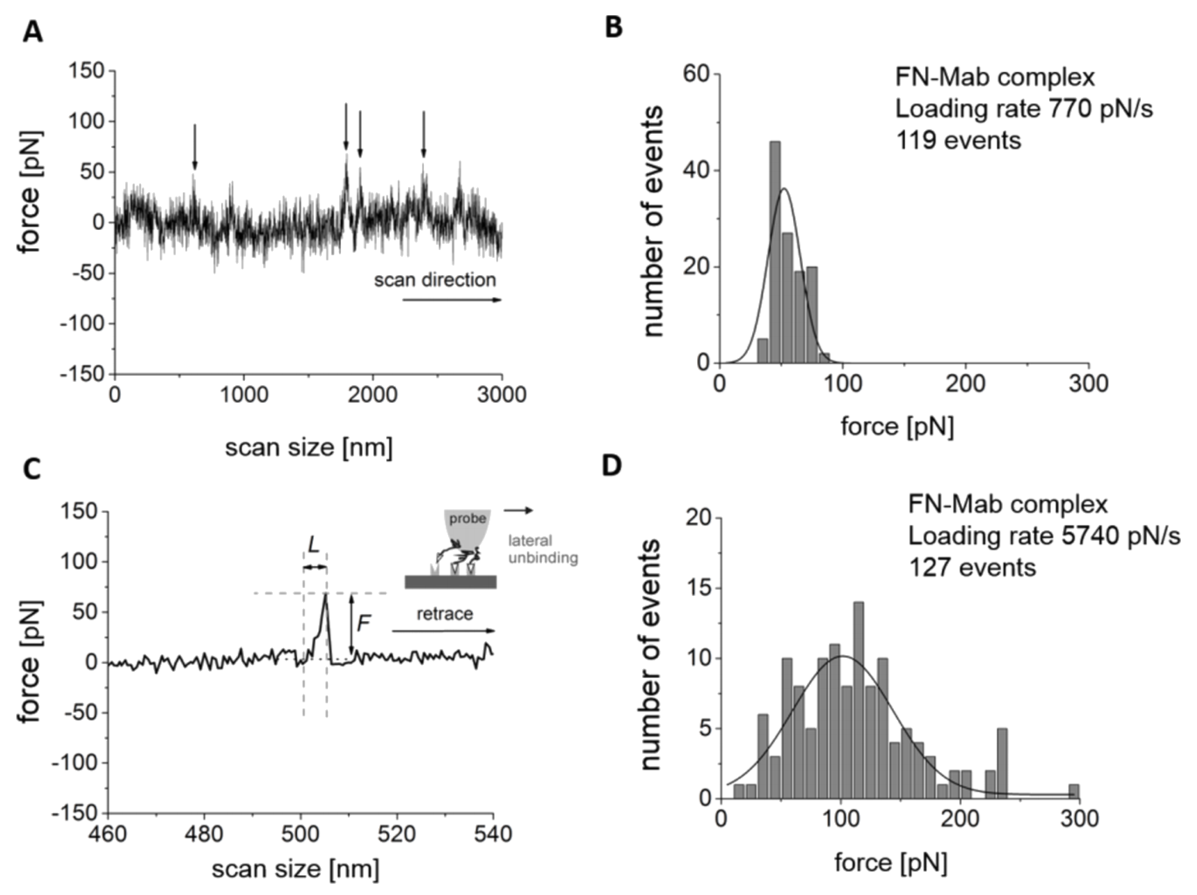

Figure 5: Unbinding of a FN-Mab complex measured by LFM. (A) An exemplary, single LFM signal showing peaks that were attributed to specific interactions between FN-Mab molecules. The arrows indicate events that are suspected to show only the specific interaction. (B) For each spike, an unbinding force, *F*, and an unbinding length, *L*, were determined. (C and D) Histograms of the unbinding force determined for two loading rates, 770 pN/s and 5740 pN/s.

probing tip functionalized with Mab molecules (Figure 5A). At a higher magnification (each line contains 2048 data points) the unbinding character similar to that observed in the previous AFM-FS experiments (Figure 4A) was revealed.

The unbinding force, *F*, and length, *L*, were determined analogous to the classical AFM-FS measurement (see Figure 5B, where a base line was subtracted for simplicity). Next, *F* and *L* were used to calculate the force required to laterally unbind a single FN-Mab complex. The loading rate in LFM has a similar effect on the most probable unbinding force as in AFM-FS, that is, a higher loading rate value showed a wider distribution of the unbinding force, with its center shifted towards larger force values (Figure 5C). The unbinding probability was calculated as a number of unbinding events divided by the number of points recorded along a single scan line. The resulting unbinding probability was around 6% but less than 10%. Inhibition experiments carried out after 30 min of incubation with a solution containing free antibody molecules showed a remarkable decrease in the unbinding events with a maximum of 1% (only a few peaks were observed in the torsional cantilever deflection signal).

Loading rate dependence

The effect of the loading rate on the unbinding force was observed by AFM for many distinct pairs of molecules, bringing deeper insight into the molecular mechanisms of the bond breaking processes [19-22]. For fibronectin interacting with its monoclonal antibody (Clone F-15), our AFM-FS experiments revealed two regimes of loading rates (open dots in Figure 6). A similar trend was observed for the unbinding determined from the torsional cantilever deflection (LFM, black squares in Figure 6).

The experimental points obtained from LFM overlap with those obtained using AFM-FS (Figure 6). Independent of the method used to study the FN-Mab interaction, the presence of two energy barriers can be noticed. Based on the Bell–Evans model, the parameters describing the unbinding process were calculated (Table 1).

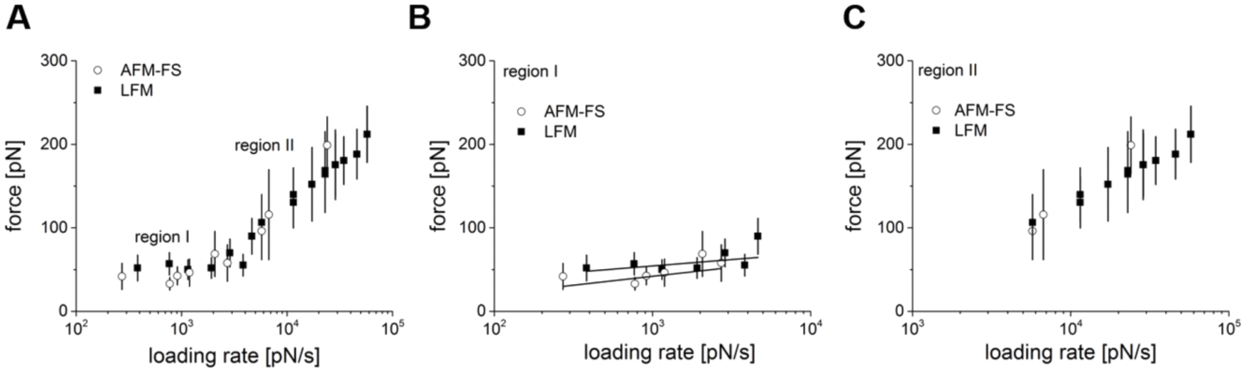

Figure 6: Unbinding force–loading rate dependence obtained for FN-Mab complexes using AFM-FS and LFM. (A) A loading rate dependence obtained for all data showing two regions of linear trends for both applied methods. (B) Region I with a fitted line obtained for lower loading rates. (C) Region II related to higher loading rates values.

Table 1: Kinetic parameters derived from the Bell–Evans model and applied to the data obtained by both classical force spectroscopy and lateral force microscopy.

AFM-FS - Classical force spectroscopy			
	x_b [nm]^a	k_{off} [s^{-1}]^b	$\tau = 1/k_{off}$ [s]^c
region I	0.43 ± 0.11	1.18 ± 2.47	0.846
region II	0.06 ± 0.01	20.12 ± 11.52	0.050
LFM - Lateral force spectroscopy			
	x_b [nm]^a	k_{off} [s^{-1}]^b	$\tau = 1/k_{off}$ [s]^c
region I	0.60 ± 0.22	0.53 ± 0.25	1.894
region II	0.09 ± 0.01	11.6 ± 5.51	0.086

[a] x_b is the position of the energy barrier.
[b] k_{off} is the dissociation rate.
[c] τ is the bond lifetime.

Based on the data obtained from AFM-FS, we infer that region I corresponds to the outermost energy barrier located at the position of 0.43 ± 0.11 nm, while region II (see Figure 6) is related to an inner barrier situated at a distance of 0.06 ± 0.01 nm. Qualitatively, similar positions of the energy barriers were observed for the same unbinding process in this complex using the LFM located at 0.60 ± 0.22 nm (the outer barrier, region I) and 0.09 ± 0.01 nm (the inner barrier, region II). The “unphysically” low values of the energy position of the internal barrier (region II) are perhaps related to the limitations of the Bell–Evans phenomenological model. The dissociation rate calculated using both applied methods shows systematically lower dissociation rates in the LFM data for each energy barrier observed (1.18 s^{-1} versus 0.53 s^{-1} and 20.12 s^{-1} versus 11.6 s^{-1}, respectively, Table 1).

Discussion

The unbinding measurements realized by the conventional AFM-FS method are one of the most tedious experiments due to the necessity of high statistics and the low number of unbinding events corresponding to single molecule interactions in a single experimental run [23]. LFM has high potential for performing such experiments in a much more effective way. The first attempt showing that specific interaction forces can be observed in the LFM signal has been applied to lectin–carbohydrate systems [24]. In that work, the specific interactions based on considerations of the frictional forces between a glycoprotein-functionalized AFM probe and a surface modified with lectins were investigated. Such measurements were possible under the assumption that specific forces strongly dominate over non-specific (friction) forces. Moreover, the lack of a reliable and accurate calibration method precluded a comparison of the obtained results with other works carried out for lectin interactions. In our work, we present the direct comparison between the FN-Mab unbinding process measured using LFM and AFM-based force spectroscopies under the assumption that unbinding of molecular complexes is independent of the direction (normal vs lateral [25]). Such a comparison enables the validation of the proposed LFM calibration method and the verification of whether it is possible to obtain similar unbinding characteristics when AFM-FS and LFM methods are applied to study the same type of molecular complex.

To obtain reliable results from the LFM method, the torsion force calibration issue was addressed and a new method was proposed in this paper. Typically, there are two approaches that would deliver either (i) a lateral photodetector sensitivity and a torsional spring constant (in two steps) or (ii) a factor that correlates the raw, uncalibrated signal of the torsional cantilever deflection with the calibrated force value (one step procedure).

The two-step calibration procedure requires separate calibrations of the lateral detector sensitivity and the lateral (or torsional) spring constant. In one approach, a mirrored substrate was tilted and the output voltage was measured as a function of the tilt angle [26]. Alternatively, the lateral sensitivity can be calculated from geometrical considerations or from the initial slope of a friction loop [27]. The angle of the cantilever twist can be estimated assuming that the tip is pinned to the substrate and that the lateral movement has been accurately calibrated. The calibration (determination) of the torsional spring constant is also not an easy task. This can be estimated from an analytical equation in which the cantilever thickness is an essential parameter, usually leading to large errors. Álvarez-Asencio et al. [28] recently proposed a hybrid model to determine the torsional spring constant under the assumption that the normal spring constant can be calibrated using the Sader method [17].

The one-step calibration seems to be much easier to perform since it is based on the direct determination of the friction force without the troublesome separate calibrations of both the lateral photodiode sensitivity and the torsional spring constant [29]. The example of a one-step calibration method has been already presented by Ruan and Bhushan [30]. Here, the cantilever was moved in the direction parallel to its long axis. The friction force was estimated as a product of the vertical spring constant multiplied by the vertical piezoelectric scanner displacement necessary to hold the cantilever deflection constant. The friction measured in this way was later used to calibrate the lateral friction measurements. Unfortunately, this method of calibration, when applied to the FN-Mab system investigated here, delivered unrealistic forces of the order of nN. The methodology of translating a lateral/torsional signal calibration into force units proposed in the current work is similar to that recently developed by Dendzik et al. [15]. However, our method is even more simple and does not require the use of special equipment.

The molecular interactions targeted in this study are between a human FN and monoclonal antibody against FN. An atomic detail basis of a typical model protein–IgG antibody interaction is shown in previous work [25]. The FN is present in the extracellular matrix (ECM) that surrounds living cells in organisms [31]. FN consists of two almost identical monomers linked together by disulphide bridges located close to the carboxyl termini of the monomer [22,32]. The knowledge of the surface topography of the FN molecules deposited on a mica surface enables verification of the quality of protein deposition by direct estimation of single molecule dimensions. Depending on the experimental conditions, fibronectin can be visible either in an elongated or a compact form [22]. Its elongated structure can result in a diameter of about 2.3 nm and a contour length in the range of 120–160 nm, determined for a dimeric FN molecule [33]. Under our conditions, FN was present in a compact, globular form with a mean height of 2.4 ± 0.9 nm. This indicates that after deposition on a mica surface, a layer composed of single molecules was formed. The compact form of FN may be rationalized by considering the electrostatic interaction occurring between different parts of the molecule. Also, the alteration of a protein conformation can be induced by a mechanical deformation during scanning in a contact mode. Interestingly, the average height of 2.4 nm determined by LFM corresponds well with the theoretical value of 2.3 nm estimated by Erickson et al. [34].

Both experimental methods, AFM-FS and LFM, applied here to study the FN–antibody interactions, detected specific unbinding events that were further characterized by two parameters, the unbinding force and rupture length. The inhibition experiments show a significant reduction in the unbinding probability (from 20% to 6%), which indicates the specificity of the interactions. Apparently, when two molecules are pulled apart in the normal direction, they presumably unbind along a different reaction coordinate from the pull in the lateral (inclined) direction. In such a case, one may expect that the energy landscape (and hence the dissociation rate and width of the energy barrier) should be very different. However, it has been theoretically shown that the unbinding of a protein–antibody complex can have a similar character for both modes of enforced “dissociation” [25], illustrating that at initial stages the unbinding proceeds perhaps along the same global reaction pathway, independent of the applied relative pulling force direction.

Another question regarding on the competition between FN unfolding and the unbinding of FN from the antibody arises. Since the whole human FN was used, one can expect that forced unbinding will be also associated with the unfolding (i.e., unfolding may occur when the interaction with the antibody is stronger than the unfolding of the FN domains). Since a sawtooth pattern was not observed in either of the experiments (AFM-FM and FFM), the FN-Mab unbinding in our experiment was weaker than the unfolding of FN domains. The rupture length, at which the unbinding occurred, varied from 10 to 25 nm. This rather high value is probably due to the use of whole, long FN molecules (and not fragments) in our experiments, which could lead to a low-force stretching phase before the unbinding. On the other hand, the calculated rupture length corresponds well to that reported for a similar type of interaction between an antigen and an antibody (i.e., bovine serum albumin and its monoclonal antibody) [35]. Our experiments do not allow for determination of which region (module) of FN interacts with Mab.

As the bond dissociation is a nonequilibrium, dynamic process, accordingly, the rupture force of an isolated bond is not a constant value. Instead, the bond strength is expected to display both a time- and loading-rate-dependent behavior. This has been shown in several experiments where the applied force–loading rate extends over a few orders of magnitude [19-23,35-38]. Figure 5 summarizes the dynamic response of the FN-Mab complex to loading rates between 200 to 70,000 pN/s. Within this range, the unbinding force showed an initial increase of 9.2 ± 3.2 pN and 6.7 ± 5.2 pN for AFM-FS and LFM, respectively. Such a gradual increase is followed by a steep rise starting from a loading rate of about 4000 pN/s. Independent of the loading rate region, the dynamic response curves of the FN-Mab complex overlapped, which may indicate that the activation enthalpy is independent from how the unbinding force is applied. A more detailed analysis of the unbinding of the FN-Mab complex was performed in terms of the Bell model. This analysis shows that both the dissociation rate constant (in the absence of the applied force) and the parameter that characterizes the relative position of the energy barrier are dependent on the mode of rupture (i.e., classical force spectroscopy or lateral force spectroscopy). This likely indicates some differences in the vertical and lateral unbinding scenarios. The computer modelling of a similar unbinding event in an MCP1-IgG antibody complex showed that lateral unbinding forces are about 30% lower than those characteristic of a normal rupture [38]. Regardless of this fact, the loading rate dependence shows two regions within the range of the experimental loading rates. Such observed changes in the slope are usually attributed to the suppression of an outer energy barrier of the energy landscape [19,39]. This suggests that during the unbinding, the single FN-Mab complex goes through a transition state, separating the inner and outer energy barriers. In nearly all molecular complexes studied to date, the dependence of the unbinding force on the logarithm of the loading rate was described by a linear line, indicating the presence of only one energy barrier in the interaction energy landscape. However, in the case of complex molecules, such as proteins, the kinetic processes can be characterized by multiple local maxima and minima in the interaction potential along the reaction coordinate. In these situations, the plot of the most probable unbinding force versus the logarithm of the loading rate displays a sequence of lines with different slopes, each corresponding to the position of a particular energy barrier.

Conclusion

The force measurements carried out for a fibronectin–antibody complex showed similarity in the unbinding process, independent of how the rupture force was applied by the AFM cantilever movement: either normal (AFM-FS) or lateral (LFM). The relation between the measured unbinding force and the loading rate applied overlapped for the AFM-FS and LFM methods. These findings demonstrate that the detection of specific protein–protein forces using lateral force microscopy (LFM) is possible. However, the appropriate calibration suitable for LFM must be performed and the assumption that specific forces dominate over non-specific must be fulfilled. In this work we presented an effective variant of the calibration of the cantilevers for the LFM measurements. Our findings on the FN-Mab antibody protein complex validate the proposed novel and simple method of a lateral signal calibration. Thus, it can be foreseen that the lateral scanning of the sample could accelerate an unbinding measurement as compared to the conventional AFM molecular recognition study. We anticipate that the LFM technique will be useful since it is not limited to proteins or biological samples; however, more experiments are needed to better understand the limitations/advantages of the use of LFM in molecular recognition processes.

Experimental

Proteins

Fibronectin from human plasma ($M_w \approx 450$ kDa, Sigma) was used in all experiments. The fibronectin was detected by the use of monoclonal antibody against human fibronectin (Mab, Clone FN-15, Sigma), produced in mouse ascites fluid after immunization of the mice with fibronectin isolated from human plasma.

Other reagents

Other reagents used in the experiments were: (a) phosphate buffered saline (PBS, ICN Biomedicals, pH 7.4, containing 10 mM of PO_4^{2-}, 137 mM of NaCl and 27 mM of KCl) was used to prepare all protein solutions; (b) 3-aminopropyltriethoxysilane (APTES, Sigma) was used for the silanization of the mica and cantilever surfaces; (c) 2.5% glutaraldehyde aqueous solution, prepared from a 25% solution of glutaraldehyde was purchased from Sigma. All solutions were prepared using deionized water (Cobrabid water purification system, 0.08 µS).

Cantilevers

Commercially available cantilevers (MLCT-AUHW, gold coated, not sharpened) purchased from Veeco were used. For all experiments, the cantilever type C was chosen. It is characterized by the nominal spring constant of 0.01 N/m, a resonant frequency of 7.0 kHz, and geometrical dimensions of 320 µm (length), 22 µm (width) and 0.6 µm (thickness). The open angle of a tip pyramid was 35° while the radius of curvature was 50 nm. As a reference, the cantilever type B was used. It is a rectangular-shaped cantilever with geometrical dimensions of 210 µm (length), 20 µm (width) and 0.6 µm (thickness). It is characterized by a nominal cantilever spring constant of 0.02 N/m and a resonant frequency of 10 kHz.

Fibronectin deposition on mica surface

As a support for the deposition of fibronectin, a modified mica surface was used. First, freshly cleaved mica was silanized with APTES. The APTES was deposited on the mica surface from gas phase for 2 h in a desiccator. Next, the sample was immersed in 2.5% glutaraldehyde aqueous solution for 20 min and afterwards rinsed with 10 mM PBS buffer. Then, the prepared sample was completely immersed in 0.1 mg/mL FN solution in PBS for 60 min, which prevented drying. Then, it was gently rinsed with PBS and immediately measured by AFM-FS or LFM.

Cantilever functionalization with Mab

The cantilevers (MLCT, type C, Veeco) used for both the AFM-FS and LFM measurements were modified using the same protocol as for the mica surface. Similar to mica surface, the cantilevers were silanized using APTES from the gas phase, then their surface was activated using a 1.5% aqueous glutaraldehyde solution and rinsed with PBS buffer. Then, the cantilevers were immersed in a drop (≈50 µL) of PBS solution of 0.05 mg/mL Mab for 30 min, and afterwards rinsed with PBS buffer. These prepared cantilevers were immediately used in the measurements.

Atomic force microscope

All measurements were carried out using commercially available devices (PSIA XE100 and XE120, Park Systems, Korea) equipped with a "liquid cell" setup, in 10 mM PBS buffer. The surface topography of a fibronectin-coated mica surface was measured in contact mode over an area of 10 × 10 µm, with set point of 0.2 nN and scan rate of 0.8 Hz.

Unbinding experiments

In AFM-based classical force spectroscopy, the unbinding forces of the interaction between fibronectin (FN) and monoclonal antibody against FN (FN-Mab) were measured using a fibronectin-coated surface and antibody-modified cantilevers always prepared in the same way. The measurements were carried out seven times, each time with a fresh AFM probe and a new sample (newly Mab-coated cantilever and freshly deposited fibronectin on the mica surface). These experiments were carried out using two cantilever types, MLCT-C and MLCT-D, characterized by nominal spring constants of 0.01 N/m and 0.03 N/m, respectively.

In lateral force microscopy, the cantilever (MLCT-C; nominal spring constant of 0.01 N/m) was moved laterally over the mica surface covered with fibronectin. The friction images always contained 2048 points per line. Three scan sizes from 1 to 6 µm were recorded at a scan rate from 0.1 Hz to 10 Hz (the scan velocity varied from 0.1 to 60 µm/s). In the classical AFM-FS experiment, the cantilever, localized in one selected point over the sample surface, was moved perpendicularly towards the FN-functionalized mica surface, followed by retraction. During this movement, the normal cantilever deflection was recorded as a function of relative scan position (i.e., force curves were collected). The force curves (2048 points per cycle, for approach and retract) were recorded as a function of retraction speed. The velocity was in a typical range of AFM retraction velocity and varied from 0.1 to 10 µm/s.

Specificity of the interaction

To assure the specificity of the interaction, the fibronectin was blocked using monoclonal antibody, same as that used for the cantilever functionalization. The inhibition experiments were carried out after 30 min of incubation with the PBS solution containing free antibody molecules. Afterwards, samples were rinsed with PBS buffer and immediately measured. The same protocol for the interaction inhibition was used in both types of experiments (AFM-FS and LFM).

Bell–Evans model

During the AFM unbinding, the external forces applied to a protein–ligand complex pull the ligand off of its initial position in the binding pocket. If the transition from bound to unbound states over the energy barrier is associated with a displacement in the direction of the acting force, the height of the energy barrier is lowered by the term $F \cdot x_b$ where x_b is the difference between the bound and unbound states [38-40]. In 1997, Evans and Ritchie introduced a model describing the bond rupture under an external force [41] for the case when the applied force F changes linearly in time t according to:

$$F(t) = k_{\text{eff}} \cdot \nu \cdot t, \tag{1}$$

where k_{eff} is the effective spring constant accounting for the AFM cantilever and the single bond spring constants, and ν is the tip velocity. The dependence of the unbinding force on the loading rate is given as [41]:

$$F = \frac{k_B \cdot T}{x_b} \ln(r_f) + \frac{k_B \cdot T}{x_b} \cdot \ln\left(\frac{x_b}{k_0 \cdot k_B \cdot T}\right), \tag{2}$$

where k_B is Boltzmann's constant, T is the temperature, x_b is the difference between the maximum of the energy barrier from the potential minimum, k_0 is the dissociation rate of the unbinding process, and r_f is the loading rate defining how fast an external force changes as a function of time.

Acknowledgements

This work was supported by Polish Funds for Science, Grant No. N202 262038 (W. N., M. L.). The study was (partly) supported by a research fellowship (M. L.) within the project “Enhancing Educational Potential of Nicolaus Copernicus University in the Disciplines of Mathematical and Natural Sciences” (Project No. POKL.04.01.01-00-081/10).

References

1. Hamon, L.; Pastré, D.; Dupaigne, P.; Le Breton, C.; Le Cam, E.; Piétrement, O. *Nucleic Acids Res.* **2007,** *35,* e58. doi:10.1093/nar/gkm147
2. Müller, D.; Janovjak, H.; Lehto, T.; Kuerschner, L.; Anderson, K. *Prog. Biophys. Mol. Biol.* **2002,** *79,* 1–43. doi:10.1016/S0079-6107(02)00009-3
3. Rotsch, C.; Radmacher, M. *Biophys. J.* **2000,** *78,* 520–535. doi:10.1016/S0006-3495(00)76614-8
4. Francis, L. W.; Lewis, P. D.; Wright, C. J.; Conlan, R. S. *Biol. Cell* **2010,** *102,* 133–143. doi:10.1042/BC20090127
5. Zhang, J.; Wu, G.; Song, C.; Li, Y.; Qiao, H.; Zhu, P.; Hinterdorfer, P.; Zhang, B.; Tang, J. *J. Phys. Chem. B* **2012,** *116,* 13331–13337. doi:10.1021/jp306882r
6. Wildling, L.; Rankl, C.; Haselgrübler, T.; Gruber, H. J.; Holy, M.; Newman, A. H.; Zou, M.-F.; Zhu, R.; Freissmuth, M.; Sitte, H. H.; Hinterdorfer, P. *J. Biol. Chem.* **2012,** *287,* 105–113. doi:10.1074/jbc.M111.304873
7. Zhu, R.; Rupprecht, A.; Ebner, A.; Haselgrübler, A.; Gruber, H. J.; Hinterdorfer, P.; Pohl, E. E. *J. Am. Chem. Soc.* **2013,** *135,* 3640–3646. doi:10.1021/ja312550k
8. Teulon, J.-M.; Delcuze, Y.; Odorico, M.; Chen, S. W.; Parot, P.; Pellequer, J.-L. *J. Mol. Recognit.* **2011,** *24,* 490–502. doi:10.1002/jmr.1109
9. Senkara-Barwijuk, E.; Kobiela, T.; Lebed, K.; Lekka, M. *Biosens. Bioelectron.* **2012,** *36,* 103–109. doi:10.1016/j.bios.2012.04.014
10. Jiang, Y.; Marszałek, P. E. *EMBO J.* **2011,** *30,* 2881–2893. doi:10.1038/emboj.2011.180
11. McCourt, C. M.; Boyle, D.; James, J.; Salto-Tellez, M. *J. Clin. Pathol.* **2013,** *66,* 58–61. doi:10.1136/jclinpath-2012-201140
12. Labuda, A.; Paul, W.; Pietrobon, B.; Lennox, R. B.; Grütter, P. H.; Bennewitz, R. *Rev. Sci. Instrum.* **2010,** *81,* 083701. doi:10.1063/1.3470107
13. Munz, M. *J. Phys. D: Appl. Phys.* **2010,** *43,* 063001. doi:10.1088/0022-3727/43/6/063001
14. Schwarz, U. D.; Köster, P.; Wiesendanger, R. *Rev. Sci. Instrum.* **1996,** *67,* 2560–2567. doi:10.1063/1.1147214
15. Dendzik, M.; Kulik, A. J.; Benedetti, F.; Marszalek, P. E.; Dietler, G. *Nanotechnology* **2013,** *24,* 365703. doi:10.1088/0957-4484/24/36/365703
16. Wang, H.; Gee, M. L. *Ultramicroscopy* **2014,** *136,* 193–200. doi:10.1016/j.ultramic.2013.10.012
17. Sader, J. E.; Larson, I.; Mulvaney, P.; White, L. R. *Rev. Sci. Instrum.* **1995,** *66,* 3789–3798. doi:10.1063/1.1145439
18. Cannara, R. J.; Eglin, M.; Carpick, R. W. *Rev. Sci. Instrum.* **2006,** *77,* 053701. doi:10.1063/1.2198768
19. Evans, E. *Biophys. Chem.* **1999,** *82,* 83–97. doi:10.1016/S0301-4622(99)00108-8
20. Neuert, G.; Albrecht, C.; Pamir, E.; Gaub, H. E. *FEBS Lett.* **2006,** *580,* 505–509. doi:10.1016/j.febslet.2005.12.052
21. Puntheeranurak, T.; Wildling, L.; Gruber, H. J.; Kinne, R. H. K.; Hinterdorfer, P. *J. Cell Sci.* **2006,** *119,* 2960–2967. doi:10.1242/jcs.03035
22. Taubenberger, A.; Cisneros, D. A.; Friedrichs, J.; Puech, P.-H.; Muller, D. J.; Franz, C. M. *Mol. Cell. Biol.* **2007,** *18,* 1634–1644. doi:10.1091/mbc.E06-09-0777
23. Scholl, Z. N.; Marszalek, P. E. *Ultramicroscopy* **2014,** *136,* 7–14. doi:10.1016/j.ultramic.2013.07.020
24. Lekka, M.; Kulik, A. J.; Jeney, S.; Raczkowska, J.; Lekki, J.; Budkowski, A.; Forró, L. *J. Chem. Phys.* **2005,** *123,* 014702. doi:10.1063/1.1949187
25. Gogolinska, A.; Nowak, W. *J. Mol. Model.* **2013,** *19,* 4773–4780. doi:10.1007/s00894-013-1972-z
26. Feiler, A.; Attard, P.; Larson, I. *Rev. Sci. Instrum.* **2000,** *71,* 2746–2750. doi:10.1063/1.1150686
27. Liu, E.; Blanpain, B.; Celis, J. P. *Wear* **1996,** *192,* 141–150. doi:10.1016/0043-1648(95)06784-1
28. Álvarez-Asencio, R.; Thormann, E.; Rutland, W. M. *Rev. Sci. Instrum.* **2013,** *84,* 079901. doi:10.1063/1.4820345
29. Ogletree, D. F.; Carpick, R. W.; Salmeron, M. *Rev. Sci. Instrum.* **1996,** *67,* 3298–3306. doi:10.1063/1.1147411
30. Ruan, J.-A.; Bhushan, B. *J. Tribol.* **1994,** *116,* 378–388. doi:10.1115/1.2927240
31. Kim, M.-C.; Neal, D. M.; Kamm, R. D.; Asada, H. H. *PLoS Comput. Biol.* **2013,** *9,* e1002926. doi:10.1371/journal.pcbi.1002926
32. Midwood, K. S.; Williams, L. V.; Schwarzbauer, J. E. *Int. J. Biochem. Cell Biol.* **2004,** *36,* 1031–1037. doi:10.1016/j.biocel.2003.12.003
33. Lai, C.-S.; Wolff, C. E.; Novello, D.; Griffone, L.; Cuniberti, C.; Molina, F.; Rocco, M. *J. Mol. Biol.* **1993,** *230,* 625–640. doi:10.1006/jmbi.1993.1174
34. Erickson, H. P.; Carrel, N. *J. Biol. Chem.* **1983,** *258,* 14539–14544.
35. Chtcheglova, L. A.; Dietler, G. *Acta Phys. Pol., A* **2003,** *104,* 321–326.
36. Fritz, J.; Katopodis, A. G.; Kolbinger, F.; Anselmetti, D. *Proc. Natl. Acad. Sci. U. S. A.* **1998,** *95,* 12283–12288. doi:10.1073/pnas.95.21.12283
37. Nishizaka, T.; Seo, R.; Tadakuma, H.; Kinosita, K., Jr.; Ischiwata, S. *Biophys. J.* **2000,** *79,* 962–974. doi:10.1016/S0006-3495(00)76350-8
38. Kienberger, F.; Kada, G.; Mueller, H.; Hinterdorfer, P. *J. Mol. Biol.* **2005,** *347,* 597–606. doi:10.1016/j.jmb.2005.01.042
39. Hänggi, P.; Talkner, P.; Borkovec, M. *Rev. Mod. Phys.* **1990,** *62,* 251–393. doi:10.1103/RevModPhys.62.251
40. Zhang, X.; Bogorin, D. F.; Moy, V. T. *ChemPhysChem* **2004,** *5,* 175–182. doi:10.1002/cphc.200300813
41. Evans, E.; Ritchie, K. *Biophys. J.* **1997,** *72,* 1541–1555. doi:10.1016/S0006-3495(97)78802-7

License and Terms

BEILSTEIN JOURNAL OF NANOTECHNOLOGY

Tattoo ink nanoparticles in skin tissue and fibroblasts

Colin A. Grant*[1,§], Peter C. Twigg[1], Richard Baker[2] and Desmond J. Tobin[2]

Full Research Paper

Open Access

Address:
[1]Advanced Materials Engineering, Faculty of Engineering and Informatics, University of Bradford, Bradford, BD7 1DP, United Kingdom and [2]Centre for Skin Sciences, Faculty of Life Sciences, University of Bradford, Bradford, BD7 1DP, United Kingdom

Email:
Colin A. Grant* - c.grant@bradford.ac.uk

* Corresponding author
§ Tel: (0)1274 234550; Fax: (0)1274 235925

Keywords:
atomic force microscopy (AFM); dermis; nanoparticles; skin; tattoo ink

Beilstein J. Nanotechnol. **2015,** *6,* 1183–1191.
doi:10.3762/bjnano.6.120

Received: 21 November 2014
Accepted: 22 April 2015
Published: 20 May 2015

This article is part of the Thematic Series "Advanced atomic force microscopy techniques III".

Guest Editor: T. Glatzel

Abstract

Tattooing has long been practised in various societies all around the world and is becoming increasingly common and widespread in the West. Tattoo ink suspensions unquestionably contain pigments composed of nanoparticles, i.e., particles of sub-100 nm dimensions. It is widely acknowledged that nanoparticles have higher levels of chemical activity than their larger particle equivalents. However, assessment of the toxicity of tattoo inks has been the subject of little research and ink manufacturers are not obliged to disclose the exact composition of their products. This study examines tattoo ink particles in two fundamental skin components at the nanometre level. We use atomic force microscopy and light microscopy to examine cryosections of tattooed skin, exploring the collagen fibril networks in the dermis that contain ink nanoparticles. Further, we culture fibroblasts in diluted tattoo ink to explore both the immediate impact of ink pigment on cell viability and also to observe the interaction between particles and the cells.

Introduction

The act of tattooing has been practised for many centuries in a number of countries including Japan, China, New Zealand as well as in regions of North Africa. The oldest recorded human tattoo was found on a well-preserved natural mummy from about 5,300 years ago, found in the Ötztal Alps in Italy, close to the border with Austria [1]. These ancient tattoos do not appear to have had decorative importance but may had have had some medical/therapeutic relevance, some appear to be close to traditional acupuncture points [2]. Today, tattooing is becoming increasingly popular across several sections of society, with increasing numbers of tattoo parlours opening for business. However, despite this striking cultural shift we know very little about the biochemical reactivity of ink particles with skin cells and tissues (including some of the key constituent components, e.g., fibroblasts and associated collagen fibrillar networks).

The tattooing process involves inserting ink pigment of the desired colour into the dermis layer of the skin. This is carried out by first dipping a needled tattoo instrument into the coloured ink before applying to the skin. The oscillating ink-coated needle punctures the skin in the range of 100 times per second, depositing the ink pigments 1.5 to 2 mm below the skin surface. Thus, the needle penetrates the skin through the epidermis and into the papillary layer of the dermis, where the ink particles accumulate. As with any type of trauma to the dermis, the first response of the body is to stop the resultant bleeding to form a clot. Then the skin tissue swells (edema) followed by a migration of immune system cells to the wound site (neutrophils and macrophages) in order to phagocytose foreign substances, cell debris and microbes. Any damaged collagen in the wounded papillary dermis is then repaired through the action of fibroblasts, ultimately laying down scar tissue. Over long periods of time the tattoo ink particles can be found to gradually move to the deeper dermis (i.e., reticular dermis), which gives the tattoo a faded and blurred appearance. Importantly, after tattoo ink insertion associated pigment particles can be found to leave the skin via its vasculature and enter the lymphatic system (nodes) [3].

Tattoo inks are commonly made up of a mixture of small organic pigments, water and isopropyl alcohol. Surprisingly, manufacturers of tattoo ink are not compelled to reveal the precise ingredients or chemical composition of their ink products despite their potential systemic absorption. Black inks are commonly made from soot (carbon black) particles. Tattoo inks can contain polycyclic aromatic hydrocarbons (PAHs) at a range of concentrations, which are reported to be carcinogenic, mutagenic and could pose other health risks to the skin [4]. Further, it was recently reported that tattooed young individuals can exhibit adverse reactions, especially with black or red ink tattoos, including photosensitivity, skin elevation and itching [5].

Nanoparticle research is currently receiving a great deal of interest due to its potential applications in biophysics, medicine, optics and electronics. A particle is generally considered to be a nanoparticle if it has dimensions below about 100 nm. For example, researchers in cancer nanotechnology are exploring methodologies to utilise functionalised quantum dots and nanocrystals to target specific tumour antigens [6]. Other medical research on nanoparticles includes the formation of a network of nanoparticles with an insulin core that can regulate and control normal blood sugar level [7]. However, despite considerable progress in nanoscience, it is often argued that the ethical and socio-legal implications of nanoparticles have been neglected [8]. Potential hazards of nanoparticles exist due to their high surface to volume ratio, which can make them very reactive [9], and their small size that can enable them to pass through cell membranes. The toxicity or biocompatibility of nanoparticles is an extremely important consideration for many of the aforementioned proposed applications. In particular carbon nanotubes, commonly used in applications such as drug delivery [10] and directed growth of neuron cells [11], have been shown to exhibit cytotoxicity potential [12], although carbon nanotube toxicity differs according to the production method used [13]. Moreover, the carbon black nanoparticles found in tattoo ink have safety profiles comparable to multi-walled carbon nanotubes [14]. Thus, there is a need to more accurately assess how tattoo ink particles directly interface with human cells and tissues. Atomic force microscopy (AFM) is one technique that can help to address this issue.

Atomic force microscopy (AFM) has been around since the mid-1980s and has become a powerful research instrument in the field of nanoscience and nanotechnology [15]. With highly specialised instrumentation and techniques, it is even possible to resolve molecular bonds [16,17]. Details of AFM operation and capabilities can be found elsewhere [18,19]. However, in brief, the AFM instrument involves a sharp probe at the end of a cantilever interacting with a surface. Not only can the AFM be used to visualise the surfaces of a wide range of materials (under various environmental conditions and over a large temperature range) the probe can also be used as a nano-indenter to ascertain mechanical properties [20] or even to carry out tensile testing of fibrils [21] or unfold protein molecules [22].

In this study we have used AFM to assess two fundamental components of skin dermis (fibroblasts and their secreted product, collagen) following interaction with tattoo ink particles. We examine the shape and size of tattoo ink particles on cellular and tissue surfaces. Further, we also investigate the cell viability of dermal fibroblasts after incubation with filtered/unfiltered diluted tattoo ink and discuss these results in the context of nanoparticle research.

Results and Discussion

Tattoo ink particle size distribution

Following three repeats of the particle size distribution procedure, the mode (peak intensity) value was 240.9 ± 2 nm. The same ink was also passed through a 220 nm filter to investigate the effect of increasing the proportion of nano-particulate pigment in the ink. Repeating the particle size analysis after filtration, the peak mode value reduced to 151 ± 2 nm (Figure 1a).

The light scattering technique used to make these measurements cannot distinguish between primary particles, aggregates and agglomerates. This means that the primary pigment particles may be smaller than the distribution suggests, although they cannot be larger. However, the agglomeration behaviour of the particles will be strongly influenced by the in vivo conditions in tattooing, or the in vitro conditions in cell culture. Agglomeration due to electrochemical processes can reduce the

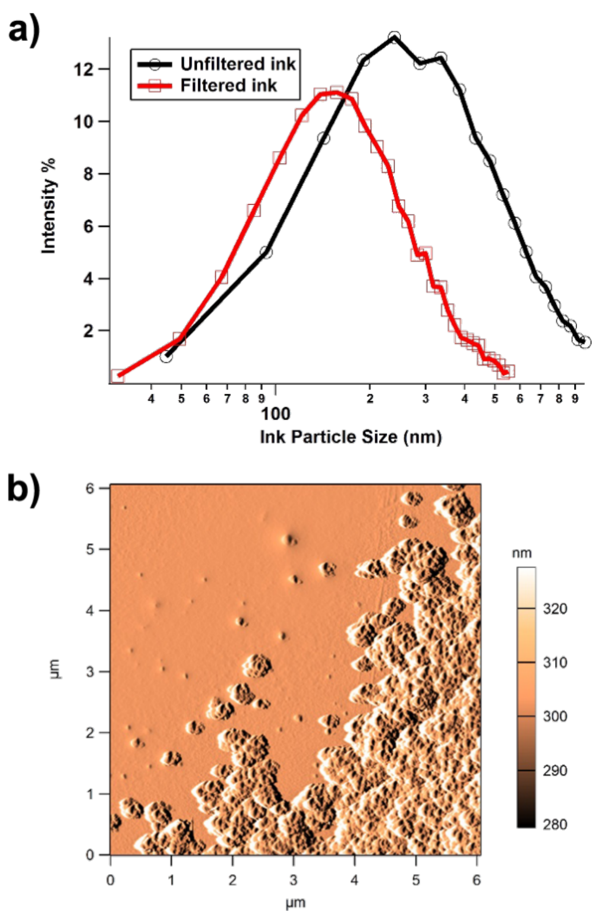

Figure 1: (a) Particle size distribution of filtered vs unfiltered commercially available tattoo ink, showing data ranging between 30 to 600 nm (filtered) and 40 to 970 nm (unfiltered). (b) Amplitude image of tattoo ink particles showing single and agglomerated particles adhered to a glass substrate.

effective number of particles by orders of magnitude and this will have a profound effect on how the particles are dealt with by cells and tissues.

AFM scanning of the tattoo ink that was adhered to the glass slide was carried out in order to isolate and measure the smallest particle size, as well as to explore agglomeration behaviour. In AFM imaging, the amplitude (error) image often gives greater clarity, as it is a more efficient edge detector and is not low-pass filtered through the electronic feedback loops [23]. The z-scale on the amplitude images reflects changes in the height moved by the piezo sensors to maintain the engage amplitude setpoint. From the amplitude image in Figure 1b it can be seen that the particles have strongly agglomerated following the deposition process, although, a small number of individual particles can be seen in the upper left portion of the image. These single, non-agglomerated particles in the AFM image (n = 16) exhibited a mean projected area of 2895 nm^2, which translates to a diameter of 60.7 nm assuming a spherical shape. For this study we have only examined one commercially available tattoo ink. However, the AFM and particle size distribution results are in strong agreement with Høgsberg et al., who carried out a large study of 58 tattoo inks of six different colours [24], where 99.94% of the volume of ink was made up from particles smaller than 100 nm.

It is clear that tattoo ink contains nanoparticles, given the peak size of the particle distribution and the AFM imaging of the ink on a glass slide. It remains unclear what potential toxicological effects tattoo ink components may have on cells, collagen fibrils etc. because of their nanometre-scale size. A gram of 60.7 nm carbon spheres would have a surface area of about 40 m^2; over 100000 times larger than the surface area of the equivalent bulk material. In addition, materials are known to behave differently at the nanometre-level in comparison with samples at the bulk level.Nanoparticle surface atoms have an increased reactivity over bulk surface atoms [9]. However, on the whole, tattoo pigments do appear to be reasonably well tolerated by the skin, and no clear relationship between tattoo exposure and skin cancer (or cancers in general) has yet been established [24]. As cancers in general can take years if not decades of toxicant exposure to materialise, we will need to monitor how the recent dramatic increase in large-scale tattooing may impact on (skin) cancer rates.

Microscopy of tattoo particles in skin tissue

Using the AFM top down optical microscope it was straightforward to manipulate the skin tissue section so that the cantilever was at the periphery of a clump of ink particles in the dermis (Figure 2a). A number of images were taken at various locations; Figure 2b shows a typical AFM height and corresponding amplitude image (Figure 2c) of a region in the upper dermis that contains tattoo ink particles. These AFM images clearly show the dense collagen fibril network with agglomerates of tattoo ink particles. The surface topography of the dermis is quite undulating with a surface roughness R_a of 30 nm over the 10 μm scan region.

The collagen fibrils here have a strong degree of parallel orientation, which would suggest that this region may well be scar tissue that was formed following the tattoo process. In a recent AFM study we compared scar tissue and healthy skin tissue and demonstrated that greater alignment of collagen fibrils occurs in scar tissue, as well as highlighting the reduction in the biomechanical performance of the scar tissue [25]. However, due to patient confidentiality it was not possible to find out more about how long the subject had the tattoo. Further, as the subject was 62 years old, the skin was also aged, including photo-aged from

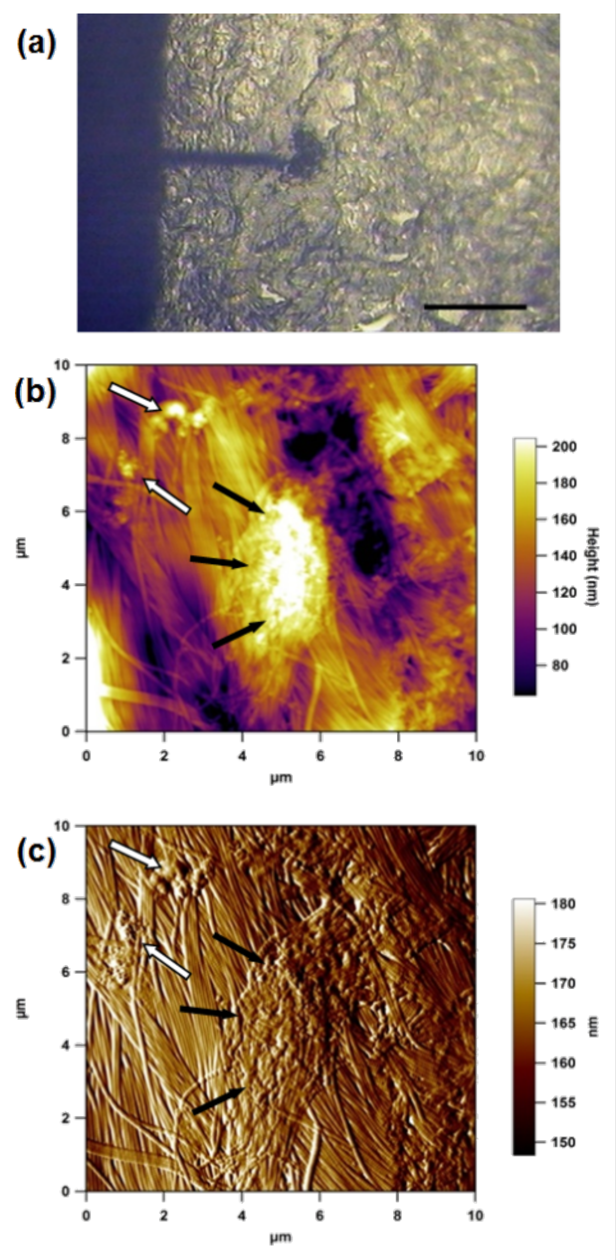

Figure 2: (a) AFM optical image (10×) showing the cantilever over a region of tattoo ink in the dermis; scale bar 200 µm. (b) 10 µm AFM height and (c) amplitude (error) image of cryosectioned tattooed skin. Black arrows indicate a large agglomerate and white arrows smaller agglomerates of tattoo ink particles.

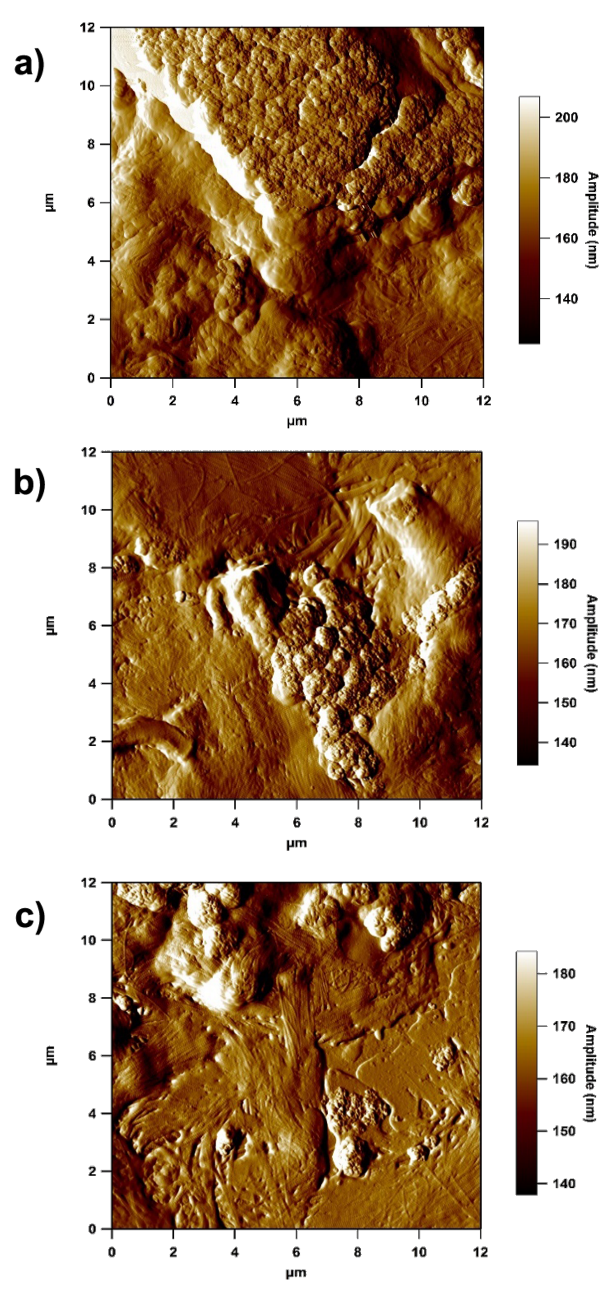

Figure 3: 12 µm amplitude images of highly agglomerated tattoo ink particles in the collagen network.

exposure of the forearm to UV irradiation. From multiple scans over a number of sections of tattooed skin tissue, it is clear that there were many regions of highly agglomerated ink particles, as shown in Figure 3. These agglomerations can be larger than the dermal cells, thereby changing the nature of the interaction between the pigment and the surrounding skin cells.

More detailed close-up scans (Figure 4a–d) also showed ink particles in close proximity to collagen fibrils. In the amplitude images (Figure 4b and Figure 4d), the periodic banding that is associated with collagen fibrils can clearly be resolved [26,27]. The inset of Figure 4e is a detailed view of the area surrounding a small cluster of particles from Figure 4d, with the corresponding line profile shown in Figure 4e. The pigment particle here has a width of 37.5 nm at half height. When measuring a spherically shaped object with a rounded AFM probe, it is common to use the dimension at half height, to try and avoid probe convoluted distortions [28]. This line section shows that

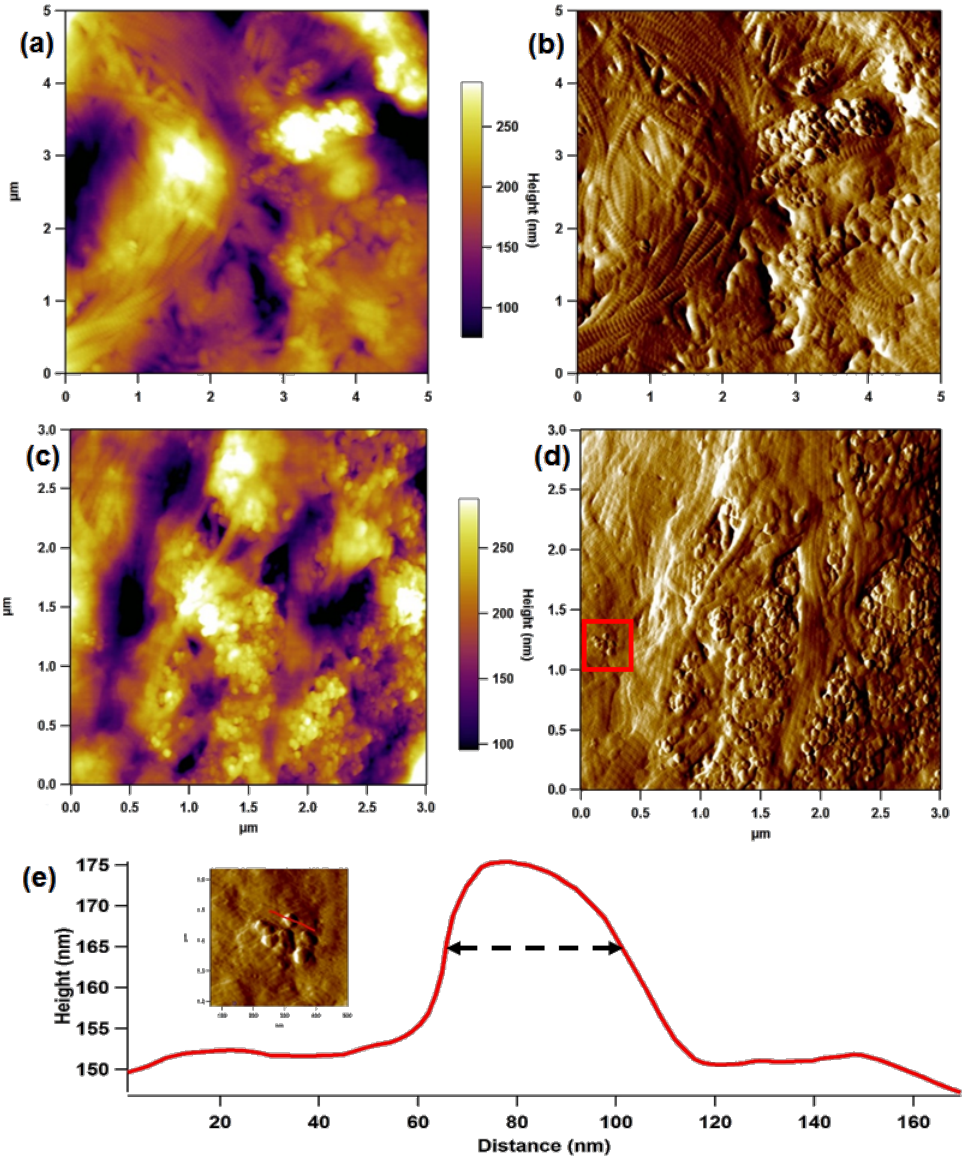

Figure 4: Height (a & c) and amplitude (b & d) images of disperse ink particles in the dermal collagen network. (Inset of (e)) 500 nm image of small cluster of ink particles from the solid red square (e) Line profile showing a particle of 37.5 nm width at half height.

the tattoo ink pigments are truly nanoparticles embedded in the dermal collagenous network, which were visible especially at the periphery of a clump of deposited particles. Wherever primary pigment particles could be resolved they were of approximately this diameter, suggesting that the observed ink particle size distribution reflects the range of agglomeration level rather than a wide range of primary particle sizes. It is also noted that images of ink particles on the control glass slide are remarkably similar to the images of the tattoo ink in the dermis (c.f. Figure 1b and Figure 3c).

It should be noted that these images are of surfaces, sectioned from bulk samples. In vivo these particles would sit within a three dimensional extracellular matrix structure where the particles do not always sit at the surface. Further, the act of sectioning might disrupt the particles, potentially breaking up agglomerates. However, every effort was taken to avoid this by controlling the cryosectioning conditions and using new blades. Even though imaging in air may lead to unknown artefacts within the tissue, the resolution is much better. Capturing a scan of the tissue under aqueous conditions in a non-tattoo part of the skin section yielded images of collagen fibril networks without particle matter, but were of lower quality (Figure 5). AFM fluid imaging has to use a cantilever spring constant that is about two orders of magnitude lower, which makes scanning trickier. Also, the tissue surface becomes softer.

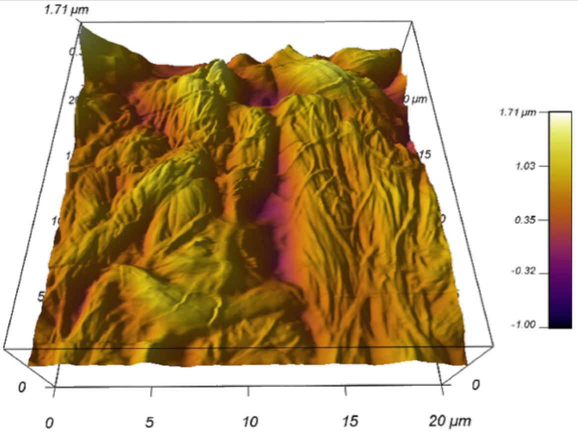

Figure 5: 3D reconstruction of AFM image on non-tattoo portion of the skin tissue under aqueous conditions (UHQ water).

Tattoos inevitably fade over time with a redistribution of the pigments deeper into the dermis and some even entering dermal blood vessels before transportation to local lymph nodes [29]. This leads one to question the extent of transportation of ink pigment particles throughout the body from the tattooing process. Light microscopy analysis of tattooed skin section revealed some interesting features. Figure 6a shows a transverse section of histologically stained tattooed skin, with the epidermal region uppermost in the image. Clumps of tattoo ink have dispersed throughout the upper and lower dermis. However, close inspection of a deep dermal blood vessel (Figure 6b) showed regions of tattoo ink scattered in the vessel wall as well as inside (peri)-vascular cells. A recent study, using a model system of mice tattooed with a commonly used ink to investigate the transportation and photo-decomposition of tattoo pigment particles [30], reported that the amount of ink in the mouse skin had reduced by 32 ± 16% of its initial value 42 days after tattooing. Furthermore, exposure of tattooed skin to simulated sun light and laser light also reduced the amount of ink particles retained in the skin [30]. A related study examined the distribution and accumulation of micrometre- and nanometre-sized silver particles following subcutaneous injection in rats, and found that silver nanoparticles were distributed throughout the main organs especially kidney, liver, spleen, brain and lungs [31]. By contrast, the micrometre-sized silver particles did not get into the blood circulation.

AFM imaging of dermal fibroblasts

Several studies have been conducted on fibroblasts using AFM to visualise both their surface and nano-mechanical properties [32-35]. Here, we show AFM images of dermal fibroblasts after incubation in diluted tattoo ink. This gives us an opportunity to visualise how tattoo ink particles may interact with dermal cells replicating the first moments following tattoo insertion in the skin. The AFM image of the fibroblast (Figure 7a) shows that the fixed cell is quite large, over 2 µm in height, therefore the small ink nanoparticles are difficult to see. However, phase imaging at a zoomed-in location on the cell surface (Figure 7b) highlights the ink particles very well. There appears to be a large number of ink particles attached to the cell surface in 200–500 nm clumps. However, it is not clear how much ink may have penetrated the cell, as the AFM technique can only probe surfaces.

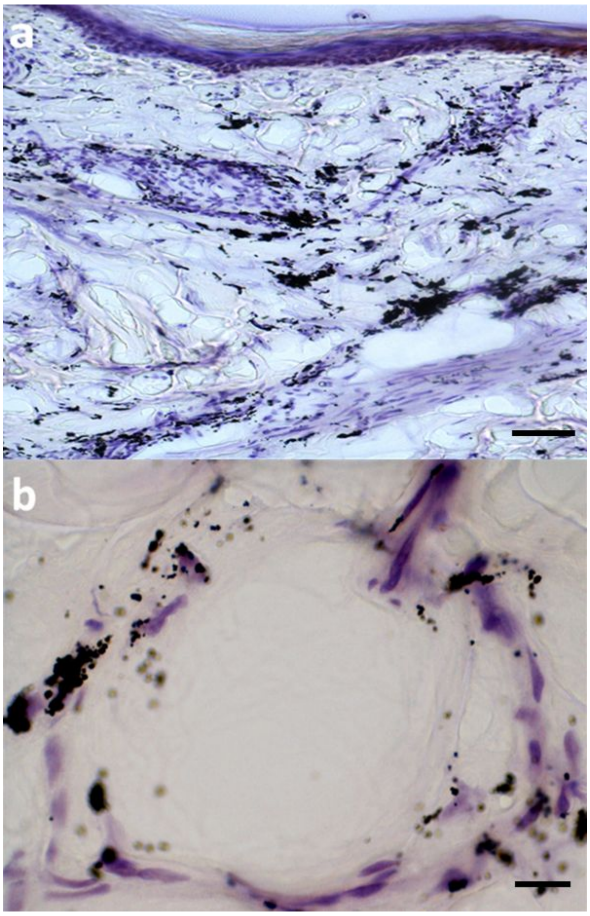

Figure 6: Light microscopy view of stained adult human tattooed arm skin. (a) Large deposits of dark ink particles distributed in a clumped manner in the dermis; scale bar 75 µm. (b) A deep dermal vessel with aggregations of ink particles in/around vessel wall and inside some associated cells; scale bar 15 µm.

The MTT (3-[4,5-dimethylthiazol-2-yl]-2,5-diphenyltetrazolium bromide) assay is a commonly used biological test on living cells, which broadly measures the in vitro cytotoxic effects of drugs on cell lines or primary patient cells [36]. Recently, an MTT assay for cytotoxicity assessment was carried out on fibroblasts exposed to two different diluted tattoo inks, which showed both cell death and inhibition of pro-collagen synthesis [37]. As that study was not carried out on skin fibroblasts it was decided to run a similar cell viability test using

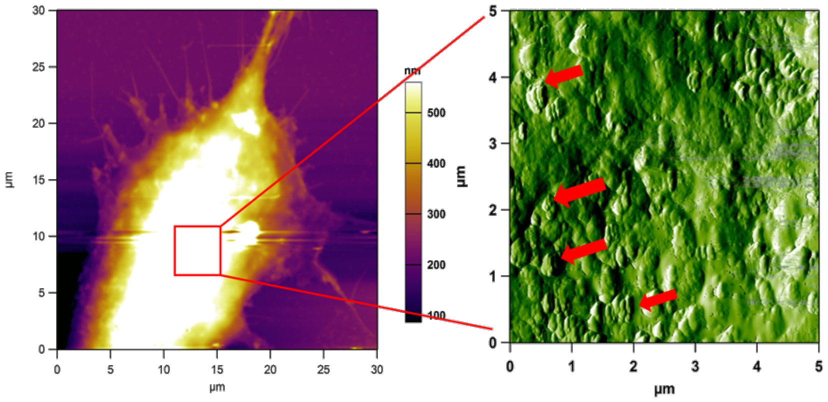

Figure 7: (a) AFM height image of a large fibroblast in vitro and incubated with diluted tattoo ink (1:10,000), followed by chemical fixation. (b) Phase image (5 μm) of the highest part of the cell body, which shows many regions (red arrows) of clumped ink particles on the cell surface.

human adult skin dermal fibroblast cells (the cells targeted in skin tattooing) with both filtered and unfiltered commercially available black ink.

The MTT assay results (shown in Figure 8) indicated that at an ink dilution of 1:100 the dermal fibroblast viability was reduced significantly after a one week exposure. A reduction in viability was also noted from similar work on gingival fibroblasts exposed to a different tattoo ink source [37]. As the MTT assay is a colourimetry-based technique, the use of dark pigments can be problematic. It was found that the lowest dilution of tattoo ink for the MTT assay to work was 1 in 100. Wamer and Yin found a phototoxic effect of eight decorative tattoo inks and permanent make-up inks that contained titanium dioxide on human dermal fibroblasts [38]. The phototoxic effect from the inks was attributed to the generation of hydroxyl radicals under UV excitation.

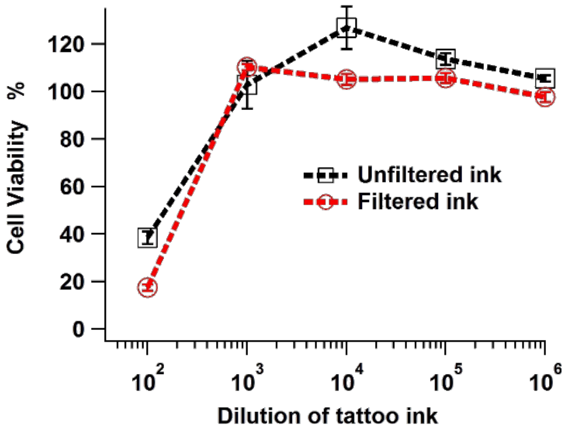

Figure 8: Cell viability of skin dermal fibroblasts incubated in diluted tattoo ink for seven days (filtered and unfiltered).

Interestingly, fibroblast viability was lowered to a greater extent in filtered (and diluted 1:100) than unfiltered ink, i.e., 17.6 ± 1.2% viability versus 38.3 ± 2.7% viability. Filtering the ink caused larger ink particles to be removed from the suspension, reducing the overall solid content of the ink. If the cytotoxicity were simply due to the amount of pigment in the culture media then filtration would be expected to reduce toxicity. It may be that in the culture media large particles act as nuclei for agglomeration of the pigment, reducing the toxic activity. Without these nucleation sites, primary nanoparticles may remain in suspension in very large numbers, thereby presenting the cell with a greater nanoparticle challenge and so interference of their cell physiology.

This finding demonstrates that smaller pigment particles cause an increase in fibroblast death over a period of one week. A further implication of this particle size reduction may occur during attempts to remove tattoos by using lasers during which tattoo ink clusters are broken up into smaller and potentially more cytotoxic particles. It is worth highlighting that the cell incubation period of a week was used here to try and replicate the initial conditions that fibroblasts may encounter during the immediate to early post-tattoo period. The long-term behaviour of the dermal fibroblasts is not likely to be damaged or hindered and will recover following the tattoo procedure.

Conclusion

In this study we have demonstrated that a commercially available black tattoo ink contains nanoparticles and that the modal particle size can be reduced by simple filtration. Atomic force microscopy can be used to successfully observe nanoparticles of tattoo ink in human skin tissue as well as on dermal fibroblasts in vitro. A single isolated nanoparticle of tattoo ink pigment in the region of 40 nm diameter was visualised from a dermal section of tattooed skin. The strong parallel orientation of the collagen fibrils was also noted in the tattooed skin, which was consistent with previous findings in wound healing/scar tissue [25].

Fibroblasts that were incubated in diluted tattoo ink also showed nanoparticles of ink pigments on their cell surface. Although it was not possible to explore using AFM methodology whether ink pigment nanoparticles could be taken up by the cells, this may be accomplished by ultrathin sectioning of such cells. However, the MTT assay using 1:100 diluted tattoo ink showed considerable fibroblast death. The amount of cell death with filtered tattoo ink was greater than the amount of cell death using unfiltered ink, which can be attributed to the subsequent reduction in tattoo ink particle size.

Experimental

Particle size distribution

The particle size distribution of the ink was determined by using a Mastersizer 3000, (Malvern Instruments Ltd., Malvern, UK). Tattoo ink (Scream Ink – Pitch Black, The Tattoo Shop, UK) was diluted in ultra-pure water (1:1000), pipetted into a disposable cuvette and then placed in the instrument. Detectors then accurately measured the intensity of light scattered by the particles in the ink for red and blue light wavelengths over a range of angles.

Tattoo skin sample

Skin samples were obtained from the forearm of a 62 year old male. Full approval was obtained from the ethics committee of the clinic and University for the use of this tissue in this research. The skin samples were frozen upon arrival in the laboratory and stored at −80 °C. Skin specimens from the tattooed region were attached to a metal chuck using optimum cutting temperature (OCT) embedding compound (Agar Scientific, Essex, England), then sectioned in a cryostat (CM1510, Leica Microsystems, Wetzlar, Germany) at 5 μm thickness and the sections collected onto polylysine-coated microscope slides. Tissue sections for light microscopy imaging (Nikon Eclipse 80i, Japan) were stained with haematoxylin and eosin, and then gently washed before mounting with a glass cover slip.

Skin tissue collection for isolation and culture of dermal fibroblasts

Normal human tissue (female, 35 years of age) was sourced from elective plastic surgery (facelift) and placed immediately in transport media. After arrival at the laboratory the skin samples were cleaned in wash solution (PBS containing 5 × Pen/Strep with antimycotics/antifungal (5 × PBS)) and any fat removed. Full approval was obtained from the ethics committee of the clinic and University for the use of this tissue. Skin was cut into 0.5 × 1.0 cm pieces then placed in 0.1% trypsin overnight at 4 °C. The following day tissue was incubated for 1 h at 37 °C to separate epidermis from dermis. The epidermis was removed and the remaining dermis placed upside down in a 75 cm^3 flask in RPMI 1640 medium (Invitrogen), then placed in a 37 °C incubator containing 5% CO_2. After five days the dermis was removed and the culture maintained. Cells were grown in RPMI 1640 supplemented with 10% fetal bovine serum (Invitrogen), 100 μg/mL Primocin (Source Bioscience) and 1% GlutaMAX (Invitrogen).

MTT assay

Dermal fibroblasts (passage 3) were trypsinised and seeded into 96-well plates at a density of 1×10^4 cells/well. The plates were maintained overnight (16 h) in RPMI 1640 medium to allow for cell attachment. The plates were incubated for 24 h in serum-starved medium (i.e., lacking fetal bovine serum) to remove exogenous sources of growth factors, before being exposed to the tattoo ink. Unfiltered and 0.22 μm filtered tattoo ink was diluted in ‘starved’ medium and added to the plate at dilutions ranging between $1{:}10^2$ and $1{:}10^6$. The plates were placed in a 37 °C incubator containing 5% CO_2 for 1 week, then washed with phosphate buffer solution (PBS) and incubated with serum-starved medium containing 0.5 mg/mL tetrazolium dye (MTT) for 4 h. The medium was carefully removed and 150 μL of dimethyl sulfoxide (DMSO) added to each well. The plate was gently shaken to achieve complete dissolution of the formazan crystals then the absorbance read on a spectrophotometer (Tecan Infinite) at 550 nm. The results were analysed and presented as a percentage of the untreated control samples.

A cell plate that did not undergo the MTT procedure but did have cells incubated with the tattoo ink was treated with 4% glutaraldehyde for 20 min in order to chemically fix the cells for AFM analysis. Chemically fixed samples were exhaustively washed and rinsed in ultra-pure water and gently dried under a stream of nitrogen.

AFM

Separate microscope slides containing the cryo-sectioned skin tissue samples and fixed fibroblast cells were placed on the sample stage of the MFP-3D AFM (Asylum Research, Santa Barbara, USA) and imaged in air in intermittent contact mode using Olympus AC160 silicon probes ($k \approx 40$N/m, tip radius ≈ 10 nm) and AC240 probes ($k \approx 2$N/m, tip radius ≈ 10nm). The AFM optics (10×) were used to identify an appropriate region of interest before scanning.

Diluted tattoo ink (1:10,000) from the particle size testing was then deposited on to a poly-L-lysine-coated glass slide for 60 s then washed off and dried in a steady stream of nitrogen. AFM imaging was carried out to examine the tattoo ink particles that were used in the particle size distribution testing.

References

1. Pabst, M. A.; Letofsky-Papst, I.; Bock, E.; Moser, M.; Dorfer, L.; Egarter-Vigl, E.; Hofer, F. *J. Archaeol. Sci.* **2009,** *36,* 2335–2341. doi:10.1016/j.jas.2009.06.016
2. Dorfer, L.; Moser, M.; Bahr, F.; Spindler, K.; Egarter-Vigl, E.; Giullén, S.; Dohr, G.; Kenner, T. *Lancet* **1999,** *354,* 1023–1025. doi:10.1016/S0140-6736(98)12242-0
3. Zirkin, H. J.; Avinoach, I.; Edelwitz, P. *Cutis* **2001,** *67,* 471–472.
4. Regensburger, J.; Lehner, K.; Maisch, T.; Vasold, R.; Santarelli, F.; Engel, E.; Gollmer, A.; König, B.; Landthaler, M.; Bäumler, W. *Exp. Dermatol.* **2010,** *19,* e275–e281. doi:10.1111/j.1600-0625.2010.01068.x
5. Høgsberg, T.; Hutton Carlsen, K.; Serup, J. *J. Eur. Acad. Dermatol. Venereol.* **2013,** *27,* 846–852. doi:10.1111/j.1468-3083.2012.04590.x
6. Nie, S.; Xing, Y.; Kim, G. J.; Simons, J. W. *Annu. Rev. Biomed. Eng.* **2007,** *9,* 257–288. doi:10.1146/annurev.bioeng.9.060906.152025
7. Gu, Z.; Aimetti, A. A.; Wang, Q.; Dang, T. T.; Zhang, Y.; Veiseh, O.; Cheng, H.; Langer, R. S.; Anderson, D. G. *ACS Nano* **2013,** *7,* 4194–4201. doi:10.1021/nn400630x
8. Anisa, M.; Abdallah, S. D.; Peter, A. S. *Nanotechnology* **2003,** *14,* R9–R13. doi:10.1088/0957-4484/14/3/201
9. Roduner, E. *Chem. Soc. Rev.* **2006,** *35,* 583–592. doi:10.1039/b502142c
10. Chen, J.; Chen, S.; Zhao, X.; Kuznetsova, L. V.; Wong, S. S.; Ojima, I. *J. Am. Chem. Soc.* **2008,** *130,* 16778–16785. doi:10.1021/ja805570f
11. Hu, H.; Ni, Y.; Montana, V.; Haddon, R. C.; Parpura, V. *Nano Lett.* **2004,** *4,* 507–511. doi:10.1021/nl035193d
12. Poland, C. A.; Duffin, R.; Kinloch, I.; Maynard, A.; Wallace, W. A. H.; Seaton, A.; Stone, V.; Brown, S.; MacNee, W.; Donaldson, K. *Nat. Nanotechnol.* **2008,** *3,* 423–428. doi:10.1038/nnano.2008.111
13. Herzog, E.; Casey, A.; Lyng, F. M.; Chambers, G.; Byrne, H. J.; Davoren, M. *Toxicol. Lett.* **2007,** *174,* 49–60. doi:10.1016/j.toxlet.2007.08.009
14. Hara, K.; Aoki, K.; Usui, Y.; Shimizu, M.; Narita, N.; Ogihara, N.; Nakamura, K.; Ishigaki, N.; Sano, K.; Haniu, H.; Kato, H.; Nishimura, N.; Kim, Y. A.; Taruta, S.; Saito, N. *Mater. Today* **2011,** *14,* 434–440. doi:10.1016/S1369-7021(11)70188-2
15. Binnig, G.; Quate, C. F.; Gerber, C. *Phys. Rev. Lett.* **1986,** *56,* 930–933. doi:10.1103/PhysRevLett.56.930
16. Gross, L.; Mohn, F.; Moll, N.; Liljeroth, P.; Meyer, G. *Science* **2009,** *325,* 1110–1114. doi:10.1126/science.1176210
17. Gross, L.; Mohn, F.; Moll, N.; Schuler, B.; Criado, A.; Guitián, E.; Peña, D.; Gourdon, A.; Meyer, G. *Science* **2012,** *337,* 1326–1329. doi:10.1126/science.1225621
18. Giessibl, F. J. *Mater. Today* **2005,** *8,* 32–41. doi:10.1016/S1369-7021(05)00844-8
19. Santos, N. C.; Castanho, M. A. R. B. *Biophys. Chem.* **2004,** *107,* 133–149. doi:10.1016/j.bpc.2003.09.001
20. Butt, H.-J.; Cappella, B.; Kappl, M. *Surf. Sci. Rep.* **2005,** *59,* 1–152. doi:10.1016/j.surfrep.2005.08.003
21. Svensson, R. B.; Hassenkam, T.; Grant, C. A.; Magnusson, S. P. *Biophys. J.* **2010,** *99,* 4020–4027. doi:10.1016/j.bpj.2010.11.018
22. Brockwell, D. J. *Curr. Nanosci.* **2007,** *3,* 3–15. doi:10.2174/157341371070301000З
23. Grant, C. A.; Brockwell, D. J.; Radford, S. E.; Thomson, N. H. *Biophys. J.* **2009,** *97,* 2985–2992. doi:10.1016/j.bpj.2009.09.010
24. Høgsberg, T.; Loeschner, K.; Löf, D.; Serup, J. *Br. J. Dermatol.* **2011,** *165,* 1210–1218. doi:10.1111/j.1365-2133.2011.10561.x
25. Grant, C. A.; Twigg, P. C.; Tobin, D. J. *Acta Biomater.* **2012,** *8,* 4123–4129. doi:10.1016/j.actbio.2012.06.042
26. Grant, C. A.; Brockwell, D. J.; Radford, S. E.; Thomson, N. H. *Appl. Phys. Lett.* **2008,** *92,* 233902. doi:10.1063/1.2937001
27. Grant, C. A.; Phillips, M. A.; Thomson, N. H. *J. Mech. Behav. Biomed. Mater.* **2012,** *5,* 165–170. doi:10.1016/j.jmbbm.2011.08.020
28. Markiewicz, P.; Goh, M. C. *J. Vac. Sci. Technol., B* **1995,** *13,* 1115–1118. doi:10.1116/1.587913
29. Anderson, L. L.; Cardone, J. S.; McCollough, M. L.; Grabski, W. J. *Dermatol. Surg.* **1996,** *22,* 92–94. doi:10.1111/j.1524-4725.1996.tb00578.x
30. Engel, E.; Vasold, R.; Santarelli, F.; Maisch, T.; Gopee, N. V.; Howard, P. C.; Landthaler, M.; Bäumler, W. *Exp. Dermatol.* **2010,** *19,* 54–60. doi:10.1111/j.1600-0625.2009.00925.x
31. Tang, J.; Xiong, L.; Wang, S.; Wang, J.; Liu, L.; Li, J.; Yuan, F.; Xi, T. *J. Nanosci. Nanotechnol.* **2009,** *9,* 4924–4932. doi:10.1166/jnn.2009.1269
32. Haga, H.; Sasaki, S.; Kawabata, K.; Ito, E.; Ushiki, T.; Sambongi, T. *Ultramicroscopy* **2000,** *82,* 253–258. doi:10.1016/S0304-3991(99)00157-6
33. Hopp, I.; Michelmore, A.; Smith, L. E.; Robinson, D. E.; Bachhuka, A.; Mierczynska, A.; Vasilev, K. *Biomaterials* **2013,** *34,* 5070–5077. doi:10.1016/j.biomaterials.2013.03.075
34. Mahaffy, R. E.; Park, S.; Gerde, E.; Käs, J.; Shih, C. K. *Biophys. J.* **2004,** *86,* 1777–1793. doi:10.1016/S0006-3495(04)74245-9
35. Müller, D. J.; Dufrêne, Y. F. *Trends Cell Biol.* **2011,** *21,* 461–469. doi:10.1016/j.tcb.2011.04.008
36. van Meerloo, J.; Kaspers, G. J.; Cloos, J. *Methods Mol. Biol. (N. Y., NY, U. S.)* **2011,** *731,* 237–245. doi:10.1007/978-1-61779-080-5_20
37. Falconi, M.; Teti, G.; Zago, M.; Galanzi, A.; Breschi, L.; Pelotti, S.; Ruggeri, A.; Mazzotti, G. *Arch. Dermatol. Res.* **2009,** *301,* 539–547. doi:10.1007/s00403-009-0953-7
38. Wamer, W. G.; Yin, J.-J. *J. Cosmet. Sci.* **2011,** *62,* 535–548.

License and Terms

The definitive version of this article is the electronic one which can be found at:
doi:10.3762/bjnano.6.120

BEILSTEIN JOURNAL OF NANOTECHNOLOGY

Nano-contact microscopy of supracrystals

Adam Sweetman[*1], Nicolas Goubet[2,3], Ioannis Lekkas[1], Marie Paule Pileni[2,3,4]
and Philip Moriarty[1]

Full Research Paper

Open Access

Address:
[1]The School of Physics and Astronomy, The University of Nottingham, Nottingham, NG7 2RD, U.K., [2]Sorbonne Universités, UPMC Univ Paris 06, UMR 8233, Monaris, F-75005, Paris, France, [3]CNRS, UMR 8233, Monaris, F-75005, Paris, France and [4]CEA/IRAMIS, CEA Saclay, 91191, Gif-sur-Yvette, France

Email:
Adam Sweetman* - adam.sweetman@nottingham.ac.uk

* Corresponding author

Keywords:
dynamic force microscopy; nanoparticle; non-contact atomic force microscopy; point contact imaging; scanning probe microscopy; supracrystal

Beilstein J. Nanotechnol. **2015,** *6,* 1229–1236.
doi:10.3762/bjnano.6.126

Received: 31 December 2014
Accepted: 04 May 2015
Published: 29 May 2015

This article is part of the Thematic Series "Advanced atomic force microscopy techniques III".

Guest Editor: T. Glatzel

Abstract

Background: Highly ordered three-dimensional colloidal crystals (supracrystals) comprised of 7.4 nm diameter Au nanocrystals (with a 5% size dispersion) have been imaged and analysed using a combination of scanning tunnelling microscopy and dynamic force microscopy.

Results: By exploring the evolution of both the force and tunnel current with respect to tip–sample separation, we arrive at the surprising finding that single nanocrystal resolution is readily obtained in tunnelling microscopy images acquired more than 1 nm into the repulsive (i.e., positive force) regime of the probe–nanocrystal interaction potential. Constant height force microscopy has been used to map tip–sample interactions in this regime, revealing inhomogeneities which arise from the convolution of the tip structure with the ligand distribution at the nanocrystal surface.

Conclusion: Our combined STM–AFM measurements show that the contrast mechanism underpinning high resolution imaging of nanoparticle supracrystals involves a form of nanoscale contact imaging, rather than the through-vacuum tunnelling which underpins traditional tunnelling microscopy and spectroscopy.

Introduction

Artificial solids comprising extended assemblies of nanocrystals with a narrow size distribution represent an especially important class of nanostructured material. In addition to their inherent tunability, this type of “designer” solid is of particular interest in the context of the evolution of mesoscopic and, indeed, macroscopic physical properties from nanoscale components [1-3]. Remarkably well-ordered 3D nanocrystal superlattices, otherwise known as supracrystals [4], can now be synthesized via slow nucleation and growth under a solvent atmosphere [5]. This assembly process produces not only supra-crystalline films (which nucleate and grow at the air–solvent interface) but also large polyhedral supracrystals arising from precipitation in the colloidal suspension.

There is a significant body of work that focuses on elucidating the electronic properties of nanocrystals and their associated 1D, 2D, and 3D assemblies. Building on the conceptual and theoretical framework put forward by Middleton and Wingreen in the early 1990s [6], a number of groups [7-11] have shown that the current–voltage ($I(V)$) characteristics of nanocrystal superlattices follow a power law dependence above a voltage threshold (which is related to the Coulomb gap for the system). The power law exponent depends both on the effective dimensionality and the amount of topological/charge disorder in the system. The distribution of nanocrystal connectivity due to this disorder plays an essential role in determining the topological "landscape" for charge transport, which can be affected at the nanoscopic, mesoscopic, and microscopic scales [12].

Although a similar power law behaviour has been observed for the $I(V)$ characteristics of both interfacial and precipitated supracrystals, Yang et al. [11,13] point out that it is somewhat counter-intuitive and surprising that supracrystals that are of order 5 µm thick (i.e, ≈700 nanoparticle layers) are sufficiently conductive for STM and scanning tunnelling spectroscopy (STS) studies. However, not only are STM and STS measurements possible, but the quality of imaging is comparable to that attained on monolayer (or submonolayer) coverages of nanoparticles on various substrates [14,15] (see, in particular, Figure 7a of Yang et al. [11].) However, bias voltages significantly higher than those conventionally used in STM measurements (as high as 9 V [13]) were sometimes necessary to image thick precipitated supracrystals. In addition to the unexpected imaging resolution, tunnelling spectra of nanocrystals were interpreted as exhibiting the collective behaviour of the ensemble with the spectral fingerprint of an isolated nanocrystal superimposed on the overall $I(V)$ characteristic [13].

Here we extend scanning probe measurements of supracrystals to an analysis based on a combination of STM and dynamic force microscopy (DFM) imaging and spectroscopy. DFM experiments, also known as non-contact AFM (NC-AFM), are carried out using a quartz tuning fork sensor in the qPlus geometry [16,17] to which a tip has been glued. Shifts in the resonant frequency of a tine of the tuning fork due to variations in the tip–sample interaction are tracked and, via the formula introduced by Sader and Jarvis [18], can be converted to force or potential energy measurements. The qPlus sensor facilitates, in principle, a straight-forward method of acquiring tunnelling current and tip–sample force maps in parallel, but there are important instrumental artefacts [19,20] and physical effects [21] that can produce crosstalk between the measurement channels and these need to be carefully considered. With this proviso in mind, the DFM-STM combination can be exploited to correlate, in parallel, the dependence of the tunnel current and the tip–sample force on the displacement of the probe.

Our combined STM-DFM measurements clearly show that STM imaging of low conductivity supracrystals involves a contact conduction mechanism, and not the through-vacuum tunnelling that is exploited in conventional tunnelling microscopy. The possibility of atomic scale point-contact imaging in STM was recognised by Smith et al. almost three decades ago [22], and in the intervening years, the relationship between the variation in the tunnel current and the tip–sample force as a function of probe displacement has been studied in considerable detail [23-27]. A recent review [28] outlines key developments in point-contact measurements, including the quantum point-contact microscopy strategy introduced by Zhang et al. [29]. State-of-the-art qPlus DFM, where both intra- [30,31] and inter-molecular [32-34] resolution are increasingly the norm, also exploits imaging in the point-contact regime for which electron repulsion underpins the contrast mechanism (as pioneered by Gross et al. [30]). We apply a similar type of contact imaging protocol to nanocrystal superlattices for the first time and demonstrate that subparticle resolution images can be acquired in constant height mode, despite the high curvature of the particle surfaces. There remains, of course, the perennial issue plaguing the interpretation of scanning probe microscopy images: the convolution of the tip and sample structure. Nonetheless, our results clearly show that there is significant potential for qPlus DFM imaging to provide high resolution images of the surfaces of nanoparticles and, for example, to lay to rest the controversy regarding molecular self-assembly and phase separation in the ligand shell of nanoparticles [35].

Experimental

The Au nanocrystals used here were synthesized using a modified organometallic reduction method [36]. Briefly, 0.25 mmol of chloro(triphenylphosphine)gold(I) was dissolved in 25 mL of toluene and 250 µL of dodecanethiol. The reducing solution was made with 2.5 mmol of tertbutylamine borane complex dissolved in 15 mL of toluene. Both solutions were heated to 100 °C and mixed together. The colourless reaction medium first turns to brown and then quickly to dark red. After five minutes the solution was allowed to cool to room temperature. The resulting nanocrystals have a mean diameter of 7.4 nm with 5% polydispersity (see Supporting Information File 1).

A portion of the colloidal solution was washed with ethanol to produce the starting solution for Au nanocrystal superlattices. The resulting precipitate was then redispersed in toluene and the self-assembly process occurred in the washed solution in a toluene-saturated atmosphere. After one week without evaporation, the toluene/air interface exhibited a deposit which appeared golden in colour [4]. A part of this interfacial deposit was withdrawn from the interface solution with a DuNouy ring and deposited on a highly oriented pyrolytic graphite substrate. High-resolution scanning electron microscopy pictures revealed that the nanocrystals organise into compact structures (see Supporting Information File 1). We note that the samples were not annealed or treated in any other way before the scanning probe experiments were undertaken.

The scanning probe data in this paper were acquired using an Omicron Nanotechnology combined low temperature STM/DFM operating under UHV conditions at cryogenic temperatures (78 K, with liquid nitrogen cooling). Commercial qPlus sensors from Omicron with an electrochemically etched tungsten wire glued to one tine of the tuning fork were first prepared on clean Si(111)-(7 × 7) samples by standard STM techniques before imaging of the nanocrystal samples. During imaging of the supracrystal surface, spontaneous and regular tip changes were observed, thus it is possible that the qPlus probe became nanocrystal- (or thiol-)terminated. Imaging was performed in constant current STM, constant frequency shift (Δf) DFM, and constant height DFM modes. In addition to traditional STM, we also carried out dynamic STM (dSTM) imaging and spectroscopy, where the tip was oscillated with a small amplitude (of order 0.1−0.3 nm, see below) normal to the surface. The use of constant height imaging (using a similar protocol to that described previously [30,33]) allows us to probe the tip–sample interaction on the repulsive branch of the frequency shift curve, which is typically not available using conventional Δf feedback on the attractive branch.

Oscillation amplitudes (A_0) between 0.1 and 0.3 nm were typically used for DFM imaging. We reduced any possible electronic crosstalk [19] or so-called “phantom force” [21] effects by ensuring DFM imaging was performed in the absence of a detectable tunnel current. Normally this was done by ensuring the gap voltage was set to 0 V, but we were also able to make force measurements without detectable tunnel currents at higher voltages (see Results and Discussion section). In the experimental set-up used for the experiments described in this paper, the tip was held at ground potential and the sample was biased. To help stabilise the imaging conditions, a custom-built atom tracking system [37] was used to apply feed-forward correction to reduce the effect of thermal drift and piezo-electric creep.

To measure the site-specific force between the probe tip and a single nanocrystal, single-point $\Delta f(z)$ spectroscopy measurements were acquired both on a particle (so-called “on” spectra), and in a region not demonstrating any site-specific interaction (so-called “off” spectra). The non-site-specific interactions were then subtracted from the “on” spectra [23,38] and the resultant short-range $\Delta f(z)$ was inverted to extract force values using the Sader–Jarvis algorithm [18,39].

Results and Discussion

In agreement with previous studies [11,13] we readily (within minutes) obtained dSTM images of the supracrystals upon approaching the tip to the sample. Figure 1A,B show constant current dSTM images obtained at moderate tip–sample biases (+2.5 V and +1.5 V respectively). After ensuring the imaging and scan conditions were stable, the tip was retracted several nm and the bias was slowly reduced to 0 V. We then reapproached the sample in constant Δf feedback and slowly increased the Δf setpoint until stable, high contrast DFM imaging was obtained. Figure 1C is an image of the same nanocrystal as shown in the centre of Figure 1B acquired in constant Δf DFM mode at a Δf of −2 Hz. We note that the appearance of the nanocrystals in DFM feedback is broadly comparable to that in dSTM, with the particles having the same approximate size and shape with little internal contrast.

After completing the DFM scan, the tip was positioned over the centre of a nanocrystal and the feedback loop turned off. The same region was then imaged in constant height DFM mode, producing a map of Δf, with dark regions corresponding to attractive interaction (more negative frequency shift), and brighter regions corresponding to repulsive interactions (more positive frequency shifts). The result of imaging the nanocrystal at progressively smaller tip–sample separations is shown in Figure 1D–F.

Due to the nature of operation, we only observe the very top of the nanocrystal in constant height mode , with the surrounding regions imaging as a featureless void. Nonetheless, a number of additional features become apparent in constant height imaging. The crystalline shape of the nanocrystal is apparently clearer in constant height mode, with a triangular appearance suggestive of faceting, as proposed recently by Goubet et al. [40]. In addition, we see an internal structure that is not apparent in either the dSTM or constant Δf DFM topographs. Interpreting these intra-nanocrystal features is challenging for a number of reasons. First, the exact nature of our tip apex is unknown, and very possibly terminated either by free thiol ligands or entire nanocrystals. Second, due to the high aspect ratio of the nanocrystal surface (as compared to an atomically flat substrate), it is difficult to image a very large area of a particle without causing very close approach over the topmost regions. Consequently, we often see a number of “slices” and tip changes during imaging, suggesting that either the apex of the tip or the

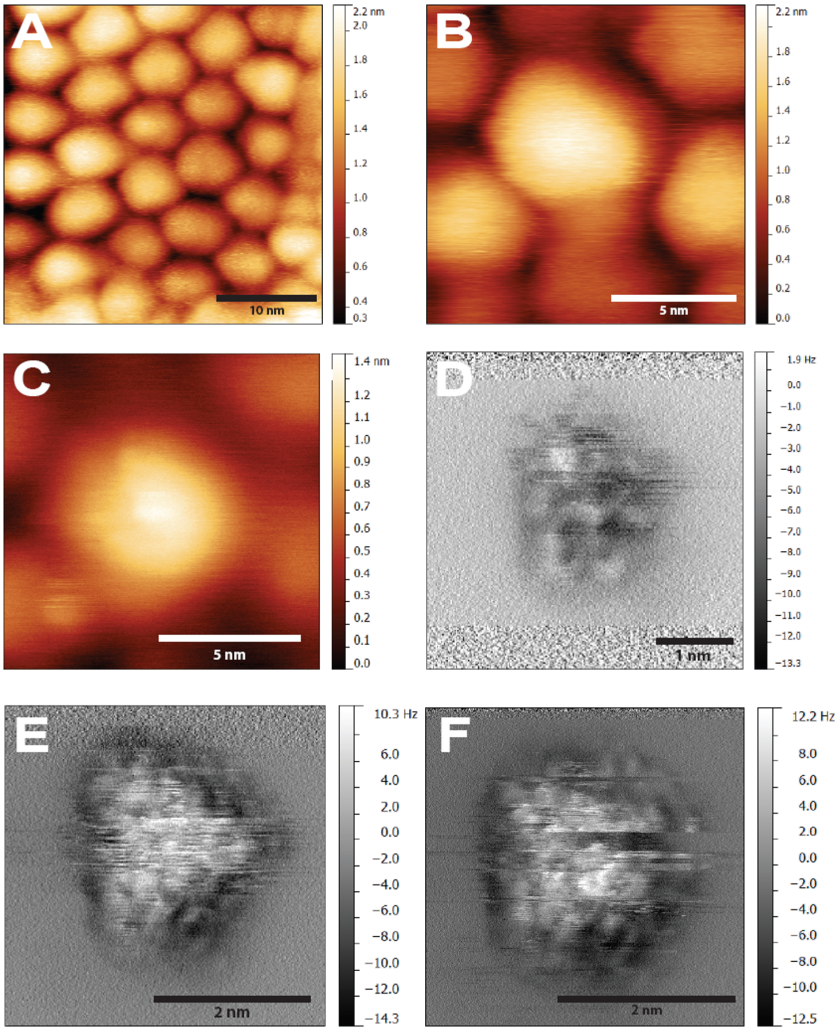

Figure 1: (A) Overview dSTM image showing packing of nanocrystals in a supracrystal. V_{gap} = +2.5 V, $< I_t >$ = 20 pA, A_0 = 1 nm. (B) High resolution dSTM image of nanocrystals. V_{gap} = +1.5 V, $< I_t >$ = 10 pA, A_0 = 0.11 nm. (C) Constant frequency shift DFM image of same region V_{gap} = 0 V, Δf = −2 Hz, A_0 = 0.11 nm. (D) Constant height image of nearby region. Estimated height relative to feedback position Δz = −0.2 nm. (E) Constant height DFM, Δz = −0.25 nm. (F) Δz = −0.3 nm. The frequent discontinuities ("slicing") in E and F are due to modifications/relaxation of the tip–sample junction. We also note that, due to instrumental drift and creep, the Δz values are likely to be systematically underestimated.

coating of the nanocrystal is undergoing changes during scanning. As such, we cannot assume a priori that a simple single atom "point-like" contact is responsible for the observed contrast. Finally, the supracrystal is composed of a mixture of single domain and polycrystalline nanocrystals [40], complicating the analysis of the DFM images.

We found that the evolution in contrast from STM, to constant Δf DFM, to constant height DFM was reproducible if we used different tip apices (prepared via gentle crashing into the sample). Figure 2A–C shows a dSTM, constant Δf DFM, and constant height DFM image all acquired using a different tip apex over a different region of the sample. During this imaging sequence we also measured the quantitative force data shown in Figure 2D,E. The peak attractive force is of order 200−400 pN, comparable to that measured between two weakly interacting (C_{60}) molecules, where the interaction is entirely due to dispersion forces [41]. However, while force–distance measurements of single molecule interactions using this technique are typically highly reproducible [31,33,41-43], we observe a very large degree of variation between different $F(z)$ spectra for the nanocrystals. Although the broad trends remain similar, there are multiple jumps and discontinuities. A plausible explanation is that while the macroscopic apex of the tip remains stable, the very apex of the tip is undergoing multiple reconfiguration events upon contact with the sample. This is perhaps unsurprising if we consider the quite likely scenario where we have both a thiol-terminated tip and thiol-coated nanocrystal, and where the thiols on both the tip and nanocrystal would be relatively free to relax as the tip approaches the sample. These

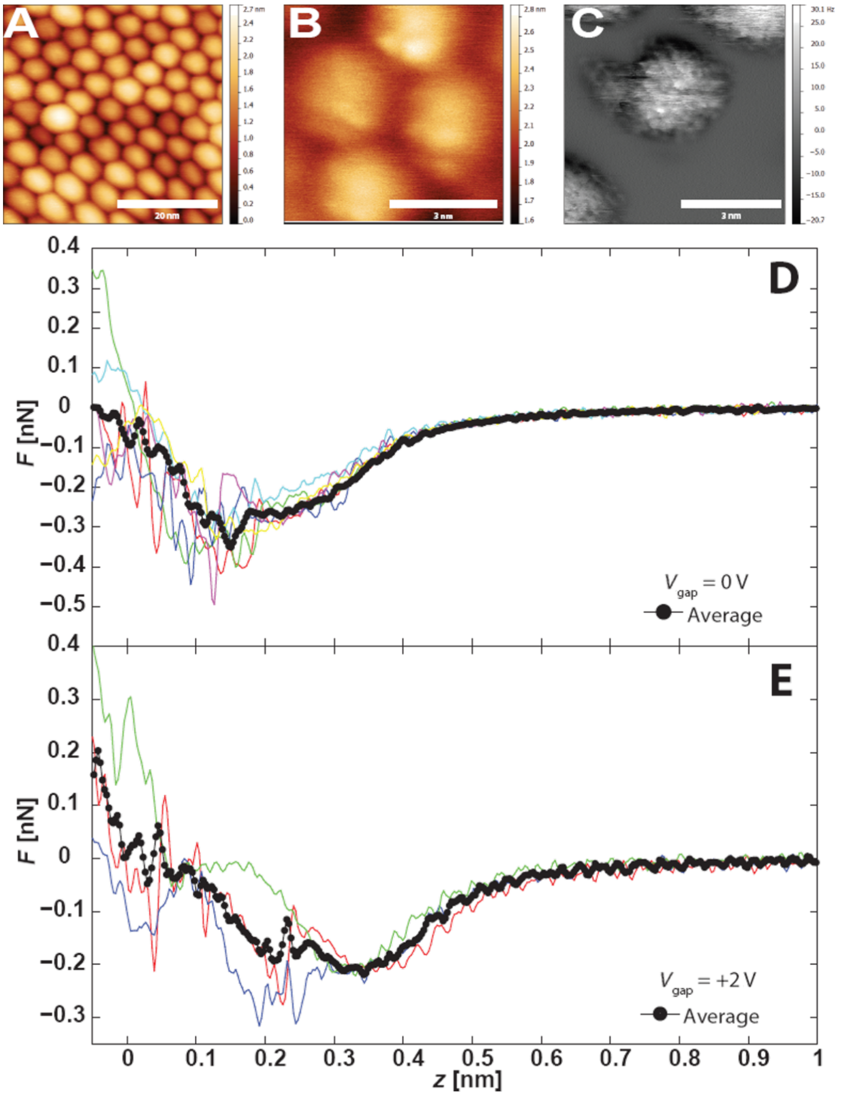

Figure 2: (A) Overview dSTM showing nanocrystal assembly, V_{gap} = +2 V, $< I_t >$ = 20 pA. (B) DFM image acquired in the region shown in A. V_{gap} = 0 V, Δf = −2.3 Hz, A_0 = 0.11 nm. (C) Constant height Δf image of nearby region Δz = −0.7 nm. (D) Site-specific tip–sample force data taken over a single nanocrystal with zero applied bias. (E) Site-specific tip–sample force data taken over the same nanocrystal and height range with an applied bias of +2 V. Note that no tunnel current was detected during this measurement.

observations are also consistent with the numerous reconfiguration events that we observe during constant height imaging (observed, for example, as discontinuities in Figure 1F).

An important conclusion from Figure 2D,E is that the constant height imaging we perform is clearly within the repulsive branch of the short range force, and consequently the tip is in contact with the sample. Despite the strong forces applied to the sample, the supracrystal remains stable, most likely due to the high cohesive energy arising both from the integrated van der Waals forces and ligand interdigitation. The question of where to define the contact point is, of course, a notoriously vexed issue, as Smith et al. pointed out in their pioneering paper on point-contact microscopy using STM [22]. However, regardless of whether we define the contact point as the tip–sample separation associated with the minimum of the potential energy curve (i.e., where $F(z) = 0$) or as the point at which the gradient of the force curve changes from positive to negative, it is clear that the STM images are acquired far beyond the tunnelling regime, in a point-contact mode.

In order to investigate the force/tunnel current relationship for this system in more detail, we gradually increased the applied bias from 0 V to +2 V, maintaining the same tip–sample separation. Repeating the force–distance measurements (Figure 2E), we observed a slight modification to the tip–sample force profiles, although we cannot rule out that the reduced peak force could also arise from a minor change in the tip apex. More striking was the observation that even at +2 V bias we observed no detectable tunnel current signal throughout the spectroscopy or imaging, despite clearly being in contact with the sample.

Having previously successfully acquired STM images in the same region at the same bias, we performed combined $\Delta f(z)$ and $I(z)$ measurements with increasing tip indentation in the same region (Figure 3A). We only began to detect comparable tunnel current signals to the STM setpoint at indentations of −1 to −1.5 nm closer to the sample than the constant height imaging position (Figure 3B), which we previously established was already at a tip–sample separation corresponding to the repulsive branch of the short range force curve. The simultaneously acquired Δf curve also shows strongly repulsive behaviour, but we note that the quantitative short range force cannot be extracted in this case as at this level of indentation there is no complementary "off" curve position that does not show site-specific interactions. Nonetheless, the Δf behaviour provides strong complementary evidence for a repulsive interaction at the tip height at which a detectable tunnel current is observed. Likewise, decreasing the tip–sample separation whilst imaging in

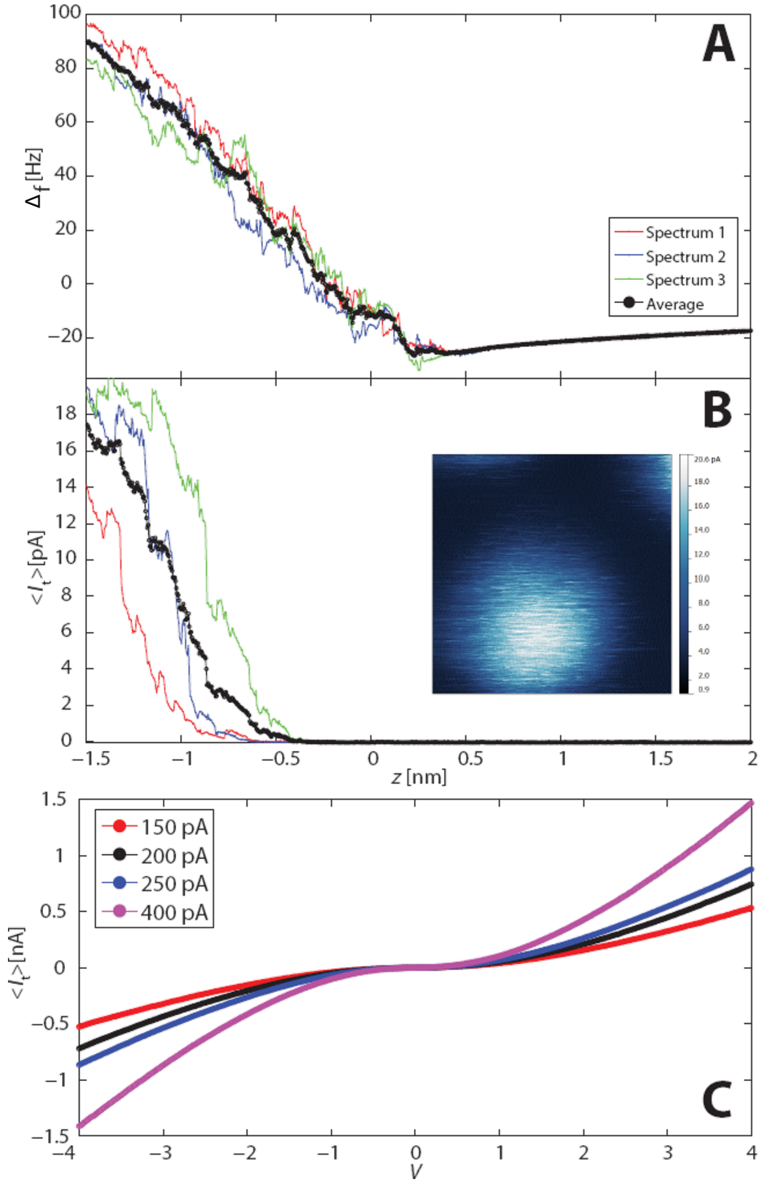

Figure 3: Simultaneous Δf (A) and I_t (B) data acquired over a single nanocrystal with an applied bias of V_{gap} = +2 V. Note the absolute z positioning is identical to that used in Figure 2. Inset: Tunnel current map for an individual nanocrystal acquired immediately after the constant height DFM images shown in Figure 2. (C) I–V data acquired using a different tip apex at various feedback stabilisation currents (stabilisation bias +2 V throughout).

constant height mode over the same region provides additional supporting evidence (inset to Figure 3B), showing a comparable tunnel current image to the previous STM imaging at a tip height −0.5 nm closer to the sample than the constant height DFM imaging shown in Figure 2C.

We note that the $I(V)$ characteristics of the supracrystals (Figure 3C) are broadly in line with those measured by Yang et al. [11] in that they are symmetric about 0 V. A key difference is that we do not observe a Coulomb gap (nor Coulomb staircase) due to the higher temperature of the sample in our experiment (77 K, as compared to Yang et al.'s measurements at 5 K.) In addition, we plot the average tunnel current values acquired over the oscillation cycle of the tip in Figure 3C, rather than the value of the current for a static tip. Nonetheless, there is a clear, almost linear dependence of the tip–sample resistance at the maximum voltage applied (4 V) on the setpoint "stabilisation" current (I_s) used to acquire each of the spectra observed in Figure 3C. The stabilisation current is the setpoint value at which the feedback loop operates before the loop is disabled to allow the $I(V)$ measurement to take place. I_s therefore provides a measure of the tip–sample separation in traditional STM where a tunnel gap exists. In our case, the stabilisation current is most likely related to the degree to which the tip is indented into the nanocrystal sample.

Conclusion

In conclusion, we have presented the first combined STM/DFM study of nanocrystal supracrystals. We readily obtain single nanocrystal resolution in STM, but are only able to resolve subparticle features by operating in constant height DFM mode. The examination of quantitative short range force spectra reveals that STM imaging occurs not by vacuum tunnelling, but by contact imaging in the repulsive force regime.

Supporting Information

Supporting Information File 1

Size distribution of Au nanocrystals used in our study and scanning electron microscope images of an interfacial supracrystal.
[http://www.beilstein-journals.org/bjnano/content/supplementary/2190-4286-6-126-S1.pdf]

Acknowledgements

P.M. and A.S. thank the Engineering and Physical Sciences Research Council (EPSRC) and the Leverhulme Trust, respectively, for Grants No. EP/G007837/1 and F00/114 BI. I.L. acknowledges funding from the European Commission's Marie Curie Actions programme through the ACRITAS Initial Training Network (grant PITN-GA-2012-317348). N.G. and M.P.P. thank the European Research Council for funding via Advanced Grant No. 267129.

References

1. Hanrath, T. *J. Vac. Sci. Technol., A* **2012,** *30,* 030802. doi:10.1116/1.4705402
2. Talapin, D. V.; Lee, J.-S.; Kovalenko, M. V.; Shevchenko, E. V. *Chem. Rev.* **2010,** *110,* 389–458. doi:10.1021/cr900137k
3. Pileni, M. P. *J. Phys. Chem. B* **2001,** *105,* 3358–3371. doi:10.1021/jp0039520
4. Pileni, M. P. *Acc. Chem. Res.* **2012,** *45,* 1965–1972. doi:10.1021/ar3000597
5. Goubet, N.; Portales, H.; Yan, C.; Arfaoui, I.; Albouy, P.-A.; Mermet, A.; Pileni, M.-P. *J. Am. Chem. Soc.* **2012,** *134,* 3714–3719. doi:10.1021/ja207941p
6. Middleton, A. A.; Wingreen, N. S. *Phys. Rev. Lett.* **1993,** *71,* 3198–3201. doi:10.1103/PhysRevLett.71.3198
7. Parthasarathy, R.; Lin, X.-M.; Jaeger, H. M. *Phys. Rev. Lett.* **2001,** *87,* 186807. doi:10.1103/PhysRevLett.87.186807
8. Parthasarathy, R.; Lin, X.-M.; Elteto, K.; Rosenbaum, T. F.; Jaeger, H. M. *Phys. Rev. Lett.* **2004,** *92,* 076801. doi:10.1103/PhysRevLett.92.076801
9. Reichhardt, C.; Olson Reichhardt, C. J. *Phys. Rev. Lett.* **2003,** *90,* 046802. doi:10.1103/PhysRevLett.90.046802
10. Ancona, M. G.; Kooi, S. E.; Kruppa, W.; Snow, A. W.; Foos, E. E.; Whitman, L. J.; Park, D.; Shirey, L. *Nano Lett.* **2003,** *3,* 135–138. doi:10.1021/nl0258224
11. Yang, P.; Arfaoui, I.; Cren, T.; Goubet, N.; Pileni, M.-P. *Phys. Rev. B* **2012,** *86,* 075409. doi:10.1103/PhysRevB.86.075409
12. Blunt, M. O.; Šuvakov, M.; Pulizzi, F.; Martin, C. P.; Pauliac-Vaujour, E.; Stannard, A.; Rushforth, A. W.; Tadić, B.; Moriarty, P. *Nano Lett.* **2007,** *7,* 855–860. doi:10.1021/nl061656e
13. Yang, P.; Arfaoui, I.; Cren, T.; Goubet, N.; Pileni, M.-P. *Nano Lett.* **2012,** *12,* 2051–2055. doi:10.1021/nl3001925
14. Durston, P. J.; Schmidt, J.; Palmer, R. E.; Wilcoxon, J. P. *Appl. Phys. Lett.* **1997,** *71,* 2940–2942. doi:10.1063/1.120222
15. Andres, R. P.; Bielefeld, J. D.; Henderson, J. I.; Janes, D. B.; Kolagunta, V. R.; Kubiak, C. P.; Mahoney, W. J.; Osifchin, R. G. *Science* **1996,** *273,* 1690–1693. doi:10.1126/science.273.5282.1690
16. Giessibl, F. J. *Appl. Phys. Lett.* **1998,** *73,* 3956–3958. doi:10.1063/1.122948
17. Giessibl, F. J. *Rev. Mod. Phys.* **2003,** *75,* 949–983. doi:10.1103/RevModPhys.75.949
18. Sader, J. E.; Jarvis, S. P. *Appl. Phys. Lett.* **2004,** *84,* 1801–1803. doi:10.1063/1.1667267
19. Majzik, Z.; Setvin, M.; Bettac, A.; Feltz, A.; Cháb, V.; Jelinek, P. *Beilstein J. Nanotechnol.* **2012,** *3,* 249–259. doi:10.3762/bjnano.3.28
20. Sweetman, A.; Danza, R.; Gangopadhyay, S.; Moriarty, P. *J. Phys.: Condens. Matter* **2012,** *24,* 084009. doi:10.1088/0953-8984/24/8/084009
21. Weymouth, A. J.; Wutscher, T.; Welker, J.; Hofmann, T.; Giessibl, F. J. *Phys. Rev. Lett.* **2011,** *106,* 226801. doi:10.1103/PhysRevLett.106.226801
22. Smith, D. P. E.; Binnig, G.; Quate, C. F. *Appl. Phys. Lett.* **1986,** *49,* 1166–1168. doi:10.1063/1.97403
23. Ternes, M.; González, C.; Lutz, C. P.; Hapala, P.; Giessibl, F. J.; Jelínek, P.; Heinrich, A. J. *Phys. Rev. Lett.* **2011,** *106,* 016802. doi:10.1103/PhysRevLett.106.016802

24. Jelínek, P.; Ondráček, M.; Flores, F. *J. Phys.: Condens. Matter* **2012,** *24,* 084001. doi:10.1088/0953-8984/24/8/084001
25. Hofer, W. A.; Fisher, A. J. *Phys. Rev. Lett.* **2003,** *91,* 036803. doi:10.1103/PhysRevLett.91.036803
26. Herz, M.; Schiller, C.; Giessibl, F. J.; Mannhart, J. *Appl. Phys. Lett.* **2005,** *86,* 153101. doi:10.1063/1.1900316
27. Sugimoto, Y.; Nakajima, Y.; Sawada, D.; Morita, K.-i.; Abe, M.; Morita, S. *Phys. Rev. B* **2010,** *81,* 245322. doi:10.1103/PhysRevB.81.245322
28. Tartaglini, E.; Verhagen, T. G. A.; Galli, F.; Trouwborst, M. L.; Müller, R.; Shiota, T.; Aarts, J.; van Ruitenbeek, J. M. *Low Temp. Phys.* **2013,** *39,* 189–198. doi:10.1063/1.4795171
29. Zhang, Y.-h.; Wahl, P.; Kern, K. *Nano Lett.* **2011,** *11,* 3838–3843. doi:10.1021/nl201912u
30. Gross, L.; Mohn, F.; Moll, N.; Liljeroth, P.; Meyer, G. *Science* **2009,** *325,* 1110–1114. doi:10.1126/science.1176210
31. Gross, L.; Mohn, F.; Moll, N.; Schuler, B.; Criado, A.; Guitián, E.; Peña, D.; Gourdon, A.; Meyer, G. *Science* **2012,** *337,* 1326–1329. doi:10.1126/science.1225621
32. Zhang, J.; Chen, P.; Yuan, B.; Ji, W.; Cheng, Z.; Qiu, X. *Science* **2013,** *342,* 611–614. doi:10.1126/science.1242603
33. Sweetman, A. M.; Jarvis, S. P.; Sang, H.; Lekkas, I.; Rahe, P.; Wang, Y.; Wang, J.; Champness, N. R.; Kantorovih, L.; Moriarty, P. *Nat. Commun.* **2014,** *5,* No. 3931. doi:10.1038/ncomms4931
34. Hapala, P.; Kichin, G.; Tautz, F. S.; Temirov, R.; Jelinek, P. *Phys. Rev. B* **2014,** *90,* 085421. doi:10.1103/PhysRevB.90.085421
35. Stirling, J.; Lekkas, I.; Sweetman, A.; Djuranovic, P.; Guo, Q.; Pauw, B.; Granwehr, J.; Lévy, R.; Moriarty, P. *PLoS One* **2014,** *9,* No. e108482. doi:10.1371/journal.pone.0108482
36. Zheng, N.; Fan, J.; Stucky, G. D. *J. Am. Chem. Soc.* **2006,** *128,* 6550. doi:10.1021/ja0604717
37. Rahe, P.; Schütte, J.; Schniederberend, W.; Reichling, M.; Abe, M.; Sugimoto, Y.; Kühnle, A. *Rev. Sci. Instrum.* **2011,** *82,* 063704. doi:10.1063/1.3600453
38. Lantz, M. A.; Hug, H. J.; Hoffmann, R.; van Schendel, P. J. A.; Kappenberger, P.; Martin, S.; Baratoff, A.; Güntherodt, H. J. *Science* **2001,** *291,* 2580–2583. doi:10.1126/science.1057824
39. Sweetman, A.; Stannard, A. *Beilstein J. Nanotechnol.* **2014,** *5,* 386–393. doi:10.3762/bjnano.5.45
40. Goubet, N.; Yan, C.; Polli, D.; Portalès, H.; Arfaoui, I.; Cerullo, G.; Pileni, M.-P. *Nano Lett.* **2013,** *13,* 504–508. doi:10.1021/nl303898y
41. Chiutu, C.; Sweetman, A. M.; Lakin, A. J.; Stannard, A.; Jarvis, S.; Kantorovich, L.; Dunn, J. L.; Moriarty, P. *Phys. Rev. Lett.* **2012,** *108,* 268302. doi:10.1103/PhysRevLett.108.268302
42. Sun, Z.; Boneschanscher, M. P.; Swart, I.; Vanmaekelbergh, D.; Liljeroth, P. *Phys. Rev. Lett.* **2011,** *106,* 046104. doi:10.1103/PhysRevLett.106.046104
43. Mohn, F.; Schuler, B.; Gross, L.; Meyer, G. *Appl. Phys. Lett.* **2013,** *102,* 073109. doi:10.1063/1.4793200

License and Terms

BEILSTEIN JOURNAL OF NANOTECHNOLOGY

Atomic force microscopy as analytical tool to study physico-mechanical properties of intestinal cells

Christa Schimpel[1], Oliver Werzer[1], Eleonore Fröhlich[2], Gerd Leitinger[3],
Markus Absenger-Novak[2], Birgit Teubl[1], Andreas Zimmer[1] and Eva Roblegg[*1,4,§]

Full Research Paper

Open Access

Address:
[1]Institute of Pharmaceutical Sciences, Department of Pharmaceutical Technology, NAWI Graz, Karl-Franzens-University of Graz, BioTechMed-Graz, Austria, [2]Medical University of Graz, Center for Medical Research, BioTechMed-Graz, Austria, [3]Research Unit Electron Microscopic Techniques, Institute of Cell Biology, Histology and Embryology, Center for Medical Research, Medical University of Graz, BioTechMed-Graz, Austria and [4]Research Center Pharmaceutical Engineering GmbH, Graz, Austria

Email:
Eva Roblegg[*] - eva.roblegg@uni-graz.at

[*] Corresponding author
§ phone: +43 316 380-8888, fax: +43 316 380-9100

Keywords:
atomic force microscopy; Caco-2 cells; elasticity; M cells; mechanical properties

Beilstein J. Nanotechnol. **2015,** *6,* 1457–1466.
doi:10.3762/bjnano.6.151

Received: 11 March 2015
Accepted: 15 June 2015
Published: 06 July 2015

This article is part of the Thematic Series "Advanced atomic force microscopy techniques III".

Guest Editor: T. Glatzel

Abstract

The small intestine is a complex system that carries out various functions. The main function of enterocytes is absorption of nutrients, whereas membranous cells (M cells) are responsible for delivering antigens/foreign substances to the mucosal lymphoid tissues. However, to get a fundamental understanding of how cellular structures contribute to physiological processes, precise knowledge about surface morphologies, cytoskeleton organizations and biomechanical properties is necessary. Atomic force microscopy (AFM) was used here as a powerful tool to study surface topographies of Caco-2 cells and M cells. Furthermore, cell elasticity (i.e., the mechanical response of a cell on a tip indentation), was elucidated by force curve measurements. Besides elasticity, adhesion was evaluated by recording the attraction and repulsion forces between the tip and the cell surface. Organization of F-actin networks were investigated via phalloidin labeling and visualization was performed with confocal laser scanning fluorescence microscopy (CLSM) and scanning electron microscopy (SEM). The results of these various experimental techniques revealed significant differences in the cytoskeleton/microvilli arrangements and F-actin organization. Caco-2 cells displayed densely packed F-actin bundles covering the entire cell surface, indicating the formation of a well-differentiated brush border. In contrast, in M cells actins were arranged as short and/or truncated thin villi, only available at the cell edge. The elasticity of M cells was 1.7-fold higher compared to Caco-2 cells and increased significantly from the cell periphery to the nuclear region. Since elasticity can be directly linked to cell adhesion, M cells showed higher adhesion forces than Caco-2 cells. The combination of distinct experimental techniques shows that morphological differences between Caco-2 cells and M cells correlate with mechanical cell properties and provide useful information to understand physiological processes/mechanisms in the small intestine.

Introduction

The human small intestine consists of a cell monolayer, which is predominantly composed of enterocytes mixed with mucus-secreting goblet cells [1]. Apart from enterocytes, membranous epithelial cells (M cells) reside throughout the small intestine as follicular-associated epithelium (FAE) that overlays lymphoid follicles (e.g., Peyer's patches) [2]. One of the most prominent features of epithelial enterocytes are the microvilli that cover the cell surface and form the so-called intestinal brush border [3]. The brush border membrane provides a greatly expanded absorptive surface, which facilitates rapid absorption of digestive products [4], but also constitutes an effective barrier against microorganisms, pathogens and foreign substances [5]. Moreover, assembly of the F-actin network in the brush border occurs due to expression and recruitment of actin-binding proteins [6]. The main proteins involved are fimbrin and villin, whereby the latter one is the key component and determines organization and plasticity of the F-actin network [7,8]. In contrast, M cells show no brush border with only sparse irregular microvilli [9,10]. Interestingly, in M cells villin accumulates in the cytoplasm and thus does neither induce extensive microvillus growth nor brush border formation [11]. The mechanism behind this is still unknown. It is suggested that villin either controls gelation of F-actin or that other proteins are involved [3,12], which block brush boarder assembly [13]. Thus, it is likely that variations in cell morphology between enterocytes and M cells may lead to differences in their physico-mechanical properties (elasticity, adhesion), which, as a consequence might impact certain cellular processes.

Apart from magnetic twisting cytometry (MTC) [14,15], micropipette aspiration [16] and magnetic/optical tweezers or optical traps [17-19], atomic force microcopy (AFM) is a versatile and potent tool for studying biological structures [20-22]. AFM enables both topographical and force curve measurements (atomic force spectroscopy) [23]. The former allow getting an image of the cell surface to observe its morphological and structural features. The latter is used to study elastic properties of a cell. Briefly, the central part of an AFM is a sharp tip, situated at the end of a flexible cantilever. The reflection of a laser beam focused at the back side of the cantilever is used to measure the movement of the tip. When the probe at the end of the cantilever interacts with the sample surface, the laser light pathway changes and is finally detected by a photodiode detector. The measured cantilever deflections vary (depending on the sample nature, i.e., high features on the sample cause the cantilever to deflect more) hence, a map of surface topography can be generated [21,22,24]. Moreover, quantitative analysis of the cell elasticity is possible by analyzing force-distance curves via monitoring the response of a cantilever once the tip is pushed against the plasma membranes. As a consequence, indentation occurs. The amount of force acting on the cantilever as a function of indentation enables an estimation of the nanomechanical properties of living cells, such as elasticity and adhesion [21,25-27].

To get a basic understanding regarding surface morphologies, mechanical properties and cytoskeleton organizations, enterocytes (Caco-2 cells) and M cells were studied in an in vitro co-culture model [28]. For this, enterocytes were cultured with Raji B cells to trigger M cell formation. AFM was used as a tool to study surface topography, elasticity and adhesion. Moreover, differences in F-actin networks were investigated via phalloidin labeling using confocal laser scanning fluorescence microscopy (CLSM) and scanning electron microscopy (SEM).

Results and Discussion

Morphological surface structures and cytoskeleton organization of Caco-2 cells and M cells

Cells display various surface architectures, which enable them to carry out different functions. For example, the FAE mainly consists of two cell types: absorptive enterocytes with a brush border and M cells without this highly organized apical specialization. The main function of enterocytes is the absorption of nutrients. M cells on the other hand provide an portal through which antigens/microorganisms can be delivered to the underlying mucosal lymphoid tissues [29]. This is due to the fact that M cells show a higher endocytic and transcytotic capacity than enterocytes. Hence, the fundamental question arises whether this is also reflected by the physico-mechanical properties of their respective cell surfaces.

SEM was used in order to firstly verify differentiation of Caco-2 cells to M cells in the presence of Raji B cells and secondly to evaluate differences in shape/surface morphology between both cell types. The SEM images show that the absorptive surface of Caco-2 cells is covered with densely packed microvilli, indicating the formation of a well-differentiated brush border structure (Figure 1A,B). In contrast, the apical surface of M cells is nearly devoid of microvilli. The few remaining villi that render the apical surface membrane appear to be sparse, short and/or truncated (Figure 1C,D). These findings are in excellent agreement with Owen et al., Bockman et al. and Gebert et al. [30-32]. They demonstrated that microvilli are less regular in M cells than in Caco-2 cells, differing in lengths as well as diameters. This suggests that the absence of a well-developed brush border in M cells may facilitate the adherence of antigens on the cell surface and, as a consequence, cellular uptake processes [2]. By contrast, the large surface area of

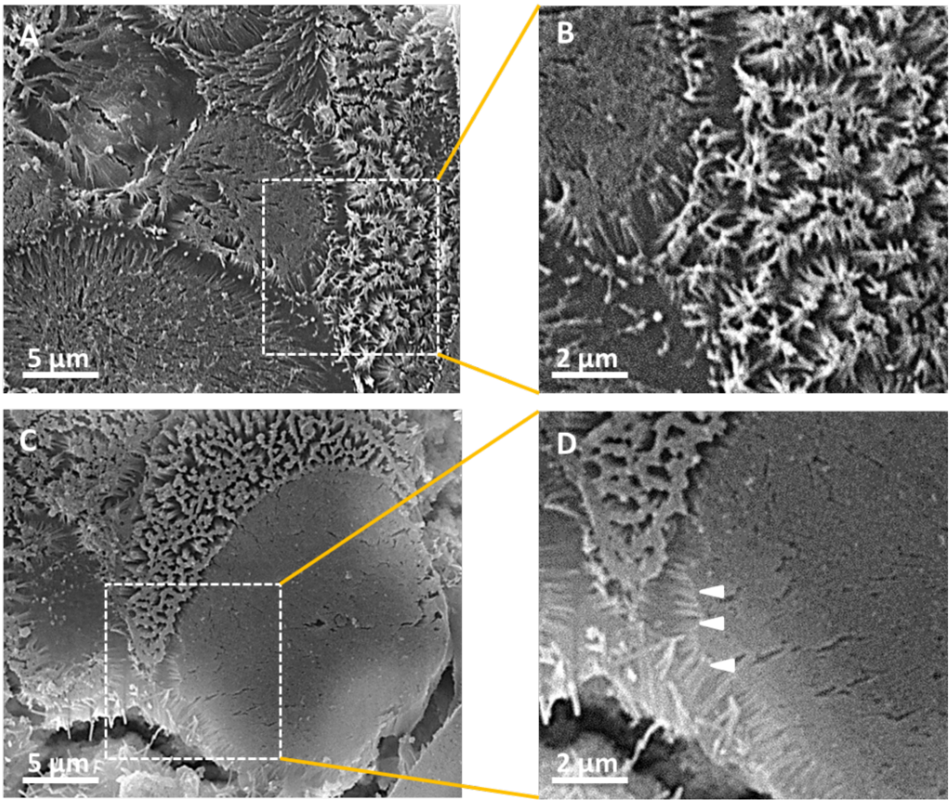

Figure 1: SEM analyses of the Caco-2 monolayer (A, B) and the Caco-2/M cell co-culture (C, D). The most prominent features on the Caco-2 cell surfaces are the microvilli that cover the surface forming the typical intestinal brush border (A, B). In contrast, M cells lack in microvilli (C). Arrowheads indicate sparse truncated microvillar structures on the edge of the cell membrane of a M cell (D).

intestinal microvilli is more appropriate for terminal digestion and absorption of soluble nutrients, electrolytes and water [33].

Although SEM typically provides nanometer resolution images of cell surfaces, a major drawback of this technique is that imaging usually requires fixation, drying and sputter coating of the samples. However, there are advanced SEM technologies available, such as environmental scanning electron microscopy (ESEM), which does not require complex sample preparation [34]. This allows preserving and analyzing of biological samples/structures at a hydrated state most closely approximating the native state. Although ESEM presents some additional beneficial features, considerable disadvantages including a high signal-to-noise ratio and/or limited resolution may arise [35].

In contrast, AFM allows high resolution (topographical) imaging of cells under (semi)hydrated, unfixed physiological conditions. Hence, complicated specimen preparation as well as destruction of native molecular conformations/structures can be avoided [36]. With this in mind, AFM was used in contact mode to explore the surface morphology of Caco-2 and M cells in more detailed. Unfortunately, it was not possible to localize M cells in the co-culture, since the large hydrated cells were highly flexible and only rough cell contours could be detected. Thus, cells were cultivated on transwell® inserts and scanned in contact mode in a semi-dry state at ambient temperatures [37,38]. The results revealed that Caco-2 cells show the typical microvilli-rich intestinal brush border upon reaching confluence. Highly densely packed microvilli projecting perpendicular to the surface (marked by arrowheads in Figure 2A) were detected. In contrast, M cells depict a flat surface and comprise only short truncated microvilli that form an arch around the edge of the M cell (see Figure 2B). Moreover, the microvilli observed in M cells appear to be rudimentary and limp.

Each microvillus consists of a bundle of 20 F-actin microfilaments containing several actin-binding proteins, such as fimbrin and villin. Villin serves as F-actin cross-linker, and is thus responsible for polymerization of monomeric actin to microfilaments and/or the linkage of single microfilaments into hexagonally packed bundles [6,39]. According to the literature, villin is localized at the apex of cells that display a well-developed brush border [40]. In M cells, however, villin was found to be

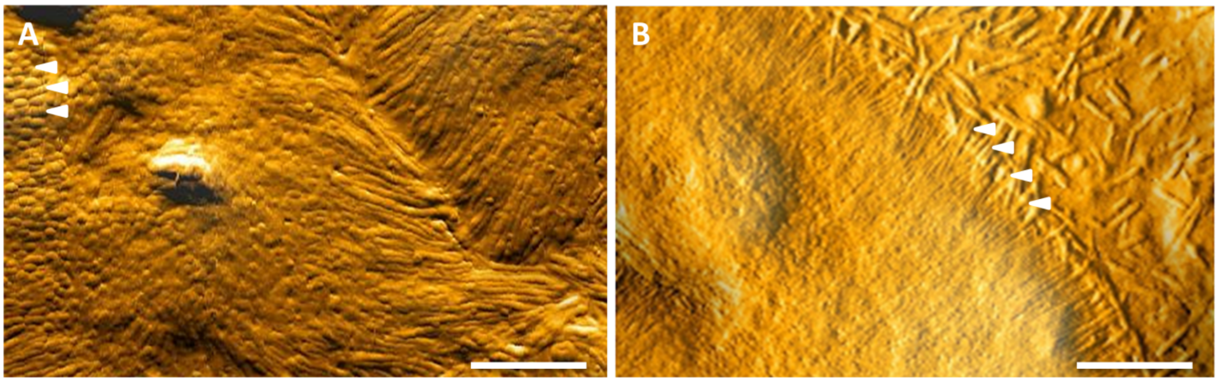

Figure 2: Topographic AFM images of a Caco-2 cell (A) and a M cell (B). The well-differentiated brush border of epithelial Caco-2 cells (A) depicts a densely packed array of upright orientated microvilli (marked by arrowheads) covering the entire surface. In contrast, the M cell surface (B) is supported by sparse truncated microvilli (marked by arrowheads) which appear shorter than those found in Caco-2 cells (scale bar = 5 µm).

diffusely distributed in the cytoplasm and no microvillus growth and brush border assembly was induced [8,11,41-43]. This is in accordance with the absence of defined microvilli at the outer M-cell surfaces as verified by the SEM and AFM images.

To further verify that the different number of microvilli reflects an altered organization of the F-actin network between M cells and Caco-2 cells labeling of cytoskeletal F-actin-fibers with rhodamine-phalloidin was performed. In Caco-2 cells, an intense F-actin labeling at the apex of the cells was obtained, indicating a fully developed brush border (Figure 3A). In contrast, F-actin staining at the apex of M cells was markedly decreased due to a reduced or absent brush border (Figure 3B–D).

Elasticity (force-indentation) measurements of Caco-2 cells and M cells

Villin is not only involved in the formation and/or regulation of the actin cytoskeleton, it also controls gelation of F-actin by inducing bundling of actin-filaments and thereby assures the stability of microvilli [42]. Hence, it is likely that differences in the mechanical properties of Caco-2 and M cells, such as elasticity and adhesion, might occur. To study this in detail, atomic force spectroscopy was used. For local force curve (indentation) measurements, the tip of the cantilever was placed over the location of interest (i.e., peripheral region/cell edge, nuclear area, cell body/cytoplasm) and the mechanical response was recorded as the cantilever was moved toward the cell surface. Such force–indentation curves of Caco-2 cells and M cells revealed variations of elastic values dependent on the cell location that was investigated. Generally, cells were more compliant at the nuclear area and became stiffer towards the periphery. Due to the higher compliance in the proximity of the cell nucleus, the loading force applied by the cantilever resulted in an increased elastic indentation of the cell by the tip due to an enlarged contact area. In contrast, indentation values obtained at positions at the cell edge were reduced.

This is in accordance with previous studies [44,45]. It was shown in astrocytes (glial cells) that the elastic modulus near

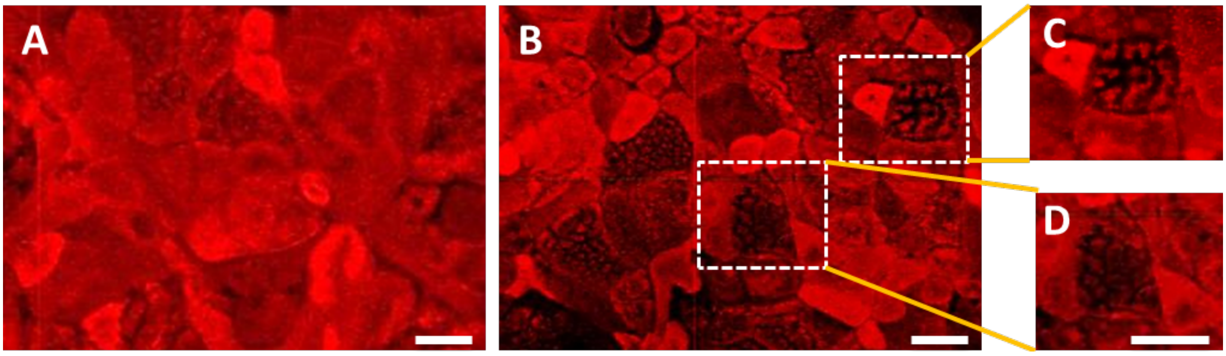

Figure 3: Optical images of the cytoskeleton organization in Caco-2 cells (A) and M cells (B–D). F-actin was stained with rhodamine-phalloidin. Caco-2 cells depict a well-differentiated brush border indicated by the intense red F-actin staining. In contrast, M cells show a reduced/absent brush border indicated by a reduced F-actin labeling (B–D) (scale bar = 20 µm).

the nuclear region was an order of magnitude higher than at the edge of the cell. However, Caco-2 cells showed a 1.7-fold reduced elasticity compared to M cells (Figure 4A–F). Specifically at regions near the nucleus, M cells revealed a significantly higher elasticity than Caco-2 cells (see Figure 4). These increased elasticity values in M cells can be attributed to a decrease in filamentous actin. During the descent of a cell from a Caco-2 cell to a M cell, the cytoskeletal structure changes, more precisely F-actin-rich microvilli forming the intestinal brush border disappear, leading to an increased compliance compared to Caco-2 cells. This is also consistent with previous results, where actin was found to be reduced by 30% in cancerous keratinocytes compared to normal keratinocytes, which consequently leads to a decreased compliance of cancer cells [46].

Moreover, macrophages, which are also immune cells, display a similar arrangement of F-actin-rich structures, also referred as podosomes [47]. In activated state, podosomes rearrange and form a belt-shaped structure (i.e., rosette) on the outer surface of the cellular membrane. The rosette triggers migration and phagocytic processes and shows a 5-fold decreased elasticity compared to podosome-free regions (nuclear area). This is in accordance with our study. Since M cells are also immune cells, it seems that the arrangement of the sparse truncated microvilli and the increased elasticity at nuclear M cell regions (3-fold compared to peripheral region) are likely to be responsible for their high endocytic and transcytotic capacity. Reduced elasticity values at the cell periphery of Caco-2 cells can be explained by cell-cell junctions. Caco-2 cells form a dense monolayer with transepithelial electric resistance values (TEER) of 422 ± 8.77 $\Omega\cdot\text{cm}^2$. This is due to the fact that cells are connected via tight junctions (TJs), which are very strong junctions that lack in intercellular spaces (compared to gap junctions or desmosomes) due to fusion of the outerleaflets of the membranes of adjacent cells. They are responsible to main-

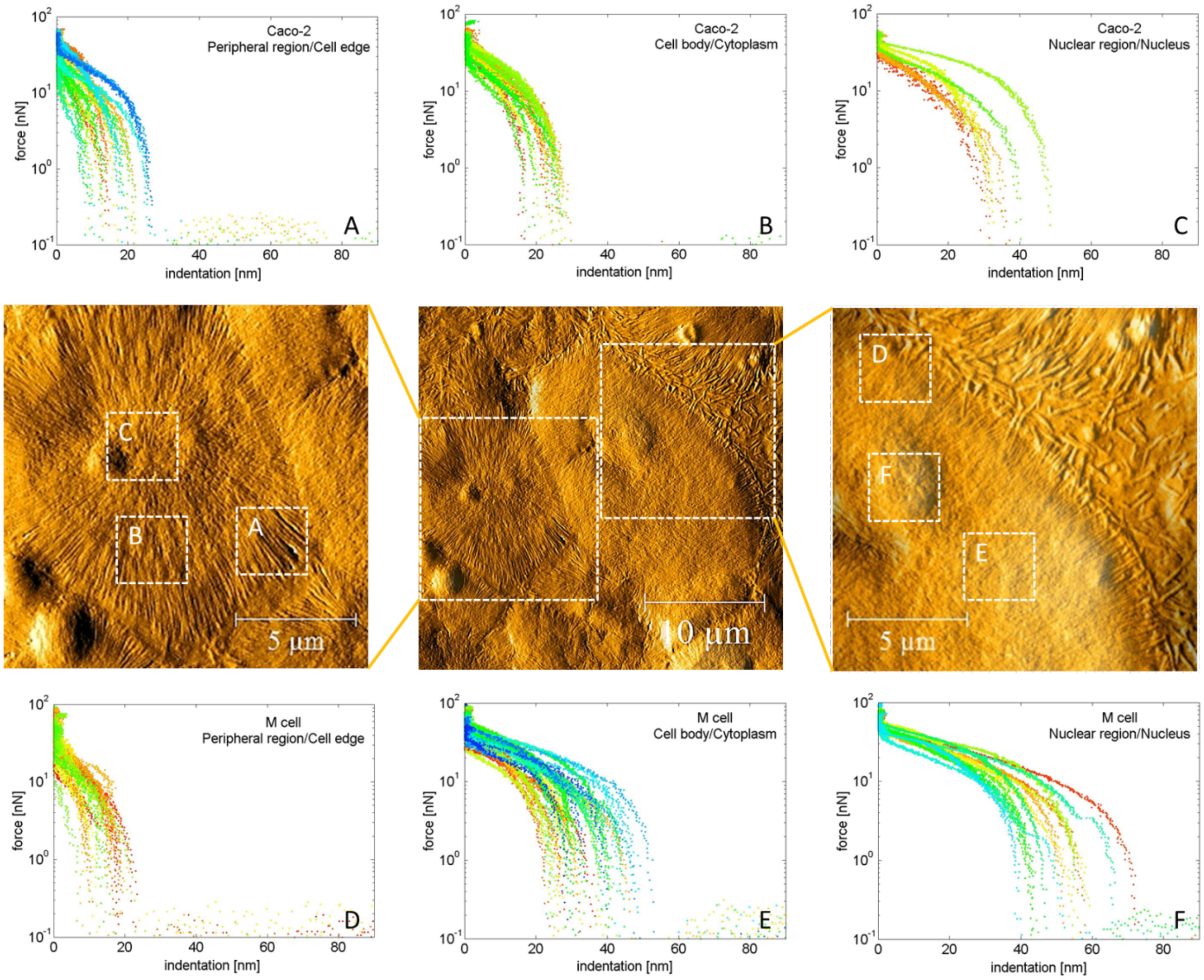

Figure 4: Force–indentation curves and topographical images of a Caco-2 cell (A–C) and a M cell (D–F) classified into peripheral region/cell edge, nuclear area and cell body/cytoplasm.

tain the integrity of the cell layer, which is likely to be associated with the cell mechanics such as high cell stiffness and reduced cell elasticity at the cell periphery. In contrast, once enterocytes are interdispersed with M cells TEER values (388 ± 2.74 $\Omega\cdot\text{cm}^2$) decrease. Studies reported by Clark and Hirst [48] and Gebert et al. [2] showed that TJs in non-FAE intestinal epithelia differ from FAE TJs. M cells show an increased depth and an altered arrangement of TJ strands. Thus, we speculate that this is reflected in the cell mechanics, such as a higher elasticity values compared to Caco-2 cells. Moreover, it is reported that the density of epithelial cell monolayers impacts cell mechanics (as well as the dynamics) due to variations of compressive forces [49,50].

To deeper understand the obtained elastic properties in the nuclear regions, representative sample force curves of Caco-2 cells and M cells were selected from the force map presented in Figure 4. One way to analyze force–indentation curves in more detail is to investigate the difference between the approaching and retracting part, which are parameters that reflect the plastic and/or elastic (deformation) behavior of the sample under load. For a mechanical response, which is ideally elastic, the indentation and retraction curve will be identical (overlap). Cells undergoing plastic deformations (i.e., the cell membrane is non-reversible distorted during increasing load) result in significantly changed retraction forces [21]. The results of our study showed that force-indentation/retraction curves nearly overlapped in both cell types, indicating a mechanical response, which is dominated by elastic contributions at large indentation. This confirms that the cell integrity remains on the contact with the sharp cantilever (Figure 5). At very low indentations, both cell types show plastic deformation but this effect is more significant in M cells (see Figure 5C,D). This can be explained by higher indentation values obtained for M cells (50 nm) compared to Caco-2 cells (30 nm). Basically, the Hertz model has been validated for indentation analysis of cell mechanical properties, providing a single parameter called the Young´s modulus of the cell. However, this model assumes that the tested sample is homogenous, linear elastic, isotropic and continuously thick [51,52]. Related to eukaryotic cells, none of these requirements apply. The microvillar structures are responsible for a rough and heterogonous cell surface. The cytoskeleton comprises accessory proteins (e.g., villin) that induce formation of F-actin filament bundles and control the length of F-actin filaments [53], resulting in non-linear elasticity. Thus, we alternatively displayed the indentation values in the nanometer range taking into account distinct cell locations of Caco-2 cells and M cells.

Evaluation of the attraction/repulsion (adhesion) forces

Elastic properties of cells can be directly linked to cell adhesion, since indentation also determines the number of adhesive bonds which are formed between cells and a surface. Hence, a smaller indentation and a consequent reduced contact area leads to a decrease in cellular adhesion [54]. Thus, we zoomed into the region, where the cantilever got in contact with the sample. Due to strong adhesion forces (van der Waals forces), the tip snapped in contact with the cell membrane. When retracting the tip, adhesion was maintained until the cantilever-force overcame the pull-off force (also referred as adhesion force) [51]. Lowest adhesion forces were found at the periphery of Caco-2 cells and slightly increased in the nuclear regions. However, in M cells adhesion was significantly higher, particularly in the nuclear region. This can be explained by the surface morphology and by the cell elasticity. M cells exhibit a smooth

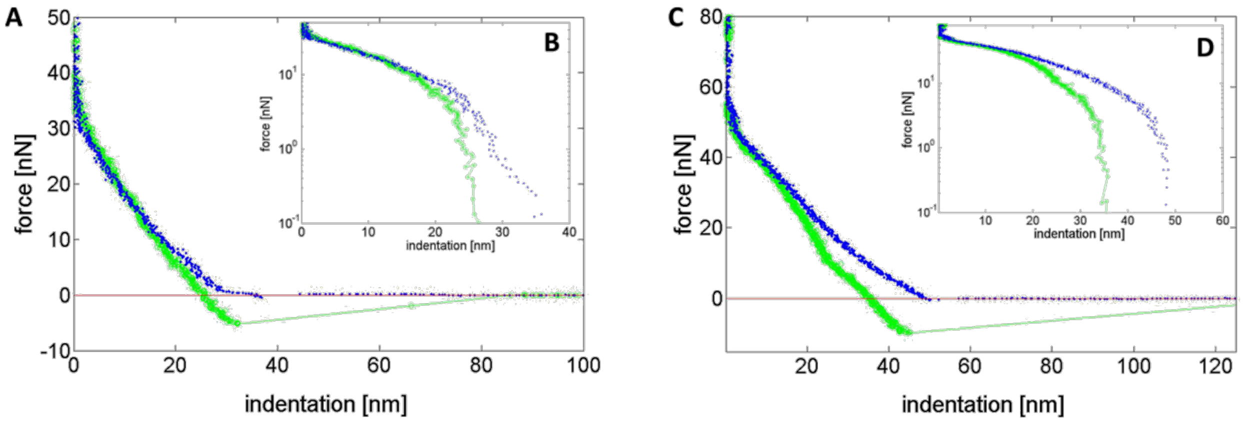

Figure 5: Representative force–indentation curves of a Caco-2 cell (A, B) and a M cell (C, D). The inset shows the force–deformation curve of the same indentation data on a logarithmic scale.

and more elastic surface due to the absence of microvilli, resulting in a significantly higher adhesion ability compared to rough Caco-2 cells [55]. Apart from surface nature, adhesive interactions of cells with other surfaces available in the (intestinal) environment are usually mediated by adhesion complexes/receptors. Such adhesion receptors include members of the cadherin, immunglobulin, selectin, proteoglycan and integrin superfamilies [56]. They trigger signaling pathways, which are involved in cellular processes (e.g., cell survival, tissue organization, binding interactions, specificity of cell–cell interactions) [56-58]. However, the cell adhesion molecule α5β1 integrin exhibits a different distribution pattern in M cells compared to enterocytes. Enterocytes display integrin only on basolateral and lateral surfaces, whereas M cells express α5β1 integrin on the apical membrane [41]. It is known that this cell adhesion molecule assists not only transformation from enterocytes to M cells but also preferential uptake by M cells [59]. This suggests that the presence of α5β1 integrin on the apical surfaces of M cells is likely to be responsible for the enhanced adhesion properties obtained via AFM.

However, it has to be added that AFM measurements performed under semi-dried conditions also show limitations, since physiological conditions are not fully reflected but are likely to change the interface between the gut lumen and the brush boarder membrane. Intestinal mucus, for instance, is continuously secreted by goblet cells and forms an efficient acellular barrier that strongly impacts adhesive interactions between intestinal epithelial cells and diverse substances/antigens. Due to intake of food, differences in the pH occur, which leads to changes in the viscoelastic properties of the mucus layer. Apart from food residuals, higher concentrations of digestive enzymes are available in the human small intestinal environment that influence transport processes through the mucus layer into the underlying tissue. Notably, bile salts, which are amphiphilic chemical derivates of cholesterol act as permeation enhancer via altering of the cell membrane integrity [60]. Moreover, bile salts form micells in aequeous solutions, enhancing transport of foreign substances [61].

This clearly shows that further research activities (e.g.; liquid-state AFM imaging using simulated intestinal fluid) are required to fill remaining data gaps on the effects of these parameters on cell mechanics/kinetics and, as a consequence, on cellular uptake processes (e.g., nanoparticulate systems/antigens).

Conclusion

The current study shows that cytoskeletal structures and the content of F-actin filaments strongly impact nanomechanical properties (i.e., elasticity, adhesion) of intestinal cells. In Caco-2 cells, F-actin filaments are organized as densely packed bundles forming a well-differentiated brush border. In M cells, F-actin filaments are arranged as short and limp structures in the cell periphery resulting in microvilli that form an arch around the edge of M cells. These morphological differences correlate with the cell elasticity: Caco-2 cells show a 1.7-fold reduced elasticity compared to M cells. Moreover, elasticity of M cells increased significantly from the cell edge to the nuclear region. Since elastic properties of cells can be directly linked to cell adhesion, adhesion to the smooth and more elastic surface of M cells is enhanced, thus, facilitating the adherence of antigens and, as a consequence, cellular uptake processes.

Experimental

Cell cultures

Raji B cells were a kind gift from R. Fuchs (Medical University of Graz, Austria) and were grown in RPMI 1640 medium supplemented with 10% fetal bovine serum (FBS) (Invitrogen GmbH, Darmstadt, Germany), 1% non-essential amino acids (NEAA) (Invitrogen GmbH, Darmstadt, Germany), 1% L-glutamine (Invitrogen GmbH, Darmstadt, Germany) and 1% penicillin and streptomycin (PenStrep) (Invitrogen GmbH, Darmstadt, Germany) at 37 °C in a humified 5% CO_2 atmosphere. Cells were cultured as previously described [62]. Caco-2 cells (ACC169, HTB-37 clone from the German Collection of Microorganisms and Cell Cultures) were cultivated at 37 °C under 10% CO_2 water saturated atmosphere in complete medium consisting of Dulbecco´s Modified Eagle Medium (DMEM) supplemented with 10% FBS, 1% NEAA, 1% L-glutamine and 1% PenStrep according to the protocol of des Rieux et al. [1].

For experimental studies the double culture (Caco-2/Raji B co-culture), comprising enterocytes and M cells, was co-cultivated following previously described protocols [1,28]. Briefly, 5×10^5 Caco-2 cells (passage 8–20) suspended in 0.5 mL supplemented DMEM were seeded onto polycarbonate 12-well Transwell® filters (Corning Incorporated, USA; 3 μm mean pore size, 1.12 cm^2 surface area). Caco-2 cells were maintained under standard incubation conditions for 14–16 days and medium both on the apical (0.5 mL) and basolateral side (1.7 mL) was changed every other day. Subsequently, 5×10^5 Raji B cells (passage 8–20), resuspended in supplemented DMEM were added to the basolateral compartment of inserts promoting the differentiation of M cells. Cell monolayer integrity and confluence were evaluated by measuring the transepithelial electrical resistance (TEER) with an Endohm culture cup connected to an epithelial volt ohm meter (World Precisions Instruments, Sarasota, USA). For AFM cell imaging/force spectroscopy inserts were washed thrice with PBS, cut and mounted on round (15 mm) glass coverslips. This coverslip containing semi-dried cells was mounted in a Quick Change

Imaging Chamber RC-40LP (Warner Instruments, USA) and measured directly afterwards.

Scanning electron microscopy

In addition, scanning electron microscopy (SEM) was used to evaluate morphological changes of cell surface architectures and examine protrusive surface structures including microvilli. For this, specimens were prepared similar as described previously [62]. After cultivation in transwell® systems cells were washed twice with PBS. Fixation was performed in Schaffer´s fixative (37% formol/100% ethanol) for 2 h [63]. Subsequently, fixed samples were dehydrated through a graded series of ethanol (80%, 90%, 100%), incubating for 20 min at room temperature in each ethanol grade. Subsequently, samples were dried with hexamethyldisilazane and the removed filter membranes were given a thin coating of gold palladium (Bal-Tec SCD 500) to improve the surface conductance of the sample and thus avoid surface charging of the sample under the beam. The samples were sputtered at 25 mA for 60 s under argon atmosphere and images were acquired using a scanning electron microscope (Zeiss DSM 950).

Topographic imaging using atomic force microscopy (AFM)

The topography of different cell types (i.e., Caco-2 cells and M cells) was investigated using a Nanosurf AFM with an Easyscan2 controller (Switzerland). All measurements were performed using a ContAl-G cantilever (Budgetsensors, Romania) with an aluminum coating. Topography measurements were performed in contact mode at a line scan rate of 0.5 s/line. Various scan sizes revealed information on different length scales. As we were unable to localize M cells in the co-culture, due to highly hydrated and flexible cells, measurements were performed in a semi-dry state as demonstrated elsewhere [37,38].

Tetramethylrhodamine (TRITC)-phalloidin staining

Visualization of the cytoskeletal F-actin network was performed using TRITC-phalloidin (Invitrogen GmbH, Darmstadt, Germany) in a similar manner as described earlier in literature [64]. In brief, cells were quickly rinsed in warm phosphate buffered saline (PBS; 0.01 M phosphate buffer, 0.15 M NaCl, pH 7.4) and fixed with 4% formaldehyde in PBS for 15 min at room temperature (RT). Next, cells were washed with PBS and permeabilized for 5 min at RT with 0.1% Triton X-100 in PBS. Subsequently, TRITC-phalloidin was added and cells were incubated for 20 min at RT in the dark. For CLSM imaging inserts were extensively washed and mounted on glass slides. Phalloidin-TRITC dyed cells were detected at 543 nm excitation wavelength using a LP 560 nm band pass detection for the red channel and images were examined with CLSM (Zeiss LSM 510 META) equipped with equipped with ZEN software (Zeiss Germany).

Atomic force spectroscopy and indentation force measurements

The mechanical properties of the cells were obtained via force curve measurements, (i.e., the deflection of the cantilever as function of the indentation was detected). Similar to the imaging, measurements were performed in a semi-dry state as demonstrated elsewhere [37,38]. The experimental data were recalculated allowing the force acting on the cantilever (respectively the cell) to be determined. For all calculations a cantilever spring constant of 0.1 N/m was assumed (specified by the manufactures). A matlab program based on Butt et al. [65] was used for data handling and plotting.

Acknowledgements

E.R. gratefully acknowledges support from NAWI Graz.

References

1. des Rieux, A.; Ragnarsson, E. G. E.; Gullberg, E.; Préat, V.; Schneider, Y.-J.; Artursson, P. *Eur. J. Pharm. Sci.* **2005,** *25,* 455–465. doi:10.1016/j.ejps.2005.04.015
2. Gebert, A.; Rothkötter, H.-J.; Pabst, R. *Int. Rev. Cytol.* **1996,** *167,* 91–159. doi:10.1016/S0074-7696(08)61346-7
3. Bretscher, A.; Weber, K. *J. Cell Biol.* **1978,** *79,* 839–845. doi:10.1083/jcb.79.3.839
4. Caspary, W. F. *Am. J. Clin. Nutr.* **1992,** *55,* 299S–308S.
5. Hollander, D. *Scand. J. Gastroenterol.* **1992,** *27,* 721–726. doi:10.3109/00365529209011172
6. Matsudaira, P. T.; Burgess, D. R. *J. Cell Biol.* **1979,** *83,* 667–673. doi:10.1083/jcb.83.3.667
7. Friederich, E.; Huet, C.; Arpin, M.; Louvard, D. *Cell* **1989,** *59,* 461–475. doi:10.1016/0092-8674(89)90030-5
8. Friederich, E.; Pringault, E.; Arpin, M.; Louvard, D. *BioEssays* **1990,** *12,* 403–408. doi:10.1002/bies.950120902
9. Neutra, M. R.; Kraehenbuhl, J.-P. *J. Cell Sci.* **1993,** , 209–215. doi:10.1242/jcs.1993.Supplement_17.29
10. Neutra, M. R.; Pringault, E.; Kraehenbuhl, J.-P. *Annu. Rev. Immunol.* **1996,** *14,* 275–300. doi:10.1146/annurev.immunol.14.1.275
11. Kerneis, S.; Bogdanova, A.; Colucci-Guyon, E.; Kraehenbuhl, J.-P.; Pringault, E. *Gastroenterology* **1996,** *110,* 515–521. doi:10.1053/gast.1996.v110.pm8566599
12. Glenney, J. R., Jr.; Kaulfus, P.; Weber, K. *Cell* **1981,** *24,* 471–480. doi:10.1016/0092-8674(81)90338-X
13. Costa de Beauregard, M.-A.; Pringault, E.; Robine, S.; Louvard, D. *EMBO J.* **1995,** *14,* 409–421.
14. Mijailovich, S. M.; Kojic, M.; Zivkovic, M.; Fabry, B.; Fredberg, J. J. *J. Appl. Physiol.* **2002,** *93,* 1429–1436. doi:10.1152/japplphysiol.00255.2002
15. Fabry, B.; Maksym, G. N.; Hubmayr, R. D.; Butler, J. P.; Fredberg, J. J. *J. Magn. Magn. Mater.* **1999,** *194,* 120–125. doi:10.1016/S0304-8853(98)00564-2
16. Hochmuth, R. M. *J. Biomech.* **2000,** *33,* 15–22. doi:10.1016/S0021-9290(99)00175-X

17. Neuman, K. C.; Nagy, A. *Nat. Methods* **2008,** *5,* 491–505. doi:10.1038/nmeth.1218
18. Gosse, C.; Croquette, V. *Biophys. J.* **2002,** *82,* 3314–3329. doi:10.1016/S0006-3495(02)75672-5
19. Simmons, R. M.; Finer, J. T.; Chu, S.; Spudich, J. A. *Biophys. J.* **1996,** *70,* 1813–1822. doi:10.1016/S0006-3495(96)79746-1
20. Binnig, G.; Quate, C. F.; Gerber, C. *Phys. Rev. Lett.* **1986,** *56,* 930–933. doi:10.1103/PhysRevLett.56.930
21. Butt, H.-J.; Cappella, B.; Kappl, M. *Surf. Sci. Rep.* **2005,** *59,* 1–152. doi:10.1016/j.surfrep.2005.08.003
22. Radmacher, M.; Tillmann, R.; Fritz, M.; Gaub, H. *Science* **1992,** *257,* 1900–1905. doi:10.1126/science.1411505
23. Lekka, M.; Laidler, P. *Nat. Nanotechnol.* **2009,** *4,* 72. doi:10.1038/nnano.2009.004
24. Leite, F.; Mattoso, L.; Oliveira Junior, O.; Herrmann Junior, P. d. P. In *Modern Research and Educational Topics in Microscopy;* Méndez-Vilas, A.; Díaz, J., Eds.; Formatex, 2007; Vol. 1, pp 747–757.
25. Alonso, J. L.; Goldmann, W. H. *Life Sci.* **2003,** *72,* 2553–2560. doi:10.1016/S0024-3205(03)00165-6
26. Kuznetsova, T. G.; Starodubtseva, M. N.; Yegorenkov, N. I.; Chizhik, S. A.; Zhdanov, R. I. *Micron* **2007,** *38,* 824–833. doi:10.1016/j.micron.2007.06.011
27. A-Hassan, E.; Heinz, W. F.; Antonik, M. D.; D'Costa, N. P.; Nageswaran, S.; Schoenenberger, C.-A.; Hoh, J. H. *Biophys. J.* **1998,** *74,* 1564–1578. doi:10.1016/S0006-3495(98)77868-3
28. Gullberg, E.; Leonard, M.; Karlsson, J.; Hopkins, A. M.; Brayden, D.; Baird, A. W.; Artursson, P. *Biochem. Biophys. Res. Commun.* **2000,** *279,* 808–813. doi:10.1006/bbrc.2000.4038
29. Mabbott, N. A.; Donaldson, D. S.; Ohno, H.; Williams, I. R.; Mahajan, A. *Mucosal Immunol.* **2013,** *6,* 666–677. doi:10.1038/mi.2013.30
30. Owen, R. L.; Jones, A. L. *Gastroenterology* **1974,** *66,* 189–203.
31. Bockman, D.; Boydston, W. *Scanning Electron Microsc.* **1982,** 1341–1350.
32. Gebert, A. *Histochem. Cell Biol.* **1997,** *108,* 455–470. doi:10.1007/s004180050186
33. DeSesso, J. M.; Jacobson, C. F. *Food Chem. Toxicol.* **2001,** *39,* 209–228. doi:10.1016/S0278-6915(00)00136-8
34. Thiberge, S.; Nechushtan, A.; Sprinzak, D.; Gileadi, O.; Behar, V.; Zik, O.; Chowers, Y.; Michaeli, S.; Schlessinger, J.; Moses, E. *Proc. Natl. Acad. Sci. U. S. A.* **2004,** *101,* 3346–3351. doi:10.1073/pnas.0400088101
35. Bogner, A.; Jouneau, P.-H.; Thollet, G.; Basset, D.; Gauthier, C. *Micron* **2007,** *38,* 390–401. doi:10.1016/j.micron.2006.06.008
36. Alessandrini, A.; Facci, P. *Meas. Sci. Technol.* **2005,** *16,* R65–R92. doi:10.1088/0957-0233/16/6/R01
37. Ivanova, E. P.; Webb, H.; Christen, R.; Zhukova, N. V.; Kurilenko, V. V.; Kalinovskaya, N. I.; Crawford, R. J. *Int. J. Syst. Evol. Microbiol.* **2010,** *60,* 1620–1625. doi:10.1099/ijs.0.014159-0
38. Ruby, E. G. *Annu. Rev. Microbiol.* **1996,** *50,* 591–624. doi:10.1146/annurev.micro.50.1.591
39. Mooseker, M. S. *Cell* **1983,** *35,* 11–13. doi:10.1016/0092-8674(83)90202-7
40. Nusrat, A.; Delp, C.; Madara, J. L. *J. Clin. Invest.* **1992,** *89,* 1501–1511. doi:10.1172/JCI115741
41. Tyrer, P.; Foxwell, A. R.; Kyd, J.; Harvey, M.; Sizer, P.; Cripps, A. *Biochem. Biophys. Res. Commun.* **2002,** *299,* 377–383. doi:10.1016/S0006-291X(02)02631-1
42. Bretscher, A.; Weber, K. *Cell* **1980,** *20,* 839–847. doi:10.1016/0092-8674(80)90330-X
43. Coluccio, L. M.; Bretscher, A. *J. Cell Biol.* **1989,** *108,* 495–502. doi:10.1083/jcb.108.2.495
44. Radmacher, M.; Fritz, M.; Kacher, C. M.; Cleveland, J. P.; Hansma, P. K. *Biophys. J.* **1996,** *70,* 556–567. doi:10.1016/S0006-3495(96)79602-9
45. Ricci, D.; Tedesco, M.; Grattarola, M. *Microsc. Res. Tech.* **1997,** *36,* 165–171. doi:10.1002/(SICI)1097-0029(19970201)36:3<165::AID-JEMT4>3.0.CO;2-O
46. Katsantonis, J.; Tosca, A.; Koukouritaki, S. B.; Theodoropoulos, P. A.; Gravanis, A.; Stournaras, C. *Cell Biochem. Funct.* **1994,** *12,* 267–274. doi:10.1002/cbf.290120407
47. Labernadie, A.; Thibault, C.; Vieu, C.; Maridonneau-Parini, I.; Charrière, G. M. *Proc. Natl. Acad. Sci. U. S. A.* **2010,** *107,* 21016–21021. doi:10.1073/pnas.1007835107
48. Clark, A. M.; Hirst, B. H. *Histochem. Cell Biol.* **2002,** *118,* 137–147.
49. Nnetu, K. D.; Knorr, M.; Pawlizak, S.; Fuhs, T.; Käs, J. A. *Soft Matter* **2013,** *9,* 9335–9341. doi:10.1039/c3sm50806d
50. Schulze, C.; Wetzel, F.; Kueper, T.; Malsen, A.; Muhr, G.; Jaspers, S.; Blatt, T.; Wittern, K.-P.; Wenck, H.; Käs, J. A. *Clin. Plast. Surg.* **2012,** *39,* 9–20. doi:10.1016/j.cps.2011.09.008
51. Radmacher, M. *Methods Cell Biol.* **2007,** *83,* 347–372. doi:10.1016/S0091-679X(07)83015-9
52. Titushkin, I.; Cho, M. *Biophys. J.* **2007,** *93,* 3693–3702. doi:10.1529/biophysj.107.107797
53. Lodish, H. F.; Berk, A.; Zipursky, S. L.; Matsudaira, P.; Baltimore, D.; Darnell, J. *Molecular cell biology;* WH Freeman: New York, 2000; Vol. 4.
54. Rico, F.; Roca-Cusachs, P.; Sunyer, R.; Farré, R.; Navajas, D. *J. Mol. Recognit.* **2007,** *20,* 459–466. doi:10.1002/jmr.829
55. Högfors-Rönnholm, E.; Norrgård, J.; Wiklund, T. *J. Fish Dis.* **2015,** *38,* 429–437. doi:10.1111/jfd.12250
56. Gumbiner, B. M. *Cell* **1996,** *84,* 345–357. doi:10.1016/S0092-8674(00)81279-9
57. Legate, K. R.; Wickström, S. A.; Fässler, R. *Genes Dev.* **2009,** *23,* 397–418. doi:10.1101/gad.1758709
58. Weber, G. F.; Bjerke, M. A.; DeSimone, D. W. *J. Cell Sci.* **2011,** *124,* 1183–1193. doi:10.1242/jcs.064618
59. Foxwell, A. R.; Cripps, A. W.; Kyd, J. M. *Hum. Vaccines* **2007,** *3,* 220–223. doi:10.4161/hv.3.5.4358
60. Aungst, B. J. *J. Pharm. Sci.* **2000,** *89,* 429–442. doi:10.1002/(SICI)1520-6017(200004)89:4<429::AID-JPS1>3.0.CO;2-J
61. Meaney, C.; O'Driscoll, C. M. *Int. J. Pharm.* **2000,** *207,* 21–30. doi:10.1016/S0378-5173(00)00526-3
62. Schimpel, C.; Teubl, B.; Absenger, M.; Meindl, C.; Fröhlich, E.; Leitinger, G.; Zimmer, A.; Roblegg, E. *Mol. Pharmaceutics* **2014,** *11,* 808–818. doi:10.1021/mp400507g
63. Schaffer, J. *Anat. Anz.* **1918,** *51,* 353–398.
64. Lázaro-Diéguez, F.; Egea, G. In *Modern research and educational topics in microscopy;* Méndez-Vilas, A.; Díaz, J., Eds.; Formatex, 2007; Vol. 1, pp 362–369.
65. Butt, R. *Introduction to Numerical Analysis Using MATLAB®;* Jones & Bartlett Learning, 2009.

License and Terms

BEILSTEIN JOURNAL OF NANOTECHNOLOGY

Lower nanometer-scale size limit for the deformation of a metallic glass by shear transformations revealed by quantitative AFM indentation

Arnaud Caron*[1,2,§] and Roland Bennewitz[1]

Full Research Paper

Address:
[1]Leibniz - Institute for New Materials, Campus D2.2, 66123 Saarbrücken, Germany and [2]current address: Korea University of Technology and Education, Department of Energy, Materials and Chemical Engineering, Chungcheongnam-do, 31253 Republic of Korea

Email:
Arnaud Caron* - arnaud.caron@koreatech.ac.kr

* Corresponding author
§ Phone: +82(0)41-560-1363

Keywords:
AFM indentation; dislocation; metallic glasses; metals; plasticity; shear transformation

Beilstein J. Nanotechnol. **2015,** *6,* 1721–1732.
doi:10.3762/bjnano.6.176

Received: 07 April 2015
Accepted: 20 July 2015
Published: 13 August 2015

This article is part of the Thematic Series "Advanced atomic force microscopy techniques III".

Guest Editor: T. Glatzel

Abstract

We combine non-contact atomic force microscopy (AFM) imaging and AFM indentation in ultra-high vacuum to quantitatively and reproducibly determine the hardness and deformation mechanisms of Pt(111) and a $Pt_{57.5}Cu_{14.7}Ni_{5.3}P_{22.5}$ metallic glass with unprecedented spatial resolution. Our results on plastic deformation mechanisms of crystalline Pt(111) are consistent with the discrete mechanisms established for larger scales: Plasticity is mediated by dislocation gliding and no rate dependence is observed. For the metallic glass we have discovered that plastic deformation at the nanometer scale is not discrete but continuous and localized around the indenter, and does not exhibit rate dependence. This contrasts with the observation of serrated, rate-dependent flow of metallic glasses at larger scales. Our results reveal a lower size limit for metallic glasses below which shear transformation mechanisms are not activated by indentation. In the case of metallic glass, we conclude that the energy stored in the stressed volume during nanometer-scale indentation is insufficient to account for the interfacial energy of a shear band in the glassy matrix.

Introduction

Hardness testing has been widely applied by materials scientists and mechanical engineers to assess the mechanical properties of materials and to predict their behavior during machining processes or under tribological loading for the last 150 years. Most generally hardness testing describes the resistance of a material surface to the penetration of a harder indenter and thus relates in the case of metals to the resistance to plastic flow. Different types of indenter geometries have been employed, such as spherical, conical, and pyramidal indenters. For each of these, different hardness numbers have been established, such as the Brinell hardness (*HB*), the Vickers hardness (*HV*) or the Knopp hardness (*HK*). They are calculated by dividing the applied load by the area of a remaining indent. While the experimental implementation of hardness testing is straightforward the obtained quantities are rather empirical and do not describe a fundamental property of the material. A first attempt to relate the hardness of metals to their intrinsic mechanical properties was made for a spherical indenter. The hardness was set equal to the mean contact pressure and the hardness was defined as the ratio of the maximal applied load to the projected area of the remaining indent. This quantity is also referred to as the Meyer's hardness (*H*) and relates to the yield stress of non-work-hardening metals according to $H \approx 3\ \sigma_y$ [1].

In industrial practice the projected area of the remaining indent is evaluated by optical microscopy and hardness measurements are limited to the macro-scale. With the development of depth-sensing indentation techniques such as instrumented nanoindentation, the recording of load–displacement curves has been recognized as a suitable alternative to determine the hardness of a material, even when the remaining indent is too small to be accurately imaged. The projected area is then determined from the penetration depth with the help of an indenter-area function [2]. Meanwhile the Berkovich indenter with a half-opening angle $\alpha = 65.27°$ is widely used for depth-sensing indentation measurements so as to match the projected area to depth characteristics of the four-sided pyramidal Vickers indenter. The preference for the Berkovich indenter arises from the accurate and reproducible processing of three sided pyramids and their ability to apply larger strains than spherical indenters. Analysis of the curvature of load–displacement curves and of the occurrence of sharp pop-ins have further been used to study mechanisms of plastic deformation such as the generation and multiplication of dislocations in crystalline metals [3] or the generation of shear bands in metallic glasses [4].

Dislocation nucleation and shear band generation are mechanisms that operate at the nanometer scale. In order to investigate the fundamental mechanisms contributing to the mechanical behavior of materials new advanced experimental techniques are required with a resolution at the level of the relevant structures. First studies of single plasticity events in nanometer scale contacts between a nanometer-sized single asperity and Au(111), (110), and (001) surfaces have been performed by means of interfacial force microscopy (IFM) [5,6]. Indentation by means of atomic force microscopes (AFM indentation) has been used to observe the nucleation and gliding of single dislocations in a KBr(100) single crystal [7] and in Cu(100) [8]. Pop-ins were observed in load–displacement curves, and the pop-in length observed in AFM-indentation was in the range of 1 Å and less. These observations demonstrate the potential of AFM indentation to detect atomistic plasticity events.

Here we present the results of AFM indentation in ultra-high vacuum to quantitatively determine hardness and the underlying fundamental mechanisms of plastic deformation of nanometer-scale contacts between an AFM-tip and a Pt(111) single crystal on the one hand, and a $Pt_{57.5}Cu_{14.7}Ni_{5.3}P_{22.5}$ metallic glass on the other hand. In order to investigate plasticity mechanisms at the nanometer-scale, AFM indentation experiments were performed with varying maximal loads and varying loading rates. We discuss our results with regard to dislocation activity in crystalline materials and to the recent discussion of plasticity mechanisms in metallic glasses, including the generation of shear bands and their incipient size and indentation size effects down to the structural length scale of metallic glasses [9-12].

Experimental

The sample preparation followed a similar method as already described in [13]. The (111) surface of a platinum single crystal was prepared by several cycles of Ar sputtering and annealing at 1000 °C. This resulted in the formation of 50 to 100 nm wide atomically flat terraces. A $Pt_{57.5}Cu_{14.7}Ni_{5.3}P_{22.5}$ metallic glass master alloy was prepared according to [14] and subsequently melt-spun on a Cu wheel to produce 20 μm thick amorphous metallic ribbons. The amorphous structure of the Pt-based metallic glass was confirmed by X-ray diffraction (XRD) with Cu Kα radiation and differential scanning calorimetry (DSC). We observed a broad diffraction peak at 39.866 degrees of 2θ, a clear glass transition at $T_g = 223$ °C, and crystallization at $T_x = 295$ °C using a heating rate $R_H = 0.67$ K/s. The surface of an as-spun Pt-based metallic glass ribbon was prepared by careful Ar-sputtering for a duration of 5 min with an energy of 1 keV to remove its native oxide layer. Both Pt(111) and $Pt_{57.5}Cu_{14.7}Ni_{5.3}P_{22.5}$ metallic glass surfaces were characterized with Auger electron spectroscopy (AES) that confirmed the absence of surface contaminants such as C, H, S, and O. For both samples non-contact (nc)-AFM imaging was used to determine the RMS-roughness R_q over a representative area of 250 × 250 nm^2. For atomically flat Pt(111) we found $R_q = 0.372$ nm, caused by atomic steps between terraces, and for $Pt_{57.5}Cu_{14.7}Ni_{5.3}P_{22.5}$ metallic glass we found $R_q = 0.375$ nm.

The nanometer-scale plastic deformation of Pt(111) and the $Pt_{57.5}Cu_{14.7}Ni_{5.3}P_{22.5}$ metallic glass was investigated in ultra-high vacuum by AFM indentation and subsequent nc-AFM imaging using a VT-AFM manufactured by Omicron Nanotechnology GmbH, Germany. In non-contact AFM an AFM cantilever is driven to oscillate close to a sample surface at its resonance frequency. The tip–sample distance is of the order of a few nanometers. Changes in tip–sample distance during scanning over a sample surface due to sample topography yield changes in the oscillation amplitude and in a frequency shift of the cantilever resonance. In order to measure topography both amplitude and frequency shift are tracked by a feedback loop so as to keep the cantilever oscillation in resonance [15]. For indentation and imaging we used a diamond-coated silicon single crystalline cantilever (Type: CDT-NCLR, manufactured by NanoSensors). The bending stiffness of the cantilever was calculated according to the beam geometry method [16] and was found to be $k_n = 46$ N/m. The sensitivity of the photo-diode was calibrated in the non-contact mode of AFM, following the method proposed in [17] and considering a conversion factor of $\sqrt{4/3}$ for the vibration energy of the cantilever determined from the optically measured deflection [18]. This allowed us for a precise measurement of the vertical deflection. AFM indentation measurements comprised the measurement of the cantilever deflection upon extension of the z-scanner of the AFM with different velocities. Given the tilt angle of the cantilever with regard to the sample surface a tilt correction was applied by moving the lateral scanner by $Z \times \tan \varphi$ during a vertical scanner extension Z, where φ is the tilt angle [19]. In this work the extension lengths Z of the z-scanner were varied from 10 to 160 nm and the extension rate $\dot{Z}$ were varied from 1 to 8 nm/s.

The plastic deformation of both sample surfaces was analyzed based on nc-AFM topographical images of the indents and on the force–distance curves recorded during AFM-indentation. Figure 1a shows a typical topographical image of a Pt(111) surface after indentation with a stiff diamond-coated AFM tip. The indent was analyzed with regard to its projected area and its pile-up volume by using the indentation analysis function of the software package Gwyddion [20]. The projected area and the pile-up volume were determined by masking the area with height values below and above a reference plane (see Figure 1b,c). The reference plane was selected by setting a relative height tolerance value, so as to not include topographical features of the undeformed surface into the calculations. The values obtained for the pile-up volume and the projected area of the indent underestimate the real values by the maximal peak value of the height signal in the undeformed region of the topographical image. Due to tip-shape convolution effects the size of indents imaged by nc-AFM are underestimated while the pile-up volume is overestimated; this effect is more pronounced for smaller indents and pile-ups.

The force–distance curves were used to calculate force–penetration (P–δ) curves (see Figures 1d,e). For an infinitely stiff and hard sample surface the cantilever deflection D upon extension of the z-scanner is equal to the extension length Z, i.e., the slope $\mathrm{d}D/\mathrm{d}Z = 1$. For a compliant sample surface, an extension of the

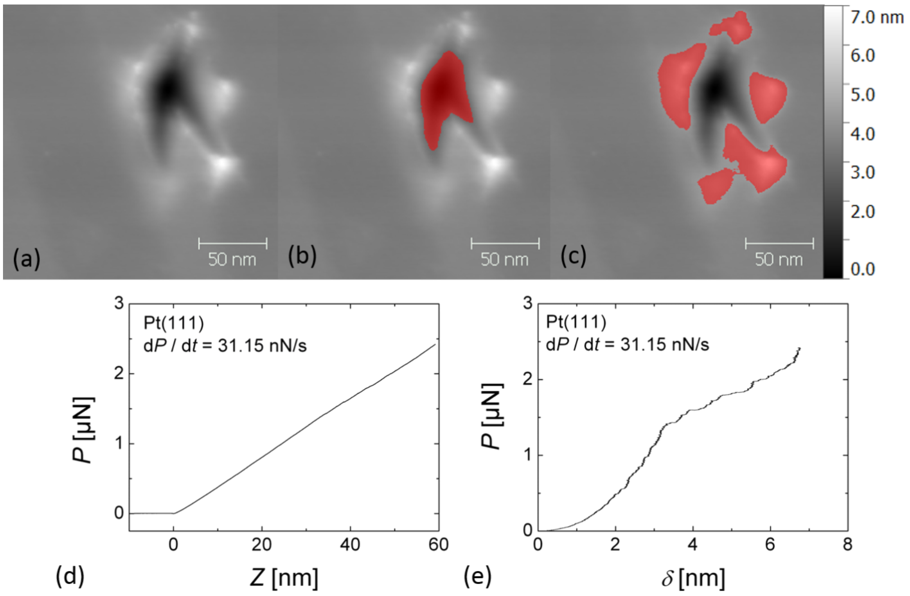

Figure 1: (a) Non-contact (nc)-AFM image of an AFM-indentation on Pt(111) (z-scale: 7 nm) and highlighted masks used to determine (b) the projected area and (c) the pile-up volume of the AFM indentation shown in (a); in (a–c) the z-scale is 7 nm; (d) force distance–curve recorded on Pt(111) at the indicated loading rate and (e) corresponding AFM indentation curve. As described in the text, (e) is extracted from (d) by subtracting the deflection of the cantilever.

z-scanner also leads to a penetration of the AFM tip into the sample surface by the penetration depth $\delta = Z - D$. While the cantilever deflection D is calibrated independently, the height value Z is subject to drift or creep effects of the piezoelectric scanner. The accuracy in δ is thus limited by piezoelectric creep of the AFM scanner. In order to minimize vertical drift, the tip position was equilibrated before each indentation by recording a slow 500 × 500 nm^2 scan of the area to be indented by AFM. Indentation measurements were then started from the position of the scanner during nc-AFM imaging, i.e., half of the oscillation amplitude or a few nanometers above the surface.

In order to further account for piezoelectric creep effects during rate-dependent measurements a drift difference ΔZ_{drift} with regard to the fastest measurement was calculated according to $\Delta Z_{\text{drift}} = \Delta\delta + \Delta D = v_{\text{drift}} \times t$, where Δδ and Δ*D* are the differences in penetration depth and deflection with regard to the fastest measurement, v_{drift} is the drift velocity and t is the time. Subsequently, the penetration depth was re-evaluated according to $\delta = Z + \Delta Z_{\text{drift}} - D$ under the assumption that $v_{\text{drift}} = \Delta Z_{\text{drift}}/t$ remained constant during the extension of the *z*-scanner. Figure 2 shows a series of rate-dependent *P*–δ curves on $Pt_{57.5}Cu_{14.7}Ni_{5.3}P_{22.5}$ metallic glass before and after correction of piezoelectric drift. The absolute values for the calculated drift velocity difference vary from 19.5 to 170 pm/s. After drift correction the indentation curves coincide as expected in the low load regime that corresponds to the elastic deformation.

A drawback of AFM indentation experiments is that no controlled manufacturing of the tip apex is available at the nanometer scale and one has to work with the shape of a given tip. Figure 3 shows a SEM image of the diamond-coated AFM tip after recorded after finishing all measurements presented in this report. One can recognize the granular structure of the diamond coating of the tip. From SEM images like this one it is usually not possible to identify which granule or crystallite at the tip apex was the actual indenter. However, the shape of the AFM tip relevant for indentation and imaging can be reconstructed using the tip analysis function of Gwyddion [20]. Figure 3b,c and Figure 3d,e show the shape of the AFM tip

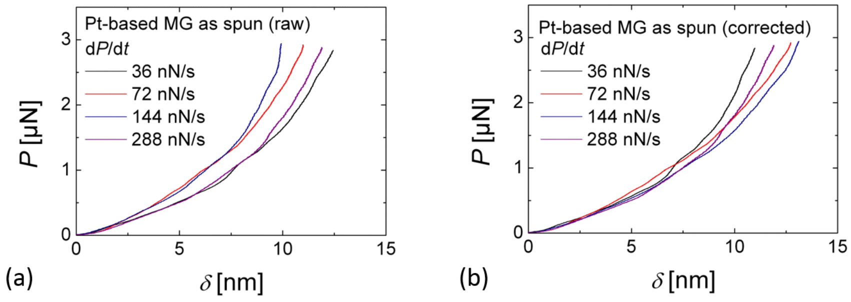

Figure 2: Series of rate-dependent AFM indentation curves (a) before and (b) after drift correction; the drift velocity difference with respect to the fastest measurements were $\Delta v = -19.5$, 46, and 170 pm/s for d*P*/d*t* = 36, 72, and 144 nN/s, respectively.

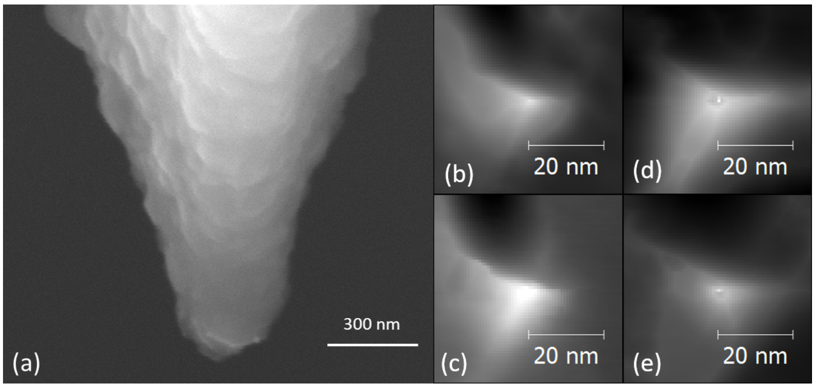

Figure 3: (a) SEM image of the diamond coated AFM tip used for all measurements presented in this report; tip geometry reconstructed from nc-AFM images on (b,c) Pt(111) (*z*-scale: 5 nm) and (d,e) $Pt_{57.5}Cu_{14.7}Ni_{5.3}P_{22.5}$ metallic glass (*z*-scale: 10 nm). The nc-AFM images used to reconstruct the tip shape in (b,d) and (c,e) were recorded several months apart.

reconstructed from nc-AFM images of indents on Pt(111) and $Pt_{57.5}Cu_{14.7}Ni_{5.3}P_{22.5}$ metallic glass, respectively. As confirmed in all reconstructions performed over several months, the tip is a stable three-sided pyramid that we assume is the corner of a single diamond nano-grain. The angle of each side with regard to the basis of the pyramid is approx. 16°, while its half opening angle is $\alpha \approx 74°$.

Results

Figure 4 shows series of nc-AFM images of indents on Pt(111) and $Pt_{57.5}Cu_{14.7}Ni_{5.3}P_{22.5}$ metallic glass for varying maximum loads and varying loading rates. The different series of this matrix have been conducted over a period of several months and on different surface preparations. Images of indents on the surface of a same sample performed at similar loads or loading rates are very similar. This similarity demonstrates the reproducibility and the stability of the tip under repeated indentation tests. For both materials remaining indents were observed only for a minimum load of $P_{\mathrm{max}} > 0.8$ µN. For both materials the projected area of the indents increases with the load with a similar trend. Indents performed on a given sample at different loading rates with the same maximal load do not show any tendency and have similar shapes. However, the height of pile-up around indents differs significantly between Pt(111) and $Pt_{57.5}Cu_{14.7}Ni_{5.3}P_{22.5}$ metallic glass. Pile-ups around indents on the metallic glass are much more prominent than on Pt(111). This indicates that the plastic deformation of Pt(111) was accommodated over much longer distances than in the case of $Pt_{57.5}Cu_{14.7}Ni_{5.3}P_{22.5}$ metallic glass. In the case of the metallic glass plastic flow was closely confined around the indenting tip. The chevron-like shape of the indent performed on Pt(111) with $P_{\mathrm{max}} > 3$ µN and low loading rates was never observed on $Pt_{57.5}Cu_{14.7}Ni_{5.3}P_{22.5}$ metallic glass. We attribute the distortion of the triangle to an anisotropic elastic relaxation of Pt(111).

Figure 5 shows the load dependence of the pile-up volume $V_{\mathrm{pile\ up}}$ and the projected area A_{p} for Pt(111) and $Pt_{57.5}Cu_{14.7}Ni_{5.3}P_{22.5}$ metallic glass as extracted from nc-AFM images of indents. Values for $V_{\mathrm{pile\ up}}$ and A_{p} recorded in different experimental series are in very good agreement. As already observed in Figure 4, $V_{\mathrm{pile\ up}}$ for the metallic glass is more than a factor of two higher than for Pt(111). The measured projected area A_{p} of indents obtained at different maximal loads are significantly smaller for $Pt_{57.5}Cu_{14.7}Ni_{5.3}P_{22.5}$ metallic glass than for Pt(111). In both cases A_{p} is observed to increase linearly with P_{max}. Given the fact that the pile-up volume has to be equal to the indent volume it is misleading that the values obtained for A_{p} on Pt(111) are larger than on $Pt_{57.5}Cu_{14.7}Ni_{5.3}P_{22.5}$ metallic glass, while the corresponding values for $V_{\mathrm{pile\ up}}$ on $Pt_{57.5}Cu_{14.7}Ni_{5.3}P_{22.5}$ metallic glass are significantly larger than on Pt(111). This apparent contradiction can be resolved by considering the lateral extension of plastic deformation. The nc-AFM images in Figure 4 distinctly show that in the case of the metallic glass plastic flow was concentrated around the indent. In this case $V_{\mathrm{pile\ up}}$ could be measured accurately. In the case of Pt(111) it appears that

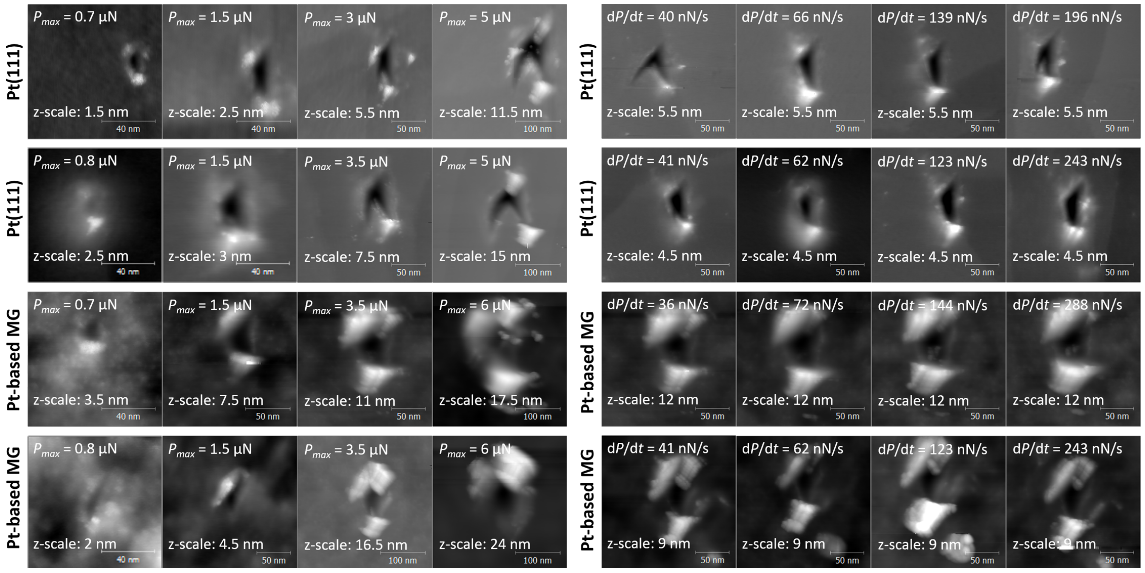

Figure 4: nc-AFM images of indented surfaces as a function of (left) the maximal loads P_{max} and of (right) the loading rate d*P*/d*t* on Pt(111) and $Pt_{57.5}Cu_{14.7}Ni_{5.3}P_{22.5}$ metallic glass; all AFM indentation measurements were performed with the same diamond-coated AFM tip that was analyzed in Figure 3.

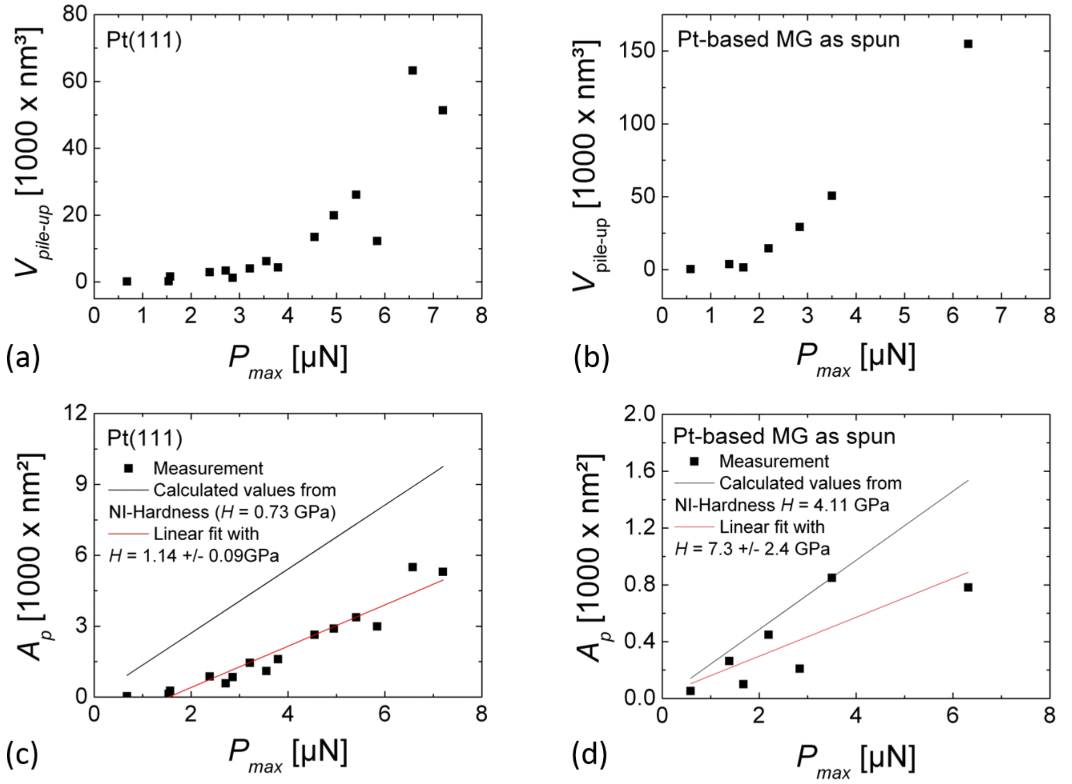

Figure 5: (a,b) Pile-up volume $V_{\text{pile up}}$, (c,d) projected area A_p as a function of $P_{\max}$ for (a,c) Pt(111) and (b,d) $Pt_{57.5}Cu_{14.7}Ni_{5.3}P_{22.5}$ metallic glass. The data points in (c) and (d) where fitted with a linear function $A_p = P_{\max}/H$ shown as a red line; for comparison the calculated values of A_p as a function of $P_{\max}$ are shown as a black line for hardness values measured by nanoindentation.

plastic deformation was accommodated over larger distances than considered in our image frames, resulting in an underestimation of $V_{\text{pile up}}$. Furthermore the steeper increase of the pile-up volume as a function of the indentation load for $Pt_{57.5}Cu_{14.7}Ni_{5.3}P_{22.5}$ metallic glass compared to Pt(111) further underlines the higher localization of plastic deformation for the metallic glass.

Using the load dependence of A_p, we further calculated the hardness of both sample surfaces according to $dA_p/dP_{\max} = 1/H$. Usually, the hardness is calculated as the ratio of a normal load to the projected area of a remaining indent. For smaller loads the hardness is, however, difficult to determine by this means due to the elastic offset. This explains why in this work the hardness was calculated as the slope $dA_p/dP_{\max}$. For Pt(111) we obtained $H = 1.14 \pm 0.09$ GPa; a slightly higher value than $H_{NI} = 0.73$ GPa which we found from nanoindentation measurements. For $Pt_{57.5}Cu_{14.7}Ni_{5.3}P_{22.5}$ metallic glass we obtained $H = 7.3 \pm 2.4$ GPa, also larger than $H_{NI} = 4.11$ GPa found from nanoindentation measurements. The larger hardness values based on nc-AFM imaging are attributed to the underestimation of the projected area of indents due to tip convolution. The corresponding error for the metallic glass is larger due to the increased difficulty to accurately measure A_p from nc-AFM images. The large pile ups in metallic glass appear to partly cover the indents after indenter retraction.

Figure 6 shows the loading-rate dependence of the pile-up volume $V_{\text{pile up}}$ and the projected area A_p for Pt(111) and $Pt_{57.5}Cu_{14.7}Ni_{5.3}P_{22.5}$ metallic glass as evaluated from nc-AFM images of indents from different series of indentations. For both samples $V_{\text{pile up}}$ was found to be independent on the loading rate dP/dt. The pile-up volume $V_{\text{pile up}}$ is again found to be significantly higher on $Pt_{57.5}Cu_{14.7}Ni_{5.3}P_{22.5}$ metallic glass than on Pt(111). For both samples the indent area A_p was found to be independent of the loading rate as well (see Figure 6).

Figure 7a and Figure 7b shows indentation curves for Pt(111) and $Pt_{57.5}Cu_{14.7}Ni_{5.3}P_{22.5}$ metallic glass for different values of $P_{\max}$. For Pt(111), the P–δ curves from different series of measurements overlap with each other, demonstrating the good reproducibility of the method. The P–δ curves on the crystalline Pt(111) show clear pop-ins. In the low load part of indentation curves ($P = 0.6$–1.4 µN) the pop-ins have a length of the order of 1 Å and are attributed to the activation of single dislocations. The load corresponding to the first pop-in event was

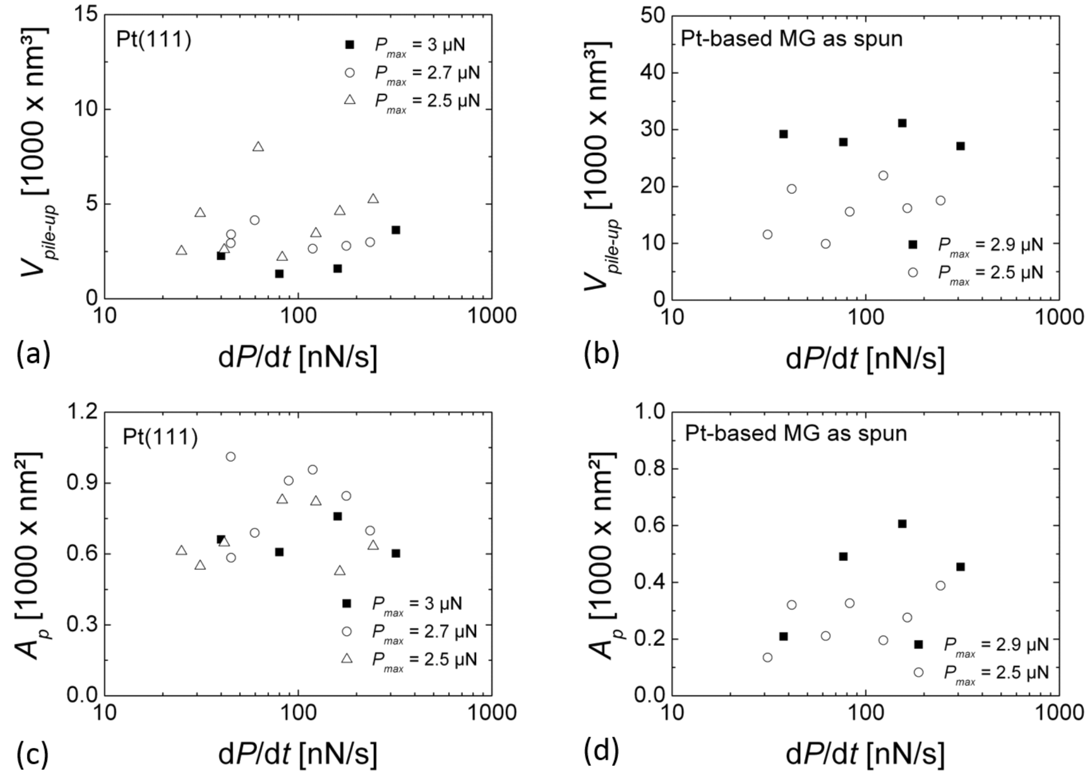

Figure 6: (a,b) Pile-up volume $V_{\text{pile up}}$, (c,d) projected area A_p as a function of d*P*/d*t* for (a,c) Pt(111) and (b,d) $Pt_{57.5}Cu_{14.7}Ni_{5.3}P_{22.5}$ metallic glass, respectively.

found to scatter from P_y = 186–633 nN at an indentation depth δ_y = 1.43–2.54 nm. With increasing load we observed an increase of the length of the pop-ins up to several nanometers, which corresponds to the simultaneous activation of several dislocations. For the metallic glass, the *P*–δ curves measured with different P_{max} values also overlap well. In contrast to the serrated flow of the crystalline Pt(111) evidenced by the occurrence of pop-ins, the plastic flow of the metallic glass is found to be continuous as demonstrated by the absence of pop-ins in the *P*–δ curves. Figure 7b and Figure 7d show indentation curves on Pt(111) and $Pt_{57.5}Cu_{14.7}Ni_{5.3}P_{22.5}$ metallic glass for varying loading rates. For both samples no loading-rate dependence could be observed: the *P*–δ curves are found to overlap eachother.

Figure 8 shows the projected area A_p as a function of the maximal indentation depth δ_{max} for both samples. In order to evaluate the geometry of the indenter the data points for both samples were fitted with a parabolic function of the type $A_p = C \times (\delta_{max} - \delta_{el})^2$, where δ_{el} is the indentation depth at the elastic limit and *C* is geometric factor that depends on the opening angle of the indenter. In this work δ_{el} was set as the maximal indentation depth corresponding to the smallest load at which a remaining indent was observed. For Pt(111) δ_{el} = 2.95 nm and for $Pt_{57.5}Cu_{14.7}Ni_{5.3}P_{22.5}$ metallic glass δ_{el} = 2.85 nm. Given the triangular shape of the indent obtained by AFM indentation the geometric factor *C* was set in analogy to a Berkovich indenter as $C = 3\sqrt{3}\tan^2\alpha$, where α is the half-opening angle of the indenter. This analogy is supported by the assumption that in our AFM measurements the indentation proceeded from the sharp corner of a single diamond nano-crystallite. From our results on Pt(111) we find *C* = 9.50 corresponding to α = 55.9° and for $Pt_{57.5}Cu_{14.7}Ni_{5.3}P_{22.5}$ metallic glass we obtain *C* = 6.47 corresponding to α = 50.7°. These results are reasonably close each other but deviate from the value of the half-opening angle of the reconstructed tip shown in Figure 3 of α = 74°. As stated above the projected area determined from nc-AFM images of indents is underestimated due to tip-convolution effects and results in an underestimated half-opening angle of the indenter.

Discussion

A single diamond-coated AFM tip was used to perform several series of indentations at various maximal loads and loading rates on Pt(111) and a $Pt_{57.5}Cu_{14.7}Ni_{5.3}P_{22.5}$ metallic glass. Throughout our experimental series results have been highly reproducible. We find very similar shape of indents and their pile ups in nc-AFM images and an excellent overlap of the corresponding *P*–δ curves. Unlike in nanoindentation experi-

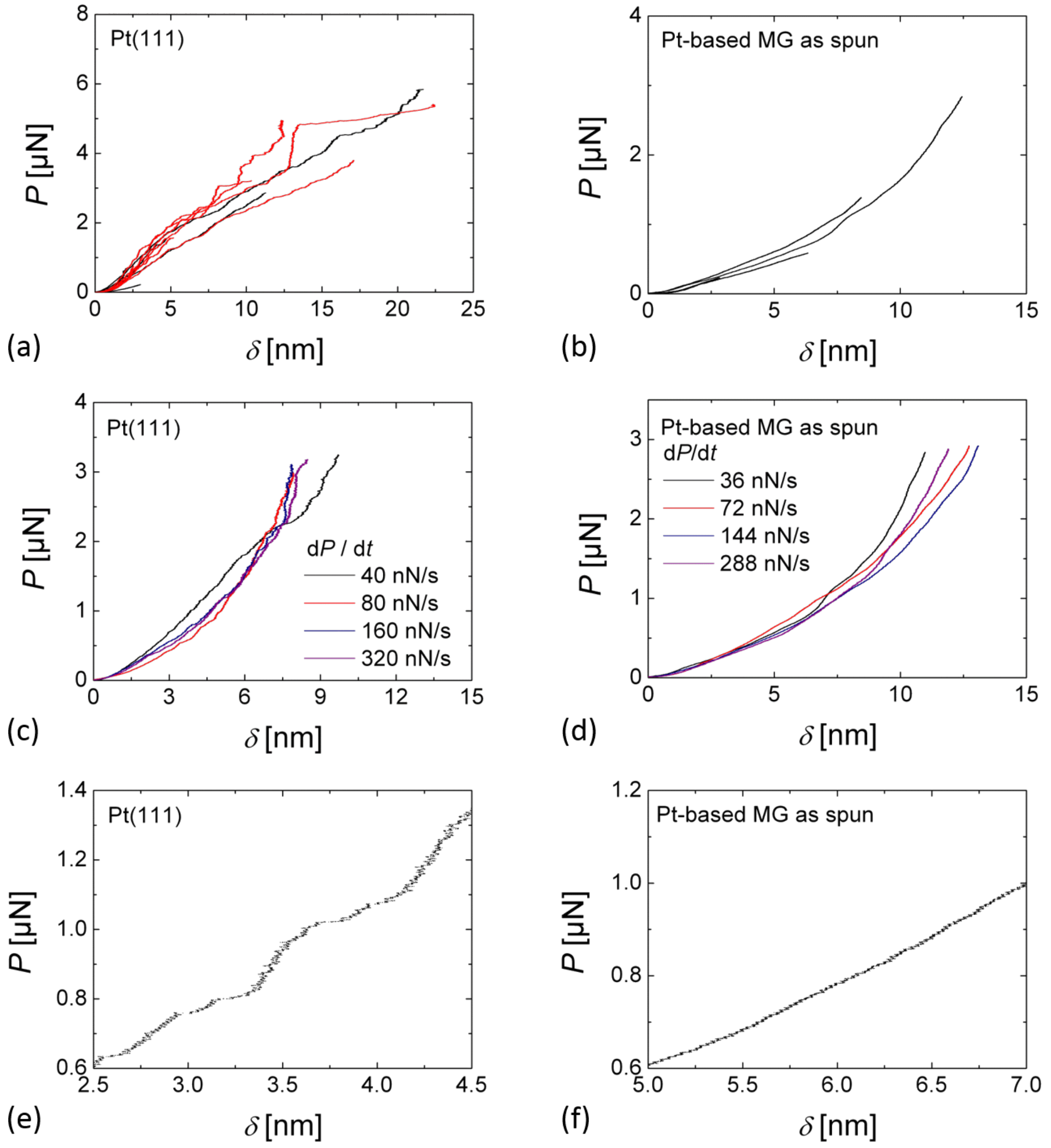

Figure 7: *P*–δ curves as a function of (a,b) the maximal load P_{max} and (c,d) the loading-rate on (a,c) Pt(111) and (b,d) $Pt_{57.5}Cu_{14.7}Ni_{5.3}P_{22.5}$ metallic glass; in (e,f) magnifications of *P*–δ curves at the plasticity on-set are shown for Pt(111) and $Pt_{57.5}Cu_{14.7}Ni_{5.3}P_{22.5}$ metallic glass, respectively.

ments with a standardized and macroscopically well-defined indenter geometry (such as a Berkovich tip), the indenter used in our AFM experiments is a diamond crystallite which is part of the diamond coating of the AFM tip. The geometry of this microscopic indenter was reconstructed from nc-AFM images selected from different experiment series on both samples recorded several months apart. Though the shape of imaged indents and of the pile-up geometry on both samples differed significantly, the reconstructed tip shape is very similar. In all cases the reconstructed tip shape is a three-sided pyramid. The angle of each side with regard to the base of the pyramid is found to be about 16°, while its half opening angle is about 74°, which may represent the corner of a single diamond nano-crystallite. We also determined the half-opening angle α of our indenter from the depth dependence of the projected area of indents and obtained α = 50–55°. As mentioned above the difference in the α values can be explained by the underestimation of the projected area from nc-AFM images of indents due to tip-convolution effects.

The stability of the microscopic indenter shape throughout our experimental study allows us to compare the nanometer-scale plastic flow of Pt(111) and $Pt_{57.5}Cu_{14.7}Ni_{5.3}P_{22.5}$ metallic glass. Our AFM indentation results reveal fundamentally different deformation mechanisms. For the crystalline Pt(111) the plastic deformation is accommodated over much larger distance than

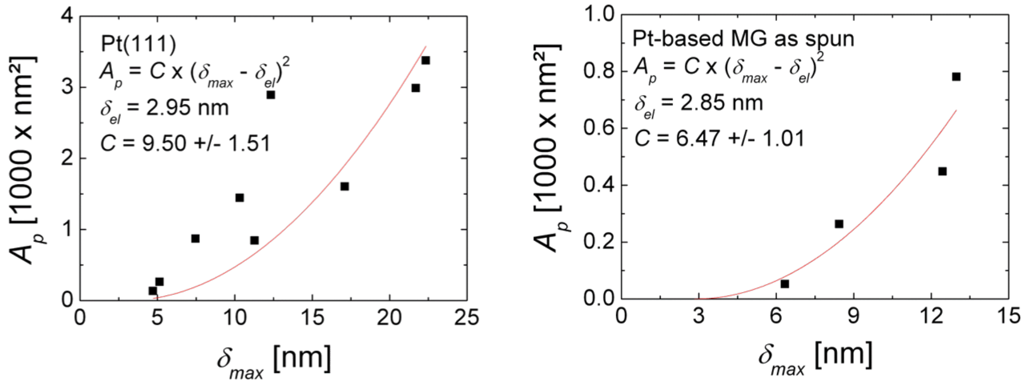

Figure 8: Projected area A_p as determined from nc-AFM images as a function of the maximal indentation depth δ_{max} as calculated from force–distance curves for (a) Pt(111) and (b) $Pt_{57.5}Cu_{14.7}Ni_{5.3}P_{22.5}$ metallic glass.

for the metallic glass. In our study the AFM indentation of Pt(111) is similar to KBr(100) or Cu(100) where plastic flow has been found to extend over several 100 nm from the AFM indentation site [7,8]. In contrast, the plastic flow of $Pt_{57.5}Cu_{14.7}Ni_{5.3}P_{22.5}$ metallic glass is highly concentrated around the AFM indenter.

In a recent study, we have compared the nano-scale wear of Pt(111) and $Pt_{57.5}Cu_{14.7}Ni_{5.3}P_{22.5}$ metallic glass by AFM scratching in UHV. The friction forces measured during reciprocal scratching with a diamond-coated silicon tip were found to be four times higher for the metallic glass than for Pt(111). This difference has been explained in [13] on the basis of the respective deformation mechanisms of crystalline and amorphous metals, namely easy dislocation mobility for Pt(111) and high resistance to plastic flow for $Pt_{57.5}Cu_{14.7}Ni_{5.3}P_{22.5}$ metallic glass. The latter was found to be mediated by thin shear bands at moderate loads of P in the range of 400 to 1.5 µN until the sliding contact merged in a single shear zone at higher load. Note that the high shear rate parallel to the surface in those scratching experiments as compared to the slower indentation experiments presented here is likely responsible for the occurrence of shear bands that can abruptly relax elastic stresses.

The nanometer-scale plastic flow of Pt(111) occurs by discrete events, i.e., pop-ins that correspond to the activation of dislocations. In the low-load regime the length of pop-ins is a few angstroms and probably corresponds to the activation of single dislocations. At higher loads, $P > 3$ µN, the pop-in length increases up to several nanometers, which corresponds to the simultaneous activation of several dislocations. These findings are again in good agreement with previous AFM indentation results on crystalline KBr(100) [7] and Cu(100) [8]. The increased pop-in length at higher loads is also in good agreement with nanoindentation results on (111)-oriented fcc-metal surfaces such as Au(111), for which burst-like dislocations activation has been observed [3]. However, the nanometer-scale plastic flow of $Pt_{57.5}Cu_{14.7}Ni_{5.3}P_{22.5}$ metallic glass is found to be continuous, without any signs of discontinuous events such as pop-ins. The observation of continuous plastic flow during AFM indentation on the metallic glass is in contrast to the observation of serrated flow in nanoindentation experiments on metallic glasses, where the occurrence of pop-ins has been associated to the generation and propagation of shear bands [4]. In nanoindentation experiments the plastically deformed volume is in the range of several cubic micrometers. Plastic deformation is mediated by the cooperative activation of several shear transformations zones (STZs) [21] and is often characterized by a serrated flow. Single pop-ins in nanoindentation load–displacement curves correspond then to the operation of single shear bands. In the following we introduce previous studies on homogeneous flow in very small metallic glass samples and relate them to our results. We will then discuss alternative concepts leading to homogeneous flow and finally the role of strain rates.

The investigation of the plastic flow of micro- and nano-fabricated test samples prepared from metallic glasses by focus ion beam (FIB) with volumes in the range of a few cubic micrometers to 0.05 µm^3 has revealed a transition from localized to delocalized plastic deformation upon reducing the sample size down to a diameter of the order of 100 nm [9]. For micrometer-sized samples studied in compression, plastic flow is characterized by visible shear steps at the sample surface and discrete load drops in the stress–strain curves that are attributed to the operation of single shear bands. Below a critical sample diameter though, the surface of samples tested in compression or tension are devoid of shear steps or shear bands and the plastic deformation has in this case been consequently described as homogeneous [10]. In [10] the size-induced transition from serrated to homogeneous plastic deformation has been discussed on the basis of an energetic argument, where below a critical sample size the elastic energy stored in the sample can no longer account for energy release to the area of a shear band traversing the sample. More recently, it has been shown that despite the disappearance of shear bands and shear steps at sample surfaces upon the decrease of sample size one could still observe intermittence in stress–strain curves [11,12]. The magnitude of plasticity events was much reduced and their frequency higher than for larger samples. This effect was attributed to local shear transformation events [12] that could not be resolved in previous works, probably due to limitations in the force and displacement resolution of nanoindentation. From these previously reported results it can be inferred that plastic deformation of metallic glasses becomes rather delocalized than homogeneous below a critical volume of ca. 0.05 μm^3 but does not lose its intermittent character. In the experimental results presented in this study, force and displacement resolution are higher than in any of the studies discussed above, and we still observe no serrated but only homogeneous flow.

The generation of a shear band has been discussed to require the storage of a sufficient amount of elastic energy within the strained volume to overcome the interfacial energy of a shear band [10,12]. In our case the elastic energy stored in the contact corresponds to $\int_0^{\delta_p} P d\delta$ where δ_p is the penetration depth at the onset of plastic deformation that can be taken as the δ_{max} value for P_{max} = 0.6 µN (see Figure 2). The shear band energy can be calculated according to $\sqrt{2}\pi r^2 \Gamma$, where r is the radius of the plastic zone and $\Gamma \approx 10$ J/m² is a higher bound for the energy per unit area of the shear band [10]. The critical shear band size can be equated as

$$r_c = \sqrt{\int_0^{\delta_p} P\mathrm{d}\delta \Big/ \sqrt{2}\pi\Gamma} \; .$$

For our measurement with P_{max} = 0.6 µN we find $\int_0^{\delta_p} P d\delta$ = 1.61×10^{-15} J and $r_c \approx 6$ nm. From Figure 4 the size of the plasticity zone can be estimated to be $r_p \approx 5$ nm by measuring the distance between pile-up and the center of the indent. The value estimated for r_p is lower than for r_c, inferring that in our AFM indentation experiments the generation of shear bands was not energetically favorable. Instead we observe that the plastic deformation of $Pt_{57.5}Cu_{14.7}Ni_{5.3}P_{22.5}$ metallic glass at the nanometer-scale occurs by a continuous material flow around the tip. The contrast between serrated and homogeneous flow for Pt(111) and $Pt_{57.5}Cu_{14.7}Ni_{5.3}P_{22.5}$ metallic glass is confirmed by the different characteristics of the remaining indents on both samples. Plastic deformation of Pt(111) was accommodated by dislocations, over larger distance than in the case of $Pt_{57.5}Cu_{14.7}Ni_{5.3}P_{22.5}$ metallic glass. The pile-up around indents in $Pt_{57.5}Cu_{14.7}Ni_{5.3}P_{22.5}$ metallic glass are also devoid of shear steps in contrast to nanoindentation experiments [22].

The difference in the mechanisms involved in the nanometer-scale plastic deformation of Pt(111) and $Pt_{57.5}Cu_{14.7}Ni_{5.3}P_{22.5}$ metallic glass is also reflected in the hardness. Although the H values determined from AFM indentation experiments are overestimated due to the underestimation of the projected area it is interesting to note that the hardness ratios for $Pt_{57.5}Cu_{14.7}Ni_{5.3}P_{22.5}$ metallic glass and Pt(111) are slightly higher from AFM indentation than from nanoindentation. The values obtained from our measurements were:

$$\left.\frac{H_{\text{Pt-based MG}}}{H_{\text{Pt(111)}}}\right|_{\text{NI}} = 5.5 \text{ from nanoindentation and}$$

$$\left.\frac{H_{\text{Pt-based MG}}}{H_{\text{Pt(111)}}}\right|_{\text{AFM}} = 6.4 \text{ from AFM indention.}$$

This may point at different size effects for the plasticity of Pt(111) and $Pt_{57.5}Cu_{14.7}Ni_{5.3}P_{22.5}$ metallic glass. For crystalline materials the indentation size effect has been rationalized on the basis of geometrically necessary dislocations with Burgers vectors normal to the plane of the surface [23]. In this case the hardness decreases with the indentation depth according to $H/H_0 = \sqrt{1+\delta^*/\delta}$, where H_0 is the hardness in the limit of infinite depth and δ^* is a characteristic length depending on the indenter geometry, the shear modulus, the Burgers vector, and H_0. For metallic glasses an indentation size effect has also been observed and has been discussed on the basis of accumulation of STZs during indentation and subsequent shear softening at larger indentation depths resulting in an increase of the hardness at smaller indentation depth [24].

In order to shed light on our AFM indentation results at different loading rates, we discuss previous observations on the effect of loading rate and homologous temperature on the plastic flow of metallic glasses during nanoindentation. At higher loading rates and homologous temperatures, the serrated character of plastic flow recorded on metallic glasses during nanoindentation disappears [4,25]. The effect of the strain rate on the transition from serrated to homogeneous plastic flow of metallic glasses has been explained by the idea that a single shear band cannot accommodate the imposed strain rapidly enough at high strain rates [4]. According to the authors, at high strain rates the applied strain is instead accommodated by the simultaneous operation of multiple shear banding events that can no longer be distinguished in load–displacement curves. Further, the effect of temperature on the transition from serrated to homogeneous plastic flow of metallic glasses has been discussed in [25] on the basis of the thermal activation of STZs [21]. On macroscopic scale, the flow stress in metallic glasses or activation of STZs has been reported to depend on the strain rate [26]. This has also been observed by nanoindentation where at higher rates the hardness increases [27] and has been used to determine the size of STZs.

In our AFM indentation experiments no rate dependence could be observed on Pt(111) or $Pt_{57.5}Cu_{14.7}Ni_{5.3}P_{22.5}$ metallic glass. Our observation of no loading-rate dependence in Pt(111) is in good agreement with the absence of strain-rate sensitivity of coarse crystalline fcc metals at low homologous temperatures. The absence of loading-rate further emphasize that during our AFM indentation experiments on $Pt_{57.5}Cu_{14.7}Ni_{5.3}P_{22.5}$ metallic glass plasticity is not mediated by shear banding or the activation of STZs but involves alternative mechanisms. Our experiments on $Pt_{57.5}Cu_{14.7}Ni_{5.3}P_{22.5}$ metallic glass were performed at a homologous temperature $T_H = 0.6$, which is far below the reported value for the transition from serrated to non-serrated flow of metallic glasses during nanoindentation [26]. For $Pt_{57.5}Cu_{14.7}Ni_{5.3}P_{22.5}$ metallic glass we claim that the volume that is plastically deformed during AFM indentation is not large enough to yield a significant accumulation of STZs and their autocatalytic multiplication, which would result in shear softening.

Conclusion

AFM indentation was used to quantitatively and reproducibly determine the hardness and deformation mechanisms of Pt(111) and a $Pt_{57.5}Cu_{14.7}Ni_{5.3}P_{22.5}$ metallic glass with unprecedented resolution in imaging and force curves thanks to operation and sample preparation in ultra-high vacuum. At the nanometer-scale the plastic deformation mechanisms of Pt(111) remain consistent with the serrated mechanisms operating at larger scale: Plasticity is accommodated over large distances by dislocation gliding and no rate dependence is observed. For $Pt_{57.5}Cu_{14.7}Ni_{5.3}P_{22.5}$ metallic glass the nanometer-scale plastic deformation is rate independent, continuous and localized around the indenter, which contrasts with the observation of serrated flow at the micrometer-scale and the rate dependence of flow stress of metallic glasses at larger scales. The results demonstrate a lower size limit for metallic glasses below which shear transformation mechanisms are not activated by indentation. In the case of metallic glass, we conclude that the energy stored in the stressed volume during nanometer-scale indentation is insufficient to account for the interfacial energy of a shear band in the glassy matrix.

Acknowledgements

We thank Prof. E. Arzt for continuing support of the project and acknowledge financial support by the Deutsche Forschungsgemeinschaft. We thank Dr. Wada from the Institute for Materials Research, Tohoku University, Japan for his contribution to the preparation of the $Pt_{57.5}Cu_{14.7}Ni_{5.3}P_{22.5}$ metallic glass sample.

References

1. Tabor, D. *The hardness of metals;* Oxford University Press, 1951.
2. Fischer-Cripps, A. C. *Nanoindentation,* 2nd ed.; Springer: New York, 2004.
3. Michalke, T. A.; Houston, J. E. *Acta Mater.* **1998,** *46,* 391. doi:10.1016/S1359-6454(97)00270-X
4. Schuh, C. A.; Nieh, T. G. *Acta Mater.* **2003,** *51,* 87. doi:10.1016/S1359-6454(02)00303-8
5. Kiely, J. D.; Houston, J. E. *Phys. Rev. B* **1998,** *57,* 12588. doi:10.1103/PhysRevB.57.12588
6. Kiely, J. D.; Jarausch, K. F.; Houston, J. E.; Russell, P. E. *J. Mater. Res.* **1999,** *14,* 2219. doi:10.1557/JMR.1999.0298
7. Egberts, P.; Bennewitz, R. *Nanotechnology* **2011,** *22,* 425703. doi:10.1088/0957-4484/22/42/425703
8. Filleter, T.; Bennewitz, R. *Nanotechnology* **2007,** *18,* 044004. doi:10.1088/0957-4484/18/4/044004
9. Greer, J. R.; De Hosson, J. T. M. *Prog. Mater. Sci.* **2011,** *56,* 654. doi:10.1016/j.pmatsci.2011.01.005
10. Volkert, C. A.; Donohue, A.; Spaepen, F. *J. Appl. Phys.* **2008,** *103,* 083539. doi:10.1063/1.2884584
11. Kuzmin, O. V.; Pei, Y. T.; De Hosson, J. T. M. *Appl. Phys. Lett.* **2011,** *98,* 233104. doi:10.1063/1.3598400
12. Chen, C. Q.; Pei, Y. T.; De Hosson, J. T. M. *Scr. Mater.* **2012,** *67,* 947. doi:10.1016/j.scriptamat.2012.08.029
13. Caron, A.; Louzguinue-Luzgin, D. V.; Bennewitz, R. *ACS Appl. Mater. Interfaces* **2013,** *5,* 11341. doi:10.1021/am403564a
14. Schroers, J.; Johnson, W. L. *Phys. Rev. Lett.* **2004,** *93,* 255506. doi:10.1103/PhysRevLett.93.255506
15. Meyer, E.; Hug, H.-J.; Bennewitz, R. *Scanning Probe Microscopy;* Springer: Berlin Heidelberg New York, 2004.
16. Nonnenmacher, M.; Greschner, J.; Wolter, O.; Kassing, R. *J. Vac. Sci. Technol., B* **1991,** *9,* 1358. doi:10.1116/1.585196
17. Giessibl, F. J. *Appl. Phys. Lett.* **2001,** *78,* 123. doi:10.1063/1.1335546
18. Butt, H.-J.; Jaschke, M. *Nanotechnology* **1995,** *6,* 1. doi:10.1088/0957-4484/6/1/001
19. Cannara, R. J.; Brukman, M. J.; Carpick, R. W. *Rev. Sci. Instrum.* **2005,** *76,* 053706. doi:10.1063/1.1896624
20. Gwyddion – Free SPM (AFM, SNOM/NSOM, STM, MFM, …) data analysis software. http://www.gwyddion.net (accessed April 6, 2015).
21. Argon, A. S. *Acta Metall.* **1979,** *27,* 47. doi:10.1016/0001-6160(79)90055-5
22. Burgess, T.; Ferry, M. *Mater. Today* **2009,** *12,* 24. doi:10.1016/S1369-7021(09)70039-2
23. Nix, W. D.; Gao, H. *J. Mech. Phys. Solids* **1998,** *46,* 411. doi:10.1016/S0022-5096(97)00086-0
24. Van Steenberge, N.; Sort, J.; Concustell, A.; Das, J.; Scudino, S.; Suriñach, S.; Eckert, J.; Baró, M. D. *Scr. Mater.* **2007,** *56,* 605. doi:10.1016/j.scriptamat.2006.12.014
25. Song, S. X.; Jang, J. S. C.; Huang, J. C.; Nieh, T. G. *Intermetallics* **2010,** *18,* 702. doi:10.1016/j.intermet.2009.11.009
26. Argon, A. S. Inelastic behavior of non-polymeric glasses. *The physics of deformation and fracture of polymers;* Cambridge University Press, 2013; pp 174–227.

27. Pan, D.; Inoue, A.; Sakurai, T.; Chen, M. W. *Proc. Natl. Acad. Sci. U. S. A.* **2008,** *105,* 14769. doi:10.1073/pnas.0806051105

License and Terms

BEILSTEIN JOURNAL OF NANOTECHNOLOGY

A simple method for the determination of qPlus sensor spring constants

John Melcher, Julian Stirling and Gordon A. Shaw*

Full Research Paper

Open Access

Address:
National Institute of Standards and Technology, Gaithersburg, MD 20899, USA

Email:
Gordon A. Shaw* - gordon.shaw@nist.gov

* Corresponding author

Keywords:
atomic force microscopy; calibration; non-contact atomic force microscopy; qPlus

Beilstein J. Nanotechnol. **2015,** *6,* 1733–1742.
doi:10.3762/bjnano.6.177

Received: 06 April 2015
Accepted: 20 July 2015
Published: 14 August 2015

This article is part of the Thematic Series "Advanced atomic force microscopy techniques III".

Guest Editor: T. Glatzel

Abstract

qPlus sensors are widely used to measure forces at the atomic scale, however, confidence in these measurements is limited by inconsistent reports of the spring constant of the sensor and complications from finite tip heights. Here we combine a numerical investigation of the force reconstruction with an experimental characterization of the flexural mechanics of the qPlus sensor. Numerical studies reveal significant errors in reconstructed force for tip heights exceeding 400 µm or one sixth of the cantilever length. Experimental results with a calibrated nanoindenter reveal excellent agreement with an Euler–Bernoulli beam model for the sensor. Prior to the attachment of a tip, measured spring constants of 1902 ± 29 N/m are found to be in agreement with theoretical predictions for the geometry and material properties of the sensor once a peaked ridge in the beam cross section is included. We further develop a correction necessary to adjust the spring constant for the size and placement of the tip.

Introduction

Non-contact-atomic force microscopy (ncAFM) has paved new inroads to the measurement of nanometer-scale properties that were previously inaccessible. By allowing the atomic-scale imaging of surfaces from insulators to conductors, the technique opens up a broad materials spectrum to the possibility of atomic-scale analysis. This new capability has led to imaging with sub-atomic resolution [1], and chemical identification of surface atoms [2] and molecules [3], as well as dynamic force spectroscopy in a wet chemical environment [4]. However, a direct comparison between theory and experiment requires that an absolute, quantitative framework for the measurement is established, as illustrated by a recent work in single dimer manipulation [5].

In recent years, quartz tuning fork sensors have emerged as an attractive alternative to traditional silicon microcantilevers for ncAFM. The stiff spring constant of the tuning fork enables precise control over the tip–sample separation at short stand-off distances despite relatively large van der Waals interactions. Moreover, the mass production of tuning forks for timing applications has provided highly-stable frequencies with self-sensing and self-actuating electromechanical properties all at low cost [6]. Tuning fork sensors were originally used as a traditional, dual-tine oscillator. This evolved into the more widely used qPlus configuration where the sensing tine oscillates and the second tine is immobilized [7,8]. If the tines are well balanced, the former benefits from high quality factors due to low inertial coupling with the stage. The later simplifies the modeling and calibration effort for quantitative force measurements [9]. With careful design and experimentation it is possible for qPlus sensors [10], and other sensors with cantilevered geometries [11], to reach quality factors in excess of 10^6 without inertial cancelling.

Several methods have been developed to reconstruct the tip–sample interaction force from the frequency shift of an oscillating tip in ncAFM [12-17]. This analysis requires four separate experimental inputs: the frequency shift $\Delta\omega$ as a probe interacts with a surface relative to the unperturbed resonant frequency ω_0, the sensor oscillation amplitude a, which is held constant, and z is the distance of nearest approach between a surface and the oscillating probe tip, and the spring constant k. The reconstructed tip–sample force $\hat{F}(z)$ is given by [17]:

$$\hat{F}(z) = 2k\int_z^\infty \left(1 + \frac{a^{1/2}}{8\left[\pi(\zeta - z)\right]^{1/2}}\right)\Omega(\zeta) - \frac{a^{3/2}}{\left[2(\zeta - z)\right]^{1/2}}\frac{\mathrm{d}\Omega(\zeta)}{\mathrm{d}\zeta}\mathrm{d}\zeta, \qquad (1)$$

where $\Omega(z) = \Delta\omega(z)/\omega_0$. The reconstruction requires that the z-separation between the tip and sample is varied while the frequency shift is monitored. Force reconstruction using other methods, such as the matrix method [15], also use the same input parameters. For a more in-depth comparison of force reconstruction methods see [18].

To extract meaningful forces from Equation 1, the input parameters must be calibrated. The accepted method for trustworthy calibrations is to establish an unbroken chain of comparisons to a internationally recognized standard, that is, to establish traceability to a primary standard. Traceability ensures that all measurements are identically scaled, allowing for consistent comparison between theory and independent measurements.

The largest source of uncertainty in ncAFM measurements currently comes from the calibration of the spring constant of the sensor. Several traceable calibration methods have been developed for micro-fabricated silicon cantilevers [19-24]. However, despite several attempts to determine spring constants for sensors based on quartz tuning forks [25-29], no comprehensive framework yet exists due to inconsistencies between results from different methods.

qPlus sensors are stiff compared to traditional microcantilever sensors and present their own set of spring constant calibration challenges. A common approach has been to estimate the spring constant from plane view geometry and the Young's modulus of the appropriate crystallographic orientation. In this case, the qPlus sensor is treated as a uniform, rectangular cantilever and the spring constant is predicted from Euler–Bernoulli beam theory [1,7]. However, qPlus sensors violate several of the assumptions inherent in this approach (see Figure 1). In particular, the cross-section of the tine is not rectangular, but rather includes a peaked ridge resulting from anisotropy in the crystal etching process [30]. The assumption of axial uniformity is violated by the chamfered edge at the base of the tine, and the assumption of base rigidity has been questioned [25]. The attachment of a tip can alter the length of the cantilever, introduce parasitic tip motion [31], and, in extreme cases, introduce additional vibratory modes [32,33].

In what follows, we develop a rigorous mathematical model for the qPlus sensor with a finite tip. The effect of the parasitic tip motion on the reconstructed interaction force is examined quantitatively from the perspective of two-dimensional grid spectroscopy. In addition, we use a traceable nanoindenter to accurately characterize the flexural mechanics of the qPlus sensor. The experimental results provide validation of a theoretical model that can be used to predict the spring constant of the qPlus sensor.

Results

In this section we develop a model for the qPlus sensor with a finite tip that is subjected to a tip–sample interaction potential. The effect of the tip height and resulting parasitic tip rotation are carefully considered in terms of the error in the reconstructed tip–sample force.

Modeling the qPlus sensor dynamics

Figure 2 provides a model schematic of the qPlus sensor. The unconstrained tine is treated as a uniform cantilever the cross-section of which is rectangular with a triangular ridge (see Figure 1). The 50 µm tungsten wire tip is modeled as a rigid, slender rod extending from the center of the distal end of the beam with height H and axial offset B. Numerical values of the modeling parameters are listed in Table 1.

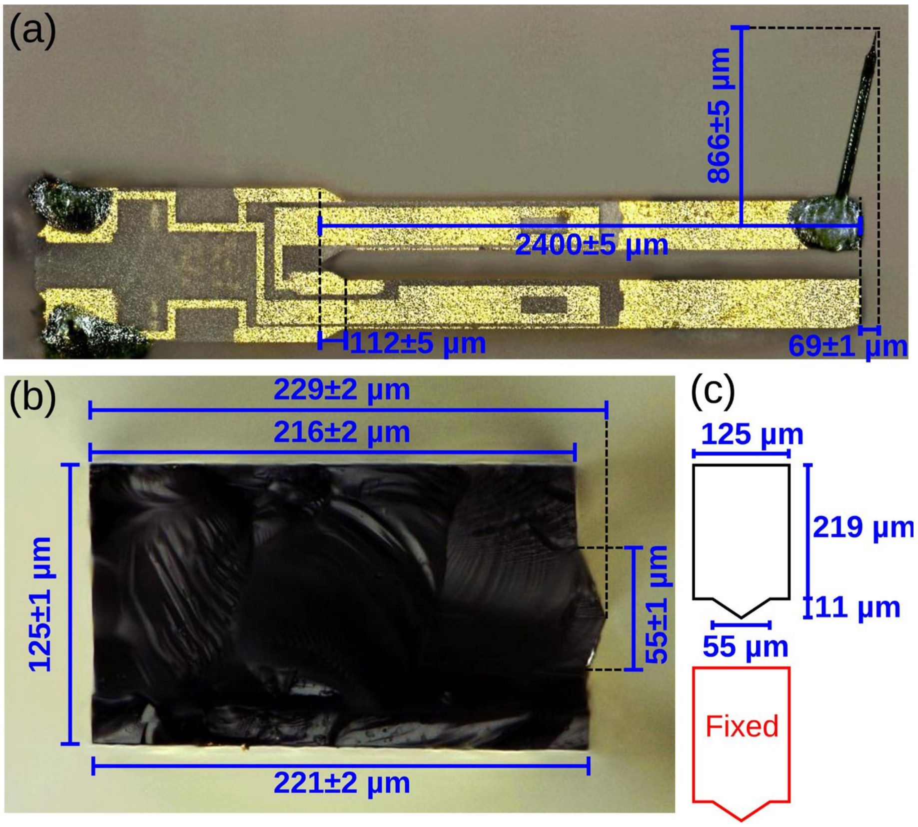

Figure 1: Optical images of a commercial qPlus sensor [8]. (a) Plane-view image consisting of an E158 quartz tuning fork (Micro Crystal, Switzerland) that is glued to a ceramic mount such that one tine is immobilized. A tungsten wire tip is attached to the distal end of the unconstrained tine. The tip height (measured from the center of the beam) is $h = 866 \pm 5$ µm. The tip also extends the length of the cantilever by 69 ± 1 µm. (b) Optical image of a cleaved E158 tine showing the non-rectangular cross-section (image is a composite of nine images at slightly different focal lengths). (c) Model schematic of the tine cross-section.

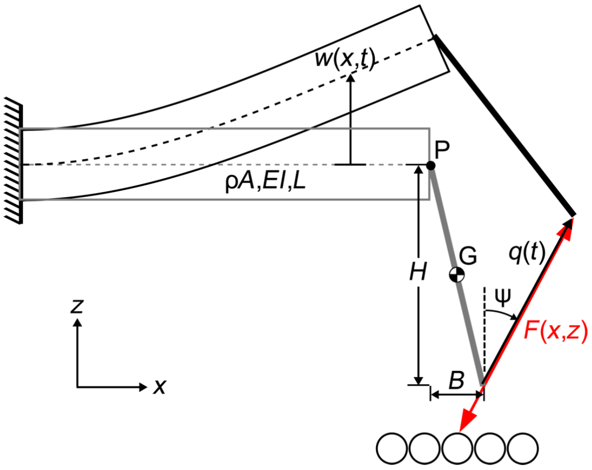

Figure 2: Model schematic for the qPlus sensor. The tine is a uniform beam with linear mass density μ, flexural rigidity *EI* and length *L*. The tip is attached to the free-end of the tine at point P corresponding to the neutral axis of the tine. The tip is modeled as a rigid, slender rod with a height *H* and axial offset *B*. Point G marks the center of mass of the tip.

Table 1: qPlus model parameters.

beam properties	
linear mass density (μ)	2650 kg/m^3
Young’s modulus (*E*)	78.6 GPa
second moment of area (*I*)	1.17×10^{-16} m^4
flexural rigidity (*EI*)	9.20 µN·m^2
length (*L*)	2.4 mm
tip properties	
mass density (ρ)	19 250 kg/m^3
diameter (*D*)	50 µm
height (*H*)	variable
axial offset (*B*)	variable

The schematic in Figure 2 highlights a kinematic property of a bending cantilever combined with a finite tip length [31]. The bending of the cantilever results in a transverse deflection of the free end. Additionally, bending causes the cross section of the beam to rotate. This rotation, coupled to a finite tip, results in an unwanted lateral displacement of the distal end of the tip. The resulting displacement of the tip occurs at an angle ψ from the normal, which depends strongly on the length of the tip. Consequently, the *z*-displacement of the sensor by the scanning stage, which is assumed to be transverse to the cantilever axis, and the tip–displacement are no longer collinear.

The dynamics of the qPlus sensor subjected to an interaction potential $V(x,z)$ can be modeled with classic Euler–Bernoulli beam theory. Let $w(x,t)$ denote the transverse deflection of the neutral axis (in this case, the midplane) of the cantilever. The kinetic and potential energy of the QTF sensor, respectively, are given by

$$\begin{aligned} T &= \frac{1}{2}\int_0^L \mu\left[\frac{\partial w(x,t)}{\partial t}\right]^2 \mathrm{d}x \\ &\quad + \frac{m}{2}\left[\frac{\partial w(L,t)}{\partial t} + \frac{B}{2}\frac{\partial^2 w(L,t)}{\partial x \partial t}\right]^2 + \frac{J_G}{2}\left[\frac{\partial^2 w(L,t)}{\partial x \partial t}\right]^2, \\ U &= \frac{1}{2}\int_0^L EI\left[\frac{\partial^2 w(x,t)}{\partial x^2}\right]^2 \mathrm{d}x \\ &\quad + V\left(x_0 + H\frac{\partial w(L,t)}{\partial x}, z_0 + w(L,t) + B\frac{\partial w(L,t)}{\partial x}\right), \end{aligned} \tag{2}$$

where the mass and moment of inertia of the tip are $m = \rho\pi D^2/4$ and $J_G = m(H^2 + B^2)/12$. Application of Hamilton's principle to Equation 2 establishes the governing partial differential equation (PDE) with the appropriate boundary conditions:

$$\begin{aligned} &\mu\frac{\partial^2 w}{\partial t^2} + EI\frac{\partial^4 w}{\partial x^4} = 0 \\ &x = 0:\ w = 0,\ \frac{\partial w}{\partial x} = 0 \\ &x = L:\ J_P\frac{\partial^3 w}{\partial x \partial t^2} + \frac{Bm}{2}\frac{\partial^2 w}{\partial t^2} + EI\frac{\partial^2 w}{\partial x^2} = H\frac{\partial V}{\partial x} + B\frac{\partial V}{\partial z} \\ &\qquad\quad m\frac{\partial^2 w}{\partial t^2} + \frac{Bm}{2}\frac{\partial^3 w}{\partial x \partial t^2} + EI\frac{\partial^3 w}{\partial x^3} = \frac{\partial V}{\partial z}, \end{aligned} \tag{3}$$

where $J_P = m(H^2 + B^2)/3$ is the moment of inertia of the tip about point P.

The unperturbed eigenmodes and eigenfrequencies of the qPlus sensor are solved for in the traditional manner by setting $V(x,z) = 0$ and substituting $w(x,t) = \Phi(x)e^{i\omega t}$ into Equation 3, where $\Phi(x)$ is the eigenfunction (See Appendix section). Here we limit our discussion to the fundamental eigenmode of the beam as it is most relevant to ncAFM. For convenience, let $X = x/L$. The tip-displacement angle is given by

$$\tan\psi = \frac{H\dfrac{\mathrm{d}\Phi(1)}{\mathrm{d}X}}{L\Phi(1) + B\dfrac{\mathrm{d}\Phi(1)}{\mathrm{d}X}}. \tag{4}$$

Figure 3 shows ψ vs H/L for $B = 0$. Results are calculated for the 50 μm tungsten wire tip and a hypothetical massless tip. ψ is shown to have strong geometric dependence on H/L in Equation 4, a weak dependence on B/L, and a weak implicit dependence on the mass and rotational inertia of the tip.

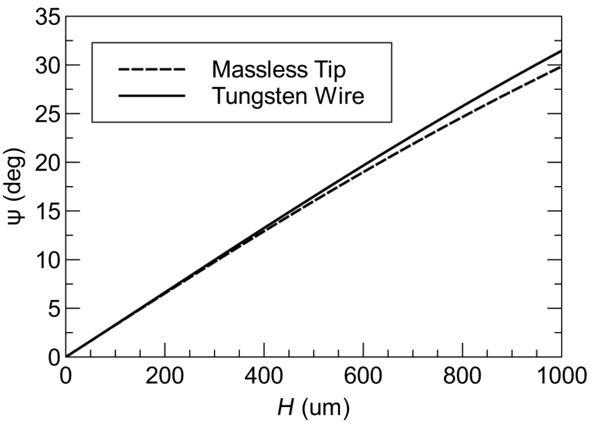

Figure 3: Tip displacement angle ψ vs tip height *H* calculated for the tungsten wire tip described in Table 1 and a hypothetical massless tip. $B = 0$ for both cases. The agreement between the two curves shows that ψ primarily depends on the tip height.

The governing PDE (Equation 3) can be reduced to an ordinary differential equation (ODE) with a single degree of freedom by approximating the motion of the beam with a single eigenmode $\Phi(x)$. The reduction of Equation 3 can be accomplished with a Galerkin discretization process (see Appendix section). Alternatively, one can follow the approach outlined in [34] and set $U = kq^2/2 + V$ and $T = k\left(\mathrm{d}q/\mathrm{d}t\right)^2 / \left(2\omega_0^2\right)$, where k and ω_0 are the spring constant and unperturbed resonant frequency of the oscillator, respectively, and q is the coordinate for the tip displacement (See Figure 2). Following either approach, it is possible to show

$$\frac{\mathrm{d}^2 q}{\mathrm{d}t^2} + \omega_0^2 q = \frac{\omega_0^2}{k}F\left(x_0 + q\sin\psi, z_0 + q\cos\psi\right), \tag{5}$$

where $F(x,z)$ is the derivative of $V(x,z)$ in the direction of the tip displacement:

$$F\left(x,z\right)=\frac{\partial V\left(x,z\right)}{\partial x}\sin\psi+\frac{\partial V\left(x,z\right)}{\partial z}\cos\psi\,. \tag{6}$$

The spring constant is $k = k_z \cos^2\psi$, where:

$$k_z=\frac{EI}{L^3}\frac{\int_0^1\left[\frac{\mathrm{d}^2\Phi(X)}{\mathrm{d}X^2}\right]^2\mathrm{d}X}{\left[\Phi(1)+\frac{B}{L}\frac{\mathrm{d}\Phi(1)}{\mathrm{d}X}\right]^2}, \tag{7}$$

is the effective spring constant in the z-direction. Note that Equation 7 represents the exact solution for the spring constant of the fundamental eigenmode according to Euler–Bernoulli theory [34]. A static approximation for k_z, which relates the transverse tip deflection to a static point load applied at the tip, is given by

$$\hat{k}_z=\frac{3EI}{\left(L+B\right)^3},\quad B\ll L. \tag{8}$$

Figure 4 shows the exact expression for spring constant k_z according to Euler–Bernoulli theory (Equation 7) alongside the approximation $\hat{k}_z$ (Equation 8). The spring constant is calculated for both a massless tip and a 50 µm tungsten wire tip with H = 400 µm. For the massless tip, the true spring constant is about 3% stiffer than the approximation. The addition of the tip mass actually shifts the true spring constant closer to the approximate value. For a 400 µm tip height, k_z is only 1.5% stiffer than $\hat{k}_z$ and for tip heights greater than 632 µm, the approximation deviates by less than 1%. In the following section, we neglect the error in the approximation, however, the small correction factor can be estimated from the theoretical model if desired.

Modeling dynamic force spectroscopy

Ultimately, the goal of the modeling and calibration effort in ncAFM is to provide a quantitative measurement of the tip–sample force and/or potential. Here we will assume that the parasitic tip motion is neglected in the model and study the resulting error in the reconstructed force. It is instructive to formulate the problem from the perspective of grid spectroscopy [35], where the tip–sample force is reconstructed for a grid of points in the xz-plane. We study the effect of the parasitic tip motion first computing the frequency shift according to the model, and second, reconstructing the force from the Sader–Jarvis formula.

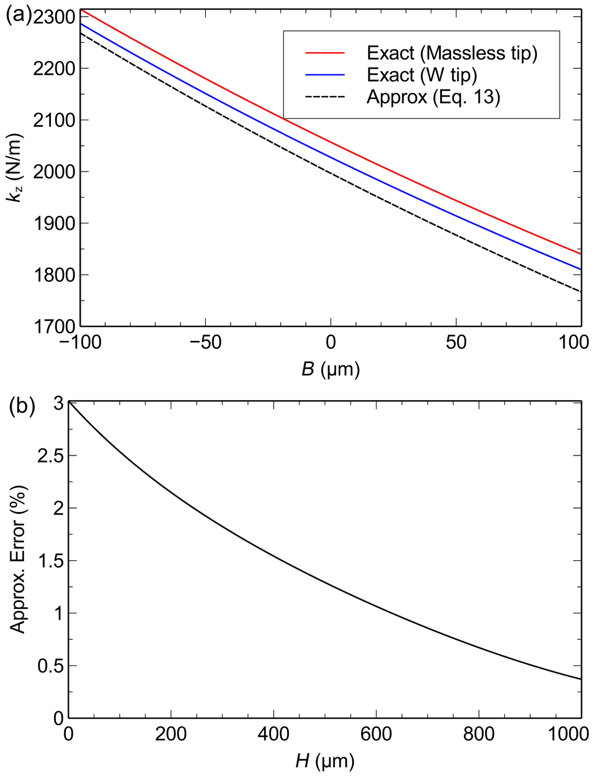

Figure 4: Theoretical prediction of the spring constant k_z. (a) k_z vs axial tip offset B. The spring constant is calculated with the exact expression (Equation 7) for a massless tip and for the 50 µm tungsten wire tip with H = 400 µm and compared to the approximate expression $\hat{k}_z$ (Equation 8). (b) Approximation error $\left(k_z-\hat{k}_z\right)/k_z\times 100$ vs H for B = 0.

First, let us consider frequency shift, which is calculated by applying a standard perturbation approach [14,17] to Equation 5:

$$\Omega=-\frac{1}{ka^2}\left\langle Fq\right\rangle, \tag{9}$$

where a is full amplitude of the tip displacement $q(t)$. A widely accepted method [31] for determining the oscillation amplitude in ncAFM employs a calibrated z-scanner and takes advantage of the large-amplitude frequency shift approximation [14]. However, this method measures only the z-component of the amplitude $a_z = a\cos\psi$. Rearranging Equation 9, we find

$$\Omega=\frac{1}{k_z a_z^2}\left\langle\left[\frac{\partial V}{\partial z}+\frac{\partial V}{\partial x}\tan\psi\right]q_z\right\rangle, \tag{10}$$

where $q_z = q\cos\psi$ is the z-component of the tip displacement. Thus, if only the z-component of the tip-displacement is measured, force measurements require knowledge of k_z. However, this approach does result in a systematic error from the tanψ term in Equation 10. For large tip heights the error is significant.

To quantify the error in the reconstructed force caused by the parasitic tip motion, we introduce a model for the tip–sample interaction given by the Morse potential for a pair of silicon atoms:

$$V_{\mathrm{Morse}}\left(x,z\right)=V_0\left\{1-\exp\left[-\frac{1}{\lambda}\left(\sqrt{x^2+z^2}-r_0\right)\right]\right\}^2, \quad (11)$$

where $\Omega=-\left(1/ka^2\right)\langle Fq\rangle$, is distance between the atoms, and $V_0 = 3.643 \times 10^{-19}$ J, $r_0 = 235.7$ pm, $\lambda = 100$ pm are taken from [36]. Using Equation 10 and Equation 11, $\Omega(x,z)$ is computed for a grid of points in the xz-plane for an oscillation amplitude $a_z = 100$ pm. The computation is repeated for tip heights $H = 0$, 200, 400, 600, 800 and 1000 µm, which correspond to $\psi = 0$, 6.5°, 13°, 19°, 25° and 30°, respectively. Substituting a_z for a, k_z for k, into the Sader–Jarvis formula (Equation 1) allows the tip-sample force to be reconstructed for the two-dimensional grid $\Omega(x,z)$.

Figure 5 shows two-dimensional grid spectroscopy images reconstructed from the Sader–Jarvis formula. For zero tip height, the image faithfully reconstructs the interaction force. However, for non-zero tip heights, the parasitic tip motion contributes an error to the reconstructed force. Most notably, the parasitic tip motion causes an overall distortion of the image by the angle ψ. Additionally, there is an error in the magnitude of the force, which can be quantified by the force minimum. For increasing tip heights, the reconstructed force minimum is −1.65, −1.67, −1.73, −1.84, −1.99, and −2.19 nN, respectively. Thus, for a tip height of 1000 µm, the error in the reconstructed force minimum is nearly 35%.

We remark here that it is possible, with accurate knowledge of ψ, to eliminate the error caused by the parasitic tip motion by changing the integration of $\Omega(x,z)$ in the Sader–Jarvis formula to be collinear with the tip displacement. However, this approach would be fairly onerous for most experimental setups where typically only a single frequency vs z curve is acquired, rather than an entire grid. Thus, the preferred method is to limit the tip height to approximately less than 400 µm.

Mechanical characterization of qPlus sensors with nanoindentation

In this section we characterize the flexural mechanics of qPlus sensors using a nanoindentation method. The nanoindenter, which is calibrated with traceability to the International System of Units (SI) [19,21,37], measures a force vs displacement curve by pressing a sharp indenter tip into the qPlus sensor surface at a known axial distance from the distal edge of the tine. From the indentation curve, a stiffness k_I is inferred, taking

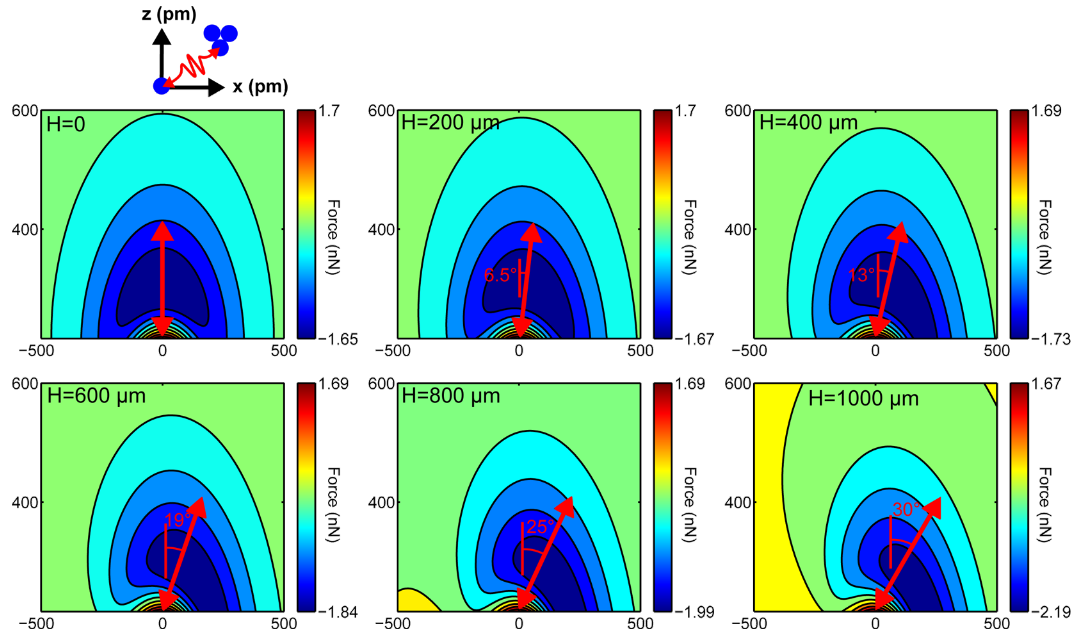

Figure 5: Reconstructed grid spectroscopy images for Si–Si Morse potential with varying tip heights. Red arrows are drawn to scale to indicate the direction of the tip motion. The extrema of the scale bar show the error in the reconstructed force.

care to remove the machine compliance and contact compliance by performing additional measurements at the base of the sensor. Applying this method at two or more distinct locations along the axis of the tine determines the flexural rigidity EI and effective cantilever length L_{eff} of the qPlus sensor. Moreover, the indentation data provides validation of Bernoulli–Euler beam theory with fixed-free boundary conditions to model the flexural mechanics of qPlus sensors.

Let $k_\text{I}(b)$ denote the force gradient measured by the nanoindenter at an offset b from the distal edge of the tine (positive in the $+x$ direction pointing away from the base of the cantilever). For a uniform cantilever beam, the Euler–Bernoulli model predicts the following relationship:

$$k_\text{I}^{-1/3}(b) = (3EI)^{-1/3}(L_{\text{eff}} + b). \qquad (12)$$

Measuring k_I for a range of offsets allows EI and L_{eff} to be determined from a linear least-squares fit regression. Note that L_{eff} differs slightly from the geometric length due to the non-ideal boundary conditions at the fixed end of the tine. With knowledge of EI, L_{eff} and the tip offset B, the spring constant k_z can be determined.

The qPlus sensors tested were custom-built. E158 tuning forks were attached to ceramic substrates obtained from Oxford Instruments using Torr Seal epoxy [8]. Two gluing configurations were tested. In the first configuration, only the bottom tine is glued to the substrate, while in the second the base of the tuning fork is also glued to the substrate (cf. Figure 6). The indentations were performed with a pre-load of 1 mN and maximum load of 1.9 mN. Measurements were acquired along the axis of the tine and additionally at the base of the sensor in order to remove the contact stiffness and machine compliance from the spring constant prediction. To avoid interference with the indenter tip, tips were not attached to the tine.

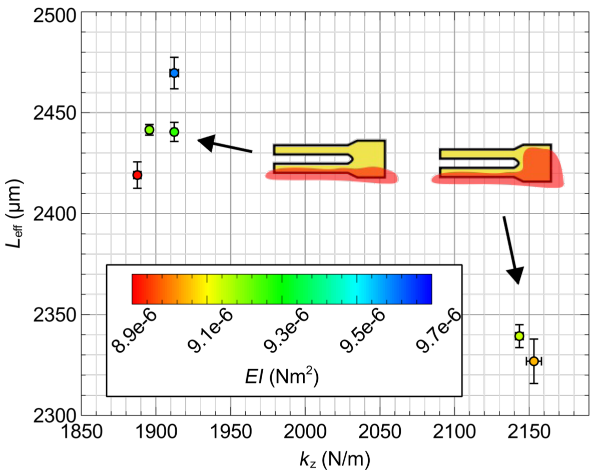

Figure 6: Dependence of the spring constant k_z on the effective length of the cantilever L_{eff}. Two distinct values of L_{eff} and corresponding k_z are observed depending on the mounting of the tine. The flexural rigidity EI is unaffected by the mounting as expected.

Figure 7 shows the indentation measurements for a single sensor (qPlus A). Plotting $k_\text{I}^{-1/3}$ vs b reveals excellent linearity as indicated by the coefficient of determination $R^2 = 0.9997$. The goodness of fit and uncorrelated residuals serve to validate the use of Euler–Bernoulli beam theory to model the flexural mechanics of the tine. A least-squares regression to indentation data determines the flexural rigidity and effective cantilever length.

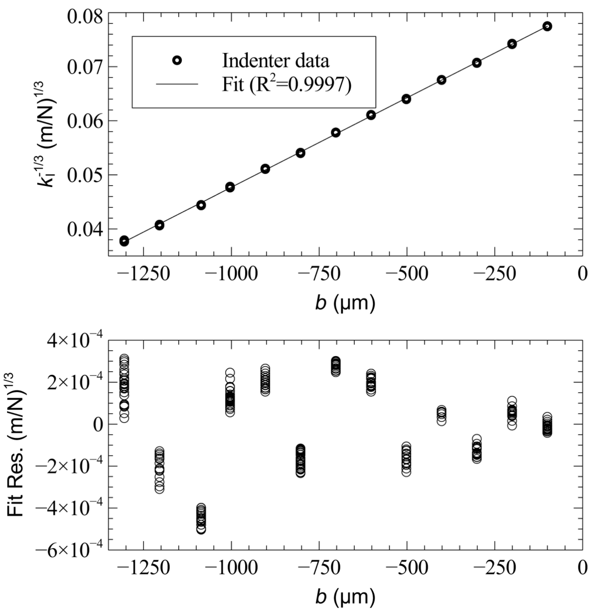

Figure 7: Nanoindenter measurements from a tunning fork tine. $k_\text{I}^{-1/3}$ vs b is plotted where k_I is the spring constant measured at an offset b from the distal edge of the tine. A linear least-squares regression determines EI and L of the tine.

The effective length, flexural rigidity, and nominal spring constant for several sensors are provided in Table 2. The combined standard uncertainty in the parameters includes Type A (statistical) uncertainty, which we estimate from the regression, and Type B (non-statistical) uncertainty, which includes (i) 1% uncertainty in the calibration of both force and indention of the nanoindenter and (ii) ±5 μm uncertainty in the positioning the indenter tip with respect to the distal edge of the tine. The details of the analysis are provided in the Appendix.

Figure 6 shows the spring constant k_z vs the effective length with a color bar for the flexural rigidity. There are two distinct

Table 2: Mechanical characterization of qPlus sensors with nanoindentation.

sensor	mounting	k_z (B = 0) (N/m)	L_{eff} (μm)	EI (μN·m^2)
qPlus A	tine	1897 ± 29	2442 ± 16	9.20 ± 0.13
qPlus B	tine	1912 ± 29	2440 ± 17	9.27 ± 0.14
qPlus C	tine	1912 ± 29	2470 ± 18	9.60 ± 0.16
qPlus D	tine	1888 ± 29	2419 ± 17	8.91 ± 0.14
qPlus E	base	2143 ± 33	2339 ± 17	9.14 ± 0.15
qPlus F	base	2153 ± 34	2327 ± 19	9.04 ± 0.18

values of the effective length directly corresponding to the two mounting configurations. The additional constraint provided by the glue at the base effectively shortens the tine leading to a stiffer spring constant. The flexural rigidity of the tine, however, is unaffected by the mounting configuration, as expected.

Assuming the reported values for the effective length and spring constant at zero tip offset, it is possible to determine the spring constant of the qPlus sensor from only the plane-view geometry and infer $k_z(B)$ simply by

$$k_z(B) = k_0 \left(1 + \frac{B}{L_{\text{eff}}}\right)^{-3}, \qquad (13)$$

where $k_0 = k_z(0)$ is the spring constant at zero offset. We estimate from Equation 13 that the spring constant of the qPlus sensor can be determined with less than 2% relative standard uncertainty for moderate tip offsets (less than ±100 μm with this method, see Appendix section).

Finally, the agreement between experiment and theory suggests that the spring constant of the tuning fork can be predicted reasonably well from the geometry and Young's modulus of the tine, being careful to include the contribution of the peaked ridge. The cross-section geometry can be determined by cleaving a tine as shown in Figure 1. Adopting this approach for the E158 tuning fork, we predict $EI = 9.20 \times 10^{-6}$ N·m^2 and $k_z = 2000 \pm 130$ N/m, where the dominant uncertainty is an estimated ±50 μm in the effective length due to the non-ideal boundary condition. This approach could be used for tuning forks other than the E158 with an estimated uncertainty of 10%.

Discussion

Because of their development for consumer timing applications, we can expect very little variation in the mechanical properties of a given commercial tuning fork. Some additional variables are introduced, however, by the attachment of a tip and the mounting of the sensor. Provided the tip height is sufficiently small (approximately less than 400 μm) and the mounting of the sensor is consistent, the additional variables can be determined from the plane-view geometry. We estimate that the nominal spring constant of the E158 qPlus sensor is 1902 ± 29 N/m, with an effective length of 2443 ± 21 μm. This spring constant, however, can be significantly higher if the base of the tuning fork is also constrained by the glue, also reducing the effective length of the beam. We note that while this value is significantly higher than the commonly-assumed spring constant of 1800 N/m [1], an estimate that gets significantly worse if the tip is inset from the end of the beam; the estimate is accurate for tips offset by about 50 μm from the end of the tine. Our values are not consistent with the range of 1480–1708 N/m estimated by Falter et al. [29]. We expect that complications from the gluing of tips between the tuning fork tine and load cell may have contributed to the poor agreement between theory and experiment found in [29]. On the other hand, the nanoindentation experiments presented here are highly reproducible and demonstrate excellent agreement with the theoretical model. There is, however, some potential for further work examining the effect of the mounting on the qPlus spring constant. We have observed a small variation (less than 3%) in stiffness by testing at a lateral offset from the beam axis.

Finally, we note that for sufficiently long tips, the compliance of the tip contributes to the parasitic tip motion [32,33]. This, in turn, influences the spring constant and force spectroscopy results presented here. To quantify the effect of the tip compliance, we construct a finite element model corresponding to our beam model and 50 μm diameter tungsten wire tip. The tip was first modelled as a rigid domain; the inertial loading of the beam gives results consistent with our analytical model. The rigid constraint was then removed, allowing the tungsten tip to deform elastically. Comparing the results for elastic and rigid tip models, we find the effect of tip compliance is negligible for tip heights below 400 μm, contributing about 1% to total parasitic tip motion and less than 0.05% to k_z. This effect becomes more pronounced for tips exceeding 750 μm, contributing over 25% to the overall parasitic tip motion and over 1% to k_z. As such, the use of shorter tips allows the parasitic tip motion to be related to the bending of the tine with negligible contribution from tip compliance.

Conclusion

In summary, we have developed a mathematically rigorous model of the qPlus sensor that includes the effect of finite tip lengths on the reconstructed tip–sample force in ncAFM. A grid spectroscopy simulation with a Morse potential shows that significant errors in the force reconstruction occur for tip heights greater than 400 μm. A quasi-static nanoindentation method is used to validate Bernoulli–Euler beam theory with fixed-free boundary conditions for modeling the flexure of the tuning fork tine. Indentation data provides the effective length, flexural rigidity, and nominal spring constant of the tine with an estimated uncertainty of 2%. Finally, we have proposed two methods for estimating the spring constants of qPlus sensors with finite tips. The first is to extrapolate the nominal value provided for the E158 for a given measured tip offset. This method has an estimated uncertainty in the neighborhood of 2%. The second is simply to estimate the spring constant from the Young's modulus and geometry of the tuning fork, taking care to measure the dimensions of the cross section. We estimate the uncertainty in this method is closer to 10%, which comes primarily from limited knowledge of the effective cantilever length.

Appendix

Discretization of the Euler–Bernoulli Equation

The process by which the partial differential equation governing the continuous tuning fork tine is reduced into a set of ordinary differential equations is referred to as discretization and is briefly described here. The process involves first solving for the normal eigenmodes of the cantilever for the case of $V = 0$ and second, using the unperturbed normal modes as a basis for the discretization.

The normal modes of the cantilever are determined by substituting $V = 0$ and $w(X,t) = \Phi(X)\exp(i\omega t)$ into Equation 3. The nontrivial solutions correspond to the roots of the characteristic equation

$$\begin{aligned} &1+\cos\beta\cosh\beta \\ &+\mathcal{M}\beta\left(\cos\beta\sinh\beta-\sin\beta\cosh\beta\right) \\ &-\mathcal{J}\beta^3\left(\sin\beta\cosh\beta+\cos\beta\sinh\beta\right) \\ &+\mathcal{M}\mathcal{J}\beta^4\left(1-\cos\beta\cosh\beta\right)=0\,, \end{aligned} \tag{14}$$

where $\mathcal{M} = m/(\mu L)$ and $\mathcal{J} = J_\mathrm{P}/(\mu L^3)$, and the dispersion relation is

$$\omega^2 = \frac{EI\beta^4}{\mu L^4}\,. \tag{15}$$

The eigenfunctions are given by

$$\begin{aligned} \Phi(X) &= \cos\beta X-\cosh\beta X-\sigma\left(\sin\beta X-\sinh\beta X\right), \\ \sigma &= \frac{\cos\beta+\cosh\beta-\mathcal{J}\beta^3\left(\sin\beta+\sinh\beta\right)}{\sin\beta+\sinh\beta+\mathcal{J}\beta^3\left(\cos\beta+\cosh\beta\right)}\,. \end{aligned} \tag{16}$$

There are countably-infinite solutions to Equation 14, which form an admissible basis for a Galerkin discretization [38] of Equation 3. Equation 5 follows from a single-term truncation.

Uncertainty Estimates

In this section we provide an analysis of the uncertainty in indentation measurements. The nanoindenter measures force F_I vs indentation δ at a specified displacement for the distal edge of the tuning fork tine. Let $F_\mathrm{I} = C_F\hat{F}_\mathrm{I}$ and $\delta = C_\delta\hat{\delta}$ where C_F and C_δ are calibration constants, both of which are estimated to have 1% relative standard uncertainties, denoted u_{C_F} and u_{C_δ}, respectively. Finally, we estimate a ±5 μm uncertainty in the positioning of the indenter tip with respect to the distal edge, which we denote U_E. Relative uncertainty estimates are summarised in Table 3.

Table 3: Relative uncertainty contributions. Type A estimates correspond to the indentation data from the qPlus A sensor.

source	$u_{k_z}(B=0)$	u_{EI}	u_{L_eff}
indenter calibration	0.014	0.014	0.0067
distal edge position	0.0061	0	0.0020
type A	0.0011	0.0031	0.0011

Let u refer to the standard relative uncertainty of a specified parameter. The relative standard uncertainty u_{k_z} in k_z is estimated by

$$\begin{aligned} u_{k_z}^2 &= u_{C_F}^2+u_{C_\delta}^2+u_{\mathrm{TypeA}}^2 \\ &\quad+\left(\frac{3U_\mathrm{E}}{L_\mathrm{eff}}\right)^2+\left[\frac{3B}{L_\mathrm{eff}+B}\right]^2\left(u_B^2+u_{L_\mathrm{eff}}^2\right), \end{aligned} \tag{17}$$

where $u_{k_z}^\mathrm{A}$ represents the type-A (statistical) uncertainty estimated from the regression. The uncertainty in the flexural rigidity is estimated by

$$u_{EI} = u_{C_F}^2+u_{C_\delta}^2+\left(3u_{EI,\mathrm{A}}\right)^2, \tag{18}$$

where, $u_{EI,\mathrm{A}}$ represents the type-A uncertainty in EI, and the uncertainty in the effective length is estimated by

$$u_{L_\mathrm{eff}}^2 = \frac{2}{9}\left(u_{C_F}^2+u_{C_\delta}^2\right)+u_{L_\mathrm{eff},\mathrm{A}}^2+\left(\frac{U_\mathrm{E}}{L_\mathrm{eff}}\right)^2. \tag{19}$$

References

1. Giessibl, F. J.; Hembacher, S.; Bielefeldt, H.; Mannhart, J. *Science* **2000,** *289,* 422–425. doi:10.1126/science.289.5478.422
2. Sugimoto, Y.; Pou, P.; Abe, M.; Jelinek, P.; Pérez, R.; Morita, S.; Custance, O. *Nature* **2007,** *446,* 64–67. doi:10.1038/nature05530
3. Gross, L.; Mohn, F.; Moll, N.; Liljeroth, P.; Meyer, G. *Science* **2009,** *325,* 1110–1114. doi:10.1126/science.1176210
4. Ebeling, D.; Oesterhelt, F.; Hölscher, H. *Appl. Phys. Lett.* **2009,** *95,* 013701. doi:10.1063/1.3152771
5. Sweetman, A.; Jarvis, S.; Danza, R.; Bamidele, J.; Gangopadhyay, S.; Shaw, G. A.; Kantorovich, L.; Moriarty, P. *Phys. Rev. Lett.* **2011,** *106,* 136101. doi:10.1103/PhysRevLett.106.136101
6. Qin, Y.; Reifenberger, R. *Rev. Sci. Instrum.* **2007,** *78,* 063704. doi:10.1063/1.2743166
7. Giessibl, F. J. *Appl. Phys. Lett.* **1998,** *73,* 3956. doi:10.1063/1.122948
8. Certain commercial equipment, instruments, or materials (or suppliers, or software, etc.) are identified in this paper to foster understanding. Such identification does not imply recommendation or endorsement by the National Institute of Standards and Technology, nor does it imply that the materials or equipment identified are necessarily the best available for the purpose.
9. Melcher, J. Eigenvalue veering in quartz tuning fork sensors and its effect on dynamic atomic force microscopy. In *Proc. ASME 2014 IDETC,* Buffalo, NY, USA, Aug 17–20, 2014; ASME: New York, NY, U.S.A., 2014; V004T09A033.
10. Pielmeier, F.; Giessibl, F. J. *Phys. Rev. Lett.* **2013,** *110,* 266101. doi:10.1103/PhysRevLett.110.266101
11. Melcher, J.; Stirling, J.; Guzmán Cervantes, F.; Pratt, J. R.; Shaw, G. A. *Appl. Phys. Lett.* **2014,** *105,* 233109. doi:10.1063/1.4903801
12. Albrecht, T. R.; Grütter, P.; Horne, D.; Rugar, D. *J. Appl. Phys.* **1991,** *69,* 668–673. doi:10.1063/1.347347
13. Durig, Ü.; Züger, O.; Stalder, A. *J. Appl. Phys.* **1992,** *72,* 1778. doi:10.1063/1.352348
14. Giessibl, F. J. *Phys. Rev. B* **1997,** *56,* 16010–16015. doi:10.1103/PhysRevB.56.16010
15. Giessibl, F. J. *Appl. Phys. Lett.* **2001,** *78,* 123. doi:10.1063/1.1335546
16. Hölscher, H.; Gotsmann, B.; Schirmeisen, A. *Phys. Rev. B* **2003,** *68,* 153401. doi:10.1103/PhysRevB.68.153401
17. Sader, J. E.; Jarvis, S. P. *Appl. Phys. Lett.* **2004,** *84,* 1801. doi:10.1063/1.1667267
18. Welker, J.; Illek, E.; Giessibl, F. J. *Beilstein J. Nanotechnol.* **2012,** *3,* 238–248. doi:10.3762/bjnano.3.27
19. Pratt, J. R.; Kramar, J. A.; Newell, D. B.; Smith, D. T. *Meas. Sci. Technol.* **2005,** *16,* 2129–2137. doi:10.1088/0957-0233/16/11/002
20. Kim, M.-S.; Choi, J.-H.; Park, Y.-K.; Kim, J.-H. *Metrologia* **2006,** *43,* 389–395. doi:10.1088/0026-1394/43/5/008
21. Shaw, G. A.; Kramar, J.; Pratt, J. *Exp. Mech.* **2006,** *47,* 143–151. doi:10.1007/s11340-006-9394-9
22. Langlois, E. D.; Shaw, G. A.; Kramar, J. A.; Pratt, J. R.; Hurley, D. C. *Rev. Sci. Instrum.* **2007,** *78,* 093705. doi:10.1063/1.2785413
23. Clifford, C. A.; Seah, M. P. *Meas. Sci. Technol.* **2009,** *20,* 125501. doi:10.1088/0957-0233/20/12/125501
24. Kim, M.-S.; Pratt, J. R.; Brand, U.; Jones, C. W. *Metrologia* **2012,** *49,* 70–81. doi:10.1088/0026-1394/49/1/011
25. Simon, G. H.; Heyde, M.; Rust, H.-P. *Nanotechnology* **2007,** *18,* 255503. doi:10.1088/0957-4484/18/25/255503
26. Morita, S.; Giessibl, F. J.; Wiesendanger, S., Eds. *Noncontact Atomic Force Microscopy;* Springer: Berlin, Germany, 2009; Vol. 2, p 131.
27. van Vörden, D.; Lange, M.; Schmuck, M.; Schmidt, N.; Möller, R. *Beilstein J. Nanotechnol.* **2012,** *3,* 809–816. doi:10.3762/bjnano.3.90
28. Berger, J.; Švec, M.; Müller, M.; Ledinský, M.; Fejfar, A.; Jelínek, P.; Majzik, Z. *Beilstein J. Nanotechnol.* **2013,** *4,* 1–9. doi:10.3762/bjnano.4.1
29. Falter, J.; Stiefermann, M.; Langewisch, G.; Schurig, P.; Hölscher, H.; Fuchs, H.; Schirmeisen, A. *Beilstein J. Nanotechnol.* **2014,** *5,* 507–516. doi:10.3762/bjnano.5.59
30. Hedlund, C.; Lindberg, U.; Bucht, U.; Soderkvist, J. *J. Micromech. Microeng.* **1993,** *3,* 65–73. doi:10.1088/0960-1317/3/2/006
31. Stirling, J.; Shaw, G. A. *Beilstein J. Nanotechnol.* **2013,** *4,* 10–19. doi:10.3762/bjnano.4.2
32. Higuchi, S.; Kuramochi, H.; Kubo, O.; Masuda, S.; Shingaya, Y.; Aono, M.; Nakayama, T. *Rev. Sci. Instrum.* **2011,** *82,* 043701. doi:10.1063/1.3569765
33. Nakayama, T.; Kubo, O.; Shingaya, Y.; Higuchi, S.; Hasegawa, T.; Jiang, C.-S.; Okuda, T.; Kuwahara, Y.; Takami, K.; Aono, M. *Adv. Mater.* **2012,** *24,* 1675. doi:10.1002/adma.201200257
34. Melcher, J.; Hu, S.; Raman, A. *Appl. Phys. Lett.* **2007,** *91,* 053101. doi:10.1063/1.2767173
35. Hölscher, H.; Langkat, S. M.; Schwarz, A.; Wiesendanger, R. *Appl. Phys. Lett.* **2002,** *81,* 4428. doi:10.1063/1.1525056
36. Pérez, R.; Štich, I.; Payne, M. C.; Terakura, K. *Phys. Rev. B* **1998,** *58,* 10835–10849. doi:10.1103/PhysRevB.58.10835
37. Seugling, R. M.; Pratt, J. R. Traceable force metrology for micronewton level calibration. In *Proc. ASPE 2004 Annual Meeting,* 2004; pp 3–6.
38. Meirovitch, L. *Principles and Techniques of Vibrations;* Prentice Hall: Upper Saddle River, NJ, U.S.A., 1997.

License and Terms

The definitive version of this article is the electronic one which can be found at:
doi:10.3762/bjnano.6.177

BEILSTEIN JOURNAL OF NANOTECHNOLOGY

Electrospray deposition of organic molecules on bulk insulator surfaces

Antoine Hinaut*, Rémy Pawlak, Ernst Meyer* and Thilo Glatzel

Full Research Paper

Open Access

Address:
Department of Physics, University of Basel, Klingelbergstrasse 82,
4056 Basel, Switzerland

Email:
Antoine Hinaut* - antoine.hinaut@unibas.ch; Ernst Meyer* -
ernst.meyer@unibas.ch

* Corresponding author

Keywords:
adsorption; electrospray; insulating surface; large molecules;
non-contact AFM; ultra-high vacuum (UHV)

Beilstein J. Nanotechnol. **2015,** *6,* 1927–1934.
doi:10.3762/bjnano.6.195

Received: 12 May 2015
Accepted: 25 August 2015
Published: 18 September 2015

This article is part of the Thematic Series "Advanced atomic force
microscopy techniques III".

Associate Editor: A. Gölzhäuser

Abstract

Large organic molecules are of important interest for organic-based devices such as hybrid photovoltaics or molecular electronics. Knowing their adsorption geometries and electronic structures allows to design and predict macroscopic device properties. Fundamental investigations in ultra-high vacuum (UHV) are thus mandatory to analyze and engineer processes in this prospects. With increasing size, complexity or chemical reactivity, depositing molecules by thermal evaporation becomes challenging. A recent way to deposit molecules in clean conditions is Electrospray Ionization (ESI). ESI keeps the possibility to work with large molecules, to introduce them in vacuum, and to deposit them on a large variety of surfaces. Here, ESI has been successfully applied to deposit triply fused porphyrin molecules on an insulating KBr(001) surface in UHV environment. Different deposition coverages have been obtained and characterization of the surface by in-situ atomic force microscopy working in the non-contact mode shows details of the molecular structures adsorbed on the surface. We show that UHV-ESI, can be performed on insulating surfaces in the sub-monolayer regime and to single molecules which opens the possibility to study a variety of complex molecules.

Introduction

Large complex molecules with tunable electronic properties are building block candidates for functional materials with special electrochemical and photophysical properties, which are of fundamental interest for many applications such as hybrid-photovoltaic [1] or molecular electronics [2]. Information at the single molecular level, even if challenging, is required to foresee the interplay between nanoscale structures and geometries and the device properties. For reliable investigations of such systems, a well defined environment is necessary and therefore ultra-high vacuum (UHV) conditions are required for these fundamental studies. However, thermal evaporation, the most commonly employed technique under UHV conditions, may lead to a fragmentation of large molecules generally happening before reaching the sublimation temperature. Therefore the study of such complex molecules with high resolution and precision is hindered. Recently, other deposition techniques have been introduced, e.g., direct deposition from a liquid solution (droplet casting) on a freshly prepared surface or pulsed valve deposition in UHV. Although these techniques are compatible with molecular resolution, the pollution from solvents remains a problem [3-5].

Electrospray ionization (ESI), first developed by Fenn et al. [6] allows for the introduction of large organic molecules in vacuum. Originally developed for mass spectrometry and protein studies, it has since been used with many other types of molecules. In ESI, molecules are directly ionized from solution, allowing to select and analyze them with electrostatic lenses. Following this initial use, numerous experimental setups have been built to deposit such ionized molecules on surfaces. For such ESI deposition systems, the combination with filtering devices, made of quadrupoles, octopoles and other electrostatic stages allows one to filter ions and guide them towards the sample surface [7-10]. An advantage of theses systems, in addition to the selection of the ion species, is the use of a soft landing deposition where additional electrostatic lenses are used to reduce the kinetic energy of the molecules [11-13]. Moreover it lowers the chance of fragmentation by impacting surfaces. However the complexity of the setup as well as the proper adjustment somehow limits their usability.

An easy and commercially available ESI system has already proven its capability to deposit simple [14,15] or more complex molecules [16-20] on various surfaces such as metals or TiO_2. The setup is aligned in straight line and no selection or deviation elements are used. As a result, all species introduced in vacuum that are not pumped are directed towards the surface. Consequently, the use of contaminant-free solvent, as well as appropriate spray parameters is primordial to successful deposition of single molecules.

With the prospect of studying the intrinsic properties of large molecules, their decoupling from the metal surface is desirable. Deposition and analysis on insulating films or crystals is thus mandatory and requires high resolution imaging. Therefore, for the characterization at the atomic-scale, atomic force microscopy (AFM) is mandatory. Numerous experimental AFM studies have shown the possibility to image molecular islands [21-27], small aggregates [28], single molecules [29] as well as trapped single molecules [30-32] at room temperature on insulating surfaces. The use of ESI now allows one to study even larger and more complex molecules which are more suitable for future devices and could incorporate additional functions and anchoring groups.

In this work we present the adaptation of a UHV-ESI system to deposit triply fused porphyrin molecules on a bulk insulator KBr(001) sample and the analysis of theses deposits by high resolution AFM measurements at RT and under UHV conditions. First, it is shown that the applied solvents do not impact the deposits and the measurements. The coverage of the molecules on the bulk insulator surface can be controlled and adopted to the needs of the AFM measurement. However, at large coverage, charging of the surface was observed, which could be successfully overcome by a moderate annealing of the surface. The formation of various molecular assemblies was achieved and even isolated molecules could be analyzed at room temperature.

Results and Discussion

UHV-ESI of solvent

UHV-ESI has been performed with a modified commercial MolecularSpray setup [33], of which a scheme is shown in Figure 1. The mixture of solvent and molecules is introduced by a syringe pump and a needle (1) into the first vacuum chamber (3) trough a capillary (2) by applying a bias of several kilovolts (1 to 5 kV). Behind the entrance capillary, three chambers (3, 4, 5) are used to pump solvent molecules and to reach the high vacuum level in the preparation chamber (7). The extra vacuum chamber (6) was added to further decrease the vacuum level during deposition, typical vacuum ranges are indicated in millibars. Two type of pumps are employed, i.e., primary and turbo pumps and the chamber separations are skimmer cones for the first two chambers and inlets for the others.

To confirm that residual solvent molecules introduced with the UHV-ESI process will not interfere with adsorbed molecules on the surface, we performed a deposition of the solvent solution only, i.e., toluene/isopropanol in the ratio 2:1 on a clean KBr(001) surface. Figure 2a shows a topography image

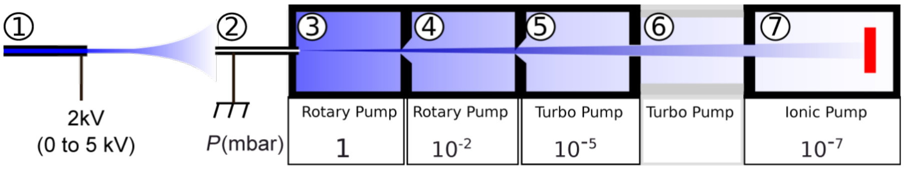

Figure 1: Scheme of the commercial ESI setup [33] (1 to 5) connected to the UHV chamber (7), i.e., sample preparation chamber. The additional vacuum chamber (6) was added to further enhance the performance of the deposition system.

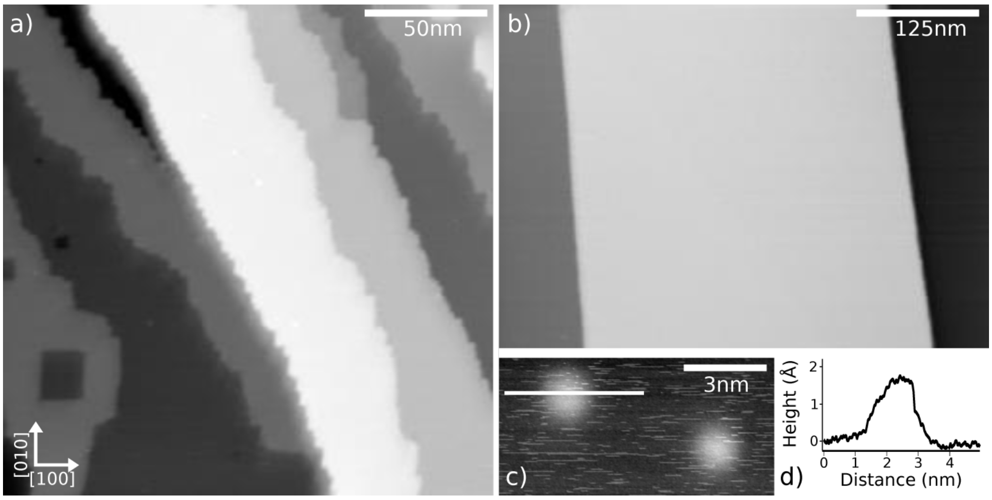

Figure 2: a) Topography image of the KBr(001) surface after the application of UHV-ESI with a mixture of toluene/isopropanol (2:1) over the course of 30 min. b) Topography image of clean KBr(001) surface obtained after UHV cleavage and following annealing at 400 K for 1h. c) Topography image of two protrusions with a profile (c) along the line. Parameters: a) *A* = 5 nm, Δ*f* = −10 Hz, b) *A* = 2 nm, Δ*f* = −60 Hz, c) *A* = 2 nm, Δ*f* = −25 Hz.

acquired by nc-AFM at room temperature on a KBr(001) surface after a total time of 30 min of UHV-ESI deposition of the pure solvent. This is a long exposure time compared to the generally applied molecules deposition time of 1–5 min. As can be seen, terraces remain large and flat, and step-edges remain clean from adsorbates. However, some pits are observed on the terraces and step-edges present lots of kinks. Such pits are known from the bombardment of ionic surfaces by electrons or UV light and are attributed to a reorganization of color centers towards the surface [34].

The surface should be compared to the clean, UHV prepared, KBr(001) surface as presented in Figure 2b. Here, large terraces and step-edges aligned along the non-polar directions, e.g., [010] or [100] can be observed. Some protrusions can also be found on the surface, however their number remains small. In Figure 2b, a zoom on two of these protrusions is presented with a profile in Figure 2c. The protrusions all appear with similar shape, i.e., circular with a diameter of 2 nm maximum. Since the solvents we used were high purity solvents, excluding any pollution, these protrusions can be attributed to solvent molecules or clusters. Another indication of the presence of the solvent are the spikes observed on this image. Most probably solvent molecules are still on the surface but are diffusing to fast for nc-AFM imaging.

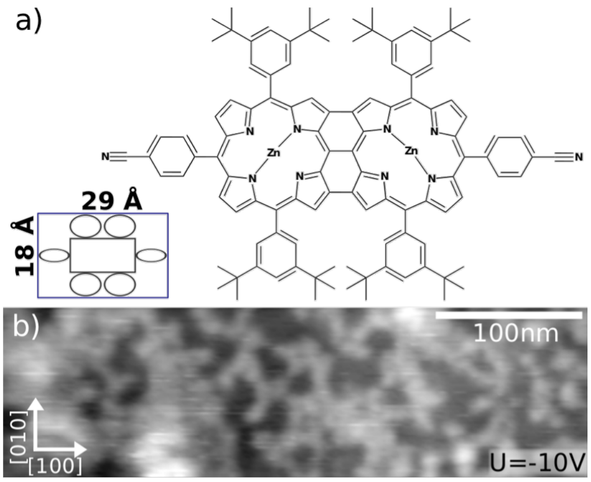

Figure 3: a) Chemical structure of the used triply fused diporphyrin molecule derivative prepared according to the synthetic protocols by D. Bonifazi et al. [39]. The inset shows a molecular scheme and the dimensions. b) Topography image after the UHV-ESI deposition of the porphyrins on KBr(001) for 5 min. Scan parameter: *A* = 2 nm, Δ*f* = −25 Hz, *U* = −10 V.

Large coverage UHV-ESI of triply fused diporphyrins

The complex porphyrin-based molecules under study are schematically shown in Figure 3a. It is a triply fused diporphyrin molecule including two 3-cyanophenyl groups and Zn metal cores. Similar molecules have already been thermally deposited on surfaces in UHV and are known to form self-assemblies on metallic substrates [35,36]. These molecules are rather complex compared to others, however the deposit by UHV-ESI can still be compared with the thermally deposited ones. Furthermore, the 3-cyanophenyl groups are known to enhance the binding to ionic substrates by electrostatic interaction [37,38]. For the UHV-ESI deposition, molecules were diluted at 1 µL/mL in a mixture of toluene and isopropanol with a 2:1 ratio. Deposition was performed for 5 min at a constant rate of injected solution of 5 µL/min, a maximum applied high voltage of 1.5 kV, and a pressure in the vacuum chamber below 2×10^{-7} mbar.

A topographic image acquired by nc-AFM after UHV-ESI deposition of the diporphyrin on the clean KBr(001) surface is displayed in Figure 3b. Large molecular features are homogeneously distributed all over the surface and appear up to 3 nm high. However, no clear organization of the molecules was observed. Large electrostatic forces have been observed and measured via frequency shift versus voltage curves $df(V)$ [40] after the deposition process. These could not be compensated during measurements by applying a bias voltage of up to ±10 V, which is the limit of the AFM system. These large electrostatic forces induced difficult scan conditions and we were not able to study the organization of the molecules in more detail. Indeed, surfaces charges of bulk insulator samples have already been studied in detail [41,42]. Due to cleavage many charges can be created resulting in large electrostatic forces. Sample preparation with soft annealing is well-established and leads to only a few remaining isolated charges [42]. Since the sample was prepared with such procedure before UHV-ESI deposition, we thus attribute this charging to the deposition process. During the deposition of only the solvent, we have not observed charging of the surface (Figure 2), whereas the presence of molecules in the solution always induces the surface charging for high coverage. Since the deposition time (minutes) is short compared to the charge compensation time (days), a charged surface is obtained. In our setup, a positive bias is applied to the solution containing the diporphyrin molecules. Therefore, droplets produced during ESI as well as the molecules reaching the surface are positively charged. This positive charging of the surface is in agreement with the estimated large negative bias voltages needed to compensate the surface potential of approximately −30 V.

A major disadvantage of UHV-ESI for insulating surfaces is thus the surface charging of the crystals, increasing with the deposition time and resulting in difficult scan conditions. High electrostatic forces in presence are also impacting the self-assembly of the molecules resulting in the molecular domains observed. Furthermore, above a certain amount, surface charges act as electrostatic barriers and prevent the landing of further molecules and high coverages are difficult to obtain.

Triply fused diporphyrins UHV-ESI after annealing

Annealing of the sample was performed at 350 K for 1 h to remove the surface charges. Electrostatic force compensation was then reduced to −1.1 V, which is typical for KBr surfaces [43]. The topography image shown in Figure 4 reveals the surface modification due to the annealing in presence of the molecules. Indeed, pits, hills and a circular shape for the step-edges are observed instead of straight step-edges that are normally observed. Molecules are adsorbed at KBr step-edges (arrow 1) and also form small aggregates (arrow 3) at terraces or even larger islands (arrow 4). Their presence at step-edges is visible in Figure 4 as bright lines. Exceptions are step-edges oriented along the non-polar [010] and [100] directions (arrow 2), which are standard directions for KBr(001). The rounding of the normally straight step-edges is induced by the surface annealing in presence of molecules. Such phenomena have already been observed and described for truxene molecules containing similar cyanophenyl functional groups [31]. The circular shapes are created during deposition and annealing and allow the adsorbed molecules to be stabilized by reaching an overall energetic minimum. A result of this is the creation and stabilization of KBr pits and islands, which are not present on the untreated surface. Molecular islands can therefore be observed in theses pits [30] or on the KBr islands and present distinct height differences.

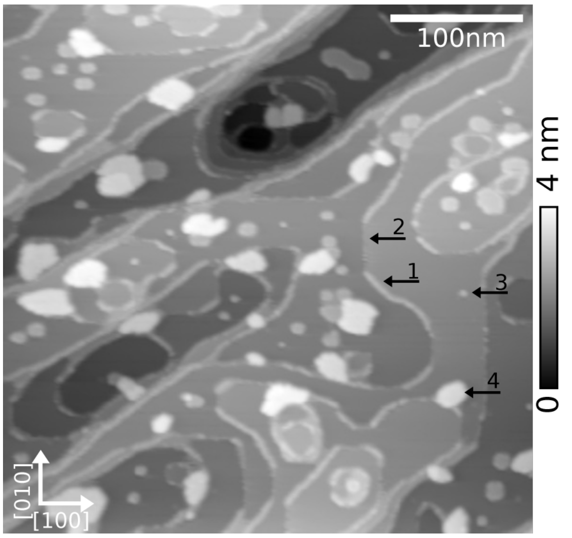

Figure 4: Topography image (400 × 400 nm^2) of diporphyrins on KBr(001) after 1 h of annealing at 350 K. Different areas: covered (1) and non-covered (2) step edges, small aggregates (3), and molecular islands (4). Parameters: A = 4 nm, Δf = −10 Hz.

A more detailed topography image of such an island is presented in Figure 5a with the corresponding dissipation image (Figure 5b). Using the dissipation image, the identification of the areas with and without molecules is facilitated due to two different contrasts (bright or dark). This phenomenon was already related [24]. The KBr terraces present a brighter contrast and molecules are observed in form of islands, at step-edges, in small aggregates and trapped in regions where successive step-edges are close. The profile presented in Figure 5c is

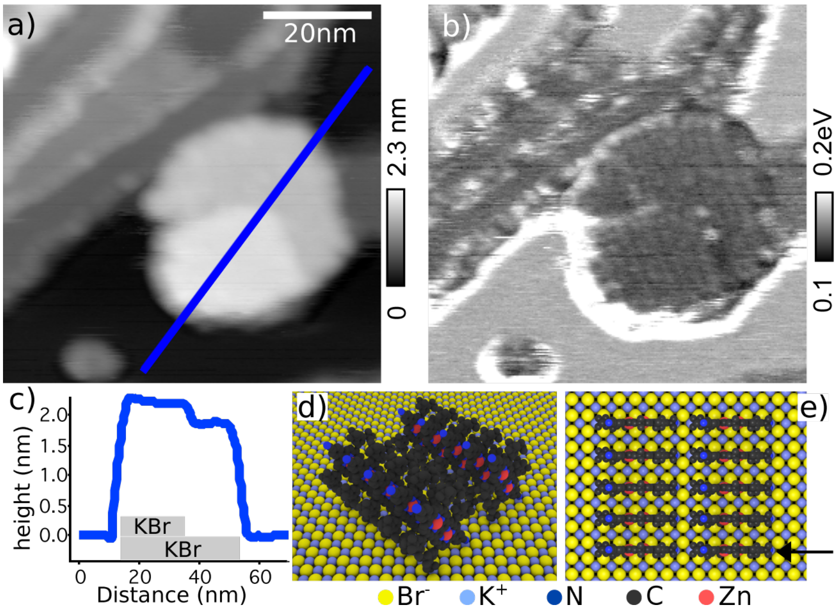

Figure 5: a) Topography image of a diporphyrin island on KBr(001). b) Corresponding dissipation image. c) Island profile, blue line in a). Scheme of the molecular arrangement in side view d) and in top view e). Black arrow point toward CN group anchored to K^+ ions. Parameters: A = 5 nm, Δf = −8 Hz.

acquired on the topography image and helps to understand the shape of the island. It shows two different heights, of 2.3 and 2.0 nm, compared to the KBr terrace. The difference corresponds to the height of a single KBr step meaning that the self-assembly partly sits on the KBr terrace and an island.

A better understanding of the molecular self-assembly is obtained by the dissipation image where single molecular rows are visible. A columnar organization of the rows with a length of 20–50 nm, and spaced by roughly 3 nm, compose the islands. This is in good agreement with the molecular size of 2.8 nm (Figure 5d,e) in a tilted position. Inside one molecular island and also for different islands, several line orientations can be observed (not shown here). Despite different tries and the intra islands resolution in the dissipation image, we were not able to achieve similar resolution in the topography images to know the exact commensurability between substrate and molecules. Few reasons can be mentioned related to a reduced imaging stability of this system. The molecules present a cyanophenyl group facing towards the tip and carrying a dipole moment which influences the electrostatic field distribution and with this also the imaging stability. Furthermore, this functional group is known to be quite flexible and will therefore, especially at room temperature conditions, prevent high-resolution imaging.

A schematic model of an island is proposed in Figure 5d and Figure 5e showing a possible molecular arrangement. In this configuration, columnar stabilization can be explained by a dominant molecule–molecule interaction by π–π-stacking [29,37,44,45]. Due to the symmetric arrangement of the two 3-cyanophenyl groups the electrostatic binding to the surface is only small and the molecular wires might easily flip or rearrange explaining the low stability in the AFM measurements and the different behaviour compared to smaller molecules [44,45]. The smaller features also visible at the surface can be attributed to molecular aggregates, but due to the high mobility at room temperature they were not investigated in more details.

Low coverage of UHV-ESI porphyrins

To enable the analysis of single molecules, annealing of the sample should be avoided to restrict diffusion processes. Different parameters that could lead to a reduced amount of deposited molecules and charges can be tuned, like reducing deposition time or molecule concentration in the solution. Furthermore, deposition of solvent molecules should be reduced to a minimum which was achieved by the implementation of an additional pumping chamber to the spray setup (Figure 1), which helps to reduce the base pressure at the sample during spray deposition by an order of magnitude.

Figure 6 presents the surface obtained after diporphyrin deposition at low coverage by UHV-ESI. Topography images is acquired at the 2nd flexural mode which allows one to enhance the sensitivity to short range forces by using small oscillation amplitude (400 pm) [46]. The topography shows two terraces

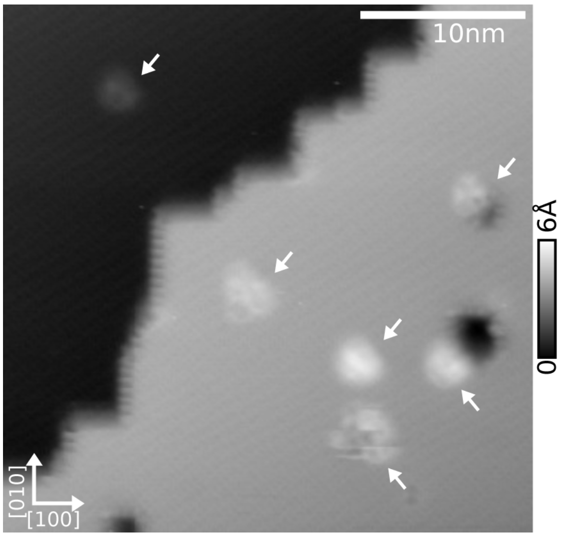

Figure 6: Topography image (40 × 40 nm^2) of the KBr(001) surface with a low coverage of diporphyrin molecules deposited by UHV-ESI for 2 min. Parameters: f_{2nd} = 1.02 MHz, A_{2nd} = 400 pm, Δf_{2nd} = −57 Hz.

separated by a kinked step-edge. Pits similar to what can be obtained after electron irradiation of the surface are visible [47]. Sample charging was not observed and bias remained in the ±1 V range. Small objects with sizes compatible with single molecules decorate both terraces. Due to the shorter deposition time, 2 min compared to 30 min in Figure 2, solvent molecules should only appear as traces on the surface and are unlikely to be observed here. However, two different contrasts have been observed, a stable and a slightly less stable one as can be seen in the distorted molecule at the bottom part of the image. Some of the single molecules are attached to the pits corners.

A high resolution image of a stable molecule presenting even the internal structure is shown in Figure 7. The image was acquired on the same sample but at another area. The simple superposition of the molecule drawing, is used to show that the observed object size fits with a single molecule. The molecule lay flat at the surface and binds through the 3-cyanophenyl groups to the KBr(001) substrate [29,31] indicated by the two symmetric protrusions. The two elongated features are attributable to the four 3,5-di(*tert*-butyl)phenyl moieties of the diporphyrin having a slightly higher topographic signature.

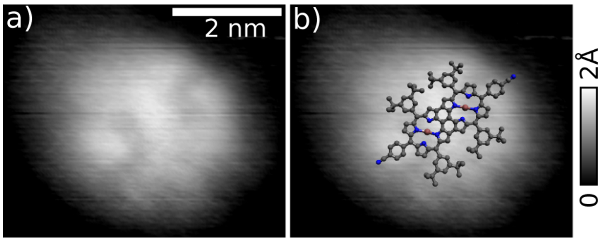

Figure 7: a) High resolution topography image of a single diporphyrin on KBr(001) at room temperature. b) Same image with added molecular model. Parameters: f_{2nd} = 1.02 MHz, A_{2nd} = 400 pm, Δf_{2nd} = −70 Hz.

Conclusion

The deposition of large functionalized molecules on surfaces with low contamination is important for fundamental studies. We show that UHV-ESI deposition, where molecules are contained in solution, fulfill theses conditions on insulating surfaces. This leads to the possibility to access molecular electronic properties at the single molecule level with scanning probe microscopy. We first demonstrated that solvent deposition from ESI has a weak influence on the KBr(001) surface. Then a complex molecule based on a triply fused diporphyrin was successfully deposited at various coverages on the KBr(001) surface. For a coverage of more than a few isolated molecules per 10 × 10 nm^2 we have observed charging of the sample due to ion deposition. This charging can be easily overcome by annealing, leading to the formation of large molecular islands. We characterized theses islands showing molecular assemblies stabilized by π–π stacking organization and anchoring through the cyano group of the molecules and K$^+$ ions of the surface. To achieve single molecule deposition, we added a pumping chamber in the setup that lowered the number of molecules reaching the surface. Due to the small amount of species on the surface we lowered the charging effect. In this way, we demonstrated the deposition of single molecules, down to few units per 100 × 100 nm^2. For some adsorption geometries, where the molecules are laying flat on the surface, we obtained intra-molecular resolution at room temperature.

Experimental

All experiments were performed under UHV conditions ($p < 10^{-10}$ bar) with our home-built non-contact atomic force microscope (nc-AFM), operating at room temperature (RT) [48]. Bulk insulator KBr(001) crystals surfaces (from MaTeck GmbH) were prepared in situ by cleavage followed with an annealing at 400 K for 1 h to remove residual charges. PPP-NCL cantilevers (Nanosensor) with typical resonance frequency of $f_{1st} \approx 170$ kHz and first harmonic of $f_{2nd} \approx 1$ MHz were used. Sensor preparation consists of annealing for 1 h at 400 K and tip sputtering for 90 s at 680 eV at an Ar$^+$ pressure of $p = 3 \times 10^{-6}$ bar.

The ESI setup (Figure 1) is connected to the UHV preparation chamber of the system. It is a commercial system from MolecularSpray [14,33]. After the spray is formed in air, highly charged droplets [49-51] enter by a capillary into the differential pumping system composed of the three chambers separated by leak orifices. During this differential pumping system, initial droplets undergo successive droplet solvent pumping and coulomb fission leading to ionized molecules only. The spray quality in air was controlled during deposition with a camera. The base pressure in the sample chamber was in the low 10^{-10} mbar range, and increase to low $p \approx 10^{-7}$ mbar during spray deposition. Typical parameters for UHV-ESI are 1.3–2.0 kV, sometimes adjusted to maintain spray quality during deposition. The deposition time was tuned to obtain different coverages between 1–30 min at controlled flux, by the use of a syringe pump, of 2–10 μL/min. The molecules were diluted in a solution of toluene/isopropanol made from high purity solvents (Sigma-Aldrich) with a ratio of 2:1. Molecule concentration in solution was 1 μg/mL.

Molecules, see Figure 3, are based on a triply fused double porphyrin and include two metallic core atoms (zinc) and two cyanophenyl groups. More information on the synthesis of the molecules can be found in [35,36,39]

Acknowledgements

The authors thank Prof. D. Bonifazi and Prof. F. Diederich for the synthesis of the molecules. The Swiss National Science Foundation (SNF), the Swiss Nanoscience Institute (SNI), and the Joint Swiss–Polish Research Programme PSPB-085/2010 are acknowledged for financial support. All images have been processed with the WSxM [52] software.

References

1. O'Regan, B.; Grätzel, M. *Nature* **1991,** *353,* 737–740. doi:10.1038/353737a0
2. Joachim, C.; Gimzewski, J. K.; Aviram, A. *Nature* **2000,** *408,* 541–548. doi:10.1038/35046000
3. Pang, C. L.; Ishibashi, T.-a.; Onishi, H. *Jpn. J. Appl. Phys.* **2005,** *44,* 5438. doi:10.1143/JJAP.44.5438
4. Tanaka, H.; Kawai, T. *J. Vac. Sci. Technol., B* **1997,** *15,* 602–604. doi:10.1116/1.589299
5. Zambelli, T.; Boutayeb, Y.; Gayral, F.; Lagoute, J.; Girdhar, N. K.; Gourdon, A.; Gauthier, S.; Blanco, M.-J.; Chambron, J.-C.; Heitz, V.; Sauvage, J.-P. *Int. J. Nanosci.* **2004,** *03,* 331–341. doi:10.1142/S0219581X04002115
6. Fenn, J. B.; Mann, M.; Meng, C. K.; Wong, S. F.; Whitehouse, C. M. *Science* **1989,** *246,* 64–71. doi:10.1126/science.2675315
7. Rauschenbach, S.; Stadler, F. L.; Lunedei, E.; Malinowski, N.; Koltsov, S.; Costantini, G.; Kern, K. *Small* **2006,** *2,* 540–547. doi:10.1002/smll.200500479
8. Hamann, C.; Woltmann, R.; Hong, I.-P.; Hauptmann, N.; Karan, S.; Berndt, R. *Rev. Sci. Instrum.* **2011,** *82,* 033903. doi:10.1063/1.3553010
9. Kley, C. S.; Dette, C.; Rinke, G.; Patrick, C. E.; Čechal, J.; Jung, S. J.; Baur, M.; Dürr, M.; Rauschenbach, S.; Giustino, F.; Stepanow, S.; Kern, K. *Nano Lett.* **2014,** *14,* 563–569. doi:10.1021/nl403717d
10. Hauptmann, N.; Scheil, K.; Gopakumar, T. G.; Otte, F. L.; Schütt, C.; Herges, R.; Berndt, R. *J. Am. Chem. Soc.* **2013,** *135,* 8814–8817. doi:10.1021/ja4036187
11. Rauschenbach, S.; Vogelgesang, R.; Malinowski, N.; Gerlach, J. W.; Benyoucef, M.; Costantini, G.; Deng, Z.; Thontasen, N.; Kern, K. *ACS Nano* **2009,** *3,* 2901–2910. doi:10.1021/nn900022p
12. Hauptmann, N.; Hamann, C.; Tang, H.; Berndt, R. *J. Phys. Chem. C* **2013,** *117,* 9734–9738. doi:10.1021/jp311420d
13. Bodin, A.; Laloo, R.; Abeilhou, P.; Guiraud, L.; Gauthier, S.; Martrou, D. *Rev. Sci. Instrum.* **2013,** *84,* 095104. doi:10.1063/1.4818961
14. Satterley, C. J.; Perdigão, L. M. A.; Saywell, A.; Magnano, G.; Rienzo, A.; Mayor, L. C.; Dhanak, V. R.; Beton, P. H.; O'Shea, J. N. *Nanotechnology* **2007,** *18,* 455304. doi:10.1088/0957-4484/18/45/455304
15. Saywell, A.; Magnano, G.; Satterley, C. J.; Perdigão, L. M. A.; Champness, N. R.; Beton, P. H.; O'Shea, J. N. *J. Phys. Chem. C* **2008,** *112,* 7706–7709. doi:10.1021/jp7119944
16. Saywell, A.; Sprafke, J. K.; Esdaile, L. J.; Britton, A. J.; Rienzo, A.; Anderson, H. L.; O'Shea, J. N.; Beton, P. H. *Angew. Chem., Int. Ed.* **2010,** *49,* 9136–9139. doi:10.1002/anie.201004896
17. Rienzo, A.; Mayor, L. C.; Magnano, G.; Satterley, C. J.; Ataman, E.; Schnadt, J.; Schulte, K.; O'Shea, J. N. *J. Chem. Phys.* **2010,** *132,* 084703. doi:10.1063/1.3336747
18. Handrup, K.; Richards, V. J.; Weston, M.; Champness, N. R.; O'Shea, J. N. *J. Chem. Phys.* **2013,** *139,* 154708. doi:10.1063/1.4825382
19. Svatek, S. A.; Perdigão, L. M. A.; Stannard, A.; Wieland, M. B.; Kondratuk, D. V.; Anderson, H. L.; O'Shea, J. N.; Beton, P. H. *Nano Lett.* **2013,** *13,* 3391–3395. doi:10.1021/nl4017557
20. Wieland, M. B.; Perdigão, L. M. A.; Kondratuk, D. V.; O'Shea, J. N.; Anderson, H. L.; Beton, P. H. *Chem. Commun.* **2014,** *50,* 7332–7335. doi:10.1039/C4CC02629B
21. Pfeiffer, O.; Gnecco, E.; Zimmerli, L.; Maier, S.; Meyer, E.; Nony, L.; Bennewitz, R.; Diederich, F.; Fang, H.; Bonifazi, D. *J. Phys.: Conf. Ser.* **2005,** *19,* 166. doi:10.1088/1742-6596/19/1/027
22. Kunstmann, T.; Schlarb, A.; Fendrich, M.; Wagner, T.; Möller, R.; Hoffmann, R. *Phys. Rev. B* **2005,** *71,* 121403. doi:10.1103/PhysRevB.71.121403
23. Mativetsky, J. M.; Burke, S. A.; Fostner, S.; Grütter, P. *Small* **2007,** *3,* 818–821. doi:10.1002/smll.200600699
24. Hinaut, A.; Lekhal, K.; Aivazian, G.; Bataillé, S.; Gourdon, A.; Martrou, D.; Gauthier, S. *J. Phys. Chem. C* **2011,** *115,* 13338–13342. doi:10.1021/jp202873f
25. Pawlak, R.; Nony, L.; Bocquet, F.; Oison, V.; Sassi, M.; Debierre, J.-M.; Loppacher, C.; Porte, L. *J. Phys. Chem. C* **2010,** *114,* 9290–9295. doi:10.1021/jp102044u
26. Neff, J. L.; Götzen, J.; Li, E.; Marz, M.; Hoffmann-Vogel, R. *Beilstein J. Nanotechnol.* **2012,** *3,* 186–191. doi:10.3762/bjnano.3.20
27. Kittelmann, M.; Rahe, P.; Gourdon, A.; Kühnle, A. *ACS Nano* **2012,** *6,* 7406–7411. doi:10.1021/nn3025942
28. Schütte, J.; Bechstein, R.; Rohlfing, M.; Reichling, M.; Kühnle, A. *Phys. Rev. B* **2009,** *80,* 205421. doi:10.1103/PhysRevB.80.205421
29. Hinaut, A.; Pujol, A.; Chaumeton, F.; Martrou, D.; Gourdon, A.; Gauthier, S. *Beilstein J. Nanotechnol.* **2012,** *3,* 221–229. doi:10.3762/bjnano.3.25
30. Nony, L.; Gnecco, E.; Baratoff, A.; Alkauskas, A.; Bennewitz, R.; Pfeiffer, O.; Maier, S.; Wetzel, A.; Meyer, E.; Gerber, C. *Nano Lett.* **2004,** *4,* 2185–2189. doi:10.1021/nl048693v
31. Such, B.; Trevethan, T.; Glatzel, T.; Kawai, S.; Zimmerli, L.; Meyer, E.; Shluger, A. L.; Amijs, C. H. M.; de Mendoza, P.; Echavarren, A. M. *ACS Nano* **2010,** *4,* 3429–3439. doi:10.1021/nn100424g

32. Trevethan, T.; Such, B.; Glatzel, T.; Kawai, S.; Shluger, A. L.; Meyer, E.; de Mendoza, P.; Echavarren, A. M. *Small* **2011,** *7,* 1264–1270. doi:10.1002/smll.201001910
33. Molecularspray Ltd.. http://www.molecularspray.co.uk/ (accessed July 30, 2015).
34. Such, B.; Czuba, P.; Piatkowski, P.; Szymonski, M. *Surf. Sci.* **2000,** *451,* 203–207. doi:10.1016/S0039-6028(00)00028-5
35. Bonifazi, D.; Spillmann, H.; Kiebele, A.; de Wild, M.; Seiler, P.; Cheng, F.; Güntherodt, H.-J.; Jung, T.; Diederich, F. *Angew. Chem., Int. Ed.* **2004,** *43,* 4759–4763. doi:10.1002/anie.200460562
36. Bonifazi, D.; Kiebele, A.; Stöhr, M.; Cheng, F.; Jung, T.; Diederich, F.; Spillmann, H. *Adv. Funct. Mater.* **2007,** *17,* 1051–1062. doi:10.1002/adfm.200600586
37. Maier, S.; Fendt, L.-A.; Zimmerli, L.; Glatzel, T.; Pfeiffer, O.; Diederich, F.; Meyer, E. *Small* **2008,** *4,* 1115–1118. doi:10.1002/smll.200701259
38. Zimmerli, L.; Maier, S.; Glatzel, T.; Gnecco, E.; Pfeiffer, O.; Diederich, F.; Fendt, L.; Meyer, E. *J. Phys.: Conf. Ser.* **2007,** *61,* 1357. doi:10.1088/1742-6596/61/1/268
39. Bonifazi, D.; Scholl, M.; Song, F.; Echegoyen, L.; Accorsi, G.; Armaroli, N.; Diederich, F. *Angew. Chem.* **2003,** *115,* 5116–5120. doi:10.1002/ange.200352265
40. Guggisberg, M.; Bammerlin, M.; Loppacher, C.; Pfeiffer, O.; Abdurixit, A.; Barwich, V.; Bennewitz, R.; Baratoff, A.; Meyer, E.; Güntherodt, H.-J. *Phys. Rev. B* **2000,** *61,* 11151–11155. doi:10.1103/PhysRevB.61.11151
41. Barth, C.; Henry, C. R. *Phys. Rev. Lett.* **2007,** *98,* 136804. doi:10.1103/PhysRevLett.98.136804
42. Barth, C.; Henry, C. R. *Nanotechnology* **2006,** *17,* S155–S161. doi:10.1088/0957-4484/17/7/S09
43. Bocquet, F.; Nony, L.; Loppacher, C.; Glatzel, T. *Phys. Rev. B* **2008,** *78,* 035410. doi:10.1103/PhysRevB.78.035410
44. Glatzel, T.; Zimmerli, L.; Koch, S.; Kawai, S.; Meyer, E. *Appl. Phys. Lett.* **2009,** *94,* 063303. doi:10.1063/1.3080614
45. Glatzel, T.; Zimmerli, L.; Kawai, S.; Meyer, E.; Fendt, L.-A.; Diederich, F. *Beilstein J. Nanotechnol.* **2011,** *2,* 34–39. doi:10.3762/bjnano.2.4
46. Kawai, S.; Kitamura, S.-i.; Kobayashi, D.; Meguro, S.; Kawakatsu, H. *Appl. Phys. Lett.* **2005,** *86,* 193107. doi:10.1063/1.1923200
47. Kolodziej, J. J.; Such, B.; Czuba, P.; Krok, F.; Piatkowski, P.; Struski, P.; Szymonski, M.; Bennewitz, R.; Schär, S.; Meyer, E. *Surf. Sci.* **2001,** *482–485,* 903–909. doi:10.1016/S0039-6028(01)00936-0
48. Howald, L.; Meyer, E.; Lüthi, R.; Haefke, H.; Overney, R.; Rudin, H.; Güntherodt, H.-J. *Appl. Phys. Lett.* **1993,** *63,* 117–119. doi:10.1063/1.109732
49. Kebarle, P.; Tang, L. *Anal. Chem.* **1993,** *65,* 972A–986A. doi:10.1021/ac00070a001
50. Fenn, J. B. *J. Am. Soc. Mass Spectrom.* **1993,** *4,* 524–535. doi:10.1016/1044-0305(93)85014-O
51. Gaskell, S. J. *J. Mass Spectrom.* **1997,** *32,* 677–688. doi:10.1002/(SICI)1096-9888(199707)32:7<677::AID-JMS536>3.0.CO;2-G
52. Horcas, I.; Fernández, R.; Gómez-Rodríguez, J. M.; Colchero, J.; Gómez-Herrero, J.; Baro, A. M. *Rev. Sci. Instrum.* **2007,** *78,* 013705. doi:10.1063/1.2432410

License and Terms